Lymph node imaging with magnetic resonance, positron emission tomography and fluorescence techniques

A thesis submitted in fulfilment of the requirements for the degree of Doctor of Philosophy

Giovanni Mandarano

B. App. Sci. (Medical Radiations), Grad. Dip. (Business Administration),

Grad. Cert. (Magnetic Resonance Imaging), Grad. Cert. (Higher Education)

School of Medical Sciences

College of Science Engineering and Health

RMIT University

June, 2015

Declaration

I certify that except where due acknowledgement has been made, the work is that of the author alone; the work has not been submitted previously, in whole or in part, to qualify for any other academic award; the content of the thesis is the result of work which has been carried out since the official commencement date of the approved research program; any editorial work, paid or unpaid, carried out by a third party is acknowledged; and, ethics procedures and guidelines have been followed.

Giovanni Mandarano

June, 2015

Acknowledgements

There are many I wish, and need, to thank. The work presented in this thesis borrows from many facets of the physical sciences and medical sciences, including – nuclear physics (NMR) and clinical MRI; the chemistry of iron oxide nanoparticle production and conjugation to FITC, R-PE and also DTPA anhydride; cell biology and flow cytometry; *in vivo* and *in vitro* experimental processes; and radiolabelling, radiochemistry and PET imaging. Primarily, these could not have been possible without the supervision and guidance of my PhD research supervisors, Dr Dodie Pouniotis, Mr Peter Eu and Professor Owen Woodman.

From RMIT University, I also wish to thank and acknowledge the Discipline of Applied Chemistry at RMIT University, specifically Dr Jos Campbell and Associate Professor Vipul Bansal in relation to the synthesis of iron oxide nanoparticles; from the School of Health Sciences I thank Professor Stephen Robinson for the Vascular Perfusion Fixation process with mice; from the Cancer and Tissue Repair Group (CTRG) Laboratory, I would like to thank Associate Professor Ian Darby for his advice with respect to H&E staining and also microscopy imaging; from the Discipline of Laboratory Medicine, I need to thank Associate Professor Janine Danks for her advice on Perls Prussian blue and PAS staining (and also for teaching me about the need for having a positive control tissue sample), also from Laboratory Medicine, a special thank you to Mr Robert Brown for his valuable technical advice when preparing wax blocks, using the microtome and preparing microscope slides; and from the RMIT Microscopy and Microanalysis Facility (RMMF) I would like to thank Mr Phil Francis, Mr Peter Rummel and Dr Matthew Field for their support and expert advice with TEM and SEM. My understanding of MTS assays and their graphing could not be complete without the

input of Associate Professor Terry Piva, Dr Bryce Feltis and fellow PhD candidate, Mr Griffin D'Costa.

From Peter MacCallum Cancer Centre, I wish to thank Dr Carleen Cullinane (Rebecca and Susan), Noelene Bergen (T2 weighted imaging for iron oxide nanoparticle samples at 3T), Dr Jacki Doughton, Dr Andrew Mallia, Dr Michael Hoffman and Professor Rod Hicks for their advice and support with experiments, MRI and PET imaging performed there.

From the Austin Hospital, I wish to thank Ms Emma Hornsey for MRI imaging at 1.5T field strength and from Western Health, Ms Jennifer Montgomerie for MRI imaging at 3T to test for T1 weighted imaging possibilities with iron oxide nanoparticles.

I would also like to thank the Australian Institute of Radiography (AIR), as I was a recipient of the AIR Research Scholarship and aspects of this research was made possible with the funding associated with this research award.

Most importantly, I must thank my family for their support and patience throughout this journey, as this would not have been possible otherwise. They have been very forgiving with the many late evenings and weekends I spent in the university laboratories, the many late evenings analysing data and writing and the very early start to days involving certain experimental processes.

Finally, I must pay a special acknowledgement to my mother who helped me with my primary school work when I was struggling; and from this early age had taught me the importance of learning. This foundation has served me well. Thank you.

Table of Contents

List of Abbreviations

^{111}In	Indium 111 (a radio-isotope of indium, with a half-life of 2.8 days)
^{111}In-oxine	Indium 111 Oxyquinolone (a diagnostic radiopharmaceutical used to radio-label autologous leukocytes
^{125}Iodine	Iodine 125 (a radio-isotope of iodine, with a half-life of 59.4 days)
^{18}F	Fluorine 18 (a radio-isotope fluorine, with a half-life of 109 minutes)
^{18}F-FDG	Fluorodeoxyglucose
^{18}F-FECH	Fluoroethylcholine
3D	Three dimension(al)
7AAD	7-Aminoactinomycin D
^{64}Cu	Copper 64 (a radio-isotope of copper, with a half-life of 12.7 hours)
^{67}Ga	Gallium 67 (a radio-isotope of gallium, with a half-life of 3.3 days)
^{68}Ga	Gallium 68 (a radio-isotope of gallium, with a half-life of 67.7 minutes)
^{68}Ge	Germanium 68 (a radio-isotope of germanium, with a half-life of 270.95 days)
^{89}Zr	Zirconium 89 (a radio-isotope of zirconium, with a half-life of 78.4 hours)
^{99m}Tc	Technetium 99m (where m is the abbreviation for metastable)
A549	Human alveolar cancer cells (adenocarcinoma of the alveolar basal epithelial cells)
AAS	Atomic absorption spectrometre

AlbG	Albumin globulin
AlkP	Alkaline phosphatase
ALT	Alanine aminotransferase
Amy	Amylase
ANOVA	Analysis of variance
APC-Cy	Allophycocyanin (APC) – Cyanine (Cy)
apo E-KO	Apolipoprotein E Knockout mice
ASL	Arterial spin labelling
AST	Arterial spin tagging
b-value	Describes effect of gradients on diffusion weighted images; increasing the b-value increases the diffusion weighting.
B_1	Radiofrequency field strength; externally applied magnetic field
BiliT	Bilirubin total or total bilirubin
BM-DC	Bone marrow derived dendritic cell
BM-DCs	Bone marrow derived dendritic cells
B_o	Main magnetic field strength
BSA/PBS	Bovine seum albumin / Phosphate buffered saline
C57BL/6	Mouse used for experiments, strain C57 black mouse, type 6
CBA	Cytometric bead array
CCR	Chemokine receptor

CD	Cluster of differentiation
cDC	Conventional dendritic cell
cDCs	Conventional dendritic cells
CE certified	Confomité Européenne (conforming to European definition of minimal risk to the public)
CIN	Contrast induced nephropathy
cm	Centimetre
cMRI	Cellular magnetic resonance imaging
CNR	Contrast to noise ratio
CNS	Central nervous system
CO_2	Carbon dioxide
COR	Coronal
CreaC	Creatinine clearance (also alternative nomenclature for estimated glomerular filtration rate, eGFR)
CT	Computed Tomography
Cy5.5	Cyanine 5.5
Cy7	Cyanine 7
DC	Dendritic cell
DCs	Dendritic cells
DCi	Dendritic cell immunotherapy

Dextran T10	Dextran with a molecular weight of 10,000 daltons
DICOM	Digital imaging and communications in medicine
DMSA	Dimercaptosuccinic acid
DNA	Deoxyribonucleic acid
DPX	Distyrene (a polystyrene), plasticiser (tricresyl phosphate) and xylene
DTPA	Diethylene triamine pentaacetic acid (also known as pentetic acid)
EB	Evans blue
eGFR	Estimated glomerular filtration rate
EDS	Energy dispersive spectroscopy
EMEA	European Medicines Evaluation Agency
EMT-6	Murine breast cancer cells (subcutaneous mammary tumours)
emu/g	electromagnetic unit per gram (unit for mass magnetisation)
EPPT1	A synthetic peptide
ETL	Echo train length
FACS	Fluorescence activated cell sorting
FBS	Fetal bovine serum
FcR	Constant fragment receptor
FDA	Food and Drug Administration
FDG	Flurodeoxyglucose

FESEM	Field emission scanning electron microscopy
FITC	Fluorescein Isothiocyanate
FID	Free induction decay
Flt3	FMS-like tyrosine kinase 3 (also known as CD135)
FMS	McDonough feline sarcoma viral (v-fms) oncogene homolog; also known as colony stimulating dactor 1 receptor (CSF1R)
g	Gram
GA	General anaesthesia
GE	Gradient echo
GFR	Glomerular filtration rate
GGT	Gamma-glutamyl transferase
g/L	grams per litre
GM-CSF	Granulocyte-Macrophage Colony Stimulating Factor
GTV	Gross tumour volume
HeLa	Human cervical carcinoma cell line
HEPES	Hydroxyethyl-piperazineethane-sulfonic acid
HER2	Human Epidermal Growth Factor Receptor 2
HEV	High endothelial venules
Hi-Myc	High (Hi) expression of a regulator gene (Myc) that encodes transcription factors (proteins) for cell cycle, apoptosis and cell transformation.

HLA-DR	Human leukocyte (lymphocyte) antigen – D related
hMSC	human mesenchymal stem cell
hMSC	human mesenchymal stem cells
hr	hour
iDC	Immature dendritic cell
iDCs	Immature dendritic cells
IFN-α	Interferon-alpha
IFN-β	Interferon-beta
IgG	Immunoglobulin G
IHC	Immunohistochemical staining
IL-4	Interleukin-4
IONP	Iron Oxide Nanoparticle
IONPs	Iron Oxide Nanoparticles
K_2EDTA	Potassium ethylene diamine tetraacetic acid
KB	Human cane cell line derived from epilthelial carcinoma of the nasopharynx
kD	KiloDalton
keV	Kiloelectronvolt
kg	Kilogram
kv	Kilovolts

LN	Lymph node
LNs	Lymph nodes
M	Molar concentration
mA	Milliampere
MBq	Mega Becquerel
MCF-7	Human breast cancer cell line, named after the Michigan Cancer Foundation, tumourigenic variety.
MCF-10A	Human breast cancer cell line, named after the Michigan Cancer Foundation, nontumourigenic variety.
MCP-1	Monocyte chemoattractant (or chemotactic) protein-1
MFI	Mean fluorescence intensity
MHC	Major histocompatibility complex
mDC	Myeloid type dendritic cell
mDCs	Myeloid type dendritic cells
MDCT	Multi-detector computed tomography
MFI	Mean fluorescence intensity
mg	milligrams
MHC class II	Major histocompatibility complex class II molecule
MHz	Mega Hertz
ml	Millilitre

mmol/L	Millimole per litre
MMP-9	Matrix metalloproteinase 9
Mo-DC	Monocyte derived dendritic cell
Mo-DCs	Monocyte derived dendritic cells
MR	Magnetic resonance
MRA	Magnetic resonance angiography
MRI	Magnetic Resonance Imaging
ms	millisecond
MTS	3-(4,5-dimethylthiazol-2-yl)-5-(3-carboxymethoxyphenyl)-2-(4-sulfophenyl)-2H-tetrazolium
MUC-1	A high molecular weight protein containing glycoconjugates
mV	milliVolt
µg	micrograms
µl	microlitre
µmol/L	micromole per litre
N1	A solution of 80 % acetone and 0.15 Molar concentration of hydrochloric acid in MilliQ water
N2	A solution of 97.56 % acetone and 0.05 Molar concentration of hydrochloric acid in MilliQ water).
NBF	Neutral buffered formalin

NBIA	Neurodegeneration with brain iron accumulation
ng	nanograms
NK cells	Natural killer cells
NIR	Near infra-red
NIR830	Near infra-red, requiring an absorption wavelength of 830 nanometres
nm	Nanometre
NMR	Nuclear magnetic resonance
NMV	Net magnetic vector
NSF	Nephrogenic Systemic Fibrosis
PBMC	Peripheral blood mononuclear cell
PBMCs	Peripheral blood mononuclear cells
pDC	Plasmacytoid type dendritic cell
PE-Cy	Phycoerytherin-Cyanine
PEG	polyethylene glycol
PEGlygated	PEG attached or boded to another molecule (such as a drug or protein)
Pen/Strep	Penicillin/Streptomycin
PET	Positron Emission Tomography
PET/CT	A scanner or imaging device that combines PET and CT
PET/MRI	A scanner or imaging device that combines PET and MRI

PFA	Paraformaldehyde
pg	Picogram
pH	The concentration or activity of hydrogen ions in a solution
PSMA	Prostate specific membrane antigen
R-PE	R-Phycoerytherin
R_1	Longitudinal relaxation rate (the reciprocal of the T_1 relaxation time)
R_2	Transverse relaxation rate (equals the reciprocal of the T_2 relaxation time)
R^2	Correlation co-efficient
RANZCR	Royal Australasian and New Zealand College of Radiologists
RBC	Red blood cell
RBCs	Red blood cells
rcf	relative centrifugal force
RES	Reticuloendothelial system
rf	Radiofrequency
rh	Recombinant human
rm	Recombinant murine
ROI	Region of interest
ROS	Reactive oxygen species
rpm	Revolutions per minute

RPMI	Roswell Park Memorial Hospital (RPMI-1640 mammalian cell media)
SA PET	Small Animal Positron Emission Tomography scanner
SE	Spin echo
SEM	Scanning electron microscope
SLN	Sentinel lymph node
SNR	Signal to noise ratio
SPECT	Single Photon Emission Computed Tomography
SPECT/CT	A scanner or imaging device that combines SPECT and CT
SPION	Superparamagnetic iron oxide nanoparticle
T10	Dextran with a molecular weight of 10,000 daltons
T_1	Longitudinal relaxation time
T_2	Transverse relaxation time
T	Tesla
TE	Time to echo (or echo time)
TF	Turbo factor
TGA	Therapeutics goods administration
TI	Time from inversion
TLC	Thin layer chromatography
TNFα	Tumour Necrosis Factor – Alpha

TP	Total protein
TR	Repetition time
U/L	Units per litre
USPION	Ultra small superparamagnetic iron oxide nanoparticle
VPF	Vascular perfusion fixation
w/v	Weight per volume
XRD	X-ray diffraction

List of Figures

List of Tables

List of Equations

Abstract

The knowledge that unbound gadolinium was responsible for NSF highlighted the need for alternative and safer imaging agents for MRI applications. Nanoparticles (used in conjunction with MRI) were identified as offering the potential and promise, to be safer across a multitude of applications; some dedicated for the investigation of specific disease processes. In particular, iron oxide nanoparticles have been considered as offering the greatest possibility as an MRI contrast (imaging) agent in both the research and clinical arenas.

Advantages offered by T10 dextran coated iron oxide nanoparticles include human biocompatibility with a safe and known excretion pathway. The dextran coating can be functionalised, thus providing opportunities for creative compounds to be created. For example, experimental work contributing to this thesis has resulted in T10 dextran coated iron oxide nanoparticles being radiolabelled with ^{68}Ga – and this is being presented for consideration as a potential imaging agent for PET/MRI; that is, ^{68}Ga providing an imaging agent effect on PET imaging while the iron oxide component provides simultaneous imaging contrast with MRI. ^{68}Ga itself provides an advantage over ^{99m}Tc (the most commonly used PET imaging agent); it has an improved imaging sensitivity over ^{99m}Tc and is less costly to generate, requiring ^{68}Ge (a radio-isotope of germainium) and a gallium generator. The clinical benefit to developing iron oxide nanoparticles radio-labelled with ^{68}Ga is also to improve the imaging of lymph nodes in oncology patients (as well as a PET/MRI contrast agent). Also presented here are the PET imaging findings, identifying the prostate draining lymph nodes, from four prostate cancer patients having had these nanoparticle preparations directly injected into their prostate glands.

Iron oxide nanoparticles can also be loaded into immune cells, *in vitro*; for this thesis, murine dendritic cells (bone marrow derived) and human dendritic cells (monocyte derived) were used, as dendritic cells are known to migrate to lymph nodes.

The combination of iron oxide nanoparticles radiolabelled with ^{68}Ga, and *in vitro* cell loading, offer the potential to re-visit cellular MRI to determine if imaging advances can be made in this area.

To support these achievements and claims, this thesis includes *in vitro* murine dendritic cell and *in vitro* human dendritic cell studies and also *in vivo* murine and *in vivo* human imaging studies.

Chapter 1 provides a review of the literature, identifying; the advantages of iron oxide nanoparticles over the limitations of gadolinium based contrast agents; their relevance to MRI and also their capabilities of being internalised by certain cells for targeting imaging applications. The overall aims of the thesis are presented.

Chapter 2 explains in detail the materials used, the methods employed and the physical and chemical processes that underpin all of the *in vitro* and *in vivo* experiments. The processes used draw upon knowledge from a range of disciplines, including cell biology, immunology, chemistry, physics, medical imaging, nuclear medicine and radiopharmaceuticals. This chapter describes how the iron oxide nanoparticles were prepared and the radiolabelling process used. The functionalised method used for the T10 dextran coating is explained, thus providing attachment sites for either ^{68}Ga or fluorescent markers such as FITC or R-PE for *in vitro* (murine and human) and *in vivo* (murine) experiments. Also described are the *in vitro* cellular (murine and human) experimental process with dendritic cells and iron oxide nanoparticles, investigating dose dependent and time dependent uptake.

Chapter 3 provides an analysis of the physical characteristics of the laboratory produced T10 dextran coated iron oxide nanoparticles (using TEM and SEM) and an important assessment of how these nanoparticles behaved in a magnetic environment, namely at 1.5T and 3.0T clinical MRI environment; calculating and graphing the R_2 and T_2 relaxivity rate values of nanoparticle concentration at a specific TE value and magnetic field strength. The methodology of radiolabelling these nanoparticles with ^{68}Ga is described and the results of TLC are provided, demonstrating the levels of bound and unbound ^{68}Ga. Any effects T10 dextran coated iron oxide nanoparticles could cause on cell proliferation was assessed with PBMC using the MTS assay technique and compared with the effect that Dotarem® (safest gadolinium based contrast agent) may have on these same cells.

Chapter 4 investigates the characterisation of nanoparticle uptake by murine bone marrow derived dendritic cells (GM-CSF and Flt3) *in vitro,* with dose (concentration) dependent and time dependent uptake studies. These same BM-DCs were observed for apoptotic effects, *in vitro,* using various nanoparticle concentrations over a 24 hour incubation period. A murine CBA kit was used to also ascertain any inflammatory response in these BM-DCs to the presence of nanoparticles; assessed using the supernatant from *in vitro* experiments

Chapter 5 reports on the characterisation of nanoparticle uptake by human monocyte derived DCs, *in vitro.* Dose (concentration) dependent and time dependent uptake in CD14+ and CD11+ cells were identified. *In vitro* supernatant assessment for an inflammatory response using a human CBA kit was used. Dose dependent uptake, *in vitro,* was also quantified in other cells that play varying roles in an immune response; namely PBMC, lymphocytes, granulocytes/monocytes.

Chapter 6 examines *in vivo* applications of nanoparticle preparations; murine and human. Lymphatic drainage to the popliteal and inguinal lymph nodes in C57/BL6 female mice were assessed using flow cytometry; following local subcutaneous injection of T10 dextran coated

iron oxide nanoparticles tagged with FITC. To observe any systemic effects of these nanoparticles in these mice, biochemical analysis of blood serum was conducted and histopathological assessment performed, using H&E and Perls Prussian Blue, of the heart, lungs, liver, spleen and kidneys and PAS staining of the kidneys (to observe the basement membrane). Following footpad injections of T10 dextran coated IONPs tagged with FITC and radiolabelled with ^{68}Ga, separate PET and MRI imaging of mice was conducted and on both imaging modalities, image contrast effects due to ^{68}Ga (PET) and iron oxide nanoparticles (MRI) were identified. Most importantly, PET imaging results from patients (positive for prostate cancer) undergoing insertion of gold seeds (for later radiotherapy treatment) having T10 dextran coated IONPs radiolabelled with ^{68}Ga demonstrated observed drainage to lymph nodes with the PET component of a PET/CT scanner.

1.0 Chapter 1 – Introduction to MRI and nanoparticles

Ever since MRI emerged as a clinical utility in the mid 1980's, it has continued to be exploited in so many ways, creatively, to encounter new clinical frontiers and research applications. What was new and experimental even ten years ago, is now mainstream and common place. MRI has continued to evolve to meet emerging challenges and has persistently proven its imaging flexibility in novel approaches to scanning, data collection and image reconstruction techniques. In Australia, from the mid 1990's, MRI started to become a mainstream imaging modality in radiology departments. This also co-incided with the emergence of a new era of medicine; that of patient tailored treatment and therapies.

MRI scanning often involves the use of contrast media to improve diagnostic capabilities. The most commonly used agents are based upon a gadolinium chelation, however, alternatives do exist. Specifically relevant to this thesis, iron oxide nanoparticles have been explored as one alternative – not only as an imaging agent for MRI. Iron oxide nanoparticles, coated with dextran, can provide avenues beyond standard MRI imaging. These include radiolabelling with ^{68}Ga as a potential PET/MRI dual modality or bimodal contrast agent. Such a radiolabelled nanoparticle could be used to perform an MRI imaging procedure analogous to lymphoscintigraphy; thus providing a non-ionising radiation alternative with superior spatial resolution. This thesis will also report that these specific iron oxide nanoparticles with a dextran surface layer, are well tolerated by MD-DC; thus opening up further imaging possibilities which include targeted imaging.

1.1 Magnetic resonance imaging

A typical MRI scanner is comprised of a cylindrical magnet and the most common field strengths used currently are either 1.5 T or 3.0 T[1]. Each cylindrical magnet has a bore of approximately 60 cm wide and 2.0 m long, for a patient to be positioned within. This magnet is surrounded by gradients coils or bands. These gradients are immersed in a cryogen bath (filled with liquid helium) to reduce electrical impedance, permitting the gradients to carry powerful electrical currents to perform functions such as delivering rf energy to the required imaging volume, slice selection (axial, coronal, sagittal or oblique) and the encoding of the phase and frequency of the emitted rf energy from the imaging volume[1-3]. The rf energy that is delivered into the imaging volume has a specific frequency and wavelength to resonate the hydrogen nuclei, found in abundance in the human body, in the form of water, fat, proteins and carbohydrates. The MRI scanner also needs to fill k-space creatively so that imaging times can be kept to a minimum, while maintaining acceptable imaging quality with spatial and contrast resolution appropriate to the anatomy and pathology located within the imaging volume – all this is co-ordinated with pulse sequences[3, 4].

A summary of the fundamental physics of Nuclear Magnetic Resonance (NMR) now follows. There are three known types of motion present with respect to the atom. These are; the motion of electrons spinning about their axis; the motion of electrons orbiting the atom's nucleus; and the nucleus itself spinning about its own axis[3-5]. The physics and imaging principles of MRI depend upon this third motion – the motion of certain nuclei spinning about their own axis and present within biological tissue. Such nuclei are referred to as being MR active nuclei or NMR nuclei[2, 3, 5]. Only nuclei having an odd mass number are NMR nuclei;

where the number of neutrons within the atomic nucleus is greater or lesser than the number of protons; thus, such atoms have a net charge.

Therefore, the motion of the nucleus spinning about its own axis, results in a net spin or angular momentum, when compared with the motion of the electrons[3, 6]. Faraday's law of electromagnetic induction associates the three forces of charge, motion and magnetism; and clearly defines that when any two of these are present, the third is automatically induced[1-3]. Hence, MRI active nuclei, possessing net charge and also (spinning) motion; will have magnetism referred to as a magnetic moment and this magnetic moment allows such nuclei to align themselves with an applied magnetic field[1, 3, 6]. In the clinical setting, this occurs with hydrogen nuclei aligning themselves with the main magnetic field of the MRI scanner. Hydrogen nuclei have an odd mass number of one, and are abundant in biological tissue.

Ordinarily, in biological tissue, hydrogen nuclei are randomly oriented. When placed in an MRI scanner, or a strong external magnetic field is applied to the biological tissue, the net population of the hydrogen nuclei are aligned with the direction of the applied magnetic field[3, 6]. It is the magnetic moments of the hydrogen nuclei that actually align parallel to the applied magnetic field[1, 2] and this net alignment results in the net magnetic vector (NMV) and is the starting point for the MRI imaging signal[3, 4]. Any pulse sequence used in MRI imaging, always firstly interacts with the NMV. The externally applied magnetic field is denoted by B_o on diagrams and in equations[2, 3].

As each hydrogen nuclei has its own angular momentum and the externally present main magnetic field, $B_{o,}$ induces a further spin on the magnetic moment of the hydrogen nuclei. This further spin is termed precession[1, 2, 4, 5] and results in the magnetic moment of hydrogen nuclei to form a circular path[2, 3] around, or about, the direction of $B_{o.}$ The precessional frequency is the speed of the magnetic moment following its precessional path about Bo.

The Larmor equation[1-6] is used to calculate the precessional frequency. The Larmor equation is stated as:

$$\omega 0 = Bo \times \lambda \qquad \text{Equation 1.1}$$

where: ω_0 is the precessional frequency

B_o is the main magnetic field strength

λ is the gyromagnetic ratio

The gyromagnetic ratio is specific for a MR active nuclei and defines the relationship between the nuclei's angular momentum and the magnetic moment[1, 5]. The gyromagnetic ratio of hydrogen nuclei is 42.57 MHz/T [2, 4]. Therefore, in a standard 1.5 T (value of B_o) MRI scanner, the precessional frequency, ω_0, of hydrogen nuclei is 63.86 MHz. This then means that for the hydrogen nuclei in the NMV, to be incorporated into an imaging pulse sequence, the rf energy from either a Gradient Echo or Spin Echo pulse sequence that is sent into the imaging volume, would need to be transmitted with a an equivalent frequency in order to cause resonance of these nuclei. Graphically, B_o, is represented as being in the longitudinal plane[1-3].

The duration of the transmitted rf energy determines the degree of tip or flip of the NMV from the longitudinal axis[1, 3, 4]. A Spin Echo pulse sequence always commences with the NMV being tipped or flipped exactly 90 degrees from the longitudinal plane to the transverse plane; whereas; a Gradient Echo pulse sequence commences with an rf energy pulse that can tip or flip the NMV 90 degrees or less (commonly, less than 90 degrees) from the longitudinal plane[1-5].

Regardless of whether the initial transmitted rf energy pulse results in a flip angle of 90 degrees or less, and also regardless if this initial rf energy pulse was delivered by a Spin Echo or Gradient Echo pulse sequence; when the rf energy pulse is switched off, the NMV (comprised of the net magnetic moments of the net hydrogen nuclei), effected by the main magnetic field, $B_{o,}$ commences to re-align itself with the main magnetic field, B_o [1-6]. For this to occur, the hydrogen nuclei need to release the rf energy they have received from the transmitted rf pulse; in a process called relaxation[1-3, 5]. As this relaxation process occurs, the magnetisation in the longitudinal increases and is referred to as recovery, or longitudinal recovery or T_1 recovery[1-3]. Simultaneously, the magnetisation in the transverse plane decreases and is referred to as decay or transverse decay or T_2 decay[1-3]. Longitudinal recovery and transverse decay are said to take place independent of each other and this independence is due to inhomogeneities or non-uniformities in the magnetic field, T_2* (pronounced as "T_2 star")[1, 2, 5, 6]. As transverse decay takes place, that is, the transverse magnetisation is reduced in magnitude, so too is the signal (induced voltage) in the signal receiver coil. The detection of this signal decaying is the Free Induction Decay (FID)[1-6]. The echoes generated by this FID is what is measured in MRI imaging.

Longitudinal recovery, or T1 recovery, results from nuclei transferring their rf energy to their immediate environment lattice and can thus also be referred to as spin-lattice relaxation[1-3, 5]. The nuclei in the surrounding lattice absorb this rf energy and their magnetic moments recover to align with the longitudinal plane, re-forming the NMV. This recovery rate is an exponential process[1, 3, 5]. The T_1 relaxation time, is the recovery time constant, which is defined as the time taken for 63 %[1-6] of the longitudinal magnetisation in biological tissue to recover.

Transverse decay, or T_2 decay, results from the magnetic fields of adjacent nuclei interacting with one another and thus, termed spin-spin relaxation[1-3, 5]. The decay or loss in transverse

magnetisation not only is reduced in magnitude, but also results in a loss of coherence of nuclei; as magnetic fields of hydrogen nuclei spins within water and within fat, for example, with interact with each other differently, even though together, they comprised the NMV (along with other biological tissue). T_2 decay is also an exponential process[1, 3, 5]. The T_2 relaxation time of a specific biological tissue, is also a time constant (of decay) and is defined as the time taken for 63 % reduction of the transverse magnetisation and only 37 % magnitude of transverse magnetisation remaining[1-6]. Only the coherent component of magnetisation in the transvers plane is capable of inducing a voltage signal in the receiver coil, however[1-3].

1.1.1 Pulse sequences

What exactly is an MRI pulse sequence? It is effectively a set of instructions, carefully designed, to co-ordinate equipment involved with the generation, delivery, detection and reconstruction of rf energy signals. Crucially, pulse sequences contain instructions for carefully controlling the duration and timing of rf pulses and gradient pulses.

There are two main types of pulse sequences; Gradient Echo and Spin Echo[1-4]. All clinically used pulsed sequences are based on these two types of pulse sequences, and from each of these, come further pulse sequences where the variations or modifications are designed for specific clinical applications and/or body regions; such as the 3D Time of Flight Gradient Echo[1, 2] pulse sequence to image the Circle of Willis.

Regardless of sequence type, all have timing values which can be modified to alter the image contrast or image weighting[1-3]. These timing values are the repetition time, or TR[1-4], which co-ordinates the application of rf energy into the imaging volume; and; the echo time, or TE[1-

[4)], which listens to, or detects and receives, the resonating rf energy signal from the imaging volume. Both TE and TR are measured in milliseconds.

The TR period is the time from one excitation rf pulse to the next[(1-6)]. This determines the amount of relaxation allowed to occur from one excitation rf pulse to the next and thus, the TR determines the amount of T_1 relaxation that has occurred during the pulse sequence[(1-3)]. The TE is the time from the application of the excitation rf pulse to the peak signal strength as detected by rf receiver coil[(1-6)]. This controls the amount of T_2 relaxation and therefore determines the level of T2 decay along the transverse plane is allowed to occur before the rf signal is read[(1-3)].

T_1 recovery and T_2 decay are intrinsic contrast parameters specific to a particular tissue and cannot be changed. At the MRI operating console, parameters that can be altered, and that can also alter resulting image contrast and appearances include TR, TE and flip angle. Depending on the variation in pulse sequences, additional parameters that can be manipulated include; Time from Inversion, TI; Echo Train Length, ETL (also known as Turbo Factor, TF) and b-values[(1)].

In biological tissue, hydrogen nuclei is abundant; due to their presence in fat and water. These two tissues will be used as examples to demonstrate T_1 weighted and T_2 weighted image contrast[(1-3)]. Firstly, before proceeding; an explanation of T_1 recovery and T_2 decay in fat tissue and likewise with water.

Fat or adipose or lipid molecules contain hydrogen bonded with oxygen and carbon. These are comparatively large molecules and are arranged very close together[(1, 2)]. Their molecular tumbling rate are considered to be slow[(3, 6)].

With water molecules, hydrogen is only bonded with oxygen. Water molecules are further apart and their molecular tumbling rate is regarded as fast (compared to fat molecules)[1-3, 6]. The way that hydrogen is arranged in water, results in it having a greater Larmor frequency compared to the arrangement of hydrogen in fat[1, 2].

Therefore, compared to hydrogen in water; the hydrogen in fat has a quicker longitudinal recovery (or T_1 recovery or spin-lattice relaxation or T_1 relaxation time) and its loss of transverse magnetisation (or T_2 decay or spin-spin relaxation or T_2 relaxation time) is more rapid[1-4, 6]. Due to these time differences, the arising MRI signal from water and fat will mean that they will appear different on the resulting MRI images.

The MRI operator's selection of specific TE and TR values, weights an image to demonstrate either mostly T_1 values and contrast mechanisms or alternatively, to have T_2 characteristics, dominate a resulting image.

1.1.2 T1 weighted imaging

The T_1 relaxation time of fat is shorter than the T1 relaxation time of water[1-4]. Once the rf pulse is switched off (after the NMV has been flipped from the longitudinal plane), the NMV begins to re-align itself with the longitudinal plane, B_o,[1-6] and the vector from each tissue (in this example we will only consider fat and water) will commence to de-phase or become incoherent from the transverse plane[2, 3]. The shorter T_1 relaxation time of fat will allow it (the fat vector) to re-align with the longitudinal plane, B_o, sooner than the water vector[1-3]. Thus, more of the fat signal has recovered (compared to water) and is ready to be excited, again. Following the expiration of the TR period (and this TR period will be less than the total relaxation times of the biological tissues being imaged), the pulse sequences commences

again, sending an rf excitation pulse into the biological tissue. Compared to water, as there is a greater vector from fat contributing to the NMV in the longitudinal plane; after the RF excitation pulse has flipped the NMV into the transverse plane, the recovery signal from fat will be greater (compared to water) and therefore contribute more to the FID[2-4]. The signal from fat will be higher compared with the signal from water and therefore fat will appear as a hyperintense signal on the resulting T_1 MRI image. The comparatively lower water vector and resulting signal, leads to water appearing hypo-intense in the same image.

As the TR duration of a pulse sequence determines the extent of vectors recovering to re-align in the longitudinal plane[1, 3]; to allow for T_1 weighted images to be created, the TR value needs to be of a short duration; thus not allowing the fat and water vectors to fully recover in their longitudinal plane and re-align with B_o[1-4]. A TR value longer than the T1 recover times of fat and water will mean that both tissues would fully recover their longitudinal megnetisations and when the next rf excitation energy pulse is applied, the MRI signal differences related to their T1 relaxation times cannot be demonstrated nor imaged[1, 2].

Overall therefore, the TR value of a pulse sequence provides control over the degree of T_1 weighting; and for T_1 weighted images to be generated, the TR must be short – shorter than the longitudinal recovery times of the biological tissues needing to be imaged[1-4].

1.1.3 T2 weighted imaging

The T_2 relaxation time of fat is also shorter than the T2 relaxation time of water[1-4]. As T_2 relaxation or decay, is indicative of T2 signal;[1, 2] this means that at the point in the pulse sequence when the FID is recorded, there will be a greater signal component from the water

vector[3, 4]. Hence, compared to fat, water will contribute a larger signal and appear relatively hyperintense on the resulting T_2 image[2, 3].

An image that has been generated containing T_2 influences, results from the contrast mechanisms being dependent on the T_2 relaxation times of fat and water, along with other biological tissue from the imaging volume. From a pulse sequence, the duration of the TE determines the degree of T_2 decay that is permitted to occur before the FID signal is identified and read[1-4]. To generate an image that is considered to be T_2 weighted, the TE value needs to be sufficiently long, allowing both fat and water to decay via their spin-spin lattice interactions[1-3]. If, however, the TE value is too short, and fat and water are unable to demonstrate sufficient T_2 decay, their T_2 signal characteristic differences will not be able to be detected and not imaged.

Overall therefore, the TE value of a pulse sequence provides control over the degree of T_2 weighting[1-4]; and for T_2 weighted images to be generated, the TE must be of sufficient duration – allowing T_2 decay in the transverse plane to be detected. This is designed to take advantage of fat having a short T_2 decay time and water having a longer T_2 decay time.

1.1.4 T2* weighted imaging

T_2* results from either inhomogeneities in the main magnetic field[1-6], or, from susceptibility effects within the imaging volume[1-3]; which, in effect, is a local magnetic field disturbance[1, 3]. Local susceptibility imaging effects, due to iron deposits in an imaging volume, can be seen in patients suffering from a number of health conditions; including; haemorrhagic stroke (iron rich components of blood products such as met-haemoglobin or haemosiderin)[1], neuroferritinopathy (iron in the basal ganglia)[7-9], genetic conditions such as

haemochromatosis (inherited iron overload disorder)[10-12], haemosiderosis (iron overloads in the RES organs)[13-15] and neurodegeneration with brain iron accumulation (NBIA)[16, 17]. These local susceptibility imaging effects can be used by radiologists and clinicians to narrow the differential diagnosis.

Whether due to main magnetic field inhomogeneities or from local susceptibility effects, T_2* arises from molecular interactions (spin-spin relaxation)[1-3]. The MRI active nuclei experiencing these field variations will precess at slightly different frequencies[1-4] because these spins are oriented at a slightly different angle[1] to the main magnetic field. This T_2* effect leads to a rapid loss in phase coherence and transverse magnetisation[1-4]. T_2* time is less than T_2 time[1-6] and is observed in the FID[1, 3]. Thus, the spins within the biological tissue being imaged experiencing such inhomogeneities will also experience different local magnetic fields[1, 3]. This, in turn, affect the relaxation of the spins after an rf pulse; speeding up the apparent spin-spin relaxation T_2* time[1]. Relative to the T_2 decay time of the same spins in a uniform magnetic field, the T_2* transverse magnetisation decay is quicker – but spin-lattice relaxation is not affected[1]. SE pulse sequence can correct for this effect by having 180 degree rephrasing rf pulses written into their pulse sequences; but GE pulse sequences cannot, as they use a gradient in an attempt to re-phase the magnetic moments[1-4]. The gradient used by GE pulse sequences is essentially a reversal of current direction in the coils (or gradients) surrounding the main magnet[1, 3]. This gradient cannot re-set any phase differences between the spins and thus cannot compensate for magnetic field inhomogeneities[1-3]. GE images therefore result from the apparent spin-spin relaxation time, T_2* time. For a given tissue, the T_2* time closely approximates its T_2 time; therefore, GE T_2* images can be similar in appearance to images generated with a SE T_2 pulse sequence[1, 3, 4].

It is also said that the T_2* is a reflection of the quality of the main magnet within the MRI scanner. As a magnet in the Tesla strength range required for clinical and research purposes

cannot be produced with a perfectly uniform magnetic field; T_2* therefore, are effects due to a non-uniform magnetic field[1, 3].

Specifically to iron oxide nanoparticles, the local susceptibility imaging effects can be exploited with MRI imaging to introduce obvious image contrast and characteristics. Iron oxide nanoparticles will induce local susceptibility effects and therefore T_2* weighted images should be used to best demonstrate their effects on MRI images[1, 2] or contribution to image contrast and diagnosis. There are two most likely ways this can be achieved. Firstly, cells can be removed from a patient, then loaded with iron oxide nanoparticles in safe medical laboratory conditions and then administered to the same patient[18-20]. Secondly, the iron oxide nanoparticles themselves can be directly administered to the patient[21]. In both instances, MRI can be used to track their progress or movement from injection site to their final destination (an organ or site of pathology).

1.1.5 Contrast media and MRI

Broadly defined, a contrast agent or medium is any substance that can be used together with an imaging technique to provide additional and useful information. Contrast media can be either exogenous or endogenous. Endogenous material which can be used include water molecules inherent within the blood stream when performing Arterial Spin Labelling (ASL) or Tagging (AST). Exogenous substances include the already well known paramagnetic gadolinium-based agents and now emerging from literature, we are noting an increasing experimental usage of superparamagnetic iron oxide nanoparticle.

When MRI first became a clinical reality, it was thought that no contrast media would ever be needed because of MRI's superior contrast and spatial (isotropic voxels) resolution compared

with other modalities[3]. It was soon realised that a contrast media was needed to improve the specificity of MRI[1].

In 1988 the first MRI-specific contrast media preparation was approved by the Food and Drug Administration (FDA) for intravascular administration in clinical use[22, 23]. This was needed to define a pattern of contrast enhancement so that a characteristic enhancement pattern of a particular disease process could be recognised and also to narrow the differential diagnosis. This contrast media preparation contained gadolinium as its base. There have always been some concerns in relation to this preparation. These include its expense (cost per millilitre and patents are strongly held and continually renewed) and its degradation with exposure to ambient light. The way that such gadolinium-based contrast media is chemically altered and eliminated by the body is not entirely understood[24]. For some time now, a condition known as "cross reactivity" has existed. It cannot be entirely explained, however, it is thought to result either from the chelated molecules or elements, or the chelated structure themselves[25]. Within the last decade or so, a more serious condition has been attributed to gadolinium-based preparations. This condition is referred to as nephrogenic systemic fibrosis (NSF) and can lead to eventual death. NSF is almost always seen in patients with reduced renal function (less than normal glomeruli filtration rate, GFR) and there have been a number of deaths recorded and attributed to NSF. In early 2008, the Royal Australian and New Zealand College of Radiologists (RANZCR) has recommended that all clinical centres offering gadolinium-based contrast media for MRI scanning examinations to establish a new policy concerning intravascular administration and, in particular, with respect to NSF and patients with impaired renal function[26]. Due to these trends, anecdotal reports suggest more caution and less reliance upon gadolinium-based contrast media even though no alternative currently exists in Australia. The current commercially available contrast media is gadolinium-based and also referred to as para- magnetic and only benefits T_1-weighted MR imaging. No mainstream commercially available contrast media for T_2-weighted imaging is currently

available in Australia. There are benefits attributed to contrast media if it can be prepared for T_2-weighted MR imaging[24]. Coincidently, an increasing trend is underway towards clinical MRI scanners with higher field strengths such as 3.0 Tesla. The main drivers are improved capital and running costs and increased signal-to-noise (SNR) ratio. However, at higher field strengths such as 3.0 Tesla, T_1 and T_2 relaxation times of human tissue are altered compared to 1.5 Tesla. Gadolinium-based contrast media results in shortening T_1 tissue relaxivity values and therefore only T_1 optimised sequences can be used (T_2 relaxivity values are not altered significantly for MR imaging practicality). It is proposed that contrast media preparations based on nanoparticles can overcome all of the abovementioned challenges related to MRI scanning while simultaneously addressing the current medical safety concerns[24, 27]. More specifically, iron oxide nanoparticles have the following attractive attributes:

- it can offer T_2-weighted imaging opportunities
- it has a well-recognised and understood pathway for breakdown and excretion from the human body
    - Degradation causes iron to enter plasma, where it is processed by the body
    - Risk of iron overload is minimal
    - Average dose of iron in contrast agent is comparable to iron contained in less than one unit of blood
- It provides "negative" enhancement

Depending on the physio-chemical property of the coating (surrounding the iron oxide nanoparticle), both generalised and specific contrast media can be created[27, 28]. The term "specific" means that contrast media preparations can be targeted to a particular organ within the body or a particular disease process. If this can be achieved, then it follows that not only can diagnostic imaging be successful, but also therapeutic drugs/medication can be tagged to

the preparation so that it can reach and work on the target tissue. At one point, it was estimated that 30 % to 40 % of MR examinations were performed with intravascular contrast media[25]. With the awareness of NSF, no hard data currently exists to determine if the use of intravascular contrast media has decreased or remains at the same level. The most commonly available intravenous contrast media contains gadolinium. A gadolinium ion has seven unpaired electrons in its outer shell[2] and is considered a paramagnetic substance because it has an overall positive effect on the local magnetic field[3]. In brief, when placed within a magnetic field, the negatively charged gadolinium ion demonstrates characteristics such as a magnetic moment, producing a large time-varying magnetic field in its vicinity, allowing rapid exchange of bulk water, altering the relaxation rates (both T_1 and T_2, or longitudinal and horizontal) of adjacent water protons[2, 3, 25]. Gadolinium is referred to as a T_1 enhancement contrast agent as it affects T_1 to a greater extent than it does T_2. The act of molecular tumbling and local magnetic field alterations occur near the Larmor frequency value. This leads to a reduction of the T_1 relaxation value of adjacent water protons, which in turn, leads to an increased signal strength on T_1 weighted images[2]. This is due to an increased rate of longitudinal magnetisation recovery[1, 25]. For acceptable biocompatibility, gadolinium is chelated to other molecules. This reduces any acute toxicity effects, and also allows the gadolinium-based agent to remain circulating within the body for a relatively longer period (than without chelation)[1] with an elimination half-life of between 1 hour to 2 hours[2, 3]. Currently available paramagnetic contrast agents are commonly administered intravenously. Its biodistribution is into the blood stream and then into the extra cellular space. It is therefore not taken up by any specific body organ, tissue type or pathologic lesion. Hence, gadolinium compounds are also regarded as non-specific contrast agents[3]. Enhancement patterns, however, are known to be characteristic of certain pathology groups. For example, a hyperintense circular rim with a hypointense centre may be representative of a cystic lesion.

1.1.5.1 Gadolinium and current concerns

Up until about ten or twelve years ago, gadolinium-based contrast agents had been regarded as having a relatively excellent safety record[29]. NSF was originally referred to as nephrogenic fibrosing dermopathy by Cowper et al. in 2000[30]. It was described as being scleromyxoedema-like cutaneous disorder and thought to only affect the skin or dermis. It was noted in patients undergoing renal dialysis[30, 31]. As additional cases became recorded and further understanding of the pathology grew, the currently used term of NSF has become accepted. This is due to the now recognised systemic nature of the pathology[32, 33]. Commonly, NSF commences with swelling at the distal aspects of the extremities. This may then resolve, however, leaving behind thick, firm plaques over the affected skin. In the majority of patients, initial skin lesions appear on the legs, then the arms and lastly on the trunk of the body. It has also been reported that the skin lesions are often symmetrical and bilateral. It may then progress to a point where the patient has significantly reduced range of motion of their extremities and joints[34]. In addition to the flexion and joint contractures accompanying extremity skin lesions[35, 36], fibrotic effects may also be widespread and penetrating; involving organs including the liver, lungs and heart, among others[36, 37]. Today, the only successful approach in treating NSF is to restore the normal renal function. This can only be achieved by renal transplant surgery[34, 36]. NSF is almost always seen in patients with less than normal renal function or patients requiring ongoing renal dialysis. Therefore, NSF may be a resulting consequence in patients with renal impairment because the contrast media excretion half-life is markedly increased[38]. This situation then permits disassociated or de-chelated gadolinium ions an increased circulation time. Some authors consider NSF to be an, "adverse reaction to gadolinium contrast agents in particular the less stable gadodiamide"[39]. Even though all gadolinium-based preparations carry a level of risk, there is published

evidence to suggest that some gadolimium-based contrast agents offer a greater risk than others in inducing NSF[39]. This variation in risk is linked to the overall molecular structure of the gadolinium-based contrast agent and in particular, its level of chemical stability within the human body[40]. Gadodiamide has been associated with the greatest incidence of induced NSF[39, 40]. On its own, gadolinium is highly toxic; and not only can it cause injury to the liver and spleen, but it can also inhibit secretions of certain enzymes and it can induce haematological ailments[40-42]. To minimise such toxic consequences, the gadolinium ion is chelated to other chemical elements and compounds[40]. This improves its biocompatibility. The molecule or atom that is bonded to the gadolinium can be referred to as a ligand. The gadolinium ion is chelated in either a linear or macrocyclic fashion and prepared as either ionic or non-ionic formulations[25, 40]. Published data reflect that the least stable preparations are non-ionic linear chelate formulations such as gadodiamide (Omniscan, GE healthcare, Chalfort, ST Giles, UK) and Gadoversetamide (OptiMark, Covidien, St Louis, USA). Gadodiamide has been reported to have a kinetic stability of 35 seconds; that is, at a pH of 1.0, half of the preparation will shed the linearly chelated material; thus leaving free gadolinium ions to search for other metals (body cations) to bind to within the body. These would include iron, copper, zinc and calcium. This process is referred to as transmetallation. Of the above body cations, zinc has the highest relative concentration (55- 125 micromole per litre) within the blood stream[40]. The most stable gadolinium-based preparation is the ionic, macrocyclic chelate formulation; namely, gadoterate. Public communications by the FDA in 2009 and 2011 (no later public notices or communications can be found), state that no cases of NSF linked to any macrocyclic formulation has been reported [40] or confirmed by the International Centre for Nephrogenic Fibrosing Dermopathy Research[43] in the USA. It is suggested that this is due to a macrocyclic structure providing a relatively superior protection of the gadolinium ion; that is, the gadolinium ion is caged by the chelating agent[25, 40, 44, 45]. Conversely, a linear chelate is referred to as being a flexible open chain and thus not

providing a strong bond to the gadolinium ion. Gadoterate is documented to have kinetic stability of greater than one month[40]. High et al. [29] obtained paraffin embedded tissue samples from the NSF registry (the International Centre for Nephrogenic Fibrosing Dermopathy Research). These tissue samples had histopathologic diagnosis of NSF. This research group demonstrated with energy dispersive spectroscopy (EDS), a device used to characterise chemical elements, that in four of seven patients, gadolinium was able to be identified and all detectable gadolinium particles were less than 1 micrometre in size. Further analysis with field emission scanning electron microscope (FESEM) demonstrated that in all of the positive tissue samples, gadolinium particles were present within the intracellular space and most probably located within, or adjacent to, the lysosome structures. Also noteworthy was an excessive amount of iron deposition within the tissue samples. While the exact cause of NSF has not been conclusively established[36, 37, 45-49] and precise pathologic pathways are yet to be determined[31], there is however, convincing evidence that gadolinium may be responsible somehow[48, 50]. The most probable theory is that de-chelation occurs[51], resulting in the release of free gadolinium ions, which in turn may or may not lead to transmetallation[52, 53].

1.2 What are Nanoparticles

Nanotechnology is the manufacture and manipulation of materials in the nanoscale range of 1 nm to 1,000 nm[54]. Nanoparticles are defined as particulate matter and being less than 100 nm in one of their dimension, they are most likely to be spherical, but can also be shaped as rods, cages or stars[55]. In broad terms, a colloidal system is comprised of a dispersing medium and a dispersed medium. Both of these media can be gas, liquid or solid. Solid

particles in a liquid are termed dispersions; a liquid medium in another liquid medium is referred to as emulsions; and solid particles in a gas are known as aerosols[55].

For biomedical applications, a nanoparticle often has at least two components[56-58]. The core material and a surface layer. A nanoparticle is often referred to by its core material. For example, an iron oxide nanoparticle with have an iron oxide core, however, its surface layer may be dextran, silica or another material. The core material provides the fundamental properties of the nanoparticle, while the surface layer can be designed to provide added benefits such as preventing agglomeration and also being capable of functionalisation to improve imaging capabilities or drug delivery or other intended benefits such as increased blood circulation time[59]. Another layer, known as a shell, can be incorporated between the core material and the surface layer.

Iron oxide, as a material for the nanoparticle core, demonstrates the required characteristics necessary for MRI imaging; as the iron oxide core behaves as a single magnetic domains (just like NMR active nuclei) in the presence of an external magnetic field.

Dextran, as the surface layer material provides the interface between the iron oxide core and its immediate environment[28]. Dextran acts as a physical barrier between the iron oxide and its surroundings, to protect and stabilise the core and prevent oxidation[24, 28]. Further, dextran is capable of being functionalised to allow it to be tagged with FITC; meaning that in addition to MRI imaging detail, further data can be obtained with FACS flow cytometry and also confocal microscopy can be performed.

1.3 Nanoparticles and imaging

In medical imaging, the development of nanoparticles has attracted a phenomenal amount of research, particularly for applications in molecular imaging. Nanoparticles can be tailored with unique characteristics providing them with capabilities to maximise imaging signals and increase image contrast for improved visualisation, detection and diagnosis[27, 60].

In the Nuclear Medicine field, nano-scale sulphur colloids were first popularised in the 1970's for imaging lymph nodes in lymphoscintigraphy by being radiolabelled with ^{99m}Technetium (^{99m}Tc)[61, 62].

For a brief period in the 1980's, some serious research was conducted with iron oxide nanoparticles as a possible patient administrable contrast agent in MRI scanning[63, 64]. The technological capabilities were not available at the time to reduce the nanoparticle size below 200nm. The ability for nanoparticles to improve MRI imaging flexibility was first noticed and reported in the late 1970s[65].

With the incorporation of nanoparticles, various imaging modalities have transitions from simply imaging anatomy and pathology towards more sophisticated capabilities to include cell tracking and targeted imaging; with improved sensitivity and specificity[27]. For example, with iron oxide nanoparticles less than 100 nm in diameter and having a surface layer capable of being conjugated to biomarkers; these two factors can facilitate cellular uptake while the superparamagnetic properties of the iron will allow the target site to be identified on an MRI image. Nanoparticles can potentially be incorporated with many conventional imaging modalities and techniques[66]. Some conventional imaging modalities, such as x-ray imaging, ultrasound and CT, on their own, lack dual benefits of high sensitivity and high spatial resolution needed for molecular imaging. The benefits of MRI include having high spatial resolution, does not use ionising radiation, provides multi-planar imaging capabilities and is

non-invasive. PET and SPECT imaging, both nuclear medicine modalities offer greater sensitivity to molecular processes but have significantly reduced spatial resolution capabilities (when compared to MRI). Hybrid imaging, such as PET/MRI, merges the benefits of both modalities and each modality overcomes the drawbacks of the other. A radio-labelled iron oxide nanoparticle, thus, provides the promise of one contrast agent serving the purposes of both imaging modalities.

There are a number of examples in the literature of innovative uses of various types of nanoparticles being used together with common imaging modalities of planar x-ray, CT and Ultrasound.

X-ray imaging has traditionally incorporated iodinated contrast media to improve conspicuity and sensitivity in images; however, iodine has been associated with severe adverse events; ranging from allergy-type responses, respiratory arrest, laryngeal oedema, cardiovascular responses and nephrotoxicity. These adverse events can also be attributed to large and repeated doses being necessary.

De La Vega et al[67] has explored alternatives to iodine by way of a review of the literature. Elements with high atomic numbers are required in order to exhibit high absorption of x-rays photons on the generated images. Nanoparticles synthesised from elements with atomic numbers greater than iodine have been reported to have superior imaging properties, longer blood circulation times and lower toxicity than the conventional iodine based contrast agents. A study performed by Hainfield *et al*[68] focussed on nanoparticles containing a gold core; as gold has an atomic number of 79 (iodine has an atomic number of 53) providing it (gold) with a higher mass x-ray absorption (or attenuation) co-efficient; 5.16 cm^2/g (at 100 keV) compared to iodine's 1.94 cm^2/g (at 100 keV). Using these figures, gold can provide 2.7 times greater imaging contrast compared to iodine (5.16 cm2/g ÷ 1.94 cm2/g = 2.7). To observe and asses the biodistribution and contrast enhancement, these same investigators

injected these gold nanoparticles into the tail vein of Balb/C mice containing EMT-6 subcutaneous mammary tumours. Their results showed that the gold nanoparticles allowed high contrast visualisation of angiogenic and hypervascularised areas pertaining to tumours for approximately one hour following peak opacification. The detailed imaging of the vasculature were also attributed to the size of the gold nanoparticles, being approximately 2 nm. The gold nanoparticles were then eliminated via the urinary system, as noted by the image enhancement of the kidneys and urinary bladder. Standard planar x-ray imaging was used to image mice in this study.

Chien *et al*[69] also used gold nanoparticles to assess tumour related micro-vasculature in tumour bearing mice; however, their aim was to measure the dimension of the smallest identifiable vessel. Their results were achieved using gold nanoparticles conjugated with heparin and were able to image *in vivo* blood vessels as small as 3-5 μm. They achieved this imaging with the use of synchrotron assisted microradiology imaging techniques.

Kobayashi *et al*[70] demonstrated that gold nanoparticles with a silica outer layer can be retained within a mouse for 6 hours and allowing imaging of internal organs (such as heart, liver and spleen). Kobayashi *et al* concluded that the 54.8 nm sized silica coated gold nanoparticles provided contrast enhancement greater than currently commercially available iodine based contrast media. This was assessed by CT imaging and observing the CT numbers or Hounsfield Units of the enhancing organs.

Cormode *et al*[71] successfully used gold nanoparticles coated with a high density lipoprotein to identify calcification and stenosis of atherosclerotic plaques via macrophage uptake. Apolipoprotein E knockout (apo E–KO) mice were used as the animal model for atherosclerosis. The imaging capabilities of the high density lipoprotein coated gold nanoparticles were compared with a commercially available iodine based contrast agent and also compared with calcium phosphate; in phantom studies. *In vivo*, multi-colour spectral CT

successfully imaged the gold nanoparticles being deposited in the aortas of the subject mice. Post mortem microscopy assessment of the aortas demonstrated that the nanoparticles were contained within the macrophages. These investigators concluded that such nanoparticles, together with spectral CT, can demonstrate atherosclerotic plaque composition due to uptake of these nanoparticles by macrophages.

Gold nanoparticles were also used by Lie *et al*[72] for *in vitro* and *in vivo* targeted CT imaging of the KB cancer cell line (human epilthelial carcinoma). Their nanoparticles were functionalised with folic acid, which allowed them to target the KB cancer cell line *in vitro* and *in vivo* with xenograft tumour bearing rats; via their over expressing folic acid receptors.

CT imaging and contrast enhancement assessment (CT number or Hounsfield Units) of the tumour *in vivo* was used to compared the contrast enhancement produced by these gold nanoparticles to that produced by a clinically available contrast agent. Identical concentrations of both contrast agents were used. Their results demonstrated that the gold nanoparticles functionalised with folic acid provided the tumour with greater enhancement or contrast, compared to that induced by the commercially available iodine based contrast agent. The greatest difference in image contrast was noted at 1 hour post administration.

Titanium dioxide nanoparticples have also been successfully used with ultrasound *in vitro* by Ninomiya et al[73] to perform sonodynamic cancer therapy. Such therapy is not dependent upon the thermal effects of oscilating or reverberating molecules due to the ultrasound frequency waves, but rather, based on sonochemical effects of low frequency ultrasound waves and sonosensitzer (cancer fighting drugs). The titanium dioxide nanoparticles are preferentially internalised and accumulated in cancerous tissue and low frequency ultrasound then used to activate the drug. It was discovered by these investigators (in an earlier study) that titanium dioxide, when activated with ultrasound, can act as a sonocatalyst; enhancing hydroxyl radical generation. The titanium oxide then produced reactive oxygen species

capable of killing cancerous cells. Prior to this, it was thought that titanium dioxide could only induce reactice oxygen species in the presence of ultraviolet irradiation. In their *in vitro* study, Ninomiya et al identified that 80 % of the human breast cancer cells (MCF-7) ingested the titanium oxide and one day following treatment with 1 MHz ultrasound, the cell viability of MCF-7 cells was at 68 %.

1.4 Iron Oxide Nanoparticles and MRI

The most common form of iron oxides used in nanoparticle preparations are magnetite (Fe_3O_4) and maghemite (γFe_2O_3)[74, 75], and research with these has intensified over the past decade. They are both insoluble in water and because of their size, these superparamagnetic substances only exhibit their magnetic properties when placed within a magnetic field[3, 18]. The hydrodynamic size of a nanoparticle preparation is the term used to describe its overall size, that is, the iron oxide core plus the coating plus any additional ligand attachments and the thin electric dipole layer of the solvent layer attached to the particle as it moves under the influence of brownian motion. If the overall hydrodynamic size is greater than 50 nm, then the preparation is referred to as a superparamagnetic iron oxide nanoparticle (SPION).

Iron oxide nanoparticle preparations are highly complex. There are numerous production methods which can be used to generate them. Each method can result in iron oxide nanoparticles having specific dimensions, as well as unique imaging and therapeutic characteristics. Each manufacturing method is undertaken in a strict controlled environment to ensure consistency of dimensions, characteristics and biostability.

The physiochemical properties of iron oxide nanoparticles are determined by the size of the iron oxide core, its overall charge and the zeta charges between coatings and the overall hydrodynamic size. With respect to magnetic resonance imaging, the above factors also play a fundamental role in determining their efficacy (or imaging efficacy), stability within the body's environment, biodistribution, opsonisation, metabolism, clearance from vascular system and then excretion from the body[56].

1.4.1 Nanoparticle coating

An understanding of the bonding and the geometry of the coating will help us appreciate the pharmokinetic pathways and biodistribution of contrast agents composed with iron oxide nanoparticles[18, 76-78]. From a chemical perspective, the iron oxide core is coated for four main reasons. Firstly, to prevent destabilisation; secondly, to prevent agglomeration (aggregation or sedimentation) as it will be a colloidal suspension; thirdly, it allows for the iron oxide nanoparticle formulation to be soluble in an aqueous solution or a biological medium; fourthly, it determines either the role it performs within the body (diagnostic magnetic resonance imaging, cell tracking or therapeutic purposes such as tailored drug delivery) or the ligand that can be bonded to it to support the imaging, tracking or therapeutic roles. The coating used can also facilitate the method of endocytosis[79]. For example, it has been shown that IONP coated with monomer citrate (overall hydrodynamic size of 8nm) demonstrated cell entry via phagocytosis. When the same iron oxide nanoparticles were coated with polymer carboxydextran (overall hydrodynamic size of 31 nm), cell entry or penetration was demonstrated by pinocytosis. In both examples, the same cell line was used[76, 78].

A new field of nanoparticle research is emerging, termed theranostic, whereby either the core material or the surface layer can be loaded with drugs or nucleic acid; providing the nanoparticle with both therapeutic and diagnostic imaging capabilities – 'thera' from therapy and 'nostic' from diagnostic[59].

1.4.2 Stabilisation

High density coatings have been reported to be effective in stabilising iron oxide nanoparticles[18, 80-82]. Such high density coatings are commonly polymeric and monomeric materials or species. Polymeric coatings include dextran, carboxymethylated dextran, carboxy dextran and starch. Whereas monomeric coatings include dimercaptosuccinic acid (DMSA), amino acids and α-hydroxamates (such as citric, tartaric or gluconic acids).

1.4.3 Hydrodynamic size

There is evidence to suggest that USPION is less prone to phagocytosis by the liver; whereas SPION greater than 50 nm are rapidly phagocytosed[18]. Therefore, hydrodynamic size can affect biodistribution and blood half life in a time dependent manner[83]. Eventually, USPIO will actually be processed by the liver.

1.4.4 Biodistribution

Iron oxide nanoparticles greater than 50 nm are readily macrophaged by the reticulo-endothelial system (RES). This namely refers to the Kuppfer cells of the liver, the spleen and bone marrow[18]. Iron oxide nanoparticles less than 50 nm have been used to demonstrate uptake by lymph nodes[18, 56, 84-87]. Of the available iron oxide-based contrast agents which are currently on the market and also undergoing clinical trials, the blood half-life values can vary considerably from 40 mins to up to 36 hours. There is thus a link between the hydrodynamic size and the biodistribution and blood half-life. As has been established, particles greater than 50nm are readily taken up by the liver in a matter of minutes. USPION are not readily phagocytosed by the liver and can have a longer blood half-life and thus reach other structures within the body[18]. It must also be emphasised that the coating itself can be responsible for aspects of biodistribution as well as ligands; for example the targeting of specific cells or organs[18, 56, 85].

1.4.5 Metabolism and excretion

The manner in which the body metabolises iron oxide nanoparticles is determined by their overall chemical composition. In particular the immediate coating and any ligands are strong determinants as to the site (that is, which particular organ or body system) of metabolism and thus also the rate of metabolism and excretory pathways. The commonly used dextran coating should ideally be of low molecular weight. This is vital as higher molecular weight dextrans, such as those used as plasma substitutes, have a reported association with adverse reactions. Immunoglobulin G (IgG) antibodies have been reported to be reactive to such high

molecular weight dextrans[88]. Low molecular weight dextrans will initially undergo dextranases which is an intracellular level breakdown process. The majority of the breakdown components are excreted with urine over a period of nearly 2 months[18]. Once the low molecular dextran has metabolised in this manner, the iron oxide core has been found to enter the normal iron store of the body. Such iron elements can also be found as haemoglobin with the body's red blood cells[89]. This iron then follows the same excretory pathway as endogenous iron. That is, approximately one-fifth is eliminated mostly with the faeces and over a three-month period. Therefore, as both dextran and iron from iron oxide nanoparticles are incorporated into the body's normal metabolic pathways, without raising these levels noticeably, and with the evidence available today, it can thus be stated that these substances do not trigger any long-term toxicity. In the average healthy adult, normal total human iron stores is about 3500 mg with the liver containing an average of 0.2 mg of iron per gram[89]. From the currently approved iron oxide nanoparticles for diagnostic MR imaging, a regular adult dose can contain 50-200 mg of iron. This value can be considered relatively small compared to the human body's iron store. Chronic iron toxicity is known to occur when the concentration of iron within the liver reaches a level of 4mg of iron per gram of liver[74].

1.4.6 Phenomenon of superparamagnetism

From a physics perspective, there are four variations of magnetic susceptibility. In order of weaker magnetism to stronger, these are diamagnetic, paramagnetic, superparamagnetic and ferromagnetic. Materials identified as diamagnetic demonstrate very weak magnetic susceptibility effects and in fact, produce a magnetic field in the opposite direction to the externally applied magnetic field. Paramagnetic items demonstrate a relatively stronger

susceptibility effect as their own magnetic field is in the same direction as the externally applied magnetic field. Biological tissue components that are paramagnetic and their paramagnetic nature can be exploited to improve image contrast, through the use of pulse sequences, include met-haemoglobin and deoxy-haemoglobin. The gadolinium incorporated into MRI contrast media is also a known paramagnetic substance. Superparamagnetic describes material that induce a susceptibility effect in magnitude somewhere between paramagnetic and ferromagnetic substances. Ferritin and haemosiderin are naturally occurring (in the body) superparamagnetic substances and are also capable of being exploited through creative pulse sequences to aide in diagnosis. Items referred to as being ferromagnetic are material that experience introduced into an external magnetic field and thus demonstrate the strongest magnetism. Iron, and materials embedded with iron are highly magnetic – introducing ferromagnetic items into an MRI scanning facility is prohibited.

Iron oxide nanoparticles, as discussed here, are referred to as being superparamagnetic. The superparamagnetic phenomenon is observed when the thermal energy of the medium is sufficient to alter the crystallite or nanoparticles's magnetisation direction by overcoming coupling forces. When crystallite or nanoparticles are placed within an external magnetic field, its magnetic moment will align with the externally applied magnetic field. At least two points distinguish superparamagnetism from paramagnetism. Firstly, with paramagnetism, it is each individual atom or ion that becomes aligned with an externally applied magnetic field. Secondly, superparamagnetism will occur when the crystal or hydrodynamic size is less than its ferromagnetic domain. Authors report this size to be less than 30 nm[18], with the "critical size" being about 15 nm[77, 90, 91].

When not in the presence of an externally applied magnetic field, superparamagnetic particles are not magnetised, nor do they demonstrate any remnants of magnetism once removed from the magnetic field. When the crystals or particles are under the influence of an applied

magnetic field, their magnetic spins are considered to be in perfect alignment and very high local magnetic field gradients are generated. These gradients then cause spin dephasing of the surrounding water protons; thus reducing their T_1 and T_2 relaxivity[3, 90, 92]. It must also be noted that there is a relationship between the iron oxide nanoparticle size and the level of superparamagnetic saturation. As the particle size decreases, so too does the superparamagnetic saturation. This then has an effect on reducing the observed relaxivity or further reducing T_1 and T_2 relaxation.

Gadolinium based contrast agents are the most widely used paramagnetic contrast agents. They are designed to demonstrate pathology as a hyper-intense signal on T1 weighted images. Commercially available brand names include containing gadolinium in their formulation include Magnevist®, Optimark™, Prohance® and MultiHance® [93].

Concerns have arisen relating to gadolinium dissociating from its chelating agents once administered into patients. Deaths have resulted due to dissociated gadolinium inducing nephrogenic systemic fibrosis [37, 94-97].

Among the superparamagnetic agents, iron-based particles have been the most widely used and researched[77]. There are also commercially available iron-based particles, such as Revosist®, Feridex®, Gastromark® and Abdoscan® [98]. These commercial iron-based nanoparticles are marketed for with MRI in imaging the liver, spleen and gastrointestinal lumen.

1.4.7 IONP Influence on magnetic resonance image characteristics

Compared to a paramagnetic material such as gadolinium, the relatively high magnetic moment of superparamagnetic species, such as iron oxides, are sometimes referred to as super spins[18, 99]. The dipolar interactions between the super spins and adjacent water protons result in both high longitudinal (R_1) and transverse (R_2) relaxation values. IONPs therefore increase T_2* relaxation rates through the susceptibility effect and thus have their greatest visual impact on T_2* weighted images produced with gradient echo-based pulsed sequences[81, 82, 100, 101]. The accelerated phase loss due to local field gradients generated by super spins, all stem from the (induced magnetisation) high susceptibility level of iron oxide. At the common clinically available field strengths of 1.5 T and 3.0 T, published literature[18] indicate that any aggregation of SPION will only slightly decrease R_1 (longitudinal relaxation) and dramatically increase R_2 (horizontal relaxation).

1.4.8 Magnetic resonance imaging with iron oxide nanoparticles

Even though images composed with gradient echo pulse sequences possess lower signal-to-noise ratio and spatial resolution compared to spin echo pulse sequences, they are currently the most appropriate imaging sequence to use with SPIONs. This is often termed magnetic susceptibility imaging[1, 3, 82, 102]. The contrast enhancement captured on an MR image is dependent upon a number of factors. Most notable are the biodistribution and opsonisation of SPIONs.

1.4.9 Iron oxide nanoparticles as contrast agents for MRI

In addition to their superior biocompatibility, IONP MRI contrast agents have been documented to increase diagnostic sensitivity and specificity[56, 79, 103-105] in both animal model experimentation and in human trials. This improved accuracy has been attributed to their superparamagnetic effects and relaxation times[103, 105, 106]. Efficacy of IONPs as MRI dedicated contrast media also largely depends upon their physiochemical properties[56]. Such attributes include: size (both of the iron oxide core and the overall hydrodynamic dimensions); coating (dextran derivative or other); and the zeta surface charges. Their efficacy can be further increased with complex surface modifications. This is achieved by bonding or attaching active material such as monoclonal antibodies, receptor ligands and also proteins[56]. For intravascular administration, the hydrodynamic diameter of IONPs are very rarely greater than 150 nm. The iron oxide core itself is usually no more than about 15 nm[107]. The coating itself is preferably composed of dextran, or a derivative, of a low molecular weight. These are positive properties, as the dextran is biodegradable and its low molecular weight minimises possibilities of adverse reactions[88]. IONPs have also been incorporated into oral contrast media[56].

1.4.10 Imaging challenges to consider and overcome

There are a few imaging challenges with the use of IONPs[108]. They are in relation to commonly encountered artefacts in MRI imaging. On their own, they can be frustrating to deal with in everyday imaging, however, when IONPs are included in the imaging regime, a further layer of complication is added. The first criticism is that it is difficult to determine or

differentiate a signal void induced by IONPs compared to signal voids generated as artefacts by materials such as metal (susceptibility artefact). The second artefact is that of partial volume averaging. IONPs are capable of being involved in processes occurring at a cellular level. Hence, signal voids induced by IONPs that are smaller than the spatial resolution of the MRI image will not be represented as distinct and within a voxel; as individual signal intensities within a voxel are averaged together [1-3, 108].

1.4.11 Emerging trends: Applications of iron oxide nanoparticles and the role of MRI

Where possible and practicable, medical investigators and clinicians would prefer an investigation means that is non-invasive or minimally invasive. This approach is safer for patients, it expedites the medical management of patients, and can negate morbidity and mortality consequences. IONP preparations, combined with MRI, have the potential to revolutionise a number of investigative and treatment procedures. This would be achieved by combining the advantages provided by IONP together with MRI, leading to safer and superior imaging alternatives. IONPs as MRI contrast agents have already been discussed in this thesis. To re-iterate, they promise improved levels of toxicity and increased diagnostic sensitivity and specificity. These are achieved through careful chemical preparations, leading to IONPs having the required characteristics for biocompatibility and MRI image enhancement. It is recognised that further research is required to overcome the challenges mentioned. A discussion on the innovative uses of IONPs combined with MR techniques will now follow. These promise to revolutionise clinical therapies and improve patient outcomes. Molecular imaging is a broad term concerning the imaging of biological events at the cellular

or molecular level. It should also be non-invasive and the imaging characteristics representing the biological activity should be quantifiable[109]. MRI is seen as having an emerging and innovative role. Molecular imaging can be possible with MRI when IONPs are conjugated with biologically active materials such as antibodies. The near future looks promising for MRI, together with IONPs, to have a positive impact in leading non- invasive imaging of biological and biochemical processes. Not only can such processes be diagnosed; but also progression and treatment can be imaged over time.

1.4.11.1 Angiogenesis

Angiogenesis, the growth of new blood vessels (for development, wound repair or tissue reproduction), is related to tumour growth and progression[66]. There are several known molecular markers associated with angiogenesis. That is, endothelial cells active in angiogenesis express known surface receptors compared to endothelial cells not partaking in angiogenesis[110]. The commonly occurring receptors include integrins and vascular endothelial growth factor receptors. Antibodies or drugs to seek out angiogenic markers, can be conjugated to IONPs and imaged with MRI. Thus, the angiogenic process can be identified and any success in treatment can be accurately monitored. This can be achieved by exploiting the increased permeability of newly formed tumour vessels compared to normal healthy vessels[111].

1.4.11.2 Apoptosis

Apoptosis is the self destruction of cells. When determined by cell age or cell health status, the nucleus triggers this process. It requires metabolic activity by the dying cell and is commonly characterised by a redistribution of phosphatidylsenine in the cell membrane[66]. It can even be associated with tissue development and homeostasis[110]. The degree of apoptosis can determine how successful chemotherapy and radiation therapy can be. Identifying apoptotic events *in vivo* would hence further evaluate treatment regimes and progression of pathology[110]. It is known that apoptotic cells express lipid phospatidylserine (a phospholipid) on their cell membrane. Synaptotagmin I is a protein that is used to detect this phospholipid. When this protein was conjugated to IONPs, apoptosis was demonstrated *in vivo* with mice[112]. The capability to image apoptosis can allow for almost real-time monitoring of efficacy of drug therapies[90].

1.4.11.3 Targeted drug delivery with IONP and MRI

Many therapeutic drugs that are available, can be considered non-specific in nature. By non-specific, it is meant that such drugs are administered intravascularly and are thus distributed randomly. This can lead to unwanted effects on healthy tissue[113]. Specificity for target tissue or cells can be achieved by conjugating IONPs with ligands[110]. Such ligands include antibodies (in particular for targeting cancerous tissue or cells), proteins, peptides and other biological markers. Targeted drug delivery, as provided by superparamagnetic colloid suspensions, can be guided by an external magnetic field to the site of interest[56], thus, having the capability to minimise both side effects and required dose[113-115]. Therefore,

pharmaceutical drugs can be bound to IONPs designed to reach a specific, or target, organ, and then be released there[56, 77]. The emerging breakthroughs that make magnetic drug targeting possible and promising are the new classes of IONPs less than 50nm. This allows for improved circulation time, thereby permitting delivery to the target site without the likelihood of being sequestrated by the RES before this can occur[56]. With the original classes of IONPs that became commercially available over ten years ago, RES uptake occurred within a few minutes following intravascular administration (hence, their original application as dedicated contrast agents for the liver)[56]. Drug targeting can be achieved by passive, active or physical means[56]. Magnetic drug targeting falls into the category of physical means; as the pharmaceutical is attached to a carrier system (the IONP) and its distribution is facilitated with an external influence (the magnetic field). Not all therapeutic drugs can be conjugated to one single variety of IONP. Characteristics of IONPs that can determine attachment of therapeutic drugs include their size, surface charges (zeta charges) and capacity for protein absorption[56]. The process of cell uptake is determined by the overall size of the nano-system (IONP, surface coating/s and pharmaceutical); phagocytosis or pinocytosis. Pinocytosis occurs for items less than 150 nm[56, 113]. The condition under which a cell finds itself in, may alter its susceptibility to a nano-system. For example, under normal conditions, walls of endothelial cells are permeable to objects 10nm or smaller. However, when involved in pathologic processes such as tumour infiltration and inflammation, the endothelial wall can be permeable to objects up to as large as 700 nm[56]. Zeta charges need to be carefully managed. They determine whether or not nanoparticles aggregate or if they remain suspended in its medium. More importantly, they also play a part in endocytosis. It is noted that the likelihood of phagocytosis increases with a higher zeta charge[56, 116], while time spent within the circulatory system is reduced. There is an electrostatic process involved when particles and substances are absorbed by a cell's outer membrane[117]. Understanding nanosystem interaction with proteins is vital, as when they are injected into the vascular

system, their first interaction is with the plasma proteins. Therefore, the manner in which nanosystems are capable of interacting with opsonins (proteins that encourage phagocytosis such as IgG) and dysopsonins (proteins inhibiting phagocytosis) also determine if they are readily phagocytosed by the RES or if they can reach their intended target and release their pharmaceuticals. Hence, protein repulsive molecules such as polyethylene glycol (PEG) can be used to modify the surface of nano- systems to reduce their recognition by the RES[113] and reduce non-specific cellular uptake[118]. A phase I/II clinical trial of IONPs combined with epirubicin designed to image and treat solid tumours (such as sarcomas), showed that these nanosystems were reasonably well tolerated by the fourteen patients involved. No organ toxicity attributable to iron oxide was noted; however, toxicity responses to epirubicin were recorded at doses greater than 50 mg/m^2[119].

1.4.11.4 Thermal applications for cancer cells: magnetocytolysis and hyperthermia with IONP and MRI

Compared to normal healthy cells, cancer cells are known to be sensitive to temperatures above 42 ^{o}C. Normal cells can survive at higher temperatures[77]. In cancer cells, at temperatures above 42 ^{o}C, protein function is disrupted which can lead to apoptosis[114]. Thus, hyperthermia is a proposed treatment regime for certain cancers. Until recently, hyperthermic approaches have included irradiation with radiofrequency, ultrasound and microwaves. One known criticism of these approaches is the likelihood of hyperthermic injury extending to healthy tissue. The term, magnetic induction hyperthermia, now refers to cancer tissue being exposed to an alternating magnetic field[77].

Hyperthermia using IONPs together with MRI has demonstrated positive results in pre-clinical evaluation studies. With this combined approach, magnetic nanoparticles can be either directly injected into a tumour volume or designed to be selectively uptaken by a tumour site. This target-selective capability improves local heating treatment to the tumour while dramatically minimising potential for injury to surrounding healthy tissue[120]. Furthermore, the alternating magnetic field (not absorbed by tissue), together with appropriately prepared IONP, can allow hyperthermia treatment[56] to be applied to areas deep within the body[77]. Radiofrequency pulses provided by MRI can be designed to provide frequencies and amplitudes to increase local cell temperature up to 55 ^{o}C[114], thereby inducing cytolysis. This process, therefore, can be used to generate heat to target cells[121]. For magnetic hyperthermia to be successful, it requires accurate delivery of magnetic nanoparticles to the tumour site. A number of experiments report successful use of magnetic induction hyperthermia in cancerous cell models and also in animal models[77, 120, 122]. Salado et al.[123] successfully demonstrated in a rat model, with *in vivo* MRI imaging, that the IONPs which they developed were capable of providing positive contrast enhancement of induced liver tumour and also successfully treated these liver tumours with MRI-induced hyperthermia; thereby, demonstrating that IONPs can have both a diagnostic and therapeutic use. Analysis of the rats following the experimental study demonstrated no vascular embolisms (the IONP preparation was injected through the ileo-colic vein) and specimens of the liver demonstrated insignificant inflammatory changes. Xu et al.[124] have produced nanoparticles containing a core composed of iron and cobalt and a gold shell. These nanoparticles demonstrated a specific magnetisation value far greater (226 emu/g) than that achievable with commercially available iron oxides (78.8 emu/g). This higher magnetic moment is claimed to improve heating efficiency in hyperthermia applications; however, their publication did not mention any results or discussion of toxicity or biocompatibility studies.

Initial success of magnetic hyperthermia with small groups of human patients provides a promising outlook for future clinical applications. Plotkin et al.[125] reports a study on eleven consecutive patients (mean age 44 years), each with recurrent supratentorial glioblastoma. All patients had previously undergone surgery, nine patients also had radiation therapy and eight patients also had chemotherapy. Based on the prognosis following these treatments, these eleven patients were eligible as candidates for hyperthermia using nanoparticles and MRI. Nanoparticles were then administered directly into the tumour volume. MRI hyperthermia, or nano cancer therapy, followed and in ten patients, the mean reduction in gross tumour volume (GTV) was 74 % as indicated with PET/CT fusion imaging.

1.4.11.5 Cancer imaging with IONP and MRI

Diagnosing cancer in its early stages significantly improves patient outcomes and survival rates. The initial use for IONPs was directed at imaging liver tumours[126]. This was due to the nanoparticles being greater than 60nm and therefore readily phagocytosed by the liver. This has been occurring for several years now and there are a few commercially available preparations for this specific purpose. This author will therefore discuss IONPs in relation to other cancers. Current MRI techniques allow for the detection of tumour sizes in the order of one centimetre cubed. By conjugating known cancer antibodies with IONPs, then MRI can be used to identify cancerous tissue of smaller dimensions through molecular interactions. This is an improved sensitivity for cancer markers, compared with current cancer marker

detection probes[127]. IONP can be coated with DMSA, a bi-functional chelating agent and ligand. Herceptin, a monoclonal antibody, uses elements from within the immune system to stop tumour progression by binding to HER2 receptor and triggering a response by natural killer (NK) cells[128]. With a 1.5 Tesla clinical MRI scanner, Lee et al.[127] successfully demonstrated how to identify cancer sizes as small as 50mg in mice using IONPs conjugated with Herceptin. The above approach improves patient outcomes compared with just chemotherapy alone. This principle has also been used to target other tumour antigens. IONPs conjugated with EPPT1 (a synthetic peptide) are able to target under-glycosylated MUC-1 (mucin 1); which is a tumour antigen expressed by many epithelial cell adenocarcinomas such as pancreatic, colorectal, gastric and prostate[90]. The role that lymph nodes play in cancer staging has not gone unnoticed by researchers in this field. IONPs and MRI can be used to image the condition of lymph nodes and more accurately determine the extent of metastatic spread[109]. Oghabian et al.[129] demonstrated 98% detection sensitivity with *in vivo* imaging of a rat model at 1.5 Tesla. They also concluded that the type of surface coating and its thickness were factors in determining MRI signal intensity. Today, prostate cancer is still a leading cause of death in men. Current treatment, among others, involves brachytherapy, and as a procedure, it has its own level of invasiveness, morbidity and mortality. Wang et al.[130] have conjugated IONPs with prostate specific membrane antigen (PSMA) and also with doxorubicin, a chemotherapy drug. By performing whole cell assays on human cell lines, Wang et al. demonstrated that their conjugate can detect, with high sensitivity, prostate cancer cells expressing PSMA, thereby, promising the possibility of a multifunctional (diagnostic and therapeutic) nanoparticle system. IONPs can also be used to better identify tumour boundaries within the brain[109, 126, 131, 132]. This leads to improved quantification of tumour volumes. Compared with gadolinium-based contrast agents for MRI and also taking into consideration oedema surrounding a tumour volume, IONPs can define tumour margins for longer time periods[109, 131, 133]. This is as a result of the IONPs being

endocytosed by tumour cells. Thus being internalised, their elimination rate from the tumour is longer compared to extracellular gadolinium-based contrast media.

1.4.11.6 Cell labelling and tracking; including stem cell therapies

MRI imaging of cells labelled or endocytosed with IONPs is considered an indirect imaging technique. This is because changes in MRI signal intensity is in relation to the amount of IONPs and not due to the number of cells. One concern is the MRI signal characteristic and change over a time period. As stem cells rapidly divide, the fixed amount of IONPs is spread throughout the volume of newly divided daughter cells[108, 115]. This will be a relative decrease in MRI signal not accurately reflecting the activity of cells. The second noteworthy concern is the possibility of false positive signal findings. This is a result of iron presented from cells undergoing apoptosis or lysis[108]. Despite these challenges, possibilities are being created for many biomedical applications[117]. The possibility of imaging stem cells in therapeutic applications with MRI is becoming an ever increasing area of active research. Published research so far indicates that IONPs combined with peptides or transfection agents can be used for stem cell uptake[115]. A study using stem cells with IONPs injected into the infarcted myocardium of pigs was able to be successfully imaged at 1.5 Tesla *in vivo*[134]. Following this, histological analysis revealed that the MRI signal appearance attributed to IONPs corresponded with stem cells that had taken up IONPs. Heymer et al.[135] combined human mesenchymal stem cells (hMSCs) with IONPs; placed these in collage type I hydrogel (clinically approved for the repair of articular cartilage) and imaged them in an 11.7 Tesla MRI scanner. Iron uptake was confirmed by histological analysis and correlated with hypo-intense regions demonstrated on the MRI images. Their technique offers the possibility to use

MRI to track the migration of IONPs loaded with hMSCs following implantation for articular cartilage repair. Stem cell research is highly regarded as offering possible treatment solutions for patients with neuronal pathologies and injuries. Guzman et al.[136] proved that IONPs themselves do not alter survival rates, migration patterns or differentiation capabilities of stem cells from the human central nervous system (CNS), compared with unlabelled human CNS stem cells. They demonstrated this by administering the combined human CNS stem cells and IONPs into neonatal, adult and injured rodent brains. MRI was then used to track the migration of stem cells and confirmed the image findings histologically. Stem cells labelled with IONPs have been widely used in animal models (mice, rats and pigs) to demonstrate regeneration of the myocardium following infarction[137]. The limitation of this technique is that the conjugation of IONPs and stem cells need to be injected directly into the myocardium. This introduces an element of invasiveness, however, the region of infarct can be clearly delineated[138]. So far, administration of stem cell and IONP conjugations for myocardial regeneration via a vascular route (intravenous or intracoronary), has not been as successful as direct injection into the infarcted myocardium. Furthermore, comparative high volumes are needed[137, 139].

1.4.11.7 Cardiovascular imaging with IONP and MRI

IONPs have also demonstrated capabilities in imaging cardiovascular pathologies including atherosclerosis, thrombosis and myocardial infarcts[90, 140]. Atherosclerosis is considered both a progressive disease and chronic inflammation. The endothelial cells of the vascular wall express receptors from their cell membrane to attract monocytes. Monocytes establish themselves in the sub-endothelial space and then differentiate into macrophages. The

macrophages then take up oxidised low density lipoproteins and this lipoprotein can be conjugated to IONPs and used to identify active regions of atherosclerosis with MRI. This approach has been often used in studies involving animal models[141]. Furthermore, apoptosis leads to plaque instability and is known to occur before plaque rupture[141]. Identifying apoptic plaques *in vivo* with MRI is seen as advantageous in improving patient outcomes, as inflammatory activity of atherosclerotic plaques may be associated with an increased risk of rupture[137]. Aortic valve disease is also an inflammatory response with macrophage involvement[115]. Ruehm *et al* successfully used commercially available IONPs to demonstrate (with MR imaging) in hyper-lipidemic rabbits that atherosclerotic plaques containing macrophages take up these nanoparticles[142]. This was confirmed with histopathogical evaluation techniques on samples removed from the aorta. The MRI appearance demonstrated an aorta with irregular pattern where the signal dropout occurred at plaque sites containing macrophages endocytosing the IONPs.

IONPs can also be used to target fibrin containing thrombi. This approach may be considered a sensitive method of identifying patients at risk of more serious cardiovascular consequences[143]. A study by Winter et al.[144] demonstrated that by using anti-fibrin antibodies together with nanoparticles, clots in canine plasma *in vitro* could be identified with MRI (at 4.7 Tesla).

1.4.11.8 Blood pool contrast agent

There has been a high level of success in using IONPs as blood pool agents; in both animal models and in human subjects. One study[145] investigated size and dose of IONPs as a blood pool agent for MR angiography in New Zealand White rabbits. The rabbits were divided into a control group (administered with gadopentate dimeglumine), and three other groups (each receiving a different concentration of IONPs). MR angiography was performed at varying time points; ranging from first pass to 24 hours post-intravascular administration. Assessment included signal enhancement of the abdominal aorta, renal arteries and the iliac arteries. Results demonstrated that the highest level of signal enhancement was identified during the first pass imaging strategy. It was also noted that enhancement in the abdominal aorta was greatest with the smallest nanoparticle size of 21 nm. In addition to this, a concentration of 40micromole of iron per kilogram was recognised as the dose providing signal enhancement comparable to gadopentate dimeglumine. The size and dose of IONPs provided sufficient signal changes to allow imaging from first pass time-point up to 25 minutes post-intravascular administration. In this 25-minute window, multiple imaging acquisitions and measurements are possible. Another study[146] successfully demonstrated the use of IONPs as a blood pool agent in rats with induced myocardial injuries. Here, a commercially available blood pool agent, Clariscan, was used with an MRA technique. The image findings were also compared with post-mortem histochemical stains of the infarcted rat myocardium. It was found that the Clariscan-enhanced MR angiogram images over-estimated the infarcted myocardial regions when compared with histology inspection. The use of Clariscan identified the presence and dimensions of both transmural and non-transmural microvasculature insults. The peri-infarcted zone was seen to be over-estimated to a greater extent in rats with non-transmural ischaemic injuries. Overall, there was an over-estimation of the size of the true infarct but an under-estimation of the region at risk.

Another commercially available IONP preparation (Resovist) has been used to assess the abdominal aorta and the inferior vena cava in a human pilot study[147]. With a 3D MRA (T1-weighted) acquisition technique at 1.5 Tesla, first pass imaging was achievable with results being comparable to those obtained by MRA with conventional Gadolinium based contrast agents. Ferumoxytol has also been used for first pass enhanced 3D MRA of blood vessels of varying dimensions in 12 human subjects. The following vessels were investigated: the carotid arteries, thoracic aorta, abdominal aorta and peripheral arteries[148]. With delayed MRA imaging it was noted that both arterial and venous structures displayed enhancement characteristics.

1.4.11.9 Nanosensor

A critical and relatively new-found application of IONPs is to include them in preparations to produce what is now termed "nanosensors". Nanosensors, in their broadest definition, are IONP preparations that have been designed to detect the presence of a specific biological interaction. Protease specific nanosensors have been developed for *in vivo* detection of enzyme activity with MRI[149]. In particular, T2* MRI together with nanosensors of 25 nm (hydrodynamic size) have demonstrated the involvement of the metalloproteinase 9 (MMP-9) enzyme in processes including inflammation, atherosclerosis and tumour spread. This opens the potential for early diagnosis of pathologies with altered protease activity and also the monitoring of treatment and therapies that act on protease enzymes. Protein functionalised nanosensors have also demonstrated capabilities in identifying and measuring the concentration of anti-human serum albumin antibodies[150]. One of the additional benefits of the combined approach of MRI with nanosensors is that the NMR capabilities can allow for

detection in natural human substances such as blood and urine. Nanosensors have also been developed with the capability to detect single human alveolar cancer cells (A549) within 15 mins, in blood, *in vitro*[151]. High density folic acid, when conjugated to polyacrylic acid coated IONPs were designed to interact with A549 cancer cells expressing the folate receptor.

1.4.11.10 Metal doped IONPs

Metal doping of IONPs is designed to provide a comparatively higher level of magnetism at the nano scale and also allow successful magnetic tuning[152]. Such metal doped IONPs can increase MRI signal contrast by as much as 14 times compared to conventional IONPs. The implication of this is that a lower dose or lower concentration can be administered to the patient. Their magneto-thermic effects can also increase by a factor of 4. Lanthanide metals have also been used to dope IONPs[153]. The advantages that lanthanide metals can offer include optical imaging properties, detection by neutron activation, utilised in neutron capture therapy procedures and also being detectable by time resolved fluorescence. IONPs doped with manganese have shown to improve the quality of contrast-enhanced MR imaging of the liver[154]. These nano systems have a mean diameter of 80nm. The highest level or change in signal intensity occurs at 5 mins post-intravascular administration. However, unlike early IONPs, the imaging window for IONPs doped with manganese can last for approximately 36 hours.

1.5 Targeted imaging

Targeted imaging is the term used to describe the directing of a nanoparticle to an intended site or destination within the body; such as an organ or a tumour. A site can be targeted for imaging purposes only, or for drug delivery or both. Such features are introduced at the design or synthesis stage of manufacturing nanoparticles, or, alternatively, prior to administering nanoparticles, the surface layer is functionalise such that the nanoparticle can carry out such tasks.

Targeting can also be performed by loading nanoparticles into cells. This can be performed by simple incubation. The cells that are selected to be carriers are cells that are known to migrate to the organ of interest or cells involved in the pathological process under investigation.

In the field of nuclear medicine, it has been known for decades that certain radio-active tracers or labels can be used to identify pathology via biochemical pathways. For example, a radio-active form of fluorine, ^{18}F, is used to make fluorodeoxyglucose (FDG) for PET imaging to assess glucose metabolism in the brain. FDG is also used in PET imaging of many forms of cancer, as it accumulates in cancerous tissue with high metabolic activity.

Monitoring the location, distribution and long-term engraftment of administered cells is critical for demonstrating the success of a cell therapy.

1.5.1 Targeted imaging with cells loaded with IONP and MRI

Nanoparticles can be tracked with MRI, as they migrate from their administered site to their destination. In particular, stem cells have been used together with MRI to monitor experimental treatments.

Jendelova et al[155] used IONP loaded the bone marrow stromal cells from rats and also loaded into the embryonic stem cells from mice. They were implanted into animals having been deliberately given either a spinal cord compression or a cortical lesion; the implantation was on the contralateral side. Migration towards the injury site was imaged. Migration took approximately one week. MRI was used to track their path. The cells with IONPs deposited in intracerebrally were capable of providing a hypo-intense MRI signal for over 50 days.

McFadden et al[156] successfully labelled 231BR-Her2 cells with IONP and administered these into female nude mice via a left ventricle injection. One day later, these loaded cells were detectable in the brain of these mice with 3T MRI, *in vivo*. The particles used were 35 nm in diameter and labelled with Rhodamine-B. Such a particle was not only capable of providing MRI signal, and thus being capable of being tracked over time, but the Rhodamine-B allowed the particle to be identified and confirmed in tissue samples with a fluorescent microscope.

1.5.2 Targeted imaging with radio-labelled IONP and MRI

With the introduction PET/MRI, superparamagnetic IONP radio-labelled with radio-active tracers can potentially provide capabilities for high spatial resolution imaging (MRI), high contrast resolution imaging with high sensitivity and biochemical assessment (PET). Studies

have already been conducted, attempting to use the well-known targeting capabilities certain radio-tracers labelled with IONP.

Wong et al[157] has demonstrated a proof of principle that ^{64}Cu can be labelled to IONP and postulates their use with PET/MRI. They focussed on rapid production techniques using microwave techniques (while minimally impacting on the radio-active decay time of ^{64}Cu) while delivering consistently uniformly size nanoparticles. Pombo-Garcia et al[158] also used ^{64}Cu to radio-label ultrasmall IONP and conducted *in vitro* assessment with human serum, noting time dependent internalisation with human umbilical vein endothelial cells. These investigators also postulate the potential for their use in tumour imaging with PET/MRI.

^{99m}Tc is a standard SPECT radio-active label. Madru et al[159] has successfully radio-labelled ^{99m}Tc to IONP (with a surface layer of polyethylene glycol) with the intention of imaging the sentinel lymph node, *in vivo*, in Wistar rats after they received sub-cutaneous injections of their right paw. Imaging was performed at 4 hours post injection, initially with SPECT , then followed with 3.0 T MRI.

Madru et al has also experimented with radiolabelling ^{68}Ga to IONP with polyethylene glycol as its surface layer, and successfully demonstrated their capabilities in imaging the sentinel lymph node in white Wistar rats[159].

1.6 Sentinel Lymph Node Imaging

The sentinel lymph node (SLN) is recognised as the first lymph node to be reached by metastatic cancer cells. The mechanism of which, is directly related to the anatomical

arrangement of the lymphatic system and also its function; relative to the tumour. From a broad physiological perspective, the entire lymphatic system is designed to monitor fluid homeostasis and immune competence [160]. Further to this, the lymphatic system acts as a physical pathway for dendritic cells to facilitate their role in an immune response. The entire lymphatic system has been considered to be a unidirectional and open ended system [161] that serves to drain excess interstitial fluid, large molecules, or cells that cannot re-enter the cardiovascular system. Lymphatic vessels can be detected in almost all organs and interstitial tissue throughout the human body [162]. A tumour can transmit cells to its SLN either through afferent lymphatic vessels (which surround the tumour itself) or through the new development of lymph vessels originating from the tumour [163]. Hence, the realistic likelihood of metastatic cancer cells being present in the SLN.

The identification of the SLN is of paramount importance in a patient's diagnosis with certain cancers, in particular, cancers which are solid tumours and are in close proximity to lymph node clusters. The establishment of malignant cancer cells in the SLN determines the subsequent prognostic pathway for a patient [164]. Clinicians can then make appropriate decisions relating to treatment, therapy and overall medical management [165]. Such decisions need to be made and acted upon in a precise, safe and timely manner. The clinical intent is to have improved outcomes for such patients.

1.6.1 Current methods

The two most popular, current and valid imaging techniques are lymphoscintigraphy and computed tomography (CT). They each have their own advantages and disadvantages in determining the SLN. Once the SLN is identified, it will be either biopsied or surgically excised; then followed with histopathology assessment. Hemotoxylin and eosin staining (H&E) and also cytokeratin immunohistochemical staining (IHC) are performed to determine the presence of cancer cells [166, 167]. If no cancer cells are identified, then the likelihood of other lymph nodes (other than the SLN) being infiltrated by cancer cells is less than 0.1% [166]. If cancer cells are present within the SLN, then the treatment and therapy that a patient receives would be more intense and aggressive. In melanoma patients, following metastatic lymph node removal, the five year survival rate is in the range of 44 % to 60 %, whereas delaying surgical removal of lymph nodes has an associated five year survival rate of 25 % [167].

From a medical radiations perspective, both lymphoscintigraphy and CT are imaging modalities with their own disadvantages, when attempting to identify the SLN. Lymphoscintigraphy has very low spatial resolution [168]. CT requires a high volume of iodine based contrast media and also needs a number of volume data acquisitions to be made, thus, delivering a high dose of ionising radiation to the patient [169, 170]. Pre-operative imaging with either CT or Magnetic Resonance Imaging (MRI), without contrast agents, does not provide adequate sensitivity for clinicians to decide whether or not to surgically remove lymph nodes [171]. MRI, combined with iron oxide nanoparticles (IONP) as a contrast agent, has the potential to overcome the negatives associated with both lymphoscintigraphy and CT; and also MRI scanning without a contrast agent [172-175].

1.6.1.1 Lymphoscintigraphy and its role in current clinical practice

In broad terms, lymphoscintigraphy can be defined as the imaging of the lymphatic pathways and lymph nodes by using radio-active material. It is an established and routine nuclear medicine imaging procedure that captures information about lymphatic drainage [166] and the SLN [160].

There are a variety of radio-active colloids and agents that are in current use. These include ^{99m}Tc labelled sulphur colloid [161], ^{99m}Tc labelled human serum albumin, ^{99m}Tc labelled dextran [166] and also ^{99m}Tc trisulfidecolloid [163]. Collectively, these are also referred to as ^{99m}Tc nanocolloids .[171] To improve detection sensitivity rates to higher than 90% [176], medical blue dyes can be used such as isosulfan blue, patent blue V or Evans blue (EB) [160] in combination with ^{99m}Tc nanocolloids. These blue dyes aid macroscopic identification of lymphatic pathways [177]. These radio-active agents emit gamma rays. Thus, standard nuclear medicine gamma cameras and equipment are used to image their level of radio-activity. As they become localised in the SLN, the gamma activity level is imaged as being representative of the SLN.

The fundamental concept that underpins SLN imaging by lymphoscintigraphy is that the radio-active material that has been injected in close proximity to the primary tumour will then be taken up by adjacent lymph vessels and carried to the SLN. In the current clinical setting, there are two approaches of injecting radio-active agents into patients for lymphoscintigraphy. Both are valid, can be complimentary and are still subject to ongoing debate [163, 178].

The first is deep tissue injection such as subcutaneous, parenchymal, peri-tumoural and intra-tumoural injections; commonly, by a single injection of radio-active material [171]. The second method is by superficial injection into the epidermal or dermal regions. This includes

intradermal and subdermal injections, as well as peri-areolar and sub-areolar injections in breast cancer patients. Here, a clinician will most likely perform four intradermal injections surrounding the tumour mass [179]. The usual range of radio-active dose per injection is between 7 MBq and 10 MBq [180].

The passage followed by the injected imaging agents is identical to that of malignant cells extending from the tumour mass to the SLN. Such imaging agents can be either the medical blue dyes or radio-active agents previously discussed, or, as will be proposed here, iron oxide nanoparticles. Tumour cells are transported to the SLN by the afferent lymph. They arrive either as individual cells or as emboli of cell agglomerations [163]. These malignant cells initially settle in the sub-capsular sinus and the cortex of the SLN. These regions of a lymph node are located in close proximity to afferent lymph vessels, thus, providing an explanation for being the usual commencement sites of neoplastic tumour growth [181]. The lymphatic communication, from tumour mass to SLN, can occur along existing afferent vessels, or along new peri-tumoural lymphatic vessels.

1.6.1.2 Clinical concerns and limitations of lymphoscintigraphy

Even though identifying the SLN with lymphoscintigraphy is vitally important in cancer patients, the procedure of lymphoscintigraphy itself has a number of significant drawbacks. Firstly, the resulting lymphoscintigraphy images have poor quality spatial resolution. From the images, the exact location of the SLN cannot be confidently ascertained [166] and as a result, a hand-held gamma probe (or nuclear stethoscope) must be used intra-operatively to locate the SLN immediately prior to surgical removal. Secondly, lymphoscintigraphy lacks

specificity, as it relies on natural uptake of the radio-active agents from the interstitial spaces by the lymphatic vessels [182].

There is also a significant level of operator dependency when using the gamma probe and the technique and experience of the operator is linked to the successful identification of the SLN [161].

Ionising radiation is used and while the radiation dose that the patient receives may be considered low, the repeated radiation dose to the fingers received by staff that handle the resected SLN (such as the surgeon and the histopathologist) can accumulate over many years [161].

Finally, proper injection technique must be observed when administering the radio-active imaging agent, or there may be focal contamination or pooling of the radio-active agent. This can mimic the appearance of a SLN and lead to false positive assessments [179].

1.6.1.3 The role of computed tomography (CT)

Computed tomography (CT) provides improved spatial resolution as an imaging modality compared to lymphoscintigraphy. CT is readily available and imaging examinations are relatively straight forward with minimal discomfort for patients.

Identifying lymph nodes with CT imaging can, however, become complex, particularly when they are involved with a pathologic process. On CT imaging, normal healthy lymph nodes have an oval or eliptical shape. As they become involved in a pathologic process (such as malignancy, infection, inflammation), lymph nodes take on a circular shape. Their short axis dimension also increases to over one centimetre. The challenge for CT is to distinguish such

lymph nodes from nearby blood vessels. Both arteries and veins have a circular appearance in their short axis. The challenge for CT becomes even greater when blood vessels have a short axis of just over one centimetre [183].

Current clinical practice for CT imaging is to scan the anatomical area of interest dynamically with iodine based intravascular contrast media. CT images are taken of the anatomical area of interest without intravascular contrast media; then the same area is imaged with iodine based contrast media in the arterial phase (contrast media flowing through arteries); next, the same anatomy is scanned with the contrast media flowing through the veins (venous phase); finally, after approximately 10 minutes, the same anatomical area is scanned again. This last acquisition is referred to as a delayed post contrast phase. It is in this phase that pathologically affected lymph nodes may demonstrate positive enhancement (appear hyper-dense or bright). The arterial phase will demonstrate contrast filled arteries, while the venous phase will show veins filled with contrast media. Lymph nodes will not enhance with contrast media during the arterial and venous phases.

CT imaging of lymph nodes also has inherent disadvantages. First, it uses ionising radiation. Considering that up to four acquisitions can be needed (non-contrast, arterial, venous and delayed post-contrast), the radiation dose received by the patient can be large – significantly greater than the radiation levels used with lymphoscintigrahy. Second, iodine based contrast media is required, which, in certain patient groups, can lead to contrast induced nephropathy (CIN). Also, patients may experience adverse events ranging from minor events such as a warm flush or sensation throughout their body to more severe and serious events such as anaphylaxis. Third, the identification of a suspect lymph node is made, based upon its shape and short axis measurement [163, 183]. This, of course, cannot account for normal variants or anomalies. Thus, lymph node size is an ineffective parameter for attempting to diagnose metastatic progression to lymph nodes [184]

Fourth, with the recent clinical introduction of PET/CT (positron emission tomography combined with computed tomography), the combination of a radio-active agent for lymph node imaging with PET followed by CT imaging acquisitions for lymph node; will further compound the radiation dose received by the patient.

1.6.1.4 Magnetic resonance imaging

As an imaging modality, magnetic resonance imaging (MRI) offers a number of advantages compared to nuclear medicine imaging with radio-active tracers and also when placed alongside CT. MRI uses pulse sequences composed of radio-frequency pulses and also time varying magnetic (or gradient) fields, to generate images, thus, MRI does not image with ionising radiation [(185)]. In addition, MRI has superior spatial resolution, compared to both lymphoscintigraphy and CT [(3)]. This is due to the capability of image voxels having dimensions of less than one millimetre on all sides. In fact, volume or 3D acquisitions can be achieved with isotropic voxels. Therefore, the same level of spatial resolution can be maintained when reformations are performed from volume or 3D data sets [(186)]. Reformations in a variety of planes (non-orthogonal) can be achieved, to help locate the SLN and such reformations would be tailored to an individual patient's anatomy.

As the magnetic field strength of an MRI scanner increases, so too does its signal-to-noise ratio, which leads to an improved contrast resolution [(186)]. Even with the higher level of spatial resolution offered by MRI, it does not seem to have the contrast resolution to identify a metastatic lymph node from a healthy one. In a study conducted by Kortewegg *et al*[(187)], 114 lymph nodes that had been surgically removed from positively diagnosed cancer patients; were scanned with a 7.0 Tesla MRI scanner. The 7.0 T MRI image findings were compared

with the definitive histopathologic assessments. The findings were that, even with spatial resolution and signal-to-noise ratio offered by a 7.0 Tesla MRI scanner, there was poor discrimination between healthy and diseased lymph nodes. Morphological aspects that were scrutinised on MRI images were: the fatty centre, the volume, the length-width ratio, and the cortical thickness of the lymph nodes [188]. It should be noted that as this study only scanned dissected lymph nodes, there was no opportunity to incorporate a contrast agent into the experiment. Also noteworthy, is that 7.0 Tesla is an extremely high field strength for an MRI scanner – most current clinical MRI scanners are either 1.5 Tesla or 3.0 Tesla.

MRI also has its own specific contrast media, based on gadolinium, however, it is not used for identifying the SLN. It has an established clinical role for imaging a variety of disease processes such as infection and oncology (primary tumours and metastases), however, not the SLN. A meta-analysis of data published over a 20 year period concluded that the accuracy of MRI with gadolinium contrast media in detecting lymph node metastases is considered moderate [189] compared to MRI imaging of lymph nodes without gadolinium contrast media.

In recent years, concern has arisen over the use of gadolinium [190] as it is now recognised as the trigger for nephrogenic systemic fibrosis (NSF) in a variety of patient groups, including patients with Type 1 diabetes and patients with an estimated glomerular filtration rate (eGFR) of less than 60 ml/min [26].

Gadolinium based contrast media is categorised as an extracellular contrast media as it circulates through the extracellular spaces and should not enter cells. When placed within the imaging environment of an MRI scanner, gadolinium shortens the T_1 recovery (or longitudinal relaxation) of the surrounding tissue. Therefore, gadolinium appears hyper-intense (or bright) on MRI images produced with T_1 weighted pulse sequences. Gadolinium has negligible effect on T_2 decay (transverse relaxation) and thus, no intensity changes are able to be detected by the human eye (or observer).

Iron oxide nanoparticles (IONP) behave in the opposite manner to gadolinium. Their effect on T_1 signal intensity cannot be observed by the human eye, however, they have magnetic susceptibility effects on T_2 weighted and T_2* (T_2 star) weighted pulse sequences. The resultant image will demonstrate marked areas of hypo-intensity (or dark) where the IONP have accumulated [186, 190].

A review of the literature confirms that there has been some interest in imaging lymph nodes with MRI together with IONP. Lymph nodes less than 8 mm in size have been detected in humans [175]. The commonly reported method is to administer the IONP by intravenous infusion. The type of IONP used in these instances, are referred to as ultra small superparamagentic iron oxide (USPIO). The brand most commonly used is feumoxtran-10 (Combidex, Advanced Magnetics, Boston, MA, USA) [166, 191, 192]. Feumoxtran-10 is presented in a dry, powder type form and needs to be suspended in saline for intravenous infusion over a time period of 30 minutes, with a recommended dose of 2.6 mg/kg of body weight [165, 166]. Following entry into the venous system, the USPIO then extravasates into the interstitial space [191, 193]. From here, they are transported through lymphatic vessels to the lymph nodes [160]. Due to their dimensions (20 nm), USPIO are also capable of traversing capillary walls into the medullary sinuses of lymph nodes. When the nanoparticles reach a normal healthy lymph node, they become phagocytosed by macrophages [160, 163, 190, 191, 193]. The resulting accumulation of nanoparticles within macrophages leads to the magnetic susceptibility effect responsible for reduced signal intensity, or hypo-intense appearance of lymph nodes, seen on T_2 weighted and T_2* weighted MRI images. In lymph nodes containing cancer cells, macrophages are unable to phagocytose the nanoparticles [160, 163, 190, 191]. Therefore, cancer affected lymph nodes do not contain nanoparticles and so, do not display any change in signal intensity on T_2 weighted and T_2* weighted images.

The case for IONP as a worth-while contrast agent for detecting lymph nodes is supported by Harisinghani *et al*[21] who scanned 58 male and 19 female (a total of 77) patients with MRI, 24 hours following drip infusion of ferumoxtran-10. In these patients, they were able to image collectively, 169 lymph nodes. The findings of reporting radiologists were compared to that of the histopatholgy findings. The diagnosis made by an experienced radiologist was noted to be not statistically different (p=0.88) to the histopathology results [21].

Further, McCauley *et al*[194] investigated 9 healthy volunteers who received interstitial injections of ferumoxtran-10. The interstitial dose used to visualise the lymph nodes was one-tenth that of the dose used with an intravenous drip infusion. Thus, McCauley *et al* concluded that an interstitial administration route would allow identification of lymph nodes at a significantly lower dose. The researchers also noted the limitations of their study, which included a small number of subjects, and there was no independent confirmation of the number of lymph nodes in each patient [195].

There are some disadvantages to imaging cancer affected lymph nodes following intravenous infusion of ferumoxtran-10. The first is that USPIO are very slowly transported to the SLN, delaying MRI imaging to 24 to 36 hours following administration of USPIO [160, 163]. Second, MRI and USPIO can be referred to as an indirect method of identifying cancer affected lymph nodes, as it is the absence of USPIO uptake that is used to diagnose metastatic involvement of lymph nodes [163]. Third, image interpretation can also be time consuming. This is due to the low contrast ratio between lymph nodes and their surrounding anatomy. Fourth; the Food and Drug Administration (FDA) and the European Medicines Evaluation Agency (EMEA) have not approved USPIO for human clinical use for the detection of lymph nodes because of concerns surrounding the high dose of USPIO used to detect a signal change in healthy lymph nodes[163].

In the management of patients with cancer (in particular tumours such as prostate, breast, head and neck cancers, and melanoma), identifying the SLN will allow patient tailored treatment options to be considered. Even though the current imaging method of lymphocintigraphy has been widely used, it has a number of negative aspects; some of which can be overcome by MRI (without IONP). The combination of MRI imaging with IONP may prove to be a more effective avenue for SLN detection, as it provides improved spatial resolution and does not involve ionising radiation.

1.7 Cellular MRI (cMRI)

Cellular magnetic resonance imaging (cMRI) is a method of imaging cells *in vivo*, and prior to administration, these cells would have been labelled with a contrast agent *ex vivo*. Such a methodology has been experimented with in assessing the utility of cell-based therapies *in vivo*. A promising branch of cancer immunotherapy that is gaining attention by researchers is DC-based vaccines; whereby, DCs are required to migrate to secondary lymphoid organs (such as lymph nodes) and interact with T cells to initiate tumour specific immune responses[196], thus, potentially, a patient's own immune system can be used to battle cancer. DCs, and possible other antigen presenting immune cells, can be utilised as cell-based vaccine, due to their abilities to trigger immune responses. cMRI can be used to non-invasively observe the migration of DCs (loaded with an imaging agent) from their administration site to their destination.

The most promising attempts made, and widely used in experimental studies, has been an *ex vivo* approach to generate DCs *in vitro* from hematopoietic precursor cells; which are then

loaded with suitable antigen and then administered to their original cancer patient. The added benefit is that DCs are prepared in a non-immunosuppressive environment.

For DC-based immunotherapy to be successful and genuinely offer effective treatment, the *ex vivo* prepared and *in vivo* generated DCs and loaded with antigen material; must reach lymph nodes. Initial publications reporting their results identified between 3% and 5% of administered DCs were capable of migration to lymph node; thus resulting in minimal success. This can be explained by the tumour antigen specific response (by T cells), the magnitude of which is proportional to the quantity of DCs that reach the paracortices and T-cell zones of lymph nodes (and interact with T cells). cMRI may not only provide data about DC migration from administration site to lymph node; but also which other sites they are capable of reaching and the length of time taken.

To date, a variety of contrast agents have been used in attempts to image the DC migratory path. These included nanoparticles (of varying compositions) and also radioactive materials such as ^{19}Fluorine-based perfluorcarbon nano-emulsioncombined with PET imaging but to date, have been found to be less sensitive, and its utility to detect DC migration in humans remains to be demonstrated using clinical scanners presently available. Iron oxide nanoparticles can provided the imaging sensitivity needed for cMR.

Of vital importance is the need to load DCs and other immune cells safely, *ex vivo*, with sufficient IONPs (or suitable imaging agent) so that their *in vivo* migration can be imaged and assessed quantitatively and qualitatively. This can provide insight to DC activation and maturation, which in turn, may help with immunotherapy in cancer patients.

1.8 Dendritic Cells

Dendritic cells (DCs) were first identified in mice and described by Steinmen and Cohn in 1973[197]. Since then, our understanding of DCs has increased to the point where DCs are being used for cancer immunotherapy experiments with potential translational possibilities. The commonly accepted definition of DCs is based on their function; that is, DCs have the unique capabilities to internalise, process and present antigens[198] to naïve T cell lymphocytes[199] (and B cell lymphocytes) and prime an immune response[200, 201]. Further, DCs are also defined by phenotype as being lacking in certain lineage specific markers (Lin-) and expressing elevated levels of Major Histocompatibility Complex (MHC) molecules (class II); this phenotype is represented as $^{-}$HLA-DR^{+} [198].

From a progenitor cell perspective, DCs can be categorised into two main groups or originating from either one of two lineages: conventional DCs (cDC) and plasmacytoid DC (pDC)[202]. cDC are also referred to as myeloid DC (mDC)[203]. DC progenitor cells originate in the bone marrow and are carried by blood to lymphoid organs and peripheral tissue; where, *in situ;* they develop into mDC[202]. pDC develop or differentiate in the bone marrow first and then subsequently colonise lymphoid organs[202]. pDC precursors produce significant quantities of type I interferons, such as IFN-α and IFN-β[204]. A further distinction is that mDCs are progressively migrating from their peripheral tissue base to the corresponding region's draining lymph node (LN), while DCs originating from lymphoid organs remain localised there throughout their cell life cycle.

DCs can also be categorised as either immature DCs or mature DCs. Commencing from their progenitor cell origins, the presence of GM-CSF and the Flt3 ligand, allow these progenitor cells to initially become immature DCs.

Immature DCs (iDCs) continually sample their immediate environment and have a high phagocytic capacity. If iDCs ingest a pathogen, or in the presence of other relevant stimulants, iDC enter a phase of developing maturity. This triggers a maturity signal and a complex interplay of chemicals is orchestrated. Prior to this maturity signal, however, iDC (murine) are identified as having the following phenotype and attributes[203, 205]:

- High intracellular levels of MHC II (and FcR)
- Low expression levels of costimulatory markers: CD80, CD86, CD40 and CD83
- Low expression levels of IL-12 cytokine

CD, or cluster of differentiation, are proteins found on cells and these proteins provide a costimulatory signal necessary for T cell activation. Low expression levels of certain CD signify that iDC have not been activated or have not received a maturation signal. IL-12 is a cytokine, a small protein; affecting the migration of iDCs to its destination, as it matures and affecting the subsequent behaviour of T cells (once the iDCs become mDCs and meet with T cells). Chemokines, interferons and interleukins are classified as cytokines.

As DCs mature, their physical chemotaxic transition into, and through, afferent lymphatic vessels requires cytokine stimulation and induction of the CCR7 chemokine receptor[201]. The expression of CCR7 is triggered when immature DCs become activated. Activation of DCs result in up regulation of CCR7 and down regulation of inflammatory cytokine receptors to facilitate chemotaxis migration to draining lymph nodes[200].

Following the maturation signal and as iDCs evolve to mDCs, they will migrate to their destination site (such as lymph nodes or sites of infection). mDCs (murine) have been identified with the following phenotype and expression levels[20, 203, 206]:

- High intracellular levels of MHC II (and FcR)
- High expression levels of CD80, CD86, CD40, CD25 and CD83
- High expression levels of IL-12 cytokine

Mature DCs that have migrated to secondary lymphoid organs (such as the lymph nodes or spleen) are also characterised has having a very minimal capacity for phagocytosis, (compared to iDC), thus, alternatively, a lower capacity to capture antigens; however, they develop capability to efficiently present antigen material to naïve T cells to stimulate an immune response – hence, their potential pivotal role in immunotherapy[20].

DCs can also be triggered to migrate to lymph nodes by indirect methods. Firstly, under normal physiological conditions and in the immunological steady state, the normal movement of lymph fluid along afferent lymphatic vessels is by gentle pulsatile motion[200]; secondly, signals originating from B-cells located from within activated lymph nodes can initiate a migration of DCs[200].

1.8.1 Fundamental principles of DC migration

The migration[207] of iDCs from their initial environment to the high endothelial venules (HEV) and the T cell zone (within lymph nodes), together with the simultaneous transition from immature to mature; is a rather complex series of events. pDC enter lymph nodes

directly with the blood supply, whereas other types of DCs enter lymph nodes via the afferent lymphatic vessel[201]. It is this afferent lymphatic vessel that drains nearby tissue and thus providing the physical migratory pathway.

DC precursor cells originate in bone marrow and migrate to all areas of the body where they can exist in an immature state, sampling their immediate environment and awaiting antigens[200]. Upon stimulation with a suitable antigen, iDCs commence a sentinel function to home to secondary lymphoid organs and structures, especially lymph nodes, where they interact with naïve T cells and also central memory T cells[200].

Chemokines are mediators of iDC migration, whereby, intracellular signalling pathways are triggered to commence cell migration and activation to maturity[200]. Chemokine and chemokine receptors are pivotal in shifting DCs to LNs through afferent lymphatic vessels and also from blood[200]. Via afferent lymphatic vessels, DCs enter the subcapsular sinus and then migrate to the T-cell zone of the LN cortex. DCs from the blood stream enter the HEV and then migrate from the HEV, through the endothelial wall, and into the T-cell zone for efficient and effective interaction with naïve T cells.

1.8.2 The importance of DCs in an immune response and potential immunotherapy with cMRI

Along with DCs antigen presenting characteristics, comes their unique talent to encourage an immune response from T cells. This is the broad and guiding principle of Dendritic Cell Immunotherapy (DCI)[207]. DCs also provide a link between the innate (non-specific) and adaptive (acquired) immune systems.

Cellular MRI is a method of detecting cells *in vivo*, after they have been labelled *ex vivo* with a contrast agent, commonly IONP. This technology and methodology has been applied by researchers to generate iDC from bone marrow progenitor cells, incubate iDC with IONP preparations, then administer these loaded cells into a live specimen and observe their migration and subsequent fate with MRI, *in vivo*. The advantages offered by cellular MRI include that it is non-invasive imaging to live specimens, it uses non-ionising radiation and produces images of exquisite image quality.

DCs and cellular MRI are both central in experimental techniques for cancer immunotherapy – where an individual's immune cells and system can be activated to combat cancer cells. Tumours can be targeted with the use of antigen-specific vaccine; that is, DCs are loaded with cancer vaccines with tumour specific antigen (peptides or proteins) and used to initiate an anti-tumour response[20]. For DC-based cancer immunotherapy to be considered effective, DCs would need to migrate to secondary lymph organs such as lymph nodes and the spleen. Early attempts were not wholly successful; as the methodology used to attempt to load antigens into DCs and have them try to migrate to secondary lymph organs to commence and immune reaction were not efficient. Essentially, tumour antigen and adjuvant were introduced *in vivo* by either intradermal, subcutaneous or intramuscular injection; from here, local DCs were supposed to internalise the antigen, process it and migrate to lymph nodes. This was not successful because tumours can release immunosuppressive substances and also self-tolerance to the tumour antigen can exist; combined together, these can inhibit an effective immune response. At present, researchers are overcoming this is with an *ex vi*vo approach – iDCs are generated *in vitro* from haematopoietic precursor cells in non-immunosuppressed conditions, then loaded with antigen and then administered into the live specimen.

1.8.3 The behaviour of DCs in an immune response

Upon activation, DCs commence a migratory progression to lymph nodes and during this migration process, DCs process uptaken antigens, place these on their cell surface (along with MHC molecules) for presentation to T cell lymphocytes and upregulate costimulatory markers. These costimulatory markers are expressed as the DCs transition from an immature to mature state and also facilitate interaction with T cell lymphocytes[204]; as only mature DCs are capable of activating T cell lymphocytes. T cells require three different signals in order to be effectively and efficiently activated. Firstly, the T cell receptors must recognise and accept the antigen presented by the DC (together with MHC molecules). Secondly, T cells require the costimulatory molecules that have been upregulated and presented with mature DCs. Thirdly, a paracrine (cell-to-cell) signal from soluble molecules in the form of cytokines and/or chemokines produced by the mature DCs[204].

1.9 The aims of this PhD research and thesis

The preceding discussion allows an informed opinion to be formed; that from the current clinical status quo, a new path or direction can be taken to widen the capabilities of MRI through improvements in contrast agents. These may include introducing safer alternatives to ionising radiation imaging procedures being eventually established; and with the advent of PET/MRI, providing a dual modality contrast agent from one injection. All this can improve diagnostic precision and, importantly, better serve patients.

The over-arching hypothesis is that iron oxide nanoparticles (IONP) will enhance magnetic resonance imaging (MRI images), to enable identification of the sentinel lymph node (SLN).

The main research aims of this thesis are to:

1. Manufacture and characterise prototype iron oxide nanoparticles (IONP).

2. Characterise IONP uptake and toxicity in murine cells *in vitro*.

3. Characterise the migration of IONP *in vivo* with C57BL/6 mice.

4. Characterise IONP uptake and toxicity in human cells *in vitro.*

5. Radio-label the IONP with ^{68}Ga.

6. Perform *in vivo* studies with IONP radio-labelled with ^{68}Ga.

2.0 Chapter 2 – Materials and Methods

2.1 Chemicals and reagents

Chemical or Reagent	Catalogue Number	Supplier or Manufacturer
(3-Aminopropyl) triethoxy-silane (minimum 98%)	A-3648	Sigma-Aldrich (St. Louis, USA)
10% Neutral Buffered Formalin (NBF)	NBF-5L	Amber Scientific (Midvale, WV, Australia)
25% Ammonia Solution (aqueous ammonia)	4.10011.2500	Merk (Hohenbrunn, Germany)
Acrylamide	814349	ICN Biomedicals (Irvine, USA)
Ammonium Acetate	1112914 33504101	FlukaChemme GmbH (Germany)
D-Glucose	101805	Univar Ajax Chemicals (N.S.W., Australia)
Gelatine (G-2500)	2500-500G	Sigma-Aldrich (St. Louis, USA)
N'N-methylenebisacrylamide (BIS)		Sigma-Aldrich (St. Louis, USA)
Paraformaldehyde or PFA	8.18715.10000	Merck-Schuchardt (Hohenbrunn, Germany)
Sodium Azide	0313620	BDH Ltd., (England)

Table 2.1: List of chemicals and reagents used.

2.2 Kits used in *in vitro* experiments

Kit	Catalogue Number	Supplier
BD Pharmingen™ Annexin V-PE Apoptosis Detector Kit I	559763	BD Biosciences (San Diego, USA)
CellTiter 96 Aqueous One Solution Cell Proliferation kit	G3580	Promega (Madison, USA)
FluoroTag™ FITC Conjugation Kit	FITC1-1KT	Sigma-Aldrich (San Diego, USA)
Human Inflammatory Cytokine Kit BD™ Cytometric Bead Array (CBA)	551811	BD Biosciences (San Diego, USA)
Mouse Inflammation Kit BD™ Cytometric Bead Array (CBA)	552364	BD Biosciences (San Diego, USA)

Table 2.2: A list of kits purchased and used in *in vitro* experiments.

2.3 Antibodies and conjugates

Antibody or Conjugate	Catalogue Number	Supplier
Recombinant Murine Antibodies		
CD11c (APC)	550261	BD Pharmingen™ (BD Biosciences, San Diego, USA)
CD197(CCR7) (PE)	560682	BD Pharmingen™ (BD Biosciences, San Diego, USA)
CD86 (PE)	553692)	BD Pharmingen™ (BD Biosciences, (San Diego, USA)
Recombinant Human Antibodies		
Lineage Cocktail 1 (FITC)	340546	BD Biosciences (San Diego, USA)
HLA-DR (APC-Cy™7)	335831	BD Biosciences (San Diego, USA)
CD123 (APC)	560087	BD Pharmingen™ (BD Biosciences, (San Diego, USA)
CD14 (V500)	562693	BD Biosciences (San Diego, USA)
CD11c (PE-Cy™7)	561356	BD Biosciences (San Diego, USA)
CD80 (FITC)	557226	BD Pharmingen™ (BD Biosciences, (San Diego, USA)
CD83 (FITC)	556910	BD Pharmingen™ (BD Biosciences, (San Diego, USA)
CD83 (PE-Cy™5)	551058	BD Pharmingen™ (BD Biosciences, (San Diego, USA)
CD86 (APC)	555660	BD Pharmingen™ (BD Biosciences, (San Diego, USA)
Fluorescein Isothiocyanate Isomer I (FITC)	F7250-250MG	Sigma-Aldrich (St. Louis, USA)
R-Phycoerythrin (R-PE)	P801	Life Technologies (Carlsbad, USA)

Table 2.3: A list of antibodies and conjugates used.

2.4 Tissue culture reagents, drugs and equipment

Tissue culture media, reagents, drugs or equipment	Catalogue or serial or model number	Supplier or manufacturer
1.5 ml microtube	72.690.001	Sarstedt (Numbrecht, Germany)
1.5 Telsa Whole Body Clinical MRI Scanner	Siemens Trio Magnetom	Siemens Medical Solutions (Erlangen, Germany)
15 ml sterile tube Corning®CentriStar™	430791	Corning Incorporated (NY, USA)
3ml Pasteur Pipette	200CS01	Copan S.p.A. (Brescia, Italy)
3.0 Telsa Whole Body Clinical MRI Scanner	Siemens Trio Magnetom	Siemens Medical Solutions (Erlangen, Germany)
50 ml sterile tube Corning®CentriStar™	430829	Corning Incorporated (NY, USA)
6 well, well plate F-bottom	3516	Costar, Corning Incorporated (NY, USA)
24 well, well plate	662.160	Greiner Bio-one Cellstar (Frickenhausen, Germany)
^{68}Ga Generator		iThemba LABS (Somerset West, RSA)
96 well, well plate (V-bottom)	651101	Greiner Bio-one (Frickenhausen, Germany)
Mice	C57/BL6	Animal Resources Centre (Perth, Australia)
Atomic absorption spectrometer (AAS)	Varian AA280FS Fast Sequential	Varian (California, USA)
BD Falcon FACS tubes	352008	BD Biosciences (San Diego, USA)
BD Falcon cell strainer	352360	BD Biosciences (San Diego, USA)
Bovine Serum Albumin	A7906-100G	Sigma-Aldrich (St. Louis, USA)
Carbon coated copper grids	GYCu200	ProSciTech (Thuringowa, QLD, Australia)
Centrifuge	Allegra X-22	Beckman Coulter (California, USA)
Blood serum biochemical immunoassay analyser	Abbott Architect Plus ci4100	Roche Diagnostics (Melbourne, Australia)
DMEM cell media	11965-092	Gibco® by life technologies™ (NY, USA)
Dotarem® contrast agent for MRI	Batch 14GD008B	Guerbet (Aulnay-sous-bois, France)
DPX with colour fast mounting media	11023DPX	Fronine (Rivertone, Australia)
DTPA Anhydride (Diethylenetriaminepenta – Acetic Acid Anhydride)	D-6148	Sigma-Aldrich (St. Louis, USA)
Endotoxins Meter	4108	Charles River Laboratories Endosafe-PTS

Eppendorf Mini Spin Plus Centrifuge		Eppendorf (Hamburg, Germany)
FACS Canto™ II Flow Cytometer	V96300723	BD Biosciences (San Jose, CA, U.S.A.)
Fetal bovine serum	SFBS-F	Bovogen Biologicals (Victoria, Australia)
Ficoll®-Paque Premium	GE17-5442-02	GE Healthcare Bio-Sciences AB, Sweden)
Fluorescent mounting medium	S3023	Dako Australia Pty Ltd (N.S.W., Australia)
FluoroDish™ (flat bottom glass)	FD35COL	World Precision Instruments (Sarasota, USA)
Growth factor Murine GM-CSF	315-03	PeproTech (Rocky Hill, USA)
Growth factor Murine Flt3	250-31L	PeproTech (Rocky Hill, USA)
Growth factor Human GM-CSF	215-GM	R&D Systems (Minneapolis, USA)
Growth factor Human IL-4	204-IL	R&D Systems (Minneapolis, USA)
Growth factor Human IL-4	200-04	PeproTech (Rocky Hill, USA)
Haematocrit capillary tubes	9100175	Hirschmann Laborgerate (Eberstadt Germany)
Haemocytometer	Depth 0,100nm 0,0025 mm^2	Hirschmann EM Techcolor (Heilbronn, Germany)
HEPES 1M Buffer Solution	15630-80	Gibco® by life technologies™ (NY, USA)
Histopathology Tissue Processor	ASP 200 S	Leica Biosystems (NSW, Australia)
Incubator – animal cells	Heat Force® THF-212-UV	Thermoline L+M (NSW, Australia)
Incubator – human cells	Heraeus BB15	Thermo Scientific (NSW, Australia)
Lipopolysaccharides	L4391-1MG	Sigma-Aldrich (St. Louis, USA)
Magnetic hot plate and Stirrer	CH 2091.001	U-Lab (Eltham, Australia)
Menzel-Glaser Superfrost® Plus Microscope Slides (25x75x1.0mm)	SF41296SP	Lomb Scientific Pty Ltd (NSW, Australia)
Microscope	Nikon TMS 300 754	Grale Scientific (Melbourne, Australia)
Microscope Cover Glass (22x22mm)	CCS2222100	Mikro-Glass (Australia)
Microtome	RM 2235	Leica Microsystems Nussloch GmbH (Germany)
Murine FLT-3 Ligand	250-31L	PeproTech (Rocky Hill, USA)
Murine GM-CSF Ligand	315-03	PeproTech (Rocky Hill, USA)
Orbital mixer	EOM5	Ratek Instruments Pty Ltd

	206127780	(Victoria, Australia)
Penicillin/Streptomycin	15070-063	Gibco (Invitrogen) (Aukland, New Zealand)
Petrie Dish	616201	Greiner Bio-one (Frickenhausen, Germany)
Phosphate Buffered Saline (PBS)	21600-010	Invitrogren Corporation (New Zealand)
Qualtex drying oven	Model 70, Serial 3964.1	Watson (Victoria, Australia)
Radio-isotope Dose Calibrator	CRC-15PET	CAPINTEC Inc. (USA)
Ratek water bath	WB20D	Ratek Instruments Pty Ltd (Victoria, Australia)
RPMI 1640 cell media	11875-093	Gibco® by life technologies™ (NY, USA)
Sartorius Weigh Scale	BP211D	Sartorius AG (Gottingen, Germany)
Scanning Electron Microscope	Nova NanoSEM™	FEI (Oregon, USA)
Small Animal PET Scanner	MOSAIC Animal Imaging	Philips Healthcare (DA Best, The Netherlands)
Sonicator	00002939	Thermoline Scientific (N.S.W., Australia)
Sterilizer (autoclave)		Siltex (Bentleigh East, Australia)
Thin layer chromatography scanner	Rita Star TLC-01 2003123	Raytest (Straubenhardt, Germany)
Tissue/Wax Embedding Centre workstation	Shandon Histocentre™ 3	Thermo Electron Corporation (Madison, USA)
Transmission Electron Microscope	JEOL 2010 EM 135 003-8	JEOL (Tokyo, Japan)
Trypan blue solution (1.4%)	T8154	Sigma-Aldrich (St. Louis, USA)
Trypsin-EDTA solution (0.25% trypsin, 1 mM EDTA)	25200-056	Gibco® by life technologies™ (NY, USA)
Vacutte with K2EDTA	10ml	Greiner Bio-one (Frickenhausen, Germany)
Water bath	WB20 D	Ratek Instruments (Boronia, Australia)
Weigh scale	HR-200 12304600	A and D Company (Tokyo, Japan)
X-ray Diffractometer	Bruker D8 ADVANCE	Bruker Corporation (Massachusetts, USA)
Whatman® filter paper	1001 090	GE Health Care (Pittsburgh, USA)
Zetasizer	Malvern Nano-ZS ZENN3600 MAL1073053	Malvern Instruments (Worcestershire, England)

Table 2.4: A list of tissue culture reagents, drugs and equipment used in the laboratory.

2.5 Software for analyses

Software	Version	Provider
ImageJ	1.48v	National Institutes of Health (U.S.A.)
GraphPad Prism	6.05	GraphPad Software Inc.(U.S.A.)
Microsoft Excel	Microsoft Office Home & Student 2013	Microsoft Corporation (U.S.A.)

Table 2.5: A list of software programs used to analyse data throughout this thesis.

2.6 Human Cells

2.6.1 Monocyte derived dendritic cells (Mo-DC)

Monocytes were obtained from peripheral blood mononuclear cells (PBMC). To isolate the PBMC, the buffy coat was separated from whole blood of healthy donors by using a gradient centrifugation technique with Ficoll®-Paque Premium (Sigma-Aldrich, St. Louis, USA) (described in section 2.6.4).

A cell count was performed using trypan blue (Sigma-Aldrich, St. Louis, USA) and a haemocytometer (Hirschmann EM Techcolor, Heilbronn, Germany). In a fume hood, $1.5x10^6$ cells per ml were cultured in complete RPMI 1640 (Gibco® by life technologies™, NY, USA) cell media in a 6 well plate (Costar, Corning Incorporated, NY, USA). A total of $4.5x10^6$ cells in 3ml were placed in each well and 20ng/ml (w/v) of GM-CSF (R&D Systems, Minneapolis, USA) and 20ng/ml (w/v) of IL-4 recombinant cytokines (R&D Systems, Minneapolis, USA) were added and placed in an incubator (Heraeus BB15, Thermo Scientific, NSW, Australia) at 37 ^oC and 5% CO_2. At the end of third day, the well plate was removed from the incubator, placed in a fume hood and the spent media was carefully removed with a sterile pipette. Fresh complete media and cytokines were added and the well plate returned to the incubator where they remained for three further days; making a total of 6 days. On the seventh day, the *in vitro* experimental process commenced with the Mo-DC.

2.6.2 Buffy coat

Ethics approval (Project Number 19/13) was received from the Human Research Ethics Committee at RMIT University to approach the Australian Red Cross Blood Service and request orders for buffy coats. Once the order was approved, the buffy coat was collected from the Australian Red Cross Blood Service.

The buffy coat was collected from the Australian Red Cross Blood Service the night before the experimental procedure. The Australian Red Cross Blood Service provided the buffy coat (approximate volume of 50 ml) in a plastic collection bag, tagged with record numbers; placed in a polystyrene foam package and placed in a cardboard box. This was kept overnight at room temperature, until the experimental process commenced in the morning. The first step was always gradient centrifugation technique with Ficoll®-Paque Premium (GE Healthcare Bio-Sciences AB, Sweden), described in Section 2.5.4. Once the white blood cell components were isolated, *in vitro* experiments were undertaken.

2.6.3 Blood from volunteers

Adult consenting colleagues volunteered to provide a sample of approximately 15 ml of whole blood. Blood was withdrawn by experienced and qualified personnel within the Haematology Department, RMIT University. The date that this occurred and the name of the volunteer were recorded in the log book in the Haematology Blood Collection Room. Whole blood was collected in a vacuette (Greiner Bio-one, Frickenhausen, Germany) containing K_2EDTA to prevent coagulation. The blood then underwent gradient centrifugation technique with Ficoll®-Paque Premium (described in Section 2.5.4) so that the white blood cell component was isolated for *in vitro* experiments.

2.6.4 Separation by Ficoll®-Paque Premium gradient centrifugation

The following gradient density separation technique was used to isolate the white blood cell components; from either the buffy coat supplied from the Australian Red Cross Blood Service or from whole blood kindly donated by consenting colleagues at RMIT University.

Either whole blood or buffy coat was transferred into two sterile 50 ml tubes, with equal volume of blood in each tube. A volume of sterile PBS (Invitrogren Corporation, New Zealand), equivalent to the volume of whole blood or buffy coat in each tube was added to each 50 ml tube. The contents of one tube (sterile PBS with either whole blood or buffy coat) was slowly and carefully transferred (with pipette controller and glass pipette) into another 50 ml tube that already contained 15ml of Ficoll®-Paque Premium. This was repeated with the other 50 ml tube (containing sterile PBS with either whole blood or buffy coat). Both of these tubes were then removed from the fume hood and placed in a centrifuge (Beckman Coulter, California, USA) and spun at 1,500 rpm (433 rcf) for 30 minutes; no brake was used to stop the centrifuge spinning at the end of the 30 minute period.

White blood cells (PBMC) were collected, transferred into a new sterile 50ml tube and washed a further two times with sterile PBS (first wash was at 2,000 rpm, 771 rcf, for 15 minutes and the second wash was at 1,800 rpm, 624 rcf, for 10 minutes). On completion of all washes, the PBMC pellet was resuspended in 10ml of complete media and a cell count performed.

2.6.5 Dose response with R-PE tagged dextran coated iron oxide nanoparticles

Mo-DC were generated as discussed in Section 2.5.1. In a 6 well, well plate containing 4.5 x 10^6 per 3 ml. Different concentrations of nanoparticles (200 µg/ml, 100 µg/ml, 50 µg/ml, 20 µg/ml, and 5 µg/ml) were added. A control well with no nanoparticles was included for all experiments. Nanoparticles tagged with R-PE (Life Technologies, Carlsbad, USA) were sonicated (Thermoline Scientific, NSW, Australia) for 10 minutes, prior to being added to the Mo-DC cultures and incubated for 24 hours.

Following incubation, the supernatant was carefully removed, placed in a labelled microtube (Sarstedt, Numbrecht, Germany) and then stored at -80 ^{o}C for further cytokine analysis. Mo-DCs were removed using sterile PBS to. Collected Mo-DCs were centrifuged at 1,500 rpm (433 rcf) for 5 minutes, the supernatant discarded and resuspended in 0.5% BSA/PBS (w/v). Mo-DCs were added to a sterile 96 well v-bottom well plate (Greiner Bio-one) and centrifuged at 1,500 rpm (433 rcf) for 5 minutes.

The supernatant was discarded and 0.5% BSA/PBS (w/v) antibody were added and incubated at 4 ^{o}C for 30 minutes. Following incubation, cells were centrifuged at 1,500 rpm (433 rcf) for 5 minutes, supernatant discarded and cells resuspended in FACS fix for flow cytometry analysis (FACSCanto II, BD Biosciences, San Jose, USA).

2.6.6 Dose response with FITC tagged dextran coated iron oxide nanoparticles

Monocyte derived dendritic cells (Mo-DC) were generated as discussed in section 2.5.1. In a sterile 6 well plate containing 4.5 x 10^6 cells in 3 ml, different conditions of nanoparticles (200 µg/ml, 100 µg/ml, 50 µg/ml, 20 µg/ml, and 5 µg/ml) were added. A control well with no nanoparticles was included for all experiments. Nanoparticles tagged with FITC (Sigma-Aldrich, St. Louis, USA) were sonicated for 10 minutes, prior to being added to MoDC cultures and incubated for 24 hours.

Following incubation, the supernatant was carefully removed, placed in a labelled micro tube and then stored at -80 ^{o}C for further cytokine analysis. MoDCs were removed using sterile PBS to lift off any cells adhering to the bottom of each well. Collected MoDCs were centrifuged at 1,500 rpm (433 rcf) for 5 minutes, the supernatant then discarded and resuspended in 0.5% BSA/PBS (w/v). MoDCs were added to a sterile 96-well v-bottom well plate and centrifuged at 1,500 rpm (433 rcf) for 5 minutes. The supernatant was discarded and 0.5% BSA/PBS (w/v) antibody were added and incubated at 4 ^{o}C for 30 minutes. Following incubation, cells were centrifuged at 1,500 rpm (433 rcf) for 5 minutes, supernatant discarded and cells resuspended in FACS fix for flow cytometry analysis.

2.6.7 Time course with FITC

Monocyte derived dendritic cells (Mo-DC) were generated as discussed in section 2.5.1. In a sterile 6 well plate containing 4.5 x 10^6 cells in 3 ml, six conditions were established: one well served as a control and received no nanoparticles; the remaining wells received 200 µg/ml of

FITC tagged nanoparticles at different time points (24 hours, 18 hours, 6 hours, 4 hours and 1 hour). The nanoparticles were sonicated for 10 minutes, prior to being added to MoDC cultures and then incubated for 24 hours.

On completion of the treatment periods, the supernatant was carefully removed, placed in a labelled micro tube and then stored at -80 ^{o}C for further cytokine analysis. MoDCs were removed using sterile PBS was used to lift off any cells that had adhered to the bottom of each well. Collected MoDCs were centrifuged at 1,500 rpm (433 rcf) for 5 minutes, the supernatant discarded and resuspended in 0.5% BSA/PBS (w/v). MoDCs were added to a sterile 96 well v-bottom well plate; 2 x 200 µl from each tube (representing each original condition). Therefore, each original condition (from the flat bottom 24 well plate) was divided into two (and placed in a 96 v-bottom well plate). The 96 well plate was then centrifuged at 1,500 rpm (433 rcf) for 5 minutes and the supernatant was then discarded.

One well of each original condition, was resuspended with 200 µl of cold 0.5% BSA/PBS (w/v) and the other corresponding condition was resuspended with 200 µl of cold 0.5% BSA/PBS (w/v) that contained antibody. The 96 well plate was then incubated at 4 ^{o}C for 30 minutes. Following incubation, cells were centrifuged at 1,500 rpm (433 rcf) for 5 minutes, supernatant discarded and cells resuspended in FACS fix for flow cytometry analysis.

2.6.8 Human Inflammatory Cytometric Bead Array (CBA) Analyser

Supernatant from specified (dose response and time course) *in vitro* human experiments were stored at -80 ^{o}C. Frozen samples were thawed and used to assess cytokine levels by CBA analysis (BD™ Cytometic Bead Array, BD Biosciences, San Diego, USA) as per

manufacturer's instructions and read on flow cytometry. The specific cytokines analysed were: IL-8, IL-1β, IL-6, IL-10, TNF and IL-12p70.

2.6.9 Nanoparticle uptake in whole PBMC and peripheral blood dendritic cell subsets, *in vitro*

Blood was withdrawn from volunteers as described in Section 2.5.3 and was then followed by Ficoll®-Paque Premium gradient centrifugation as discussed in Section 2.6.4.

Peripheral blood mononuclear cells (PBMC) were suspended in complete RPMI 1640 media and set up in sterile 6 well plates and the following uptake conditions were investigated: control (no nanoparticles), 200 µg/ml of R-PE tagged nanoparticles, 100 µg/ml of R-PE tagged nanoparticles, 200 µg/ml of FITC tagged nanoparticles and 100 µg/ml of FITC tagged nanoparticles; incubated at 37 ^{o}C with 5% CO_2 for 24 hours.

Following incubation, the supernatant was carefully removed and stored at -80 ^{o}C. Sterile PBS was used to resuspend cells and lift them off the bottom of each well and centrifuged at 1,500 rpm (433 rcf) for 5 minutes. The cells were re-suspended in 0.5 % BSA/PBS (w/v) with the following conditions: control (no nanoparticles), 200 µg/ml of R-PE tagged nanoparticles and 100 µg/ml of R-PE tagged nanoparticles control. 200 µl from each condition was placed in 9 wells of a 96 well v-bottom well plate. The cells in the following conditions were resuspended in 400 µl of 0.5 % BSA/PBS (w/v): 200 µg/ml of FITC tagged nanoparticles, 100 µg/ml of FITC tagged nanoparticles – and 200 µl from each condition was placed in 2 wells of the same 96 well v-bottom well plate.

The 96 well plate was then centrifuged again at 1,500 rpm (433 rcf) for 5 minutes, the supernatant discarded and the cells stained with the following antibody combinations: Control (no stain), Lin 1, HLA-DR, CD11c, CD123, CD14, mix*, CD80 and CD83. The mix* treatment was composed of Lin 1, HLA-DR, CD11c and CD123. The antibodies were suspended in cold 0.5 % BSA/PBS (w/v). All stains were from BD Biosciences, San Diego, USA.

The cells were incubated at 4 ^{o}C for 30 minutes. Following incubation, cells were washed in PBS and centrifuged at 1,500 rpm (433 rcf) for 5 minutes, fixed in FACS fix buffer and analysed by flow cytometry.

2.7 Mice

All mice used were approved for experimental use by the RMIT University Animal Ethics Committee (AEC1210 and AEC1320). Female C57/BL6 mice aged between 8 and 12 weeks, supplied by Animal Resources Centre (Perth, Australia) were used for all experiments and experimental mice were allowed to acclimatise for 48 hours within the RMIT Animal Facility before any procedures were performed.

A maximum of 4 mice were housed in standard sized cages for “tissue mice” used for stem cell extraction and subsequent *in vitro* experiments (AEC 1210); with approval for these mice to be killed by CO_2 asphyxiation.

For *in vivo* experiments (project number AEC 1320), C57BL/6 mice were housed in larger cages, at a maximum of 5 mice per cage; with approval for these mice to be killed by the

Vascular Perfusion Technique under strong intraperitoneal anaesthesia provided by sodium pentobarbitone.

2.7.1 Method of killing mice approved by RMIT University Animal Ethics Committee

RMIT University Animal Ethics Committee (AEC) provided the following approval for killing mice.

For *in vitro* experiments approved under AEC 1210, tissue mice were killed by CO_2 asphyxiation. The cage housing 4 mice were collected from the housing room and brought into one of the procedure rooms, of the RMIT Animal and Aquatic Facility. A CO_2 cylinder was connected to a Perspex box positioned on a bench top. CO_2 was allowed to fill this Perspex box. After several minutes, one of the 4 mouse was collected from the housing cage and placed into the CO_2 filled Perspex box. One minute after the mouse stopped moving, paw reflexes were tested and signs of breathing cessation were scrutinised. When no response was observed, the mouse was removed from the CO_2 filled Perspex box and placed in an opaque carrying container. The mice in the housing cage were not able to observe these events and were returned to the housing room. The killed mouse in the opaque carrying container was brought to the laboratory for bone marrow stem cell extraction, as described in Section 2.10.

For *in vivo* experiments approved under AEC 1320, C57BL/6 mice were housed in larger cages, at a maximum of 5 mice per cage; with approval for these mice to be killed by the Vascular Perfusion Technique under strong intraperitoneal anaesthesia provided by sodium pentobarbitone. Anaesthesia was provided by intraperitoneal injection of sodium pentobarbitone, 150 mg/kg, using a 25 gauge needle; and the standard method of Vascular Perfusion Fixation was performed by an experienced researcher. Once the mouse appeared

anaesthetised, its reflexes were assessed to ensure that the mouse was fully anaesthetised; and the vascular perfusion fixation procedure commenced as described in Section 2.12.2.

2.8 Buffers and solutions

The following buffers and solutions were used in various experimentations, *in vitro*, throughout the PhD project.

2.8.1 FACS fix buffer

FACS fix is a cell preserving fixative used to suspend cells for analysis by flow cytometry.

As needed, a total volume of 500ml FACS fix was made using the following substances and technique. 10 g of 2 % glucose (Univar Ajax Chemicals, NSW, Australia), 100 mg of 0.02 % sodium azide (BDH Ltd, England) and 5 g of PFA (Merck-Schuchardt, Hohenbrunn, Germany) were each weighed and placed in a clean laboratory jar. This jar was filled to the 500ml indicator mark with PBS (pH of 7.4). A magnetic stir bar was placed in this jar and a clean cap screwed in place. The jar and contents were placed on a magnetic plate (U-Lab, Eltham, Australia) and stirred until dissolved – as determined by visual inspection of no particulate matter.

2.8.2 Phosphate buffered saline

Phosphate Buffered Saline (PBS) (GIBCO™ Invitrogen Corporation, New Zealand) without calcium and magnesium was prepared as per manufacturer's instructions.

2.8.3 0.5% BSA/PBS (w/v) buffer

This buffer was used to wash and suspend cells when preparing them for antibody surface staining; for flow cytometry.

When required, a total volume of 500 ml was prepared. 0.5 % weight per volume of BSA (Sigma-Aldrich, St. Louis, USA) was used. 2.5 g ((0.5/100) x 500 ml) of BSA was weighed and placed in a clean laboratory jar. A magnetic stirrer was placed in the jar and a clean cap screwed in place. This jar was filled to the 500 ml indicator mark with PBS (pH of 7.4). The jar and contents were placed on a magnetic plate and stirred until dissolved. This was determined visually when no particulate matter was apparent.

2.8.4 2% PFA/PBS (w/v)

2 % PFA was used for cell preservation and the cells were imaged with confocal microscopy.

When required, a total volume of 50 ml was prepared. 2 % weight per volume of PFA (Merck-Schuchardt, Hohenbrunn, Germany) was used. One gram ((2/100) x 50 ml) of PFA was weighed and placed in a clean laboratory jar. A magnetic stirrer was placed in this jar and a clean cap screwed in place. This jar was filled to the 50 ml indicator mark with PBS (pH of 7.4). The jar and contents were placed on a magnetic plate and stirred until dissolved. This was determined visually when no particulate matter was observed.

2.9 Iron oxide nanoparticles (IONPs)

Following a review of the relevant literature, it was determined that superparamagnetic iron oxide nanoparticles (SPIONs) with a coating of low molecular weight dextran (10,000 Daltons, also referred to as T10) would be suitable; provided that the overall dimension of the SPION would not exceed 50 nm. Vipul Bansal and Jos Campbell from the Department of Applied Chemistry at RMIT University were approached for their expertise and such particles were manufactured.

2.9.1 Synthesis, dextran coating and characterisation

The iron oxide core, magnetite (Fe_3O_4), were produced using a technique based on that published by Park *et al* and with modifications introduced by Campbell and Bansal.

Iron chloride and sodium oleate were combined in a solution of ethanol, distilled water and hexane; to form an iron oleate. To create the iron oleate, the solution was refluxed for 4 hours at 70 ^{o}C. A separatory funnel system was then used to collect the upper organic layer, which then was washed and the hexane evaporated away.

The iron oleate was then dissolved with oleic acid and 1-octadescene and then refluxed under nitrogen gas conditions; which occured at 320 ^{o}C for 30 minutes and then allowed to cool to room temperature. Ethanol was then added to the room temperature solution and the Fe_3O_4 magnetite particles were separated by centrifugation with three ethanol wash cycles. T10 dextran was then coated onto the iron oxide nanoparticles by heating them, along with the dextran, in an aqueous medium. The diameter of the iron oxide core was measured at 15 nm and together with the T10 dextran coating, the overall dimension of the SPIONs were 20 nm; with Transmission Electron Microscopy (TEM).

2.9.2 Characterisation

Assessments were performed to characterise these specialty produced IONPs. Iron content quantification was assessed with atomic absorption spectrometer (AAS) (Varian, California, USA). The sample was atomised by flames at a temperature of at least 2,200 ^{o}C. The atomiser aerosol contained iron atoms and their electrons were excited to a higher energy state by absorbing energy delivered by a known wavelength. The selectivity of AAS was provided by such a wavelength, as it delivered a defined quantity of energy to allow the electrons to transition to a higher energy state (in a known element). The wavelength then continued through to monochromators to select and transmit the iron specific wavelength to a detector. The Beer-Lambert Law was then used to quantify the iron content of the sample.

X-Ray Diffraction (XRD) spectra were collected at room temperature using a Bruker D8 ADVANCE X-Ray Diffractometer (Bruker Corporation, Massachusetts, USA). The sample was air dried at room temperature, placed onto the glass sample holder and then irradiated with copper k-alpha radiation with a wavelength of 1.5418 nm. The diffraction patterns were measured at 40 kV with 35 mA. Spectral peaks were determined by computer integration of the diffraction patterns.

To measure the diameter of the iron oxide nanoparticle with the T10 dextran coating, transmission electron microscopy (TEM) was performed with a JEOL 2010 TEM (JEOL, Tokyo, Japan) that used a lanthanum boron six crystal as its electron source. In a fume hood, ten µl of colloid suspension of the dextran coated iron oxide nanoparticles was pipetted onto the carbon coated surface of the 3mm diameter copper holey grid. The grid was placed onto Whatman filter paper (copper surface was in contact with the Whatman filter paper); these were placed in one of the wells of a sterile 24 well plate and allowed to dry overnight. The copper grid was loaded into the JOEL2010 TEM as instructed and transmission electron microscopy performed.

To observe the surface of the T10 dextran coating, scanning electron microscopy (SEM) was performed using a FEI Nova Nano SEM, (FEI, Oregon, USA). An aluminum circular mounting disc was prepared with a circular double sided sticking carbon tape and twenty µl of the colloid suspension of the dextran coated iron oxide nanoparticles was pipetted onto the circular double sided sticking carbon tape. This was allowed to air dry at room temperature for 1 hour. Pressurised air was sprayed onto the prepared surface to dislodge any particles that had not adhered to the carbon tape. The mounting disc was loaded into the vacuum chamber and SEM imaging performed.

The surface charge was assessed with a Malvern Zetasizer Nano (Malvern Instruments, Worcestershire, England). Dextran coated iron oxide nanoparticles were stored under

different conditions and their surface charge determined. The particles were first sonicated for 10 minutes, then transferred to the dedicated cell chamber and inserted into the Zetasizer Nano unit. The feature to read nanoparticle surface charge was selected and the data recorded. On completion, the dedicated cell chamber was removed from the unit and the solution containing nanoparticles was discarded.

The iron oxide nanoparticles were also observed for their behavioural characteristics (in a magnetic field environment) in response to a spin echo T_2 weighted pulse sequence. This assessment was performed on both a 1.5 T and 3.0 T clinical MRI scanner. Both scanners were made by Siemens (Erlangen, Germany), used the Syngo operating platform and had access to the same pulse sequence; referred to as: t2_se_COR_16-echoes. Different concentrations of nanoparticles were suspended in gel, in 15 ml plastic tubes (with screw tops). A plastic tube rack was glued into a rectangular plastic tub. When MRI scanning took place, these 15 ml tubes were positioned into the rack and the rectangular tub was filled with water. This volume of water provided three valuable functions; firstly, it provided sufficient MRI signal (hydrogen) to be detected (so that an image could be reconstructed); secondly, it provided image contrast adjacent to the 15 ml tubes containing nanoparticles in gel suspension, as the image appearance of the gel suspension was expected to change as the TE value (in the pulse sequence) increased; and thirdly, the water bath minimised and/or eliminated susceptibility artefacts from the air interface with tubes (that contained gel and nanoparticles).

The gel suspension was prepared in the following manner with the following ratio of ingredients: 59 % MilliQ water, 29 % iron oxide nanoparticles, 5 % gelatine (Sigma-Aldrich, St. Louis, USA), 3 % BISacrylamide (Sigma-Aldrich, St. Louis, USA) and 3 % acrylamide (ICN Biomedicals, Irvine, USA). This made a total volume of 100 ml gel suspension. Ten 15 ml plastic tubes were labelled and filled with varied concentrations of iron oxide

nanoparticles. The preparation procedure was conducted in a fume hood. Five grams of gelatine (G-2500), three grams of BISacrylamide and three grams of acrylamide were separately weighed. MilliQ water (59.333 ml) and 29.666 ml of iron oxide nanoparticles (also in MilliQ water) were also obtained. The MilliQ water was poured into a glass conical flask and placed on a magnetic hot plate and the temperature set to 50 ^{o}C. At temperature, a magnetic stirring bar was placed in the flask and the gelatine was firstly poured in slowly. Once the gelatine was dissolved, the BISacrylamide was added and when this also dissolved into the solution, acrylamide was finally added. When this final ingredient was dissolved, a pipette was used to collect a volume of 5 ml and mix (and resuspend) with the nanoparticles in the plastic tubes. The following table lists the volume of gel material and iron oxide nanoparticle. The concentration of nanoparticles was 1,000 µg/ml.

Percentage concentration of 29% volume for iron oxide nanoparticles	Volume of iron oxide nanoparticles (ml)	Volume of MilliQ Water to required to reach maximum 29% (1.67 ml) of total volume of 5 ml	Gel material (ml)	Total volume (ml)
100	1.67	0	3.33	5.0
90	1.5	0.167	3.33	5.0
80	1.33	0.331	3.33	5.0
70	1.17	0.498	3.33	5.0
60	0.99	0.665	3.33	5.0
50	0.832	0.832	3.33	5.0
40	0.665	0.999	3.33	5.0
30	0.498	1.17	3.33	5.0
20	0.331	1.33	3.33	5.0
10	0.164	1.5	3.33	5.0

Table 2.6: Percentages and volumes of materials used to compose the gel phantoms.

Ten concentration points were used, each 10 % apart from one another. This strategy was used in anticipation for ease of generating graphs and determining if T_2 decay times would be exponential or have a linear component. A further ten 15 ml tubes were filled with just gel material and no iron oxide nanoparticles. These ten tubes served as controls and were also imaged at 1.5 T and 3.0 T with the same pulse sequence.

The t2_se_COR_16-echoes pulse sequence was a Siemens specific pulse sequence whereby the TR was fixed at 3,000 ms and the TE varied from 22 ms to 352 ms with incremental values of 22 ms; therefore, generating 16 spin echoes (from 22 ms to 352 ms inclusive). The tubes filled with the combined gel and nanoparticles were imaged and so too were the control tubes (tubes filled with only gel and no nanoparticles). Coronal oriented sections were obtained and the contrast changes generated by the nanoparticles were assessed with ImageJ software, version 1.48v. Circular region of interest (ROI) areas (same size) were created and placed over the images of the gel (no nanoparticles) and gel with nanoparticles and their MRI signal intensity changes (if any) were measured in arbitrary units. These details were entered into a spreadsheet.

Firstly, T_2 decay changes were graphed from the ROI values and as the rate of change from one signal intensity (data point) to the next was known (22 ms), a power trendline was therefore used to assess the data points and understand the behaviour of the iron oxide nanoparticles suspended in gel. Secondly, from both sets of ROI measurements, calculations made using the following T2 signal intensity and relaxivity equation.

$$\text{SignalSE} = \text{SignalO}e^{(-R_2 \times TE)} \qquad \text{Equation 2.1}$$

Where:

Signal_{SE} is the spin echo signal (in arbitrary units) intensity that results from a contrast agent; thus, the ROI signal intensity measured with ImageJ over the gels with nanoparticles;

$Signal_O$ is the signal intensity with no contrast material; thus, the ROI signal intensity measured with ImageJ over the gels with no nanoparticles (control tube corresponding to the same position in the rack as the tube gel and nanoparticles);

R_2 is the relaxation rate, or relaxivity; which is the inverse if T_2 ($R_2 = 1/T_2$); and,

TE is the echo time at which $Signal_{SE}$ and $Signal_O$ were measured.

To calculate a value for R_2, Equation 2.1 was solved and transposed as follows:

$$Signal_{SE} = Signal_O e^{(-R_2 \text{ x } TE)}$$

$$\ln(Signal_{SE}) = \ln(Signal_O e^{-R_2 \text{ x } TE})$$

$$\ln(Signal_{SE}) = \ln Signal_O + In(e^{-R_2 \text{ x } TE})$$

$$In(Signal_{SE}) = (InSignal_O) - (R_2 \text{ x } TE)$$

$$In(Signal_{SE}) - (InSignal_O) = - (R_2 \text{ x } TE)$$

$$(In(Signal_{SE}) - (InSignal_O)) / (- TE) = R_2 <=> 1 / T_2$$

$$R2 = (In(SignalSE) - (InSignalO)) / (-TE) <=> 1 / T2$$

These calculations were performed for all tube samples that contained iron oxide nanoparticles at every TE value ranging from 22 ms to 352 ms inclusive. The relaxivity, or rate of change from one time point to the next, denoted with ΔR_2 was also graphed.

2.9.3 Functionalising amine chain on T10 dextran

To facilitate conjugations with FITC, R-PE, DTPA Anhydride (Sigma-Aldrich, St. Louis, USA) and radiolabelling with ^{68}Ga, the amine chain on the dextran coating was functionalised.

The process commenced with a stock concentration of 1,000 µg/ml per ml of dextran coated iron oxide nanoparticles. These were sonicated for 10 minutes until well dispersed. In a fume hood, 10 ml of the stock solution was collected and transferred into a sterile 50 ml tube. This was placed in a centrifuge (along with another 50 ml containing water, for balance) at 8,000 rpm for 10 minutes. At completion of this centrifugation step, the supernatant was discarded and 20 ml of ethanol (99%) was added. This was then sonicated for 10 min (until well dispersed). 2 ml of 28 % aqueous ammonia was then added and also 500 µl of (3-Aminopropyl) triethoxy-silane (minimum 98%). The tube was then placed on a rotary shaker for 2 hours at room temperature.

2.9.4 Conjugating FITC to IONP

At the completion of process described in Section 2.8.3, once the tube had completed two hours on the rotary shaker at room temperature; the tube was removed and placed in a centrifuge at 8,000 rpm for 10 minutes (along with a balance tube).

The buffer used to dissolve the FITC powder and to buffer the conjugation reaction was provided in the FluoroTag™ FITC Conjugation Kit and prepared, as per manufacturer's instructions (Sigma-Aldrich, St. Louis, USA). Simply, the contents of one capsule was added

to 50 ml of deionized water and vortexed until dissolved; thus 0.1 M solution of sodium carbonate-bicarbonate buffer that had a pH of 9.0 was produced.

Following 10 minutes of centrifugation, the supernatant was removed, a wash performed with 0.1 M solution of sodium carbonate-bicarbonate buffer (pH of 9.0) and then placed in a sonicator for less than 10 minutes, until well dispersed, as observed visually. A lesser duration of sonication was needed at this point, as the functionalised amine permitted the nanoparticles to disperse more readily. Following sonication, the tube was centrifuged again at 8,000rpm for 10 minutes, the supernatant was removed and 2 ml of buffer added (0.1 M solution of sodium carbonate-bicarbonate buffer having a pH of 9.0). This was then sonicated for 5 minutes until well dispersed.

The FITC was then prepared by carefully weighing 1 mg of FITC power and adding 1 ml of 0.1 M solution of sodium carbonate-bicarbonate buffer (pH of 9.0). The sample was vortexed until the FITC powder dissolved. IONP dispersed in 2 ml of buffer was then placed on a vortex at very low speed and the 1 ml of dissolved FITC solution was added to the nanoparticles drop-wise. The 50 ml tube with the IONP and FITC sample was then covered with aluminium foil placed on a gentle stirrer for 2 hours at room temperature. At the completion of that step, the IONP-FITC conjugation was stored at 4 ^{o}C until required.

2.9.5 Conjugating R-PE to IONP

The amine chain on the T10 dextran coating was functionalised as described in Section 2.8.3. The IONP were further prepared as per Section 2.3.4 with the exception of not adding

dissolved FITC; instead, R-PE was added as received from the supplier (Life Technologies, Carlsbad, USA) without any modification.

2.9.6 Conjugating DTPA Anhydride

DTPA Anhydride (Sigma-Aldrich, St. Louis, USA) was conjugated to both iron oxide nanoparticles that had the T10 amine chain functionalised as per Section 2.8.3 and also to the same nanoparticles that had already been conjugated with FITC as described in Section 2.8.4.

1 mg of DTPA Anhydride was weighed and added to 500 µl of colloid suspension of either nanoparticle preparation. The sample was vortexed until the DTPA Anhydride powder was dissolved (less than 30 seconds), was wrapped in aluminium foil and placed on a shaker at room temperature for a minimum of two hours.

2.9.7 Radiolabelling with ^{68}Ga (IONP + DTPA Anhydride + ^{68}Ga)

Following the methodology discussed in section 2.8.6, IONPs were centrifuged at 14,000 rpm for 5 minutes and the buffer supernatant removed and replaced with an equivalent volume of 0.5 M ammonium acetate (FlukaChemme GmbH, Germany). This was repeated three times. On the third instance, the ammonium acetate supernatant was not replaced. Next, the gallium generator (iThemba LABS, Somerset West, RSA) was prepared. The lead shield was lowered and 3 ml of 5 M hydrochloric acid was used to flush and clean the generator tubes. This was followed with 3 ml of MilliQ water. Air was then pushed through the tubing to clear it of any MilliQ water. Germanium-68 (^{68}Ge) was the parent isotope, with a half-life of 271 days, and

the gallium generator was used to extract ^{68}Ga (a positron emitting isotope) from a sample of decaying ^{68}Ge. 5 ml ^{68}Ge was slowly infused through the tubing over a 1 minute period.

The elution process was then performed. 1 ml of Solution 1, or N1, was infused through the tubing and this was followed by 1 ml of Solution 2, or N2 – (N1 was a solution of 80 % acetone and 0.15 M of hydrochloric acid in MilliQ water and N2 was a solution of 97.56 % acetone and 0.05 M of hydrochloric acid in MilliQ water). Dislodgement occurred – the elution process dislodged ^{68}Ga from ^{68}Ge; along the column that was in between the two three-way-taps and that dislodgement process took approximately 2 minutes.

That process dispensed ^{68}Ga into a glass vial containing 1.5 ml of ammonium acetate and thus made gallium acetate. This occurred at a temperature of approximately 80 ^{o}C for about 5 minutes (to evaporate the acetone) and was performed until condensation was visualised in the neck of the glass vial. The tubing was then cleared by pushing through 3 ml of air. 500 µl of liquefied ^{68}Ga was added to the IONP sample and resuspened and placed behind lead bricks for an incubation period of 15 minutes. Thin layer chromatography (TLC) was then performed to assess bound ^{68}Ga from free (unbound) ^{68}Ga.

When radiolabelled (68Ga) dextran coated IONPs were to be administered to humans, an endotoxin screen was performed by the Quality Assurance Radio-Chemist with an endotoxins meter (Charles River Laboratories).

2.9.8 MTS assay

PBMC were extracted from human buffy coat by using the gradient centrifugation technique with Ficoll®-Paque Premium as described in Section 2.6.4. A cell count was performed using trypan blue and a haemocytomter, under microscopy. PBMC were then suspended in complete RPMI 1640 media (10% FBS, 2% HEPES buffer and 1 % Pen/Strep). Cells were seeded at 5.0 x 10^5 per ml. A 24 well plate was used to test the PBMC's response to varying concentrations of T10 dextran coated IONPs and a second 24 well plate was used to test the PBMC's response to equivalent concentrations of gadoteric acid, the gadolinium based MRI agent in Dotarem® (Guerbet, Aulnay-sous-bois, France). According to the product label, the concentration of gadotreric acid was 279.32 mg/ml. The equivalent concentrations tested are presented in table 2.7.

IONP (µg/ml)	200	100	50	20	5	0 (control)
Dotarem® (µg/ml)	72	40	20	7	2	0 (control)

Table 2.7: The equivalent doses of each contrast agent tested in µg/ml concentration values.

Each concentration of either the IONPs or the Dotaren® tested, was tested three times for each experiment, that is, in triplicate or three replicates; as demonstrated in Tables 2.8 and 2.9. Each treatment condition had a corresponding well that contained all components of the treatment condition minus the PBMCs; this served as the background value to be subtracted from the average triplicate values. This was each performed five times, n = 5.

Control 5.0×10^5 cells	200 µg/ml 5.0×10^5 cells	100 µg/ml 5.0×10^5 cells	50 µg/ml 5.0×10^5 cells	20 µg/ml 5.0×10^5 cells	5 µg/ml 5.0×10^5 cells
Control 5.0×10^5 cells	200 µg/ml 5.0×10^5 cells	100 µg/ml 5.0×10^5 cells	50 µg/ml 5.0×10^5 cells	20 µg/ml 5.0×10^5 cells	5 µg/ml 5.0×10^5 cells
Control 5.0×10^5 cells	200 µg/ml 5.0×10^5 cells	100 µg/ml 5.0×10^5 cells	50 µg/ml 5.0×10^5 cells	20 µg/ml 5.0×10^5 cells	5 µg/ml 5.0×10^5 cells
Control No cells	200 µg/ml No cells	100 µg/ml No cells	50 µg/ml No cells	20 µg/ml No cells	5 µg/ml No cells

Table 2.8: The arrangement of the well plate for testing the cell viability of PBMC with IONPs using the MTS assay. Total volume in each well is 1 ml, prior to adding 200 ml of MTS. In the fourth row, which served to create a background value from the plate reading, the volume to 1 ml was made up with complete media and the vehicle that carried the nanoparticles, which in this case was MilliQ water.

Control 5.0×10^5 cells	72 µg/ml 5.0×10^5 cells	40 µg/ml 5.0×10^5 cells	20 µg/ml 5.0×10^5 cells	7 µg/ml 5.0×10^5 cells	2 µg/ml 5.0×10^5 cells
Control 5.0×10^5 cells	72 µg/ml 5.0×10^5 cells	40 µg/ml 5.0×10^5 cells	20 µg/ml 5.0×10^5 cells	7 µg/ml 5.0×10^5 cells	2 µg/ml 5.0×10^5 cells
Control 5.0×10^5 cells	72 µg/ml 5.0×10^5 cells	40 µg/ml 5.0×10^5 cells	20 µg/ml 5.0×10^5 cells	7 µg/ml 5.0×10^5 cells	2 µg/ml 5.0×10^5 cells
Control No cells	72 µg/ml No cells	40 µg/ml No cells	20 µg/ml No cells	7 µg/ml No cells	2 µg/ml No cells

Table 2.9: The arrangement of the well plate for testing the cell viability of PBMC with Dotarem® (279.32 mg/ml of gadoteric acid) using the MTS assay. Total volume in each well was 1 ml, prior to adding 200 ml of MTS. In the fourth row, which served to create a background value from the plate reading, the volume to 1 ml was made up with complete media and the vehicle that carried the gadoteric acid, which in this case was apyrogenic water for injection.

The well plates were placed in an incubator (37 ^{o}C and 5% CO_2) and at 22 hours incubation, MTS (Promega, Madison, USA) added according to the manufacturer's instructions of a ratio of 5:1 to the total well volume; thus 200 ml of MTS was added to each well. The well plates were returned to the incubator for a further 2 hours; completing a total of 24 hours incubation. Each plate was then placed into a plate reader and scanned with a wavelength of 490 nm, as per the instructions of the MTS manufacturer.

2.10 Bone marrow derived murine dendritic cell cultures, *in vitro*

This section recounts the method of extracting bone marrow stem cells, adding cytokines and generating DC. This was performed in aseptic conditions in a fume hood. The following were sprayed with 70 % ethanol and allowed to air dry: the interior of the fume hood itself, a cork board, tube rack, 50 ml tubes, tubes with warmed cell media, tube with red blood cell lysis buffer, PIPETTEBOY, glass pipettes tips, pipette and the exterior of three Petrie dishes. Dissecting tools (scissors and forceps) were placed in a beaker and soaked in 70 % ethanol.

The killed mouse was sprayed with 70 % ethanol and pinned to the cork board using sterile needles. Scissors were used to cut the fur layer horizontally across the mouse, above the level of the pelvis. This was then pulled down towards the hind paws so that the pelvis and lower limbs were exposed. The muscle tissue of the lower limbs were then carefully cut away. Scissors were used to cut at the ankle joints (separate the paws), knee joints and the hip joints; to free the tibia and femur in both lower limbs. These were then placed for several seconds in a Petrie dish which contained 70 % ethanol and then transferred to a second Petrie dish with complete RPMI 1640 media (10 % FBS, 2 % HEPES buffer and 1 % Pen/Strep).

The mouse carcass was then placed in a plastic bag and kept in a freezer within the laboratory, until ready to return to the university's animal and aquatic facility for ethical disposal.

One of the bones (either a tibia or a femur) was transferred to a third Petrie dish that contained complete RPMI 1640 media. With a tibia, scissors were used to make a complete cut/sever above the ankle at the lower quarter of the tibia and another complete cut/sever was made at the tibial plateau. With a femur, a complete cut/sever was made at the femoral condyle and at the femoral head. A 26 gauge needle was attached to 3 ml syringe, media from the Petrie dish

was drawn and passed through each bone (one at a time) until all marrow contents were removed.

A sterile Pasteur pipette was used to collect the Petri dish contents (complete media and marrow cells) and transfered into a sterile 50 ml tube. This was centrifuged at 1,200 rpm (277 rcf) for 4 minutes with acceleration and brake both set at level seven. The supernatant was then discarded and 3 ml of red blood cell lysis buffer was added and the cell pellet re-suspended and allowed to stand for 5 minutes. Complete RPMI 1640 media was then added to the 25 ml indicator mark. A new sterile 50 ml tube was obtained and a cell strainer was inserted and sterile Pasteur pipette used to add the cells drop-wise onto the cell strainer and allowed to drip into the sterile tube. Once all contents were transferred, the cell strainer was removed and the top screwed in place securely and this tube was then centrifuged using the same settings as previous. The supernatant was discarded and 10 ml of complete RPMI 1640 media was added to the cell pellet and re-suspended.

A cell count was performed using trypan blue and a haemocytometer. Ten microliters of the cell suspension was placed in a well of a 96 well plate and 10 µl of trypan blue was added to the same well and mixed together. A sample of this was placed under a glass cover slip on the haemocytometer and a cell count performed using a microscope. One million cells per ml were added to wells in a 24 well plate (maximum 3 million cells in a 3 ml volume in a well). Cytokines (either GM-CSF or Flt3) were added at 20 ng per ml. The well plate was then placed in an incubator with a temperature of 37 ^{o}C and 5 % CO_2.

2.11 *In vitro* studies

Experimental *in vitro* studies with murine cells were approved by the RMIT University Animal Ethics Committee, AEC Project Number 1210. Cells were collected as described in Section 2.9. The *in vitro* experiments described in Sections 2.10.1, 2.10.2, 2.10.3 and 2.10.4 with both myeloid DC (5 days following the addition of GM-CSF to murine bone marrow stem cells) and with combined myeloid and plasmacytoid DC (8 days following the addition of IL-4 to murine bone marrow stem cells).

2.11.1 Dose response (uptake)

Cells mentioned in Section 2.11 were placed in a sterile 24 well plate with 3 x 10^6 cells in 3 ml in each well. Six conditions were established: one well served as a control and received no nanoparticles, the remaining wells received different concentrations of nanoparticles (200 µg/ml, 100 µg/ml, 50 µg/ml, 20 µg/ml, and 5 µg/ml). Nanoparticles tagged with FITC were sonicated for 10 minutes, prior to being added to cells cultures and incubated for 24 hours.

Following incubation, the supernatant was carefully removed, placed in a labelled micro tube and then stored at -80 ^oC for further cytokine analysis. Sterile PBS was used to lift off any cells that had adhered to the bottom of each well. The collected cells from each well were placed in labelled tubes and centrifuged at 1,500 rpm (433 rcf) for 5 minutes, the supernatant then discarded and cells resuspended with 0.5% BSA/PBS (w/v). Cells were then added to a sterile 96 well v-bottom well plate and centrifuged at 1,500 rpm (433 rcf) for 5 minutes. The

supernatant was then discarded and cold 0.5% BSA/PBS (w/v) antibody were added and incubated at 4 ^{o}C for 30 minutes. Following incubation, cells were centrifuged at 1,500 rpm (433 rcf) for 5 minutes, supernatant discarded and cells resuspended in FACS fix for.

2.11.2 *In vitro* assessment of maturation marker on *in vitro* grown DCs by flow cytometry

Cells mentioned in 2.11 were placed in a sterile 24 well plate with 3 x 10^6 cells in 3 ml in each well. Six conditions were established: one well served as a control and received no nanoparticles, the remaining wells received different concentrations of nanoparticles (200 µg/ml, 100 µg/ml, 50 µg/ml, 20 µg/ml, and 5 µg/ml). Nanoparticles tagged with FITC were sonicated for 10 minutes, prior to being added to cells cultures and incubated for 24 hours.

Following incubation, the supernatant was carefully removed, placed in a labelled micro tube and then stored at -80 ^{o}C for further cytokine analysis. Sterile PBS was used to lift off any cells that adhered to the bottom of each well. Collected cells were centrifuged at 1,500 rpm (433 rcf) for 5 minutes, the supernatant discarded and resuspended in 0.5% BSA/PBS (w/v). Cells were resuspended and each original cell culture (or well) condition was divided into 4 equal volumes and transferred into a sterile 96 well, v-bottom well plate. Therefore, each original condition (from the flat bottom 24 well plate) was divided into four (and placed in a 96 v-bottom well plate). The 96 well plate was centrifuged at 1,500 rpm (433 rcf) for 5 minutes. The supernatant was then discarded.

As each original condition was divided into four; the contents of one well was resuspended with 200 µl of cold 0.5% BSA/PBS; the second well was resuspended with 200 µl 0.5% BSA/PBS that contained antibody CD86; the third well was resuspended with 200 µl 0.5% BSA/PBS that contained combined antibodies CD11c and CD86 and the fourth division was

resuspended with 200 µl 0.5% BSA/PBS that contained combined antibodies CD11c and CCR7.

The 96 well plate was then incubated at 4 ^{o}C for 30 minutes, then centrifuged at 1,500 rpm (433 rcf) for 5 minutes, the supernatant was then discarded and cells resuspended in FACS fix for flow cytometry analysis.

2.11.3 *In vitro* assessment of apoptosis on *in vitro* grown DC's by flow cytometry

Cells mentioned in 2.11 were placed in a sterile 24 well plate with 3 x 10^6 cells in 3 ml in each well. Six conditions were established: one well served as a control and received no nanoparticles, the remaining wells received different concentrations of nanoparticles (200 µg/ml, 100 µg/ml, 50 µg/ml, 20 µg/ml, and 5 µg/ml). Nanoparticles tagged with FITC were sonicated for 10 minutes, prior to being added to cells cultures and incubated for 24 hours.

Following incubation, the supernatant was carefully removed, placed in a labelled micro tube and then stored at -80 ^{o}C for further cytokine analysis. Sterile PBS was used to lift off any cells that adhered to the bottom of each well. Collected cells were centrifuged at 1,500 rpm (433 rcf) for 5 minutes, the supernatant discarded and resuspended in 0.5% BSA/PBS (w/v). Cells were resuspended and each original cell culture (or well) condition was divided into 4 equal volumes and transferred into a sterile 96 well, v-bottom well plate. Therefore, each original condition (from the flat bottom 24 well plate) was divided into four (and placed in a 96 v-bottom well plate). The 96 well plate was centrifuged at 1,500 rpm (433 rcf) for 5 minutes. The supernatant was then discarded.

As each original condition was divided into four; the contents of one well was resuspended with 50 µl of binding buffer (provided in the kit); the second well was resuspended with 50 µl of binding buffer that contained Annexin V (BD Biosciences, San Diego, USA); the third well was resuspended with 50 µl of binding buffer that contained 7AAD (BD Biosciences, San Diego, USA); and the fourth well was resuspended with 50 µl of binding buffer with both Annexin V and 7AAD.

The 96 well plate was then wrapped in aluminium foil, placed on a laboratory bench top for 30 minutes at room temperature, then uncovered and centrifuged at 1,500 rpm (433 rcf) for 5 minutes. The supernatant was then discarded and cells resuspended in FACS fix for flow cytometry analysis within 30 minutes of this final step.

2.11.4 Time course (time dependent uptake)

Cells mentioned in 2.11 were placed in a sterile 6 well plate containing 4.5 x 10^6 cells in 3 ml, six conditions were established: one well served as a control and received no nanoparticles; the remaining wells received 200 µg/ml of FITC tagged nanoparticles at different time points (24 hours, 18 hours, 6 hours, 4 hours and 1 hour). The nanoparticles were sonicated for 10 minutes, prior to being added to cell cultures and then incubated for 24 hours.

On completion of the treatment periods, the supernatant was carefully removed, placed in a labelled micro tube and then stored at -80 ^{o}C for further cytokine analysis. Cells were removed using sterile PBS was used to lift off any cells that had adhered to the bottom of each well. Collected cells were centrifuged at 1,500 rpm (433 rcf) for 5 minutes, the supernatant discarded and resuspended in 0.5 % BSA/PBS (w/v). Cells were added to a sterile 96 well v-bottom well plate; 2 x 200 µl from each tube (representing each original condition).

Therefore, each original condition (from the flat bottom 24 well plate) was divided into two (and placed in a 96 v-bottom well plate). The 96 well plate was then centrifuged at 1,500 rpm (433 rcf) for 5 minutes and the supernatant was then discarded.

One well of each original condition, was resuspended with 200 µl of cold 0.5 % BSA/PBS (w/v) and the other corresponding condition was resuspended with 200 µl of cold 0.5 % BSA/PBS (w/v) that contained antibody. The 96 well plate was then incubated at 4 ^{o}C for 30 minutes. Following incubation, cells were centrifuged at 1,500 rpm (433 rcf) for 5 minutes, supernatant discarded and cells resuspended in FACS fix for flow cytometry analysis.

2.11.5 Mouse Inflammatory Cytometric Bead Array (CBA) Analyser

Supernatant from specified (dose response and time course) *in vitro* murine experiments were stored at -80 ^{o}C. Frozen samples were thawed and used to assess cytokine levels by CBA analysis (BD™ Cytometic Bead Array, BD Biosciences, San Diego, USA) as per manufacturer's instructions and read on flow cytometry. The specific cytokines analysed were: IL-8, IL-1β, IL-6, IL-10, TNF and IL-12p70.

2.12 *In vivo* studies

In vivo studies performed with mice and their tissues were approved by the RMIT University Animal Ethics Committee (AEC Project Number 1320).

2.12.1 Murine strain and lymph node tracking, *in vivo*

Female mice, C57BL/6, aged between 8 to 12 weeks were used for all lymph node tracking experiments, *in vivo*.

2.12.2 Mouse injections (injection methods and sites)

All mice received unilateral hock injections of iron oxide nanoparticles (coated with dextran and tagged with FITC) suspended in saline. A maximum volume of 100 µl at a concentration of 200 µg/ml was administered into the hock, subcutaneously. The use of a hock injection was designed to be more sympathetic and humane (compared to a foot pad injection), while still providing lymphatic drainage to the popliteal lymph node. In addition to the hock injections, each mouse received subcutaneous injections into their flanks, on the same side. Again, a maximum volume of 100 µl at a concentration of 200 µg/ml was used for these flank injections.

The injection into the flank was used to determine lymphatic drainage into the inguinal lymph node. Following the time period to be assessed, either one hour or one day, the mice were

heavily anaesthetised (intraperitoneal injection of sodium pentobarbitone, 150 mg/kg with a 25 gauge needle) and the standard method of Vascular Perfusion Fixation was performed. Once the mouse appeared anaesthetised, its reflexes were assessed to ensure that the mouse was fully anaesthetised; an incision across below the rib cage was made, the descending aorta was clamped, a needle was inserted through the left ventricle and its tip was positioned in the ascending aorta. The injection or perfusion then took place with heparinised phosphate-buffered saline to flush out the blood, followed by 4% paraformaldehyde in phosphate buffered saline until fixation tremors were noted. This indicated the point of death. The mouse, thus, died humanely on completion of the Vascular Perfusion Fixation process, under anaesthesia. The mouse was then dissected and the required tissues and organs removed. The inguinal and popliteal lymph nodes were removed from one leg (right leg) and underwent further analysis by flow cytometry and confocal microscopy. The other lymph nodes (left side) remained in the mouse for further analysis (imaging with MRI). Other organs/tissues assessed were the liver, spleen, kidneys, heart and lungs; with histological staining techniques). A blood sample (for blood serum biochemical assay) was also taken just prior to the commencement of the Vascular Perfusion Fixation process via a retro-orbital sinus. The remainder of the mouse was preserved with 10 % neutral buffered formalin (NBF).

2.12.3 Preparation of iron oxide nanoparticles

The dextran coated iron oxide nanoparticles were functionalised as described in Section 2.8.3 and then conjugated with FITC as stated in Section 2.8.4. To wash unbound FITC, the required volume of particles were centrifuged at 5,000 rpm for 5 minutes and resuspended in saline. This was performed three times. The mice received injections of FITC tagged nanoparticles suspended in saline.

2.12.4 Lymph node removal and preparation for FACS flow cytometry

Popliteal and inguinal lymph nodes were removed by surgical dissection, *post mortem* and placed in 10% NBF. To prepare the lymph nodes for flow cytometry, they were placed in 0.5% BSA/PBS (w/v), fatty tissue surrounding the lymph node was carefully removed and the soft rubber end of a syringe plunger was used to rupture the capsule of the lymph node and release its capsular contents. The cellular contents were then collected centrifuged at 4,000 rpm for 4 minutes and resuspended in 0.5% BSA/PBS (w/v). Lymph node cells were divided into two staining conditions: (1) no antibody (control) and (2) CD11c antibody as per manufacturer specification. Antibody staining was performed at 4 ^{o}C for approximately 25 minutes, after which they were centrifuged at 4,000 rpm for 4 minutes, washed and resuspended in FACS fix buffer for flow cytometry.

2.12.5 Organ removal for histological analysis

On completion of the Vascular Perfusion Fixation process, all mice were then dissected and organs were removed for histological analysis. Organs included the liver, spleen, kidneys, heart and lungs; which were fixed in 10% NBF for further analysis.

2.12.6 Histological analysis

Organs (liver, spleen, kidney, heart and lungs) fixed for histopathological analysis were processed using a histopathology tissue processor (Leica ASP200S, NSW, Australia) using a protocol specifically designed for rodent tissue. The automated process included preparing these tissues with 10 % NBF, 70 % ethanol, 90 % ethanol, 100 % ethanol and xylene for exact durations and temperatures.

On completion, the tissues were embedded in paraffin wax using an embedding station (Shandon Histocentre 3, Thermo Electron Corporation, Madison, USA) and wax blocks containg murine organs were created. 4 µm thick sections were cut using a microtome (RM 2235, Leica Microsystems, Nussloch, Germany)) and placed on Superfrost Plus (positively charged) glass microscope slides, then positioned in racks and placed in a drying oven (Watson, Victoria, Australia) at 60 ^{o}C for one hour.

2.12.7 Biochemical analysis of blood serum

A blood sample (for blood serum biochemical assay) was taken just prior to the commencement of the Vascular Perfusion Fixation process, while mice were heavily anaesthetised, via their retro-orbital sinus. The blood sample was taken using a haematocrit capillary tube (Hirschmann Laborgerate, Eberstadt Germany) transferring blood into a micro tube, allowed to clot for at least 1 hour and then centrifuged at 2,000 rpm (771 rcf) for 10 minutes. Serum was collected and stored -80 ^{o}C for further analysis. The blood serum samples were later analysed for various biochemical parameters at the Department of

Pathology Peter MacCallum Cancer Centre using a blood serum biochemical immunoassay analyser (Abbott Architect Plus, ci4100, Roche Diagnostics, Melbourne, Australia).

2.12.8 FACS flow cytometery analyser

All FACS flow cytometry experiments were performed using the FACS Canto™ II Flow Cytometer (BD Biosciences, San Jose, USA) located within the RMIT Flow Cytometry Facility (RMIT University, Bundoora West Campus, Australia).

2.13 MRI imaging studies

MRI imaging of gel phantoms with suspended iron oxide nanoparticles (as set out in section 2.8.2) were performed with both a 1.5 T Siemens MRI scanner at The Austin Hospital (Studley Road, Heidelberg, 3084, Victoria, Australia) and a 3.0 T Siemens at Peter MaCallum Cancer Centre, (St. Andrews Place, East Melbourne, Victoria, Australia). In both instances, a head coil was used with the MRI imaging process. To ensure that the gel phantoms were positioned within the isocentre volume of the MRI magnet, and that the imaging plane co-incided with this, a specially designed foam pad was fashioned to elevate the desired imaging plane of the gel phantoms to be within the central horizontal plane (z-direction) of the head coil.

Mice were scanned with a 3.0 T Siemens MRI scanner at Peter MaCallum Cancer Centre. The mice were imaged using a wrist coil (an MRI imaging coil designed for imaging the

human wrist). This coil approximated the dimension of the mice and allowed the mice to be as close as possible to the coil, acting as a receiver for the MRI signal emanating from the mice); thus maximising SNR. The mice had been killed by cervical spine dislocation immediately prior to MRI imaging.

2.14 PET imaging studies

For PET imaging, the radiotracer used was ^{68}Ga. The radiolabelling process was as described in section 2.8.7. For PET imaging in mice, ^{68}Ga was radiolabelled to dextran coated iron oxide nanoparticles tagged with FITC and for PET imaging in humans, the ^{68}Ga was radiolabelled to dextran coated iron oxide nanoparticles (without FITC).

Mice were imaged with a Small Animal PET (Philips Healthcare, DA Best, The Netherlands) scanner and were anesthetised with 2% isoflurane in medical air (20 % oxygen and 80 % nitrogen) with a total flow rate of 0.8 litres per minute. PET imaging commenced 1 hour after the mice received a foot-pad injection of radiolabelled nanoparticles (a volume of 100 µl and a nanoparticle concentration of 1,000 micrograms per ml).

The Human Ethics Committee (Peter MacCallum Cancer Centre) granted approval for experimental research in patients diagnosed with prostate cancer. These patients provided their consent to this imaging procedure. They received general anaesthesia, were brought to the operating theatre and positioned supine on the operating table with their legs in stirrups. An ultrasound machine and rectal probe were used to identify the prostate gland. The radiolabelled nanoparticles – 1,000 µg/ml in a total volume of 1,000 ml – were divided into 8 equal fractions or doses (125 µl), and directly injected into the prostate by a radiation oncologist, using ultrasound guidance. Four injections were into the peripheral zone of the prostate and the remaining four doses were injected into the prostate's inner zone. 1 hour post

procedure, the patient was brought to the PET/CT scanner for imaging. The patient was positioned supine on the PET/CT imaging table and entered the gantry head-first.

2.15 Histopathology staining

2.15.1 Haematoxolin and Eosin staining

Organs processed for histopathology analysis were stained with haematoxylin and eosin (H&E) according to the following protocol:

1. Xylene (5 minutes).
2. Xylene (3 minutes).
3. Absolute alcohol (2 minutes).
4. Absolute alcohol (2 minutes).
5. Rinse in tap water (1 minute).
6. Haemotoxolin (30 seconds).
7. Rinse in tap water (20 seconds).
8. Scott's tap water (30 seconds).
9. Rinse in tap water (20 seconds).
10. Eosin (20 seconds).
11. Rinse in tap water (20 seconds).
12. In 70 percent alcohol (1 minute).
13. Absolute alcohol (1 minute).
14. Absolute alcohol (1 minute).
15. Xylene (20 seconds)

16. Xylene. The Superfrost Plus glass microscope slides remain in this bath until they were glass cover-slipped with xylene based DPX colourfast mounting media (Fronine, NSW, Australia).

2.15.2 Perls Prussian Blue Staining for Haemosiderin

Organs processed for histopathology analysis were stained with Perls Prussian Blue according to the following protocol:

1. Tissue sections on positively charged microscope slides were dewaxed as per the following process:
    a. Xylene (2 minutes)
    b. Xylene (1 minute)
    c. Absolute alcohol (2 minutes)
    d. Absolute alcohol again (1 minute)
    e. 70 percent alcohol (2 minute).
2. Bring to water
3. Positively charged microscope slides were dewaxed sections placed n tank with equal volume mixture of hydrochloric acid and potassium ferrocyanide (5 minutes)
4. Washed in distilled water
5. Counterstained in nuclear fast red (20 minutes)
6. Washed in tap water (1 minute)
7. Dehydrated according to the following process:
    a. 70 percent alcohol (2 minutes)
    b. Absolute alcohol (1 minute)
    c. Absolute alcohol again (1 minute)

d. Xylene (2 minutes)
e. Xylene again (2 minutes)

8. Cleared and mounted with xylene based DPX colourfast mounting media and glass cover slip

2.15.3 Periodic Acid Schiff's (PAS) reaction staining

The kidney tissue sections processed for histopathology analysis underwent the PAS reaction staining protocol as follows:

1. Tissue sections on positively charged microscope slides were dewaxed as per the following process:
    a. Xylene (2 minutes)
    b. Xylene (1 minute)
    c. Absolute alcohol (2 minutes)
    d. Absolute alcohol again (1 minute)
    e. 70 percent alcohol (2 minutes)
2. Bring to water
3. Oxidisation with 1 percent periodic acid (10 minutes)
4. Washed in distilled water (1 minute)
5. Placed in Schiff's reagent at room temperature (20 minutes)
6. Washed well in water (5 minutes)
7. Counterstained with Mayer's Haematoxylin (90 seconds)
8. Placed to blue in Scott's tap water (30 seconds)
9. Washed in water
10. Dehydrated according to the following process
    a. 70 percent alcohol (2 minutes)

b. Absolute alcohol (1 minute)

c. Absolute alcohol again (1 minute)

d. Xylene (2 minutes)

e. Xylene again (2 minutes)

11. Cleared and mounted with xylene based DPX colourfast mounting media and glass cover slip.

2.16 Generation of graphs and statistical analysis

The following graphs – Figures 3.13 to 3.38, and, Figures 3.41 to 3.66 – presented in Chapter 3 and in the Appendix 1, were created using Microsoft Excel (Microsoft Corporation, USA). The trendlines presented in Figures 3.13 to 3.22 inclusive and Figures 3.41 to 3.50 inclusive contain power trendlines because the rate of change in the pulse sequence is known to be 22 ms from one TE to the next. The feature of adding a power trendline to a data set is not possible with GraphPad Prism 6 (GraphPad Software Inc. USA). Figures 3.67 and 3.68 are 3D graphs (data sets presented on a 3D graph) and this feature was also not available with GraphPad Prism 6.

The remaining graphs throughout this thesis were generated using GraphPad Prism 6. Where statistical analysis was performed, the following was applicable.

- The alpha, α, value (threshold significance level), was set at 0.05
- As GraphPad Prism was used to generate the graphs and statistical data, their statistical terminology and references were used and summarised in Table 2.9.
- Where no asterisk/s appear on a graph, no statistical significance was identified.

P value	Wording	Summary
< 0.0001	Extremely significant	****
0.0001 to 0.001	Extremely significant	***
0.001 to 0.01	Very significant	**
0.01 to 0.05	Significant	*
≥ 0.05	Not significant	ns

Table 2.9: The correlation of calculated P value, statistical wording and summary (as indicated with asterisk/s) according to GraphPad Prism, version 6.05. Throughout this chapter, when calculated statistical P values conformed to any of the ranges indicated, the corresponding wording was used and asterisks were incorporated into the graphs.

3.0 Chapter 3 – Characterisation of iron oxide nanoparticle in the clinical magnetic environment, radiolabelling with ^{68}Ga and *in vitro* cytotoxicity

3.1 Introduction

For almost a decade now, there has been progressively increased research efforts into exploiting certain attributes of iron oxide nanoparticles for a variety of imaging techniques, incorporated with MRI. These include using iron oxide nanoparticles as MRI contrast agents, for cell tracking[208-210], for drug delivery[211, 212] and for hyperthermia therapy[213, 214]. One facet of current research interest is the possibility of multimodal imaging flexibility offered by nanoparticles that can be radiolabelled with a suitable radionuclide[215, 216]. In this respect, recent research activities have turned to designing imaging agents for the hybrid imaging modes of PET/MRI. At this time, no PET/MRI for patients is available in Australia, however, there is anticipation that this will soon change in major hospitals offering oncology and related surgical services. For any nanoparticle to be primarily considered as a PET/MRI contrast agent, it would need to be radiolabelled with a positron emitting radionuclide.

Compared to current PET only imaging and to MRI only imaging, a hybrid or multimodal approach with a suitable contrast agent offers improved contrast-to-noise ratio amongst anatomical structures defined by the spatial resolution offered by MRI. This would thereby improve the specificity of these modalities, particularly MRI; and also provide further diagnostic capabilities to referring clinicians for their patients.

For iron oxide nanoparticles to be utilised as imaging agents, they would need to be designed with several favourable characteristics that can be maximised by either MRI or PET or combined imaging processes. For MRI, iron oxide nanoparticles would need to have their own magnetic properties, be compatible in the MRI and magnetic field environments,

demonstrate T_2 spin-spin relaxation behaviour and respond to pulse sequence directions. For *in vivo* administration, iron oxide nanoparticles need to; be biocompatible, be evenly distributed in a colloidal suspension (no chemical agglomeration or aggregation), and each have a consistent size throughout the sample.

Their size, that is, the physical dimension of nanoparticles, can determine their *in vivo* biodistribution[109]. Iron oxide nanoparticles greater than 50 nm are readily isolated by organs of the reticulo-endithelial system (RES), namely the liver and spleen[18, 217]. This is especially true when these nanoparticles are administered by an intravascular route and their sequestration occurs within minutes. Commercially available iron oxide nanoparticle preparations (such as Resovist® and Endorem™) have been marketed specifically as a contrast agent for imaging the liver with MRI. For improved biodistribution *in vivo,* iron oxide nanoparticles would need to be less than 50 nm, as this would also provide them with a greater circulation time throughout the body[18, 56].

Physical properties of the iron oxide nanoparticles used for the purposes of experiments pertaining to this thesis were that they were less than 50 nm, specifically, 20nm, approximately. They were coated with T10 dextran for *in vitro* and *in vivo* biocompatibility. The biocompatibility or safety profile afforded by T10 dextran is that it is a very low molecular weight dextran, as opposed to higher molecular weight dextrans that have been shown to induce an IgG response *in vivo*[218]. Dextran has already proven itself to be a successful biocompatible coating in commercially approved iron oxide contrast agents for intravenous (Resovist®, Endorem™, Feridex®).

The iron oxide core itself; if it can be demonstrated that low concentrations of iron oxide nanoparticles (with high magnetic properties) can induce a visually noticeable signal intensity change on MRI images, then a small quantity would need to be administered *in vivo*; and if such nanoparticles were radiolabelled, this in turn would signify that less ionising

radiation[219] would be present but still generate PET image data due to PET's contrast-to-noise ratio (CNR) sensitivity. Iron (oxide) is normally found in the human body; and with commercially available and FDA approved iron oxide nanoparticle preparations, any risk of iron overload in the liver is rendered minimal or negligible[18]. The excretory pathway of iron oxide from the human body, however, is well known and understood. Dextran coated iron oxide nanoparticles are incorporated as phagolysosomes within phagocytic cells[18]. From here, intracellular dextranase enzymes cleave the dextran from the nanoparticle and the iron oxide is solubilized into iron ions, which then progress into the haemoglobin pool, and as with endogenous iron, it is eliminated via the RBC cycle and the liver[220]. The safety profile of iron oxide nanoparticles have been established at concentrations up to 200 µg/ml and concentrations greater than this have demonstrated intracellular toxicity due to high levels of reactive oxygen species (ROS)[221]. One method of assessing cytotoxicity of nanoparticles is by performing a MTS assay. MTS is the compound [3-(4,5-dimethylthiazol-2-yl)-5-(3-carboxymethoxyphenyl)-2-(4-sulfophenyl)-2H-tetrazolium] and is combined with an electron coupling agent (phenazine ethosulfate; PES). MTS is bioreduced by cells into a formazan product that is soluble in tissue culture medium. The conversion of MTS into the aqueous soluble formazan product is accomplished by dehydrogenase enzymes found in metabolically active cells. The absorbance of formazan is measured at a wavelength of 490 nm in a plate reader. The quantity of formazan product as measured by the amount of 490nm absorbance is directly proportional to the number of living cells in culture[222].

For *in vitro* experimentation, the physical size of the iron oxide nanoparticles were also critical, as size is one determining factor for ease of ingestion by cells. The outer surface of the T10 dextran coating should be smooth to not restrict or adversely affect ingestion by cells. The surface charge of nanoparticles may also be a factor in determining the degree of cell internalisation in a variety of cells, particularly in healthy cell and in cancer cell types.

These desired characteristics are also applicable if cell tracking were to be pursued[18, 208, 210], that is, cells can be loaded with iron oxide nanoparticles; with features designed specifically to facilitate cell entry. The cells would then be re-administered to their original host and they would be imaged with MRI to observe their migration from their administration site to their eventual destination, *in vivo*. Biocompatibility features, embedded in their fabrication, would also ensure no cytotoxity or rejection.

The principle of withdrawing cells from a patient, adding a feature and then administering these cells to the patient; has been a standard practice within the Nuclear Medicine field for decades; that is, *ex vivo* radiolabelling of cells and returned for *in vivo* imaging applications. For example, labelling white blood cells (leukocytes) with Indium-111 (^{111}In) to image acute infective process is common-place; whereby a blood sample from a patient is taken, the white blood cells isolated, incubated with ^{111}In, re-administered to the same patient and imaging then performed. In a very similar process, radio-active gallium is used to label neutrophils to image long-standing infective processes such as osteomyelitis (gallium binds to the membrane of neutrophils). Nuclear Medicine can also image the activity in the liver and spleen by radiolabelling technetium (^{99m}Tc) to red blood cells; whereby the majority of the radio-activity conjugates to haemoglobin, but more specifically, in the beta chain component of the globin. These Nuclear Medicine imaging procedures can encounter challenges that limit their clinical utility under certain condition. For example, patients being medicated with heparin would not be suitable candidates for RBC labelling and imaging, as ^{99m}Tc will bind to heparin rather than RBCs. Likewise, radiolabelling of lymphocytes[223] and leukocytes[224] with ^{99m}Tc has been demonstrated to induce chromosomal aberrations. These limitations can be addressed and overcome by radiolabelling nanoparticles, as the nanoparticles (instead of cells) will serve as a carrier for the radionuclide.

Further supporting the case for incorporating nanoparticles with Nuclear Medicine is that the size of iron oxide nanoparticles are analogous to the size of various antimony sulphide colloids already widely used for a number of radionuclide imaging procedures and administered to patients. ^{99m}Tc antimony sulphide is administered intravenously and targets bone marrow in patients experiencing bone marrow related conditions such as avascular necrosis of the femoral head and also bone metastases. In an imaging technique referred to as intramammary lymphoscintigraphy, ^{99m}Tc antimony sulphide can be used to map lymph drainage in patients with breast cancer, prior to surgery for lymph node removal. ^{99m}Tc antimony sulphide has been measured at less than 100nm and rhenium sulphide is approximately 40nm[225].

The specific aims of this chapter were to:

1. Assess the physical characteristics of the specially fabricated iron oxide nanoparticles.
2. Measure the surface charge on the outer T10 dextran coating
3. Observe the behavioural characteristics of these iron oxide nanoparticles in a clinical MRI scanner, at 1.5 T and 3.0 T, namely their spin-spin relaxivity (T_2) and behaviour.
4. Radiolabel ^{68}Ga to the iron oxide nanoparticles.
5. Perform cell viability (MTS) assays.

3.2 Results

3.2.1 Physical characterisation of dextran coated iron oxide nanoparticles

3.2.1.1 Transmission Electron Microscopy (TEM)

A JEOL 1010 TEM operating at an accelerating voltage of 100 kv and a JEOL 2010 HRTEM that incorporated a lanthanum boron six crystal as its electron source and operating at an accelerating voltage of 200 kv; were used to assess the nanoparticles' physical characteristics. The size and shape of the iron oxide core and the T10 dextran coating were identified and measured. On the TEM images, the iron oxide core appeared to be circular (and not quasi-cuboid) and of suitable density. The T10 dextran coating was demonstrated as almost being translucent and with an even thickness encompassing the dense, circular iron oxide core. The iron oxide core was measured to be approximately 15 nm, the T10 dextran coating providing a coat of approximately 5nm thickness; thus, these particles have an overall diameter of approximately 20 nm.

The TEM images also demonstrate the sample on the carbon coated copper grid to be uniform in size and this uniformity was consistent throughout the samples that were imaged, that is, the nanoparticles were monodispersed. Samples of nanoparticles were prepared for TEM imaging at the commencement of this project, at the mid-way point and also at the end of this research. This was to ensure that the specifically fabricated nanoparticles maintained their physical characteristics throughout this study.

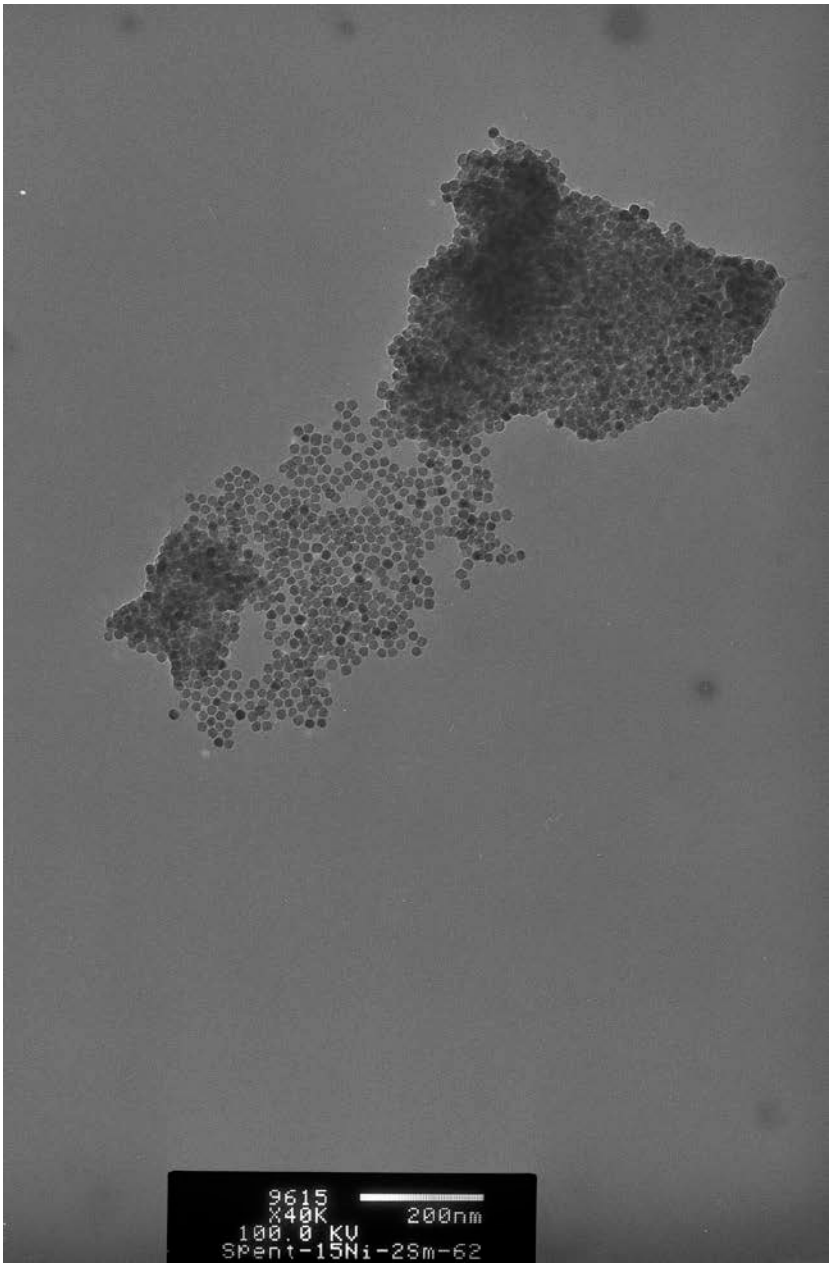

Figure 3.1: TEM image of dextran coated iron oxide nanoparticles to ascertain physical dimensions post fabrication (40,000 magnification taken in March 2011).
This micrograph was taken in March 2011 with a JEOL 1010 TEM containing a lanthanum boron six crystal as its electron source. This image forms part of a series of images taken to determine the physical dimensions and monodispersity of the laboratory manufactured nanoparticles.

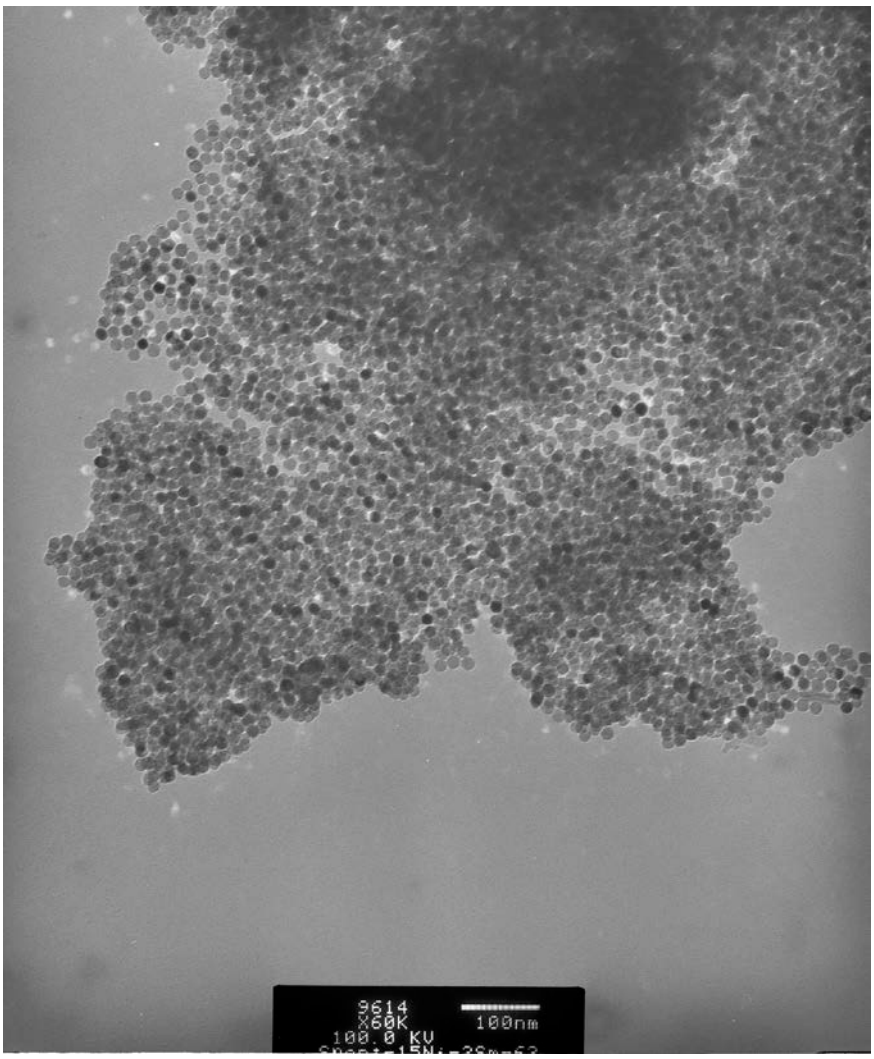

Figure 3.2: TEM image of dextran coated iron oxide nanoparticles to ascertain physical dimensions post fabrication (60,000 magnification taken in March 2011).
This micrograph image (60,000 magnification) was taken in March 2011 with a JEOL 1010 TEM containing a lanthanum boron six crystal as its electron source. This image is from the same sample (3mm copper grid with nanoparticles prepared for TEM) as the nanoparticles presented in Figure 3.1.

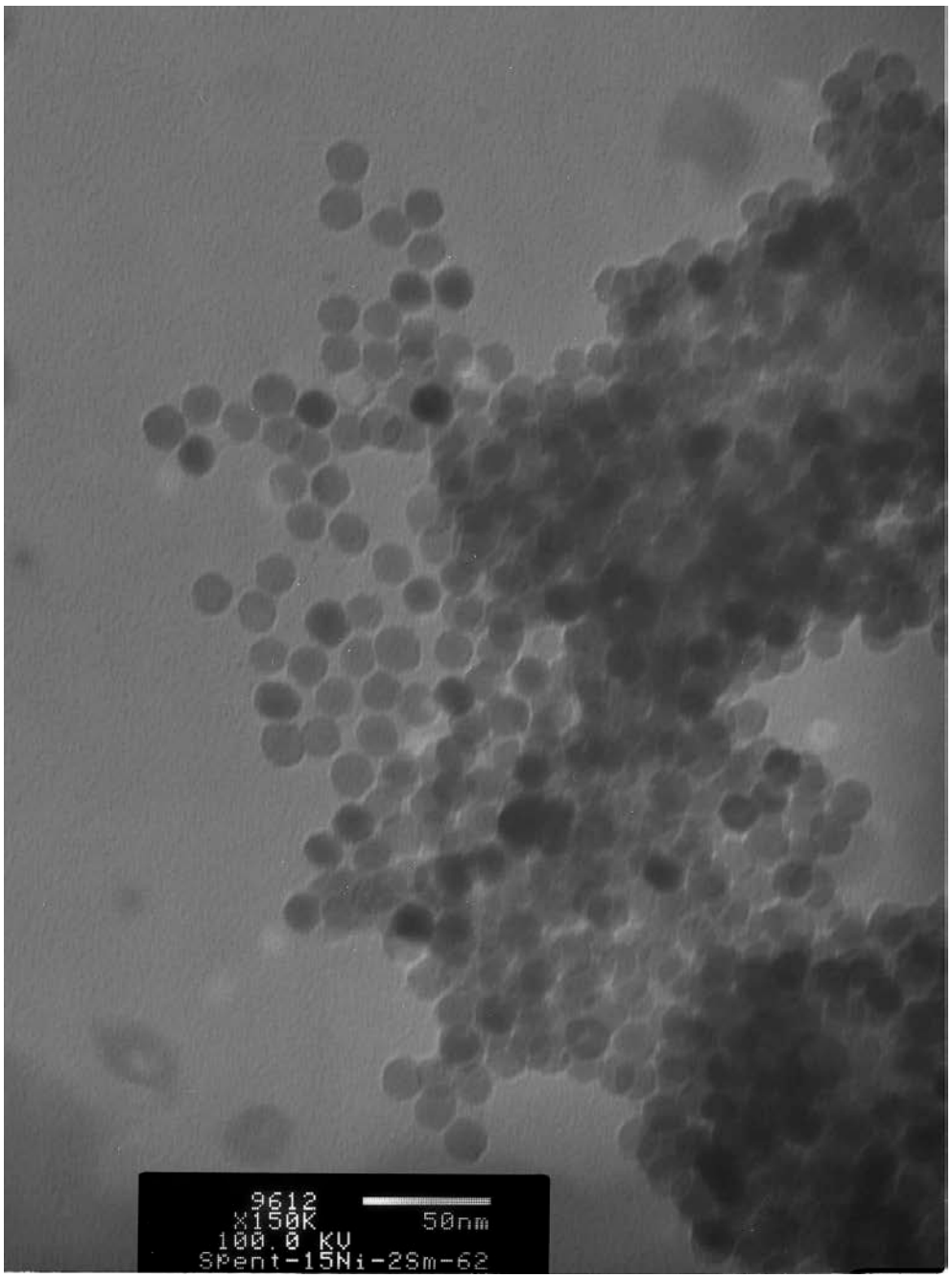

March 2011

Figure 3.3: TEM image of dextran coated iron oxide nanoparticles to ascertain physical dimensions post fabrication (150,000 magnification taken in March 2011).
This micrograph image (150,000 magnification) was taken in March 2011 with a JEOL 1010 TEM containing a lanthanum boron six crystal as its electron source. This image is from the same sample (3mm copper grid with nanoparticles prepared for TEM) as the nanoparticles presented in Figures 3.1 and 3.2.

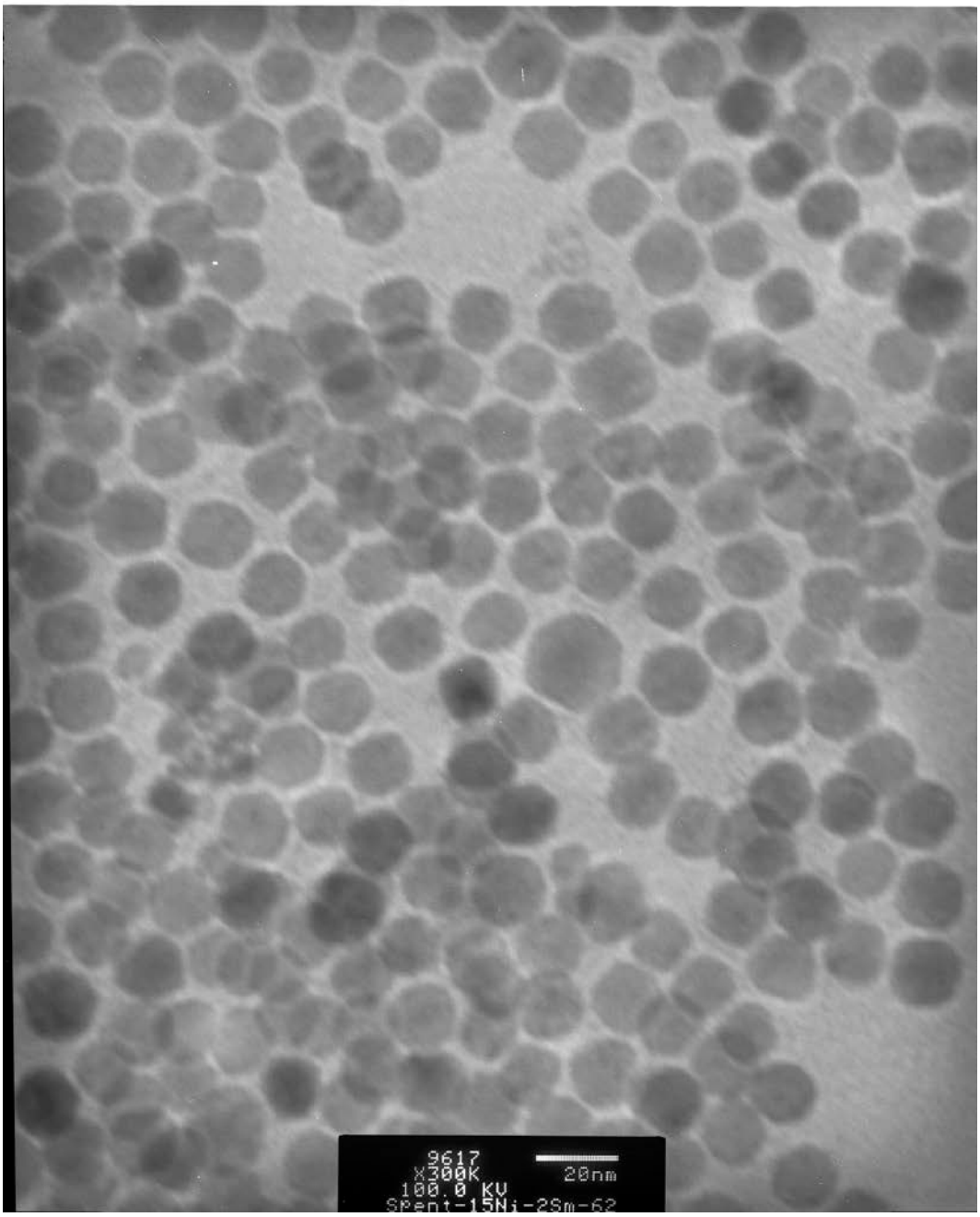

Figure 3.4: TEM image of dextran coated iron oxide nanoparticles to ascertain physical dimensions post fabrication (300,000 magnification taken in March 2011).
This micrograph image (300,000 magnification) was taken in March 2011 with a JEOL 1010 TEM containing a lanthanum boron six crystal as its electron source and is from the same sample (3mm copper grid with nanoparticles prepared for TEM) as the nanoparticles presented in Figures 3.1 to 3.3.

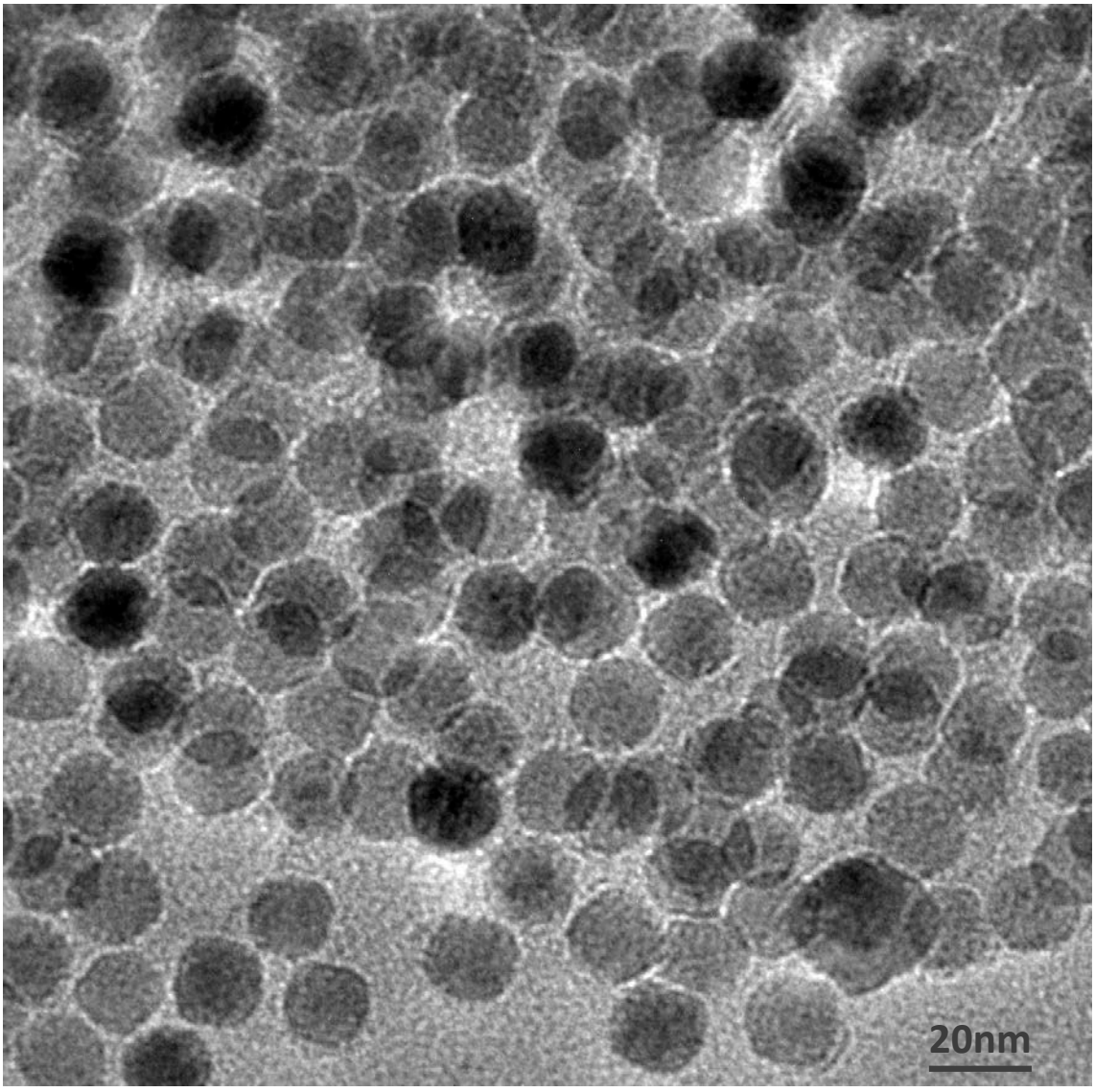

Figure 3.5: High resolution TEM of dextran coated iron oxide nanoparticles taken at the midway time-point of PhD thesis (350,000 magnification taken in June 2013).
This micrograph image (350,000 magnification) was taken in June 2013 with a JEOL 2010 TEM containing a lanthanum boron six crystal as its electron source. The physical dimensions of the dextran coated iron oxide nanoparticles were evaluated for consistency in physical dimension and monodispersity at approximately the midway time-point of the experiments supporting this PhD thesis.

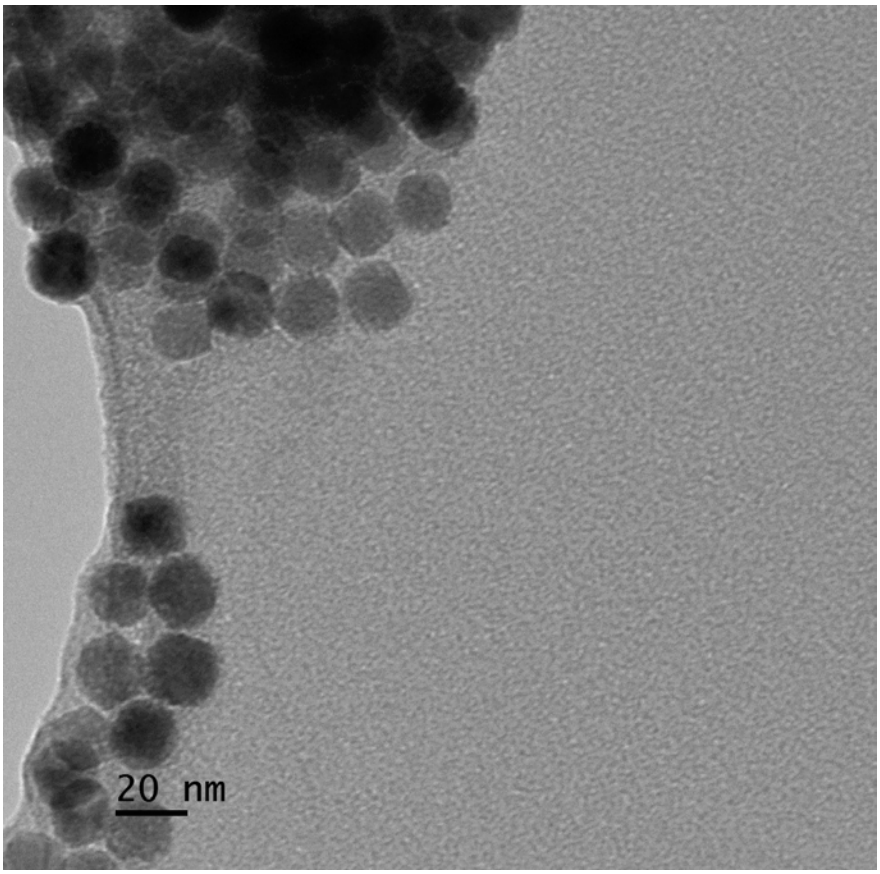

Figure 3.6: TEM of dextran coated iron oxide nanoparticles taken at approximately the end time-point of PhD thesis (75,000 magnification taken in November 2014). This image (100,000 magnification) was taken in November 2014 with a JEOL 1010 TEM containing a lanthanum boron six crystal as its electron source. At approximately the end time-point of the experiments supporting this PhD thesis, the physical dimensions of the dextran coated iron oxide nanoparticles were evaluated for a final time for consistency in physical dimension and monodispersity.

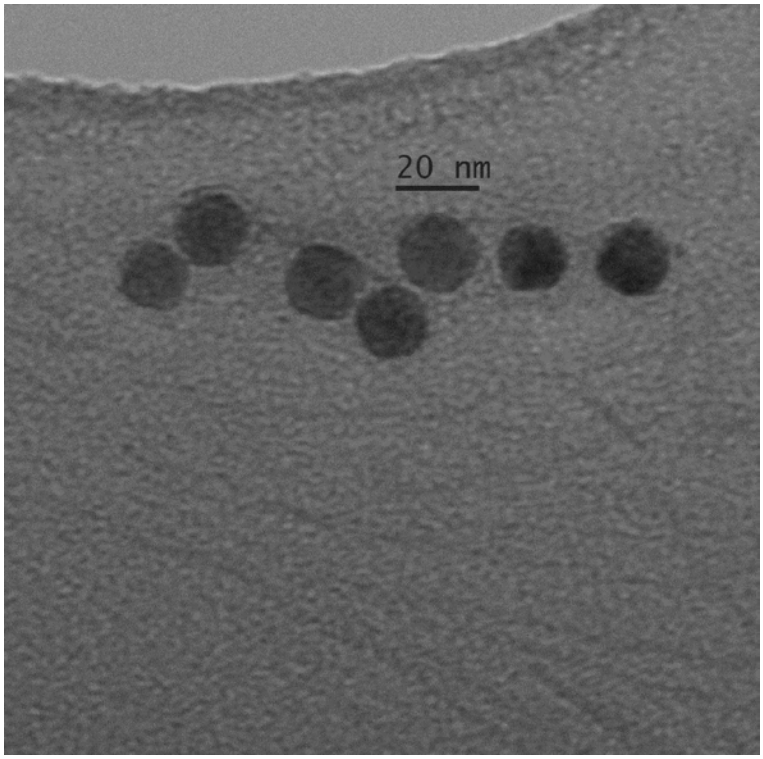

Figure 3.7: TEM of dextran coated iron oxide nanoparticles taken at approximately the end time-point of PhD thesis (100,000 magnification taken in November 2014). This image (100,000 magnification) was taken in November 2011 with a JEOL 1010 TEM containing a lanthanum boron six crystal as its electron source and is from the same sample (3mm copper grid with nanoparticles prepared for TEM) as the nanoparticles presented in Figure 3.6.

3.2.1.2 Scanning Electron Microscope

A FEI NovaNano SEM was used to observe the iron oxide nanoparticles from another dimension and specifically the outer surface of the T10 dextran coating surrounding the iron oxide core. The nanoparticles displayed a spherical morphology. The surface coating was noted to have a smooth appearance and this was consistent across all samples imaged. A smooth surface (as opposed to an inconsistent exterior) was designed to facilitate ingestion by cells when *in vitro* experiments were conducted.

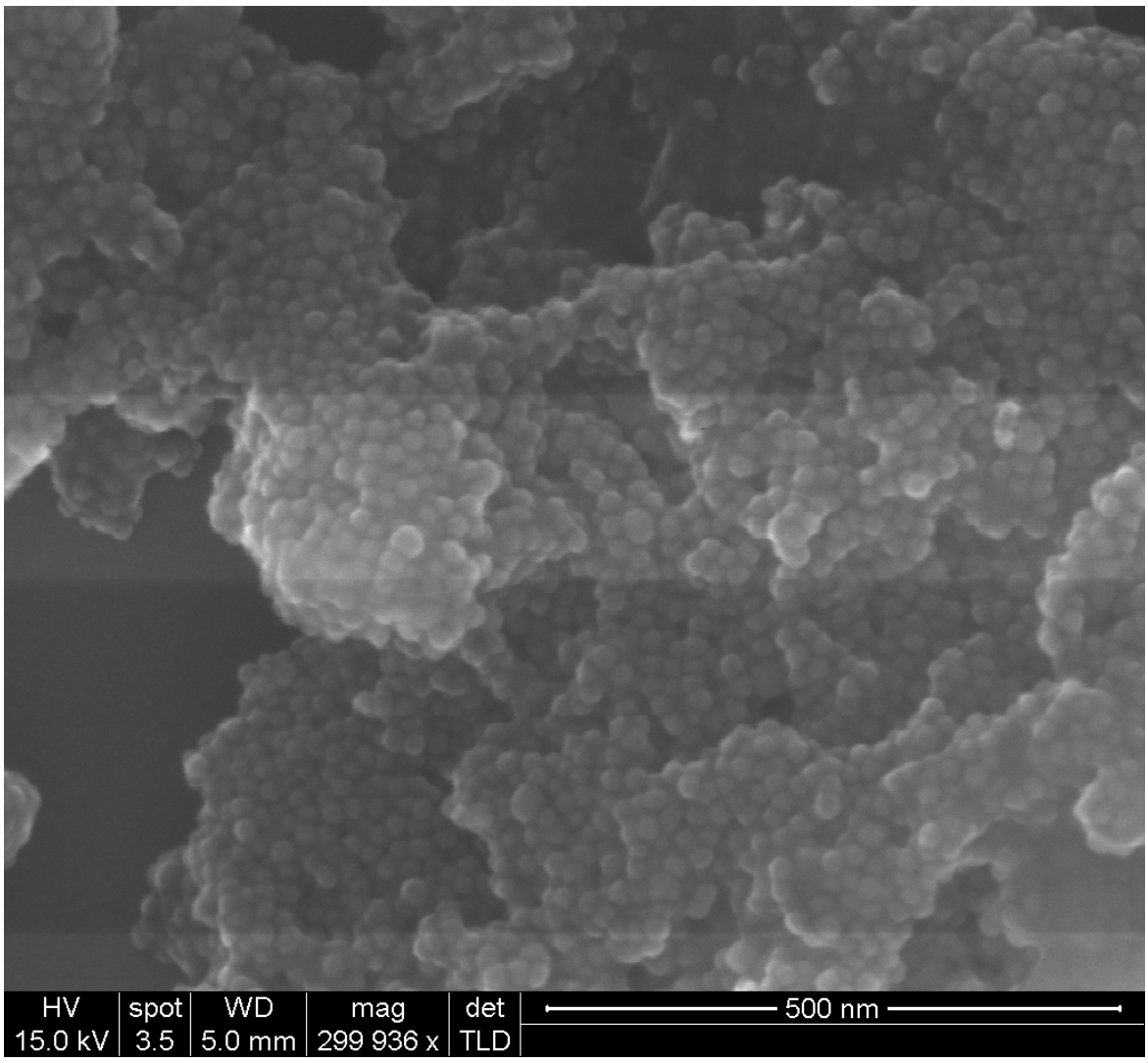

Figure 3.8: SEM image to ascertain physical dimensions post fabrication (approximately 300,000 magnification, March 2011). This SEM image was taken in March 2011 with a FEI NovaNano to determine the surface characteristic of the laboratory fabricated dextran coated iron oxide nanoparticles.

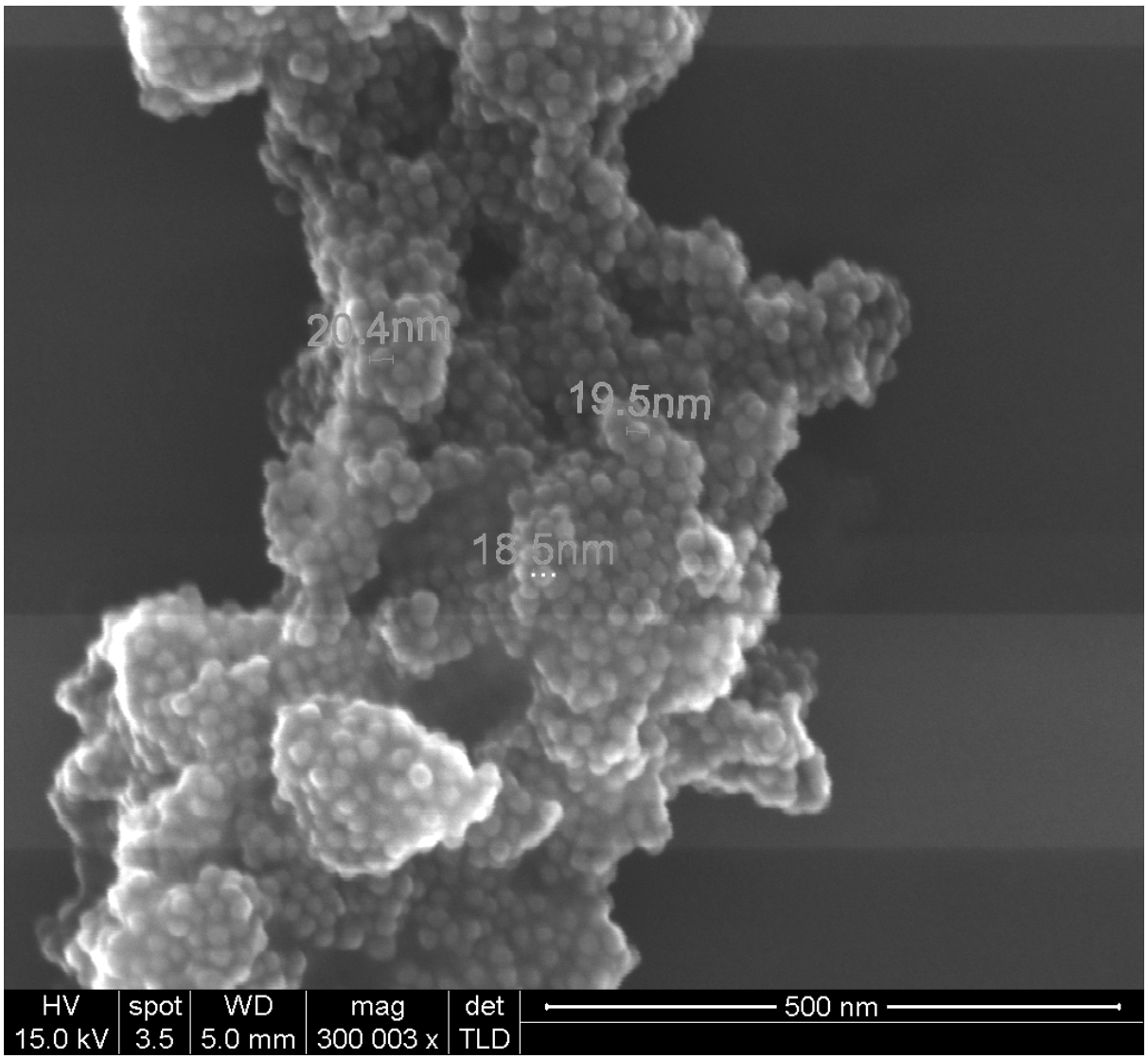

Figure 3.9: SEM image of another sample to ascertain physical dimensions post fabrication, including dimension measurements (approximately 300,000 magnification, taken in March 2011). This SEM image was taken in March 2011 with a FEI NovaNano SEM. In addition to observing the surface characteristics with SEM, their dimensions were also measured under SEM imaging.

3.2.2 Surface charge of dextran coated iron oxide nanoparticles

A Malvern Nano-ZS zetasizer was used to measure the surface charge of the nanoparticles. At the commencement of this thesis, a colloid suspension of 1.5 ml of MilliQ water containing nanoparticles at a concentration of 100 µg/ml were placed in micro tubes with room air and also in nitrogen filled glass vials. A total of ten micro tubes and ten nitrogen filled glass vials were used. The samples were stored in the following conditions:

- a standard fridge at 4 ^{o}C
- a standard freezer at -20 ^{o}C
- a long tern storage freezer at -80 ^{o}C

Throughout this thesis, samples were prepared for surface charge readings. The surface charges, measured in millivolts, from the six readings are tabulated and graphed.

Storage Condition	Mean Surface Charge (millivolt)	Standard Error of the Mean
Fridge (4 ^{o}C) Sample stored under air	-15.62	9.083
Fridge (4 ^{o}C) Sample stored under nitrogen	-20.80	8.681
Freezer (-20 ^{o}C) Sample stored under air	-30.50	4.300
Freezer (-20 ^{o}C) Sample stored under nitrogen	-19.32	3.455
Freezer (-80 ^{o}C) Sample stored under air	-23.17	0.8793
Freezer (-80 ^{o}C) Sample stored under nitrogen	-20.50	2.436

Table 3.1: The mean of six readings of particle surface charge (millivolts), stored under common laboratory or clinical conditions. The standard error of the mean (SEM) is also presented and used as error bars when graphed.

As like charges repel each other, consistent like-charges would assist the nanoparticles in minimised chemical aggregation and agglomeration. The nanoparticles selected for use with *in vitro* and *in vivo* experimentation were from those stored in a standard 4 ^{o}C fridge, under normal room air, as these had the least negative charge.

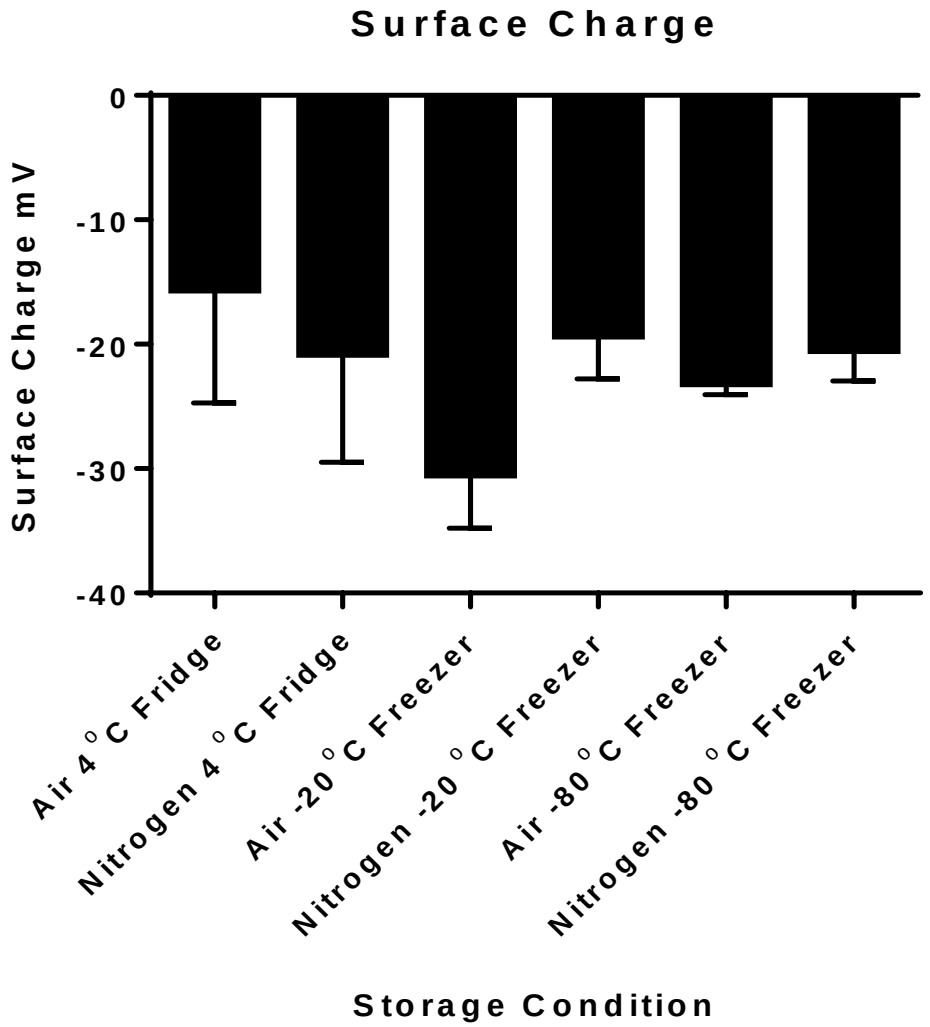

Figure 3.10: Surface charge (millivolts) of T10 dextran coating on iron oxide nanoparticles kept under different storage conditions. Iron oxide nanoparticles coated with T10 dextran were kept under different storage conditions and their surface charge was read and recorded with a Malvern Zetasizer (n=6) on six separate occasions throughout this thesis. At each reading, a new sample of particles was prepared and used, from the individual storage condition. The results presented are shown as the mean value of the six readings with standard error of the mean as error bars.

3.2.3 IONP gel phantoms in the magnetic environment of clinical MRI scanners

The iron oxide nanoparticles were observed for their behavioural characteristics (in a magnetic field environment) and their capabilities to provide contrast changes in MRI images; in response to a spin echo T_2 weighted pulse sequence. The assessment was performed on both a 1.5 T and 3.0 T clinical MRI scanner and with a 12-channel head coil. Both scanners were made by Siemens, used the Syngo operating platform and had access to the same pulse sequence; referred to as: t2_se_COR_16-echoes.

Under clinical conditions, an MRI image contains recorded signal intensity detail directly related to the magnetic or proton relaxation of nuclear spins of protons (hydrogen protons of water molecules). To allow the MRI clinical scanner to detect a hydrogen signal and to minimise and/or eliminate susceptibility artefacts from the air interface with tubes that contained gel and iron oxide nanoparticles, the plastic container (with the securely glued rack holding the tubes filled with nanoparticles) was filled with water. MRI imaging was performed with a Siemens clinical MRI scanner at both 1.5 T and 3.0 T and a 12-channel head coil was used.

The strength of a contrast agent and the extent to which it provides a presence within an MRI image, is based on the agent's ability to alter either the spin-lattice relaxation time, T_1, such as gadolinium; or spin-spin relaxation time, T_2. Such factors, which primarily affect the performance of all MRI contrast imaging agents, are also applicable to iron oxide nanoparticles. Thus, the resulting relaxation effects of iron oxide nanoparticles are a combination of factors; including the iron oxide core, the applied magnetic field strength and the local environment or condition or tissue that the iron oxide nanoparticle find themselves in.

The addition of nanoparticles, with an iron oxide core, generates a further (localised) magnetic field of its own, due to its iron content, induced magnetic field inhomogeneities localised to their location. These induced inhomogeneities lead to an increased transverse relaxation rate (a decrease in T_2 thus appearing hypo-intense), also known as spin-spin relaxation time (T_2). This was observed with an increase in nanoparticle concentration (μg/ml) in the prepared gel phantoms resulted in a decrease in MRI signal, hence a hypo-intense image appearance. Iron oxide nanoparticles demonstrated relaxation changes that would allow them to be classified as a spin-spin relaxation contrast agent.

Compared to a 1.5 T clinical MRI scanner; a progression to an increased magnetic field strength, as with high magnetic field strength clinical MRI scanners, 3.0 T or greater, the proton relaxivities of substances become more rapid. The relaxivity rate $1/T_2$ at 3.0 T was thus more rapid compared to 1.5 T. The T_2 spin echo pulse sequence used was composed of 16 echoes. The TE values ranged from 22 ms (echo number 1) to 352 ms (echo number 16) inclusive. All other echoes were 22 ms apart; as presented in Table 3.2.

Echo number	TE value (ms)
1	22
2	44
3	66
4	88
5	110
6	132
7	154
8	176
9	198
10	220
11	242
12	264
13	286
14	308
15	330
16	352

Table 3.2: The echo numbers and their corresponding TE values.
Siemens MRI scanners, 1.5 T and 3.0 T, each used the same spin echo pulse sequence; t2_se_COR_16-echoes; and one image at each echo was created.

One MRI image at each echo was generated and in each of these images, the signal intensity changes at each tube was assessed, therefore, a total of 160 data ROI were created and used to calculate graphs that demonstrated the spin-spin relaxation of the iron oxide nanoparticles.

ImageJ software was used to quantitate (in arbitrary units) the MRI signal intensity changes induced by the iron oxide nanoparticles interacting with the magnetic field. These data were entered into Excel. The T_2 spine echo contrast intensity change formula; $Signal_{SE} = Signal_O e^{(-R_2 \times TE)}$; was transposed to $R_2 = (In(SignalSE) - (InSignalO)) / (-TE) <=> 1 / T_2$; and relaxation curved generated.

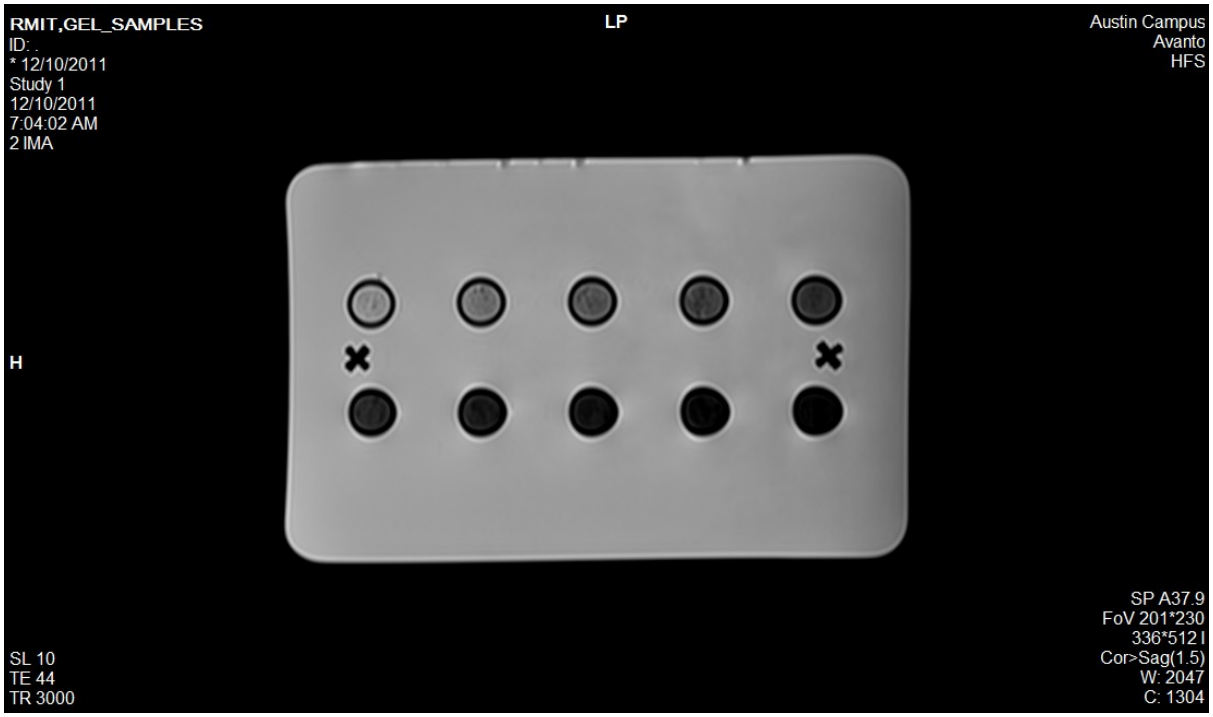

Figure 3.11: Top view of plastic container filled with water and containing plastic tubes filled with gel of increasing concentration of iron oxide nanoparticles; scanned at 1.5 T. A T_2 weighted image generated from a 16 echo spin echo pulse sequence at 1.5 T. This image was acquired with a TE value of 44ms and a TR value of 3,000 ms and a 12-channel head coil was used.

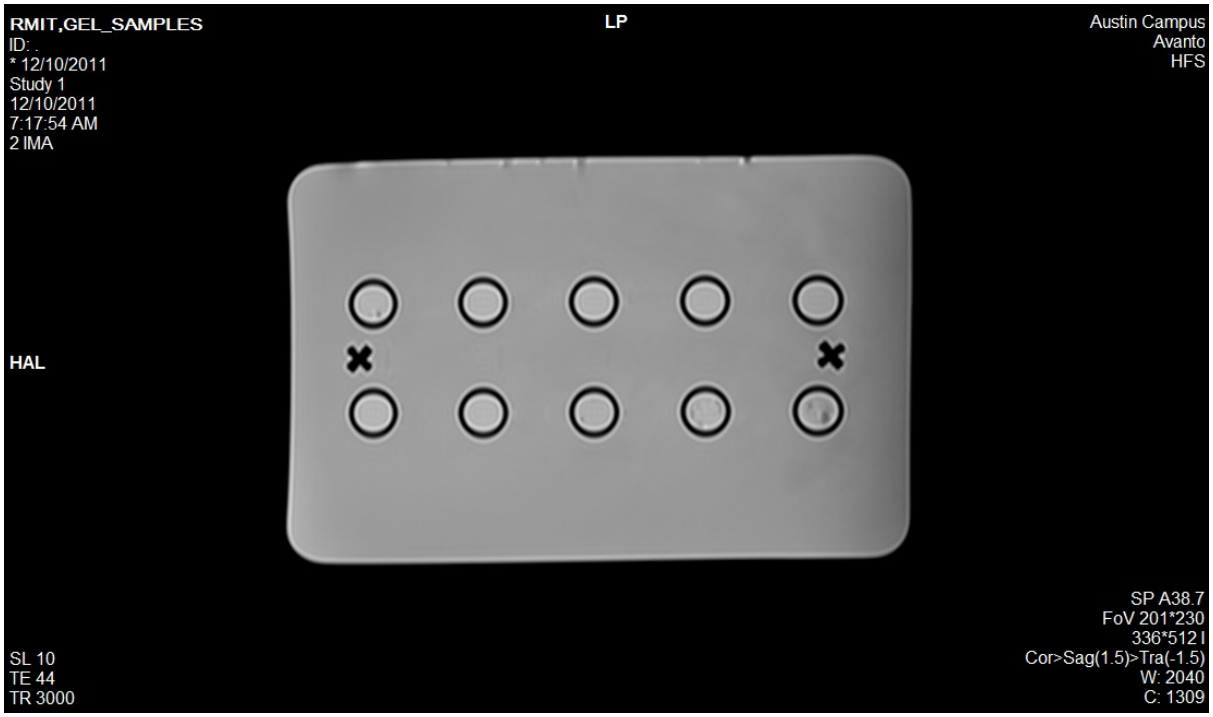

Figure 3.12: Top view of plastic container filled with water and containing control tubes – plastic tubes filled with gel only (no iron oxide nanoparticles); scanned at 1.5 T

A T_2 weighted image generated from a 16 echo spin echo pulse sequence at 1.5 T. This image was acquired with a TE value of 44 ms and a TR value of 3,000 ms and a 12-channel head coil was used.

Firstly, the signal intensity changes were calculated for the tubes that contained gel and iron oxide nanoparticles. Secondly, the signal intensity changes were calculated for the tubes that contained only gel and no iron oxide nanoparticles. Thirdly, the values calculated for the gel only tubes were used to subtract from the values calculated for the tubes that contained both gel and nanoparticle. This served two purposes. As both sets of tubes were imaged in the same position, the subtraction allowed for any image contract effects due to the gel to be eliminated and also, any magnetic field inhomogeneities inherent to the individual scanner would also be accounted for; as magnetic field inhomogeneity can accelerate localised de-phasing of spins and therefore alter local relaxivity.

The time between each echo (in the 6 echo pulse sequence) is known and thus, power trend lines have been applied to graphed measurements.

The following series of supporting graphs have been inserted in Appendix 1: A series of graphs (Figure 3.13 to Figure 3.22) that demonstrate the change in T_2 relaxivity, ΔR_2 response (or intensity decay profile), for each concentration sample across the 16 echoes in the pulse sequence, at 1.5 T. The next series of graphs (Figure 3.23 to Figure 3.38) record the linear fit to the T_2 relaxivity as a function of nanoparticle concentration and each of the known 16 TE echoes in the pulse sequence used, at 1.5 T. The same graphs and calculations were produced at 3.0T and are also presented in Appendix 1 (Figure 3.41 to Figure 3.66). An image of the gel phantoms with varying concentrations of iron oxide nanoparticles (Figure 3.39) and without nanoparticles (Figure 3.40) generated at 3.0T, appears in sequence prior to Figure 3.41).

On the following pages, Figure 3.67 represents the composite of Figures 3.13 to 3.22, Figure 3.68 represents the composite of Figures 3.41 to 3.50; Figure 3.69 displays the combination of Figures 3.23 to 3.38; and Figure 3.70 displays the combination of Figures 3.51 to 3.66.

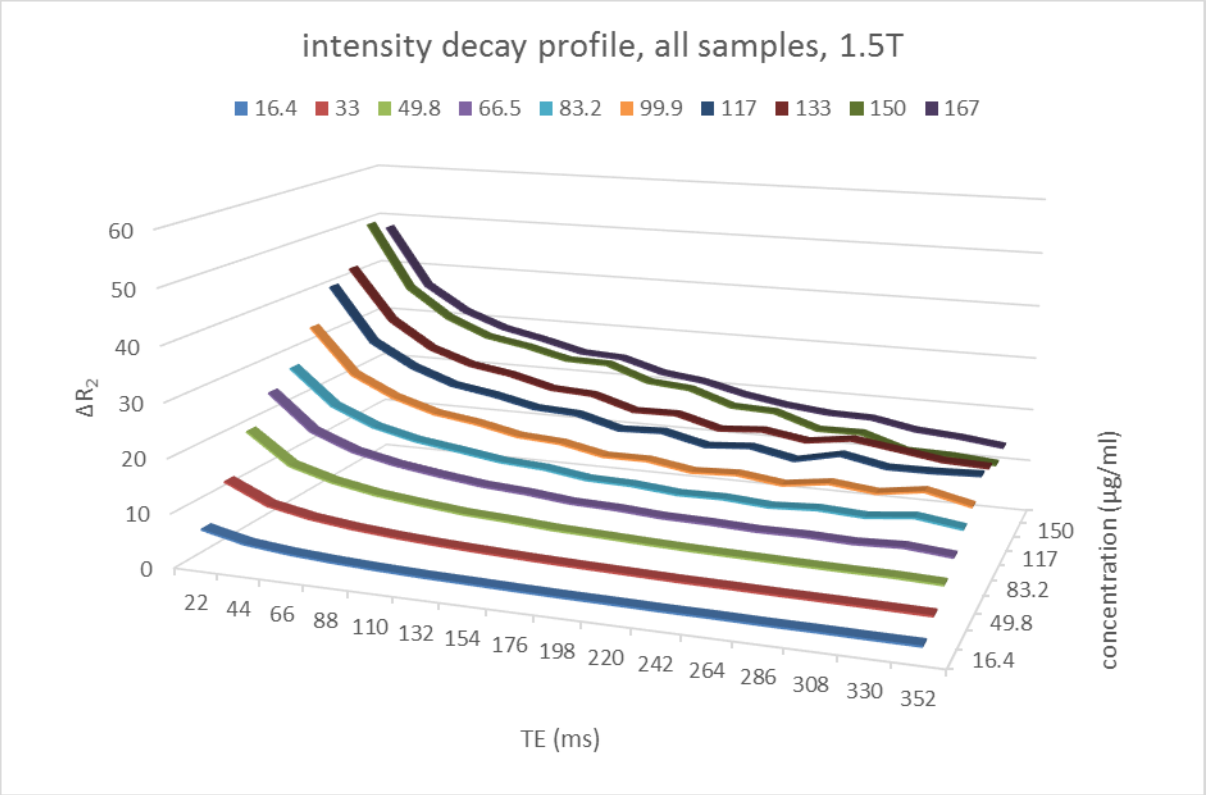

Figure 3.67: A comparison of the change in R_2 relaxivity, intensity-decay profile of all iron oxide concentration samples, as determined at 1.5 T. This 3D graph demonstrates the intensity decay profiles of all samples and compares the subtle differences between them across all TE values of the spin echo pulse sequence t2_se_COR_16-echoes at 1.5 T.

µg/ml	graph equation	R^2
16.4	$y = 23.635x^{-0.413}$	$R^2 = 0.9969$
33	$y = 45.607x^{-0.416}$	$R^2 = 0.9966$
49.8	$y = 68.059x^{-0.408}$	$R^2 = 0.9955$
66.5	$y = 82.358x^{-0.394}$	$R^2 = 0.9914$
83.2	$y = 79.628x^{-0.351}$	$R^2 = 0.9751$
99.9	$y = 101.4x^{-0.366}$	$R^2 = 0.9699$
117	$y = 119.56x^{-0.365}$	$R^2 = 0.977$
133	$y = 141.24x^{-0.386}$	$R^2 = 0.9884$
150	$y = 250.76x^{-0.486}$	$R^2 = 0.9394$
167	$y = 204.36x^{-0.443}$	$R^2 = 0.9669$

Table 3.3: A comparison of R^2 values of intensity decay profiles of all concentration samples at 1.5 T. Note that as the concentration of nanoparticles increases, the R^2 values commences to move away from the value of 1, indicating inhomogeneity and dephasing of spins, particularly at a concentration of 150 µg/ml.

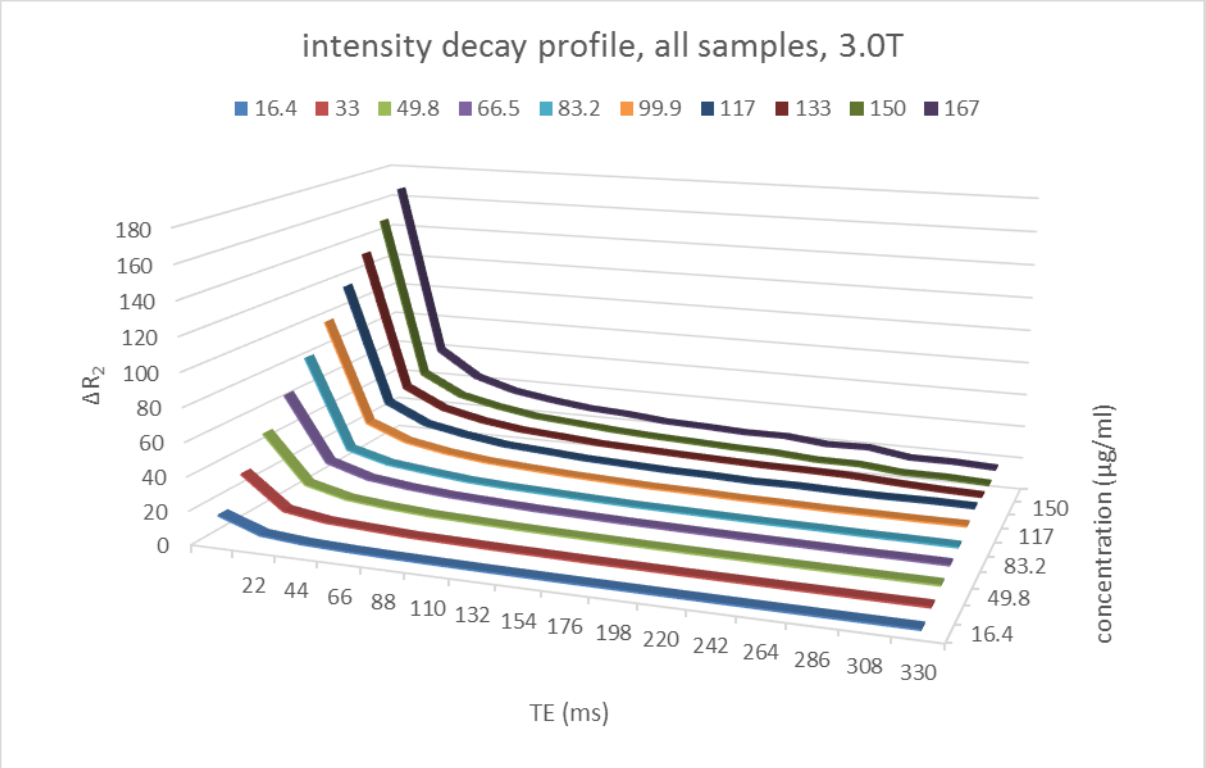

Figure 3.68: A comparison of the change in R_2 relaxivity, intensity-decay profile of all iron oxide concentration samples, as determined at 3.0 T. This 3D graph demonstrates the intensity decay profiles of all samples and compares the subtle differences between them across all TE values of the spin echo pulse sequence t2_se_COR_16-echoes at 3.0 T.

µg/ml	graph equation	R^2
16.4	$y = 29.66x^{-0.448}$	$R^2 = 0.9989$
33	$y = 48.054x^{-0.419}$	$R^2 = 0.9968$
49.8	$y = 74.54x^{-0.417}$	$R^2 = 0.9967$
66.5	$y = 95.261x^{-0.415}$	$R^2 = 0.9969$
83.2	$y = 90.05x^{-0.382}$	$R^2 = 0.9966$
99.9	$y = 119.29x^{-0.386}$	$R^2 = 0.9901$
117	$y = 119.29x^{-0.386}$	$R^2 = 0.9901$
133	$y = 170.11x^{-0.413}$	$R^2 = 0.9845$
150	$y = 225.67x^{-0.466}$	$R^2 = 0.9756$
167	$y = 274.1x^{-0.478}$	$R^2 = 0.9701$

Table 3.4: A comparison of R^2 values of intensity decay profiles of all concentration samples at 3.0 T. Note that as the concentration of nanoparticles increases, the R^2 values commences to move away from the value of 1, indicating inhomogeneity and dephasing of spins, particularly at 133 µg/ml, which is one concentration value less than at 1.5 T, confirming the NMR principle of rapid dephasing at higher field strengths.

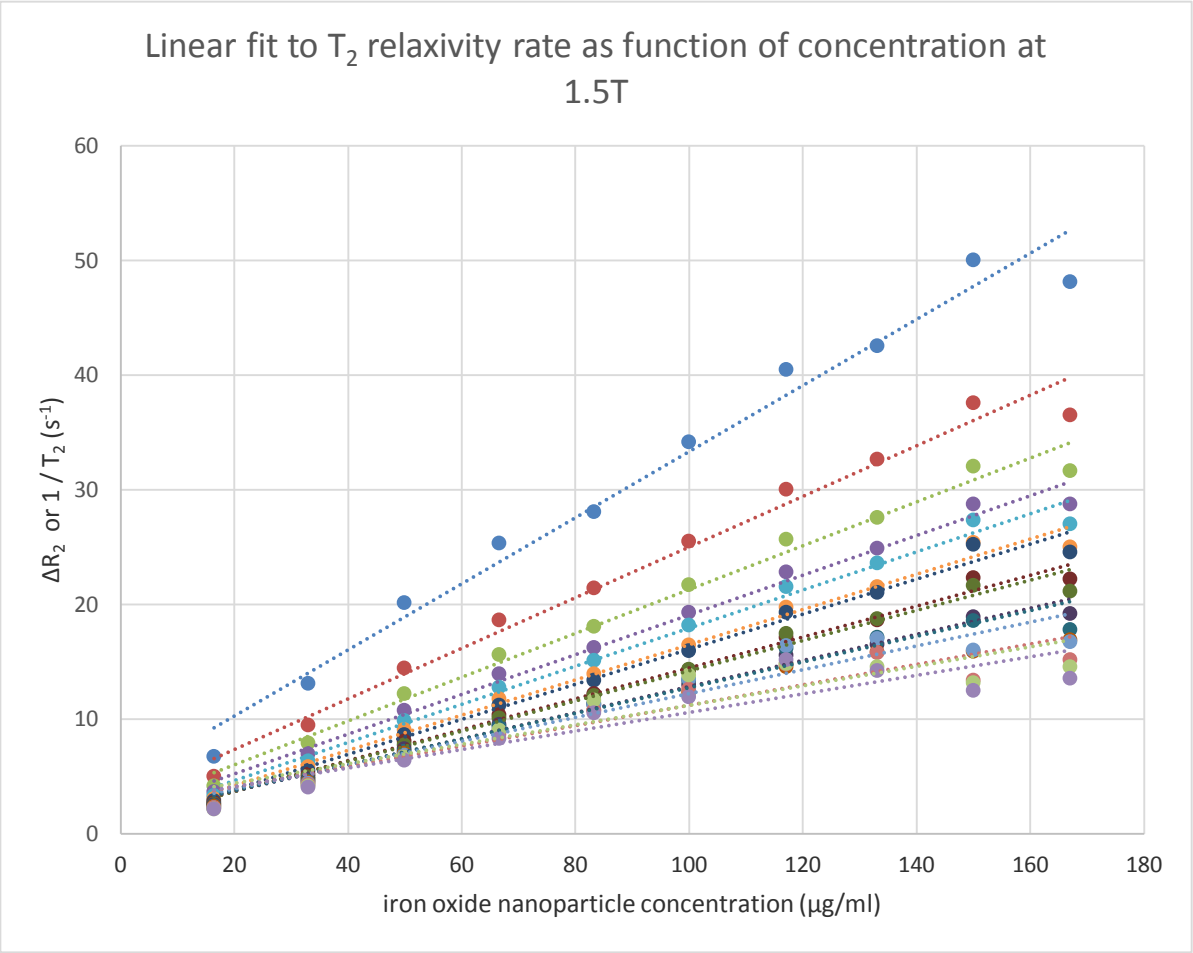

Figure 3.69: Comparison of the linear fit to the T_2 relaxivity rates as a function of iron oxide nanoparticle concentration, of all samples at 1.5 T.

Echo number	TE value (ms)	graph equation	R^2
1	22	y = 0.2882x + 4.5173	R^2 = 0.9779
2	44	y = 0.221x + 2.9077	R^2 = 0.983
3	66	y = 0.1911x + 2.1912	R^2 = 0.9867
4	88	y = 0.1735x + 1.7393	R^2 = 0.9895
5	110	y = 0.1663x + 1.2965	R^2 = 0.9889
6	132	y = 0.1536x + 1.1375	R^2 = 0.9894
7	154	y = 0.153x + 0.7817	R^2 = 0.9886
8	176	y = 0.1344x + 1.0287	R^2 = 0.9909
9	198	y = 0.1316x + 1.0451	R^2 = 0.9852
10	220	y = 0.1139x + 1.4566	R^2 = 0.9877
11	242	y = 0.112x + 1.5628	R^2 = 0.9629
12	264	y = 0.099x + 1.8665	R^2 = 0.9679
13	286	y = 0.104x + 1.8328	R^2 = 0.9244
14	308	y = 0.0889x + 2.3182	R^2 = 0.8891
15	330	y = 0.0846x + 2.7387	R^2 = 0.8359

Table 3.5: Comparison of R^2 of linear fit equations, as a function of nanoparticle concentration at 1.5 T. These figures support the dephasing, and resulting image signal intensity changes observed, according to TE values at 1.5 T. Note that as TE values increase, the linear fit becomes less accurate, indicating dephasing effects on the iron oxide nanoparticles.

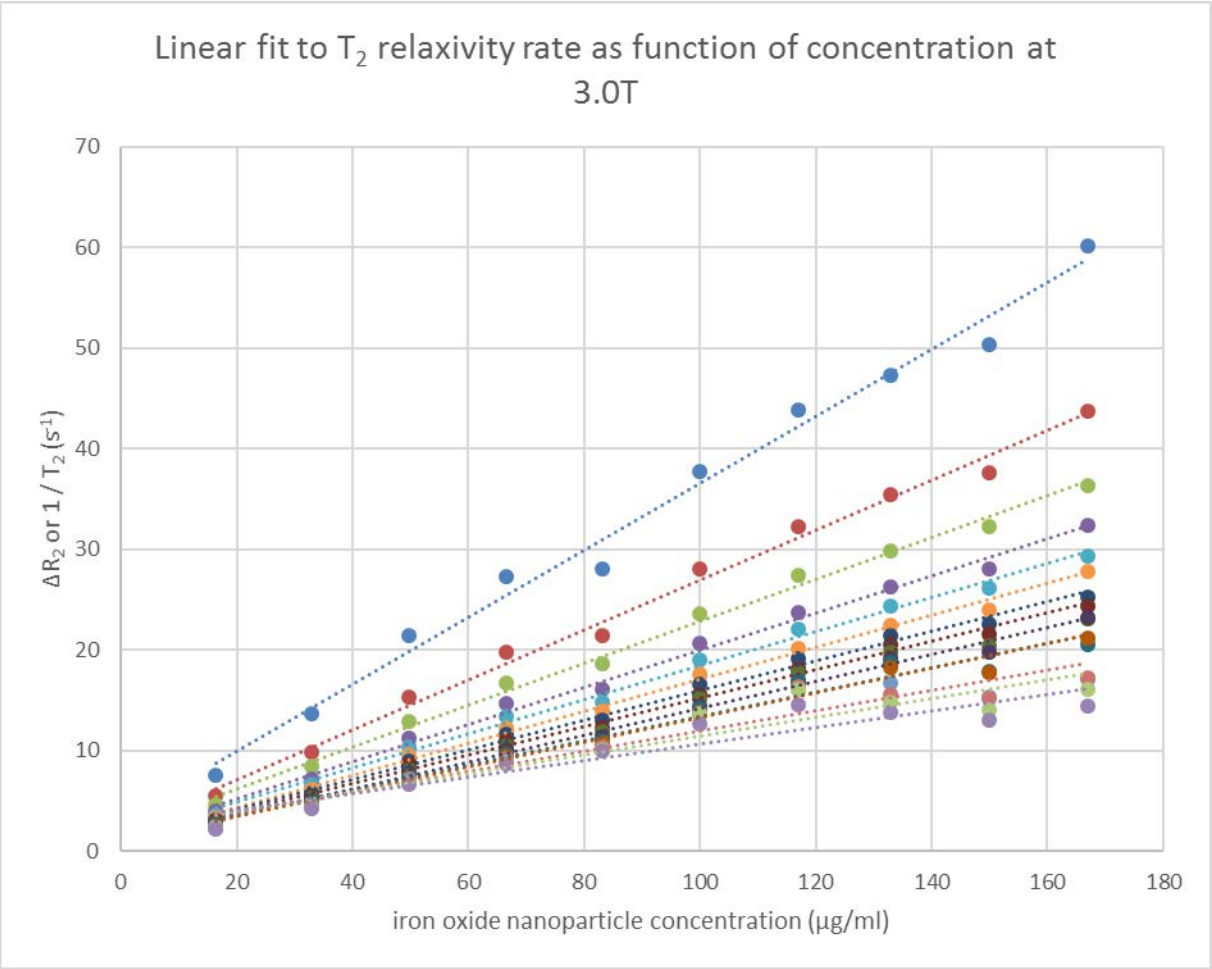

Figure 3.70: Comparison of the linear fit to the T_2 relaxivity rates as a function of iron oxide nanoparticle concentration, of all samples at 3.0 T.

Echo number	TE value (ms)	graph equation	R^2
1	22	y = 0.3332x + 3.2128	R^2 = 0.9882
2	44	y = 0.248x + 2.1639	R^2 = 0.993
3	66	y = 0.2082x + 2.0011	R^2 = 0.9945
4	88	y = 0.1845x + 1.5138	R^2 = 0.9945
5	110	y = 0.1696x + 1.4361	R^2 = 0.9942
6	132	y = 0.1587x + 1.1653	R^2 = 0.9957
7	154	y = 0.147x + 1.2744	R^2 = 0.9933
8	176	y = 0.1419x + 1.0113	R^2 = 0.9942
9	198	y = 0.1352x + 1.0715	R^2 = 0.9911
10	220	y = 0.1336x + 0.7622	R^2 = 0.994
11	242	y = 0.1212x + 1.2905	R^2 = 0.9719
12	264	y = 0.1227x + 0.939	R^2 = 0.9834
13	286	y = 0.1014x + 1.9394	R^2 = 0.9285
14	308	y = 0.1005x + 1.8697	R^2 = 0.9309
15	330	y = 0.0932x + 2.1364	R^2 = 0.8946
16	352	y = 0.0821x + 2.4585	R^2 = 0.8817

Table 3.6: Comparison of R^2 of linear fit equations, as a function of nanoparticle concentration ant 3.0 T. These figures support the dephasing, and resulting image signal intensity changes observed, according to TE values at 3.0 T. Note that as TE values increase, the linear fit becomes less accurate, indicating dephasing effects on the iron oxide nanoparticles and this occurs at a much earlier TE values compared with 1.5 T.

3.2.4 Radiolabelling of dextran coated iron oxide nanoparticles with ^{68}Ga

At the end of the incubation period with eluted ^{68}Ga, the dextran coated iron oxide nanoparticles underwent TLC to determine the level of purity of radiolabelling. The radiolabelling efficiency, as measured by TLC was 87.59 % (n=3); that is, when the radiolabelled sample of dextran coated iron oxide nanoparticles is prepared, 87.59% of the ^{68}Ga was bound to the nanoparticles and 12.41% was free or unbound. This is summarised in Figure 3.69. An example of the TLC spectral assessment is provided in Figure 3.70.

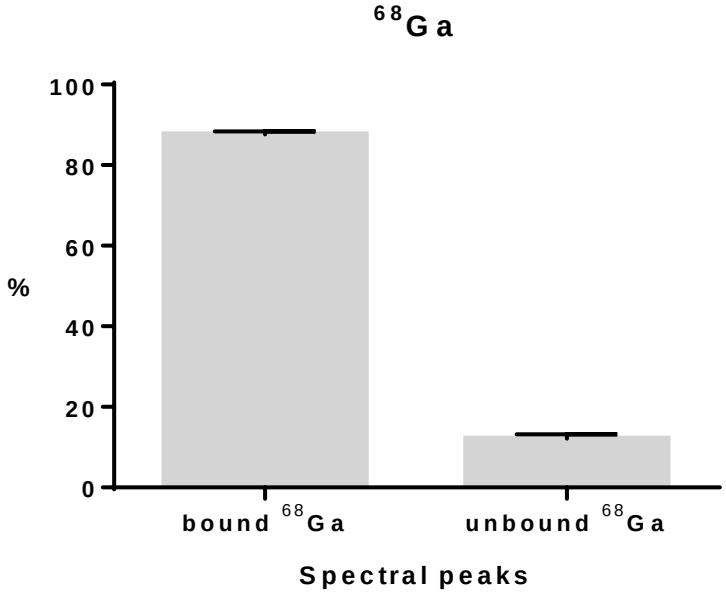

Figure 3.71: The ratio of ^{68}Ga bound to nanoparticles to unbound ^{68}Ga following the radiolabelling process. The error bars represent the standard error of the mean (n=3). The minimal error indicates that the radiolabelling process is robust and reproducible.

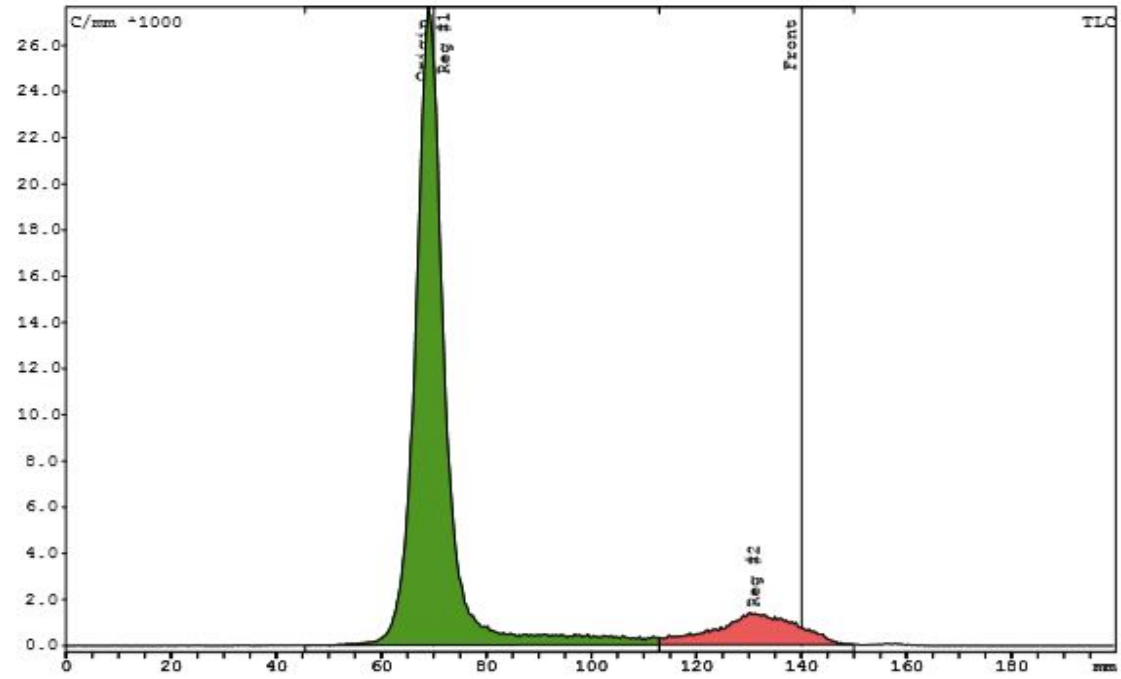

Sample description

Study:	QC 2013		
Measurement:	Spion DTPA Anhydride 151113 small spot.rta, started: 15/11/2013 1:07 PM		
Method:	Ga-Dex DTPA		
Origin:	70 mm	Front:	140 mm
Meas. time:	0:05:00	Resolution:	0.37 mm
Tray number:	1	Scan position:	100.0 mm
High voltage:	1650.0 V		
Mobile Phase: 0.1 M trisodium citrate			
TLC Plate: silica gel 60 F254			
Radio detector: raytest RITA			

Integration TLC

Substance	R/F	%Total %	Type	Area Counts	%Area %
Reg #1	-0.010	85.66	BD(	180490.2	88.01
Reg #2	0.864	11.67	DB(	24582.3	11.99
Sum in ROI				205072.6	
Total area				210716.0	
Area RF				104948.0	
Ext. BKG				0.00 C/mm	

Figure 3.72: A TLC chromatogram of a nanoparticle sample radiolabelled with ^{68}Ga. The green coloured peek quantifies the ^{68}Ga in the sample that is bound and the red coloured peek identifies the amount of ^{68}Ga that is free or unbound or not labelled; to the T10 dextran coated iron oxide nanoparticles.

3.2.5 MTS assay of T10 dextran coated iron oxide nanoparticles

FDA approval of commercially available dextran coated iron oxide nanoparticles imply that they are biocompatible and safe to administer to humans at the recommended dose per body mass. Published results have demonstrated that, commonly, iron oxide nanoparticles offer a very safe profile with signs of cytotoxicity becoming apparent at concentrations greater than 200 µg/ml, *in vitro*[221]. To assess the cytocompatibility of the iron oxide nanoparticles especially prepared for use throughout this thesis, MTS Cell Proliferation Assays were conducted, *in vitro*, with human peripheral blood mononuclear cells (PBMC), n = 5.

Figure 3.71 shows the results of the MTS assays performed with PBMCs following a 24 hour incubation time with nanoparticle concentrations of 200 µg/ml, 100 µg/ml, 50 µg/ml, 20 µg/ml and 5 µg/ml. Each experiment had three replicate values and the average of these replicates were compared with control wells (no nanoparticles). MTS assays were also performed with the safest known gadolinium based MRI contrast agent, Dotarem® (gadoteric acid)[40, 226-228], n = 5. These were also structured identically as per the PBMCs and nanoparticle experiments; with three replicates for each experiment with PBMCs and compared with control wells (no Dotarem®). The results from both sets of MTS assays, nanoparticle and Dotarem®, were compared.

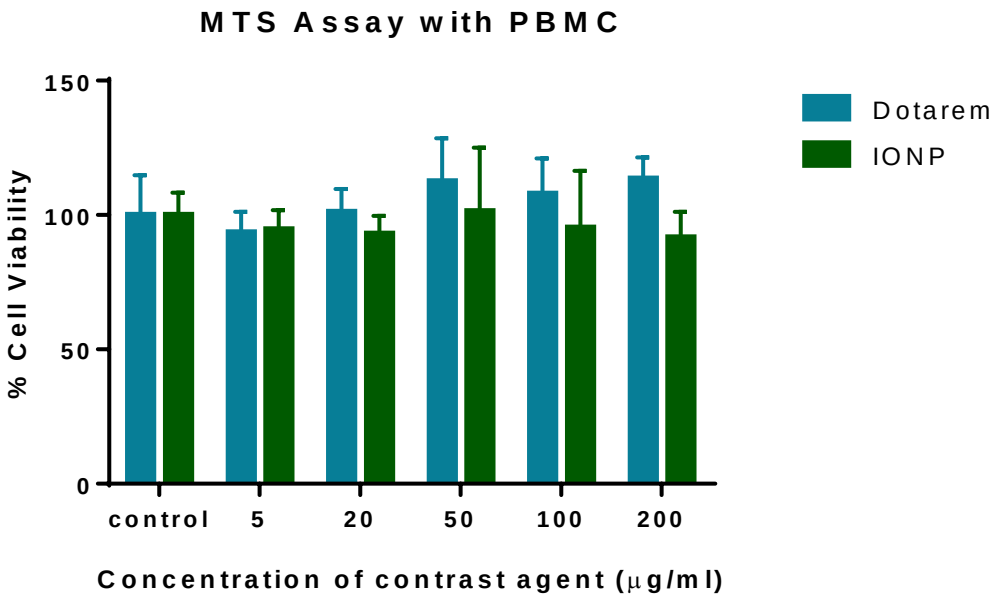

Figure 3.73: MTS Cell Proliferation Assay comparison with human PBMCs and T10 dextran coated IONPs and with human PBMCs and Dotarem®.
Percentage cell viability of human PBMCs following an incubation time of 24 hours with varying concentrations of T10 dextran coated iron oxide nanoparticles and separately with Dotarem®. The data is representative of triplicate assessments, performed five times (n = 5) and the error bars are the standard error of the mean. Statistical comparison was performed using a two-way ANOVA statistical post-test analysis with the Tukey's multiple comparison test (multiple comparison test comparing each group with the other group). No statistical significance was identified.

3.3 Discussion

For the intended purposes of experiments needed to be conducted throughout this thesis, there were a number of factors considered to be of equal and of paramount importance. These factors included the composition of the nanoparticle, its size and morphology. If these features are considered at the conception and design stage and followed through with incorporation into the fabrication process, such favourable characteristics will allow such nanoparticles to be included into a variety of laboratory experimental procedures to support the possible or eventual applications to new imaging possibilities.

At the commencement of this thesis, a review of the literature was performed. Published results identified that of all the possible combinations for nanoparticle composition, the least toxic and most biocompatible combination would be a nanoparticle composed with an iron oxide core with a dextran coating or outer shell[18, 56, 229]. Further exploration of the published revealed that high molecular weight dextrans were linked with allergic reactions and IgG responses in some humans[88, 218]. Therefore, a low molecular weight dextran would be more appropriate in order to improve biocompatibility. The overall size of the nanoparticles is also critical; to perform *in vitro* experiments with murine and human cells, the nanoparticles would need to be of a size that would allow them to be ingested. The nanoparticle size becomes even more critical when applied in *in vivo* studies. It has been established that, *in vivo*, nanoparticles greater than 60nm are readily identified and taken up by the RES[18]. A commercially available preparation of low molecular weight dextran coated iron oxide nanoparticles, Resovist®, is FDA approved and has been TGA approved, for use as a contrast agent specifically for imaging liver with MRI. Even though Resovist® is composed of iron

oxide core with a dextran coating, it's overall size is greater than 60nm; meaning that it is readily taken up by the Kupffer cells of the liver and other cells of the RES (spleen and bone marrow) and provides T_2 signal change characteristics on MRI images. Nanoparticles with a lesser size would evade sequestration of the RES and thus increase *in vivo* circulation time.

The nanoparticles used throughout this thesis, conformed to these desired characteristics, that is, an iron oxide core, low molecular weight dextran coating (T10) and a dimension of 20 nm with a smooth surface. The iron oxide core provided suitability for MRI imaging with T_2 characteristics and their 20 nm size allowed for *in vivo* and *in vitro* experiments. The low molecular weight dextran served two purposes; firstly to improve biocompatibility and secondly, to increase the range of imaging possibilities as the dextran's amine chain could be functionalised. The functionalise amine chain facilitated conjugation with FITC or R-PE and also with DTPA Anhydride for radiolabelling with ^{68}Ga.

Publications regarding the role of nanoparticles surface charge are not all in agreement; it is difficult to state with certainty if any statement made with respect to nanoparticles having either a positive, neutral or negative surface charge. It is clear, however, that with the different cells that have been examined, the resulting data have demonstrated their own preferential uptake of differently charged nanoparticles. For example, Villanueva *et al*[230] demonstrated that human cervical carcinoma cells (HeLa) preferentially internalised negatively charged nanoparticles; compared to the same nanoparticles with a positive or neutral charge. The postulation is that there are strong non-specific interactions with the plasma membrane, even though plasma membranes are known to be negatively charged. The mechanism of internalisation is believed to occur through nonspecific binding and clustering effects of cationic sites on the plasma membrane. Zhang *et al*[231] also reported iron oxide nanoparticles with a negative surface charge being internalised by both healthy breast epithelial cells (MCF10A) and with breast epithelial cancer cells (MCF7) and the

accompanying TEM images identified internalisation via endocytosis. These investigators further suggested that internalisation could be mediated by certain proteins; theorising that proteins from the cell culture medium could be located on the nanoparticle surface and induce receptor-mediated endocytosis. To support this theory, Zhang et al referred to studies with similar findings and suggestions. The findings of Koudelka *et al*[232] are put forward to also support for their theory, in that the 54 kD protein found on plasma membranes of both human and murine cells could be responsible for mediating the endocytosis of negatively charged nanoparticles.

Human mesenchymal stem cells were shown to internalise approximately equal quantities of negative, positive and neutral charged nanoparticles, as reported by Lorenz *et al*[233]. These investigators, in the same publication, also reported that HeLa cells showed internalisation of greater amounts of positively charged nanoparticles, which counters the findings reported by Villanueva. Thiele *et al*[234] reports that positively charged FITC-tagged nanoparticles tend to remain stuck to the outer cell membranes of human derived macrophages and human dendritic cells and purports that the phagocytic activity of positively charged particles, by these cells, is attributable to multiple factors such as the bulk material that both the particles and cells are held in, in addition to the size, charge and coating of the particles. BSA in the cell culture medium was attributed to the continuing phagocytic activity of these cells. They confirmed this by using trypan blue to quench the FITC of the particles adhered to the outer cell membrane, prior to performing flow cytometry.

Similar findings were supported by Foged *et al*[235] where immature DC (derived from human mononuclear cells) demonstrated greater uptake of negatively charged particles (100 nm) compared to positive charged particles, over a 4 hour incubation time; and assert further that negatively charged particles of a smaller size could offer superior interactions with immature

DC, compared to positive charged particles, as the negative charged particles will have less non-specific interactions with other cells.

Two commercially available iron oxide preparation, FDA approved for intravenous administration, have a dextran coating (Feridex®) and a carbodextran coating (Resovist®) and are both anionic. The nanoparticles used for this thesis had a negative charge, in the order of -15.62 ± 9.083 mV. Results of *in vitro* studies presented in the following chapters will demonstrate that these nanoparticles are internalised by both murine and human cells *in vitro* and *in vivo*.

It has been conclusively established that iron oxide nanoparticles demonstrate T_2 characteristics on MRI images; which is directly attributable to the iron oxide core[1, 2]. In the magnetic field environment of a clinical MRI scanner, the iron oxide core can behave analogous to a small magnet. At the nano scale, considering the surface area-to-volume ratio, collectively, the iron oxide cores can generate large scale imaging signal changes.

During the imaging process, under the application of a pulse sequence, the recovery to the magnetic equilibrium state (for iron oxide nanoparticles) is via the T_2 process of spin-spin relaxation; that is, the signal loss in the transverse plane. In the region where iron oxide nanoparticles are located (analogous to a contrast agent at a site of pathology, or the different concentrations of iron oxide nanoparticles suspended in gel), the presence of such particles creates an additional magnetic field. This, in turn, induces local magnetic field inhomogeneities which increase the rate of transverse relaxation (T_2) of proton adjacent and nearby protons. This rapid decrease of T_2 is demonstrated on an MRI image as a region of hypo-intensity, or darker that the surrounding biological tissue.

This physics principle has been adequately demonstrated by the specially fabricated dextran coated iron oxide nanoparticles. Ten gel samples were prepared with different concentrations of particles (as described in chapter two, section 2.12) and imaged with a spin echo, T_2

weighted, pulse sequence with 16 TE values. MRI imaging performed at both 1.5 T and 3.0 T demonstrated that these particles behave as desired in the magnetic field environments of these clinical MRI scanners. For all nanoparticle concentrations, their change in R_2 relaxivity, ΔR_2, or intensity-decay profile were graphed for 1.5 T and for 3.0 T. Also, the linear fit to the T_2 relaxivity rate, 1/T2, as a function of iron oxide nanoparticle concentration, at each TE value was also graphed at both 1.5 T and at 3.0 T. The signal intensity changes demonstrate rapid loss of T_2, particularly at 3.0 T compared to 1.5 T. These signal intensity changes render imaging changes contributed by these nanoparticles readily identifiable, therefore, demonstrating these nanoparticles' capabilities as suitable T_2 contrast agent at both 1.5 T and 3.0 T

MRI imaging also confirmed the even distribution of nanoparticles, as a contrast agent, within the gel suspension. In addition to visually comparing MRI signal intensities of the gel and nanoparticle filled tubes, quantitative analysis was conducted with their DICOM images being imported to ImageJ software program, and the signal intensity changes resulting from the presence of the nanoparticles were assessed. From this information graphs were generated demonstrating the capabilities of these nanoparticles across the 16 TE values. The control gel samples were also imaged and quantitated with the same method and subtracted from the values recorded for the corresponding nanoparticle-gel tubes; to account for magnetic field variations at those spatial locations and, important, to remove any signal contribution that may be attributed to the gel itself.

Imaging modalities that can complement one another are able to deliver more clinically useful imaging information than either modality can provide individually. PET and MRI are two such modalities that, when combined, the united advantages overcome their individual limitations. The use of nano-radiotracers is under development by many research groups with some success being published, and are designed for specific applications, using a variety of

nanoparticle composites and radionuclides to target the relevant biochemical process under investigation. Multimodal molecular imaging techniques (incorporating nanotechnology and radionuclides) are now seen as essential tools in translational and preclinical studies to evaluate new techniques[236, 237]. Clinical molecular imaging is seen as offering earlier detection, improve the accuracy of disease characterisation and also assess treatment efficacy earlier (and alter and improve treatment if necessary).

Even though MRI demonstrates excellent soft tissue definition with high levels of spatial interpretation, still, with certain available iron oxide nanoparticle preparations, the volume required to generate noticeable signal changes on MRI images has been reported to vary from 2 mg and 20 mg of iron per kilogram body mass[219]. The addition of a suitable radionuclide, such as ^{68}Ga (a PET agent) – as PET offers a higher order of magnitude in detection sensitivity (compared to MRI), – thus, the use of lower concentrations or volumes per kilogram of body mass of iron oxide nanoparticles would be needed – and together – molecular information can be provided with less ionising radiation.

Nanoparticles, therefore, can allow for creative opportunities for molecular imaging. Publications inform us that required capabilities can be engineered at the fabrication stage or (also at the synthesis stage) conjugated certain functional elements to the outer surface of nanoparticles. For this thesis, ^{68}Ga labelled iron oxide nanoparticles were prepared and evaluated with a TLC (to ascertain radiochemical purity) for bound and unbound ^{68}Ga. TLC results demonstrated a very high average radiolabelling yield of 87.59 %. This result was at the pre-wash stage; that is, immediately on completion of the incubation period of ^{68}Ga with dextran coated iron oxide nanoparticles. From here, the radio-active sample was centrifuged, the supernatant (containing as much unbound ^{68}Ga as possible) was removed and then resuspended in saline for *in vivo* administration. Interestingly, unbound or free ^{68}Ga results in corresponding activity being identified with PET imaging, in the liver, spleen, bone marrow

and kidneys, *in vivo*, and these same organs are responsible for collecting iron oxide nanoparticles, if their size are greater than 60 nm.

PET/MRI, with a radiolabeled nanoparticle can overcome limitations of both modalities and exploit the advantages of both; which are, using the radionuclide to maximise CNR on PET and using the nanoparticle to maximise both SNR and spatial resolution with MRI. Importantly, PET will provide functional information and MRI will contribute structural and anatomical detail[238]. Therefore, radiolabeled nanoparticles can be designed to target biochemical activity as well as demonstrate maximum soft tissue spatial definition with MRI[239]. Combining nanotechnology and molecular imaging and thus open new imaging possibilities and provide greater benefits to patients.

In vivo, Resovist® is a commercially available dextran coated iron oxide nanoparticle contrast agent specifically marketed as a liver imaging agent with MRI. It has an excellent safety profile, is well tolerated by patients, and is FDA approved. At one point, Resovist® was available in Australia.

To determine if the iron oxide nanoparticles would have severe deleterious effects on cells *in vitro*, MTS cell proliferation assays were performed using human PBMCs incubated for 24 hours with T10 dextran coated IONPs, *in vitro*, and also PBMC incubated for 24 hours with Dotarem®, *in vitro*. Of all the commercially available gadolinium based MRI contrast agents, Dotarem® has the highest level of human safety profile with no recorded incidence of NSF attributed to it[226]. Its comparatively safer profile has been attributed to its macrocyclic arrangement of gadolinium in relation to the chelating agent[40, 45, 227, 228]. The two datasets were graphed and compared; the justification being that as the ultimate intention was for the IONPs to be administered to human subjects, then they would need to be tested with human cells and compared with the safest known gadolinium MRI contrast agent (as also tested with the same type of human cells under the same *in vitro* conditions). The post-test analysis was

conducted with a two-way ANOVA and Tukey's multiple comparison test. No statistical significance could be found between any of the conditions treated with Dotarem®, nor could any statistical significance difference be found between the conditions treated with the T10 dextran coated IONPs; and importantly, no statistical significance was identified between any of the treatment conditions with nanoparticles when compared with any of the treatment conditions with Dotarem®. There was also no statistical difference between any of the treatment conditions and the control conditions. These comparisons suggest that both of these contrast agents have the same effect on the human cells tested, *in vitro,* and under the conditions of the experiment. Therefore, both the concentrations of the tested nanoparticles and Dotarem® do not impede cell viability of the human PBMC tested over a 24 hour incubation period, *in vitro*.

3.4 Conclusion

The aims of this chapter were addressed and experimental results lead to the following conclusions.

1. The dimensions and morphology of the specially fabricated dextran coated iron oxide nanoparticles were assessed. Their overall dimension was measured to be approximately 20 nm with TEM. Assessment with SEM demonstrated their morphology to be spherical and the dextran coating was smooth. Measurements taken with SEM also confirm the dimension of these nanoparticles to be approximately 20 nm.

2. The surface charge of these nanoparticles were demonstrated to be in the negative millivolt range for all storage conditions tested. The storage condition that provided the least negative millivolt charge was from nanoparticles stored in a standard refrigerator (4 ^{o}C) under room air. Nanoparticles stored under air in a standard freezer (-20 ^{o}C) revealed the greatest negative millivolt surface charge.

3. The T_2 characteristic behaviour of these nanoparticles were imaged using a spin echo pulse sequence with 16 TE values at both 1.5 T and 3.0 T (clinical MRI scanners). It was demonstrated graphically and also with phantom gel images, that the nanoparticles exhibited well defined imaging behaviour under T_2 weighted condition; generating readily identifiable and measurable signal intensity changes; thus making these nanoparticles viable as T_2 contrast imaging agents (MRI).

4. The radiolabelling process, in total, from completion of DTPA incubation to completion of ^{68}Ga incubation time, was between 2 hours and 2 ½ hours. The process resulted in high levels of radiolabelling effectiveness (87.59 %). This established the likely possibility of using this radiolabelled nanoparticle preparation as a dual modal (PET and MRI) contrast agent.

5. The cytotoxicity results, through the MTS cell viability assays, demonstrate that the tested concentrations of T10 dextran coated iron oxide nanoparticles and of Dotarem® do not reduce viability in human PBMCs compared to the control conditions. Importantly, there was no statistical significance between the effect that the nanoparticle preparation had on the human PBMCs compared to the effect that Dotarem® (the safest known gadolinium based MRI contrast agent) had on the PBMCs under the same experimental conditions, *in vitro*.

4.0 Chapter 4 – Characterisation of Iron Oxide Nanoparticle Uptake by Murine Derived Dendritic Cells, *in vitro*.

4.1 Introduction

Murine dendritic cells (DCs) were first identified and described by Steinmen and Cohn in 1973[197]. Since then, our understanding of DCs has increased to the point where DCs are being used for cancer immunotherapy experiments with potential translational possibilities. The commonly accepted definition of DCs is based on their function; that is, DCs have the unique capabilities to internalise, process and present antigens[198] to naïve T cell lymphocytes[199] (and B cell lymphocytes) and prime an immune response[200, 201]. Further, DCs are also defined by phenotype as being lacking in certain lineage specific markers (Lin-) and expressing elevated levels of Major Histocompatibility Complex (MHC) molecules (class II); this phenotype is represented as $^{-}$HLA-DR^{+} [198].

From a progenitor cell perspective, DCs can be categorised into two main groups or originating from either one of two lineages: conventional DCs (cDC) and plasmacytoid DC (pDC)[202]. cDC are also referred to as myeloid DC (mDC)[203]. DC progenitor cells originate in the bone marrow and are carried by blood to lymphoid organs and peripheral tissue; where, *in situ;* they develop into mDC[202]. pDC develop or differentiate in the bone marrow first and then subsequently colonise lymphoid organs[202]. pDC precursors produce significant quantities of type I interferons, such as IFN-α and IFN-β[204]. A further distinction is that mDCs are progressively migrating from their peripheral tissue base to the corresponding region's draining lymph node (LN), while DCs originating from lymphoid organs remain localised there throughout their cell life cycle.

DCs can also be categorised as either immature DCs or mature DCs. Commencing from their progenitor cell origins, the presence of GM-CSF and the Flt3 ligand, allow these progenitor cells to become immature DCs, *in vitro*. Immature DCs (iDCs) continually sample their immediate environment and have a high phagocytic capacity. If iDCs ingest a pathogen, or in the presence of other relevant stimulants, iDC enter a phase of developing maturity. This triggers a maturity signal and a complex interplay of chemicals is orchestrated. Prior to this maturity signal, however, iDC (murine) are identified as having the following phenotype and attributes:

- Low expression levels of costimulatory markers: CD80, CD86, CD40 and CD83
- Low secretion levels of IL-12 cytokine

CD, or cluster of differentiation, are proteins found on cells and these proteins provide a costimulatory signal necessary for T cell activation. Low expression levels of certain CD signify that iDC have not been activated or have not received a maturation signal. IL-12 is a cytokine, a small protein; affecting the migration of iDCs to its destination, as it matures and affecting the subsequent behaviour of T cells (once the iDCs become mDCs and meet with T cells). Chemokines, interferons and interleukins are classified as cytokines.

As DCs mature, their physical chemotaxic transition into, and through, afferent lymphatic vessels requires cytokine stimulation and induction of the CCR7 chemokine receptor[201]. The expression of CCR7 is triggered when immature DCs become activated. Activation of DCs result in up regulation of CCR7 and down regulation of inflammatory cytokine receptors to facilitate chemotaxis migration to draining lymph nodes[200].

Following the maturation signal and as iDCs evolve to mDCs, they will migrate to their destination site (such as lymph nodes or sites of infection). mDCs (murine) have been identified with the following phenotype and expression levels:

- High expression levels of CD80, CD86, CD40, CD25 and CD83
- High secretion levels of IL-12 cytokine

Mature DCs that have migrated to secondary lymphoid organs (such as the lymph nodes or spleen) are also characterised has having a very minimal capacity for phagocytosis, (compared to iDC), thus, alternatively, a lower capacity to capture antigens; however, they develop capability to efficiently present antigen material to naïve T cells to stimulate an immune response – hence, their potential pivotal role in immunotherapy.

DCs can also be triggered to migrate to lymph nodes by indirect methods. Firstly, under normal physiological conditions and in the immunological steady state, the normal movement of lymph fluid along afferent lymphatic vessels is by gentle pulsatile motion[200]; secondly, signals originating from B-cells located from within activated lymph nodes can initiate a migration of DCs[200].

The migration[207] of iDCs from their initial environment to the high endothelial venules (HEV) and the T cell zone (within lymph nodes), together with the simultaneous transition from immature to mature; is a rather complex series of events. pDC enter lymph nodes directly with the blood supply, whereas other types of DCs enter lymph nodes via the afferent lymphatic vessel[201]. It is this afferent lymphatic vessel that drains nearby tissue and thus providing the physical migratory pathway.

DC precursor cells originate in bone marrow and migrate to all areas of the body where they can exist in an immature state, sampling their immediate environment and awaiting antigens[200]. Upon stimulation with a suitable antigen, iDCs commence a sentinel function to home to secondary lymphoid organs and structures, especially lymph nodes, where they interact with naïve T cells and also central memory T cells[200].

Chemokines are mediators of iDC migration, whereby, intracellular signalling pathways are triggered to commence cell migration and activation to maturity[200]. Chemokine and chemokine receptors are pivotal in shifting DCs to LNs through afferent lymphatic vessels and also from blood[200]. Via afferent lymphatic vessels, DCs enter the subcapsular sinus and then migrate to the T-cell zone of the LN cortex. DCs from the blood stream enter the HEV and then migrate from the HEV, through the endothelial wall, and into the T-cell zone for efficient and effective interaction with naïve T cells.

Along with DCs antigen presenting characteristics, comes their unique talent to encourage an immune response from T cells. This is the broad and guiding principle of Dendritic Cell Immunotherapy (DCI)[207]. DCs also provide a link between the innate (non-specific) and adaptive (acquired) immune systems.

Cellular MRI is a method of detecting cells *in vivo*, after they have been labelled *ex vivo* with a contrast agent, commonly IONP. This technology and methodology has been applied by researchers to generate iDC from bone marrow progenitor cells, incubate iDC with IONP preparations, then administer these loaded cells into a live specimen and observe their migration and subsequent fate with MRI, *in vivo*. The advantages offered by cellular MRI include that it is non-invasive imaging to live specimens, it uses non-ionising radiation and produces images of exquisite image quality.

DCs and cellular MRI are both central in experimental techniques for cancer immunotherapy – where an individual's immune cells and system can be activated to combat cancer cells. Tumours can be targeted with the use of antigen-specific vaccine; that is, DCs are loaded with cancer vaccines with tumour specific antigen (peptides or proteins) and used to initiate an anti-tumour response[20]. For DC-based cancer immunotherapy to be considered effective, DCs would need to migrate to secondary lymph organs such as lymph nodes and the spleen. Early attempts were not wholly successful; as the methodology used to attempt to load

antigens into DCs and have them try to migrate to secondary lymph organs to commence and immune reaction were not efficient. Essentially, tumour antigen and adjuvant were introduced *in vivo* by either intradermal, subcutaneous or intramuscular injection; from here, local DCs were supposed to internalise the antigen, process it and migrate to lymph nodes. This was not successful because tumours can release immunosuppressive substances and also self-tolerance to the tumour antigen can exist; combined together, these can inhibit an effective immune response. At present, researchers are overcoming this is with an *ex vi*vo approach – iDCs are generated *in vitro* from haematopoietic precursor cells in non-immunosuppressed conditions, then loaded with antigen and then administered into the live specimen.

Upon activation, DCs commence a migratory progression to lymph nodes and during this migration process, DCs process uptaken antigens, place these on their cell surface (along with MHC molecules) for presentation to T cell lymphocytes and upregulate costimulatory markers. These costimulatory markers are expressed as the DCs transition from an immature to mature state and also facilitate interaction with T cell lymphocytes[(204)]; as only mature DCs are capable of activating T cell lymphocytes. T cells require three different signals in order to be effectively and efficiently activated. Firstly, the T cell receptors must recognise and accept the antigen presented by the DC (together with MHC molecules). Secondly, T cells require the costimulatory molecules that have been upregulated and presented with mature DCs. Thirdly, a paracrine (cell-to-cell) signal from soluble molecules in the form of cytokines and/or chemokines produced by the mature DCs[(204)].

For experiments pertaining to this thesis, murine DCs were generated from bone marrow precursors, *in vitro*, by incorporating the GM-CSF cytokine. A DCs progression to a mature state can be identified phenotypically by its expression of costimulatory proteins such as CD86 (and MHC class II)[(204, 240)], CD80 and CD83[(205)]. By culturing murine bone marrow

cells with the Flt3-ligand, murine pDC precursors can be generated similar to human cells[204]. Plasmacytoid pre-dendritic cells or type 1 interferon (IFN)-producing cells (IPCs), in both humans and mice, display a plasmacytoid morphology and have the capacity to produce large amounts of type 1 IFN in response to viral and bacterial stimulation[240]. Murine IPCs readily produce IL-12 in response to viruses or bacteria[240]. Human IPC do not have the ability to produce IL-12p70[240].

Are IONPs, as an introduced foreign substance to DCs, capable of being internalised by DCs and do they initiate maturation and migratory signals? A proprietary Cytometric Bead Array (CBA) Mouse Inflammation Kit can be used to test for the six most common cytokines that are known to be involved with an immune response to stimulus, the maturation process and migratory chemotaxis. This assessment techniques holds some advantages over the ELISA technique such as: a lesser supernatant volume is needed to perform the CBA assay (approximately one-sixth of the volume is required as the CBA assay can detect six cytokines in one sample), results from performing one CBA assay would be equivalent to performing six conventional ELISAs, the CBA assay is comparatively quicker and less expensive to perform. The CBA assay does, however, have a known limitation, which is, it may have a reduced sensitivity to murine MCP-1.

These following cytokines are protein molecules, secreted by DCs and used for signalling cellular activities, can be identified and quantified with a CBA assay (mouse), and it was these cytokines which were quantified by flow cytometry in conjunction with a proprietary CBA Mouse Inflammation Kit.

Mouse IL-6 (also known as B cell stimulating factor)

This is a general pro-inflammatory cytokine and also has a role in the final differentiation of B cells. IL-6 is also known to have a regulatory role of a tumour's microenvironment regulation[241]. It has also been identified that patients with advanced metastatic cancer patients have higher levels of IL-6 in their blood. One example of this is pancreatic cancer, with noted elevation of IL-6 present in patients and unfortunately correlating with poor survival rates[242]. Hence, there is an interest in developing anti-IL-6 agents as therapy against many of these diseases[243, 244]. As an anti-inflammatory cytokine, it is mediated through its inhibition of TNF-α and IL-1 and its activation of IL-1a and IL-10[245]. Il-6 has also been documented to stimulate inflammatory and auto-immune responses in patients with various pathologies including: prostate cancer, diabetes, atherosclerosis, Alzeimer's disease, multiple myeloma and rheumatoid arthritis[243].

Mouse IL-10

This is an anti-inflammatory cytokine produced by monocytes, lymphocytes and subsets of T and B cells. IL-10 inhibits the synthesis of pro-inflammatory cytokines such as INF-γ, IL-2, IL-3, TNF-α and GM-CSF, thereby supressing the ability of DCs to present antigens to T cells It also down regulates MHC II antigens and co-stimulatory molecules on macrophages.

Mouse MCP-1, monocyte chemo-attraction protein 1

(also known as CCL2, chemokine Ligand 2)

This is secreted by DCs, monocytes and macrophages to augment anti-tumour activity by monocytes themselves. MCP-1 can also direct DCs, (and memory T cells and monocytes to a lesser extent) to sites of inflammation. Whether it be tumour or inflammation, MCP-1 has a role in the chemotaxis of DCs. It has also been identified with the positive regulation of eradicating apoptotic cells.

Mouse IFN-γ (interferon-γ)

This cytokine holds important functions in both the innate and adaptive immunity systems. It is known to be produced by NK and NK T cells as part of the innate immune response and is also well known for its ability to activate macrophages. IFN-γ is secreted by myeloid cells, DCs and macrophages as a cell self-activation process during the onset period of infection. It also has anti-tumour, anti-viral and immune-regulatory properties.

Mouse TNF (tumour necrosis factor, TNF-α, also known as cachexin)

This is a monocyte derived cytotoxin that is implicated in tumour regression. It is predominately produced by activated macrophages but also by CD4+ lymphocytes, NK cells and neutrophils. Its functions include: to regulate immune cells, induce apoptotic cell death and inhibit tumourigenesis and viral replication. TNF will acts together with IL-1 and IL-6 to respond to sepsis. Prolonged periods of low concentrations of TNF has known to lead to cachexia (wasting syndrome seen in cancer patients).

Mouse IL-12p70

Murine DCs produce IL-12p70 in response to antigen stimulation. This, in turn, stimulates production of IFN-γ and TNFα from T-cells (and NK cells). Interestingly, IL-12p70 can also reduce IL-4 mediated suppression of IFN-γ and can inhibit angiogenesis, the formation of new blood vessels, by increasing IFN-γ.

Apoptosis is the programed cell death in multicellular organisms while necrosis is a form of traumatic cell death that results from acute cellular injury. Foreign substances, such as IONP, can induce apoptosis. Cells have their own tolerances to foreign material according to their dose and exposure duration. The TNF cytokine is the major extrinsic mediator of apoptosis. The apoptotic process and sequence is characterized by specific processes and morphologic traits. These include the loss integrity of the cell plasma membrane, progressive destruction and loss of cytoplasm and nucleus, and inter-nucleosomal separation of DNA.

The earliest detectable feature of cells in apoptosis is the loss of plasma membrane. Phospholipid phosphatidylserine (PS), found in the inner aspect of the cell membrane becomes exposed to the cell's external environment. Annexin V binds to cells with exposed PS as it has a high affinity for PS at this early stages of apoptosis. Successful cell staining with Annexin V occurs prior to the complete loss of cell membrane integrity which takes place at the end stages of apoptotic or necrotic cell death processes. To identify compromised integrity to the cell membrane from these events and stages, cell staining is also performed with 7-Amino-Actinomycin (7-AAD), a vital cell dye; which indicates cells in early apoptosis. Cells with a viable and intact membrane will be negative for 7-AAD, however, cells with a disrupted membrane (either damaged or dead) will allow 7-AAD to enter.

The specific aims of this chapter were:

1. To determine dose dependent uptake of IONPs by GM-CSF and Flt-3 derived murine BM-DCs, *in vitro*.
2. To determine time dependent uptake of IONPs by GM-CSF and Flt3 derived murine BM-DCs, *in vitro*.
3. To determine the potential maturation effect of IONPs on GM-CSF and Flt3 derived murine BM-DCs, *in vitro*.
4. To determine the apoptotic effect of IONPs on GM-CSF and Flt3 derived murine BM-DCs, *in vitro*.
5. To identify increased cytokine release by GM-CSF and Flt3 derived murine BM-DCs after exposure to IONPs, *in vitro*.

4.2 Results

4.2.1 Dose dependent uptake of FITC tagged IONPs by murine BM-DCs, *in vitro*

Bone marrow stem cells from female C57BL/6 mice were cultured with either GM-CSF or Flt3 as described in Section 2.10 and incubated with FITC tagged IONPs as stated in Section 2.11.1 and dose dependent uptake studies performed, *in vitro*. Flow cytometry was used to measure the uptake of FITC tagged IONPs by observing the fluorescence of the FITC and the granularity of the cells.

4.2.1.1 Dose dependent uptake of FITC tagged IONPs by GM-CSF grown murine BM-DCs, *in vitro*

Uptake of FITC tagged IONPs by CD11c+ (membrane protein of DCs) GM-CSF grown murine BM-DCs demonstrated an almost dose-dependent effect with statistical analysis identifying no statistical significance beyond an IONP concentration dose of 50 µg/ml (Figure 4.1A). The Fold Increase in MFI from the FITC itself (tagged to the IONPs) was at maximum statistical significance with an IONP concentration of 100 µg/ml (Figure 4.1B).

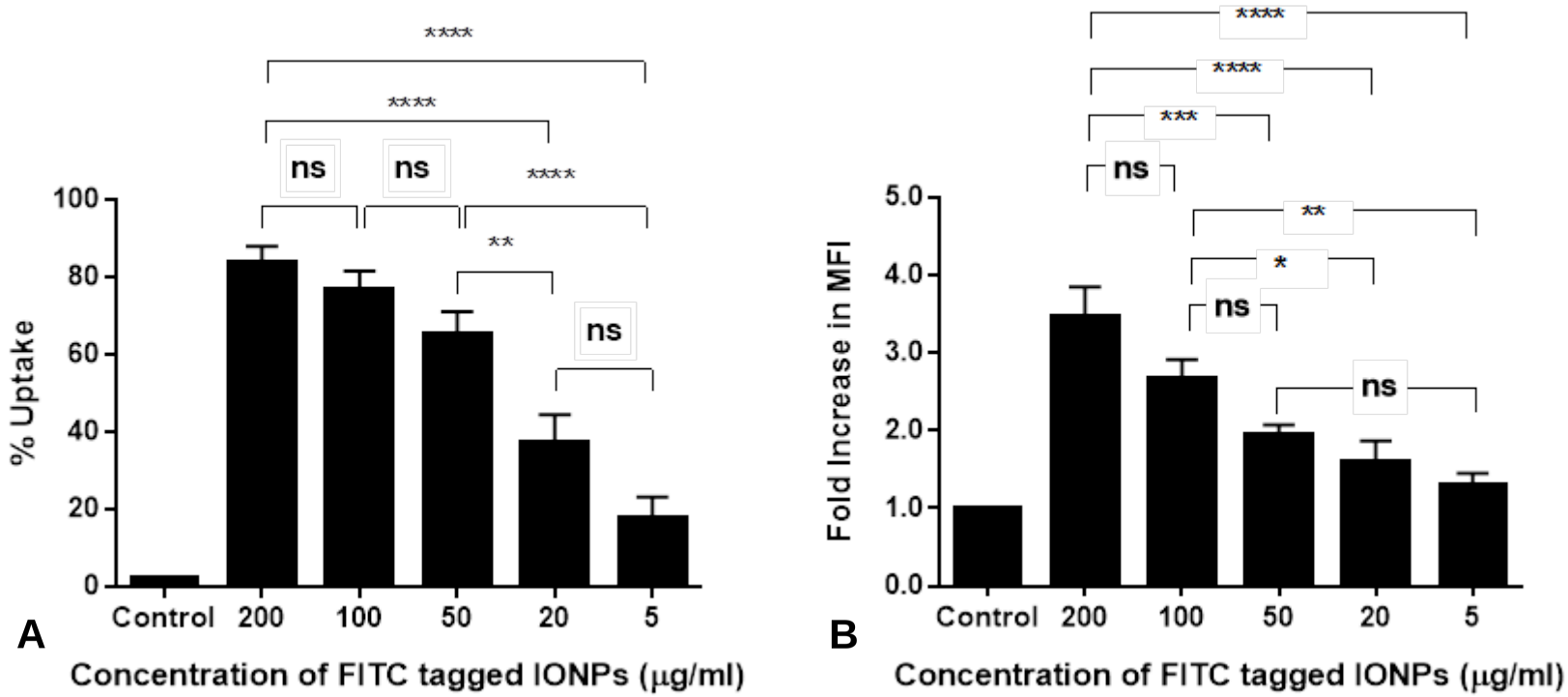

Figure 4.1: Dose dependent uptake (A, percentage uptake and B, MFI) of FITC tagged IONPs by GM-CSF grown BM-DC, *in vitro*. GM-CSF grown BM-DC (6 days) from C57BL/6 mice were incubated with varying concentrations of FITC tagged IONPs for 24 hours, *in vitro*. Uptake by CD11c+ cells was quantitated by flow cytometry and analysed using FACSDiva software (BD Biosciences), n=8. Results are shown as the mean percentage surface expression with standard error of the mean as error bars. One-way ANOVA statistical analysis with post-test analysis was conducted with the Tukey's test (multiple comparison test comparing each group with the other groups) for treatments between columns. The Dunnett's test was used to compare the control group with each treated group. **Figure 4.1A;** Percentage uptake by CD11c+ cells. **Figure 4.1B;** The fold increase in MFI from the FITC (tagged to the IONPs) from the percentage uptake by CD11c+ cells.

4.2.1.2 Dose dependent uptake of FITC tagged IONPs by Flt3 derived BM-DCs, *in vitro*

Uptake of FITC tagged IONPs by CD11c+ (membrane protein of DCs) Flt3 grown murine BM-DCs demonstrated no statistically significant difference between adjacent treatment conditions. There was no statistical significance between the control mean and treatment conditions where the IONP concentration used was 50 µg/ml or less (Figure 4.2A). Statistically significant uptake occurred with 100 µg/ml and 200 µg/ml (Figure 4.2A). The Fold Increase in MFI graph (Figure 4.2B) demonstrated no statistical significance between the control mean and any of the treatment conditions (Figure 4.2B).

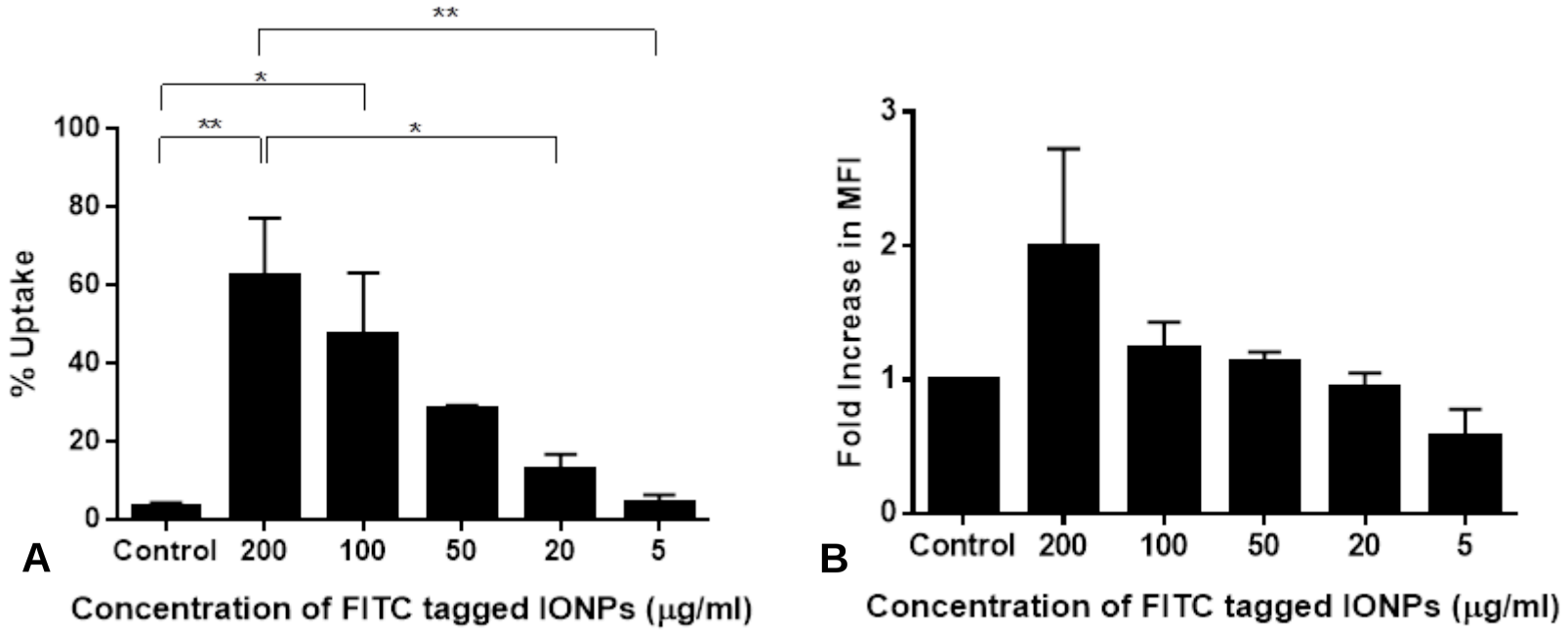

Figure 4.2: Dose dependent uptake (A, percentage uptake and B, MFI) of FITC tagged IONPs by Flt3 derived BM-DC, *in vitro*. Flt3 grown BM-DC (8 days) from C57BL/6 mice were incubated with varying concentrations of FITC tagged IONPs for 24 hours, *in vitro*. Uptake by CD11c+ cells was quantitated by flow cytometry and analysed using FACSDiva software (BD Biosciences), n=8. Results are shown as the mean percentage surface expression with standard error of the mean as error bars. One-way ANOVA statistical analysis with post-test analysis was conducted with the Tukey's test (multiple comparison test comparing each group with the other groups) for treatments between columns. The Dunnett's test was used to compare the control group with each treated group. Where no asterisks are displayed, no statistical significance was found. **Figure 4.2A;** Percentage uptake by CD11c+ cells. **Figure 4.2B;** The MFI from the FITC (tagged to the IONPs) from the percentage uptake by CD11c+ cells.

4.2.2 Time dependent uptake of FITC tagged IONPs by BM-DCs, *in vitro*

Bone marrow stem cells from female C57BL/6 mice were cultured with Flt3 as described in Section 2.10 and incubated with FITC tagged IONPs as stated in Section 2.11.4 to perform time dependent uptake studies. Flow cytometry was used to measure the uptake of FITC tagged IONPs of each treatment condition by observing the fluorescence of the FITC and the granularity of the cells.

4.2.2.1 Time dependent uptake of FITC tagged IONPs by GM-CSF grown BM-DCs, in vitro

CD11c+ (membrane protein of DCs) GM-CSF grown murine BM-DCs demonstrated the level of uptake of FITC tagged IONPs at 1 hour incubation time was statistically comparable to the uptake at 24 hours incubation time, *in vitro*, and, there was very significant statistical difference between the control mean and the mean of each treatment condition (Figure 4.3A). There was no statistical significance of the Fold Increase in MFI between the treatment conditions, however, there was statistical significance between the mean value of the control condition and the mean value of the 24 hour incubation time treatment condition (Figure 4.3B).

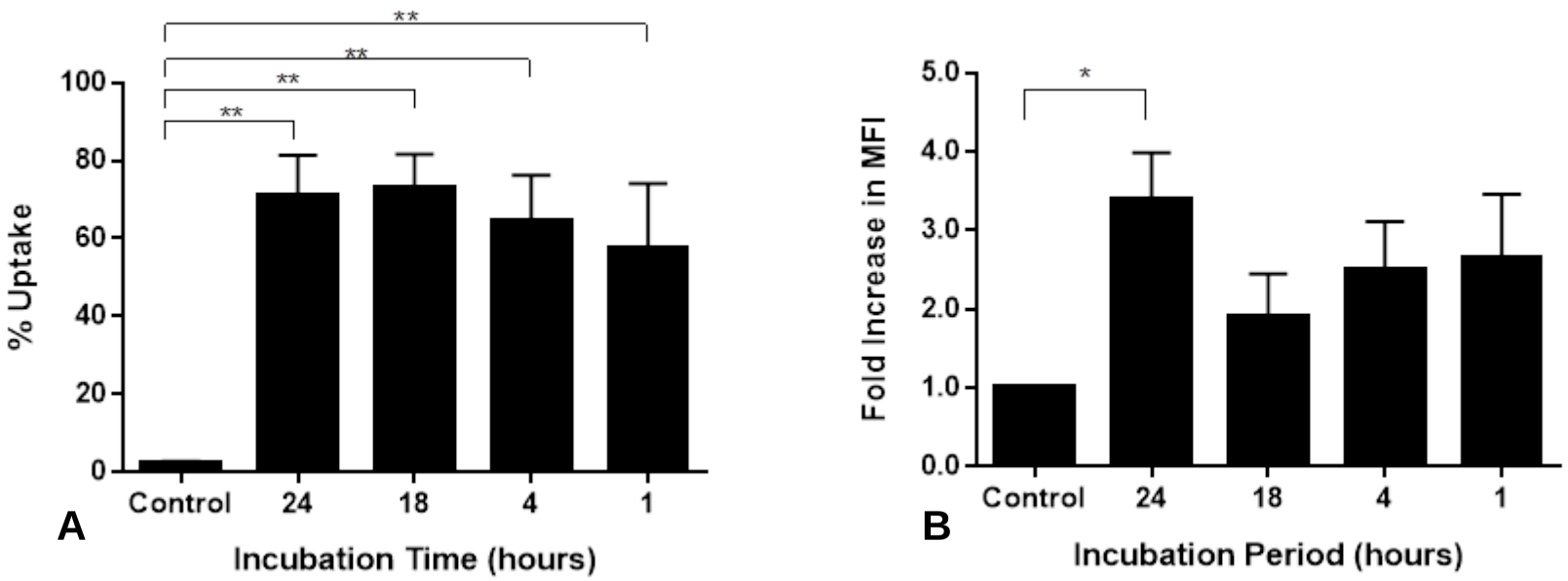

Figure 4.3: Time dependent uptake (A, percentage uptake and B, MFI) of FITC tagged IONPs by GM-CSF grown BM-DC, *in vitro*. C57BL/6 derived DM-DCs were grown for 6 days with GM-CSF and incubated with 200 µg/ml of FITC tagged IONPs for 24 hours, *in vitro*. Uptake by CD11c+ cells was quantitated by flow cytometry and analysed using FACSDiva software (BD Biosciences), n=4. Results are shown as the mean percentage surface expression with standard error of the mean as error bars. One-way ANOVA statistical analysis with post-test analysis was conducted with the Tukey's test (multiple comparison test comparing each group with the other groups) for treatments between columns. The Dunnett's test was used to compare the control group with each treated group. Where no asterisks are displayed, no statistical significance was found. **Figure 4.3A;** Percentage uptake by CD11c+ cells. **Figure 4.3B;** The MFI from the FITC (tagged to the IONPs) from the percentage uptake by CD11c+ cells.

4.2.2.2 Time dependendent uptake of FITC tagged IONPs by Flt3 grown BM-DCs, *in vitro*

CD11c+ (membrane protein of DCs) murine BM-DCs demonstrated that compared to the mean of the control condition, the level of uptake of FITC tagged IONPs became statistically significant (and thus noticeable) at 18 hours incubation time (Figure 4.4A). There was no statistical significance of the Fold Increase in MFI between the treatment conditions, nor between the control condition and any of the incubation time treatment conditions (Figure 4.4B).

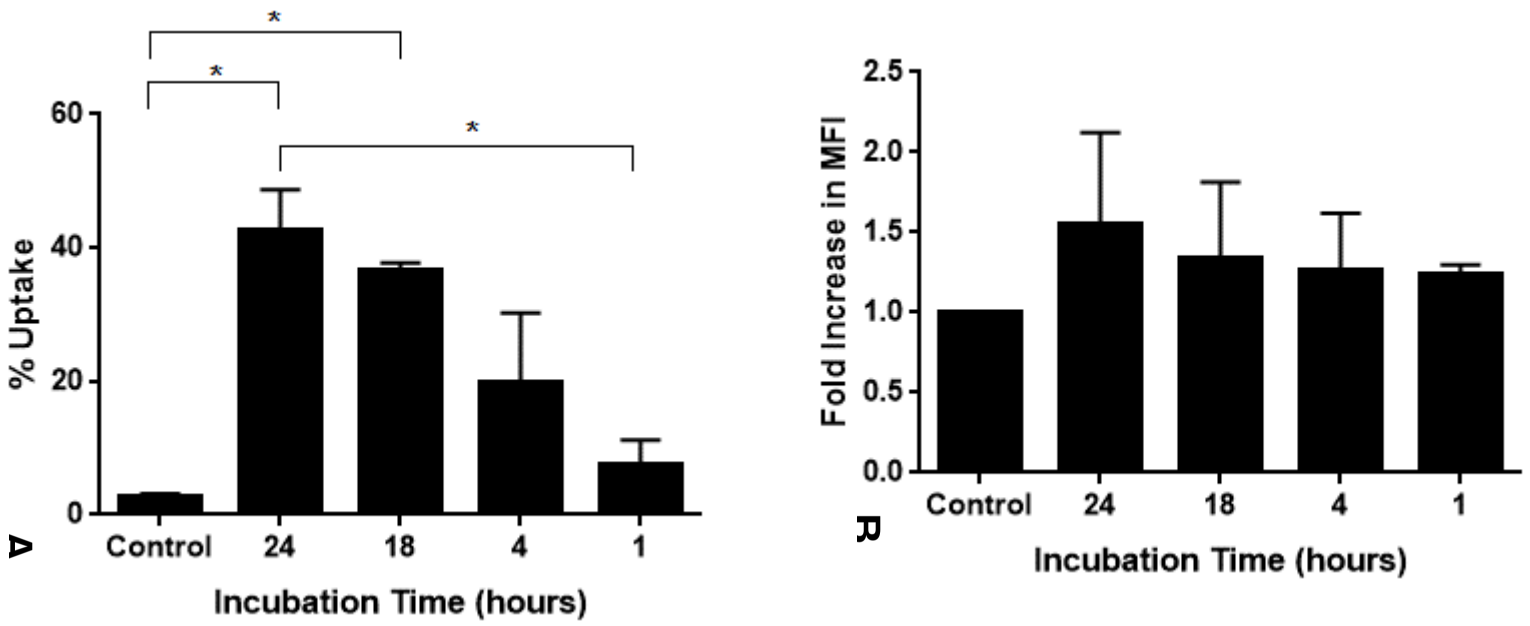

Figure 4.4: Time dependent uptake (A, percentage uptake and B, MFI) of FITC tagged IONPs by Flt3 derived BM-DC, *in vitro*. C57BL/6 derived DM-DCs were grown for 8 days with Flt3 and incubated with 200 µg/ml of FITC tagged IONPs for 24 hours, *in vitro*. Uptake by CD11c+ cells was quantitated by flow cytometry and analysed using FACSDiva software (BD Biosciences), n=3. Results are shown as the mean percentage surface expression with standard error of the mean as error bars. One-way ANOVA statistical analysis with post-test analysis was conducted with the Tukey's test (multiple comparison test comparing each group with the other groups) for treatments between columns. The Dunnett's test was used to compare the control group with each treated group. Where no asterisks are displayed, no statistical significance was found. **Figure 4.4A;** Percentage uptake by CD11c+ cells. **Figure 4.4B;** The MFI from the FITC (tagged to the IONPs) from the percentage uptake by CD11c+ cells.

4.2.2.3 Comparison of results of GM-CSF grown murine BM-DCs and Flt3 grown murine BM-DCs time dependent uptake studies

For improved comparision and understanding of time dependent uptake between GM-CSF grown and Flt3 grown murine BM-DCs, the results presented Section 4.2.2.1 (Figure 4.3) and Section 4.2.2.2 (Figure 4.4) were sumarised and tabulated (Table 4.1 and Table 4.2). Flt3 grown murine BM-DCs demonstrated less percentage up take , at all time points, compared to GM-CSF grown murine BM-DCs; and thus, the percentage up take of Flt3 grown murine BM-DCs were expressed as a percentage of the percentage uptage of GM-CSF grown murine BM-DCs.

Incubation Time	% Uptake Flt3 murine DC	% Uptake GM-CSF murine DC	% of GM-CSF
24 hours	42.70	71.08	60.07
18 hours	36.45	73.18	49.80
4 hours	19.90	64.35	30.92
1 hour	7.65	57.60	13.28

Table 4.1: Comparison of percentage uptake of FITC tagged IONPs by GM-CSF and Flt3 murine derived DCs and their corresponding differences according to incubation time, *in vitro*.

Incubation Time	FI in MFI Flt3 murine DC	FI in MFI GM-CSF murine DC	% of GM-CSF
24 hours	1.54	3.40	45.29
18 hours	1.34	1.90	70.53
4 hours	1.26	2.50	50.4
1 hour	1.23	2.65	46.42

Table 4.2: Comparison of FI in MFI of FITC tagged IONPs by GM-CSF and Flt3 murine derived DCs and their corresponding differences according to incubation time, *in vitro*.

4.2.3 Dose dependent maturation of murine BM-DCs, *in vitro*

In vitro experiments were performed to determine if the FITC tagged IONPs induced cellular maturity in GM-CSF generated murine BM-DCs. A co-staining technique was used with flow cytometry. CD11c (protein membrane identified with DCs) positive cells were identified for CD86 (a protein that can stimulate T cells) and also CCR7 (associated with the chemotaxis of murine DCs to LNs). Both CD86 and CCR7 are associated with maturing DCs.

4.2.3.1 Dose dependent maturation of GM-CSF grown murine BM-DCs, *in vitro*

There was no statistical significance of CD86 expression across the concentration dose treatment conditions or between the control mean and these same treatment conditions (Figure 4.5A); indicating that at the concentration doses tested, these BM-DCs offer no or minimal potential stimulation to T cells via CD86 expression. The corresponding Fold Increase in MFI did identify significant statistical difference between the intensity of the detectable FITC from the IONPs and the control mean , but no other (Figure 4.5B).

The surface expression of CCR7 (Figure 4.6A) and the corresponding Fold Increase in MFI (Figure 4.6B) was not statistically significant compared to the control means and there was also no significance identified between treatment conditions; thus minimimal or no LN migration capability could be induced in these BM-DCs under these tested conditions.

The level of CD86 and CCR7 expressions, compared to their control means, signify that these BM-DCs remain in a relatively immature state following 24 hours incubation with FITC taggd IONPs. The surface expression of CCR7 was approximately half the value of the surface expression of CD86 (Figure 4.7A).

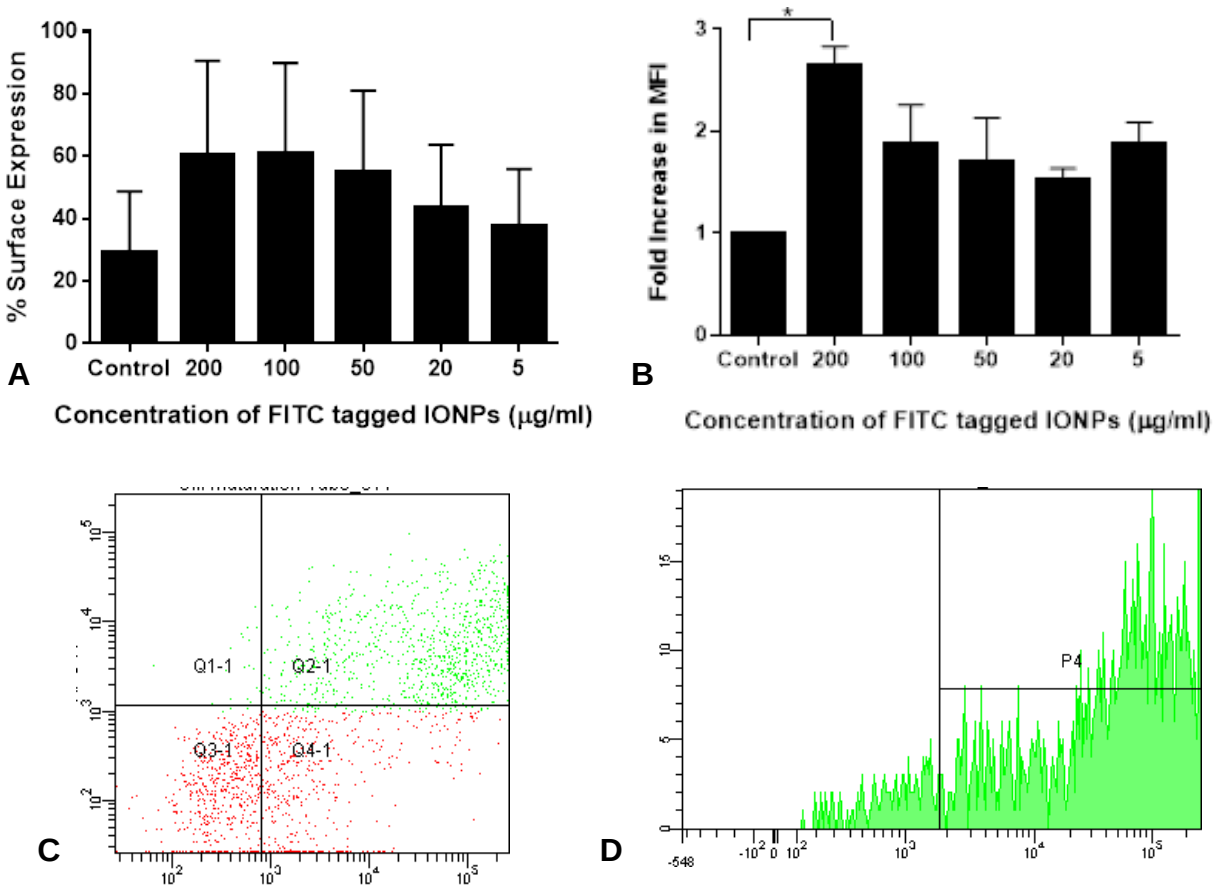

Figure 4.5: Dose dependent maturation of GM-CSF BM-DC grown over 6 days, *in vitro*. C57BL/6 derived BM-DCs were grown with GM-CSF for 6 days and incubated with varying concentrations of FITC tagged IONPs for 24 hours. Co-staining of CD86 and CCR7 with CD11c+ was quantitated by flow cytometry and analysed using FACSDiva software (BD Biosciences), n=3. One-way ANOVA statistical analysis with post-test analysis was conducted with the Tukey's test (multiple comparison test comparing each group with the other group) for treatments between columns. The Dunnett's test was used to compare the control group with each treated group. Where no asterisks are displayed, no statistical significance was found. **Figure 4.5A:** % surface expression of CD86 by CD11c+ cells. The results are shown as the mean percentage surface expression with standard error of the mean as error bars. **Figure 4.5B:** The results are shown as the mean fold increase in MFI with standard error of the mean as error bars. **Figure 4.5C:** A representative flow cytometry dot-plot of cells from the 100 µg/ml treatment condition is shown. **Figure 4.5D:** A representative flow cytometry histogram from the 100 µg/ml treatment condition, corresponding with the dot-plot presented in Figure 4.5C is shown.

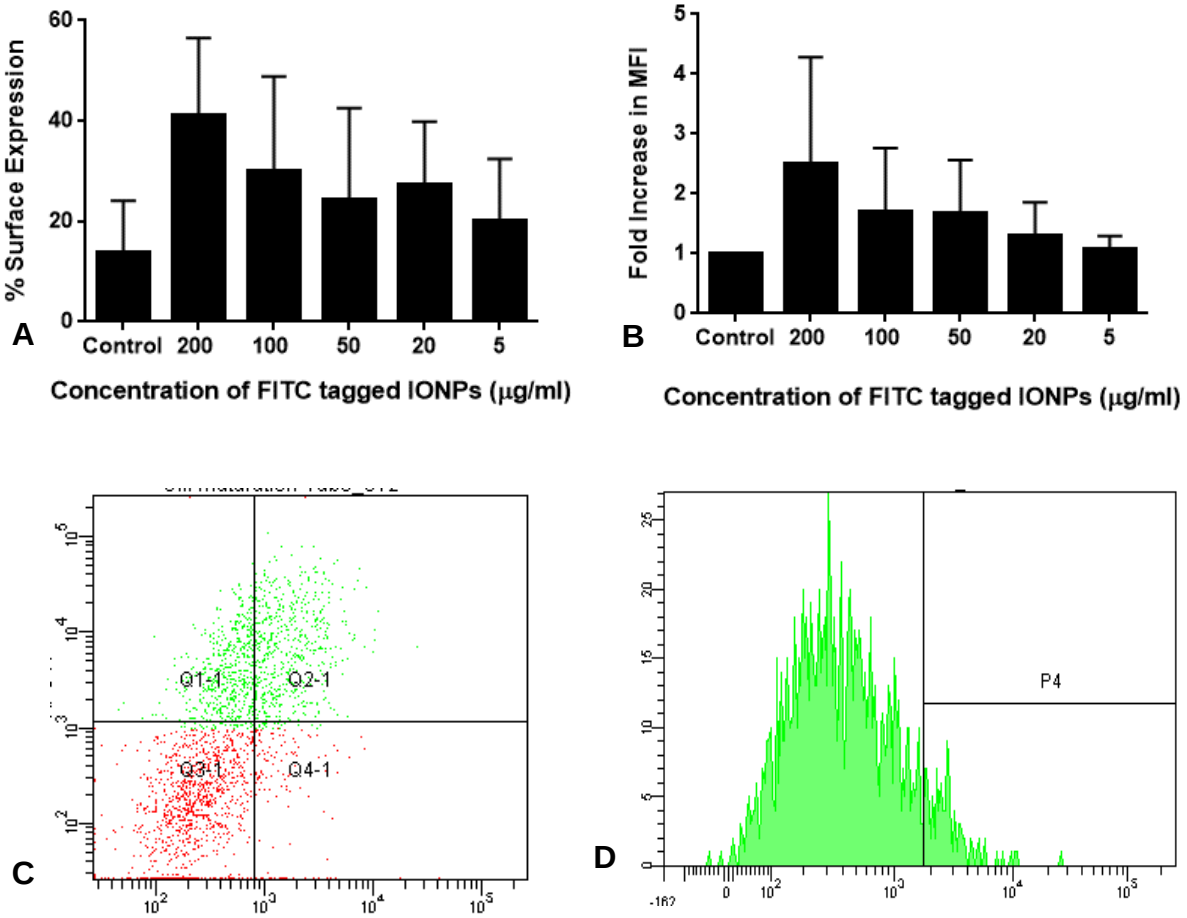

Figure 4.6: Dose dependent maturation of GM-CSF BM-DC grown over 6 days, *in vitro*. C57BL/6 derived BM-DCs were grown with GM-CSF for 6 days and incubated with varying concentrations of FITC tagged IONPs for 24 hours. Co-staining of CD86 and CCR7 with CD11c+ was quantitated by flow cytometry and analysed using FACSDiva software (BD Biosciences), n=3. One-way ANOVA statistical analysis with post-test analysis was conducted with the Tukey's test (multiple comparison test comparing each group with the other group) for treatments between columns. The Dunnett's test was used to compare the control group with each treated group. Where no asterisks are displayed, no statistical significance was found. **Figure 4.6A:** % surface expression of CCR7 by CD11c+ cells. The results are shown as the mean percentage surface expression with standard error of the mean as error bars. **Figure 4.6B:** The results are shown as the mean fold increase in MFI with standard error of the mean as error bars. **Figure 4.6C:** A representative flow cytometry dot-plot of cells from the 100 µg/ml treatment condition is shown. **Figure 4.6D:** A representative flow cytometry histogram from the 100 µg/ml treatment condition, corresponding with the dot-plot presented in Figure 4.6C is shown.

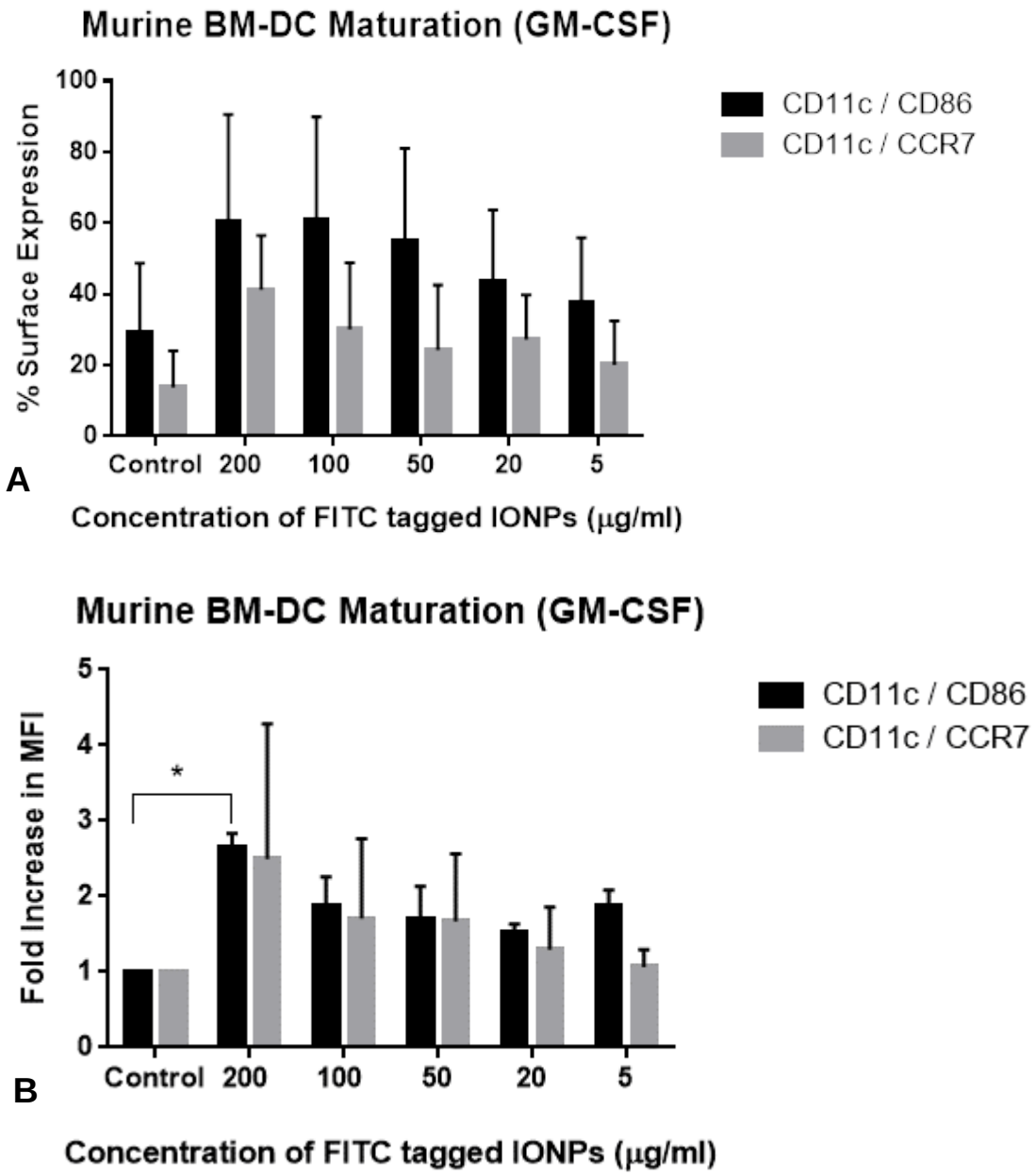

Figure 4.7: Comparison of CD86 and CCR7 surface expressions in GM-CSF grown BM-DCs, *in vitro*. **Figure 4.7A** compares the % surface expression of both CD86 and CCR7 expression and **Figure 4.7B** compares the Fold Increase in MFI of both CD86 and CCR7 expressions. Two-way ANOVA statistical analysis with post-test analysis was conducted with the Tukey's test (multiple comparison test comparing each group with the other group) for treatments between columns. The Dunnett's test was used to compare the control group with each treated group. Where no asterisks are displayed, no statistical significance was found. In Figure 4.5B, a significant statistical difference was noted between the fold increase in MFI (corresponding to % surface expression of CD86 by CD11c+ cells) between the control condition and 200μg/ml of FITC tagged T10 dextran coated IONPs; this has also been indicated in Figure 4.7B.

4.2.3.2 Dose dependent maturation of Flt3 grown BMDCs, *in vitro*

There was statistical significance in the % surface expression of CD86 of the 200 µg/ml treatment condition mean compared to the control mean. There was no further statistical difference between the control mean and any other treatment condition mean. Amongst the treatment conditions, the only statistical sigficance was found between the means of the 100 µg/ml and 5 µg/ml treatment groups (Figure 4.8A). Figure 4.8A suggests that at the concentration doses tested, these Flt3 derived murine BM-DCs offer some potential stimulation to T cells via CD86 expression pathway, namely at an IONP concentration of 200 µg/ml. The corresponding Fold Increase in MFI (Figure 4.8B) was not statistically significant compared to the control mean and there was also no significance identified between treatment conditions.

The surface expression of CCR7 (Figure 4.9A) and the corresponding Fold Increase in MFI (Figure 4.9B) was not statistically significant compared to the control means and there was also no significance identified between treatment conditions; thus minimimal or no LN migration capability could be induced in these Flt3 derived murinbe BM-DCs, under these tested conditions. The level of CD86 and CCR7 expressions, compared to their control means, signify that these BM-DCs remain in a relatively immature state following 24 hours incubation with FITC taggd IONPs. The surface expression of CCR7 was approximately half the value of the surface expression of CD86 (Figure 4.10A).

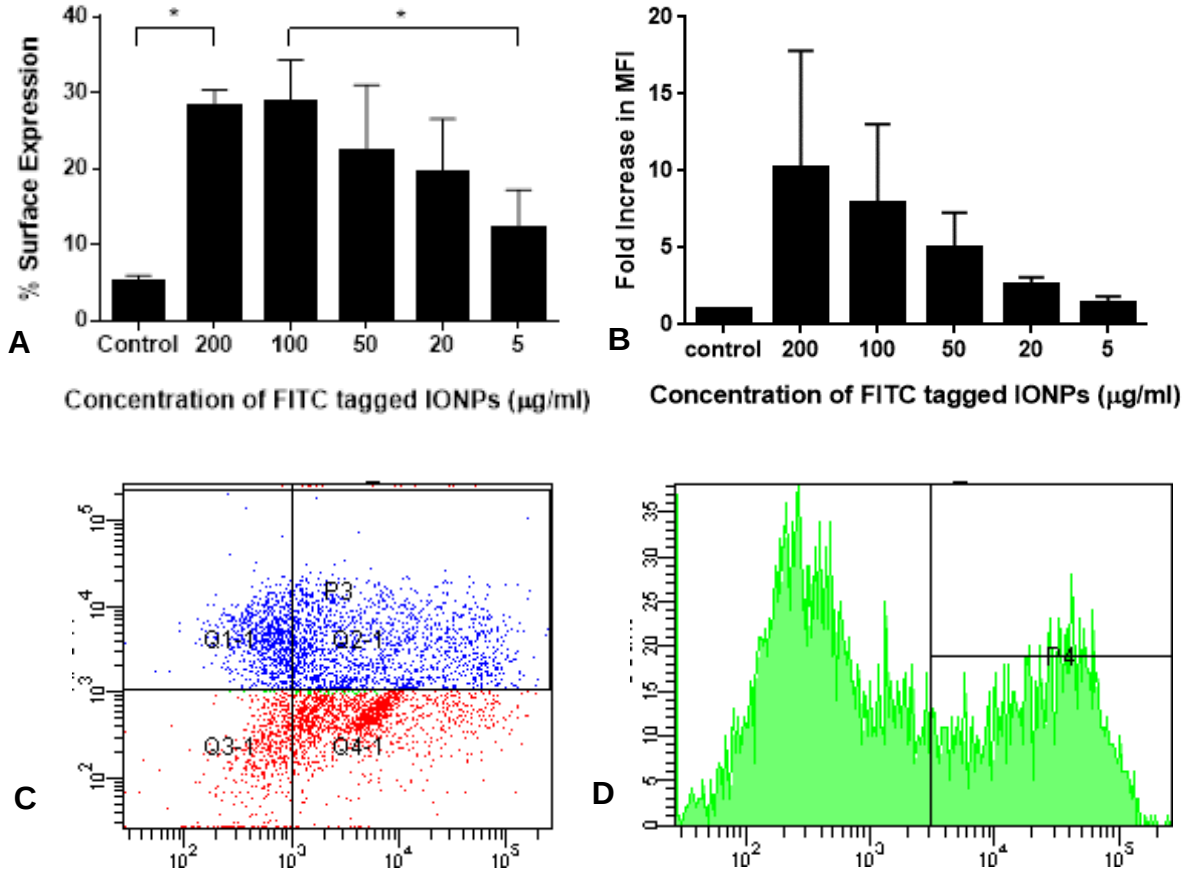

Figure 4.8: Dose dependent maturation of Flt3 BM-DC grown over 8 days, *in vitro*. C57BL/6 derived BM-DCs were grown with GM-CSF for 8 days and incubated with varying concentrations of FITC tagged IONPs for 24 hours. Co-staining of CD86 and CCR7 with CD11c+ was quantitated by flow cytometry and analysed using FACSDiva software (BD Biosciences), n=3. One-way ANOVA statistical analysis with post-test analysis was conducted with the Tukey's test (multiple comparison test comparing each group with the other group) for treatments between columns. The Dunnett's test was used to compare the control group with each treated group. Where no asterisks are displayed, no statistical significance was found. **Figure 4.8A:** % surface expression of CD86 by CD11c+ cells. The results are shown as the mean percentage surface expression with standard error of the mean as error bars. **Figure 4.8B:** The results are shown as the mean fold increase in MFI with standard error of the mean as error bars. **Figure 4.8C:** A representative flow cytometry dot-plot of cells from the 100 µg/ml treatment condition is shown. **Figure 4.8D:** A representative flow cytometry histogram from the 100 µg/ml treatment condition, corresponding with the dot-plot presented in Figure 4.8C is shown.

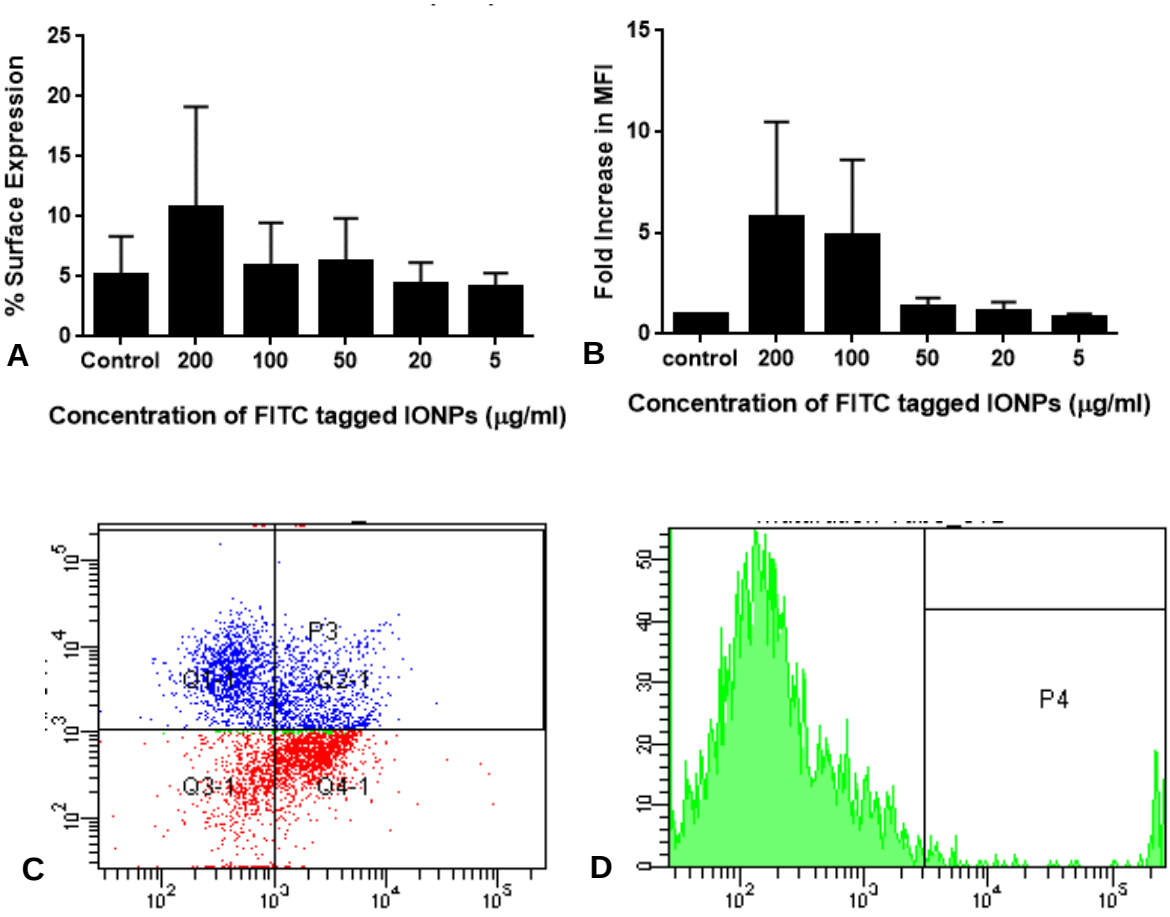

Figure 4.9: Dose dependent maturation of Flt3 BM-DC grown over 8 days, *in vitro*. C57BL/6 derived BM-DCs were grown with GM-CSF for 8 days and incubated with varying concentrations of FITC tagged IONPs for 24 hours. Co-staining of CD86 and CCR7 with CD11c+ was quantitated by flow cytometry and analysed using FACSDiva software (BD Biosciences), n=3. One-way ANOVA statistical analysis with post-test analysis was conducted with the Tukey's test (multiple comparison test comparing each group with the other group) for treatments between columns. The Dunnett's test was used to compare the control group with each treated group. Where no asterisks are displayed, no statistical significance was found. **Figure 4.9A:** % surface expression of CCR7 by CD11c+ cells. The results are shown as the mean percentage surface expression with standard error of the mean as error bars. **Figure 4.9B:** The results are shown as the mean fold increase in MFI with standard error of the mean as error bars. **Figure 4.9C:** A representative flow cytometry dot-plot of cells from the 100 µg/ml treatment condition is shown. **Figure 4.9D:** A representative flow cytometry histogram from the 100 µg/ml treatment condition, corresponding with the dot-plot presented in Figure 4.9C is shown.

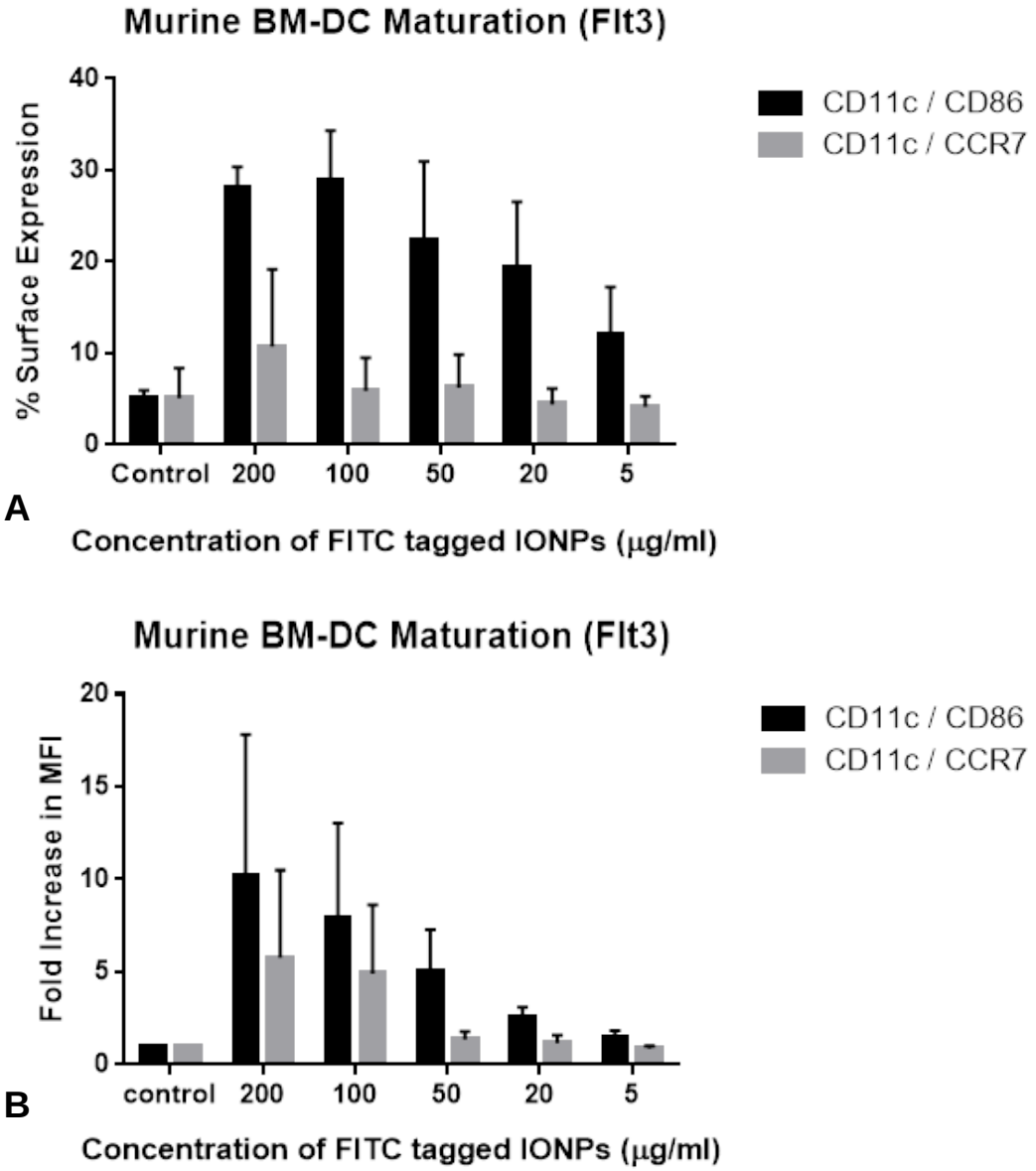

Figure 4.10: Comparison of CD86 and CCR7 surface expressions in Flt3 grown BM-DCs, *in vitro*. **Figure 4.10A** compares the % surface expression of both CD86 and CCR7 expression and **Figure 4.10B** compares the Fold Increase in MFI of both CD86 and CCR7 expressions. Two-way ANOVA statistical analysis with post-test analysis was conducted with the Tukey's test (multiple comparison test comparing each group with the other group) for treatments between columns. The Dunnett's test was used to compare the control group with each treated group. Where no asterisks are displayed, no statistical significance was found.

4.2.7 Apoptosis studies of murine BM-DCs, *in vitro*

BM-DC survival in the presence of FITC tagged IONPs, *in vitro*, was investigated to gather knowledge for considering the possibility of later *in vivo* studies; in keeping with a long term goal for extending research in this area. Apoptosis, programmed cell destruction and death, can occur when cells experience exceedingly stressful, harmful or toxic conditions. Apoptosis studies, with a double stained technique were performed using a readily available proprietary kit was used. 7-Aminoactinomycin D (7-AAD), a fluorescent marker for cellular DNA, does not traverse an intact cell membranes; therefore, BM-DCs with compromised membranes will stain with 7 AAD. Annexin V, a cellular protein, was incorporated to identify BM-DCs that have expressed on their surface membranes markers for apoptosis which include phosphatidylserine (PS) and phosphatidlethanolamine (PE). Flow cytometry was used, in conjunction with the propriety apoptosis kit and Figure 4.11 is a representation of how cell populations are identified or allocated quadrants according to their health status.

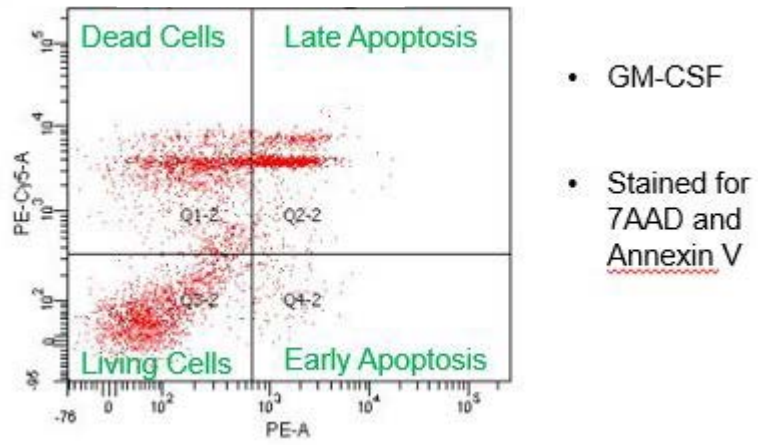

Figure 4.11: A representative dot-plot of apoptosis data from flow cytometry with GM-CSF grown murine BM-DC, *in vitro*. This is a representative example of a dot plot generated from flow cytometry analysis showing cells expressing viable/living cells (Q3-2), dead cells (Q1-2), early apoptotic (Q4-2) and late apoptotic cells (Q2-2).

4.2.7.1 Apoptosis studies of GM-CSF grown murine BM-DCs with FITC tagged IONPs, *in vitro*

Bone marrow stem cells from female C57BL/6 mice were cultured with GM-CSF as described in Section 2.10 and incubated with FITC tagged IONPs as stated in Section 2.11.1 and apoptosis studies were performed as reported in Section 2.11.3. There was uniform BM-DC population mean values present in each quadrant, contributed by a statistically even distribution BM-DC population across each treatment condition; being consistent with the control BM-DC population mean (Figure 4.12). No statistical difference between the mean value of the BM-DC control means and the treatment means could be identified, and there was also no statistical significance amongst the BM-DC population means of each treatment conditions; in each quadrant that represents the BM-DC health status as tested, *in vitro*.

As the population within each quadrant can be considered rather homogenous (only one point of statistical variation in Q2, Figure 4.12B), the average percentage mean values of each quadrant was graphed and compared (Figure 4.13). The largest overall BM-DC population was found in quadrant 3, therefore, viable/healthy, and the lowest population of these cells was found in quadrant 1, the dead cell quadrant (Figure 4.13). Figure 4.14 represents the dot-plots of these BM-DCs as identified using flow cytometry from an apoptosis study.

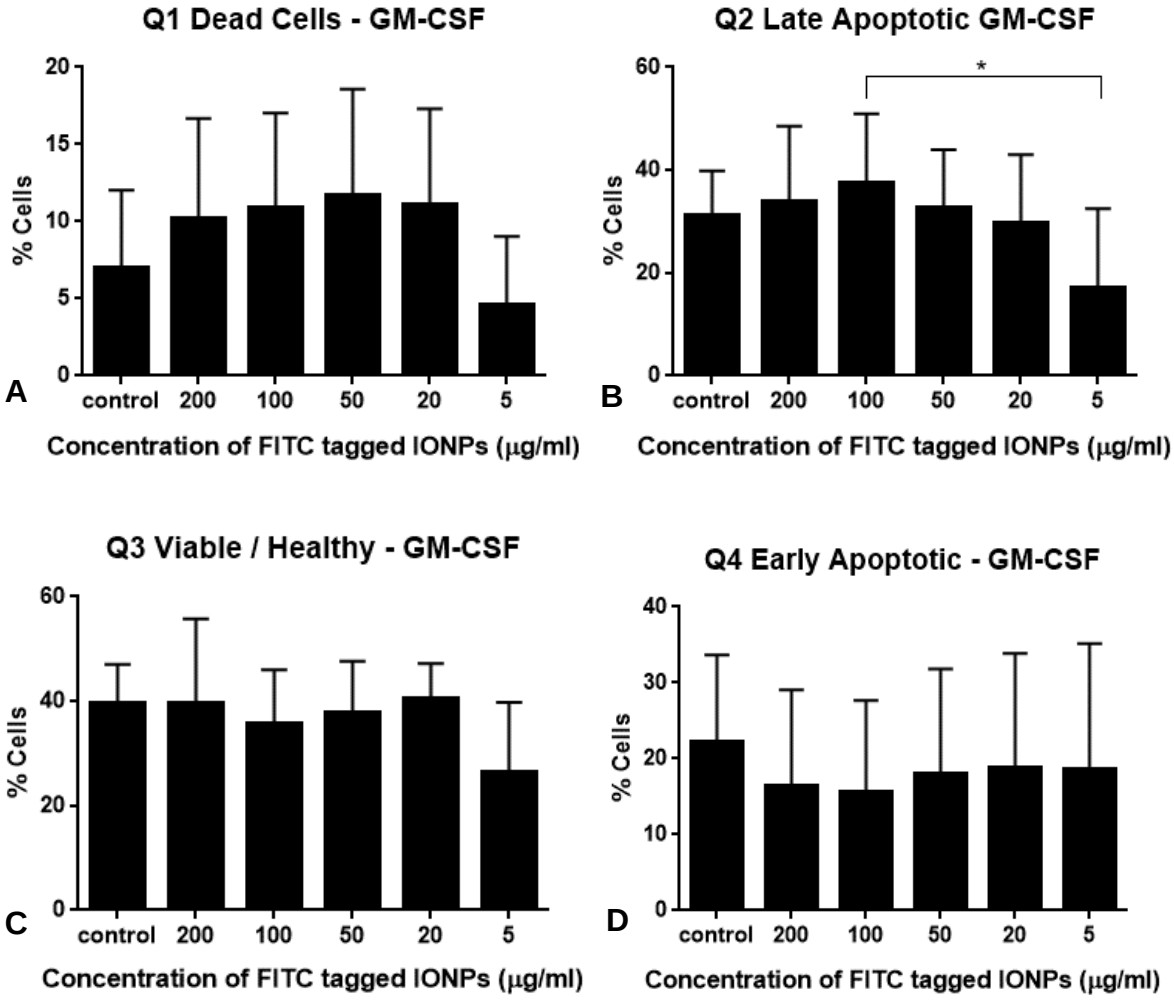

Figure 4.12: IONP induced apoptosis of GM-CSF derived BM-DCs, *in vitro*. C57BL/6 derived BM-DCs were grown with GM-CSF for 6 days and incubated with varying concentrations of FITC tagged IONPs for 24 hours. Stages of cell health were quantitated by flow cytometry and analysed, (n=3). The apoptosis study was performed with Annexin V and 7AAD. The results are shown as the mean percentage of cell population within an apoptotic quadrant with standard error of the mean as error bars. Two-way ANOVA statistical analysis with post-test analysis conducted with Tukey's test (multiple comparison test comparing each group with all other groups). Where no asterisks are displayed, no statistical significance was found. **Figure 4.12A:** Percentage of cells that were found in quadrant one, dead or necrotic. **Figure 4.12B**: Percentage of cells that were found in quadrant two, late stage apoptosis. **Figure 4.12C:** Percentage of cells that were found in quadrant three, viable or healthy. **Figure 4.12D:** Percentage of cells that were found in quadrant four, early stage apoptosis.

Quadrant (from FACS)	Definition of Quadrant	Average Percentage of Cell Population (GM-CSF)
Q1	Dead	10 %
Q2	Late Apoptosis	32 %
Q3	Alive / Viable	39 %
Q4	Early Apoptotic	20 %

Table 4.3: Average percentage figures (rounded up to nearest whole number) of GM-CSF induced murine DCs in varying stages of apoptosis, death or viability. From Figure 4.12, this table was composed, demonstrating the average percentage figures of cells in varying stages of apoptosis, death or viability as identified by the apoptosis double staining technique and flow cytometry and analysed using FACSDiva software (BD Biosciences) and shown here, (n=3).

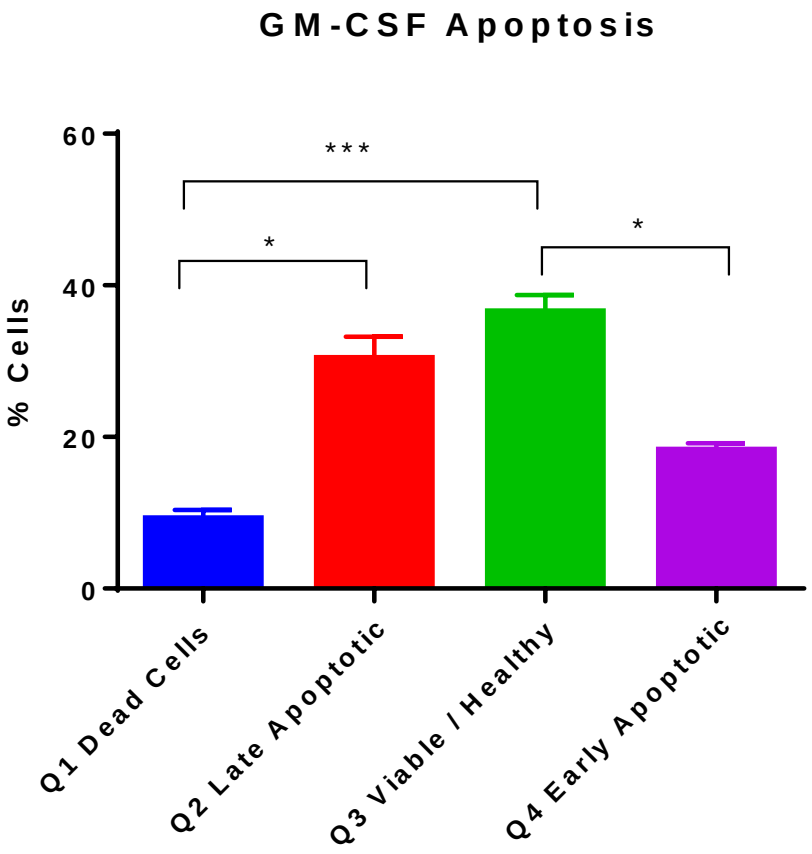

Figure 4.13: The average mean percentage figures of GM-CSF grown BM-DCs population from the quadrants representing the stages of cell health. As there was no statistical variation of the individual components (control means and treatment means) within each quadrant, the average percentage mean values of each quadrant is represented here and statistically compared. A two-way ANOVA with Tukey's multiple comparison test was used to compare each quadrant with one another.

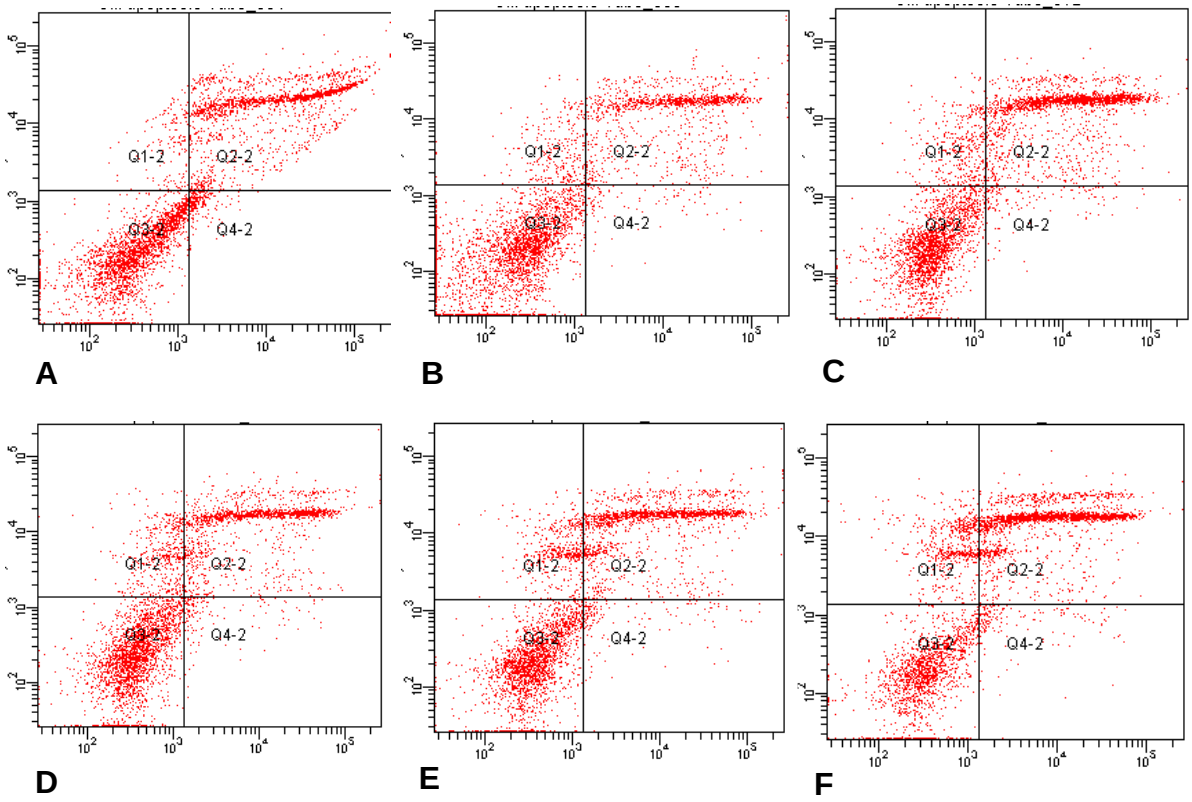

Figure 4.14: IONP induced apoptosis of GM-CSF derived BM-DCs, *in vitro*. C57BL/6 derived BM-DCs were grown with GM-CSF for 6 days and incubated with varying concentrations of FITC tagged IONPs for 24 hours. Stages of cell health were quantitated by flow cytometry and analysed, (n=3). The apoptosis study was performed with Annexin V and 7AAD. The dot-plots shown are representative of cells in the four identified stages of apoptosis, ranging from dead or necrotic cells (quadrant one), late stage apoptosis (quadrant two), viable or healthy cells (quadrant 3) and early stage apoptosis (quadrant four). **Figure 4.14A:** Representative dot-plot of apoptosis study of cells in the control condition, following 24 hours incubation. **Figure 4.14B:** Representative dot-plot of apoptosis study of cells incubated with 200 µg/ml of FITC tagged IONP for 24 hours. **Figure 4.14C:** Representative dot-plot of apoptosis study of cells incubated with 100 µg/ml of FITC tagged IONP for 24 hours. **Figure 4.14D:** Representative dot-plot of apoptosis study of cells incubated with 50 µg/ml of FITC tagged IONP for 24 hours. **Figure 4.14E:** Representative dot-plot of apoptosis study of cells incubated with 20 µg/ml of FITC tagged IONP for 24 hours. **Figure 4.14F:** Representative dot-plot of apoptosis study of cells incubated with 5 µg/ml of FITC tagged IONP for 24 hours.

4.2.7.2 Apoptosis studies of Flt3 grown BM-DCs with FITC tagged IONPs, *in vitro*

Bone marrow stem cells from female C57BL/6 mice were cultured with Flt3 as described in Section 2.10 and incubated with FITC tagged IONPs as stated in Section 2.11.1 and apoptosis studies were performed as reported in Section 2.11.3. Again, there was uniform BM-DC population mean values present in each quadrant, contributed by a statistically even distribution BM-DC population across each treatment condition; being consistent with the control BM-DC population mean (Figure 4.15). No statistical difference between the mean value of the BM-DC control means and the treatment means could be identified, and there was also no statistical significance amongst the BM-DC population means of each treatment conditions; in each quadrant that represents the BM-DC health status as tested, *in vitro*.

As the population within each quadrant can be considered rather homogenous (only one point of statistical variation in Q3, Figure 4.15C), the average percentage mean values of each quadrant was graphed and compared (Figure 4.16). The largest overall Flt3 grown murine BM-DC population was found in quadrant 3, therefore, viable/healthy, and the lowest population of these cells was found in quadrant 4, the early apoptotic quadrant (Figure 4.16). Figure 4.17 represents the dot-plots of these BM-DCs as identified using flow cytometry from an apoptosis study.

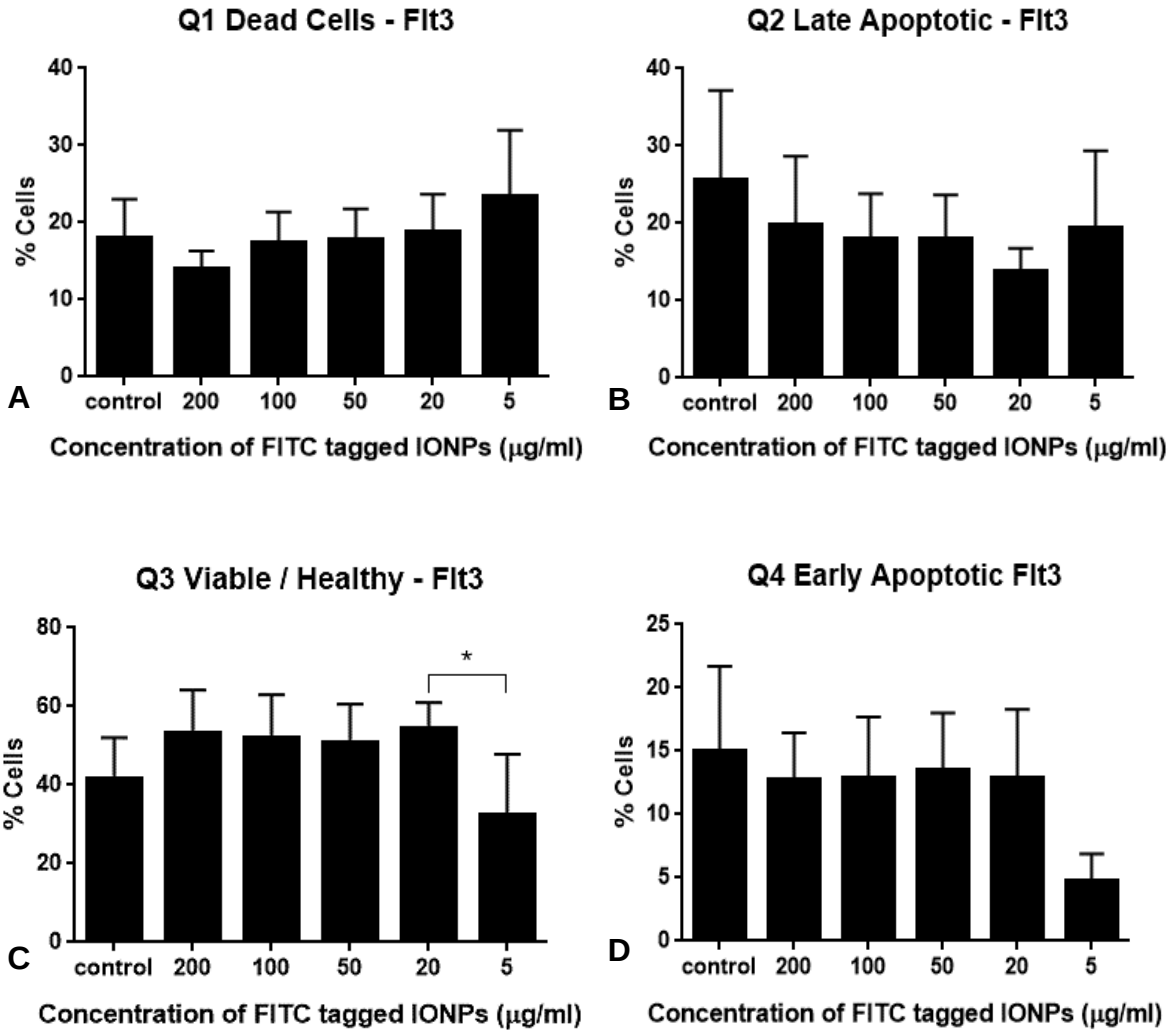

Figure 4.15: IONP induced apoptosis of Flt3 derived BM-DCs, *in vitro*. C57BL/6 derived BM-DCs were grown with Flt3 for 8 days and incubated with varying concentrations of FITC tagged IONPs for 24 hours. Stages of cell health were quantitated by flow cytometry and analysed, (n=5). The apoptosis study was performed with Annexin V and 7AAD. The results are shown as the mean percentage of cell population within an apoptotic quadrant with standard error of the mean as error bars. Two-way ANOVA post-test analysis was conducted with the Tukey's test (multiple comparison test comparing each group with the other group). Where no asterisks are displayed, no statistical significance was found. **Figure 4.15A:** Percentage of cells that were found in quadrant one, dead or necrotic. **Figure 4.15B**: Percentage of cells that were found in quadrant two, late stage apoptosis. **Figure 4.15C:** Percentage of cells that were found in quadrant three, viable or healthy. **Figure 4.15D:** Percentage of cells that were found in quadrant four, early stage apoptosis.

Quadrant (from FACS)	Definition of Quadrant	Average Percentage of Cell Population (Flt3)
Q1	Dead	19 %
Q2	Late Apoptosis	20 %
Q3	Alive / Viable	49 %
Q4	Early Apoptotic	12 %

Table 4.4: Average percentage figures (rounded up to nearest whole number) of Flt3 induced murine DCs in varying stages of apoptosis, death or viability. From Figure 4.15, this table was composed, demonstrating the average percentage figures of cells in varying stages of apoptosis, death or viability as identified by the apoptosis double staining technique and flow cytometry and analysed using FACSDiva software (BD Biosciences) and shown here, (n=5).

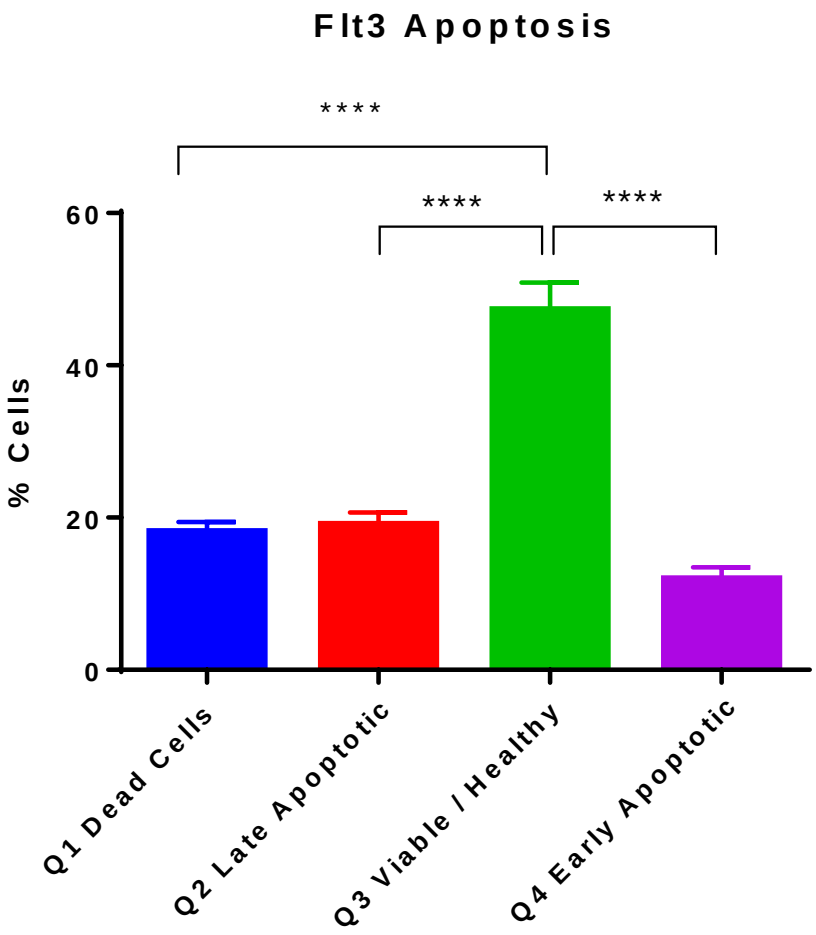

Figure 4.16: The average mean percentage figures of Flt3 grown BM-DCs population from the quadrants representing the stages of cell health. As there was no statistical variation of the individual components (control means and treatment means) within each quadrant, the average percentage mean values of each quadrant is represented here and statistically compared. A two-way ANOVA with Tukey's multiple comparison test was used to compare each quadrant with one another.

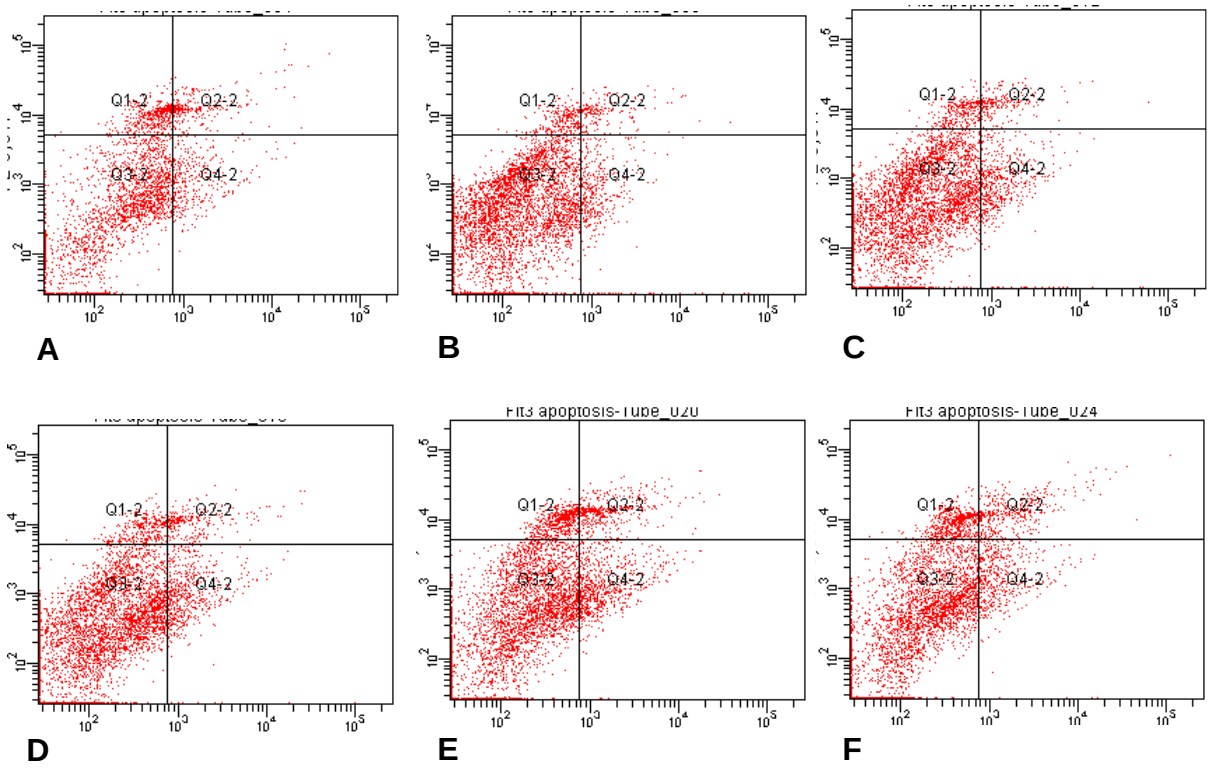

Figure 4.17: IONP induced apoptosis of Flt3 derived BM-DCs, *in vitro*. C57BL/6 derived BM-DCs were grown with Flt3 for 8 days and incubated with varying concentrations of FITC tagged IONPs for 24 hours. Stages of cell health were quantitated by flow cytometry and analysed, (n=5). The apoptosis study was performed with Annexin V and 7AAD. The dot-plots shown are representative of cells in the four identified stages of apoptosis, ranging from dead or necrotic cells (quadrant one), late stage apoptosis (quadrant two), viable or healthy cells (quadrant 3) and early stage apoptosis (quadrant four). **Figure 4.17A:** Representative dot-plot of apoptosis study of cells in the control condition, following 24 hours incubation. **Figure 4.17B:** Representative dot-plot of apoptosis study of cells incubated with 200 µg/ml of FITC tagged IONP for 24 hours. **Figure 4.17C:** Representative dot-plot of apoptosis study of cells incubated with 100 µg/ml of FITC tagged IONP for 24 hours. **Figure 4.17D:** Representative dot-plot of apoptosis study of cells incubated with 50 µg/ml of FITC tagged IONP for 24 hours. **Figure 4.17E:** Representative dot-plot of apoptosis study of cells incubated with 20 µg/ml of FITC tagged IONP for 24 hours. **Figure 4.17F:** Representative dot-plot of apoptosis study of cells incubated with 5 µg/ml of FITC tagged IONP for 24 hours.

4.2.7.3 Comparison of results of GM-CSF grown murine BM-DCs and Flt3 grown murine BM-DCs apoptosis studies

Compared to GM-CSF grown murine BM-DCs, Flt3 grown murine BM-DCs appear to better tolerate the FITC tagged IONPs at the completion of 24 hours incubation time with the nanoparticle concentrations tested. This was demonstrated by approximately 49% of the Flt3 grown murine BM-DC population identified in the quadrant 3 (viable) by flow cytometry; and thereby having the remainder of their cell population in non-viable quadrants (dead, late apoptosis and early apoptosis). GM-CSF grown murine BM-DCs had 39% of their cell population in the viable quadrant and their remaining cell populations were in the non-viable quadrants, as determined with flow cytometry. Statistically, however, there was no significance between the values of average cell populations of GM-CSF grown murine BM-DCs and Flt3 grown murine BM-DCs found in each quadrant.

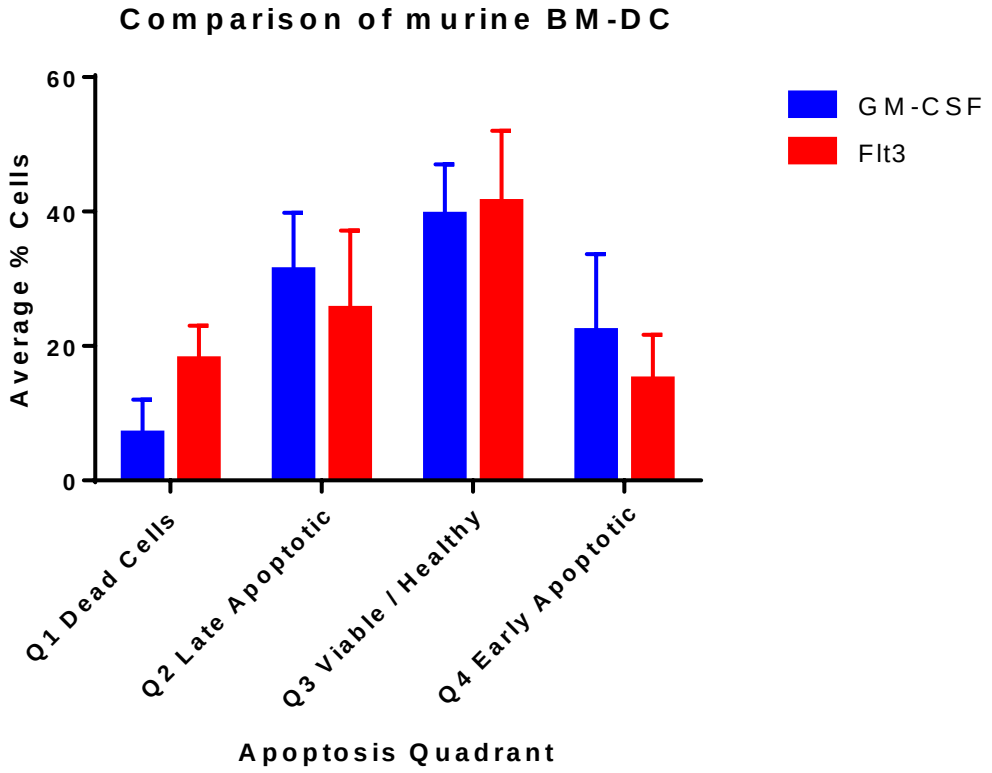

Figure 4.18: Comparison average mean values of cell populations from apoptosis studies. The average percentage mean values of each quadrant from both the GM-CSF grown BM-DC and Flt3 grown DC apoptosis *in vitro* are represented here and statistically compared. A two-way ANOVA with Tukey's multiple comparison test was used to compare each quadrant with one another. A two-way ANOVA with Tukey's multiple comparison test was used to compare each quadrant with one another. Where no asterisks are displayed, no statistical significance was found.

4.2.8 Dose dependent cytokine secretion of murine BM-DC following incubation with FITC tagged IONPs for 24 hours, *in vitro*

To ascertain if the presence of FITC tagged IONPs triggered an inflammatory response from GM-CSF grown and Flt3 grown, murine BM-DCs, a readily available propriety cytometric bead array kit was used to detect the expression of inflammatory cytokines the supernatant from *in vitro* dose dependent uptake experiments. The kit was able to detect the following cytokines: IL-p70, TNF, IFN-γ, MCP-1, IL-10 and IL-6. The supernatant from dose dependent studies tested, *in vitro*, only three cytokines were expressed in elevated levels: TNF, MCP-1, and IL-6.

For both types of murine BM-DCs, the cytokine expressions were not dependent upon the concentration of FITC tagged IONPs tested, following 24 hours incubation, *in vitro* (Figures 4.19 and 4.20). The expression levels of the TNF, MCP-1, and IL-6 cytokines found in the supernatant of dose dependent in vitro studies from Flt3 grown murine BM-DCs was approximately half the value expressed by GM-CSF grown murine BM-DCs.

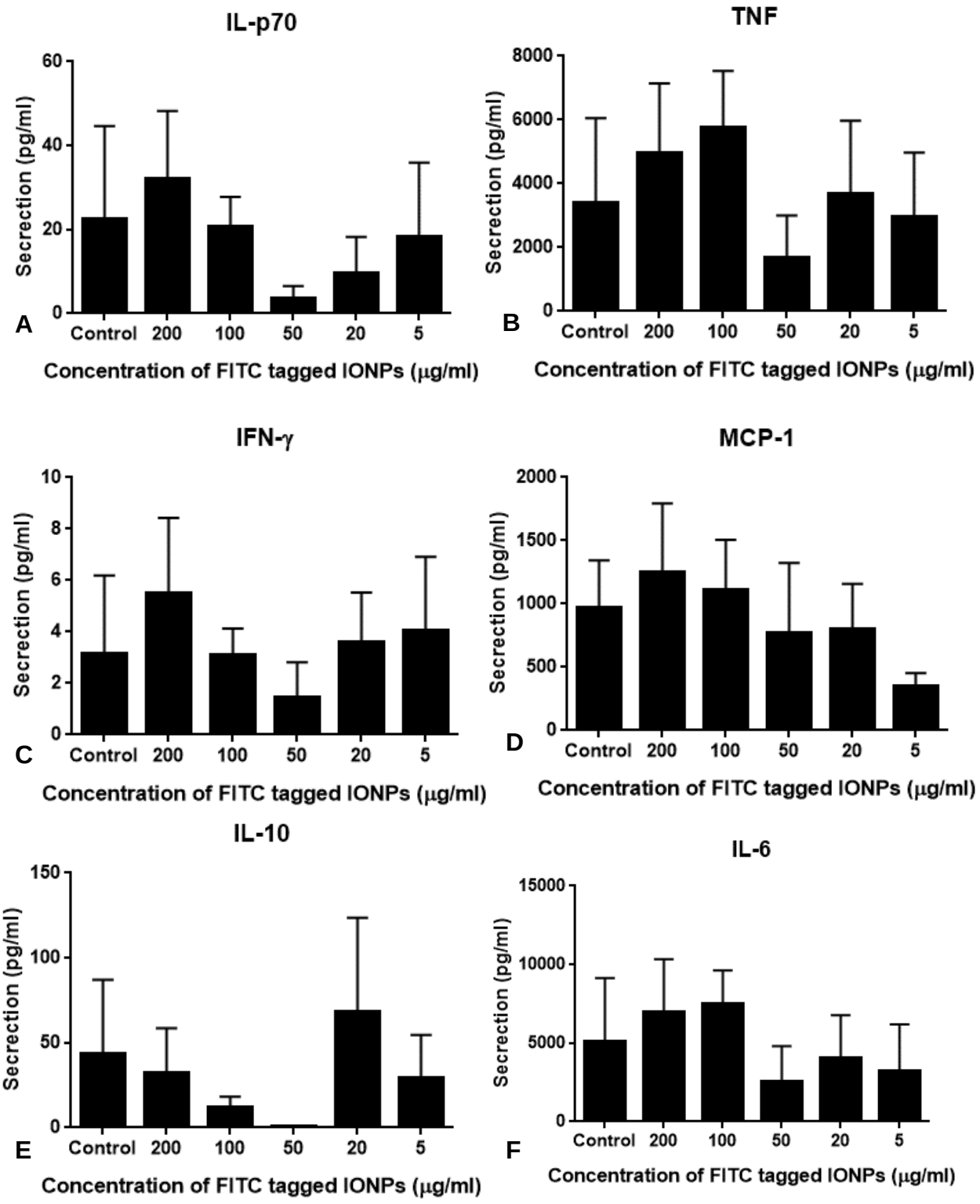

Figure 4.19: Dose dependent cytokine expression of GM-CSF grown BM-DC following incubation with FITC tagged IONPs for 24 hours, *in vitro*. C57BL/6 derived BM-DCs grown with GM-CSF for 8 days were incubated with varying concentrations of FITC tagged IONPs for 24 hours, *in vitro*. Supernatants were collected and stored at -80 ^{o}C for future cytokine analysis. Cytokine expression was quantitated using the CBA Murine Inflammatory Kit (BD Biosciences) and analysed using flow cytometry, n=3. Cytokine levels are shown as mean values with standard error of the mean represented as error bars. One-way ANOVA (nonparametric) multiple comparison test (as a post-test analysis) was performed with the Tukey's multiple comparison test. Where no asterisks are displayed, no statistical significance was found.

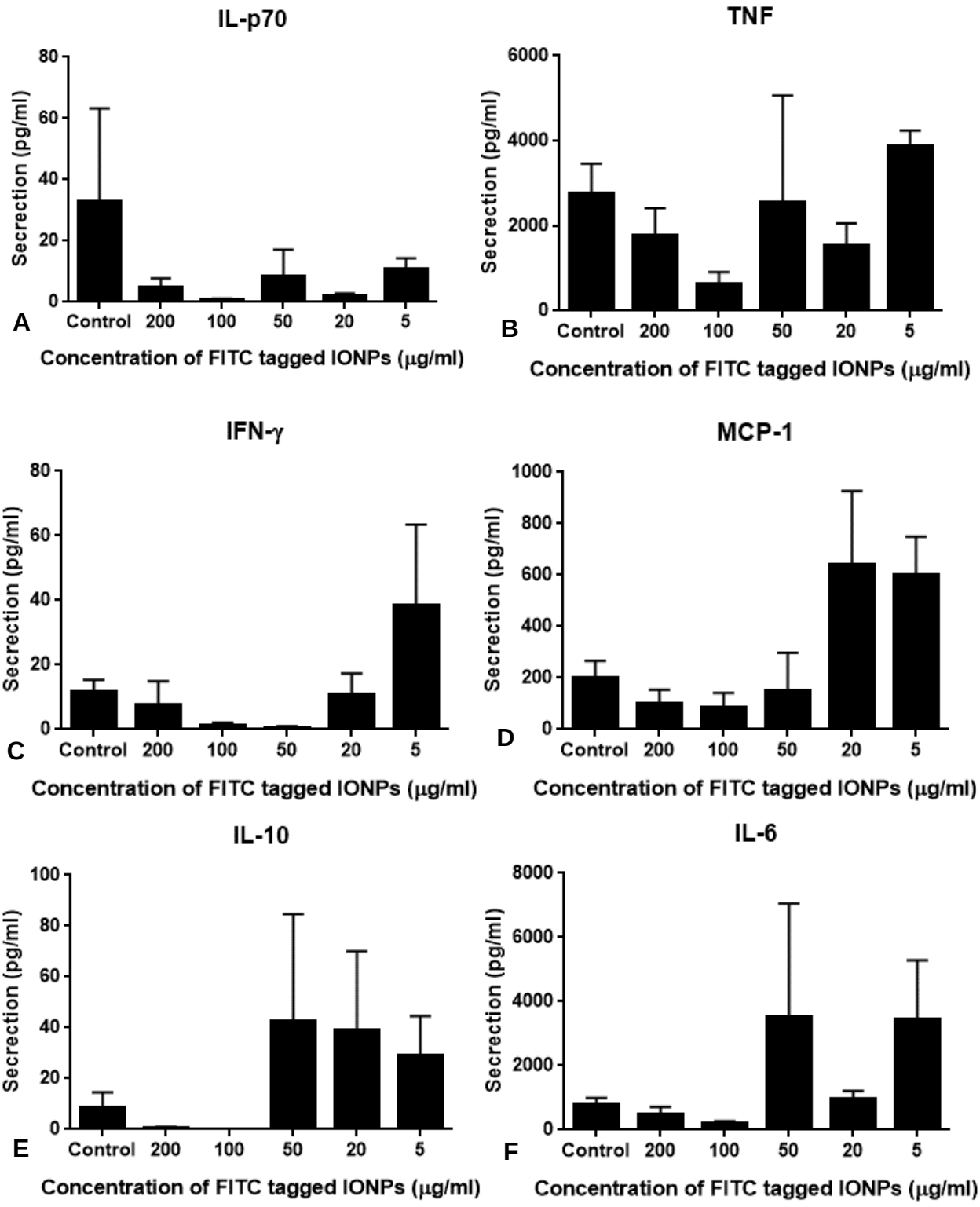

Figure 4.20: Dose dependent cytokine expression of Flt3 grown BM-DC following incubation with FITC tagged IONPs for 24 hours, *in vitro*. C57BL/6 derived BM-DCs grown with Flt3 for 8 days were incubated with varying concentrations of FITC tagged IONPs for 24 hours, *in vitro*. Supernatants were collected and stored at -80 ^{o}C for future cytokine analysis. Cytokine expression was quantitated using the CBA Murine Inflammatory Kit (BD Biosciences) and analysed using flow cytometry, n=3. Cytokine levels are shown as mean values with standard error of the mean represented as error bars. One-way ANOVA multiple comparison test (as a post-test analysis) was performed with the Tukey's multiple comparison test. Where no asterisks are displayed, no statistical significance was found.

4.3 Discussion

Murine DCs were generated from bone marrow precursors, *in vitro*, by incorporating either the GM-CSF or Flt3 cytokine or growth factor, as described in Section 2.1. Following an incubation period of 24 hours with IONPs at 5 % CO_2 at 37 ^oC, Figure 4.1A demonstrates that GM-CSF BM-DCs, uptake FITC tagged IONP in a dose dependent fashion, also known as a titration effect or response. Reviewing the post-test statistical analysis with the Tukey's test (to identify any statistical significance between treatment groups), there was very significant (**, P = 0.001 to 0.01) statistical difference between the means of the cells exposed to 50 µg/ml and 20 µg/ml concentrations. There was no statistical difference (ns, $P \geq 0.05$) recorded with the remaining cell population means, graphically positioned adjacent to each other; that is, there was no statistical difference recorded between cell populations incubated with 200 µg/ml and 100 µg/ml; between 100 µg/ml and 50 µg/ml; and between 20 µg/ml and 5 µg/ml. Therefore, even though a concentration of 50 µg/ml is more than double that of 20 µg/ml, these cells manage to respond and internalise the FITC tagged IONPs. As there is no statistical difference identified beyond this concentration (50 µg/ml); it can be deduced that this concentration is at or near the maximum capabilities of the cells (BM cells seeded at 3 x 10^6 cells in 3 ml in each well). An increase to either 100 µg/ml or 200 µg/ml results in no statistically significant greater uptake of IONP by the cells.

The corresponding graph depicting Fold Increase in MFI (Figure 4.1B) from the GM-CSF stimulated murine DCs, again, show no statistical difference between the FITC tagged IONPs concentrations of 100 µg/ml or 200 µg/ml; closely reflecting the uptake findings of Figure 4.1A at these two higher doses. Across the range of concentrations tested, graphically, the treatment means also visually demonstrate a dose dependent effect. For both the control and 200 µg/ml conditions, there was extremely significant (****, P < 0.0001) statistical difference identified by the Dunnett's test; denoting that the GM-CSF induced murine DCs successfully

had uptaken FITC tagged IONPs. The Tukey's test resulted in no statistical significance between means of adjacent treatment conditions; that is, there was no significance between 5 µg/ml and 20 µg/ml, between 20 µg/ml and 50 µg/ml, between 50 µg/ml and 100 µg/ml, and so on. This response further supports a dose dependent effect and that the GM-CSF induced murine DCs are capable of internalising the FITC tagged IONPs.

The dose uptake experiments performed with the Flt3 induced murine DCs (Figure 4.2A) also demonstrate a dose dependent effect, however, the uptake by Flt3 is approximately 75% to that of the GM-CSF DCs. For example, at a concentration of 200 µg/ml, the mean uptake by GM-CSF DCs is 80 %, whereas at this same concentration, the uptake by Flt3 DCs is 60 % (60 % is ¾ of 80 %). This pattern is followed throughout the remaining concentration levels. The Tukey's test demonstrates that there was no statistical significance (ns, $P \geq 0.05$) between the means of adjacent treatment conditions; that is there was no significance between 5 µg/ml and 20 µg/ml, between 20 µg/ml and 50 µg/ml, between 50 µg/ml and 100 µg/ml, and so on. The Dunnet's test cannot identify any statistical significance (ns, $P \geq 0.05$) between the control mean and the 50 µg/ml concentration mean and less, for Flt3 primed murine DCs; therefore, statistically noticeable percentage uptake commences with a FITC tagged IONP concentration of 100 µg/ml (*, statistically significant, P = 0.01 to 0.05) and continued to very significant (**, P = 0.001 to 0.01) between control and 200 µg/ml; at 24 hours incubation.

Figure 4.2B, demonstrates Fold Increase in MFI for the Flt3 murine DCs. The Fold Increase in MFI values identified with Flt3 murine DCs is approximately 57 % compared with GM-CSF murine DCs. At the FITC tagged IONP concentration of 200 µg/ml, for instance, a mean value of 1.9 is recorded for Flt3 murine DCs and approximately 3.5 for GM-CSF murine DCs (2.0 is 57 % of 3.5). This, for Flt3 murine DCs, corresponds with its reduced uptake identified in Figure 4.2A, compared with GM-CSF murine DCs (Figure 4.1A). Tukey's test for treatments between columns, resulted in no statistical significance (ns, $P \geq 0.05$) between adjoining treatment concentration means. Dunnett's test was used to compare the control

group with each treated group; resulted in no statistical significance (ns, $P \geq 0.05$) between the control condition and all treatment conditions.

The maximum concentration of 200 µg/ml of FTC tagged IONP, as tested during the dose uptake studies, was used to perform time course experiments with both GM-CSF and Flt3 murine DCs. With GM-CSF murine DCs (Figure 4.3A), the Tukey's test was unable to identify any statistical significance between any of the treatment groups, meaning that uptake of IONPs by GM-CSF murine DCs at 24 hours offered no statistical difference compared to the minimum incubation period tested of 1 hour. Therefore, the level of IONP uptake at 1 hour is comparable to that at 24 hours, thus, no real advantage was offered by the addition 23 hours of incubation. The Dunnett's test, however, did recognise a very significant (**, P = 0.001 to 0.01) statistical significance between the control mean and the mean of each treatment condition. The corresponding Fold Increase in MFI graph plotted in Figure 4.3B, was assessed with the Tukey's test and no statistical significance (ns, $P \geq 0.05$) was found between treatment conditions. The Dunnett's test identified a significant statistical difference (*, P = 0.01 to 0.05) between the control and highest concentration (200 µg/ml) means. This same test (Dunnet's) reported no statistical significance (ns, $P \geq 0.05$) between the control mean and the means of the remaining treatment conditions. Therefore, there was a benefit to the 24 hour incubation period, which was that it allowed the maximum difference between control and the highest concentration treatment in terms of Fold Increase in MFI; and with respect to percentage uptake, the 24 hour and 18 hour time points were considered approximately equivalent and both were statistically very significant (**, P = 0.001 to 0.01) compared to the control.

With Flt3 murine DCs, the percentage uptake pattern (Figure 4.4A) visually appeared to be time dependent, that is, as the incubation time increased, so too did the percentage uptake. The Tukey's statistical assessment discerns that there was statistical significance (*, P = 0.01 to 0.05) between the mean values of the 24 hour and 1 hour time points and no statistical

significance (ns, $P \geq 0.05$) between all other combinations of treatment time points. The Dunnett's test identified significant (*, P = 0.01 to 0.05) statistical difference between control and 24 hour and between control and 18 hour time points. Accordingly, therefore, with Flt3 murine DCs, statistically suitable percentage uptake was identified at 18 hours of incubation with IONPs; whereas with GM-CSF murine DCs the equivalent occurred at the 1 hour incubation time point.

Compared to GM-CSF, the actual percentage values of uptake of IONPs by Flt3 murine DCs were lower, as presented in Table 4.1. These tabulated and calculated figures also demonstrate that even at 1 hour incubation of GM-CSF murine BM-DCs with IONPs, a greater percentage of these cells (71.08 %) had uptaken IONPs compared to Flt3 murine DCs at completion of the longest incubation time tested of 24 hours (42.7 %). The Fold Increase in MFI graphs revealed findings of a similar nature, that is, the Fold Increase in MFI of the Flt3 murine BM-DCs (Figure 4.4B) are at a level lesser than the GM-CSF and are tabulated in Table 4.2.

To determine if the FITC tagged IONP triggered a maturation signal in either the GM-CSF or Flt3 induced murine DCs, maturation experiments were performed. Cells that were positive for CD11c, a protein associated with dendritic cells, were also assessed for CD86 and CCR7 expressions. CD86 is a protein expressed by many DCs and is known to facilitate activation for T-cell lymphocyte proliferation by providing costimulatory signals; thus, an indicator of DC maturation. CCR7 is expressed by lymphoid cells, such as DCs, and is considered as a migratory marker – it stimulates and controls the co-ordinated movement of memory T-cell lymphocytes to lymph nodes and other secondary lymph organs. It directs responding cells to traverse the endothelial wall of the HEV and transition to the T-cell zone of lymph nodes. CCR7 also has the ability to stimulate maturation of DCs.

CD11c positive murine DCs arising from GM-CSF stimulation, demonstrated levels of CD86 that graphically appeared elevated, compared to its expression of CCR7 (Figure 4.6A). The CD86 surface expression, demonstrated a dose dependent effect (graphically) with respect to treatment with IONP at concentrations from 5 µg/ml to 50 µg/ml and plateauing or peaking at 100 µg/ml. CCR7 also demonstrated a dose dependent effect, however, expressed in lesser quantities; approximately half the value compared to CD86; for all treatment conditions and also with control conditions (Figure 4.7). The data contributing to Figure 4.7 was assessed and no statistical significance was identified between CD86 and CCR7 for all treatment conditions; in relation to percent surface expression (Figure 4.7A) and Fold Increase in MFI (Figure 4.7B). It can be argued that, visually, according to the graph presented, there could possibly be a dose-dependent effect, however, more importantly, no statistical significance was found between treatment conditions. Significant (*, P = 0.01 to 0.05) statistical difference was identified, however, in fold increase in MFI between control and the level of CD86 expressed in response to 200 µg/ml of FITC tagged IONP (Figure 4.5B). The only possible explanation that can be offered for this was the maximum possible presence of FITC (in the 200 µg/ml treatment group) compared with no FITC (in the control group).

The expression of CD86 by Flt3 murine DCs demonstrated a dose-dependent response between 5 µg/ml to 50 µg/ml (Figure 4.8). The levels of CCR7 expressed was approximately between one-quarter to one-third of the CD86 expression, across the treatment concentrations. When these results are compared to those of GM-CSF derived murine DCs, the secretion of CD86 is approximately at 40 %. The corresponding Flt3 murine DCs Fold Increase in MFI (Figure 4.8B), reflected the percentage surface expression; confirming a titration or dose-dependent effect. Therefore, from these results, under these experimental conditions, the IONP have a greater maturation and migratory effect on GM-CSF murine DCs than on Flt3 murine DCs.

Apoptosis, programmed cell destruction and death, can occur when cells experience exceedingly stressful, harmful or toxic conditions. Apoptosis studies, with a double stained technique, was performed as described in Section 2.11.3 using a proprietary kit containing PE Annexin V, 7AAD and Annexin Binding Buffer. Following a 24 hour incubation period with FITC tagged IONPs, the apoptosis studies (n = 3) identified average GM-CSF murine cell populations to be in the following stages of apoptosis (Table 4.3).

Table 4.3 is a tabulated representation of the graphs presented in Figure 4.12 and Table 4.4 is representative of Figure 4.15. Flt3 derived DCs can better tolerate FITC tagged IONPs at these tested concentrations at the completion of the 24 hour incubation period. Comparing the two murine DC populations (GM-CSF and Flt3 derived), approximately half (49 %) of the Flt3 murine DCs remained alive and viable rather than 39 % of GM-CSF murine DCs (Figure 4.18). With respect to quadrants 1 (dead cells); 19 % of the Flt3 derived murine DCs were identified as dead, whereas, about half this figure, 10 % of GM-CSF murine DCs were deceased. GM-CSF murine DCs had a greater percentage of cells in both early apoptosis (quadrant 4), 20 % and in late apoptosis (quadrant 2), 32 % - while Flt3 murine DCs had 12 % and 20 % of their cell populations in these apoptotic states, respectively. With respect to quadrants 1 (dead cells), 2 (late apoptotic) and 3 (early apoptotic); there were a combined 62 % of the GM-CSF murine DC cell population experiencing these apoptotic stages and a combined 51 % of Flt3 murine DCs. In summary, while Flt3 derived murine DCs had a greater population percentage as dead cells, overall, there was a greater percentage of viable cells as fewer cells were in early and late apoptosis; thus Flt3 murine DCs demonstrated greater survival capabilities under these treatment conditions.

A number of possible reasons can be offered to explain these differences. Firstly, the apoptosis studies were performed 3 times with GM-CSF murine DCs, as opposed to 5 times with Flt3 murine DCs. As the replicates are different for these to cell types, there is a greater long-term averaging of n = 5 replicates compared to n = 3 replicates. Secondly, the large

error bars for both cell types, could indicate that the response to treatment conditions are variable. Thirdly, and perhaps more logically, the plasmacytoid component of the Flt3 murine DCs may be contributing to the greater viability of Flt3 murine DCs and being lesser of them in early and late apoptosis. GM-CSF murine DCs are considered to be myeloid DCs, whereas, Flt3 murine DCs are considered to have myeloid and plasmacytoid aspects. Overall, therefore, and average of 39% of the GM-CSF derived dendritic cell population are viable and healthy following 24 hours incubation with IONPs; compared with a value of 49 % of dendritic cells generated with Flt3 (viable and healthy following the same incubation period and treatment conditions).

For both derivations of murine DCs (GM-CSF and Flt3 generated), a proprietary cytometric bead array Mouse Inflammation Kit was used to simultaneously identify the secretion of pro-inflammatory cytokines IL-12p70, TNF, IFN-γ, MCP-1, IL-6 and an anti-inflammatory cytokine IL-10; as secreted in their cellular supernatants following exposure to FITC tagged IONP.

The IL-12p70 cytokine is secreted by DCs due to antigen stimulation, it initiates production of IFN-γ and TNF. IL-12p70 can also stop oncologic angiogenesis, the development of new blood vessels to supply tumours, by triggering high secretion of IFN-γ.

TNF, produced by lymphoid cells, acts as a cytotoxin for tumour regression and also induces apoptotic cell death, however, its actions are inhibited by elevated levels of IL-6. TNF has a clinical association with oncology patients reaching cachexia; as demonstrated by elevated blood serum levels of TNF.

IFN-γ is released by DCs, myeloid cells and macrophages. It plays an important role for both innate and adaptive immunity with respect to immune-regulation, it has anti-tumour properties and may also be involved with cell self-activation at the onset of infection.

MCP-1, secreted by DCs to an inflammatory response, is significant for establishing a chemotaxic effect and establishing a chemical gradient that directs migration of DCs to their destination to interact with T cells.

IL-6 has an inhibiting consequence on TNF and can activate IL-10; and interestingly is an inflammatory cytokine and an anti-inflammatory myokine.

IL-10 is an anti-inflammatory cytokine that can suppress production of pro-inflammatory cytokines, namely INF-γ and TNF (and also IL-2 and IL-3) and can also suppress the antigen presenting capabilities of DCs, in general.

Figures 4.19 and 4.20 both demonstrate that murine myeloid DCs (GM-CSF induced) and murine myeloid/plasmacytoid DCs (Flt3 induced) respond similarly to experimental conditions with elevated *in vitro* secretion of TNF, MCP-1 and IL-6.

For both cell types, when the secretion of TNF, MCP-1 and IL-6 in the presence of various concentrations of FITC tagged IONPs is compared to control conditions, there is no statistical difference (Figure 4.19 and Figure 4.20). Therefore, it can be surmised that the IONPs tested do not appear to induce a notable inflammatory response; and thus, there is no statistical difference in cytokine secretion between the treatment and control conditions.

Flt3 generated murine DCs, having myeloid and plasmacytoid characteristics, showed release of the same cytokines (TNF, MCP-1 and IL-6) but at approximately half the values to that of GM-CSF derived DCs (measured in pg/ml). These lower secretions of TNF and IL-6 could explain why there were 51 % of the Flt3 population in a combined state early apoptosis, late apoptosis and death; compared with GM-CSF murine DCs. For these Flt3 murine DCs, and considering the results from apoptosis studies, Flt3 murine DCs can better tolerate and survive these experimental treatment conditions compared to GM-CSF murine DCs.

What cannot be explained by these results for both cell types is that while IL-6 is being secreted, it does not appear to have an inhibiting effect on TNF. This may be dues to that 24 hours may be insufficient time for both IL-6 and IL-10 to fully respond and have an impact on the TNF release levels. For both cell types, IL-10 is also being released, but at very low, but detectable levels.

When the data from the apoptosis and CBA studies are reviewed with the respective maturation data; together, it can be argued that the Flt3 derived murine DCs are maturing either at a slower rate or in less numbers, compared to GM-CSF induced murine DCs. Therefore, the GM-CSF DCs are progressing through their cell-cycle towards death, at a faster rate, when incubated with IONPs under the treatment conditions presented here. Comparatively, there are less GM-CSF DCs alive or viable; greater numbers in early and late apoptosis; and the secreted cytokine data supports the apoptotic data, which, in turn, supports the maturation data – for both cell types.

4.4 Conclusion

The aims of this chapter have been addressed and the experimental results lead to the following conclusions:

1. GM-CSF derived BM-DCs demonstrated a dose-dependent response to the IONPs concentrations tested. Of the nanoparticle concentrations tested, 50 µg/ml is the concentration that is at or near the maximum capabilities of the GM-CSF stimulated murine DCs. An increase to either 100 µg/ml or 200 µg/ml resulted in no statistically significant (ns, $P \geq 0.05$) greater uptake of IONP by the cells when compared to 50 µg/ml concentration. When compared to the control condition, 5 µg/ml concentration resulted in no statistical (ns, $P \geq 0.05$) significance; whereas with all other concentrations, these DCs demonstrated percentage uptake that was statistically extremely significant (****, $P < 0.0001$) compared to control. Flt3 derived BM-DCs (myloid/plasmacytoid type DCs) demonstrated a dose-dependent response to the IONPs concentrations tested. At the nanoparticle concentrations tested, these DCs showed percentage uptake equivalent to approximately 75 % to the percentage uptake shown by GM-CSF generated murine DCs. Following 24 hours incubation, statistically noticeable (*, $P = 0.01$ to 0.05) percentage uptake occurred at 100 µg/ml (compared to control condition) and an increase to 200 µg/ml resulted in very significant (**, $P = 0.001$ to 0.01) statistically difference compared to control conditions.
2. GM-CSF induced BM-DCs (myeloid type DCs) time course experiments were performed. These DCs demonstrated maximum uptake of IONPs at 1 hour incubation with 200 µg/ml of IONPs. Time course studies with Flt3 generated BM-DCs (myloid/plasmacytoid type DCs) demonstrated that maximum uptake occurred at 4 hours incubation with 200 µg/ml of IONPs.

3. GM-CSF was used to generate myeloid type DCs and Flt3 used to generate myloid/plasmacytoid type DCs. GM-CSF generated BM-DCs expressed CD86 at twice the level that it expressed CCR7. Flt3 generated BM-DCs secreted CCR7 at a level that was 25 % to 30 % to their expression levels of CD86; or alternatively, these cells expressed CD86 at a level that was 3 to 4 times greater than their expression of CCR7. Flt3 derived BM-DCs secreted CD86 at a value that was about 40 % equivalent to the level of CD86 expressed by GM-CSF derived BM-DCs. *In vitro*, under these experimental conditions, the IONPs had a stimulatory effect on both cell types, however, the effect was greater on GM-CSF derived BM-DCs, resulting in greater expression of maturation and migratory markers from GM-CSF derived BM-DCs than from Flt3 derived BM-DCs.
4. Apoptosis, programmed cell death, studies were performed with GM-CSF generated BM-DCs (myeloid type DCs) and also with Flt3 generated BM-DCs (myloid/plasmacytoid type DCs). Under these experimental conditions; approximately half (49%) of the Flt3 murine DCs remained alive and viable compared to 39 % of GM-CSF murine DCs. GM-CSF murine DCs had a greater percentage of cells in both early apoptosis (quadrant 4), 20 % and in late apoptosis (quadrant 2), 32 % - while Flt3 murine DCs had 12 % and 20 % of their cell populations in these apoptotic states, respectively. Therefore, combined, 62 % of the GM-CSF murine DC cell population experienced these apoptotic stages and a combined 51 % of Flt3 murine DCs. 19 % of the Flt3 derived murine DCs were identified as dead, whereas, about half this figure, 10 % of GM-CSF murine DCs were deceased. From the results, Flt3 derived murine DCs can better tolerate FITC tagged IONPs at these tested concentrations at the completion of the 24 hour incubation period; while Flt3 derived murine DCs had a greater population percentage as dead cells, overall, there was a greater percentage of viable cells as fewer cells were in early and late apoptosis; thus

Flt3 murine DCs demonstrated greater survival capabilities under these treatment conditions.

5. The supernatant from dose uptake experiments were assessed using a CBA Murine Inflammatory Kit. Murine myeloid DCs (GM-CSF induced) and murine myeloid/plasmacytoid DCs (Flt3 induced) respond similarly to experimental conditions with elevated *in vitro* secretion of TNF, MCP-1 and IL-6. The ratio of released TNF and IL-6 by GM-CSF murine DCs across all IONP concentrations demonstrated an almost dose dependent expression effect and pattern of secretion levels of TNF and IL-6 were almost visually identical. Flt3 generated murine DCs, having myeloid and plasmacytoid characteristics, showed secretion of the same cytokines as GM-CSF induced DCs (TNF, MCP-1 and IL-6) but at approximately half the pg/ml values to that of GM-CSF derived DCs. For both cell types, a migratory stimulus response is occurring to the presence of IONP, *in vitro*, as MCP-1 has been noticeably released, GM-CSF murine DCs at twice the secretion level as Flt3 murine DCs. For both cell types, IL-10 is also being released, but at very low, but detectable levels.

5.0 Chapter 5 – Characterisation of Iron Oxide Nanoparticle Uptake by Human Monocyte Derived Dendritic Cells, *in vitro*

5.1 Introduction

Cellular magnetic resonance imaging (cMRI) is the imaging cells *in vivo*, with MRI[20]. The cells commonly used in cMRI are DCs – which have been either extracted from a patient and labelled with IONPs, *ex vivo*, and then returned to the patient; or; precursor cells from a patient have been used to generate DCs, *in vitro*, then labelled with IONPs and then returned to the patient[196]. The need for detailed understanding of cellular interactions is leading to innovative research activity and new knowledge gained is rapidly being applied to DCs in preclinical strategies for diagnosing and treating a variety of human disease. Once immature DCs are triggered with a "maturation/danger" signal, they commence migration to secondary lymphoid organs[203]. This process is also in response to certain necessary chemokines and as the immature DCs migrate, they become mature DCs upon arrival at their destination. The mature DCs then present antigen material to naïve T cells.

The two main lineages of DCs, plasmacytoid DCs (pDCs) and myeloid DCs (mDCs) have their own identifiable phenotypes. pDCs are known to be $CD123^+$ (and CD11c) and mDCs are $CD11c^+$ ($CD123^-$). $CD11c^+$ DCs have characteristics similar to immature DCs; having low expressions of costimulatory molecules (CD80, CD86), maturation marker (CD83), and chemokine receptor CCR7 (migration marker)[203, 246, 247]. To study human DCs, monocytes are isolated from peripheral blood mononuclear cells and DCs generated with the addition of recombinant cytokines, *in vitro*. This is currently the most common method used. In human blood, DC progenitor cells only account for approximately 0.1 % of cells and have the

potential to differentiate into immuno-stimulatory DCs if cultured *in vitro* with GM-CSF, IL-4 and TNF-α[206]. For the experiments performed in this thesis, this method was used to generate DCs, *in vitro,*as described in Section 2.6.1.

DCs can actually be extracted from human peripheral blood, by a process known as either haemapheresis, apheresis or leukopheresis ; however, due to their significantly low numbers, their isolation by haemapheresis in sufficient numbers for clinical or research applications can be overwhelmingly laborious[206, 248]. Therefore, *in vitro* generation of DCs from peripheral blood monocytes is currently the preferred method used to collect DCs in sufficient numbers for clinical or research use[206, 249]. Monocytes are cultured with GM-CSF and IL-4 to develop into CD11c+ DCs. These DCs have a phenotypic expression similar to immature DCs, having low expression levels of CD80, CD83, CD86 and MHC-II (induced by IFN-γ). Also, like other immature DCs, these *in vitro* generated DCs are capable of antigen uptake[206]. The lymphoid lineage shows characteristics that distinguish them from myeloid DCs. Plasmacytoid DCs (pDCs) can secrete high levels of type I interferon (IFN) and also have an important role within the innate immune system[250]. pDCs migrate to the LNs through blood and HEV pathways and are comparatively inefficient at taking up exogenous microbes and are more adept to presenting viral antigens. pDCs can be distinguished by their expression of CD123[251]. The migration of DCs from peripheral tissues or organs into their respective draining LNs is key for the adaptive immune system to respond[206].

DCs also have the ability to modify their function as they mature. For example, immature DCs have a high capacity for phagocytosis, they can carry out micropinocytosis and express surface receptors that mediate endocytosis. Immature DCs have greater capabilities to internalise exogenous reagents compared to mature DCs[252].

Upon uptake of antigens, DCs undergo a maturation process. From here, the maturation process can be recognised by changing surface expression levels of MHC-I, MHC-II; and the

CD80 and CD86 costimulatory markers[206] and IL-12 is also secreted in larger quantities[253]. Furthermore, maturation also includes a reduced capacity for antigen uptake and an increase in the expression of CCR7 (also referred to as CD197), a chemokine receptor to facilitate migration to secondary lymphoid tissue[254, 255].

Mature DCs become resistant to the immunosuppressive effects of IL-10; a tumour derived cytokine[256]. Mature DCs are more potent than their immature counterparts in inducing CD8+ cytolytic T-lymphocyte responses *in vitro*, and they are resistant to the immunosuppressive effects of tumour-derived IL-10.

A variety of immune cells exist in human blood. Of relevance to this thesis are the common myeloid progenitor and common lymphoid progenitor which both arise from multi-potential haematopoietic stem cells. One of the lineages descending from the common myeloid progenitor cell line, is the myeloblast. The myeloblast can differentiate into basophils, neutrophils and eosinophils (collectively known as granulocytes) and also monocytes. These monocytes can further differentiate into either macrophages or myeloid DCs. The common lymphoid progenitor can differentiate into lymphocytes and lymphoid DCs. These collective lymphocytes are comprised of small lymphocytes (B cell and T cell lymphocytes) and large granular lymphocytes (natural killer cells)[257].

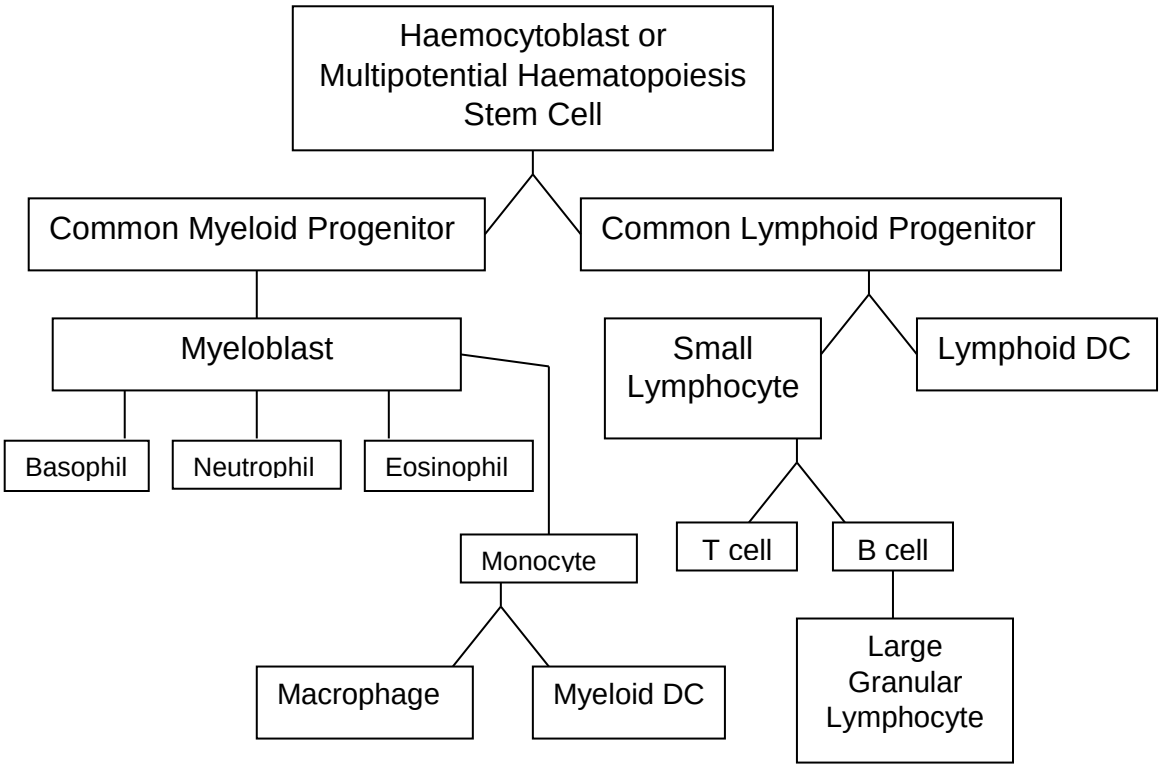

Figure 5.1: Schematic representation of haematopoiesis of human blood cells. This representation does not depict the complete haematopoiesis of human blood cells, but rather only the summary of that relevant to the experimental processes of this thesis[258, 259].

To identify and quantitate the relevant sub-sets of immune cells, multi-colour assays were performed; using a variety of fluorophores and flow cytometry. Collectively, DCs are phenotypically defined as Lin^- $HLA\text{-}DR^+$ cells; with a heterogenous DC population mix. The strategy behind a multi-colour assay is to identify lymphoid DCs which are $CD123^+$ and myeloid DCs which are $CD11c^+$. As $CD123^+$ and $CD11c^+$ are not specific to only DCs, additional markers are used; HLA-DR and Lineage Cocktail 1 which combines CD3, CD14, CD16, CD19, CD20 and CD56[260].

CD11c is also expressed by monocytes, as well as DCs; and CD123 is expressed by monocytes, granulocytes and lymphocytes, in addition to DC[260]s. Both DCs types express high levels of HLA-DR and low levels of markers for monocytes, lymphocytes and large granular lymphocytes (natural killer cells) all of which are contained within the Lineage Cocktail 1. Basophils can be identified by the lack of HLA-DR expression[260]. Hence, the relevant cell population sub-sets within a heterogeneous population of human PBMC monocyte derived DC preparations, can be identified by multi-colour assay with flow cytometry. In this case, the Lineage Cocktail 1 marker used the FITC fluorophore; and therefore, the IONPs used were tagged with R-PE as outlined in Section 2.9.5. CD123 used the APC fluorophore, while HLA-DR used APC-CY™ and the fluorophore for CD11c was PE-CY™7.

Supernatant from dose uptake and time course were collected and stored at -80 ^{o}C for later experimental requirements. This supernantant was used with a Cytometric Bead Array (CBA) Inflammation Kit to identify the levels of cytokine secretion. A proprietary Cytometric Bead Array (CBA) Human Inflammation Kit can be used to test for the six most common cytokines that are known to be involved with an immune response to stimulus, the maturation process and migratory chemotaxis. These following cytokines are protein molecules, secreted by DCs and used for signalling cellular activities, can be identified and quantified with a CBA assay (human);IL-8, IL-1β, IL-6, IL-10, TNF and IL-12p70. The IL-6, IL-10, TNF and IL-12p70 cytokines were described in Section 4.1 and that content is applicable here.

IL-8

Macrophages are known to secrete the IL-8 chemokine cytokine in in response to inflammation[261]. The IL-8 cytokine is also known to induce chemotaxis in target cells, triggering migration to infection sites where the target cells then perform phagocytic activity[262]. In oncology patients, IL-8 plays a role in promoting angiogenesis for tumour expansion and metastases[263].

IL-1β (also known as Catabolin)

The IL-1β cytokine is produced by monocytes and activated macrophages[264] and is engaged with cell proliferation[265], differentiation[266] and apoptosis[267]; as well as being a mediator of inflammatory response[264].

To image DCs, *in vivo*, there are currently two main approaches taken by researchers. The first is to observe the priming kinetics of DC interactions with T-cell lymphocytes within lymph nodes; and the second is imaging of antigen activated DCs for therapeutic applications, from their site of administration to their eventual destination, from a whole body or anatomical region perspective.

The imaging of DC and T cell interactions within the lymph node micro-environment is commonly performed with two-photon microscopy in small animals, *in vivo*[206, 268, 269]. The second approach has been imaged using either nuclear medicine techniques or with MRI – in both animals and in human trials[268]. For humans, the alternative of non-ionising and high imaging sensitivity provided by MRI, affords safe, non-invasive imaging, along with ongoing data acquisition being permissible. With current technology, Nuclear Medicine imaging techniques such as PET and SPECT provide the highest contrast resolution available, whereas MRI can deliver superior spatial resolution. Current literature suggests that both nuclear medicine imaging techniques and MRI are not routinely being used during DC-based immunotherapy to image migration of DCs. The main reason for limited nuclear medicine imaging is it currently cannot overcome the major disadvantage of the need for a radio-isotope with a sufficient half-life that will allow periodic imaging of DCs for several days[206]. Another disadvantage is that the spatial resolution offered by either SPECT or PET[270] cannot compete with two-photon microscopy and MRI. Two of the most common and applicable radio-isoptes have short half-lives, which makes then capable for observing migrating DCs for less than on day; rather than the much needed two days[206]. Imaging agents; such as ^{18}F, only has a half-life of 110 minutes. Also, ^{18}F can become unstable, *in vivo*, and provide contaminated signal detection from the kidneys and urinary bladder; thus making the interpretation of image data difficult[206].

In addition to the highest spatial resolution possible from current non-invasive imaging modalities, using MRI to image DC migration, also allows capabilities for serial or dynamic imaging along with anatomical detail. MRI is currently in wide-spread clinical use, and therefore, any successful imaging of DC migration at trial stages, can easily become translational[205, 206, 271]. Iron oxide nanoparticles, with their T2 MRI image contrast capabilities, presently offers the most sensitive and practicable imaging agent, in both animal and human applications[206]. For the purpose of *in vitro* loading of DCs and then imaging their migration *in vivo*, the innovative use of IONPs together with MRI have not been fully realised. The current benefits, with translation possibilities, are that at certain dosages, IONPs can be non-toxic to DCs; once IONPs are internalised by DCs, they are compartmentalised in vesicles[205], and as IONPs become concentrated in these vesicles, they can induce a quite large local magnetic field and thus generate a relatively high image contrast with MRI[206]; and this, in turn, can provide detectable ease against lymph node tissue. The *in vitro* preparation of DCs with IONPs can take advantage of the high phagocytic capacity of immature DCs[272].

When PET/MRI becomes available in Australia, radio-labelled IONPs may offer a new avenue for imaging DC migration which can merge the advantages of PET (high image contrast) and MRI (high spatial resolution) and overcoming PET imaging's individual disadvantages. This author envisages that ^{68}Ga can be detected with PET and once there is no detectable gamma-radiation, then MRI can be used to continue serial imaging by detecting the IONPs.

For the experiments pertaining to this chapter, monocyte derived DCs were generated from adherent peripheral blood mono-nuclear cells, from donor blood, as described in Section 2.6.1. This now seems to be the preferred starting point for commencing cell-mediated immunotherapy with DCs[246, 249, 257]. In this approach, DCs are isolated from cancer patients

and incubated with exogenous and specific tumour antigens *in vitro*, and the antigen loaded DCs are then administered to the patient to enhance the immune response against tumour targets. DCs can be isolated from human peripheral blood monocytes. The relative number of DCs *in vivo* is low compared with most other cell lineages; thus their extraction in sufficient numbers for clinical use or for research can be difficult[206]. Therefore, the majority of applications currently rely on *in vitro* generation of DCs from peripheral blood monocytes[206, 270, 273]. Given their purity and abundant yield, these are the most commonly used precursor cells for generating human DCs in clinical study. Monocytes are induced to generate CD14– CD11c+ DCs after treatment with GM-CSF and IL-4[20, 273], have characteristics similar to immature DCs through their low expression of CD83, CD80, CD86 and MHC-II[20, 206] and display efficient antigen-uptake capability[206, 274].

In addition to tracking DCs, nanoparticle-based MRI can also be used for tracking other relevant cells such as stem cells, progenitor cells, monocytes, and granulocytes[20, 206, 268, 270, 275]. MoDCs can be labelled and then matured, *in vitro.* Haematopoietic precursor cells from murine bone marrow or monocytes from human peripheral blood, when treated with GM-CSF and IL-4, can differentiate into iDCs. These cells can then be incubated with imaging agents such as iron oxide nanoparticles (MRI) or per-fluorocarbon emulsions, ^{19}F (PET) before further differentiation to mature DC (maturation cytokines can be used)[20]. The translational application of DC-based therapy can be supported greatly through molecular imaging. New discoveries on DC migration and behaviour *in vivo* will lead to new advances in the treatment of a broad range of cancers.

The specific aims of this chapter were:

1. To determine the dose dependent uptake of R-PE tagged IONPs by human MoDC, *in vitro*.
2. To determine the dose dependent uptake and time dependent uptake of FITC tagged IONPs by human MoDC, *in vitro*.
3. To determine the dose dependent uptake of R-PE tagged IONPs by human peripheral blood DC subsets, *in vitro.*
4. To determine the dose dependent uptake of R-PE tagged IONPs and also FITC tagged IONPs by human peripheral blood cells (PBMC, lymphocytes and granulocytes/monocytes), *in vitro*.
5. To determine cytokine release by human MoDC after incubation with tagged IONPs, *in vitro*.

5.2 Results

5.2.1 Dose dependent uptake of human monocyte CD14+ cells and CD11c+ myeloid DCs, *in vitro*

Cells were prepared as described in Section 2.6.1 and the *in vitro* experiments established as per Section 2.6.5 and 2.6.6. A cellular staining technique was used to prepare cells for flow cytometry detection, identification and analysis.

5.2.1.1 Dose dependent uptake of human monocyte CD14+ cells and CD11c+ myeloid DCs, with R-PE tagged IONPs, *in vitro*

The uptake of R-PE tagged IONPs by CD14+ cells (Figure 5.2A) showed no statistical significance between any of the concentration of nanoparticles tested, meaning that CD14+ cells internalised the tested concentrations of IONPs equally. CD11c+ were also capable of internalising the R-PE tagged IONPs to the same extent, statistically, as CD14+ cells, at each concentration dose (treatment condition) tested (Figure 5.3); however, there was statistical significance between the higher concentrations (200 µg/ml and 100 µg/ml) and the lower concentrations (20 µg/ml and 5 µg/ml) tested within the CD11c+ *in vitro* experimental group alone. The statistical difference is due to the CD11c+ cell populations means having a lesser SEM (except the 20 µg/ml CD11c+ population) compared with the CD14+ cells; indicating that the CD11c+ cells could be more efficient or consistent at internalising the R-PE tagged IONPs (compared with CD14+ cells).

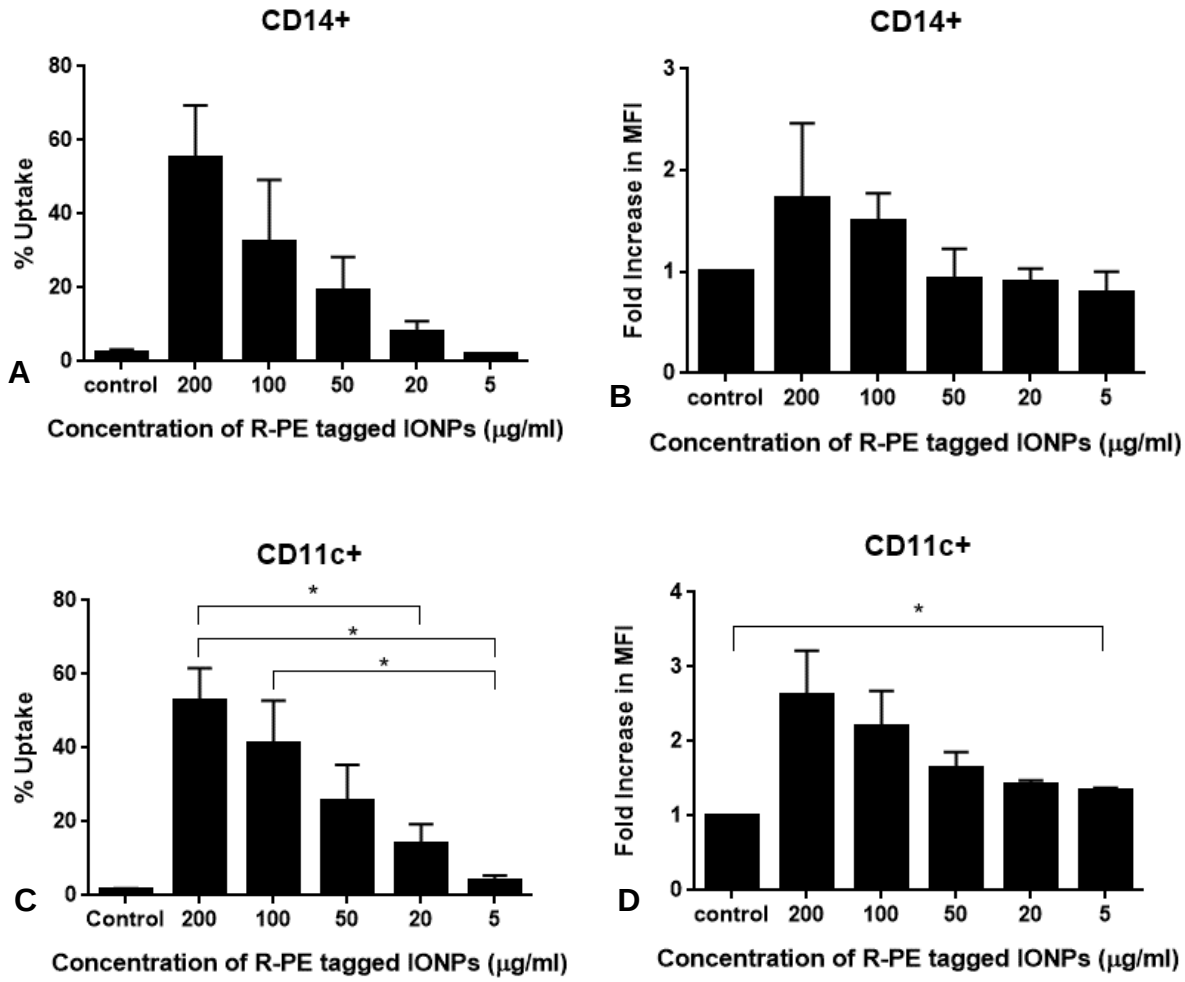

Figure 5.2: Dose dependent uptake of human monocyte CD14+ cells and CD11c+ myeloid DCs with R-PE tagged IONPs, *in vitro*. Dose dependent uptake studies were performed with cultured human Mo-DC. CD14 is expressed by DCs and also monocytes that are capable of differentiating into DCs. CD11c is expressed by human DCs but also by monocytes. CD14+ cells (**Figure A, Figure B**) and CD11c+ myeloid DCs (**Figure C, Figure D**) positive for R-PE uptake (tagged to IONP) after being incubated for 24 hours with varying concentrations of IONPs, were identified by flow cytometry, n=3. One-way ANOVA with the Tukey's multiple comparison test (comparing each treated condition with other treated conditions) and the Dunnett's text comparing the control mean with the treatment condition means were used to statistically analyse the data. Where no asterisks are displayed, no statistical significance was found.

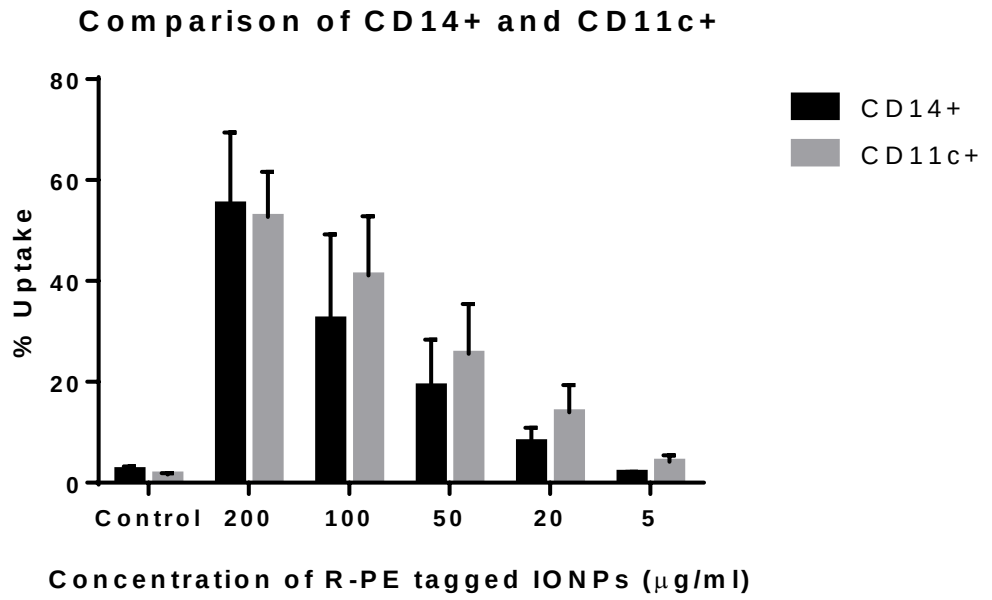

Figure 5.3: Comparison of human monocyte CD14+ and CD11c+ myeloid DC population by dose dependent uptake performed with R-PE tagged IONPs, *in vitro*. Dose dependent uptake studies were performed with cultured human Mo-DC. CD14 is expressed by DCs and also monocytes that are capable of differentiating into DCs. CD11c is expressed by human DCs but also by monocytes. Both CD14+ and CD11c+ myeloid DCs positive for R-PE uptake (tagged to IONP) after being incubated for 24 hours with varying concentrations of IONPs, were identified by flow cytometry, n=3. Two-way ANOVA was used with the Tukey's multiple comparison test, to statistically analyse the data. Where no asterisks are displayed, no statistical significance was found.

5.2.1.2 Dose dependent uptake of human monocyte CD14+ cells and CD11c+ myeloid DCs, with FITC tagged IONPs, *in vitro*

CD14+ cells demonstrated almost maximum uptake of FITC tagged IONPs across all dose concentrations tested, thus displaying efficient internalisation of these nanoparticles. CD11c+ cells demonstrated a classic dose dependent uptake pattern with a significant statistical difference between each adjacent treatment condition (except between 50 µg/ml and 20 µg/ml). When the uptake of nanoparticles by these two cell types are compared (Figure 5.5), the maximum (or near maximum) possible uptake shown by CD14+ cells and the dose dependent uptake of CD11c+ cells, are together responsible for the statistical differences seen at 50 µg/ml, 20 µg/ml and 5 µg/ml.

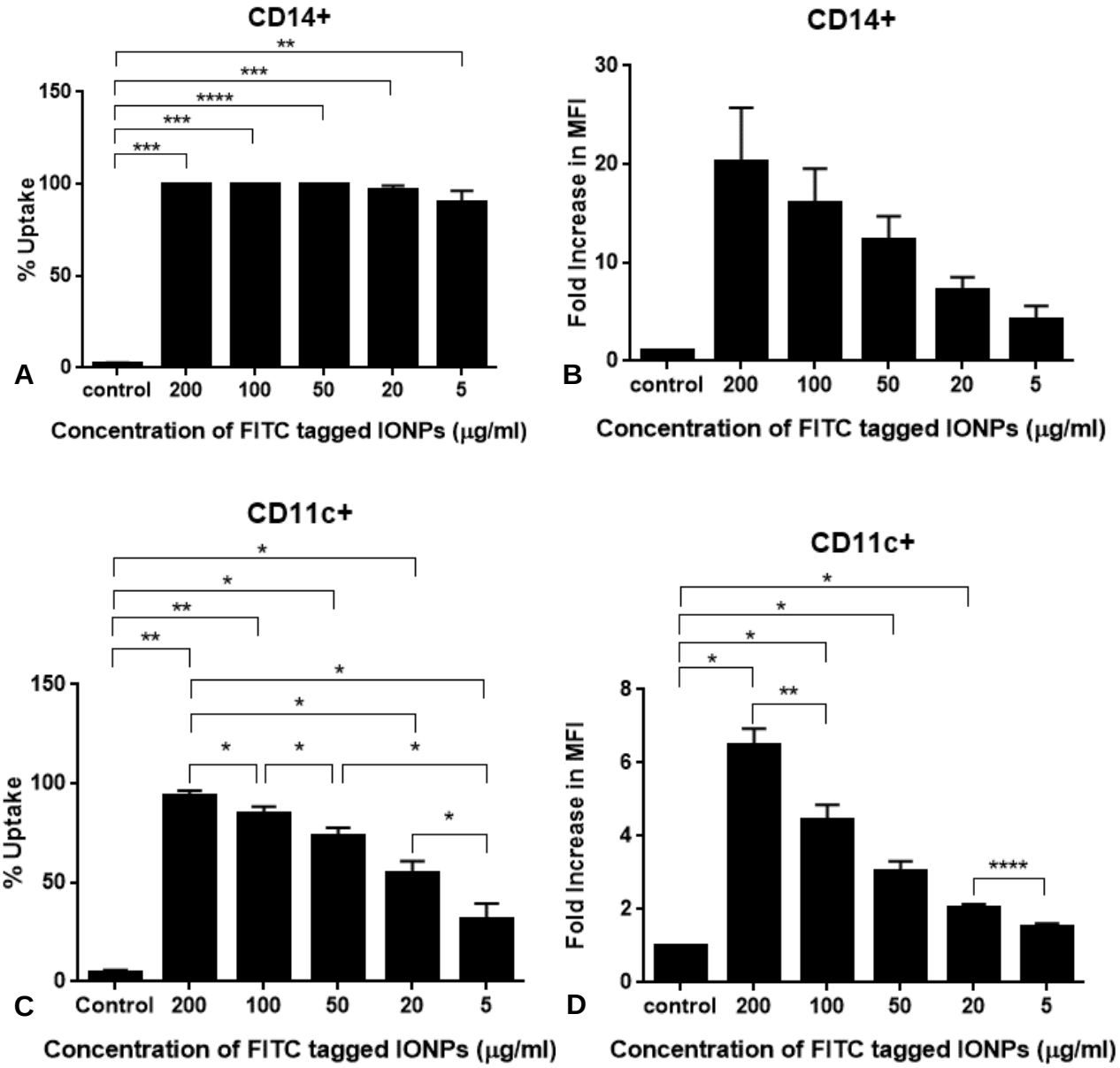

Figure 5.4: Dose dependent uptake of human CD14+ cells and CD11c+ cells with FITC tagged IONPs, *in vitro*. Dose dependent uptake studies were performed with cultured human Mo-DC. CD14 is expressed by DCs and also monocytes that are capable of differentiating into DCs. CD11c is expressed by human DCs but also by monocytes. Both CD14+ cells (**Figure A, Figure B**) and CD11c+ myeloid DCs (**Figure C, Figure D**) positive for FITC uptake (tagged to IONP) after being incubated for 24 hours with varying concentrations of IONPs, were identified by flow cytometry, n=3. One-way ANOVA was used with the Tukey's multiple comparison test (comparing each treated condition with other treated conditions) and the Dunnett's text comparing the control mean with the treatment condition means to statistically analyse the data. Where no asterisks are displayed, no statistical significance was found.

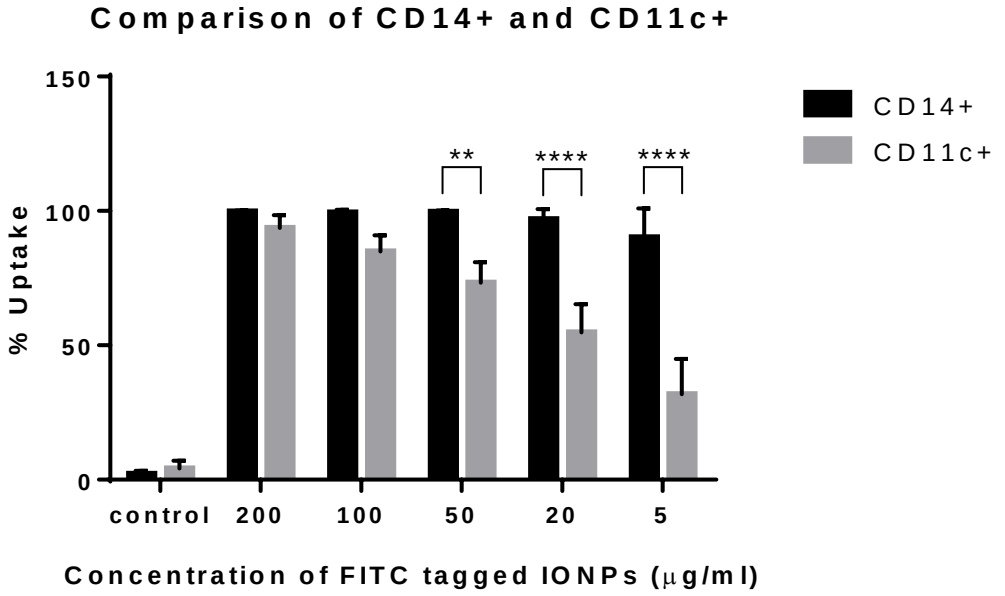

Figure 5.5: Comparison of human monocyte CD14+ and CD11c+ myeloid DC population by dose dependent uptake performed with IONPs tagged with FITC. Dose dependent uptake studies were performed with cultured human Mo-DC. CD14 is expressed by DCs and also monocytes that are capable of differentiating into DCs. CD11c is expressed by human DCs but also by monocytes. Both CD14+ and CD11c+ myeloid DCs positive for FITC uptake (tagged to IONP) after being incubated for 24 hours with varying concentrations of IONPs, were identified by flow cytometry, n=3. Two-way ANOVA was used with the Tukey's multiple comparison test to statistically analyse the data.

5.2.2 Time dependent uptake of human monocyte CD14+ cells and CD11c+ myeloid DCs, *in vitro*

Cells were prepared as described in Section 2.6.1 and the *in vitro* experiments established as stated in Section 2.6.7. A cellular staining technique was used to prepare cells for flow cytometry detection, identification and analysis.

5.2.2.1 Time dependent uptake of human monocyte CD14+ cells and CD11c+ myeloid DCs, with FITC tagged IONPs, *in vitro*

Both CD14+ cells (Figure 5.6A) and CD11c+ cells (Figure 5.6B) demonstrated maximum uptake of FITC tagged IONPs, indicating that maximum uptake was identified at 1 hour incubation; being the shortest incubation time tested. Comparing the uptake of both cell types (Figure 5.7), CD11c+ cells required at least 6 hours incubation time to reach maximum (100%) uptake, equivalent to CD14+ cells.

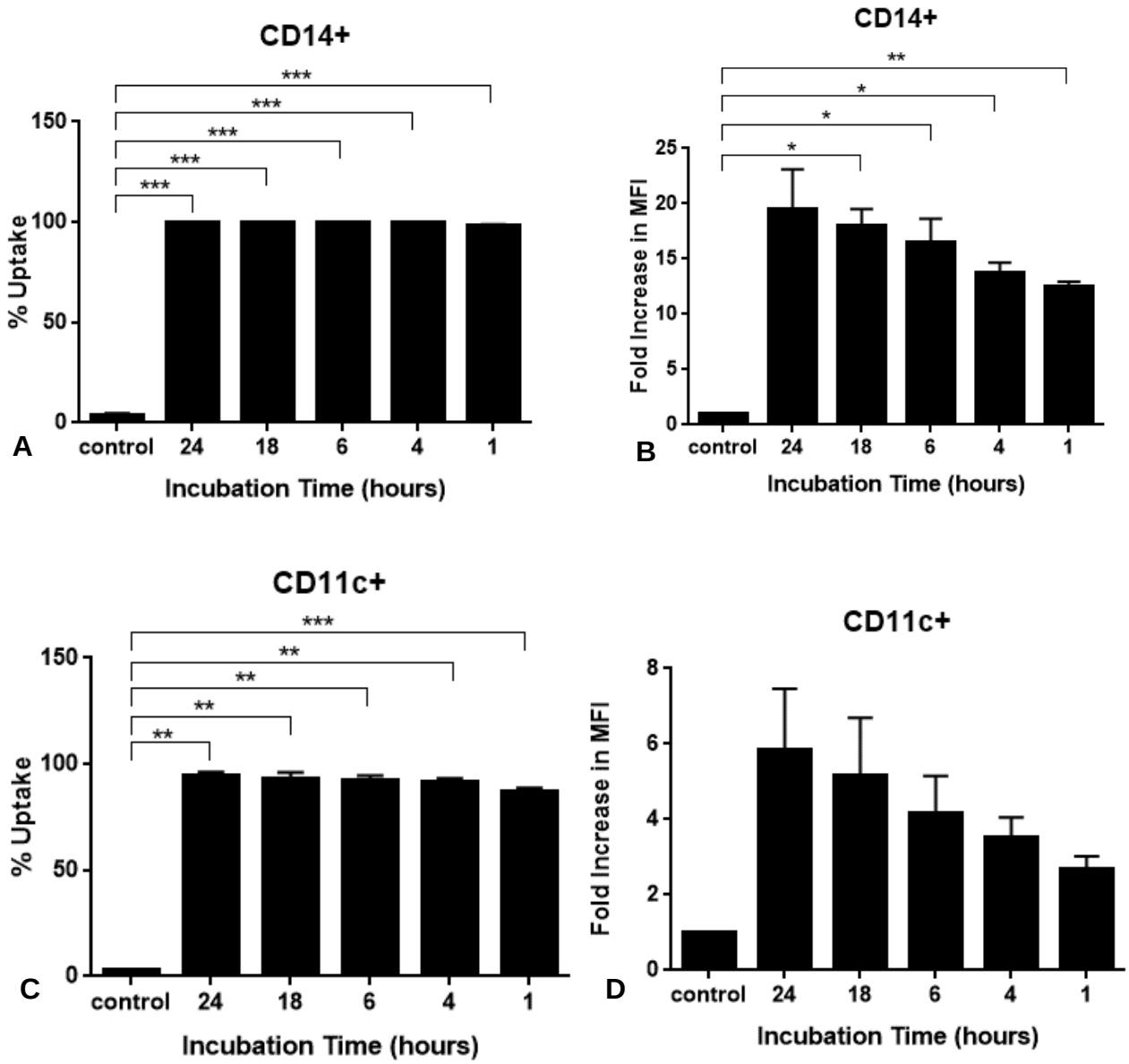

Figure 5.6: Time dependent uptake of human CD14+ cells and CD11c+ cells with FITC tagged IONPs. Time dependent uptake studies were performed with cultured human Mo-DCs, incubated with 200µg/ml of FITC tagged IONPs, over varying time periods. CD14 is expressed by DCs and also monocytes that are capable of differentiating into DCs. CD11c is expressed by human DCs but also by monocytes. Both CD14+ (**Figure A, Figure B**) and CD11c+ myeloid DCs (**Figure C, Figure D**) positive for FITC uptake (tagged to IONP), were identified by flow cytometry, n=3. One-way ANOVA with the Tukey's multiple comparison test (comparing each treated condition with other treated conditions) and the Dunnett's text comparing the control mean with the treatment condition means was used to statistically analyse the data. Where no asterisks are displayed, no statistical significance was found.

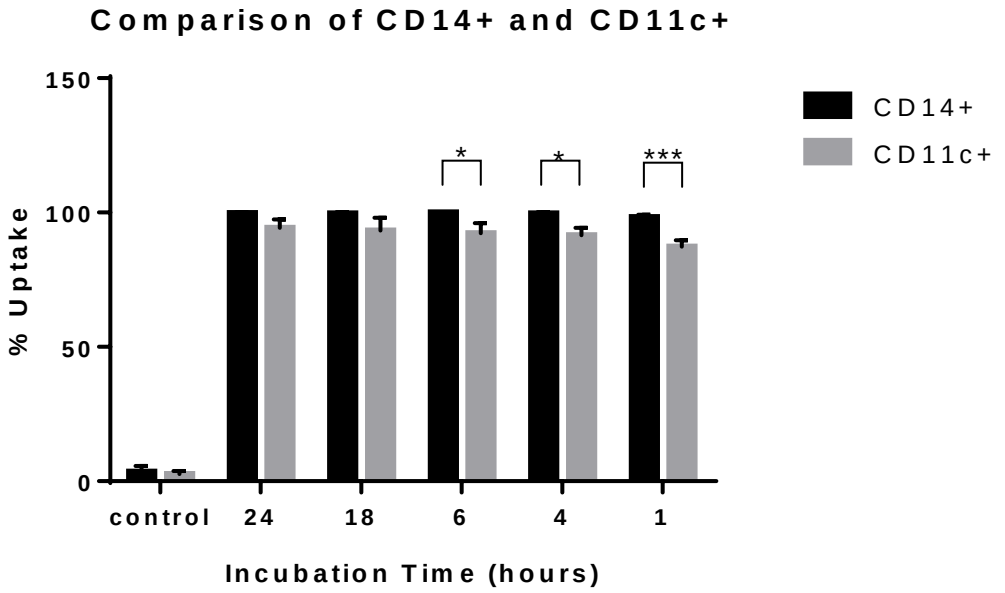

Figure 5.7: Comparison of human monocyte CD14+ and CD11c+ myeloid DC population by time dependent uptake performed with IONPs tagged with FITC. Time dependent uptake studies were performed with human Mo-DC. CD14 is expressed by DCs and also monocytes that are capable of differentiating into DCs. CD11c is expressed by human DCs but also by monocytes. Both CD14+ and CD11c+ myeloid DCs positive for FITC uptake (tagged to IONP) after being incubated for 24 hours with varying concentrations of IONPs, were identified by flow cytometry. This was performed three times, n=3. Two-way ANOVA was used to statistically analyse the data with the Tukey's multiple comparison test.

5.2.3 Dose dependent uptake of R-PE tagged IONPs by human peripheral blood DCs, *in vitro*

Cells were prepared as described in Section 2.6.1 and the *in vitro* experiments established as specified in Section 2.6.9. A cellular staining technique was used to prepare cells for flow cytometry detection, identification and analysis.

5.2.3.1 Dose dependent uptake of R-PE tagged IONPs by human peripheral blood DCs; CD123+ plasmacytoid DCs and CD11c+ myeloid DCs, *in vitro*

CD123+ lymphoid DCs demonstrated statistically equivalent capabilities at internalising the tested nanoparticles (Figure 5.8A), however, there was a significant statistical difference between how these same two nanoparticle concentrations were internalised by CD11c+ myeloid cells (Figure 5.8C). When the uptake of both cell types are compared at each individual concentration of nanoparticle tested (Figure 5.9), no statistical significance could be identified.

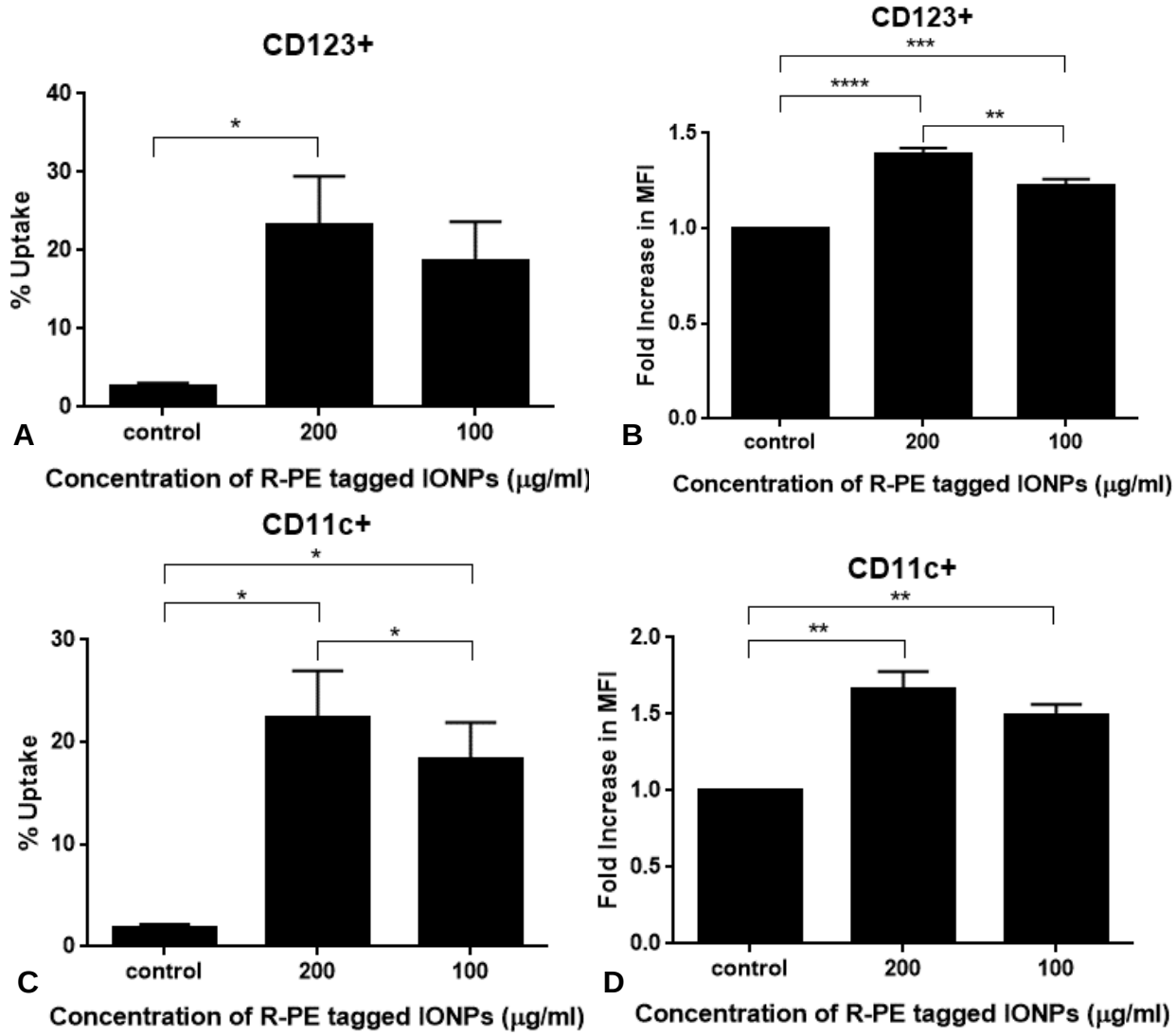

Figure 5.8: Dose dependent uptake of human peripheral blood DCs; CD123+ plasmacytoid DCs and CD11c+ myeloid DCs, positive for R-PE tagged IONPs, *in vitro*. Dose dependent uptake studies were performed with human peripheral blood DCs. Both CD123+ plasmacytoid DCs (**Figure A, Figure B**) and CD11c+ myeloid DCs (**Figure C, Figure D**) positive for R-PE uptake (tagged to IONP) after being incubated for 24 hours with varying concentrations of IONPs, were identified by flow cytometry, n=5. One-way ANOVA with the Tukey's multiple comparison test (comparing each treated condition with other treated conditions) and the Dunnett's text comparing the control mean with the treatment condition means was used to statistically analyse the data. Where no asterisks are displayed, no statistical significance was found.

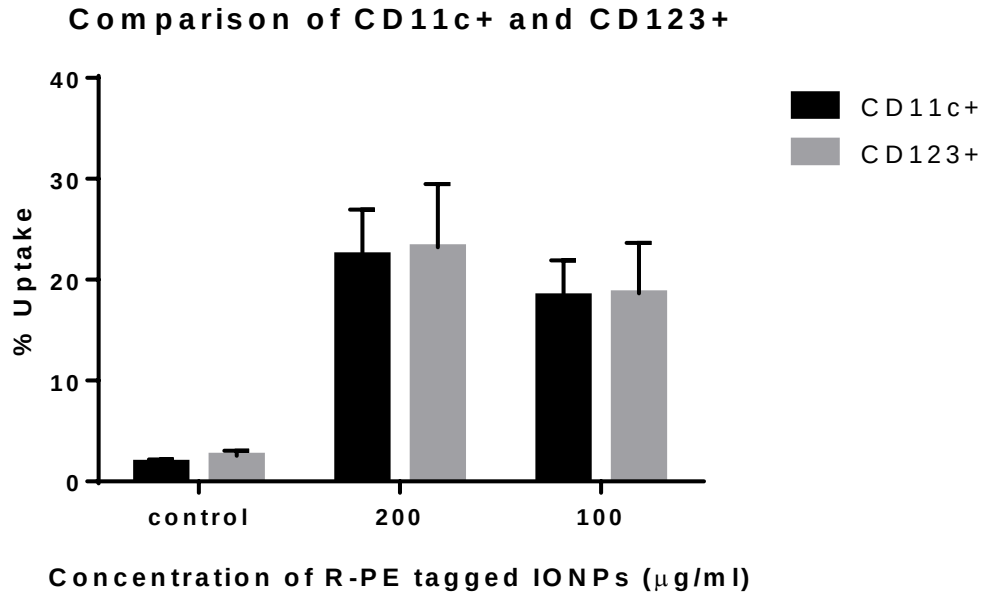

Figure 5.9: Comparison of dose dependent uptake of human peripheral blood DCs; CD123+ plasmacytoid DCs and CD11c+ myeloid DCs, positive for R-PE tagged IONPs. Dose dependent uptake studies were performed with human peripheral blood DCs. Both CD123+ plasmacytoid DCs and CD11c+ myeloid DCs positive for R-PE uptake (tagged to IONP) after being incubated for 24 hours with varying concentrations of IONPs, were identified by flow cytometry, n=5. Two-way ANOVA was used with the Tukey's multiple comparison test to statistically analyse the data. Where no asterisks are displayed, no statistical significance was found.

5.2.4 Dose dependent uptake of FITC tagged IONPs and R-PE tagged IONPs by PBMCs, lymphocytes and granulocytes/monocytes, *in vitro*

Cells were prepared and the *in vitro* experiments established as specified in Section 2.6.9. A cellular staining technique was used to prepare cells for flow cytometry detection, identification and analysis. To determine if other cell types; known to have a role in immunity and thus broadening the potential for immunotherapy or cMRI with IONPs; could be identified from multi-coloured flow cytometry assay.

5.2.4.1 Dose dependent uptake of FITC tagged IONPs and R-PE tagged IONPs by PBMCs, *in vitro*

There was no statistical difference between the internalisation of the FITC tagged IONPs at the two concentrations tested (Figure 5.10A). Like-wise can be stated with the same cell ctype and R-PE tagged IONPs (Figure 5.10C). When the uptake of both differently tagged IONPs by PBMCs are compared (Figure 5.11) at the same two concentrations, no statistical difference could be identified; thus, the PBMCs performed equally, *in vitro*, and this was in keeping with their known phagocytic capabilities.

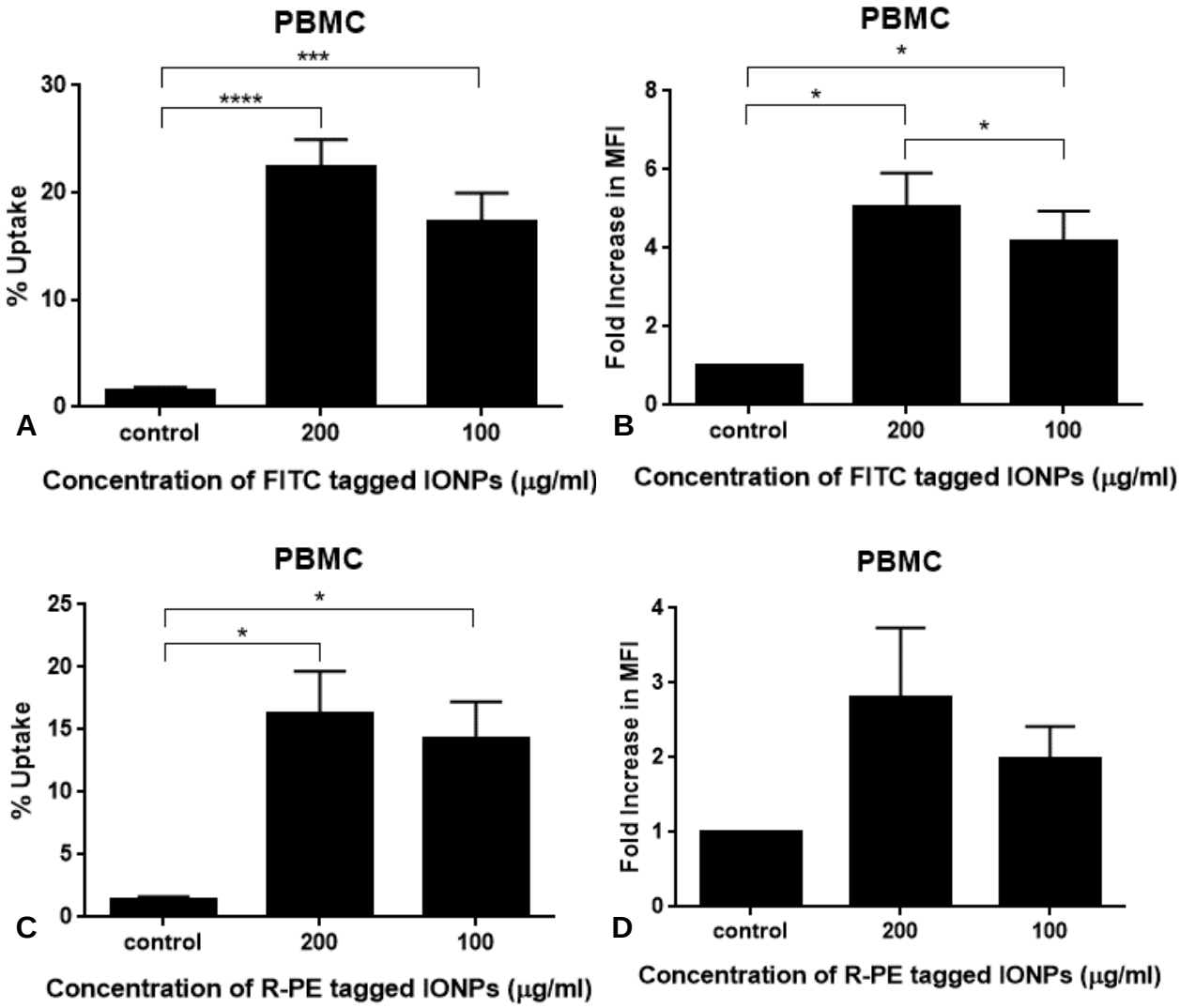

Figure 5.10: Dose dependent uptake of IONPs by human PBMC, *in vitro*. Whole PBMCs were incubated with no, 200 µg/ml and 100 µg/ml of FITC tagged IONPs (**Figure A, Figure B**) and R-PE tagged IONPs (**Figure C, Figure D**) separately for 24 hours and fluorescence was determined by flow cytometry, n=5. % uptake and fold increase in mean fluorescence intensity were determined for all experimental conditions. One-way ANOVA with the Tukey's multiple comparison test (comparing each treated condition with other treated conditions) and the Dunnett's text comparing the control mean with the treatment condition means was used to statistically analyse the data. Where no asterisks are displayed, no statistical significance was found.

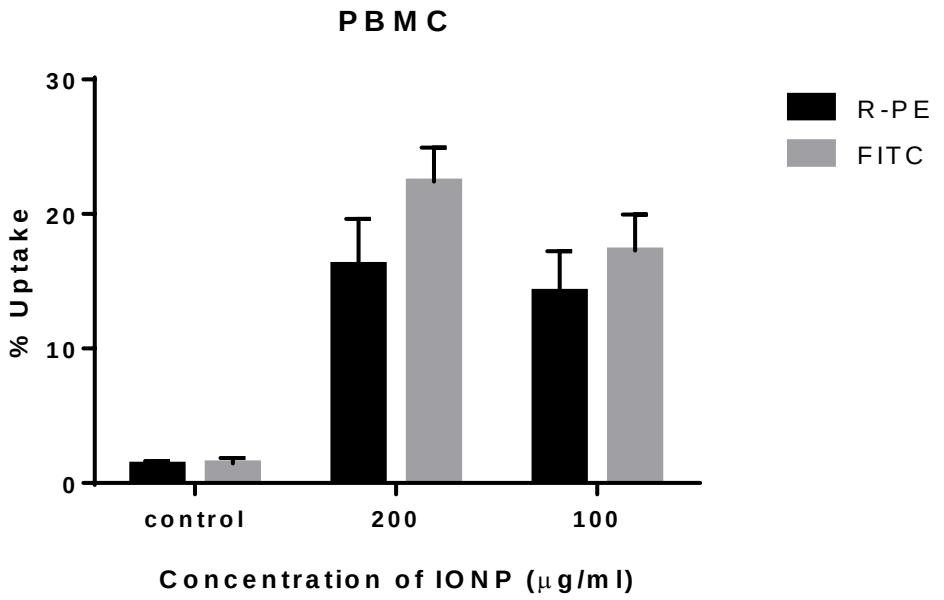

Figure 5.11: Comparison of dose dependent uptake of tagged IONPs by human PBMCs, *in vitro*. Dose dependent uptake studies were performed with whole PBMCs and assessed with flow cytometry following 24 hours incubation with varying concentrations of R-PE and FITC tagged IONPs, separately; n=5. Two-way ANOVA was used to statistically analyse the data with the Tukey's multiple comparison test. Where no asterisks are displayed, no statistical significance was found.

5.2.4.2 Dose dependent uptake of FITC tagged IONPs and R-PE tagged IONPs by lymphocytes, *in vitro*

The lymphocytes demonstrated no statistical difference in the uptake of FITC tagged IONPs at the two concentrations tested (Figure 5.12A) and the same occurred with R-PE tagged IONPs (Figure 5.12C). When the uptake of both nanoparticle varieties are compared at each treatment condition (Figure 5.13), there was no statistical difference; denoting that lymphocytes were able to internalise both nanoparticles similarly and could be identified as lymphocytes with flow cytometry.

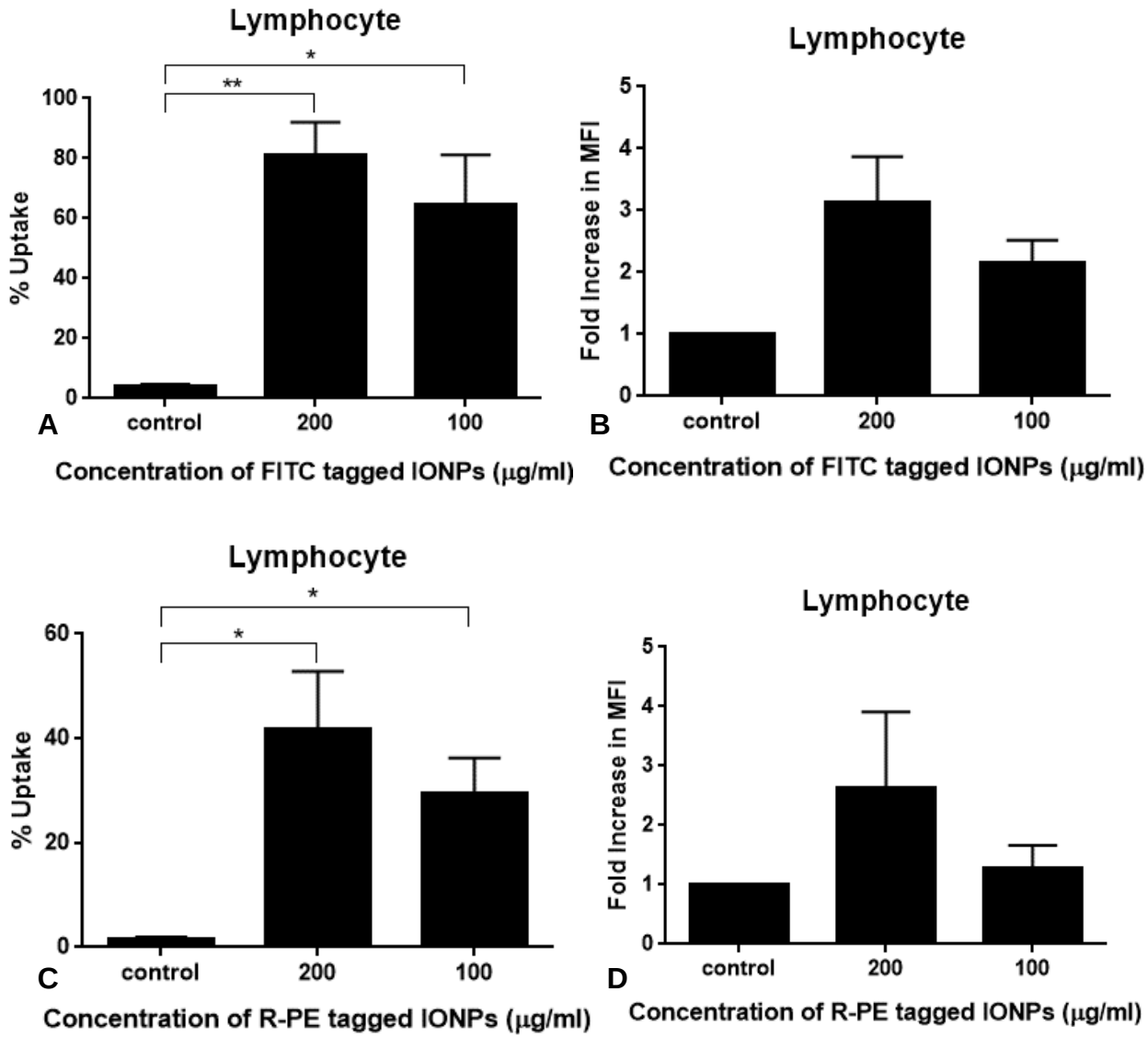

Figure 5.12: Dose dependent uptake of IONPs by human lymphocytes, *in vitro*. Whole PBMCs were incubated with no, 200 µg/ml and 100 µg/ml of FITC tagged IONPs (**Figure A, Figure B**) and R-PE tagged IONPs (**Figure C, Figure D**), separately, for 24 hours and fluorescence was determined by flow cytometry, n=5. Lymphocytes were identified using a staining technique with flow cytometery and % uptake and fold increase in mean fluorescence intensity were determined for all experimental conditions. One-way ANOVA with the Tukey's multiple comparison test (comparing each treated condition with other treated conditions) and the Dunnett's text comparing the control mean with the treatment condition means was used to statistically analyse the data. Where no asterisks are displayed, no statistical significance was found.

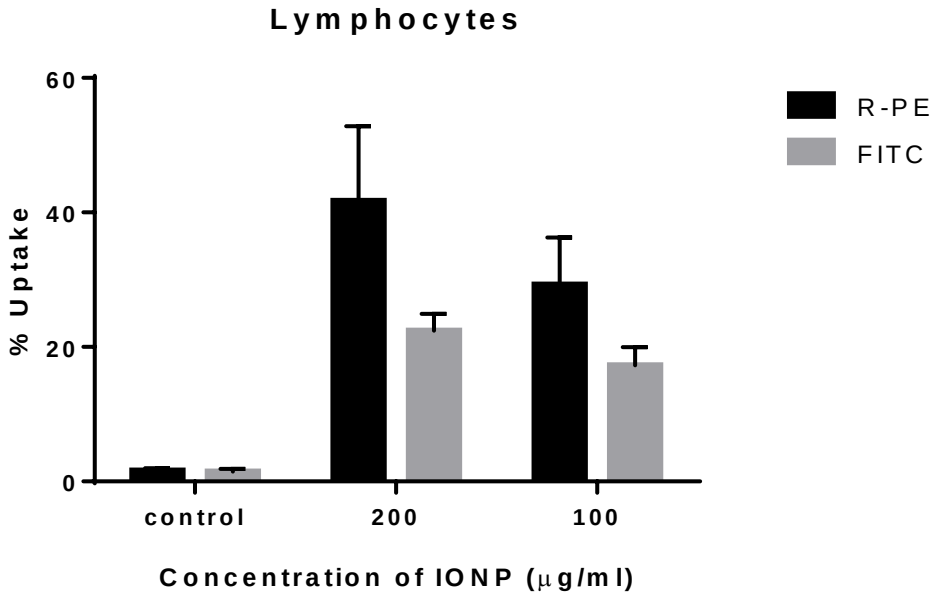

Figure 5.13: Comparison of dose dependent uptake of IONPs by lymphocytes, *in vitro*. Dose dependent uptake studies were performed with whole PBMCs and human lymphocytes were identified and assessed with flow cytometry following 24 hours incubation with varying concentrations of R-PE and FITC tagged IONPs, separately; n=5. Two-way ANOVA was used to statistically analyse the data with the Tukey's multiple comparison test. Where no asterisks are displayed, no statistical significance was found.

5.2.4.3 Dose dependent uptake of FITC tagged IONPs and R-PE tagged IONPs by granulocytes/monocytes, *in vitro*

The granulocytes/monocytes demonstrated no statistical significance in the uptake of FITC tagged IONPs at the two concentrations tested (Figure 5.14A) and the same occurred with R-PE tagged IONPs (Figure 5.14C). Interestingly, when the uptake of both nanoparticle varieties are compared at each treatment condition (Figure 5.15), the granulocytes/monocytes responded differently, *in vitro*. Granulocytes/monocytes could internalise greater quantities of the R-PE tagged IONP variety, demonstrating an extremely significant statistical difference between both nanoparticle varieties at each concentration tested, *in vitro*.

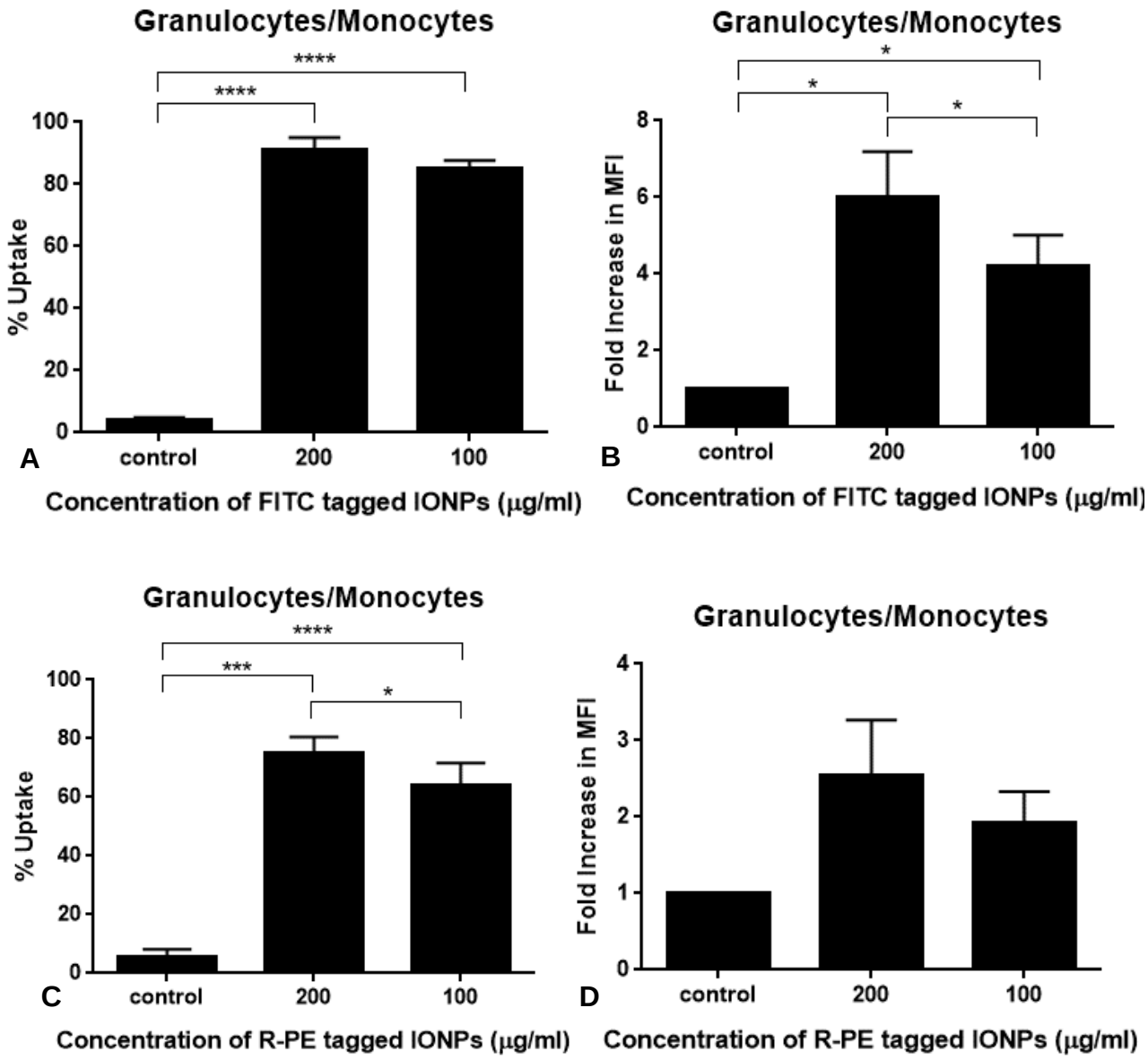

Figure 5.14: Dose dependent uptake of IONPs by human granulocytes/monocytes, *in vitro*. Whole PBMCs were incubated with no, 200 µg/ml and 100 µg/ml of FITC tagged IONPs (**Figure A, Figure B**) and R-PE tagged IONPs (**Figure C, Figure D**), separately, for 24 hours and fluorescence was determined by flow cytometry, n=5. Granulocytes/monocytes were identified using a staining technique with flow cytometery and % uptake and fold increase in mean fluorescence intensity were determined for all experimental conditions. One-way ANOVA with the Tukey's multiple comparison test (comparing each treated condition with other treated conditions) and the Dunnett's text comparing the control mean with the treatment condition means was used to statistically analyse the data. Where no asterisks are displayed, no statistical significance was found.

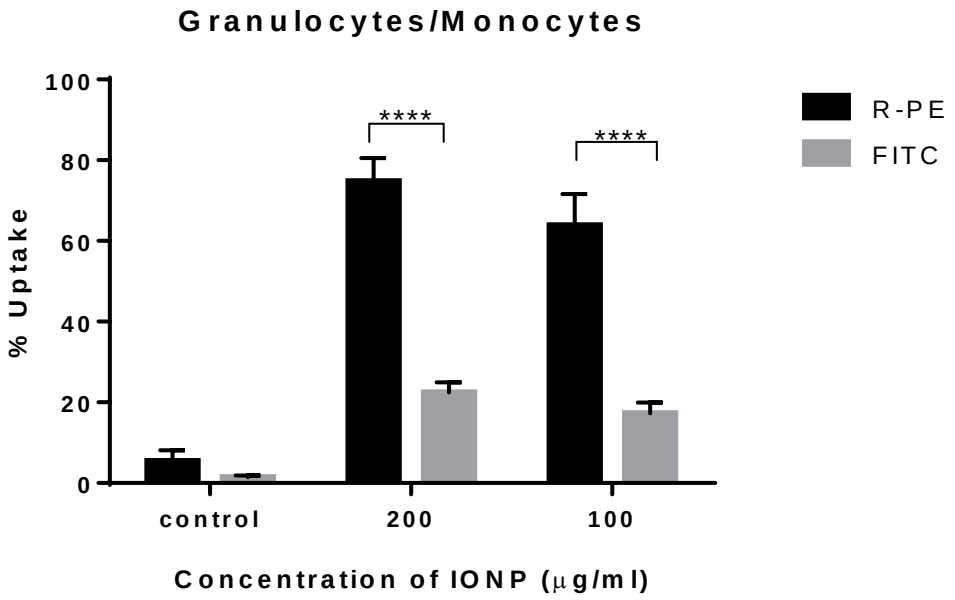

Figure 5.15: Comparison of dose dependent uptake of IONPs by human granulocytes/monocytes with, *in vitro*. Dose dependent uptake studies were performed with whole PBMCs and human granulocytes/monocytes were identified and assessed with flow cytometry following 24 hours incubation with varying concentrations of IONPs, n=5. Two-way ANOVA was used to statistically analyse the data with the Tukey's multiple comparison test. Where no asterisks are displayed, no statistical significance was found.

5.2.5 Human cytokine analysis of supernatants from dose dependent and time dependent studies with PBMC and FITC tagged IONPs, *in vitro*

To determine and identify if FITC tagged IONPs trigger an inflammatory response in PBMCs, in vitro, the supernatant from dose dependent and time dependent studies were tested with a Cytometric Bead Array kit that could test six cytokines commonly involved in an inflammatory and immune response.

With the supernatant from the dose dependent studies; in Figures 5.17B to F inclusive, there was no statistical difference between the treated conditions and the control condition; and also no statistical difference between the treated conditions themselves except for Figure 5.17B (cytokine TNF), where there was a significant statistical difference between the 200 µg/ml and 5 µg/ml treatment groups. Figure 5.15 demonstrated that the secretion of the IL-12p70 cytokine is almost dose dependent, under the conditions tested; thus, the cytokine release of IL-12p70 increased with increased concentration of IONPs.

With the supernatant from the dose dependent studies; Figures 5.18B to F inclusive revealed that there was no statistical difference between the treated conditions and the control conditions; and also no statistical difference between the treated conditions themselves except for Figure 5.17E (cytokine IL-1β), where a significant statistical difference between the treatment groups at 6 hours and 1 hour was identified.

Figure 5.18A (cytokine IL-12p70) identified a significant statistical difference between the control mean and the 24 hours incubation mean; the control mean and the 4 hours incubation mean; and the control mean and the 1 hour incubation time mean. There was very significant statistical difference between the control mean and the 18 hours incubation time mean as well

as the control mean and the 6 hour time point mean. There was no statistical significance between the treatment groups at any of the time points tested, implying that the secretion level of cytokine IL-12p70 was the same from 1 hour to 24 hour incubation times. The level of IL-12p70 release was greater than the level secreted by the same cell types under control conditions.

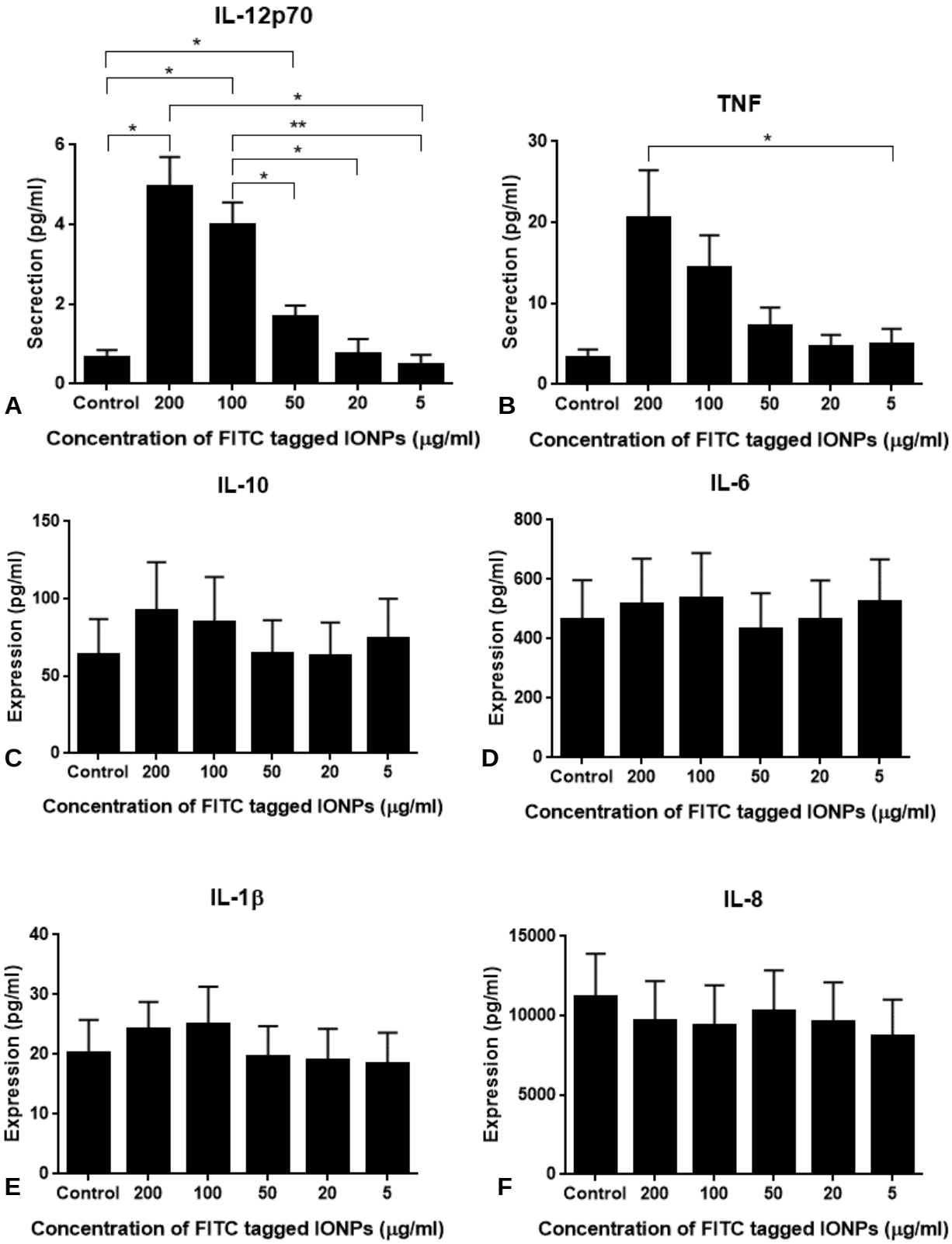

Figure 5.16: Cytokine secretion by human PBMCs after incubation with FITC tagged IONPs, from dose dependent experiments, *in vitro*. Human PBMCs were incubated with varying concentrations of FITC tagged IONPs for 24 hours, *in vitro,* and supernatants were collected for cytokine analysis by flow cytometry using cytometric bead analysis, n=3. One-way ANOVA was used to statistically analyse the data with the Tukey's multiple comparison test comparing treatment groups with each other and the Dunnett's test was used to compare the control group with the treatment groups. Where no asterisks are displayed, no statistical significance was found.

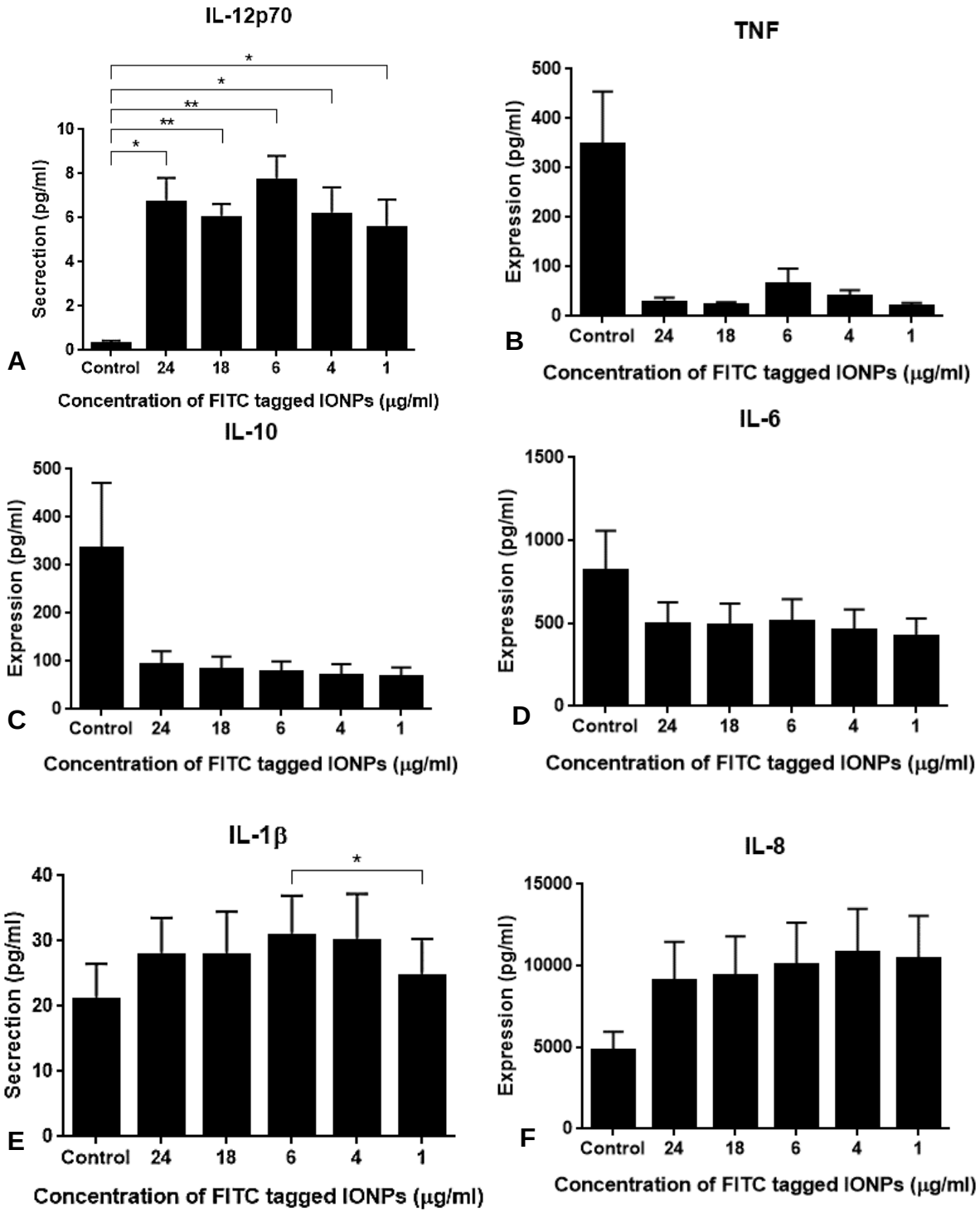

Figure 5.17: Cytokine secretion by human PBMCs after incubation with FITC tagged IONPs, from time dependent uptake experiments, *in vitro*. Human PBMCs were incubated with 200 μg/ml of FITC tagged IONPs at various time points, *in vitro*, and supernatants were collected for cytokine analysis by flow cytometry using cytometric bead analysis, n=3. One-way ANOVA was used to statistically analyse the data with the Tukey's multiple comparison test comparing treatment groups with each other and the Dunnett's test was used to compare the control group with the treatment groups. Where no asterisks are displayed, no statistical significance was found.

5.3 Discussion

Cellular imaging can be defined as the visualisation of specific cells in a living organism. Delivery of biodegradable IONP to APCs, especially DCs, has potential for immunotherapy. For cellular therapies to be successful, specific cells would need to be delivered to their intended destination. Uniquely; a cell therapy approach to stimulating an immune response would require DCs migrate to the regional lymph nodes of interest. Extending from this, researchers have used MRI to image the migration path of magnetically labelled DCs, in humans. Not only can MRI detect the magnetically labelled DCs, image their migration path, but also demonstrate all this in relation to a patient's own anatomy in multiple imaging planes. In one study[276], autologous DCs were labelled with a clinically available superparamagnetic iron oxide formulation or the radio-active tracer ^{111}In-oxine and were co-injected into the lymph nodes using ultrasound imaging guidance in melanoma patients. MRI demonstrated superior assessment of the DC migration path (inter- and intra-nodal cell migration patterns) compared with scintigraphy. MRI cell tracking using iron oxides appears safe and well suited to monitor cellular therapy in humans. Such an approach takes advantage of the high phagocytic capabilities of immature dendritic cells. Thus, immature DCs have been used by cell therapy researchers together with FDA approved nanoparticle preparations and the labelling occurred with high efficiency without compromising iDC function.

Figure 5.2 presented results showing the percentage of cells that internalised R-PE tagged IONPs, as quantitated with flow cytometry, by cells that were CD14+ (Figure 5.2A) and cells that were CD11c+ (Figure 5.2C). In relation to the literature, it is noted that human DCs and monocytes (capable of differentiating into DCs) are known to be CD14+ and human myeloid dendritic cells are CD11c+, but also, approximately, 90 % of monocytes circulating in the bloodstream are CD11c+[277]. Human myeloid DCs are negative for CD14 and their

proportion in circulating human blood has been recorded to be approximately 5 % of the PBMC population; and that the majority of circulating monocytes (CD14+) also demonstrate higher levels of phagocytosis but lower cytokine secretion[257]. Statistical analysis of Figure 5.2A identified no statistical significance (ns, $P \geq 0.05$) between treatment conditions and extremely significant (*** P = 0.0001 to 0.001 and **** $P < 0.001$) statistical difference between the control condition and any of the treatment conditions. These imply that CD14+ monocytes have the capability to internalise the varying concentrations of R-PE tagged IONPs as tested, *in vitro*, equally well. Also, the level or quantity of R-PE tagged IONPs internalised by these same CD14+ monocytes in the treatment groups was, compared to the control CD14+ monocytes, extremely significant; thus confirming their high level of phagocytic activity, consistent with the available literature[275]. Results of dose dependent experiments with CD11c+ DCs and R-PE tagged IONPs following 24 hours incubation was presented in Figure 5.2C and statistically analysed. There was statistical significance (*, P = 0.01 to 0.05) between the CD11c+ DCs incubated with 200 µg/ml of R-PE tagged IONPs and 20 µg/ml and also with 5 µg/ml concentrations. There was also statistical significance (*, P = 0.01 to 0.05) between the CD11c+ DCs incubated with 100 µg/ml of R-PE tagged IONPs and 5 µg/ml concentration. Figure 5.3 compares the percentage dose dependant uptake of cells that are CD14+ and CD11c+, side by side, and there is no statistical significance between the CD14+ monocytes and CD11c+ myeloid DCs at each corresponding concentration of R-PE tagged IONP as well as under control conditions, demonstrating that both are equally capable of internalising the tested nanoparticles under the experimental conditions tested.

The same experimented was repeated with FITC tagged IONPs and results presented in Figures 5.4 and 5.5. Figure 5.4C demonstrated a classic dose dependent uptake effect with significant statistical significance between adjacent treatment conditions (except for between 50 µg/ml and 20 µg/ml). Significant statistical (*, P = 0.01 to 0.05) difference was recorded between CD11c+ myeloid DCs under control condition compared to both the 20 µg/ml and 50

µg/ml treatment conditions and a very significant (**, P = 0.001 to 0.01) statistical significance was noted between CD11c+ cells in the control state and CD11c+ cells incubated with 100 µg/ml of FITC tagged IONP and also control conditions and 200 µg/ml concentration. Results provided in Figure 5.5 demonstrate that all CD14+ cells were healthy, viable and highly effective at internalising the FITC tagged IONP (compared to the CD11c+ cells) and thus, consistent with published literature[275].

Time dependent uptake experiments were also performed with human CD14+ monocytes and human CD11c+ dendritic cells, together with FITC tagged IONPs, and results presented in Figure 5.6. Of the time points tested, together with statistical analysis, maximum uptake of FITC tagged IONP occurred by the one hour incubation time point for both CD14+ monocytes and CD11c+ DCs. Therefore, statistically, there was no additional advantage gained in extending the incubation time to 24 hours; for each cell type. Figure 5.7 compared the time dependent uptake of both cell types. It was noted here that there was no statistical significance between the control conditions, 24 hour and 18 hour time points. There was, however, a significant (*, P = 0.01 to 0.05) statistical difference between the CD14+ monocytes and the CD11c+ DCs at the 6 hour time point and also at 4 hours incubation time. The greatest statistical significance (***, P = 0.0001 to 0.001) between these two cell types occurred at the one hour time point, thus indicating that CD14+ monocytes can perform phagocytosis of the tested nanoparticles more efficiently compared to CD11c+ DCs over the first 6 hours of incubation, with the greatest efficiency being demonstrated at the tested one hour time point; meaning thatCD11c+ cells required at least 6 hours incubation time to achieve maximum nanoparticle uptake equivalent to CD14+ cells.

Human peripheral blood contains CD123+ lymphoid DCs and these are also considered to be CD11c-[247]. CD11c+ DCs are not only present in human blood, but myeloid CD11c+ DCs can also be found in peripheral lymphoid tissue and germinal centres[260]. Such differences in

DC phenotype and their localisation in lymphoid organs had led researchers to suggest that distinct and different functional activities for CD123+ and CD11c+ DCs[198, 278].

Figure 5.8 presented results showing the percentage of cells that internalised R-PE tagged IONPs in dose dependent experiments, as quantitated with flow cytometry, by cells that were CD123+ (Figure 5.8A) and cells that were CD11c+ (Figure 5.8C). The two highest concentrations of IONPs previously used in dose uptake studies were tested, 200 µg/ml and 100 µg/ml. With Figure 5.8A, statistical assessment revealed no statistical significance in uptake between these two concentrations of R-PE tagged IONPs for CD123+ lymphoid DCs. There was significant (*, P = 0.01 to 0.05) statistical significance between the CD123+ cells in the control condition and those that internalised nanoparticles in the 200 µg/ml concentration treatment. There was no statistical significance between CD123+ cells in the control group and those incubated with 100 µg/ml. Statistical evaluation of Figure 5.8C, myeloid CD11c+ cells, showed significance (*, P = 0.01 to 0.05) statistical difference in the uptake of R-PE tagged IONPs cells incubated with 200 µg/ml and 100 µg/ml of nanoparticles. There was also significant (*, P = 0.01 to 0.05) statistical significance between the CD11c+ cells in the control condition and those that internalised nanoparticles in both the 200 µg/ml and 100 µg/ml concentration treatments. Figure 5.9 compared the percentage up of nanoparticles by both CD123+ and CD11c+ alongside each other at each treatment condition as well as under control conditions. Statistical analysis demonstrated no statistical difference between CD123+ and CD11c+ cells under these tested conditions.

Apart from DCs, other cells that have variable roles in immune responses and processes were assessed with both FITC tagged IONPs and R-PE tagged IONPs and results presented in Figures 5.10 to 5.15 inclusive. The cells experimented with were PBMCs, Lymphocytes and Granulocytes/Monocytes. With PBMCs, statistical evaluation of the treatment conditions in Figures 5.10A and 5.10C resulted in no significant (ns, $P \geq 0.05$) difference when dose

depended studies were conducted with either FITC tagged IONPs or R-PE tagged IONPs. When the PBMCs in the control condition are statistically compared with those incubated with nanoparticles for 24 hours, it is found that there was a very significant (**, P = 0.001 to 0.01) statistical difference between PBMC control cells and those treated with FITC tagged IONPs and there was an extremely significant (***, P = 0.0001 to 0.001) statistical difference between control PBMCs and those treated with R-PE tagged IONPs. When both of these projects were compared alongside each other, Figure 5.11, it was found that there were no statistical significance between how PBMCs behaved when incubated with either FITC tagged IONPs or R-PE tagged IONPs.

Results of dose dependent uptake studies with lymphocytes were presented in 5.12 and 5.13. Statistical evaluation of the treatment conditions in Figures 5.12A and 5.12C resulted in no significant (ns) difference when dose depended studies were conducted with either FITC tagged IONPs or R-PE tagged IONPs. When the lymphocytes in the control condition are statistically compared with those incubated with nanoparticles for 24 hours, it was discovered that there was a very significant (**, P = 0.001 to 0.01) statistical difference (100 µg/ml) and extremely significant (***, P = 0.0001 to 0.001) statistical difference (200 µg/ml) between lymphocyte control cells and those incubated with FITC tagged IONPs. When the same dose dependent experiments were performed with R-PE tagged IONPs, there was a significant (***, P = 0.0001 to 0.001, with 100 µg/ml) and very significant (****, P < 0.05, with 200µg/ml) statistical difference between control lymphocytes and those treated with R-PE tagged IONPs. When both of these experimental processes were compared alongside each other, Figure 5.13, it was found that there were no statistical significance between how lymphocytes behaved when incubated with either FITC tagged IONPs or R-PE tagged IONPs.

Results of dose dependent uptake studies with granulocytes/monocytes were presented in 5.14 and 5.15. Statistical evaluation of the treatment conditions in Figures 5.14A and 5.14C

resulted in no significant (ns, $P \geq 0.05$) difference when dose depended studies conducted with either FITC tagged IONPs or R-PE tagged IONPs. When the granulocytes/monocytes in the control condition are statistically compared with those incubated with nanoparticles for 24 hours, was extremely significant (****, $P < 0.0001$) statistical difference between granulocytes/monocytes under control conditions and those incubated with FITC tagged IONPs. The statistical response occurred with control granulocytes/monocytes and those treated with R-PE tagged IONPs, (****, $P < 0.0001$, with both 100 µg/ml and 200µg/ml). When both of these experimental processes were compared alongside each other, Figure 5.15, it was found that there was extremely significant (****, $P < 0.0001$) statistical significance between how granulocytes/monocytes behaved when incubated with either FITC tagged IONPs or R-PE tagged IONPs.

A proprietary CBA Human Inflammatory Cytokine Kit was used to analyse the supernatant of *in vitro* dose dependent (Figure 5.16) and time dependent (Figure 5.17) studies with human immune cells and IONPs. Statistical analysis demonstrates that for the cytokines graphed in Figures 5.18B to F inclusive, there was no statistical difference between the treated conditions and the control condition and there was also no statistical difference between the treated conditions themselves except for Figure 5.16B (cytokine TNF), where there was a significant (*, $P = 0.01$ to 0.05) statistical difference between the 200 µg/ml and 5 µg/ml treatment groups. With the graph presented in Figure 5.16A (cytokine IL-12p70), there was significant (*, $P = 0.01$ to 0.05) statistical difference between 200 µg/ml and 5 µg/ml, 100 µg/ml and 50 µg/ml, and 100 µg/ml and 20 µg/ml; and very significant (**, $P = 0.001$ to 0.01) statistical difference between 100 µg/ml and 5 µg/ml treatment groups. When the control mean was compared to the mean of the treatment groups, it was found that there was significant (*, $P = 0.01$ to 0.05) statistical difference between control and 200 µg/ml and control and 50 µg/ml treatment means; there was very significant (**, $P = 0.001$ to 0.01) statistical difference between control and 100 µg/ml treatment mean. Figure 5.16 thus demonstrates that the

secretion of the IL-12p70 cytokine is almost dose dependent, under the conditions tested; thus, the cytokine release of IL-12p70 increased with increased concentration of IONPs.

Statistical analysis was also performed for the graphs presented in Figure 5.17, analysis of cytokine production from *in vitro* time dependent studies. Statistical analysis of Figures 5.17B to F inclusive revealed that there was no statistical difference between the treated conditions and the control conditions and there was also not statistical difference between the treated conditions themselves except for Figure 5.17E (cytokine IL-1β), where there was a significant (*, P = 0.01 to 0.05) statistical difference between the treatment groups at 6 hours and 1 hour. Statistical analysis of Figure 5.17A (cytokine IL-12p70) identified that there was significant (*, P = 0.01 to 0.05) statistical difference between the control mean and the 24 hours incubation mean, the control mean and the 4 hours incubation mean and also the control mean and the 1 hour incubation time mean. There was very significant (**, P = 0.001 to 0.01) statistical difference between the control mean and the 18 hours incubation time mean as well as the control mean and the 6 hour time point mean. There was no statistical significance (ns, $P \geq 0.05$) between the treatment groups at any of the time points tested, implying that the secretion level of cytokine IL-12p70 was the same from 1 hour to 24 hour incubation times. The level of IL-12p70 secretion was greater than the level secreted by the same cell types under control conditions.

5.4 Conclusion

The aims of this chapter have been addressed and the experimental results lead to the following conclusions:

1. CD14+ and CD11c+ cells were able to be identified and their dose dependent uptake of R-PE tagged IONPs showed no statistical difference, following 24 hours incubation, *in vitro*, for the concentration of IONPs tested; thus both CD14+ and CD11c+ cells are both equally capable of internalising the tested nanoparticles under the presented experimental conditions.

2. CD14+ and CD11c+ cells were able to be identified and their dose dependent uptake of FITC tagged IONPs showed no statistical difference (ns, $P \geq 0.05$), following 24 hours incubation, *in vitro*, for the concentration of IONPs tested; thus both CD14+ and CD11c+ cells are both equally capable of internalising the tested nanoparticles under the presented experimental conditions. The time dependent *in vitro* studies demonstrated that maximum uptake of FITC tagged IONP occurred by the one hour incubation time point for both CD14+ and CD11c+ cells. Therefore, statistically, there was no additional advantage gained in extending the incubation time to 24 hours; for each cell type

3. CD11c+ and CD123+ cells were identified with the multi-coloured flow cytometry assay. There was no statistical difference (ns, $P \geq 0.05$) between the uptake demonstrated by CD11c+ and CD123+ cells for the concentrations of IONPs tested under the experimental conditions presented.

4. The use of FITC tagged IONPs and R-PE tagged IONPs were used to identify PBMCs, lymphocytes, and granulocytes/monocytes. PBMCs demonstrated no statistical difference (ns, $P \geq 0.05$) in the uptake of either FITC tagged IONPs or R-PE tagged IONPs; at the concentrations tested and experimental conditions presented, *in vitro*. Lymphocytes

demonstrated no statistical difference (ns, $P \geq 0.05$) in the uptake of either FITC tagged IONPs or R-PE tagged IONPs; at the concentrations tested and experimental conditions presented, *in vitro*. Granulocytes/monocytes demonstrated extremely significant (****, $P < 0.0001$) statistical difference in the uptake of R-PE tagged IONPs compared with FITC tagged IONPs; at the concentrations tested and experimental conditions presented, *in vitro;* the uptake of R-PE tagged IONPs was greater than the uptake of FITC tagged IONPs.

5. Assessment of the supernatant from dose effect studies identified that five (TNF, IL-10, IL-6, IL-1β, IL-8) of the six cytokines were secreted at levels statistically equivalent to the control condition. The release of the IL-12p70 cytokine is almost dose dependent, under the conditions tested; thus, the cytokine secretion of IL-12p70 increased with increased concentration of IONPs. Assessment of the supernatant from time dependent studies identified that secretion of five (TNF, IL-10, IL-6, IL-1β, IL-8) of the six cytokines were secreted at levels statistically equivalent to the control condition. The level of IL-12p70 secretion was greater than the level released by the same cell types under control conditions. The secretion level of cytokine IL-12p70 was the same from 1 hour to 24 hour incubation times with no statistical difference (ns, $P \geq 0.05$) between the incubation times tested across the 24 hours.

6.0 Chapter 6 – Application of Iron Oxide Nanoparticles *In Vivo*

6.1 Introduction

As first discussed in Section 1.6, lymphoscintigraphy with gamma emitting radio-active nano-colloids, together with blue vital dye; are the current clinical approaches used to identify the SLN and other draining lymph nodes[279]. This is then followed by surgery where the lymph nodes are exposed and a hand held gamma probe is used to identify those emitting gamma radiation. Once these lymph nodes are excised, they are treated to histopathological evaluation and based on such findings, any metastasis is staged and the corresponding treatment options considered accordingly. CT also offers a role in imaging lymph nodes and staging of cancer; by way of a series of acquisitions; firstly without iodinated intravenous contrast media and then with iodinated contrast media (arterial and venous phase aquisitions). On CT images, the overall size and shape of lymph nodes are noted and any changes from normal (from less than 1 cm diameter and oval shaped to greater than 1 cm diameter and circular shaped in cross-section) are related to metastatic spread and staging. The three major concerns regarding CT imaging of lymph nodes are that CT imaging cannot identify the SLN itself; it is unable to detect occult metastatic lymph nodes and it is unable to offer any imaging detail about the flow of lymph fluid[160].

^{99m}Tc, a nano-sized radio-colloid, was first introduced clinically in the 1960's for Nuclear Medicine imaging[280]. Since then, a variety of radio-tracers have been introduced for investigating functional organ processes and pathologies. Imaging molecular interaction with PET is considered to be the most sensitive and specific method available, *in vivo*, for humans[160]. ^{18}F-FDG is the most commonly used PET radio-tracer and has been successfully

used to identify the increased glycolytic consumption of cancer cells (compared to normal healthy cells)[281]. To date, the clinical application of this potential approach, to identify metastatic cells in lymph nodes, has not been realised. One drawback of using ^{18}F-FDG is that it is not a selective radio-tracer as other cells and organs in the body demonstrate active glucose uptake rather than just tumour cells[282]; such as the heart, brain, kidney and urinary bladder. Another limitation of ^{18}F-FDG and PET is the limited spatial resolution of PET images themselves; that is, ^{18}F-FDG will not be able to demonstrate lesions that are less than the dimension of the PET images' spatial resolution[282] which is in the order of 2.3mm[283] and is inferior to CT and MRI[284]. There is a need therefore, to improve upon such existing techniques. Iron oxide nanoparticles, together with MRI, can overcome the current limitations to lymph node imaging with CT, SPECT and of spatial resolution inherent to PET imaging. Iron oxide nanoparticles offer opportunities for creative solutions and flexibility for imaging lymph nodes. They can be superparamagnetic, meaning that a low concentration can be used to generate obvious signal changes on MRI images. They can be administered intravenously and also by conventional interstitial (subcutaneous or intradermal) means; to reach the lymph nodes. Furthermore, they have a safety profile that allows them to be loaded into immune cells that are known to migrate to lymph nodes. MRI also offers the added benefit of greater spatial and contrast resolution than CT and further still, MRI does not operate with ionising radiation. ^{68}Ga is a positron emitter with a higher energy value than ^{18}F, thus providing greater contrast resolution on PET imaging[285]. By having a shorter half-life than ^{67}Ga, ^{68}Ga offers the advantages of a quicker uptake time leading to better defined biodistribution[286]. The dosimetric advantage of ^{68}Ga also allows easier patient management; as upon completion of imaging, there is very little ionising radiation remaining – allowing immediate patient discharge and also public safety. The physical dimensions of iron oxide nanoparticles used in this thesis and commercially available isosulfan blue (vital blue dye

used in conjunction with lymphoscintigraphy) are both 20 nm, while ^{99m}Tc labelled sulphur colloid is approximately 220 nm [287].

Intravenous administration of iron oxide nanoparticles can migrate to lymph nodes; by moving through the vascular wall, into the interstitial environment where they are internalised by macrophages and then these macrophages pass through the lymph vessel walls; where they then migrate to the lymph node. As early as 2000, Moore *et al*, investigated dextran coated iron oxide nanoparticles for use in a gliosarcoma rodent model (four rats) and tabulated that 25 % of the iron content of intravenously administered dose was to be found in lymph nodes; compared to 0.11 % accumulation into the brain tumour they were investigating[288]. The 0.11 % (equating to 0.26 µg of iron relative to the injected dose) was sufficient to be detected on MRI with 1.5 T. All imaging was performed 24 hours after administration. They also successfully radio-labelled these particles with Iodine-125 (^{125}I), however, this radio-isotope is a relatively low energy gamma emitter with a half-life of 59 days. Bumb *et al*, demonstrated that a foot pad injection into nude mice using silica coated iron oxide nanoparticles, the draining lymph nodes could be successfully imaged with MRI and also with optical imaging[289]. At post mortem, microscope evaluation of H&E and Prussian blue iron stains confirmed that the particles migrated passively to the draining lymph nodes without macrophage uptake.

The successful migration of nanoparticles to lymph nodes has also been proven to be size-dependent. Zubris *et al*, assessed polymeric nanoparticles ranging from 50 nm to 120 nm in diameter by subcutaneous injection into the breast of Yorkshire pigs[290]. Images were taken 24 hours later with a Near Infra-Red (NIR) imaging system and 50 nm sized nanoparticles were observed as being capable of migrating over a distance of 20 cm from their injection site (breast) to the corresponding sentinel lymph node. This was also confirmed with surgical excision of sentinel lymph node, its histological analysis and accompanying microscopy

imaging. All other larger sized nanoparticles did not demonstrate migration capabilities to the corresponding sentinel lymph node. Zhou *et al* demonstrated that even smaller particles; 10 nm core sized iron oxide nanoparticles and 24 nm overall hydrodynamic size when conjugated with NIR830 dye; in female nude mice via a foot pad injection were capable of migrating to the draining lymph nodes[291]. The MRI (3.0 T) and NIR image findings were also confirmed with vital blue dye staining. Tseng *et al* used lipid-calcium phosphate nanoparticles of two dimensions, 25 nm and 67 nm; both radio-labelled with ^{111}In and injected into the tail vein of both C57BL/6 and nude mice[292]. SPECT/CT imaging was performed at 2 hours, 4 hours and 24 hours post tail vein injection. Their results also showed a sized dependent effect; the 25 nm sized particles performed better than the 67 nm particles. The 25 nm particles convincingly entered the lymphatic system and congregated within lymph nodes. Not only did Tseng *et al* attribute this success to the physical size of the particles, but also their slightly negative surface charge of -20 mV of the PEGlygated lipid coating; which allowed long blood circulating times and deep tissue penetration to accumulate in lymph nodes. Tseng *et al* also stated that the negative charge allowed the particles to travel as individual particles and not agglomerate. At the 2 hour and 4 hour time point, there was some activity noted in the liver and spleen (indicating uptake by the RES), however, the majority of radio-activity was found to be in the heart and the adjoining major blood vessels indicating that the radio-labelled nanoparticles were still in circulation at those time points. At 24 hours, radio-activity was noted to accumulate in the lymph nodes throughout the mice in a symmetrical arrangement; demonstrating even biodistribution, *in vivo*.

The possibility of iron oxide nanoparticles inducing adverse effects on mice, *in vivo*, need to be established. In general, iron oxide nanoparticles have a very good safety profile, *in vivo*, with patients. FDA approved preparations are available. Any immediate adverse effects on mice can be ascertained with biochemistry analysis of their blood serum. Blood serum biochemical analytes have been found to vary according to gender and age, even within the

same mouse strain and between three different mice strains. Mazzaccara *et al* performed biochemical serum analysis on three readily available mice strains, including C57BL/6[293]. Blood was extracted via the retro-orbital sinus under anaesthesia from the same mice at 1 to 2 months, then at 3 to 8 months and finally at 9 to 12 months. Male and female mice were used; 15 of each gender. The mice used for biochemical serum analysis in this thesis were 8 weeks (2 months) old and the blood sample was also retrieved from the retro-orbital sinus; therefore the majority of the findings of Mazzaccara *et al* can be used as a comparison. Further still, the same blood serum analyte has been found to provide different values based upon the blood collection method; as published by Schnell *et al* with an age and gender matched study and using the following blood collection methods; retro-orbital sinus, cardiac puncture, inferior vena cava and the tail vein[294].

Histology assessment must also be performed for two very important reasons; but also, it must be kept in mind that biochemical evaluations can vary considerably. Firstly, if any changes seen in murine biochemistry are genuine, they can be linked to structural or physical changes in the corresponding tissue. Secondly, histology assessment is performed to identify if cellular integrity is maintain or adversely affected. Generalised structural changes in cell architecture are identified with a H&E stain; a Perl stain is used to identify iron content in cells (that can presumably be attributed to the iron from the nanoparticles based on size) and a PAS reaction stain can be performed to specifically observe the basement membrane of kidney tissue samples (as this is the first structure to visually fail and demonstrate signs of structural demise)[295].

Iron oxide nanoparticles have been given consideration as MRI contrast agents since the mid 1980's[22]. The first publication documenting use of iron oxide nanoparticles in a clinical trial to image lymph nodes in humans, dates to 2003[165]. Eighty male patients (40 in the USA and 40 in The Netherlands) with diagnosed prostate cancer and undergoing surgical resection of

the prostate gland and/or pelvic lymph nodes; were administered (by intravenous drip infusion over a 20 to 30 minute time frame) with 2.6 mg of iron (from iron oxide nanoparticles) per kg of body mass. MRI at 1.5T was performed prior to nanoparticle administration and again 24 hours post administration. All MRI images were correlated with H&E histology assessment of surgically resected lymph nodes. The MRI images, taken in isolation, demonstrate conclusively that healthy and diseased lymph nodes can be differentiated from one another with the addition of iron oxide nanoparticles. Overall, the proposed technique/method, has some practical challenges that may limit its implementation as a routine clinical procedure and may not be entirely robust. These include scanning the patient pre and post nanoparticle administration and any associated difficulty in ensuring that both sets of images are equivalent or comparable or the patient can be positioned identically. Also, 24 hours may not be sufficient in some patients to have the nanoparticles reach all the relevant lymph nodes; as some authors report the need to scan at 36 hours post administration[296]. Importantly, if a number of lymph nodes demonstrate signal intensity for metastases, then this method cannot identify the actual sentinel lymph node. This published methodology relies on iron oxide nanoparticles permeating from the blood vessels into the interstitium and macrophages ingesting them and then the macrophages entering afferent lymphatic vessels leading to lymph nodes.

Iron oxide nanoparticles have also been used without MRI to successfully identify lymph nodes. Winter *et al* has recently published their results of a prospective pilot study where iron oxide nanoparticles were used, without MRI, to identify draining lymph nodes from the prostate[297]. In their study, 20 patients with prostate cancer scheduled for open radical retro-pubic prostatectomy with pelvic lymph node dissection were injected with 2 ml of iron oxide nanoparticles (concentration not reported) directly into the prostate; 20 hours (average) before surgery. At surgery, a hand held magnetometer (by SentiMag®, CE certified as a Class IIa medical device) was used to identify lymph nodes containing iron oxide nanoparticles,

Sienna+® (60 nm in diameter). The Sienna+® nanoparticles, together with the SentiMag® magnetometer, were used analogous to ^{99m}Tc nanoscale radio-colloid and hand held gamma ray detector. The imaging aspect has been removed (with gamma emitting ^{99m}Tc radio-colloid there is lymphoscintigraphy SPECT imaging performed); no MRI was performed with the Sienna+® particles. Upon surgical excision of lymph nodes (containing Sienna+® particles and detected with the SentiMag® magnetometer), histology confirmation was conducted with H&E and Perl's Prussian blue staining. The most important feature offered by this methodology is that that no ionising radiation at all is incorporated which is of benefit to patients and life-long health care professionals. The major negative here is the 20 hour time frame from injection to detection at surgery, which is significantly greater than current clinically available techniques. No further testing was reported if a shorter duration was viable while attaining similar results; as currently nano-sized radio-colloids migrate from injection site to the draining lymph node in approximately one hour.

Ravizzini *et al* also correctly identify the limitations of current clinical practice of combining nano-sized radio-colloid with vital isosulfan blue dye; and offer the possibility of gadolinium labelled nanoparticles as an alternative to overcome the known limitations with established techniques[287]. The nanoparticle is in effect a carrier of the gadolinium agent. The possibility offered by gadolinium-labelled nanoparticles, following interstitial injection, is that we have known MRI imaging pulse sequences that can be readily used with gadolinium and we have an established understanding of the image appearance of gadolinium. Also, there is no ionising radiation with MRI. The nanoparticles presented in Ravizzini *et al* were also coated with materials such as Cy5.5 to allow for Near Infra-Red (NIR) optical imaging of the lymph nodes. This approach also offers functional capabilities so that the sentinel lymph node can be recognised. The major downfall of this technique, as also recognised by the authors themselves, Ravizzini *et al*, is the possibility of gadolinium disassociating from the nanoparticle. The strength of the chemical bond between the gadolinium and the nanoparticle

may well be the key to the success of this technique. The authors also remind us that NSF is an interstitial fibrosis disease (and the gadolinium nanoparticles are injected interstitially).

In 2008, Heesakkers *et al,* offered the results of a multi-centre study of 375 consecutive patients (over a two year period) with prostate cancer where patients were imaged with iron oxide nanoparticles and MRI and these imaging findings were compared to multi-detector CT (MDCT)[298]. Patients enrolled in the study had been diagnosed with prostate cancer by tissue biopsy and were scheduled for pelvic lymph node dissection. MDCT was performed with oral contrast media and iodinated intravenous contrast media. MRI imaging was performed 24 to 36 hours following drip infusion of the iron oxide nanoparticle, Sinerem®. Their findings included that MRI imaging of lymph nodes resulted in higher sensitivity than MDCT for detecting lymph node metastases and that their post-test data analysis determined that the probability of prostate cancer lymph node metastases not appearing on MRI was low enough to omit pelvic lymph node dissection, thereby removing the need for surgery and associated mortality and morbidity risks.

To the knowledge of this PhD candidate, there are currently no publications of a possible PET/MRI contrast agent specifically used to diagnose the draining lymph nodes from the prostate gland in human patients. There have been such experiments performed in mice that have been published. The possibility of a PET/MRI contrast agent, that is, an iron oxide nanoparticle radoio-labelled with a positron emitting radio-nuclide, used for identifying draining lymph nodes from prostate gland, offers the potential to overcome limitations of current techniques (nano-sized radio-colloid with blue dye) and proposed techniques (of just magnetic nanoparticles; waiting between 20 to 36 hours). IONP radiolabeled with a positron emitter and injected directly interstitially, can allow for MRI imaging with greater image quality and non-ionising radiation compared to CT, detection by PET in approximately 1 hour post administration.

The specific aims of this chapter were to:

1. Inject iron oxide nanoparticles (coated with dextran and tagged with FITC) into the hock and flank of C57BL/6 mice and evaluate if they drained to the popliteal and inguinal lymph nodes, respectively, and quantitate this with flow cytometry.
2. Perform biochemistry assessment on the blood serum of mice undergoing step 1 above.
3. Remove organs (heart, lung, liver, kidney and spleen) of mice in experimental process in step 1 above and perform H&E, Perl's Prussian Blue and PAS to correspond with any biochemical findings.
4. Image mouse separately with PET and then with MRI, after being injected with iron oxide nanoparticles (coated with dextran and tagged with FITC) and radio-labelled with ^{68}Ga following footpad injection; then removed radio-active positive lymph node and perform uptake study on flow cytometry.
5. Remove lymph node positive for radio-activity (in step 4 above) and prepare for confocal microscopy.
6. Inject iron oxide nanoparticles (coated with dextran and radio-labelled with ^{68}Ga) into human patients and perform PET imaging (PET/CT) to observe migration from prostate gland to draining lymph nodes.

6.2 Results

6.2.1 Subcutaneous injection of T10 dextran coated IONPs tagged with FITC and quantitation with flow cytometry.

A total of ten mice, each received subcutaneous injection of 200 µl of dextran coated iron oxide nanoparticles tagged with FITC, at a concentration of 100 µg/ml, into their hocks. A hock injection is a humane method (alternative to foot pad) to ascertain if these specially prepared nanoparticles had the capability to migrate to the popliteal lymph node. These same mice also received the same volume and concentration of the same nanoparticles injected subcutaneously at their flanks, to ascertain drainage to the inguinal lymph node. One hour post injection, all mice were killed under anaesthesia when performing the vascular perfusion fixation technique. Please refer to Chapter 2, Materials and Methods, Sections 2.7 and 2.12.

A further 10 mice received the same volume and concentration of nanoparticles, injected at the same sites. Methodology followed was as described for the one hour time point, however, these ten mice, were killed under vascular perfusion fixation at 24 hours post injection.

At post mortem, the popliteal and inguinal lymph nodes were excised and prepared for flow cytometry as described in Section 2.12.4.

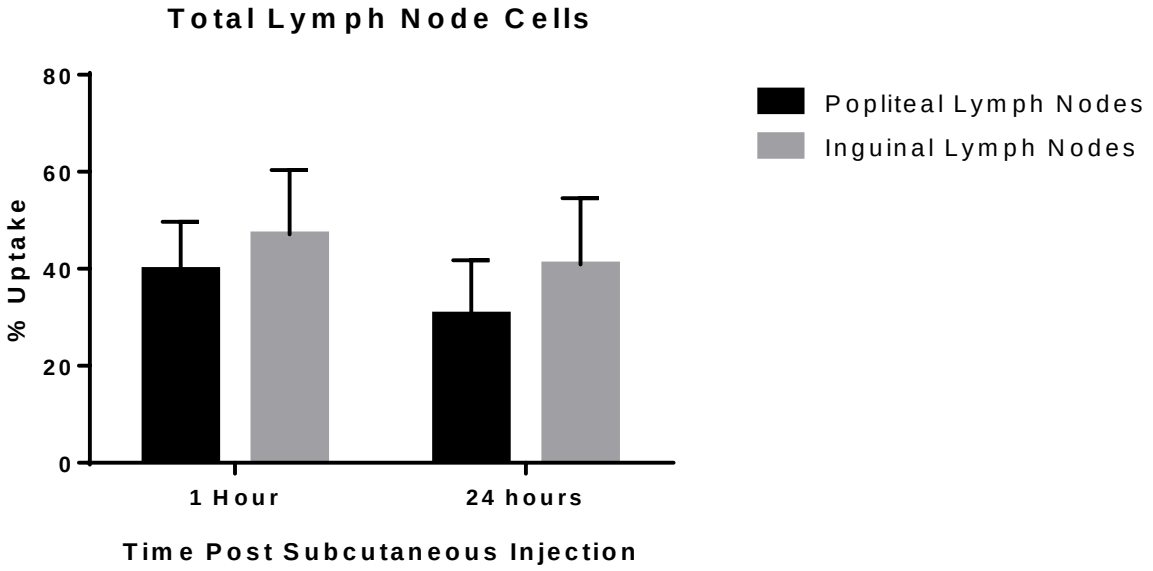

Figure 6.1: Uptake of FITC tagged IONPs by total lymph node cells extracted from the popliteal and inguinal lymph node cells, 1 hour and 24 hours post subcutaneous injection, *in vivo*. Eight week old female C57BL/6 mice were injected subcutaneously with FITC tagged IONPs in either the hock or flank and popliteal and inguinal lymph nodes were collected respectively, at 1 hour (10 mice) and 24 hours (10 mice) after subcutaneous injection, *in vivo*. Cells were collected from each lymph node and % uptake of total lymph node cells extracted that were positive for FITC tagged IONPs were assessed by flow cytometry and analysed using FACSDiva software (BD Biosciences) and shown here with error bars representing standard error of the mean. Statistical analysis was performed using GraphPad Prism 6.05. Two way ANOVA was used to statistically analyse the data with the Bonferroni multiple comparison test. There was no statistical difference between the popliteal and inguinal lymph nodes at each time point and there was also no statistical difference between each time points for either lymph nodes.

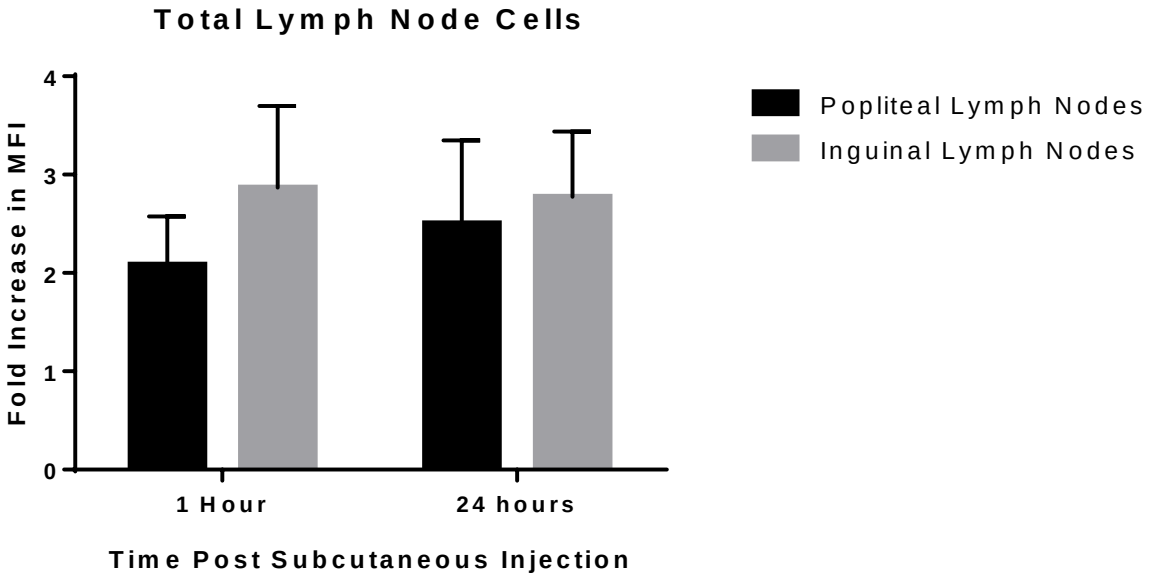

Figure 6.2: Uptake (fold increase in mean fluorescent intensity) of FITC tagged IONPs by total lymph node cells extracted from the popliteal and inguinal lymph node cells, 1 hour and 24 hours post subcutaneous injection, *in vivo*. Eight week old female C57BL/6 mice were injected subcutaneously with FITC tagged IONPs in either the hock or flank and popliteal and inguinal lymph nodes were collected respectively, at 1 hour (10 mice) and 24 hours (10 mice) after subcutaneous injection, *in vivo*. Cells were collected from each lymph node and % uptake of total lymph node cells extracted that were positive for FITC tagged IONPs were assessed by flow cytometry and analysed using FACSDiva software (BD Biosciences) and this graph demonstrates the mean fluorescent intensity (MFI) from the FITC (tagged to the IONPs), quantitated by flow cytometry and analysed using FACSDiva software (BD Biosciences) and shown here (popliteal lymph nodes, n=10 and inguinal lymph nodes, n=10). The results are shown as fold increase (compared to control) in mean fluorescent intensity with error bars representing the standard error of the mean. Statistical analysis was performed using GraphPad Prism 6.05. Two way ANOVA was use to statistically analyse the data with the Bonferroni multiple comparison test. No statistical significance (ns) could be detected between the cells from either lymph node or from either time point.

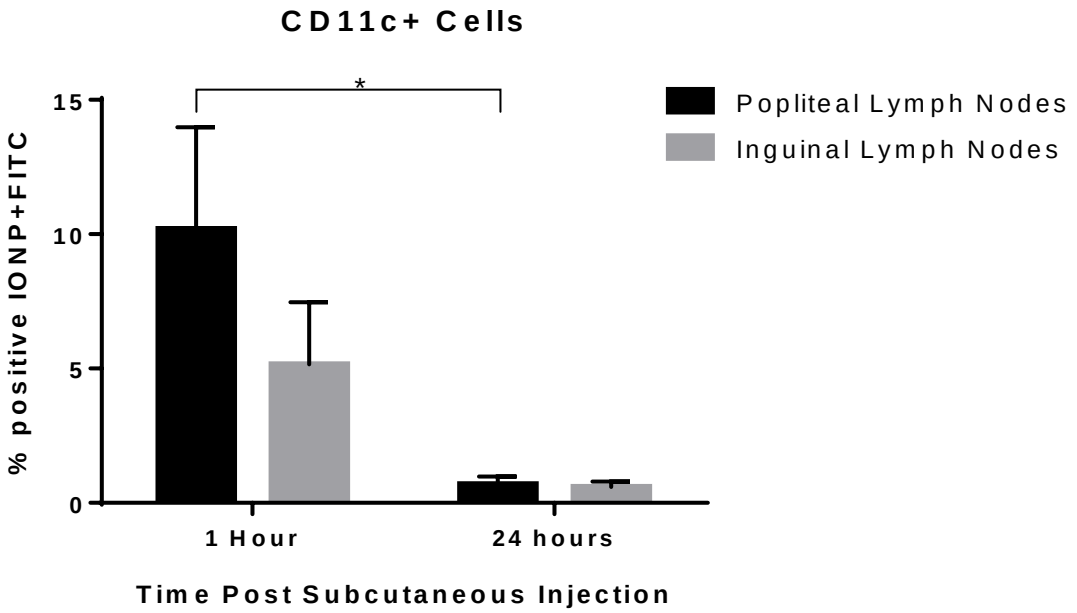

Figure 6.3: Uptake of FITC tagged IONPs by popliteal and inguinal lymph node cells, 1 hour and 24 hours post subcutaneous injection, *in vivo*. Eight week old female C57BL/6 mice were injected subcutaneously with FITC tagged IONPs in either the hock or flank and popliteal and inguinal lymph nodes were collected respectively, at 1 hour (10 mice) and 24 hours (10 mice) after subcutaneous injection, *in vivo*. Cells were collected from each lymph node and % uptake of CD11c positive cells that were also positive for FITC tagged IONPs were assessed by flow cytometry and analysed using FACSDiva software (BD Biosciences) and shown here with error bars representing standard error of the mean. Statistical analysis was performed using GraphPad Prism 6.05. Two way ANOVA was used to analyse the data with the Bonferroni multiple comparison test. An adjusted P value of 0.0180 between the popliteal lymph nodes between 1 hour and 24 hours indicates a significant statistical difference (*). The Source of Variation for this statistical difference is the time span between the two collection points with a P value summary of 0.0067 (**). There was no statistical difference between the inguinal lymph nodes between these two same time points; and no statistical significance between the popliteal and inguinal lymph nodes at 1 hour; and also no statistical difference between these same two lymph node groups at 24 hours.

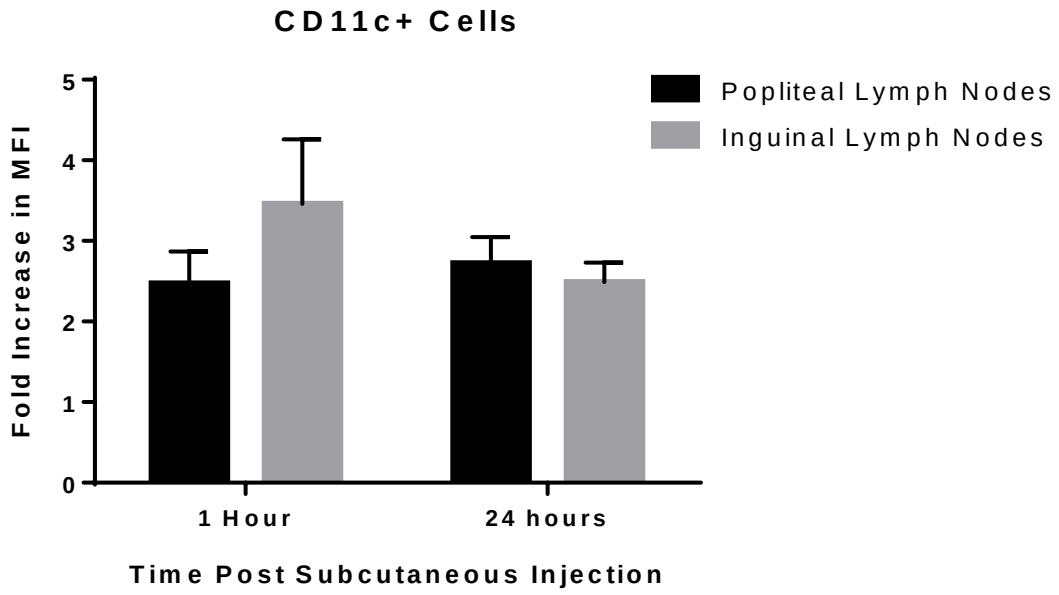

Figure 6.4: Uptake (fold increase in mean fluorescent intensity) of FITC tagged IONPs by popliteal and inguinal lymph node cells, 1 hour and 24 hours post subcutaneous injection, *in vivo*. Eight week old female C57BL/6 mice were injected subcutaneously with FITC tagged IONPs in either the hock or flank and popliteal and inguinal lymph nodes were collected respectively, at 1 hour (10 mice) and 24 hours (10 mice) after subcutaneous injection, *in vivo*. Cells were collected from each lymph node and % uptake of CD11c positive cells that were also positive for FITC tagged IONPs were assessed by flow cytometry and analysed using FACSDiva software (BD Biosciences) and this graph demonstrates the mean fluorescent intensity (MFI) from the FITC (tagged to the IONPs), quantitated by flow cytometry and analysed using FACSDiva software (BD Biosciences) and shown here (popliteal lymph nodes, n=10 and inguinal lymph nodes, n=10). The results are shown as fold increase (compared to control) in mean fluorescent intensity with error bars representing the standard error of the mean. Statistical analysis was performed using GraphPad Prism 6.05. Two way ANOVA was used to statistically analyse the data with the Bonferroni multiple comparison test. No statistical significance (ns) could be detected between the cells from either lymph node and no Source of Variation could be detected.

6.2.2 Biochemistry assessment on the blood serum of mice undergoing subcutaneous injection of T10 dextran coated IONPs tagged with FITC

While mice were under anaesthesia and just prior to performing the vascular perfusion fixation technique, haematocrit capillaries were used to retrieve blood samples from the retro-orbital sinus. The blood serum was attained from blood sample as described in Section 2.12.7 and biochemical analysis was performed.

	Mean Value (n=10)	Mean Value (n=10)	
	1 hour post injection of FITC tagged IONP	24 hours post injection of FITC tagged IONP	Units
AlbG	2.93	2.61	g/L
AlkP	198.6	196.6	U/L
ALT	35.4	47.7	U/L
Amy	1236.9	946.6	U/L
BiliT	0.152046784	0.192982456	µmol/L
CreaC	0.393413776	0.350678733	µmol/L
GGT	< 4	< 4	U/L
TP	5.15	4.57	g/L
Urea	137.52	132.12	mmol/L

Table 6.1: Biochemical analyte values obtained from murine blood serum under experimental conditions. The mice used were female C57BL/6 and 8 weeks old. The abbreviations represent the following terms: AlbG (albumin globulin), AlkP (alkaline phosphatase), ALT (alanine aminotransferase), Amy (amylase), BiliT (Bilirubin Total), CreaC (creatinine clearance or glomerular filtration rate (GFR)), GGT (gamma-glutamyl transferase), TP (total protein) and Urea (urea).

	Averages (n=10)	Averages (n=10)	Averages (n=15)	Averages (n=15)	
	1 hour post injection of FITC tagged IONP	1 day post injection of FITC tagged IONP	Mazzaccara *et al*	Schnell *et al*	Units
AlbG	2.93	2.61	Not available	3.9 ± 0.48	g/L
AlkP	198.6	196.6	221 (214 – 246)	125 ± 19.3	U/L
ALT	35.4	47.7	51 (46 – 54)	59 ± 34	U/L
Amy	1236.9	946.6	Not available	2008 ± 449.9	U/L
BiliT	2.7	3.3	6.8 (3.4 – 6.8)	5.13 ± 0 *	µmol/L
CreaC	34.6	31	35.4 (26.5 – 35.3)	79.56 ± 26.52*	µmol/L
GGT	< 4	< 4	9.5 (8 – 10)	Not available	U/L
TP	5.15	4.57	Not available	4.9 ± 0.57	g/L
Urea	137.52	132.12	7.1 (5.7 – 8.5)	25 ± 4.5	mmol/L

Table 6.2: Blood serum biochemical analyte values from the experimental process and compared with published values. Comparison was made with obtained experimental results and those published by Mazzaccara *et al*[293] (mice at 2 months of age) and Schnell *et al*[294] (mice at 6 months of age). All mice were femail C57BL/6. The asterisk (*) denotes that the figure was calculated to convert the units from mg/dl to µmol/L.

6.2.3 Histopathological Evaluation

On completion of vascular perfusion fixation, organs that may succumb to possible adverse events/reactions to contrast media (in this case dextran coated iron oxide nanoparticles tagged with FITC) were removed from the mice. These organs were the liver, kidney, spleen heart and lungs. They were preserved, embedded in wax blocks, a microtome used to cut tissue samples and set on microscope slides as described in Section 2.12.6.

H&E, Perls Prussian Blue and PAS staining were performed. The H&E stain was designed to observe the generalised cellular architecture and condition, the Perls Prussian Blue was performed to observe any iron deposits and a PAS stain was used to identify if there was any disruption to the basement membrane of the kidney tissue (as this is the first site of renal injury in response to toxicity).

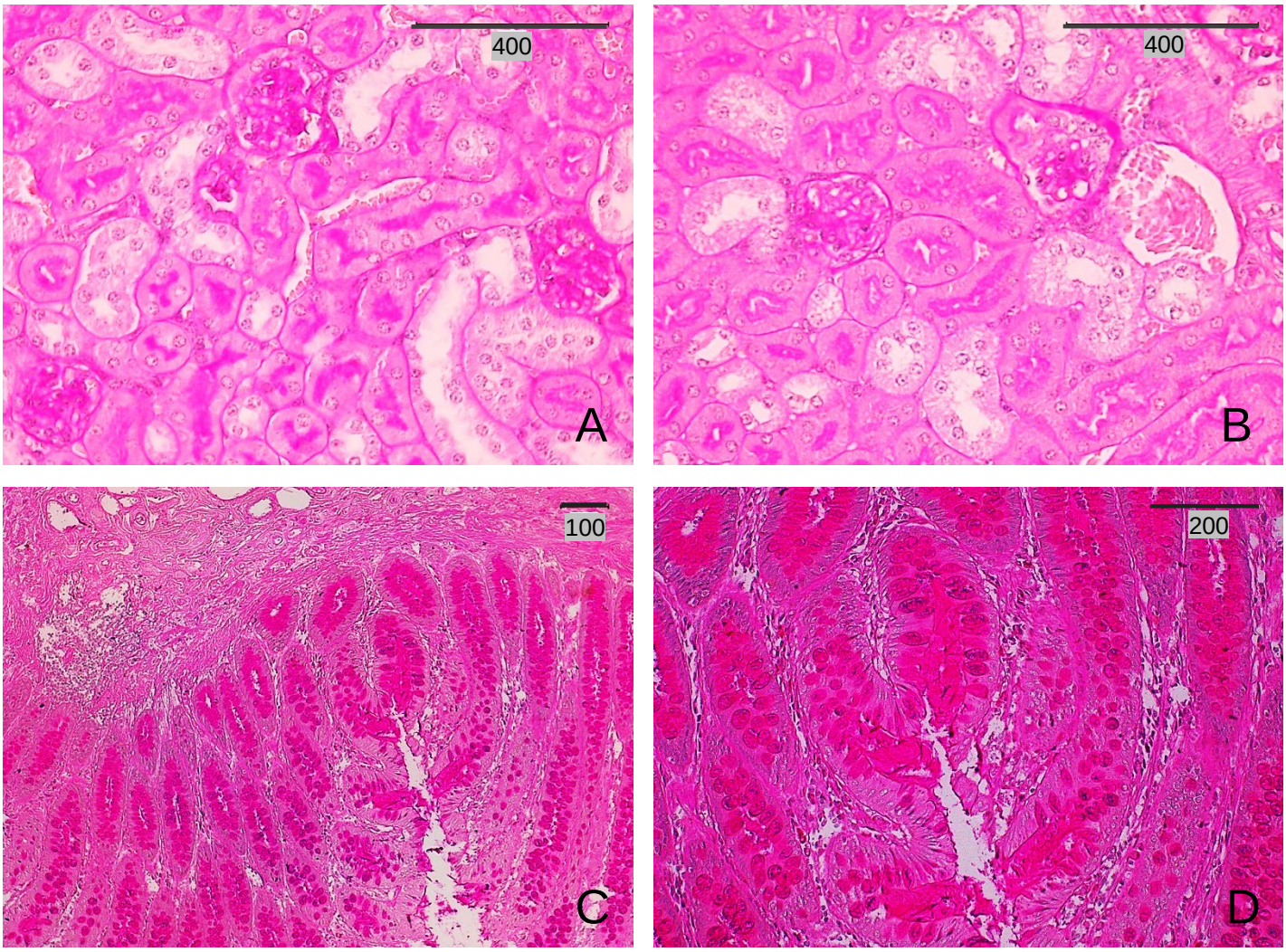

Figure 6.5: Periodic acid Schiff (PAS) stain (A and B) of paraffin embedded murine kidney sections and of known positive control tissue sections (C and D). Representative micrographs of PAS stained murine kidney sections from mice receiving iron oxide nanoparticles at 1 hour (panel A) and 24 hour (panel B) time points, post subcutaneous injections (hock and flank); both at 400x magnification. Panel C (100x magnification) and panel D (200x magnification) are known positive control tissue samples placed in the same rack as the murine kidney tissue sections and have undergone the PAS stain process simultaneously. All of the observed murine kidney sections were clear of iron deposits.

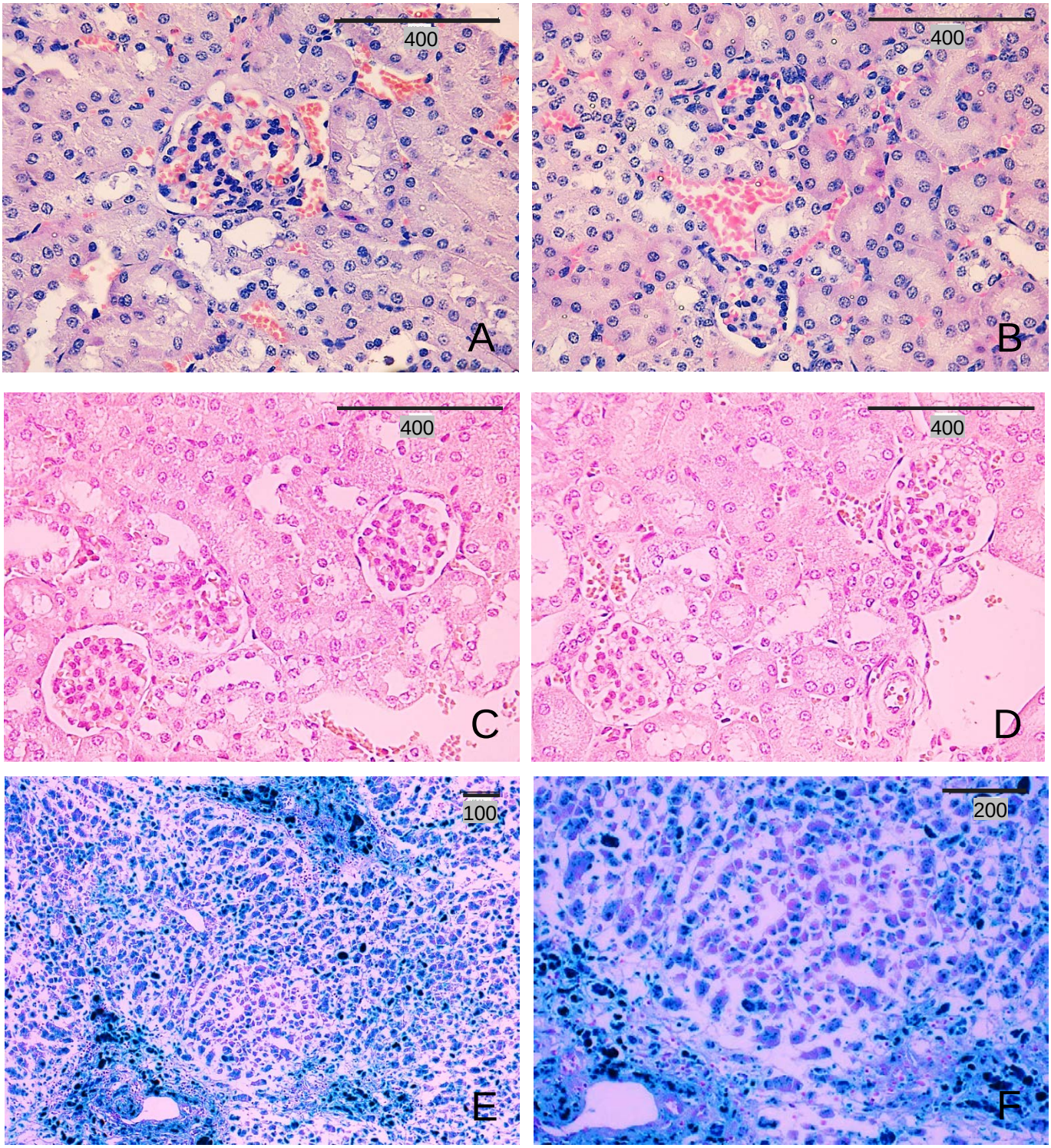

Figure 6.6: Haematoxylin and eosin (H & E) stain (A and B) and Perls Prussian blue stain (C and D) of paraffin embedded murine kidney sections and Perls Prussian blue stain of known positive control tissue sections (E and F). Representative micrographs of H & E stained murine kidney sections from mice receiving iron oxide nanoparticles at 1 hour (panel A) and 24 hour (panel B) time points post subcutaneous injections (hock and flank); both at 400x magnification. Panels C and D (both at 400x magnification) are representative micrographs of Perls Prussian blue staining of murine kidney sections, also 1 hour and 1 day post subcutaneous injections and panels E (100x magnification) and F (200x magnification) are known positive control tissue samples placed in the same rack as the murine kidney tissue sections and have undergone the Perls Prussian blue stain process simultaneously.

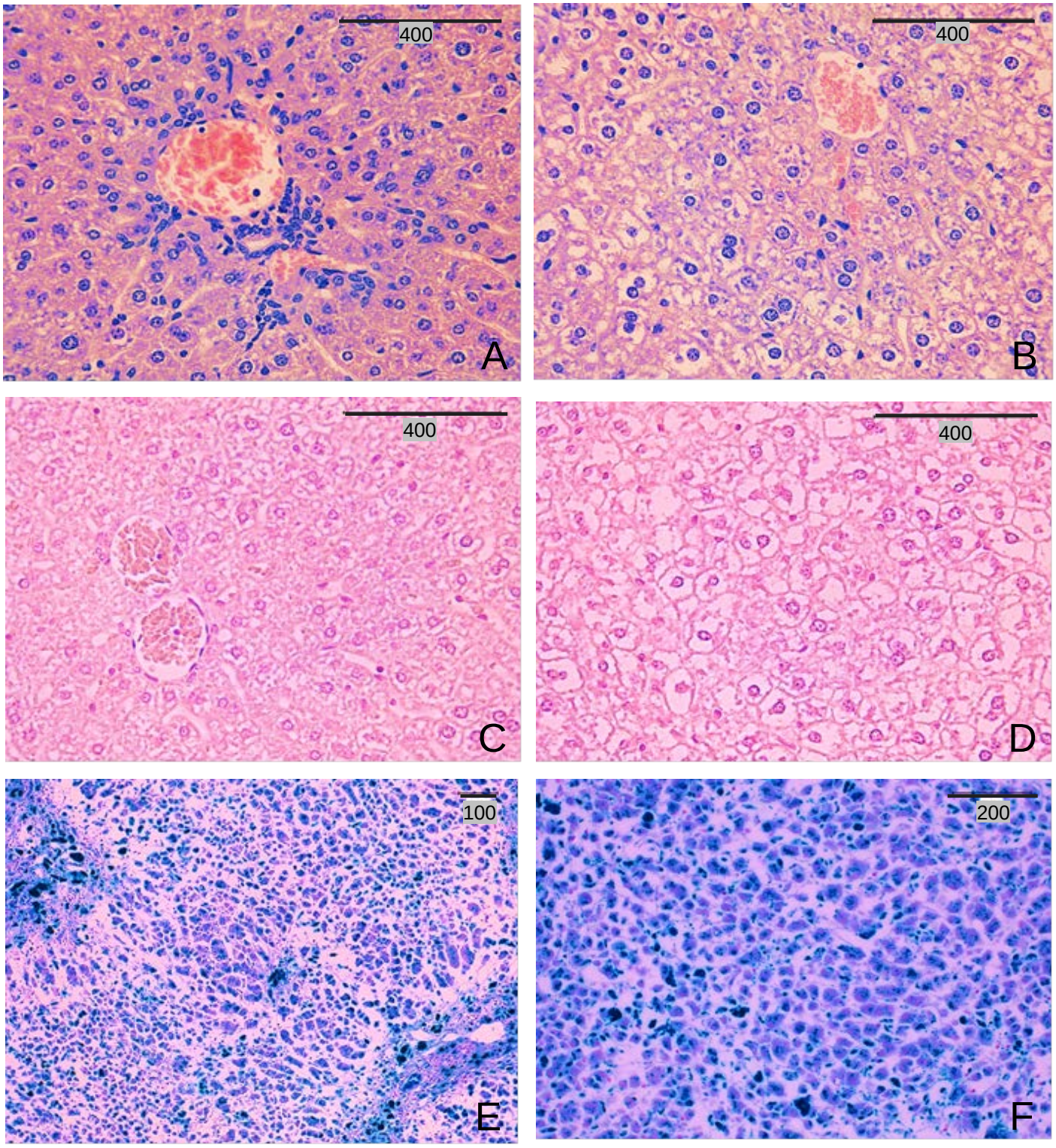

Figure 6.7: Haematoxylin and eosin (H & E) stain (A and B) and Perls Prussian blue stain (C and D) of paraffin embedded murine liver sections and Perls Prussian blue stain of known positive control tissue sections (E and F). Representative micrographs of H & E stained murine liver sections from mice receiving iron oxide nanoparticles at 1 hour (panel A) and 24 hour (panel B) time points post subcutaneous injections (hock and flank); both at 400x magnification. Panels C and D (both at 400x magnification) are representative micrographs of Perls Prussian blue staining of murine liver sections, also 1 hour and 1 day post subcutaneous injections and panels E (100x magnification) and F (200x magnification) are known positive control tissue samples placed in the same rack as the murine liver tissue sections and have undergone the Perls Prussian blue stain process simultaneously.

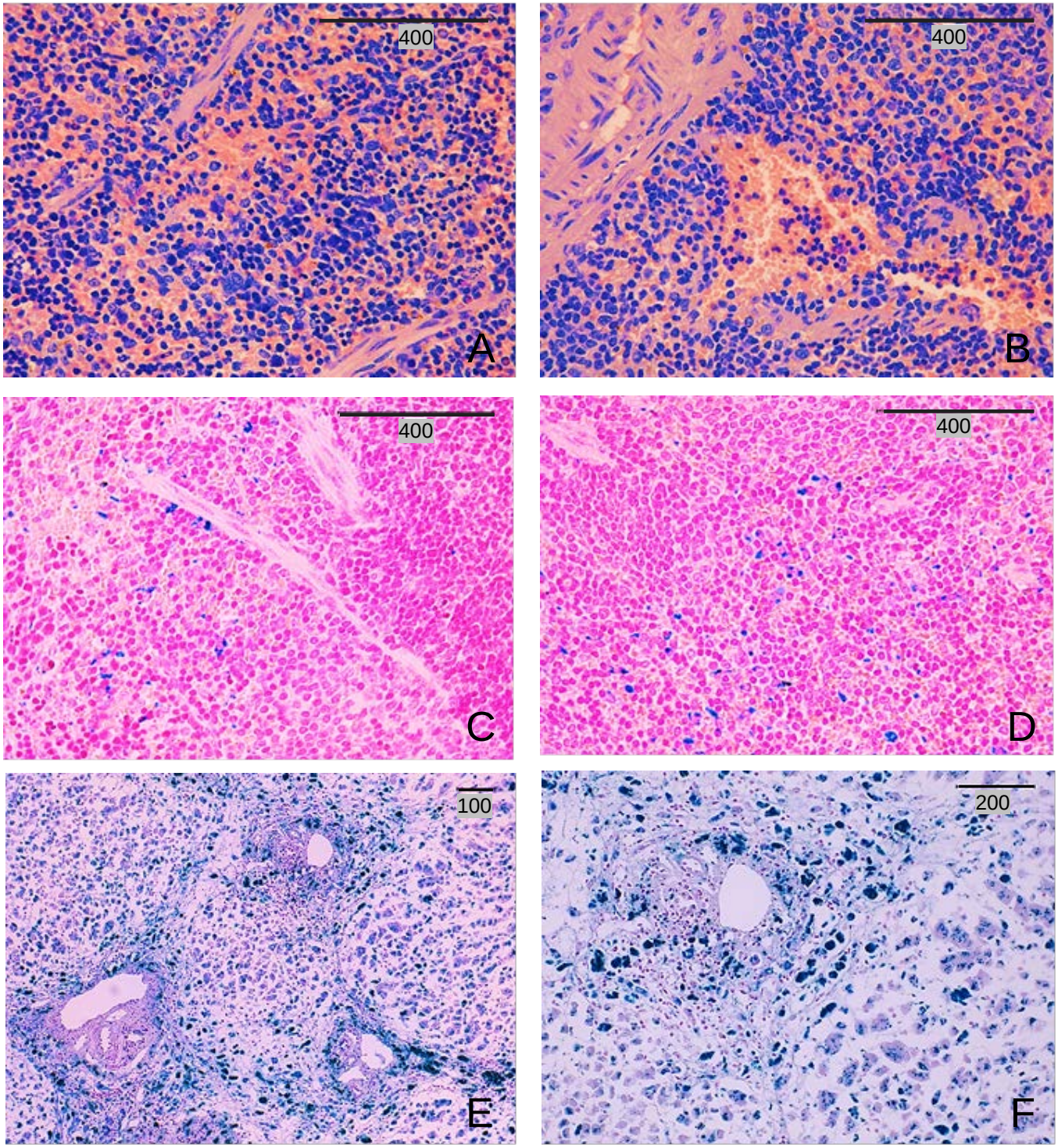

Figure 6.8: Haematoxylin and eosin (H & E) stain (A and B) and Perls Prussian blue stain (C and D) of paraffin embedded murine spleen sections and Perls Prussian blue stain of known positive control tissue sections (E and F). Representative micrographs of H & E stained murine spleen sections from mice receiving iron oxide nanoparticles at 1 hour (panel A) and 24 hour (panel B) time points post subcutaneous injections (hock and flank); both at 400x magnification. Panels C and D (both at 400x magnification) are representative micrographs of Perls Prussian blue staining of murine spleen sections also at 1 hour and 24 hour time points post subcutaneous injections and panels E (100x magnification) and F (200x magnification) are known positive control tissue samples placed in the same rack as the murine spleen tissue sections and have undergone the Perls Prussian blue stain process simultaneously.

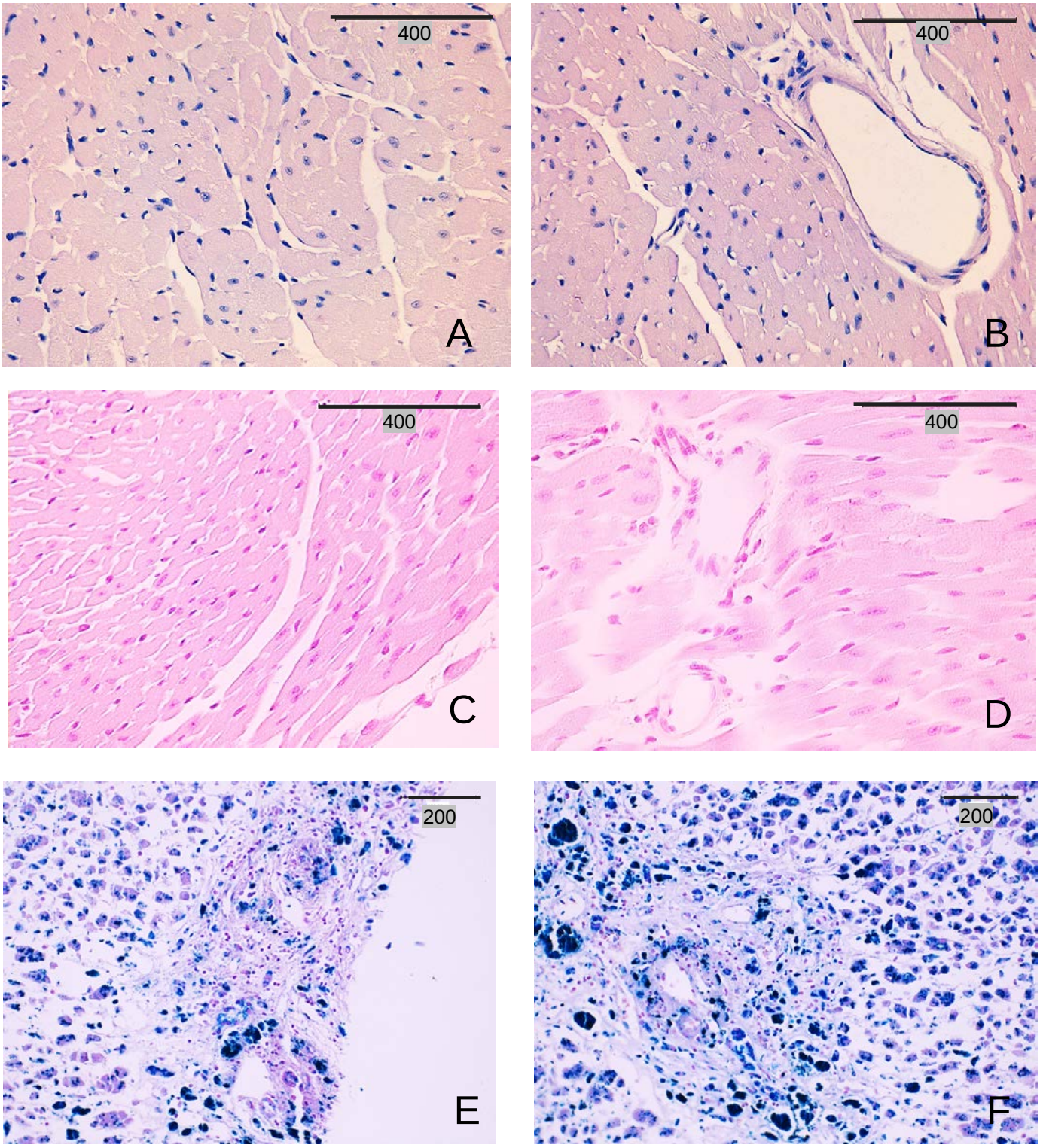

Figure 6.9: Haematoxylin and eosin (H & E) stain (A and B) and Perls Prussian blue stain (C and D) of paraffin embedded murine cardiac sections and Perls Prussian blue stain of known positive control tissue sections (E and F). Representative micrographs of H & E stained murine cardiac sections from mice receiving iron oxide nanoparticles at 1 hour (panel A) and 24 hour (panel B) time points post subcutaneous injections (hock and flank); both at 400x magnification. Panels C and D (both at 400x magnification) are representative micrographs of Perls Prussian blue staining of murine cardiac sections, also at 1 hour and 24 hour time points post subcutaneous injections and panels E and F (both at 200x magnification) are known positive control tissue samples placed in the same rack as the murine cardiac tissue sections and have undergone the Perls Prussian blue stain process simultaneously.

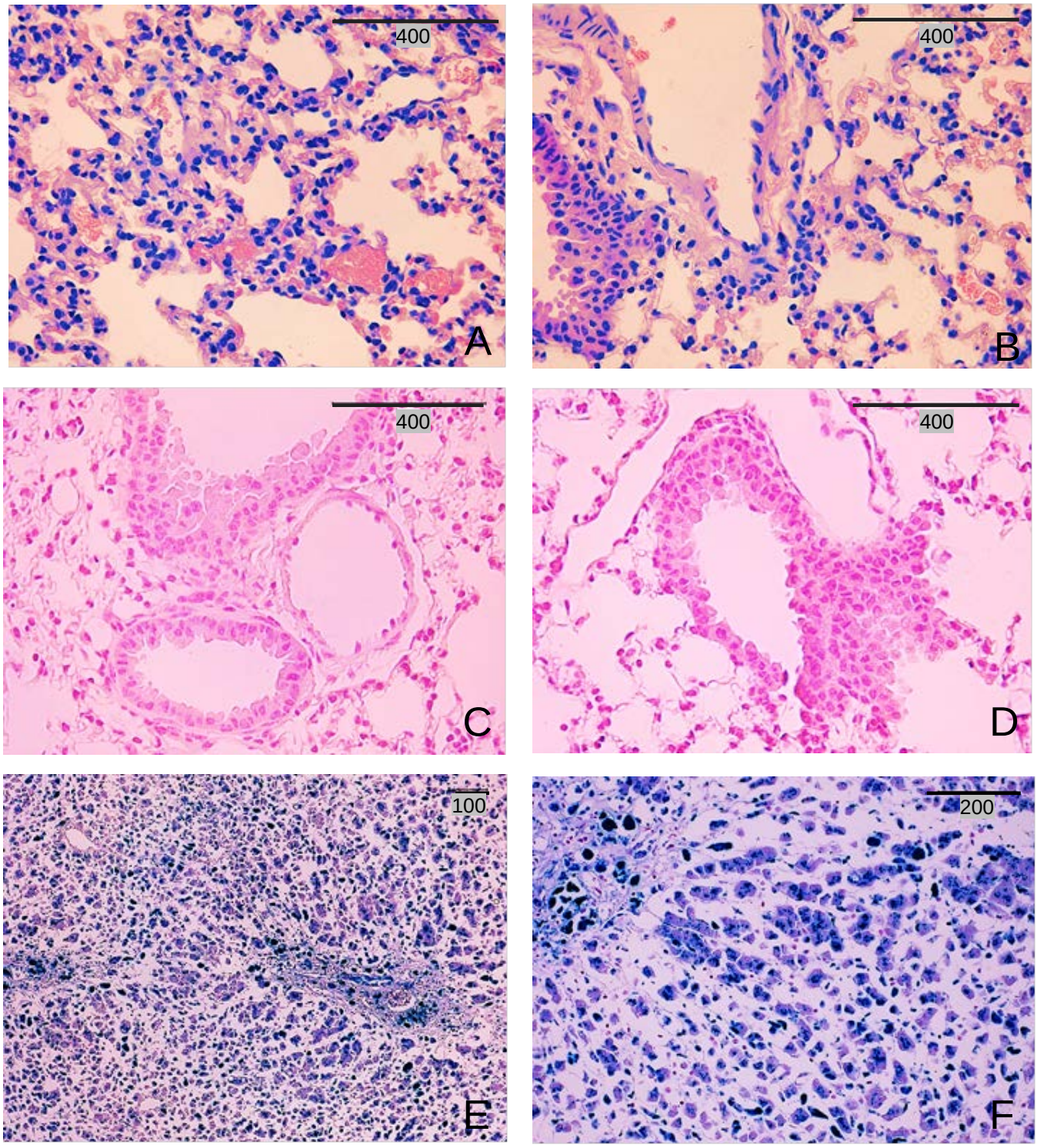

Figure 6.10: Haematoxylin and eosin (H & E) stain (A and B) and Perls Prussian blue stain (C and D) of paraffin embedded murine lung sections and Perls Prussian blue stain of known positive control tissue sections (E and F). Representative micrographs of H & E stained murine lung sections from mice receiving iron oxide nanoparticles at 1 hour (panel A) and 24 hour (panel B) time points post subcutaneous injections (hock and flank); both at 400x magnification. Panels C and D (both at 400x magnification) are representative micrographs of Perls Prussian blue staining of murine lung sections, also at 1 hour and 24 hour time points post subcutaneous injections and panels E (100x magnification) and F (200x magnification) are known positive control tissue samples placed in the same rack as the murine liver tissue sections and have undergone the Perls Prussian blue stain process simultaneously.

6.2.3.1 Comparison of Perls Prussian Blue stain for iron (Fe^{3+}) content in murine spleen and murine liver

For all mice used in the experimental process described in Section 2.12.2, the RES organs (spleen and liver) removed *post mortem* were compared for iron (Fe^{3+}) deposit by using the Perls Prussian blue stain as described in Section 2.15.2. This direct comparison was performed because no mice were used as controls for the Perls Prussian blue (please refer to discussion in Section 6.3) and also because unbound iron (Fe^{3+}) is normally found in the spleen. If iron (Fe^{3+}) from the IONPs disassociated and were responsible for iron (Fe^{3+}) deposits in the spleen, they would also be present in the liver. The logical reasoning is that if no unbound Fe^{3+} can be identified by Perls Prussian blue staining in the liver (presumably from the IONPs), then any positive Perls Prussian blue staining in spleen cannot be attributed to the IONPs. Further, the dimension of one iron oxide nanoparticle is 20 nm and therefore the iron (Fe^{3+}) component would be less than 20 nm; thus, if any iron (Fe^{3+}) did disassociate, it would be doubtful if it would be visible with the resolving power (400x magnification) of the light microscope used to image these stained sections.

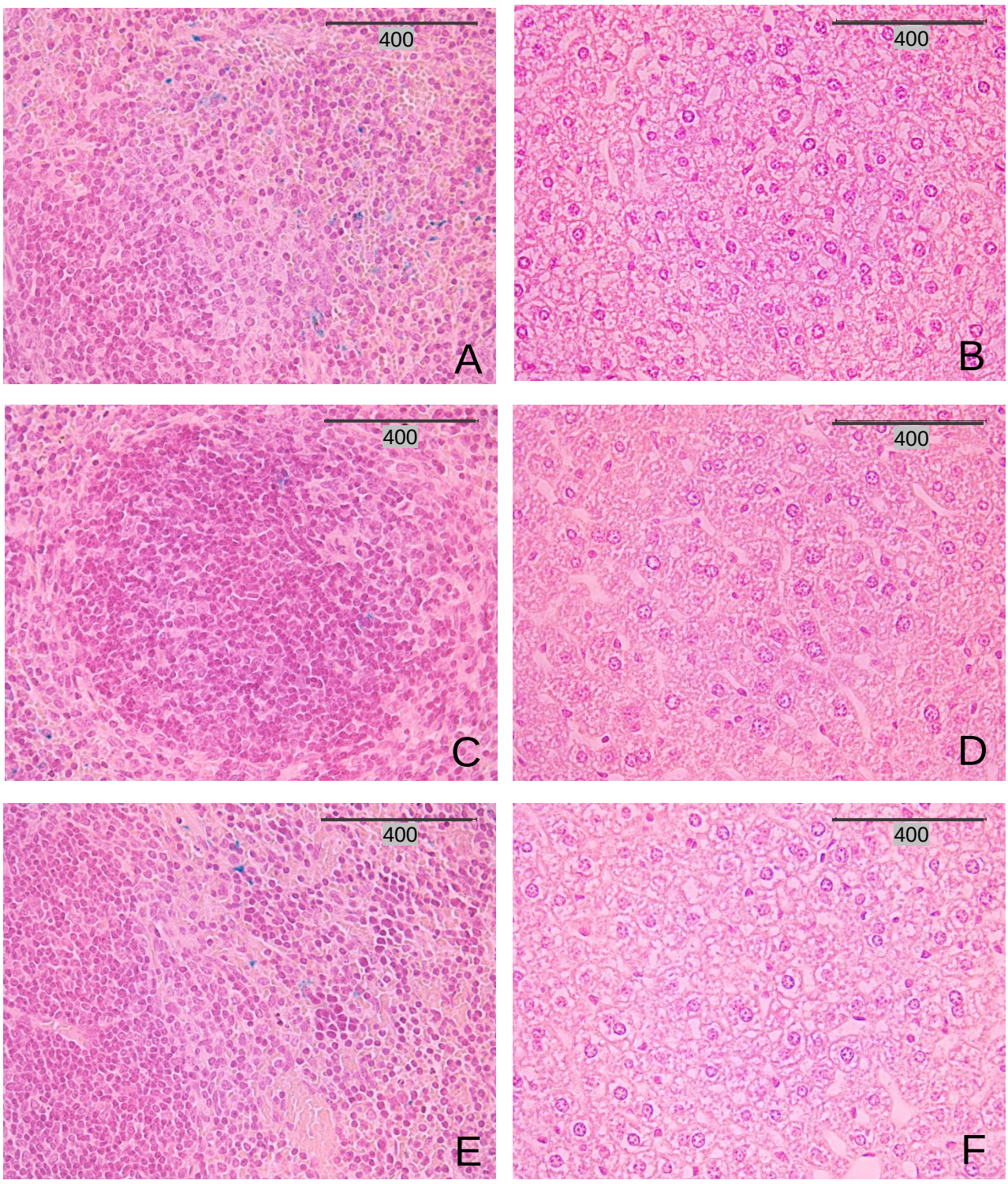

Figure 6.11: Perls Prussian blue stain of paraffin embedded murine spleen sections and corresponding Perls Prussian blue stain of liver sections from mouse number 1 (A and B), 2 (C and D) and 3 (E and F) in the first group of mice. These mice were killed 1 hour post injection of IONPs, their organs removed, fixed, sectioned and stained. Panels A, C and E are Perls Prussian blue stained spleen sections and panels B, D and F are Perls Prussian blue stained liver sections from the same mice. All representative micrographs presented here are at 400x magnification. A known positive control tissue sample placed in the same rack as these murine spleen and liver tissue sections and have undergone the Perls Prussian blue stain process simultaneously (not presented here).

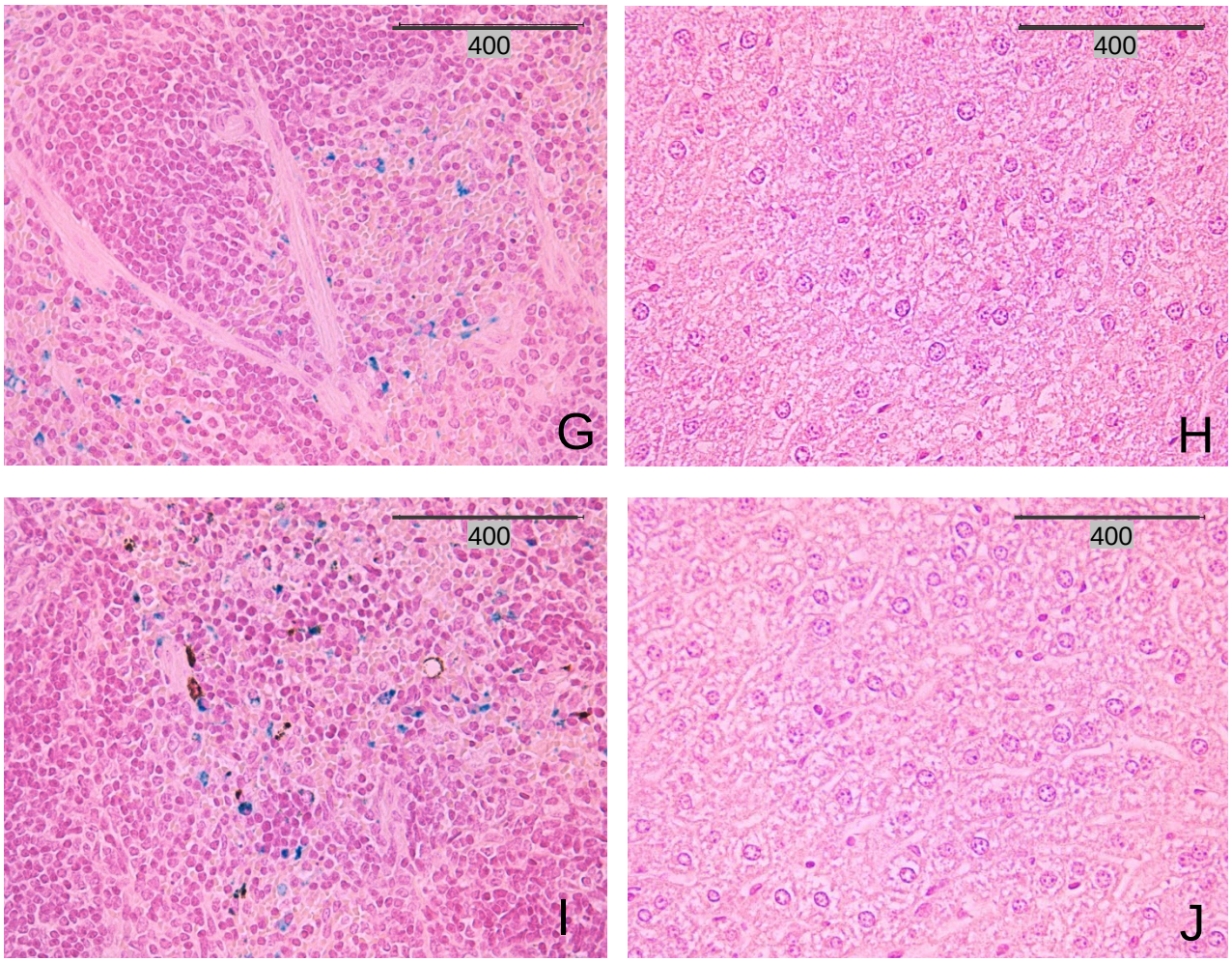

Figure 6.12: Perls Prussian blue stain of paraffin embedded murine spleen sections and corresponding Perls Prussian blue stain of liver sections from mouse number 4 (G and H) and 5 (I and J) in the first group of mice. These mice were killed 1 hour post injection of IONPs, their organs removed, fixed, sectioned and stained. Panels G and I are Perls Prussian blue stained spleen sections and panels H and J are Perls Prussian blue stained liver sections from the same mice. All representative micrographs presented here are at 400x magnification. A known positive control tissue sample placed in the same rack as these murine spleen and liver tissue sections and have undergone the Perls Prussian blue stain process simultaneously (not presented here).

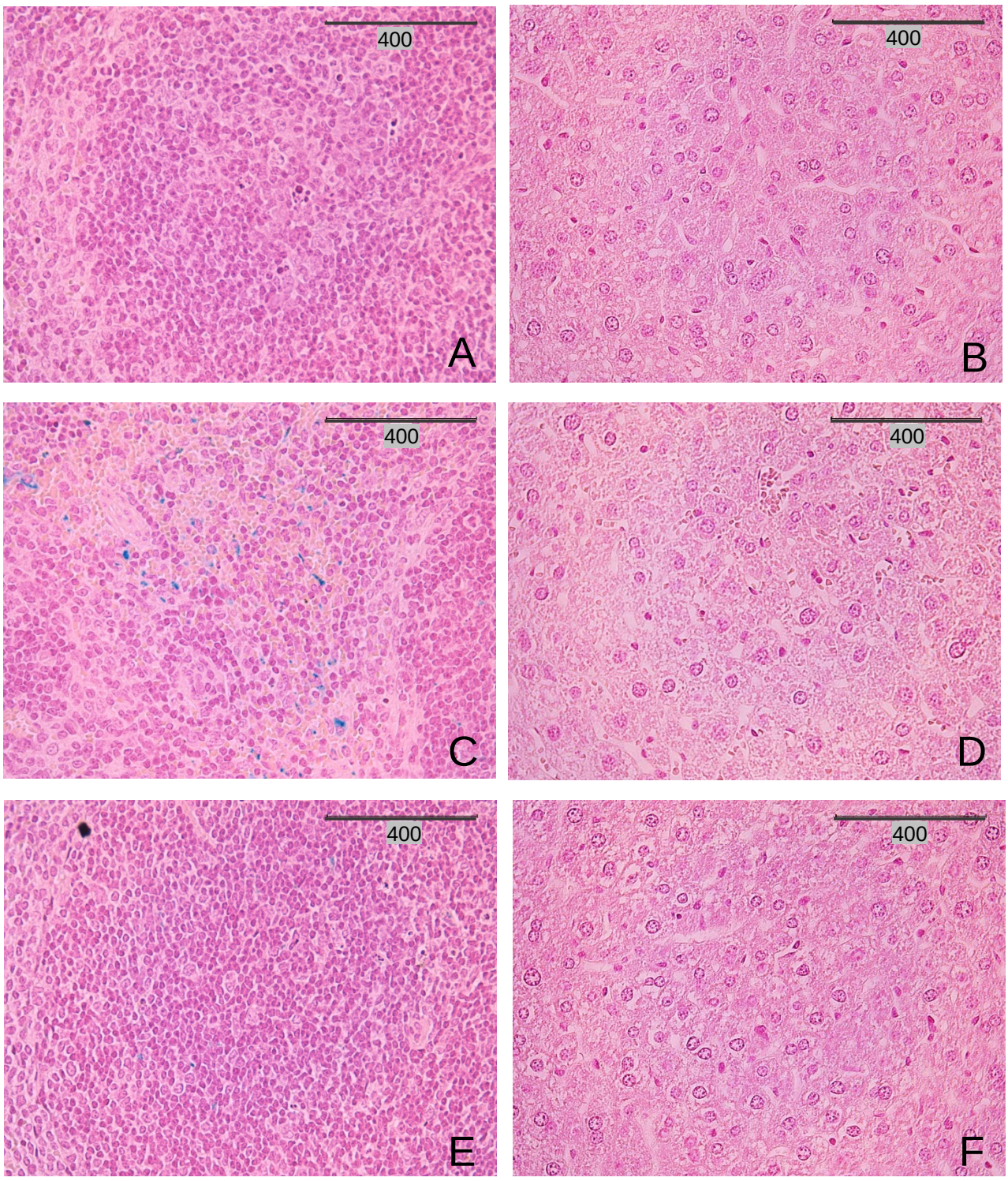

Figure 6.13: Perls Prussian blue stain of paraffin embedded murine spleen sections and corresponding Perls Prussian blue stain of liver sections from mouse number 1 (A and B), 2 (C and D) and 3 (E and F) in the second group of mice. These mice were killed 1 hour post injection of IONPs, their organs removed, fixed, sectioned and stained. Panels A, C and E are Perls Prussian blue stained spleen sections and panels B, D and F are Perls Prussian blue stained liver sections from the same mice. All representative micrographs presented here are at 400x magnification. A known positive control tissue sample placed in the same rack as these murine spleen and liver tissue sections and have undergone the Perls Prussian blue stain process simultaneously (not presented here).

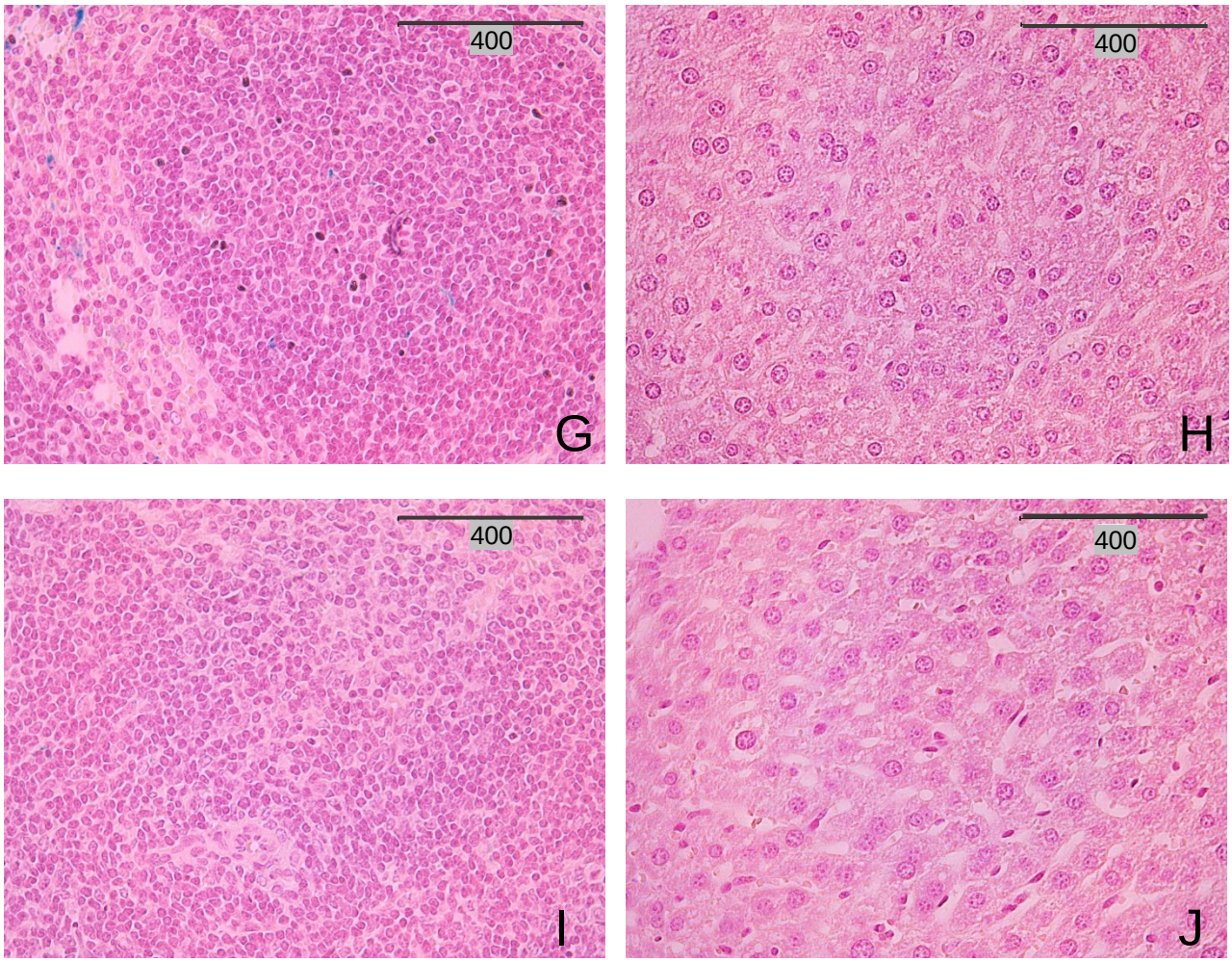

Figure 6.14: Perls Prussian blue stain of paraffin embedded murine spleen sections and corresponding Perls Prussian blue stain of liver sections from mouse number 4 (G and H) and 5 (I and J) in the second group of mice. These mice were killed 1 hour post injection of IONPs, their organs removed, fixed, sectioned and stained. Panels G and I are Perls Prussian blue stained spleen sections and panels H and J are Perls Prussian blue stained liver sections from the same mice. All representative micrographs presented here are at 400x magnification. A known positive control tissue sample placed in the same rack as these murine spleen and liver tissue sections and have undergone the Perls Prussian blue stain process simultaneously (not presented here).

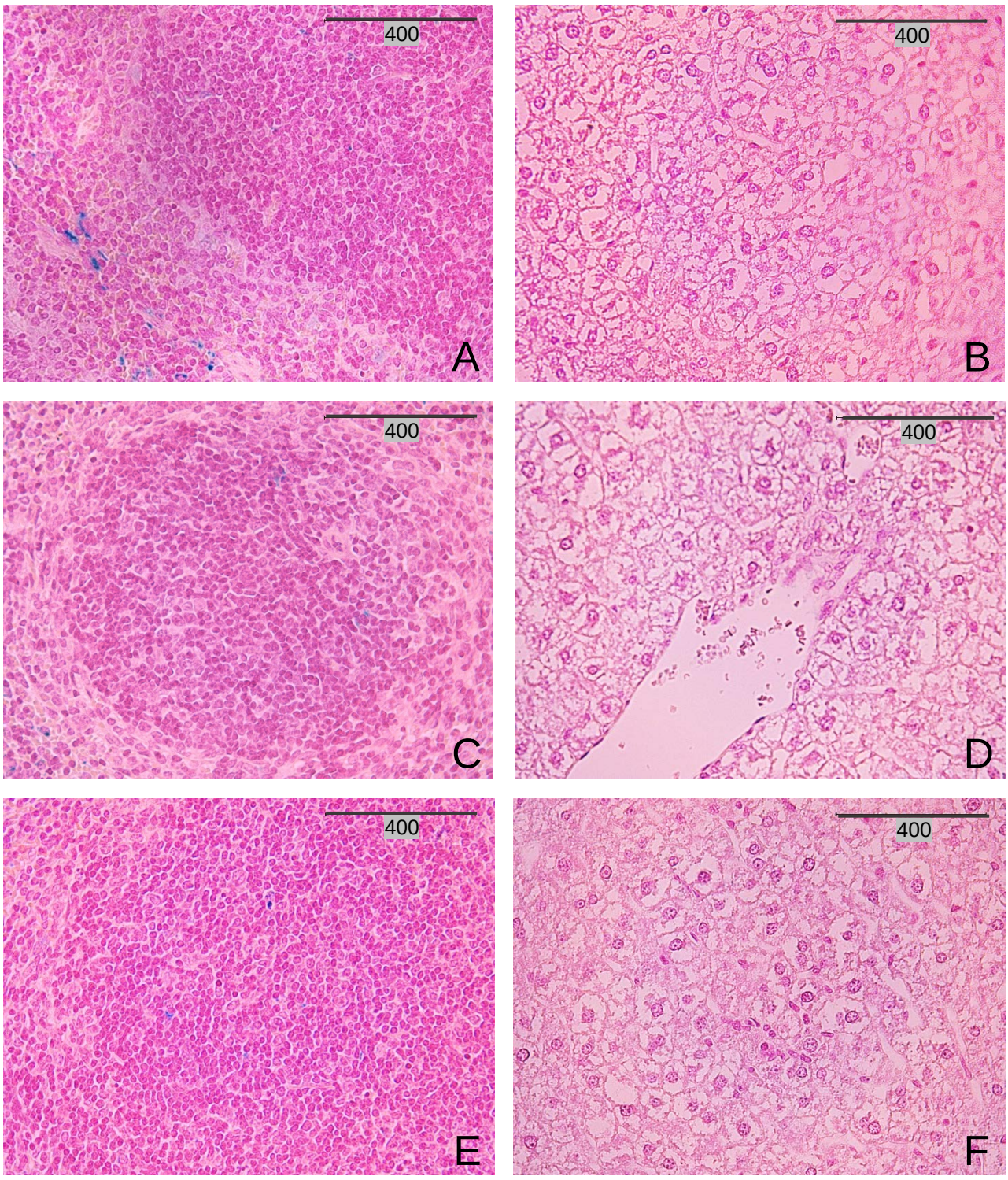

Figure 6.15: Perls Prussian blue stain of paraffin embedded murine spleen sections and corresponding Perls Prussian blue stain of liver sections from mouse number 1 (A and B), 2 (C and D) and 3 (E and F) in the third group of mice. These mice were killed 24 hours post injection of IONPs, their organs removed, fixed, sectioned and stained. Panels A, C and E are Perls Prussian blue stained spleen sections and panels B, D and F are Perls Prussian blue stained liver sections from the same mice. All representative micrographs presented here are at 400x magnification. A known positive control tissue sample placed in the same rack as these murine spleen and liver tissue sections and have undergone the Perls Prussian blue stain process simultaneously (not presented here).

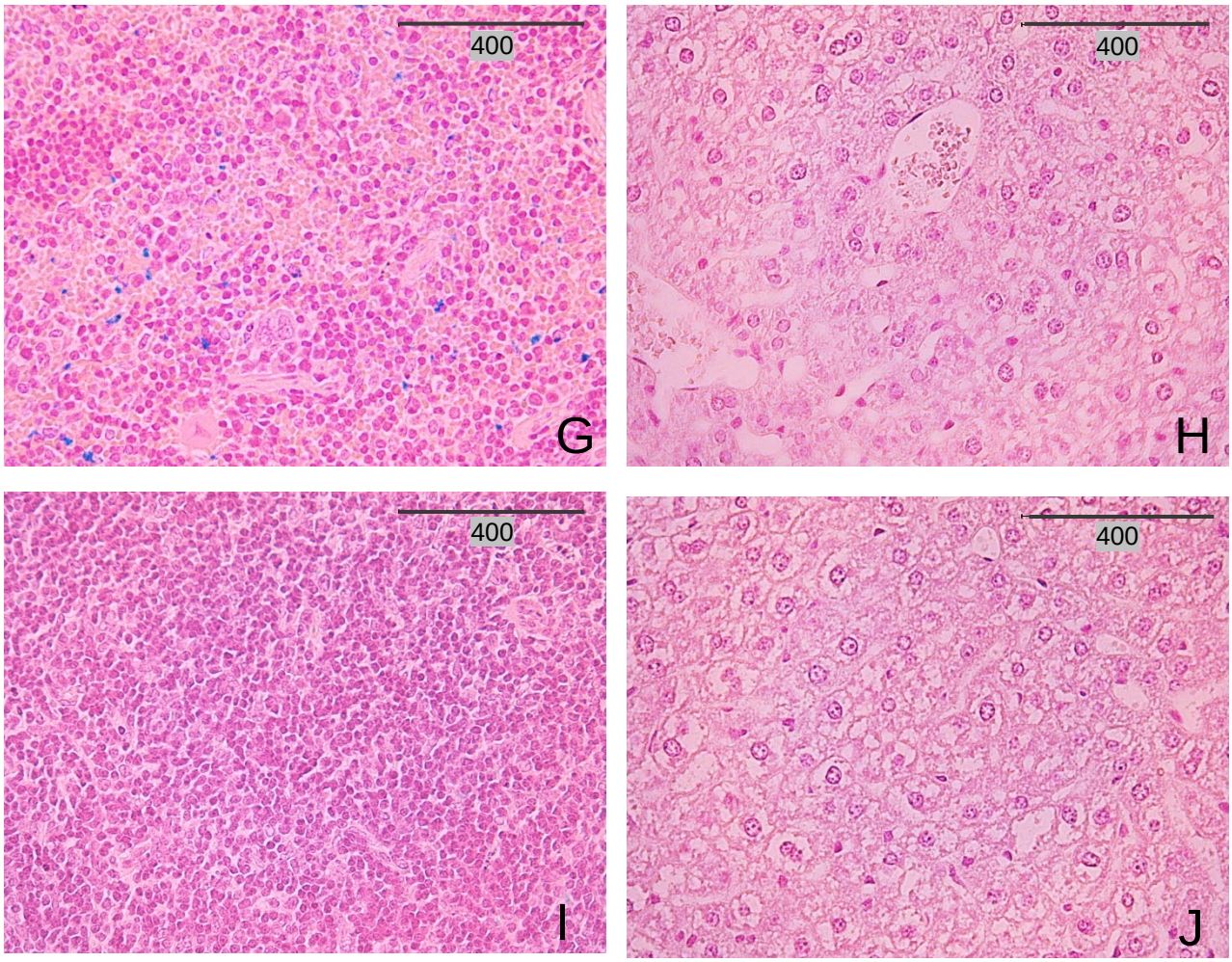

Figure 6.16: Perls Prussian blue stain of paraffin embedded murine spleen sections and corresponding Perls Prussian blue stain of liver sections from mouse number 4 (G and H) and 5 (I and J) in the third group of mice. These mice were killed 24 hours post injection of IONPs, their organs removed, fixed, sectioned and stained. Panels G and I are Perls Prussian blue stained spleen sections and panels H and J are Perls Prussian blue stained liver sections from the same mice. All representative micrographs presented here are at 400x magnification. A known positive control tissue sample placed in the same rack as these murine spleen and liver tissue sections and have undergone the Perls Prussian blue stain process simultaneously (not presented here).

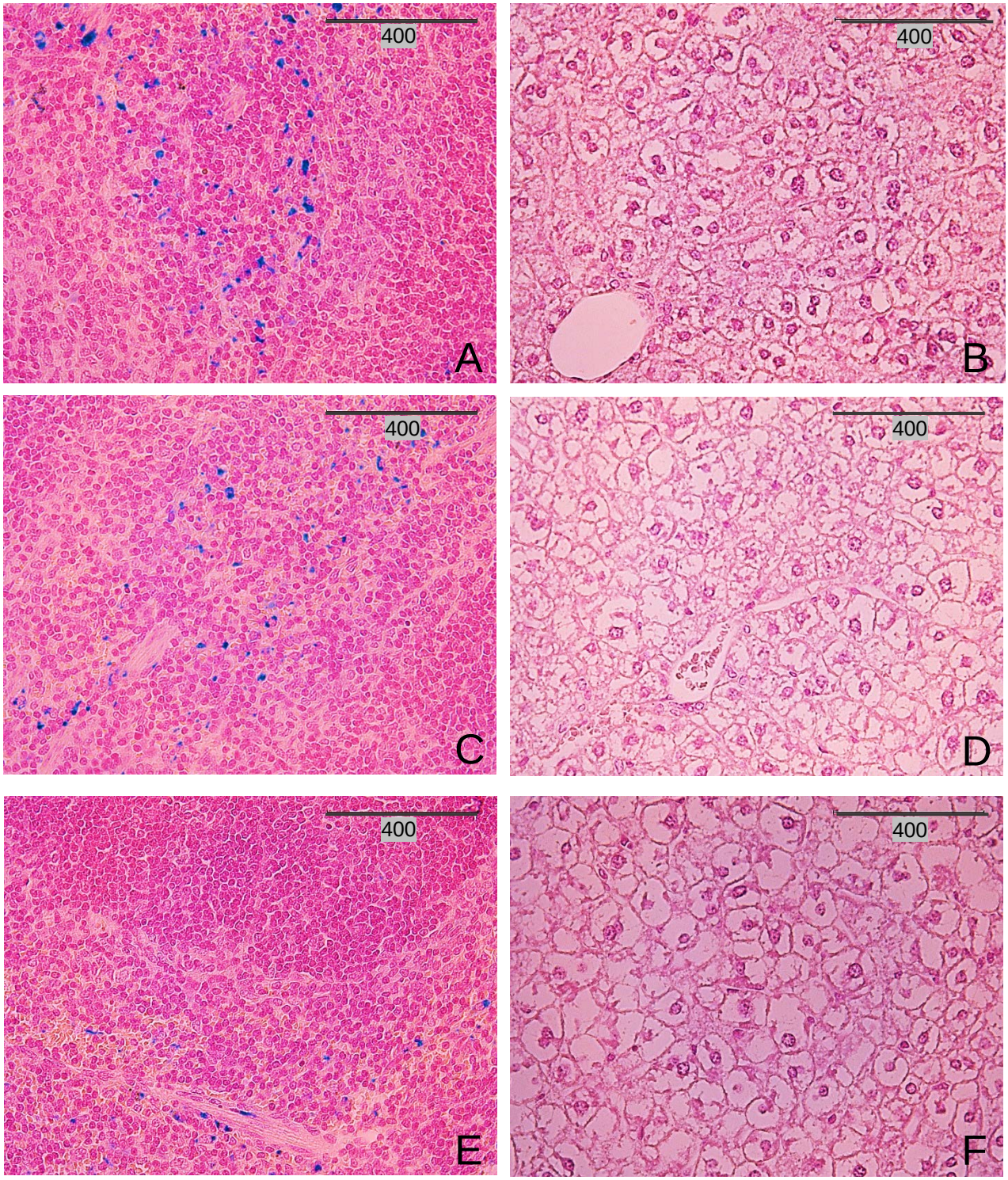

Figure 6.17: Perls Prussian blue stain of paraffin embedded murine spleen sections and corresponding Perls Prussian blue stain of liver sections from mouse number 1 (A and B), 2 (C and D) and 3 (E and F) in the fourth group of mice. These mice were killed 24 hours post injection of IONPs, their organs removed, fixed, sectioned and stained. Panels A, C and E are Perls Prussian blue stained spleen sections and panels B, D and F are Perls Prussian blue stained liver sections from the same mice. All representative micrographs presented here are at 400x magnification. A known positive control tissue sample placed in the same rack as these murine spleen and liver tissue sections and have undergone the Perls Prussian blue stain process simultaneously (not presented here).

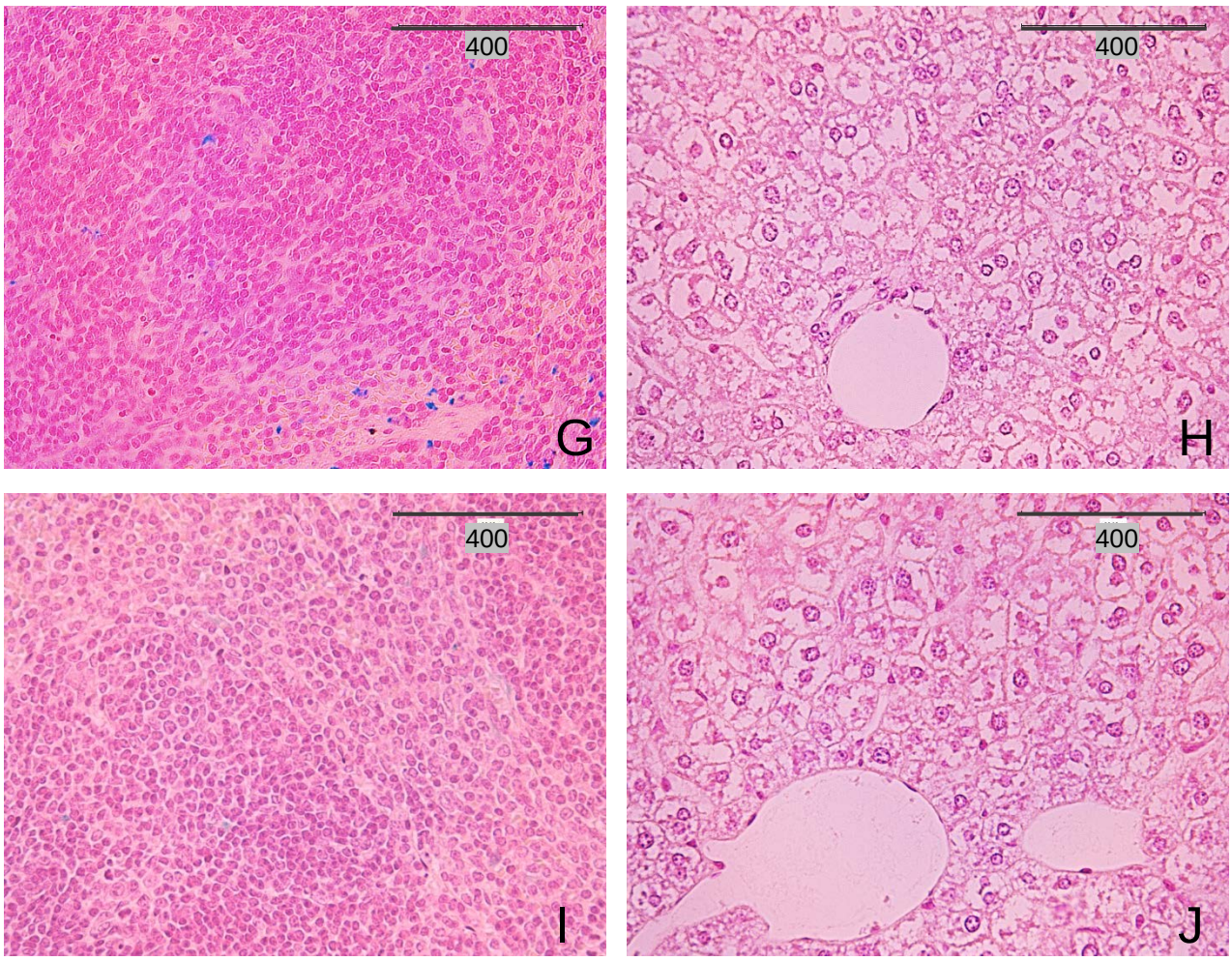

Figure 6.18: Perls Prussian blue stain of paraffin embedded murine spleen sections and corresponding Perls Prussian blue stain of liver sections from mouse number 4 (G and H) and 5 (I and J) in the fourth group of mice. These mice were killed 24 hours post injection of IONPs, their organs removed, fixed, sectioned and stained. Panels G and I are Perls Prussian blue stained spleen sections and panels H and J are Perls Prussian blue stained liver sections from the same mice. All representative micrographs presented here are at 400x magnification. A known positive control tissue sample placed in the same rack as these murine spleen and liver tissue sections and have undergone the Perls Prussian blue stain process simultaneously (not presented here).

6.2.4 PET and MR imaging of mice after being injected with T10 dextran coated IONPs + FITC and radio-labelled with ^{68}Ga following footpad injection.

The radio-labelling method described in Section 2.8.7 was used to radio-label ^{68}Ga to the dextran coated iron oxide nanoparticles tagged with FITC. The mice were imaged 1 hour after a foot pad injection with a SA PET scanner while under GA.

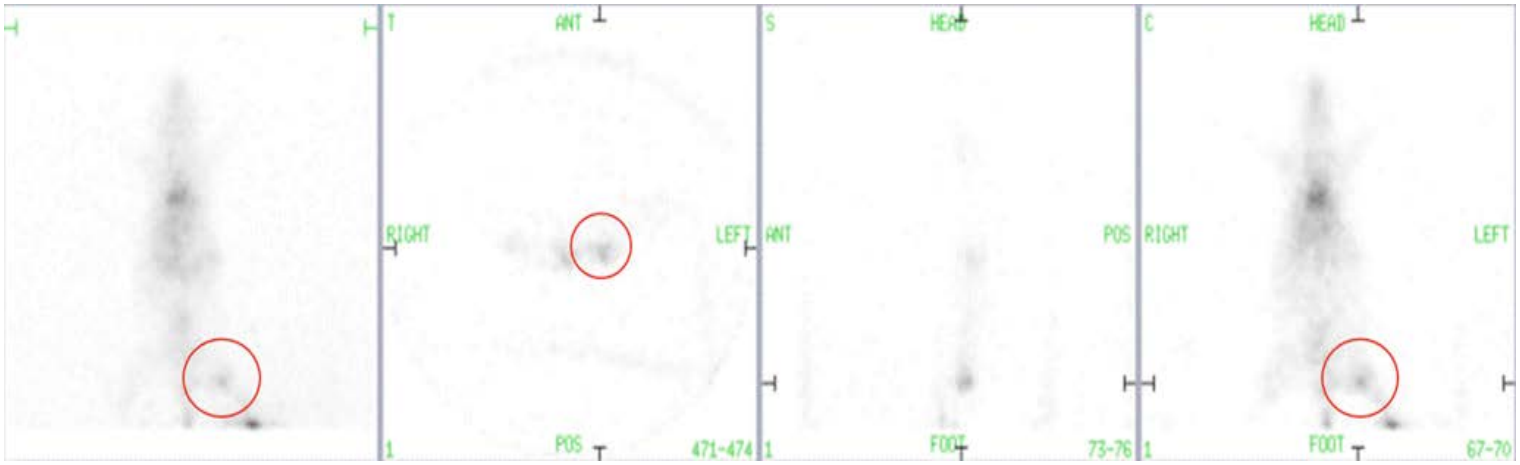

Figure 6.19: Small Animal PET images of a mouse injected (into the left foot pad) with dextran coated iron oxide nanoparticles that have been tagged with FITC and radio-labelled with ^{68}Ga. At 1 hour post injection, PET imaging was performed with C57BL/6 mouse under general anaesthesia, 2 % isoflurane and 200 ml per minute of medical air (20 % oxygen and 80 % nitrogen) with a total flow rate of 0.8 litres per minute. The area of interest (red circle) identifies the popliteal lymph node uptake of radio-active material, ^{68}Ga (radiolabelled to dextran coated IONPs tagged with FITC). The series of images are from multiple imaging perspectives.

On completion of PET imaging, the mice were killed by anaesthetic overdose. MRI was then performed, at 3.0 T, with Gradient Echo and Spin Echo pulse sequences.

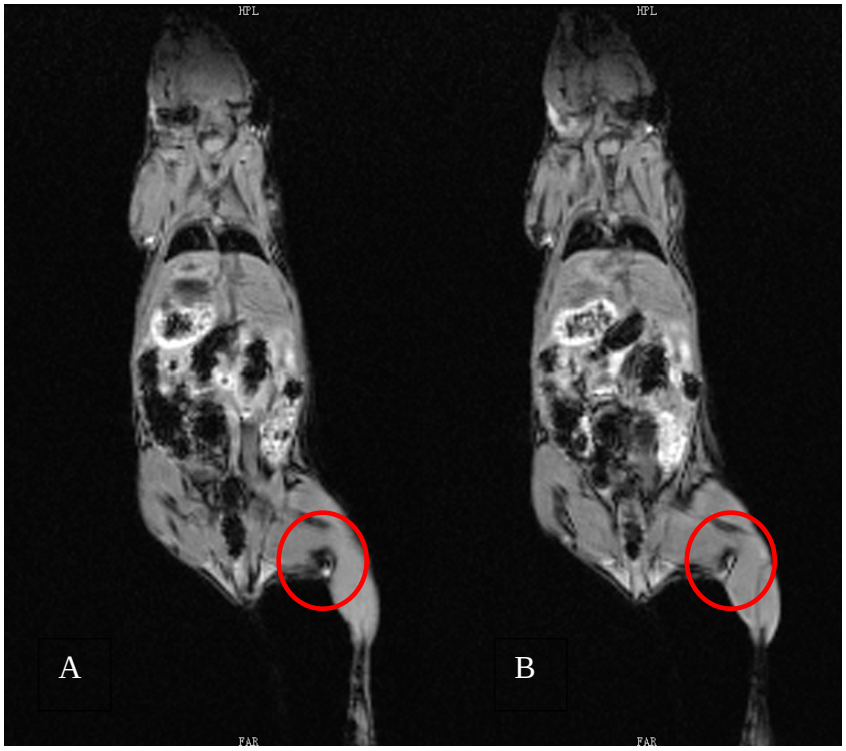

Figure 6.20: MRI images taken at 3T demonstrating identifying the popliteal lymph node (red circle) with signal intensity pattern characteristic of iron oxide nanoparticles. These images demonstrate that, with MRI, the iron oxide nanoparticles have migrated from the foot pad subcutaneous injection site to the popliteal lymph node (red circle). Importantly, also noted are the inhomogeneity imaging effects and the hypo-intense signal change; both characteristic of iron oxide nanoparticles accumulation in the popliteal lymph node. These images are of the same mouse, taken at slightly different coronal imaging levels.

The popliteal lymph nodes that appeared as hot spots on PET imaging were excised and prepared for flow cytometry as also described in Section 2.12.4.

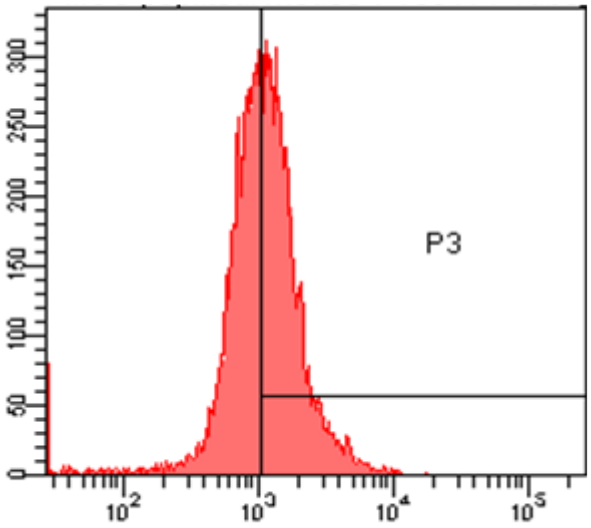

A

# Event	% Expression	MFI
5,606	53.7	1,786

B

Figure 6.21: Flow cytometry histogram (A) and data (B) indicating that 53.7% of cells extracted from the popliteal lymph node were positive for FITC and increased granularity from the iron oxide nanoparticles. On this one occasion, as a proof of concept and principle, a C57BL/6 mouse received a footpad injection of ^{68}Ga radio-labelled IONPs tagged with FITC and following 1 hour, this mouse was killed, the popliteal lymph node removed, cells extracted and prepared for flow cytometry analysis.

6.2.5 Remove lymph node positive for ^{68}Ga radio-activity and prepared for confocal microscopy.

On completion of PET imaging, the mice were killed by anaesthetic overdose. The popliteal lymph nodes that appeared as hot spots on PET imaging were excised and prepared for confocal microscopy.

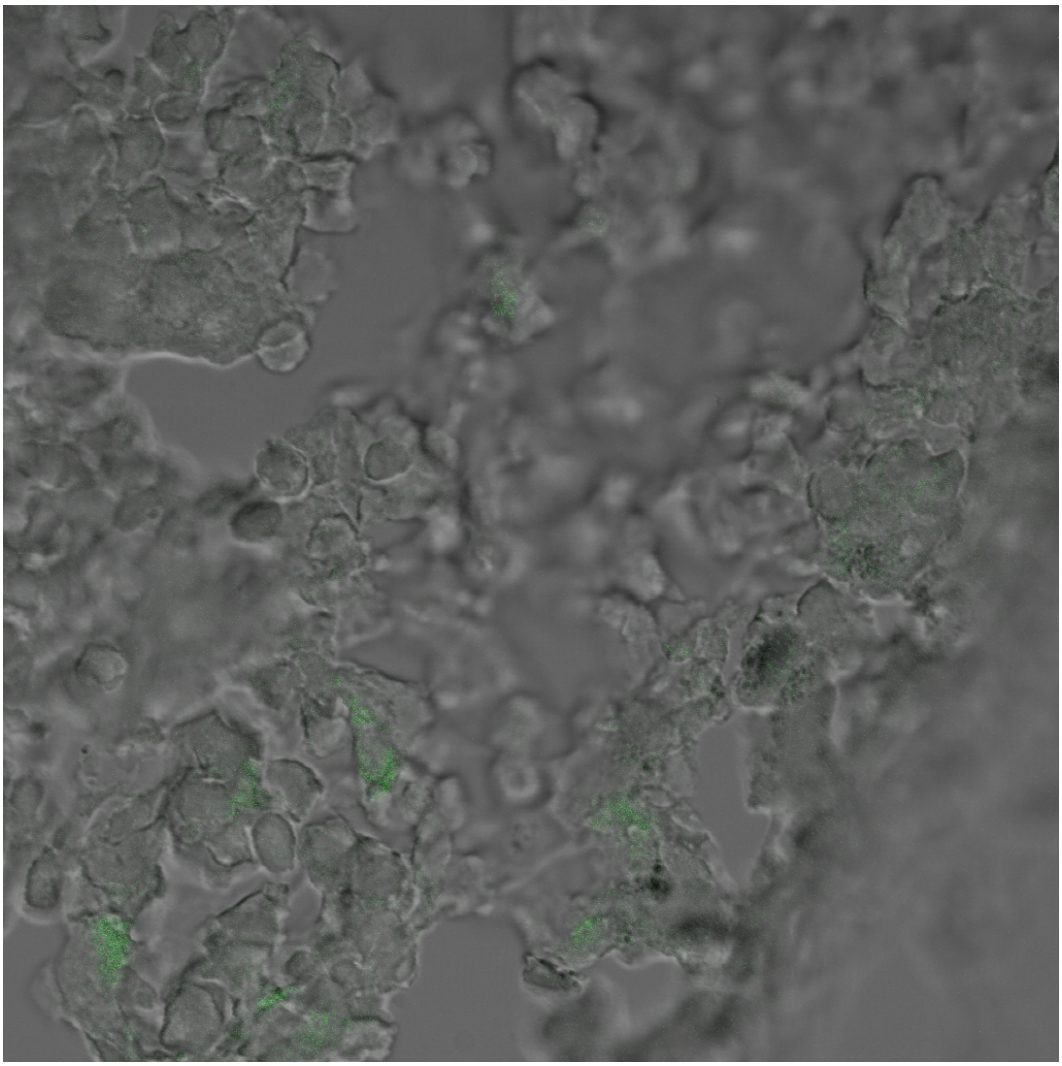

Figure 6.22: Confocal microscopy image produced with bright field and FITC laser demonstrating FITC tagged nanoparticles within cells. A C57BL/6 mouse received a footpad injection of ^{68}Ga radio-labelled IONPs tagged with FITC and following 1 hour, this mouse was killed and the popliteal lymph node was removed, sectioned and mounted on a positively charged microscope slide. Confocal microscopy imaging was performed; the fluorescent green appearance is representative of FITC and the increased black or dark regions are representative of nanoparticle accumulation within cells.

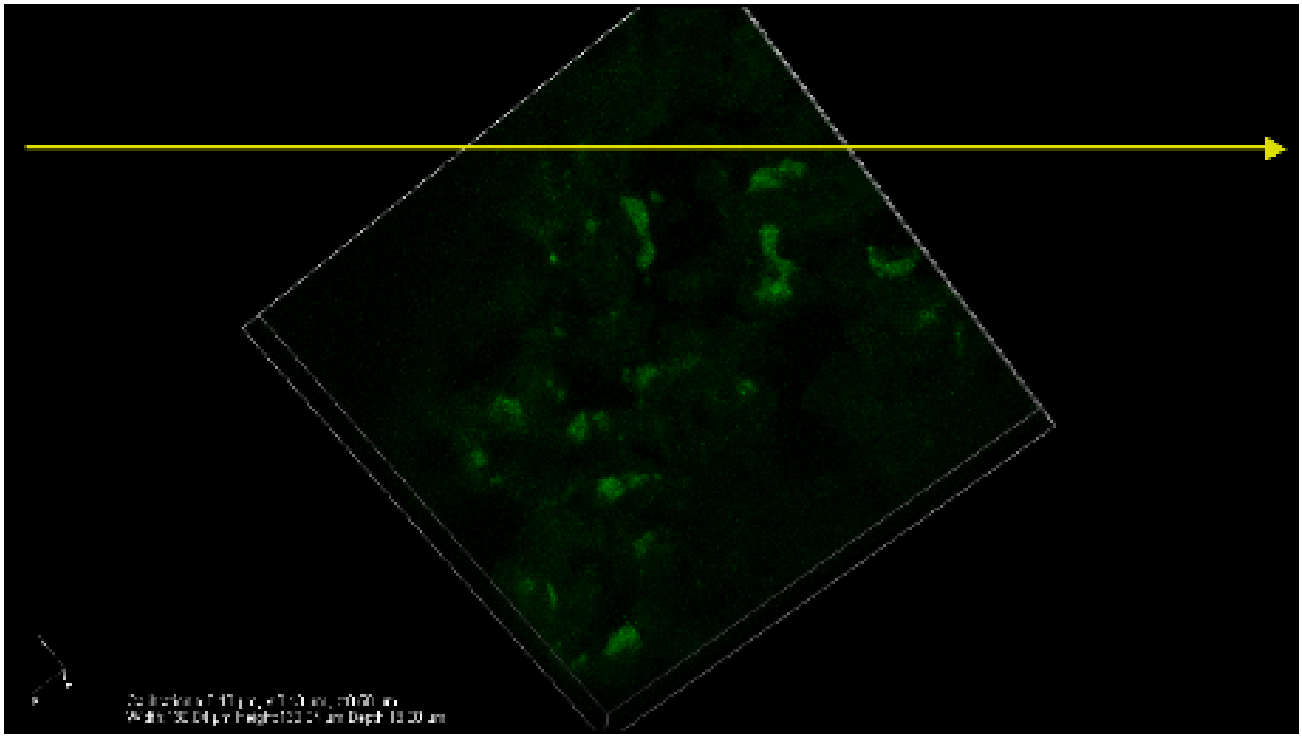

Figure 6.23: Confocal microscopy image produced with a FITC laser demonstrating FITC fluorescence from nanoparticles within cells. This image was produced from the same microscope slide used to produce Figure 6.22. A popliteal lymph node was removed from a C57BL/6 mouse, sectioned and mounted on a positively charged microscope slide. The fluorescent green appearance is representative of FITC and they appear to fill a 3D volume, presumably the internal dimensions of cells.

6.2.6 Iron oxide nanoparticles radio-labelled with ^{68}Ga injected into human patients and perform PET imaging (PET/CT) to observe migration from prostate gland to draining lymph nodes

The iron oxide nanoparticles were radio-labelled with ^{68}Ga as described in Section 2.8.7. Patients with diagnosed prostate cancer and undergoing gold seed fiducial marker implantation consented to receive the nanoparticle-^{68}Ga preparation while under general anaesthesia. Eight syringes were prepared, each with a volume of 200 µl and radioactivity ranging from between 2.5 MBq to 3.2 MBq (as measured by a dose calibrator), of which, 4 were injected into the inner prostate zone and 4 injected into the outer prostate zone.

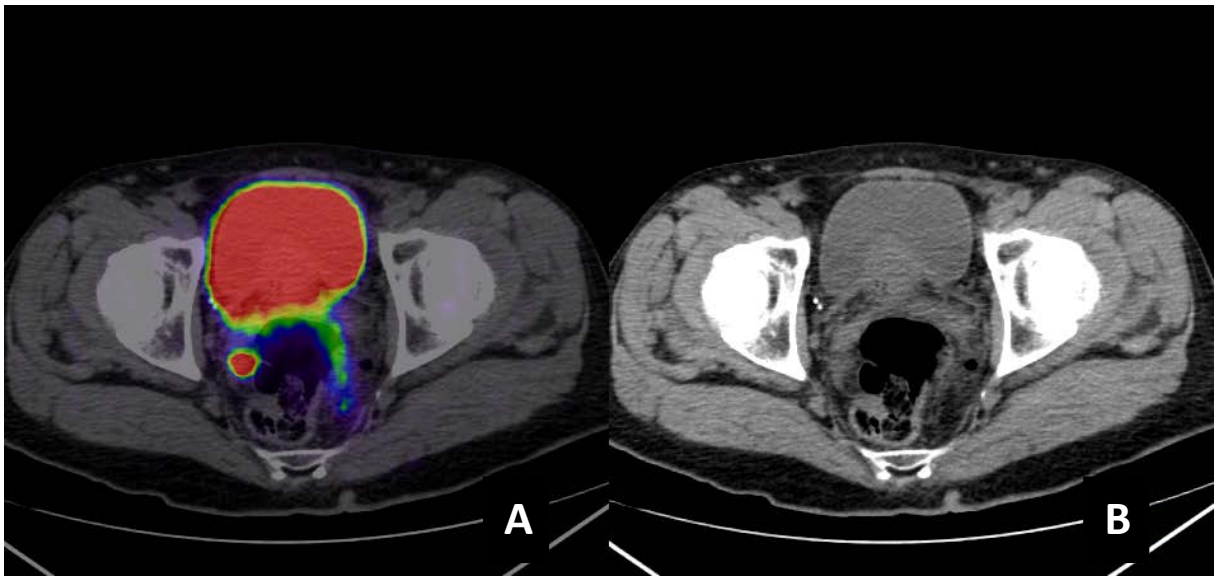

Figure 6.24: PET image co-registered with CT of a male patient following administration of nanoparticles radio-labelled with ^{68}Ga directly into the prostate gland and one hour later demonstrating radio-activity in a right sided draining lymph node (as well as the urinary bladder). The red colour signifies the greatest intensity of radio-activity by ^{68}Ga. The fused or co-registered CT image (Figure 16.24A) is a transverse slice through the pelvis at the level of the ischial spines. Figure 16.24B is the CT image only (the same as Figure 16.24A), with no overlay of PET imaging data.

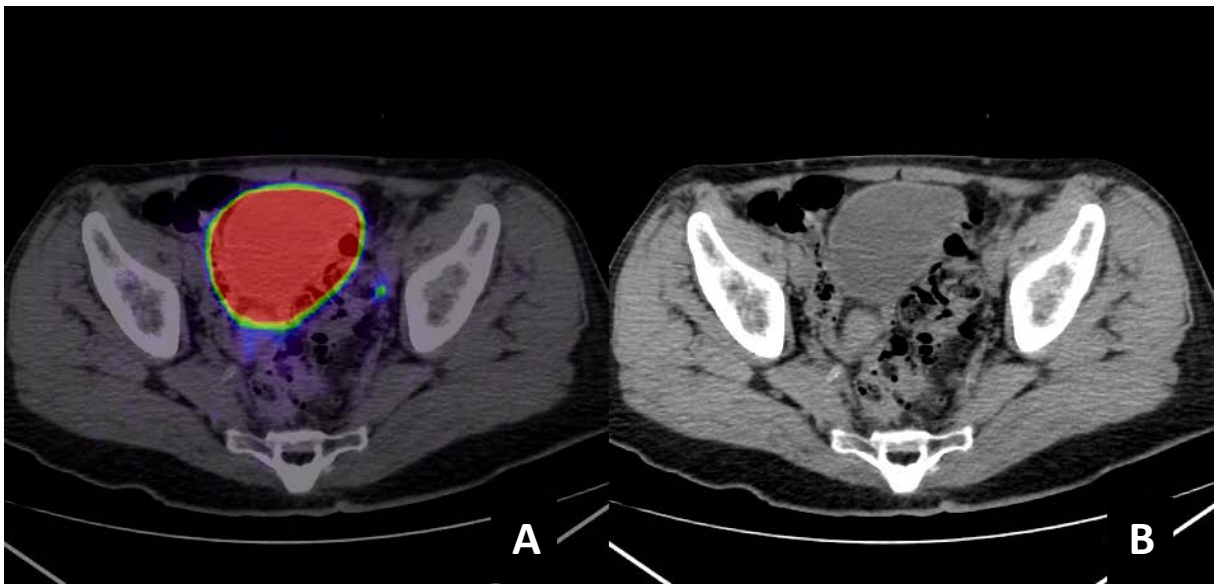

Figure 6.25: PET image (co-registered with CT) of a male patient following administration of nanoparticles radio-labelled with ^{68}Ga directly into the prostate gland and one hour later demonstrating radio-activity in a small left sided draining lymph node (as well as the urinary bladder). The red colour signifies the greatest intensity of radio-activity by ^{68}Ga. The fused or co-registered CT image (Figure 16.25A) is a transverse slice through the pelvis at the level of the ilia and lower sacrum. Without the overlay of radio-activity of ^{68}Ga obtained with PET, it would not be possible to identify this draining lymph node based on CT image (Figure 16.25B) alone.

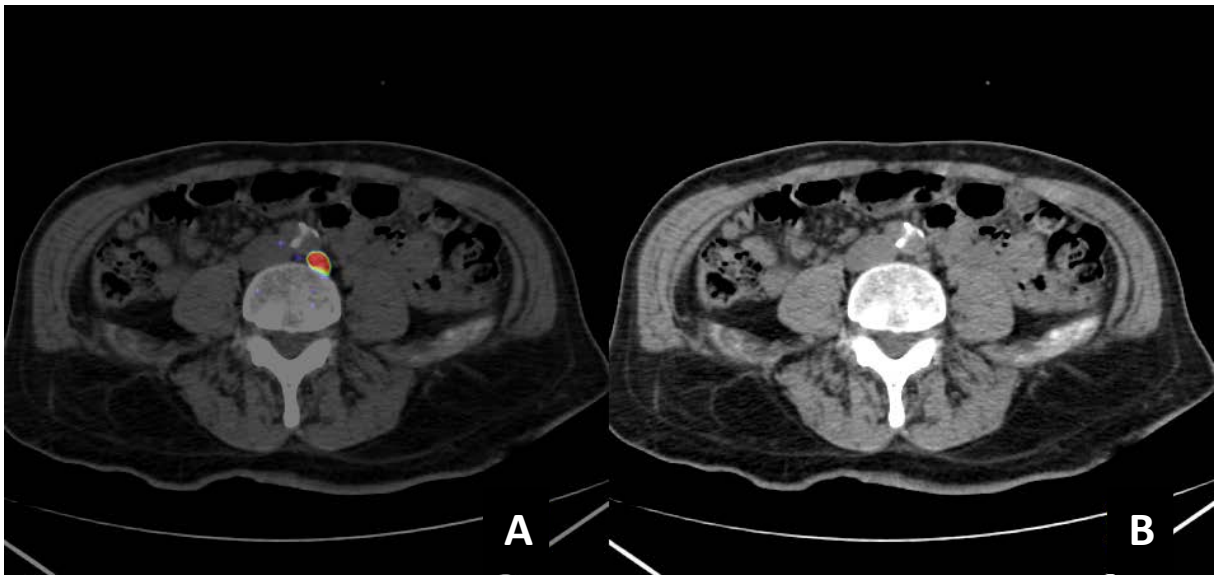

Figure 6.26: PET image (co-registered with CT) of a male patient following administration of nanoparticles radio-labelled with ^{68}Ga directly into the prostate gland and one hour later demonstrating radio-activity in a small para-aortic draining lymph node. The red colour signifies the greatest intensity of radio-activity by ^{68}Ga. The fused or co-registered CT image (Figure 6.26A) is a transverse slice through the lower abdomen, at a level superior to the iliac crests and inferior to the lower poles of the kidneys. Without the overlay of radio-activity of ^{68}Ga obtained with PET, it would not be possible to identify this draining lymph node based on the CT image (Figure 6.26B) alone as it is some distance (superiorly) from the prostate gland.

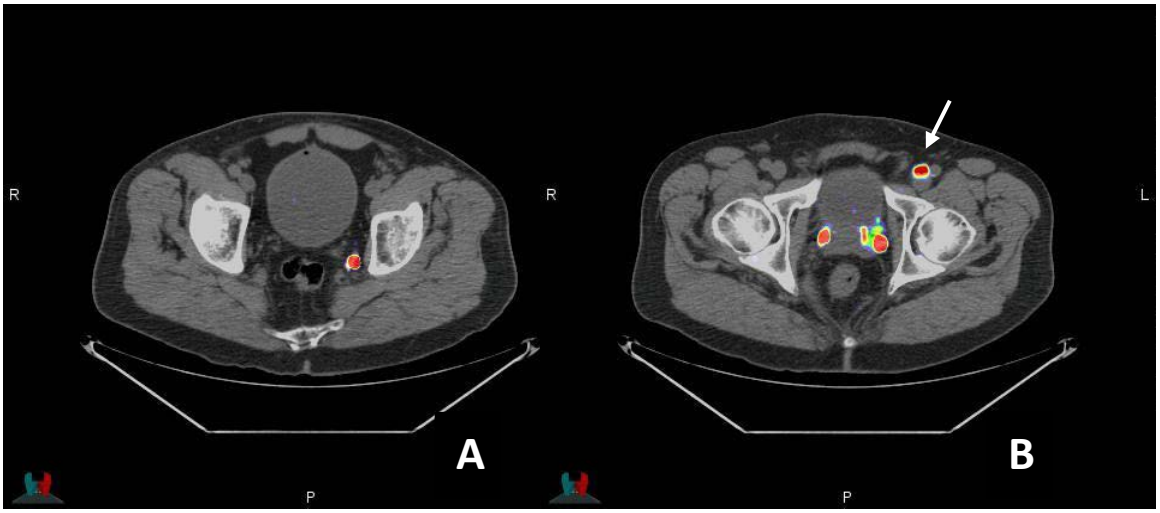

Figure 6.27: PET image (co-registered with CT) of a male patient following administration of nanoparticles radio-labelled with ^{68}Ga directly into the prostate gland and imaged one hour later demonstrating radio-activity in the draining lymph nodes. These images are of the same patient, taken at two different levels, demonstrating radioactivity from ^{68}Ga (radio-labelled to dextran coated IONPs) collecting in the draining lymph nodes of the prostate gland. Figure 6.27A demonstrates a draining lymph node nearby the prostate gland. Figure 6.27B shows more of the typical and expected draining lymph nodes adjacent to the prostate gland and, importantly, the left superficial inguinal lymph node (white arrow), which is atypical of lymphatic drainage from the prostate gland.

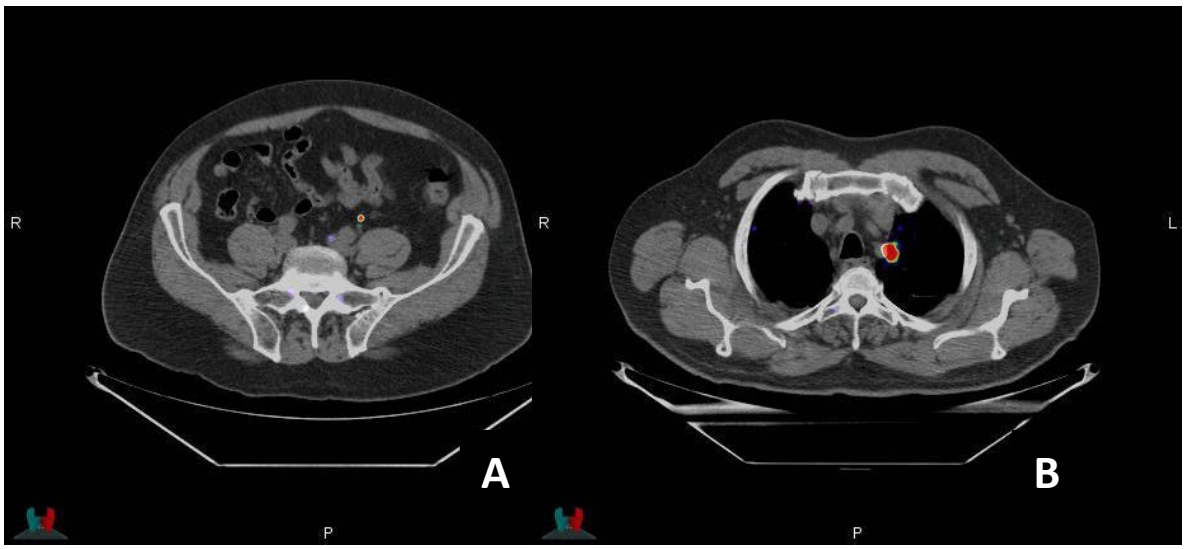

Figure 6.28: PET image (co-registered with CT) of the same male patient in Figure 6.17 following administration of nanoparticles radio-labelled with ^{68}Ga directly into the prostate gland and imaged one hour later demonstrating radio-activity in the draining lymph nodes. These PET/CT images are of the same patient, taken at two different levels, through the mid-abdomen (Figure 6.28A) and the mid thoracic cavity (Figure 6.28B), demonstrating radioactivity from ^{68}Ga (radio-labelled to dextran coated IONPs) collecting in lymph nodes draining from the prostate gland.

6.3 Discussion

There are numerous publications concerning a variety of nanoparticle preparations and *in vivo* murine studies. The results presented in Section 6.2 will be discussed relative to the most applicable publications performed with iron oxide nanoparticles, with translational potential for SLN imaging (from the prostate gland); specifically with iron oxide nanoparticles of approximately 20 nm in diameter, radiolabelled for PET imaging and also capable of imaging with MRI. Iron oxide nanoparticles have been observed, by many different imaging or detection methods, migrating from their injection site to their target site or destination. The most common imaging or detection methods includes MRI, optical imaging or luminescence (such as NIR), SPECT (if radio-labelled to a gamma emitter) and PET (for positron emitting radionuclides). The results presented in Section 6.2 demonstrate that when the iron oxide nanoparticles have reached their lymph node target *in vivo* (murine), they can be clearly identified with flow cytometry (when tagged with FITC) and with PET (when radio-labelled with ^{68}Ga) and also simply with MRI. Where the murine studies advance the knowledge presented in the current literature is with quantitation via flow cytometry and radio-labelling with ^{68}Ga; as no publications can be found with flow cytometry and FITC tagged iron oxide nanoparticles and no publications exist of ^{68}Ga being radio-labelled to these same nanoparticles. Interestingly, in December 2013, one publication was presented where ^{68}Ga was radio-labelled to PSMA ligands[299]. This publication was identified by this PhD candidate in October 2014. The laboratory notebook of this PhD candidate shows that work in this area (radio-labelling ^{68}Ga to iron oxide nanoparticles) commenced in July 2013 and was perfected in December 2013; unaware of the publication by Afshar-Oromieh *et al*[299].

Figures 6.1 and 6.2 each compare the detectable FITC (tagged to the iron oxide nanoparticles) and the granularity of cells extracted from popliteal and inguinal lymph nodes after 1 hour and 24 hours from the time of injection. At one hour post injection, 40 % of total lymph node

cells from the popliteal lymph node are positive for FITC and 45 % of inguinal lymph node cells. At 24 hours (1 day) post injection, the total lymph node cells, from mice in that specific experimental group, present a comparatively lesser value than the mice in the one hour experimental group. At 24 hours post injection, 30 % of total lymph node cells from the popliteal lymph node are positive for FITC and 40 % of inguinal lymph node cells. An explanation offered for these lesser values could be that following 24 hours, a portion of the FITC tagged nanoparticles would have transitioned through the sentinel lymph nodes (either popliteal or inguinal) and made their way to other parts of the lymphatic system. It is noteworthy that at both time points the mean and standard deviation range of the data from the inguinal lymph node is greater than that obtained from the popliteal lymph node. The most plausible explanation that can be offered to rationalise the greater mean value would be that the nanoparticles have less distance to travel when migrating from the flank subcutaneous injection site to the inguinal lymph node when compared to the hock injection site and nanoparticle migration to the popliteal lymph node. The nanoparticles used for these injections were all from the same preparation. No publications can be identified with similar or same experimental study and thus the findings presented here cannot be compared to others. The corresponding fold increase in MFI of the FITC (tagged to the nanoparticles and internalised by the cells) from the total lymph node cells also represent, and thus confirm, the same pattern observed with percentage surface expression. That is, at 1 hour post injection (Figure 6.2), the fold increase in MFI of the total lymph node cells extracted from the inguinal lymph node (fold increase of 2) is greater than the cells from the popliteal lymph node (fold increase of 3). The 50 % in fold increase (from 2 to 3), again, can, in probability, be attributed to the shorter distance that the nanoparticles need to migrate from the subcutaneous flank injection site to its draining inguinal lymph node. This same pattern is seen at 24 hours (Figure 6.2). CD11c+ cells were also specifically identified with flow cytometry from the total lymph node cell population and such cells include lymphocytes, NK cells and certain

macrophage populations – all found within lymph nodes and capable of internalising nanoparticles. The flow cytometry data, by percentage surface expression, revealed that at the 1 hour time point, twice as many CD11c+ cells from the popliteal lymph node internalised the FITC tagged nanoparticles compared to CD11c+ cells from the inguinal lymph node (Figures 6.3 and 6.4). The same figures also show that the spread of data points, the standard deviation, for CD11c+ cells from the popliteal lymph node is greater compared to CD11c+ cells from the inguinal lymph node. At the 24 hour (1 day) time point, the CD11c+ cells from both the popliteal and inguinal lymph nodes are approximately equivalent with 0.8 % and 0.7 % uptake, respectively (Figure 6.3). The correlative fold increase in MFI data (Figures 6.4) for the one hour time point differs from the percentage surface expression data. The fold increase in MFI from CD11c+ cells from the popliteal lymph node is lesser than those from the inguinal lymph node; even though by percentage surface expression, the value arising from CD11c+ cells was twice as those from the inguinal lymph node. The shorter distance from the flank to the inguinal lymph node (compared with the hock injection site to the popliteal lymph node destination) may also explain the greater fluorescence intensity captured. With respect to CD11c+ cells at the 24 hour (1 day) time point, the fold increase in MFI is relatively equal with 2.5 and 2.25 arbitrary units. One published study measured iron content in gliosarcoma brain tumours of four rats from dextran coated iron oxide nanoparticles 24 hours after intravenous administration. The iron content was found to be 0.26 μg of iron relative to the injected dose or 0.11 % of the injected nanoparticle dose[(288)], however, this was, presumably, the average iron content value detected in the gliosarcoma tumour, regardless of tumour size or the number of tumour cells in each of the four rats.

Histological tissue staining is capable of providing insight to the integrity of certain structures. Haematoxylin and eosin (H&E) stain can provide information about general cellular architecture. The H&E staining of kidney (Figure 6.6A and B), liver (Figure (6.7A and B), spleen (Figure 6.8A and B), heart (Figure 6.9A and B) and lung (Figure 6.10A and B) were assessed by an experienced and suitably qualified academic and researcher and has determined that the structural integrity of these tissue samples observed are sound and microscopically appear to be normal. A Perls Prussian blue stain identifies iron deposits; thus, with iron oxide nanoparticles, this staining technique can be used to determine if iron from the iron oxide nanoparticles was present (panels A and B in Figures 6.6 to 6.10 inclusive). It should be noted that in spleen tissue samples, naturally occurring iron deposits (due to the highly vascular nature of the spleen) can be demonstrated with Perls Prussian blue stains. Therefore, a Perls Prussian blue stain may not be the most appropriate method for assessing if iron present in splenic tissue samples have arisen from iron oxide nanoparticles. In the experimental process for this thesis, the nanoparticles were administered to mice subcutaneously and not intravascularly (venous or arterial). Iron deposits that could be attributed to the 15 nm iron oxide core from the nanoparticles were not able to be identified microscopically at 400x magnification, in the tissue samples. A Periodic Acid Schiff (PAS) stain was used specifically to detect any disruption to basement membrane (or basal laminae) of the kidneys (Figure 6.5). Tissue samples from the murine kidneys did not demonstrate any loss of integrity of the basement membrane. All tissue samples produced for H&E (kidney, liver, spleen, heart and lung), Perls Prussian blue (kidney, liver, spleen, heart and lung) and PAS (kidney) stains were obtained from all mice in the 1 hour and 24 hour experimental groups and therefore are considered to be representative.

When observing the murine spleen images (Perls Prussian blue stain) in figures 6.11 to 6.18, there are signs of haemosiderin (brown appearance) and unbound iron, Fe^{3+}, (blue appearance)[300-303]. Both presentations are normal and either are found located randomly in the spleen's white pulp, red pulp, nodule or a combination of these locations. The haemosiderin, pigment from red blood cells, infers that ferritin protein and iron (Fe^{3+}) are bound together; as haemosiderin is regarded as an iron storage complex[304-306]. Ferritin protein can be found within certain blood cells, and when bound to iron, the iron remains stored within these cells[305, 307]. Ferritin protein can also be found, unbound, in serum and in cells from the RES (liver, spleen and bone marrow)[307, 308].

The reason for this comparison (Perls Prussian blue staining of spleen and liver) is because no control mice were incorporated into the experiment design for this. Performing Perls Prussian blue and PAS stains was suggested by other researchers from RMIT University after all mice approved by the university ethics committee had been killed. The original intention was to only perform H&E staining and thus, the original experiment design included this in the following manner (to minimise the number of mice used). For each mouse, the same leg (drainage to the popliteal LN) and flank (drainage to the inguinal LN) received injection of IONPs (as described in Section 2.12.2. The contra-lateral side was not injected; therefore, each mouse served as its own control, with respect to popliteal and inguinal lymph nodes. This approach was specifically used to minimise the number of mice needed and also because the literature that was reviewed indicated that H&E staining would be sufficient to identify any damage to overall tissue architecture[295, 309]. It was only later, following consultation with other researchers and experts, that conducting additional histopathological stains; Perls Prussian blue and PAS (for kidney only) was considered. This was performed from preserved tissue specimens.

It is now acknowledged that this was not the best approach to take and that control mice specifically for Perls Prussian blue and PAS stains should have been added.

Results of imaging mice, *in vivo*, with PET and with MRI, following a footpad injection of iron oxide nanoparticles radio-labelled with ^{68}Ga was presented in Section 6.2. PET imaging occurred one hour post injection and on completion, the mouse was killed by anaesthetic overdose and then MRI scanning performed. PET image clearly demonstrates the draining lymph node from the foot pat injection site as a hot spot of increased radio-activity (Figure 6.19). From the foot pad, the popliteal lymph node is the primary draining lymph node, followed by the inguinal lymph node. The inguinal lymph node, however, receives better lymph drainage from the flank, with murine anatomy *in vivo*, as the main site. With the murine, *in vivo*, imaging data, the potential clinical utility of a positron emitter such as ^{68}Ga can be clearly noted, compared to ^{18}FDG that can accumulate in the urinary bladder and may disguise any hot spot radio-activity within nearby nodes draining from the foot pad injection site. Further still, the MRI image (Figure 6.20) is comparable with that published by Zhou *et al*[291] who used 10 nm core diameter iron oxide nanoparticles, injected into the footpad and imaging with MRI demonstrated iron oxide nanoparticles at the popliteal lymph node and confirmation performed with vital blue dye. Mori *et al* also published MRI images of iron oxide nanoparticles migrating to the popliteal lymph node following foot pad subcutaneous injection in the same strain of mice used in this thesis project, C57BL/6[310]. There were four differences tough; firstly Mori *et al* use male mice, secondly the MRI scanner had a field strength of 11.7 T, thirdly, their smallest sized nanoparticles were 50 nm and fourth, their injection site was the foot pad and not the hock. Mori *et al* also confirmed the presence of their nanoparticles in the popliteal and inguinal lymph nodes by histological means with Prussian blue staining. Despite these difference, the MRI images from this thesis and those

published by Zhou *et al* and Mori *et al* all demonstrate that, fundamentally, iron oxide nanoparticles will migrate to the draining lymph nodes, *in vivo*, and are able to be imaged with MRI.

Further to the discussion regarding flow cytometry and internalisation by cells within the lymph nodes, for this thesis, confirmation of nanoparticle presence within the lymph nodes and internalised by cells within the lymph node, when nanoparticles were tagged with FITC and radio-labelled with ^{68}Ga, the popliteal lymph node was also extracted and prepared for flow cytometry. 53.8 % of cells from the popliteal lymph node were positive for FITC from the nanoparticle preparation (IONP+FITC+ ^{68}Ga); thereby confirming the localisation of radio-labelled nanoparticles within the popliteal lymph node. Visually, this was also demonstrated with confocal microscopy video footage; from which, static images are provided in Figures 6.22 and 6.23.

Results presented in Figures 6.1 to 6.4 inclusive demonstrate unequivocally that FITC tagged iron oxide nanoparticles can migrate from hock and flank subcutaneous injection sites to the popliteal and inguinal lymph nodes, respectively. Results from Figures 6.19 to 6.21 further confirm that when the same nanoparticles are also radio-labelled with ^{68}Ga, they are also capable of reaching the draining lymph node (and imaged with PET and MRI). The iron oxide nanoparticle preparation with FITC and ^{68}Ga now provide four methods of assessment. Firstly, PET imaging can be performed due to the presence of ^{68}Ga; secondly, MRI information can be ascertained from the location of the iron oxide nanoparticles and, the FITC can be used for either flow cytometry (thirdly) or for confocal microscopy (Figures 6.22 and 6.23) imaging (fourth) or both. This can be considered a ground breaking achievement, as there is only one published study incorporating ^{68}Ga for PET imaging with mice, *in vivo*, specifically addressing the needs of prostate cancer[299].

The use of ^{68}Ga as a PET agent is progressively being considered to be superior to other existing PET radio-nuclides for oncology applications and specifically, prostate cancer. The most common PET tracer, ^{18}FDG, has been known to be recorded with cells, other than cancer cells, that have a high metabolic rate or show high levels of activity (heart, liver and urinary bladder)[311] and has low imaging specificity[312]. Comparatively, SPECT imaging, which is currently used with gamma emitting radio-nuclides for lymphoscintigrahy, has lesser image quality (spatial resolution)[160].

Biochemical analysis of murine blood serum was also performed to correlate any findings with tissue stains. Blood was extracted from 8 week old C57BL/6 female mice from the retro-orbital sinus with a capillary haematocrit. Only one published study could be found that studied blood serum biochemistry in the same strain, gender and age mice[293]. Another study was identified that performed blood serum biochemistry in the same strain and gender of mice, however, their age was far more advanced at 6 months (approximately 24 weeks)[294]. In both of these publications, there is some variability with the biochemistry analyte values, thus making certain comparison difficult.

The analytes observed were markers for liver, kidney and pancreas and general systemic wellness. Albumin (a serum protein, AlbG) was observed and this helped evaluate the murine hydration status as well as the presence of any haemorrhage, intestinal, liver or kidney disease. Values for alkaline phosphatase (AlkP) were next recorded, as an elevation of this analyte may indicate liver damage or active bone growth or Cushing's disease. To identify any immediate injury to the liver, the alanine aminotransferase (ALT) was analysed. This is a known and sensitive indicator of active liver damage, however, it cannot indicate the source of current injury to the liver and thus, any change to this analyte should be considered with the experimental process that the mouse has undergone and should also be compared with other relevant liver anayltes. The amylase (Amy) assessment reflects the health of the

pancreas. Elevations in amylase can be an indicator of pancreatitis, however, kidney disease also cannot be excluded as an elevated amylase figure may indicate kidney this. Elevation in the total bilirubin (BiliT) level also signals liver disease (and also haemolytic conditions), bile duct pathology (cancer or obstruction) and can also point to anaemia. The creatinine concentration (CreaC) levels also provides an understanding of how well the kidneys are functioning. The importance of observing the creatinine level is that is helps to discern if the cause of elevated urea levels are related to the kidneys or not. Another analyte that provided insight to liver health was gamma-glutamyl transferase (GGT). The total protein (TP) levels found in blood serum also provided further appreciation of the murine hydration status and could be also used to further understand or confirm involvement of the liver and kidneys if they were experiencing infectious diseases. The urea, or the blood urea nitrogen (BUN), denoted the quality of kidney function. Of note was that an increased level of total protein (azotemia) could be due to a variety of causes and can signify involvement of one or more organs. Elevated total protein levels could be caused by the kidneys, liver, or heart disease and could also be due to urethral obstruction, shock or dehydration.

The most appropriate comparison of the thesis experimental biochemistry data can be made with the results published by Mazzaccora *et al*[293], as both sets are matched for strain and gender and closely matched for murine age as well. In general, the liver and kidneys would be the organs most likely to suffer any acute adverse effects from contrast agents administered intravascularly; however, under the experimental process described in this thesis, the mice received subcutaneous injections of nanoparticles. With respect to the liver, an elevated alanine aminotransferase level defines acute injury and this is not the case at either 1 hour or 24 hours, as both these values are less than the value published by Mazzacora *et al*[293] and Schnell *et al*[294]. Other analytes that indicate liver health also were not elevated; these were alkaline phosphatase (no liver damage), total bilirubin (no active liver disease) and gamma-glutamyl transferase thus confirming good general liver health. Mazzacorra *et al* did not

provide values for the following analytes that also provide insight into liver health and therefore, data was compared to that published by Schnell *et al*; albumin levels indicate no liver disease present and the degree of total protein recorded also indicated no liver infection. Analytes to assess kidney well-being were also recorded, of which, some were assessed in combination with the liver indicators. The value recorded for albumin specifies no kidney disease was present at the time and the amount of amylase revealed no kidney infection. The total protein value observed also parallels the value published by Schnell *et al* and supports the amylase result of no infection of the kidney. The quality of kidney function was assessed by the blood serum creatinine concentration and the urea (or blood urea nitrogen) quantities. The creatinine figure is compliant with that published by Mazzaccara *et al,* implying that the quality of kidney function is normal. This is, however, countered by the amount of urea identified; approximately 19 times more than the value reported by Mazzaccara *et al* and about 5 times more than Schnell *et al*, however, the PAS stain of all the kidney tissue samples of all mice demonstrate no disruption to the integrity of the basement membrane. Therefore, the value of urea recorded is confounding in these circumstances and also in relation to other kidney associated analyte values of a comparably normal range. Furthermore, as analytes change greatly with age, some increase while others decrease[(293)], it is difficult to arrive at a confident understanding.

The results of *in vivo* (murine and human) imaging presented in this thesis, when assessed collectively, offer the potential of a PET/MRI imaging agent in the form of iron oxide nanoparticles radiolabelled with ^{68}Ga. Murine, *in vivo,* PET imaging provided valuable insight to the possibility of iron oxide nanoparticles being used as a carrier for the ^{68}Ga radio-isotope; as well as exploring potential as a combined PET/MRI imaging agent. This is in keeping with publications in this field. A recent publication by Bal *et al,* focussing solely on PET imaging for early detection of small tumour lesions within the prostate gland and early metastatic spread to draining lymph nodes, discuss the need for more sensitive and specific

positron emitting PET radiotracers along with improved PET spatial resolution with pixel sizes of 2 mm (along with resolution recovery and time-of-flight image reconstruction)[312]. Bal *et al*, however, do not discuss in depth the superior spatial resolution capabilities offered by MRI, either through fusion of images or through hybrid imaging in the form of PET/MRI. MRI can easily achieve voxel dimensions of 1 mm^3.

Thorek *et al* creatively modified existing FDA approved ferumoxytol (17 nm to 35 nm in diameter), Feraheme™, and radio-labelled it with ^{89}Zr and referred to these particles as ^{89}Zr-ferumoxytol[279]. These radio-labelled nanoparticles were laparoscopically inoculated into the prostate gland of Hi-Myc transgenic mice. PET/CT was performed 6 hours later and this was followed with MRI. Their results demonstrated that the PET component of PET/CT can detect the radio-activity from ^{89}Zr and that MRI can identify the signal intensity changes from the presence of Feraheme™.

With respect to prostate cancer, detailed imaging, can provide additional benefits to patients and clinicians compared with currently available techniques. These include early diagnosis, correct staging and monitoring of treatment. Since 2008, there have been a number of publications advocating the need for improved PET imaging techniques in relation to prostate cancer[313-316]. Currently, the most widely used PET radiotracer is ^{18}F-FDG, is not entirely suitable for localising primary tumour lesions within the prostate gland due to low tumour uptake (specifically, primary prostate cancer) of ^{18}F-FDG, low specificity and imaging interference from high radio-activity of ^{18}F-FDG accumulating and emanating from the urinary bladder.

The first publication of a multi-centre prospective clinical trial of patients using iron oxide nanoparticles to image lymph nodes with MRI was published in 2003[317]. To this date, there is no FDA or TGA approved nanoparticle preparation for lymph node imaging with MRI and there is also no FDA or TGA approved single contrast agent for combined PET/MRI imaging.

In relation to prostate cancer, the combined imaging results from this thesis demonstrates successful migration from the prostate gland to the draining lymph nodes in 4 consecutive patients. The radio-activity of between 2.5 MBq to 3.2 MBq (per injection into the prostate gland and there was a total of 8 injections (4 into the inner prostate zone and 4 into the outer prostate zone) from the ^{68}Ga (approximately 1 hour post administration) was capable of being identified with PET imaging within the draining lymph nodes. The imaging results with developed platform of iron oxide nanoparticles with ^{68}Ga, has demonstrated translational potential for imaging the draining lymph node from the prostate gland in patients. Figures 6.24 to 6.28 inclusive, PET/CT images, demonstrated that the IONPs radiolabelled with ^{68}Ga that had been injected into the prostate gland, were capable of migrating to the immediate draining lymph nodes. Figures 6.24 to 6.27 were taken at one hour post injection and the lymph nodes that typically drain the prostate gland were readily visualised. Figure 6.27B, specifically, and importantly, demonstrated the left superficial inguinal lymph node. This lymph node is not routinely resected for metastatic stagging as it is outside of the extended pelvic lymphadenectomy surgical region[318], however, for this patient, it would be of benefit to do so as this lymph has an association with lymphatic drainage of the prostate gland. From the prostate gland, lymphatic drainage is considered to be along a lateral pathway to the obturator lymph nodes and from there, metastases can progress to the middle and external iliac lymph nodes[319]. Metastatic positive lymph nodes in other regions are considered to be rare, however, published literature has been steadily emerging that challenges this established idea. In 2007, Weckermann *et al* stated that by excluding surgical sampling of lymph nodes from the pre-sacral, common iliac and retroperitoneal regions, the missed rate of metastatic detection can be as much as 63%[320]. A study by Mattei *et al*, in 2008, identified the superficial inguinal lymph to be positive for metastases in 0.6% of cases[321]; while in 2010, Ganswindt *et al* published their imaging findings, which observed the superficial inguinal lymph nodes to receive lymphatic drainage from the prostate gland in 0.3% of cases with

SPECT[322]. Independently of each other, Briganti *et al* (in 2012) and Joniau *et al* (in 2013) identified metastatic positive lymph nodes in the para-aortic and inferior vena cava regions in up to 15% of cases in patients positive for prostate cancer.

At two hours post injection, Figures 6.26A, 6.28A and 6.28B demonstrated that distant lymph nodes in the abdomen and in the mediastinum/thoracic cavity could be identified (using PET/CT and the T10 dextran coated IONPS radiolabelled with ^{68}Ga. As the lymphatic drainage pathway is variable and unique with each patient, the process presented here (T10 Dextran IONPs radio-labelled with ^{68}Ga, injected into the prostate gland and imaged with PET/CT) proved that a definite gain in understanding was achieved, regarding the identified lymph nodes involved with lymphatic drainage of the prostate gland – the typical and atypical lymph nodes as well as those geographically near to the prostate gland and also distant. This, therefore, introduces the realistic possibility of improving the efficacy of lymphadenectomy for metastatic staging, individualised for each patient. Thus, the imaging data collected with PET/CT allows at least three key points to be realised. Firstly, the draining lymph nodes from the prostate gland can be identified with the PET imaging component of a PET/CT scanner. Secondly, the time frame of one hour (from injection to PET imaging) is sufficient to allow the ^{68}Ga radio-labelled nanoparticles to migrate from the prostate gland to the draining lymph node. Thirdly, the radio-activity used is appropriate as it is readily detected by PET.

Two studies have been published using a prostate specific membrane antigen (PSMA) radio-labelled with ^{68}Ga demonstrating localised tumour lesions within the prostate gland. One of these studies, directly compared ^{68}Ga with ^{18}F-FECH as PET imaging agents for prostate cancer in the same patient (with elevated PSA and clinical suspicion of prostate cancer) and that PET imaging with ^{18}F-FECH was unable to detect a tumour lesion within the prostate gland[323] whereas PET imaging with ^{68}Ga radio-labelled to PSMA was capable of identifying

a tumour lesion within the prostate gland, at the peripheral zone, adjacent to the urinary bladder[299]; thereby demonstrating the clinical utility of ^{68}Ga (with PSMA) over ^{18}F-FECH.

6.4 Conclusion

The aims of this chapter have been addressed and the experimental results lead to the following conclusions.

1. Dextran coated iron oxide nanoparticles tagged with FITC migrate from their subcutaneous site of injection to the regional lymph nodes; from the hock to the popliteal lymph node and from the flank to the inguinal lymph node; *in vivo*, in C57BL/6 female mice. The amount of nanoparticles at these lymph nodes has been assessed with flow cytometry an quantitated by percent surface expression and also by fold increase in mean fluorescence intensity; in lymph node cells and also in CD11c+ cells from these lymph node cells.

2. Biochemical analysis of blood serum showed that all analytes that were measured, signified healthy functioning and no acute physiological distress. There was, however, on confounding value – elevated urea was recorded, however, other analytes indicate the mice had normal functioning kidneys with no disease or infection present at the time.

3. H&E and Perls Prussian blue stain demonstrate sound cellular integrity of heart, lung, liver, kidney and spleen tissue at 200X magnification. PAS stain of kidney tissue demonstrates an intact basement membrane, at 400X magnification. The PAS stain also reveals PAS positive staining of the brush border within the proximal tubules most likely due to PFA being delivered under pressure during the VPF procedure. This cannot explain the elevated urea level because the VPF was performed after the blood sample was taken from the mice.

4. Murine, *in vivo*, PET imaging, one hour post foot pad injection with dextran coated iron oxide nanoparticles tagged with FITC and radio-labelled with ^{68}Ga, demonstrates drainage to the popliteal lymph node. Flow cytometry quantitated the FITC coated nanoparticles in cells extracted from the popliteal lymph node.

5. Confocal microscopy confirms FITC coated nanoparticles are within cells from the popliteal lymph node.

6. Dextran coated iron oxide nanoparticles radio-labelled with ^{68}Ga that was injected into the prostate gland of 4 patients diagnosed with prostate cancer, with their consent and with human ethics approval from the hospital, demonstrated drainage to the sentinel lymph node and nearby lymph nodes as imaged with PET/CT.

7.0 Chapter 7 – Conclusions and Future Directions

7.1 Summary

This thesis has presented information pertaining to the assessment and imaging applications of iron oxide nanoparticles. A literature review, applicable to this project, identified how nanoparticles, together with MRI, are being used in novel and innovative ways to potentially improve patient health outcomes by advancing diagnostic imaging capabilities; thus aiding clinicians and patients determining the most appropriate treatment options and any such treatment options can be tailored and specific to individual patient circumstances.

For this thesis, IONP were produced, coated with T10 dextran, suspended in gel at different concentrations and MRI T_2 characteristics were assessed with 1.5 T and 3.0 T clinical MRI scanners. At the cellular level, *in vitro* experiments were performed with murine and human immune cells to ascertain the effect of these IONPs with cell viability, dose dependent uptake and time dependent uptake. The amine chain of the T10 dextran coating functionalised with aqueous ammonia to facilitate conjugation with either FITC or R-PE so that flow cytometry quantitation could be determined. The cytokine expression by the cells tested, *in vitro*, was also studied.

In vivo experiments were also performed with C57/BL6 mice and most valuably with patients diagnosed with prostate cancer. A series of i*n vivo* murine experiments involved subcutaneous injections of FITC tagged IONPs and flow cytometry evaluation of popliteal and inguinal lymph nodes, biochemical analysis of blood serum (from the retro-orbital sinus) and histopathological stains (H&E and Perls Prussian Blue) of their liver, spleen, heart and lung. The kidneys were also analysed with a PAS stain in addition to H&E and Perls Prussian Blue. The gamma emitting radio-iosotope, ^{68}Ga, was radio-labelled to the functionalised T10

dextran coating of the IONPs and also radiolabelled to the FITC tagged IONPs. Further murine *in vivo* experiments were conducted with the IONPs tagged with FITC and radiolabelled with ^{68}Ga; they were administered into the footpad and later imaged with a SA PET and then with 3.0T MRI. The non-FITC ^{68}Ga radio-labelled IONPs were directly injected into the prostate gland of prostate cancer patients (using ultrasound imaging guidance while the patients were under GA for radiation therapy gold seed implantation) and imaged with PET/CT. The importance of this procedure (performed in four patients) was to determine that the lymph nodes draining the prostate gland were able to be identified and imaged; the radio-labelling of ^{68}Ga remained intact with the IONPs while travelling *in vivo* and that the intensity of the radio-activity (the gamma radiation decay) was able to be identified and imaged using the PET imaging component of the PET/CT scanner (no PET/MRI scanner is currently available in Australia).

7.2 Overview

In determining and classifying metastatic staging, the relevant lymph nodes are always assessed, either with imaging or with surgical removal or both. When surgically excised, the lymph nodes undergo histopathological evaluation. Various imaging modalities and their unique techniques are designed to each add their own dimension to the overall diagnosis of a cancer and its metastasis. An obvious progression and benefit would be to devise and introduce a methodology or technique that will provide the advantages of many of the multi-layered imaging techniques into one; thereby saving time and money within the healthcare sector and assisting clinicians more timely and with more relevance. The inclusion of T10 dextran coated IONPs radio-labelled with ^{68}Ga with either PET alone or MRI alone or

PET/MRI combined, can provide an improved role in identifying lymph nodes, *in vivo*. Previously, cellular MRI (cMRI) demonstrated promise in understanding cell-to-cell interaction during cancer research, patient trial and pre-clinical stages; however, currently some limitations exist which may be overcome by the T10 dextran coated IONPs radio-labelled with ^{68}Ga preparations. Therefore, the clinical utility of nanoparticles, PET imaging, MRI and cellular MRI is becoming more crucial in understanding the cellular interactions involving cancer metastases and the path that cancer cells take, and can take, through the human body; in particular, correctly recognising all draining lymph nodes, including those distant from the primary site.

7.2.1 Characterisation of IONPs in the clinical magnetic environment, radiolabelling with ^{68}Ga and *in vitro* cytotoxicity

A review of the available literature allowed this author to determine ideal composition and dimension needed for nanoparticles to be used as intended for experimental processes. IONPs were manufactured in a chemistry laboratory within RMIT University, containing an iron oxide core and T10 dextran coating. The dextran coated contained amine chains that could be functionalised with aqueous ammonia to facilitated conjugation with either FITC or R-PE or ^{68}Ga, or, FITC and ^{68}Ga together; thereby increasing their innovative applications.

The physical characteristics of the T10 dextran coated IONPs were assessed with TEM and SEM. Their surface charge (mV) wase also measured, after being stored under a variety of laboratory storage conditions. T2 relaxometry data was generated with the same T_2 weighted spine echo pulse sequence incorporating 16 echo times (TE) each spaced at 22 ms intervals, performed at 1.5 T and 3.0 T. Graphs were produced that represented this data in a unique manner and graphs of these kind have not been available in the current literature. Firstly, as the echoe times within the pulse sequence are known to be separated by a time of 22 ms, a power trendline can be used as a line of best fit; where as in the literature a mono-exponential decay is almost always assumed and an exponential decay line added. Secondly, T2 decay of the tested IONPs was presented on three dimensional graphs, the y-axis showing ΔT_2, the x-axis showing the TE times and the z-axis showing the IONPs concentration suspend in gel. One of these graphs was generated for data obtained at 1.5 T and another graph for data from 3.0 T. These graphs informed this author how to be optimise MRI parameters to maximise image contrast and also which concentration of IONPs would provide the best possible image contrast due to contrast material (inhomogeneity effect).

It was also demonstrated that ^{68}Ga could be radio-labelled to functionalised IONPs, thereby providing further imaging opportunities in addition to MRI, namely PET. This also presented

the real possibility of dual modality contrast agent; PET/MRI; and this principle was demonstrated with *in vivo* murine experiments.

The cell viability of T10 coated IONPs was assessed with the Promega CellTiter96® AQueous One Solution Cell Proliferation Assay. The IONPs were tested with murine and human immune cells; and also compared with the known safest gadolinium based MRI contrast agent currently available, using human PBMCs.

7.2.2 Characterisation of IONP uptake by murine derived DCs, *in vitro*

Bone marrow stem cells from C57/BL6 mice were collected and incubated with GM-CSF (a protein that acts as a cytokine) to generate immature DCs. GM-CSF cells; mimic or behave like myeloid DC, which is a conventional type of DC. It has a myeloid lineage, most abundant of the DCs, they take up antigen, activate T cells and migrate to lymph nodes. Flt3 (also a protein with cytokine effects) was used with C57/BL6 to also develop an immature type of DC, however, these DCs are known to mimic *in vivo* DC and appear to possess characteristics of both myeloid and plasmacytoid DC (they mimic or behave like human DCs *in vivo*). The understanding gathered from *in vitro* studies with these two types of DCs provided knowledge in preparation for *in vitro* studies with human DCs.

Dose dependent *in vitro* experiments were conducted to assess the level of internalisation of FITC tagged IONPs by GM-CSF induced and Flt3 induced, murine DCs; while time dependent uptake experiments identified the time point (between 1 hour and 24 hours) at which these DCs internalised FITC tagged IONPs to maximum capacity (from a

concentration of 200µg/ml); as measured with flow cytometry by identifying the granularity of cells containing FITC.

Once IONPs were internalised by these DCs, investigations measured specific cell developmental process and activity. The cell maturation process was tested; to determine if the immature DCs were made to mature in the presence of IONPs. once the DCs internalised the IONPs, apoptosis investigations identified the population of DCs that were healthy and viable and those that were in either early or late stage apoptosis and the DCs population that had become non-viable (dead or necrotic). The supernatant from the dose dependent *in vitro* experiments were collected and the secretion of inflammatory cytokines by DCs in the presence of IONPs, were measured using a Mouse Inflammation Kit BD™ Cytometric Bead Array (CBA) kit.

7.2.3 Characterisation of IONP uptake by human derived DCs, *in vitro*

Blood samples from volunteers were collected and the PBMC extracted by using a gradient separation technique (Ficoll®-Paque Premium gradient centrifugation). When the PBMCs placed *in vitro*, 60 minutes later, the "adherence step" was performed; that is, monocyte cells would adhere to the bottom of the well plate, the remainder of the cells and media collected and discarded and fresh media added. Cytokines were added to the adhered monocytes to convert them to DCs, hence, Mo-DCs. Dose dependent and time dependent experiments with FITC tagged IONPs and also R-PE tagged IONPs were performed and quantitated with flow cytometry, using a multicolour assay technique to identify Mo-DCs.

Dose dependent experiments of related immune cells that partake in an immune response were also performed and assessed with flow cytometry and with the multicolour assay technique. These immune cells were PBMCs, lymphocytes and granulocytes/monocytes.

The supernatant from the *in vitro* Mo-DC dose dependent and time dependent experiments were collected and the secretion of inflammatory cytokines by DCs in the presence of IONPs, were measured using a Human Inflammation Kit BD™ Cytometric Bead Array (CBA) kit.

7.2.4 Application of IONPs, *in vivo*

In vivo assessment of the prototype T10 dextran coated IONPs (tagged with FITC; or tagged with both FITC and ^{68}Ga; or tagged with ^{68}Ga) was performed in C57BL/6 mice and in human patients diagnosed with prostate cancer.

Murine subjects received a subcutaneous injection of T10 dextran coated IONPs tagged with FITC, subcutaneously, into the hock to evaluate lymphatic drainage to the popliteal lymph node and another subcutaneous injection to the flank to ascertain lymphatic drainage to the inguinal lymph node. Under anaesthesia, blood was obtained from the retro-orbital sinus, then centrifuged to obtain the serum for biochemical analysis. At death, the heart, lungs, liver, spleen and kidneys were removed, preserved, embedded in paraffin wax, set onto positively charged glass microscope slides and stained for histopathological observation. Two samples from all organs were stained; one with H&E and the second with Perls Prussian Blue. A third sample from the kidneys was prepared with the PAS stain.

In vivo PET imaging was performed with mice that received a foot pad injection of T10 dextran coated IONPs tagged with both FITC and ^{68}Ga. Mice were then killed by cervical

spine dislocation, placed in a volume head coil and scanned with MRI at 3.0 T. This process was designed to identify the gamma ray emission provided by the ^{68}Ga and to image the inhomogeneity effect of the iron oxide, albeit, separately, as no combined PET/MRI scanner is currently available in Australia. The lymph nodes were removed and prepared for flow cytometry and for confocal microscopy, to determine the presence of FITC.

To determine if T10 dextran coated IONPs radiolabelled with ^{68}Ga could reach the lymph nodes draining the prostate gland, human patients undergoing implantation of gold seed markers into the prostate (under general anaesthesia and with ultrasound guidance) also consented to receive these IONPs. *In vivo* imaging was conducted with a PET/CT scanner, with the PET component detecting the gamma emissions from ^{68}Ga and this being co-registered with the cross-sectional CT images. The draining lymph nodes were identified.

7.3 Key findings and results

This thesis commenced with six aims. The first aim was to manufacture and characterise iron oxide nanoparticles (IONP). This aim was successfully achieved, noting that the IONPs were manufactured in one of the chemistry laboratories at RMIT University, according to a criteria that was informed by a review of the relevant literature. The IONPs were approximately 20 nm in total diameter; the iron oxide was approximately 14 nm to 15 nm and the T10 dextran coating added a further 4 nm or 5 nm. The T10 dextran provided a smooth surface which can facilitate internalisation by cells. These physical characteristics were confirmed with TEM, SEM. A zetasizer measured the surface charge of these IONPs, stored under different conditions. Relative to the cells used for *in vitro* and *in vivo* experiments for this thesis, importantly, the IONPs used were stored at 4 ^{o}C, under room air and had a surface charge of –

15.62 mV ± 9.083 (n = 6). A comprehensive assessment of how these IONPs behaved in a clinical MRI environment (1.5 T and 3.0 T) was presented in Section 3.3.3; demonstrating their change in R_2 (relaxivity intensity decay profile) and the linear fit to the T_2 relaxivity (as a function of IONP concentration). These data informed the optimisation of pulse sequences when mice were scanned following subcutaneous injection of these IONPs.

Any toxicity effects were assessed in the form of cell viability MTS assays; conducted with human PBMC, comparing these fabricated IONPs and the gadolinium based MRI contrast that has the best known safety profile. At the concentrations tested, there was no difference in statistical significance between the two contrast agents.

The second aim was to characterise IONP uptake and toxicity in murine dendritic cells *in vitro*. This was achieved through a series of *in vitro* experiments. The maximum uptake of IONPs by the myeloid-type GM-CSF derived DCs occurs with a IONP concentration of 50 µg/ml. Flt3 derived IONPs (myeloid/plasmacytoid type DC) displayed a dose dependent response to the various IONP concentrations tested. The uptake of IONPs by Flt3 derived DCs was approximately 75 % to that of GM-CSF derived DCs. Time course experiments identified that maximum uptake of IONPs occurred at 1 hour for GM-CSF derived DCs and at 4 hours with Flt3 derived DCs. Experiments relating to cell maturation and co-stimulation showed that both DC types expressed CD86 and CCR7. When the expression levels of CD86 and CCR7 of the two DC types were compared with each other; the IONPs had a stimulatory effect on both cell types, however, the effect was greater on GM-CSF derived BM-DCs, resulting in greater expression of maturation and migratory markers from GM-CSF derived BM-DCs than from Flt3 derived BM-DC. Apoptosis, programmed cell destruction and death, was assessed. The Flt3 generated DCs better tolerated the IONPs and demonstrated greater survival capabilities (under the treatment conditions) with a greater population of viable and healthy cells compared to GM-CSF derived DCs. Both dendritic cell types secreted TNF,

MCP-1 and IL-6 cytokines at levels greater than baseline or control. The secretion by Flt3 derived DCs was approximately half that of GM-CSF derived DCs. For both cell types, a migratory stimulus response occurred to the presence of IONP, *in vitro*, as MCP-1 had been noticeably released, in particular, GM-CSF derived murine DCs demonstrated twice the expression level of Flt3 derived murine DCs.

The third aim of the thesis was to characterise the migration of IONP *in vivo* with C57BL/6 mice. T10 dextran coated IONPs tagged with FITC migrated from their subcutaneous site of injection to the regional lymph nodes; from the hock to the popliteal lymph node and from the flank to the inguinal lymph node; *in vivo*, in C57BL/6 female mice. This was confirmed and quantitated with flow cytometry techniques (identification of FITC) in cells extracted from lymph nodes techniques and also imaged with confocal microscopy (FITC); when the radio-labelled (^{68}Ga) version of these same IONPs were used with mice *in vivo*, the migration from injection site to the draining lymph node was confirmed with PET imaging and then with MRI. Biochemical analysis of the murine blood serum showed that all measured analytes signified the mice were healthy functioning and not experiencing acute physiological distress. Elevated urea levels were recorded, which could not be explained in the context of other analytes and mice having access to water, therefore, unlikely that dehydration due to lack of water could not be a factor. The tissue staining techniques, H&E and Perls Prussian blue, demonstrated sound cellular integrity of the heart, lung, liver, kidney and spleen tissue. PAS stain of kidney tissue demonstrated an intact basement membrane, however, there was PAS positive staining of the brush border within the proximal tubules most likely due to PFA being delivered under pressure during the VPF procedure. This also cannot explain the elevated urea level because the VPF was performed after the blood sample was taken from the mice.

The fourth aim of the thesis was to characterise IONP uptake and toxicity in human cells *in vitro.* CD14+ and CD11c+ cells were identified and their dose dependent uptake of R-PE

tagged IONPs showed no statistical difference, following 24 hours incubation, *in vitro*, for the concentration of IONPs tested; thus both CD14+ and CD11c+ cells are equally capable of internalisation of IONPs. This was also applicable when FTC tagged IONPs were used. The time dependent *in vitro* studies demonstrated that maximum uptake of FITC tagged IONP occurred by the one hour incubation time point for both CD14+ and CD11c+ cells. A multi-colour technique flow cytometry assay identified CD11c+ and CD123+ cells with no statistical difference between the uptake demonstrated by CD11c+ and CD123+ cells for the concentrations of IONPs tested. The FITC tagged IONPs and R-PE tagged IONPs were used to identify PBMCs, lymphocytes, and granulocytes/monocytes. A CBA assessment of the supernatant from dose dependent studies and time dependent studies with human PBMCs identified that five (TNF, IL-10, IL-6, IL-1β, IL-8) of the six cytokines were expressed at levels statistically equivalent to the control condition. The expression of IL-12p70 increased with increased concentration of IONPs in the dose dependent studies and with the time dependent experiments, maximum expression IL-12p70 occurred at the 1 hour time point.

The fifth aim of this thesis was to radio-label the IONPs with ^{68}Ga. The radio-labelling efficiency of ^{68}Ga to the T10 dextran IONPs was measured by TLC to be at 87.59 % (n=3); that is, the technique used resulted in 87.59 % of the ^{68}Ga bound to the IONPs and 12.41% was free or unbound. The *in vivo* studies with murine and human subjects, followed with PET image, demonstrated that the radio-labelled IONPs were able to reach draining lymph nodes and behaved as particulate matter, providing evidence that the ^{68}Ga remained radio-labelled *in vivo*. With murine *in vivo* studies, the mice were also imaged with MRI and the lymph nodes demonstrating the image contrast effects due to iron oxide, co-incided with the lymph nodes that showed enhancement due to ^{68}Ga.

The sixth and final aim of this thesis was to perform *in vivo* studies with T10 dextran coated IONPs radio-labelled with ^{68}Ga. Human patients diagnosed with prostate cancer received

these radio-labelled IONPs while undergoing gold seed fiducial markers (used to later identify the prostate for external beam radiation therapy treatment) under ultrasound guidance. Imaging with PET/CT easily identified the nearby draining lymph nodes, as typically expected; however, very enlightening, the lymph nodes not routinely associated with draining the prostate gland and not routinely surgically removed for metastatic staging, also were positive for ^{68}Ga. These included the left superficial inguinal lymph node and also a lymph node in the mediastinum in one specific patient. The significance of these findings, which must not be under-estimated, is that these ^{68}Ga radio-labelled IONPs can be used to map the lymph nodes along the lymphatic drainage for each individual patient and clinicians can become aware of the path that the prostate cancer may take when metastasising along the lymphatic pathway in individual patients. This will also assist with determining correct metastatic staging. As demonstrated in four patients, the role in identifying the lymph nodes draining the prostate gland (with the tested T10 dextran coated IONPs radio-labelled with ^{68}Ga) is extremely valuable; as the typically geographically adjacent lymph nodes were identified and most importantly, the distant and atypical lymph nodes were also identified.

7.4 Discussion and future directions

Further optimisation of T_2 pulse sequences for imaging the effects of the IONPs would need to be conducted, as there are a multitude of pulse sequences; some are common across manufactures while others are unique to individual manufacturers. This would need to be repeated at both 1.5 T and 3.0 T, as these are the two most common magnetic field strengths found clinically. MRI scanners found in dedicated research facilities have higher field strengths and individualised pulse sequences; and this would add further complexity.

Correctly identifying lymph nodes that drain a tumour site is vitally important in properly staging metastases and evaluating suitably available treatment options. The results presented throughout this body of work demonstrates that the IONPs behaved ideally in an MRI clinical magnetic environment, at both 1.5 T and 3.0 T, providing excellent image contrast; thus, suitable as a potential alternative MRI contrast agent. When combined with ^{68}Ga, these IONPs collected in the lymph nodes draining the prostate gland in human patients; imaged with PET (from a PET/CT scanner). After reviewing the available literature, this author considers the work presented in this thesis (with respect to radio-labelling ^{68}Ga to T10 dextran coated IONPs and using these to identify lymph nodes draining the prostate gland in patients diagnosed with prostate cancer) as the first successful demonstration of this approach/method, clinically. This can potentially provide an immediate health care imaging application and can, of course, lead to improved health outcomes for patients by identifying the LNs along their own lymphatic drainage pathway. In principle, this can also provide an improvement over current lymphoscintigraphy imaging, as PET imaging is more sensitive to ^{68}Ga compared with current gamma emitters used for lymphoscintigraphy with sentinel lymph node imaging such as ^{99m}Tc. The preparation presented here, of T10 dextran coated IONPs radio-labelled with ^{68}Ga, also presents the possibility of being applied to other body regions such as breast cancer metastasis assessment to draining lymph nodes. The most promising possibility of the

T10 dextran coated IONP radio-labelled with ^{68}Ga and translational aspiration is that, from the work presented in this thesis, the logical progression would be to develop and optimise this preparation as a dedicated PET/MRI contrast agent for when PET/MRI scanning arrives in Australia.

The results presented in this thesis also allows for the reconsideration of, and advanced improved approach to, cellular MRI with DCs. DCs can be either isolated from a patient or developed *in vitro* in the laboratory from a patient's own precursor cells, then loaded *in vitro* with a nanoparticle preparation and then returned to the patient for *in vivo* cellular PET/MRI. In principle, the T10 dextran coated IONP radio-labelled with ^{68}Ga presents an innovative alternative to monitor cellular interactions from an imaging perspective. DCs, or DC progenitor cells, can be isolated from a patient, then at an appropriate stage of development, they can be loaded with T10 dextran coated IONPs radio-labelled with ^{68}Ga *in vitro* under controlled laboratory conditions and then returned to the patient for *in vivo* imaging with PET/MRI. These same nanoparticle preparations can assist with improving the role that cellular MRI can provide in understanding the interactions of immune cells in cancer processes, perhaps even introducing a new frontier of cellular PET/MRI, cPET/MRI? The T10 dextran coated IONP radio-labelled with ^{68}Ga can potentially solve current limitations with cMRI; the first several hours (post administration) can be imaged with the PET component (of a PET/MRI scanner); which can monitor DCs loaded with T10 dextran coated IONP radio-labelled with ^{68}Ga until the gamma radiation is depleted. From here, MRI can monitor the movement of cell groups by imaging the contrast effects of the iron oxide content. Up until now, imaging difficulty has occurred with using just IONPs alone or with a gamma emitting radio-isotope alone. If this can be successful, *in vivo*, it will increase our understanding of DC kinematics; migration and T-cell zone of LNs. Cellular MRI with these nanoparticle preparations can also be incorporated with other cells of interest for other

research applications and specific clinical use, thereby increasing the scope for considering the use of cellular MRI in humans.

8.0 Appendices

8.1 Appendix 1 – Change in R_2 relaxivity, and, T_2 relaxivity rate; at 1.5T and 3.0T (to support gel phantom studies presented in Section 3.2.3)

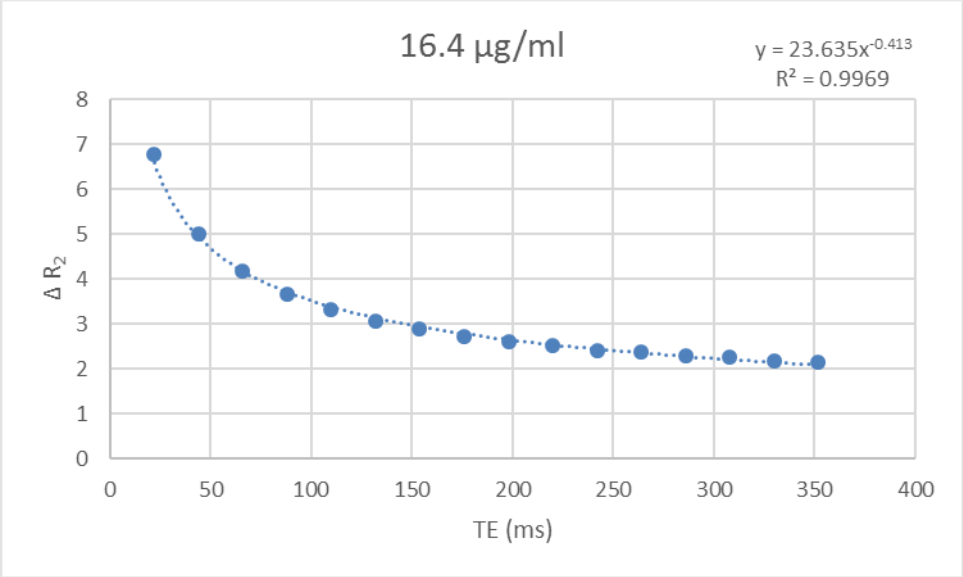

Figure 3.13: The change in R_2 relaxivity, intensity-decay profile of 16.4 µg/ml sample as determined at 1.5 T, of the dextran coated iron oxide nanoparticles has been graphed according to equation 2. A power trend line was fitted to the 16 echo data points as they were known to be exactly 22ms apart from one another. The R^2 value from the graph equation demonstrates that the curve fit is excellent. This curve was created by plotting the T_2 response of iron oxide nanoparticles at a concentration of 16.4 µg/ml to the pulse sequence t2_se_COR_16-echoes at 1.5T.

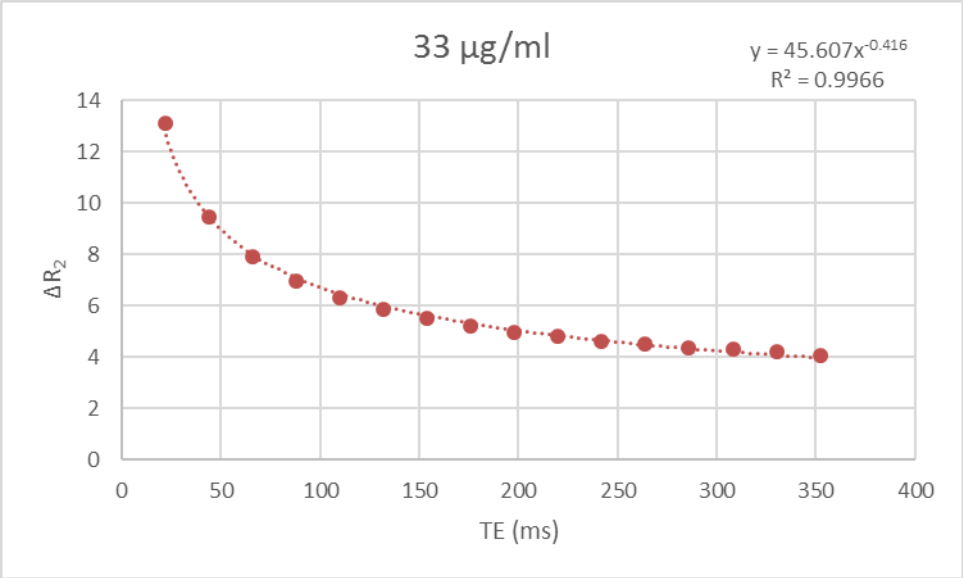

Figure 3.14: The change in R_2 relaxivity, intensity-decay profile of 33.0 µg/ml sample as determined at 1.5 T, of the dextran coated iron oxide nanoparticles has been graphed according to equation 2. A power trend line was fitted to the 16 echo data points as they were known to be exactly 22 ms apart from one another. The R^2 value from the graph equation demonstrates that the curve fit is excellent. This curve was created by plotting the T_2 response of iron oxide nanoparticles at a concentration of 33.0 µg/ml to the pulse sequence t2_se_COR_16-echoes at 1.5 T.

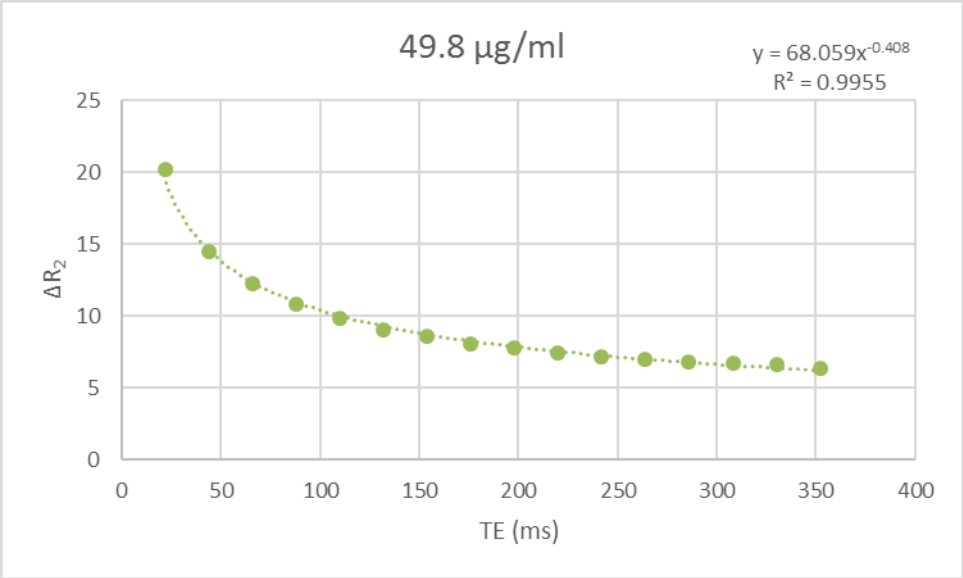

Figure 3.15: The change in R_2 relaxivity, intensity-decay profile of 49.8 µg/ml sample as determined at 1.5 T, of the dextran coated iron oxide nanoparticles has been graphed according to equation 2. A power trend line was fitted to the 16 echo data points as they were known to be exactly 22 ms apart from one another. The R^2 value from the graph equation demonstrates that the curve fit is excellent. This curve was created by plotting the T_2 response of iron oxide nanoparticles at a concentration of 49.8 µg/ml to the pulse sequence t2_se_COR_16-echoes at 1.5 T.

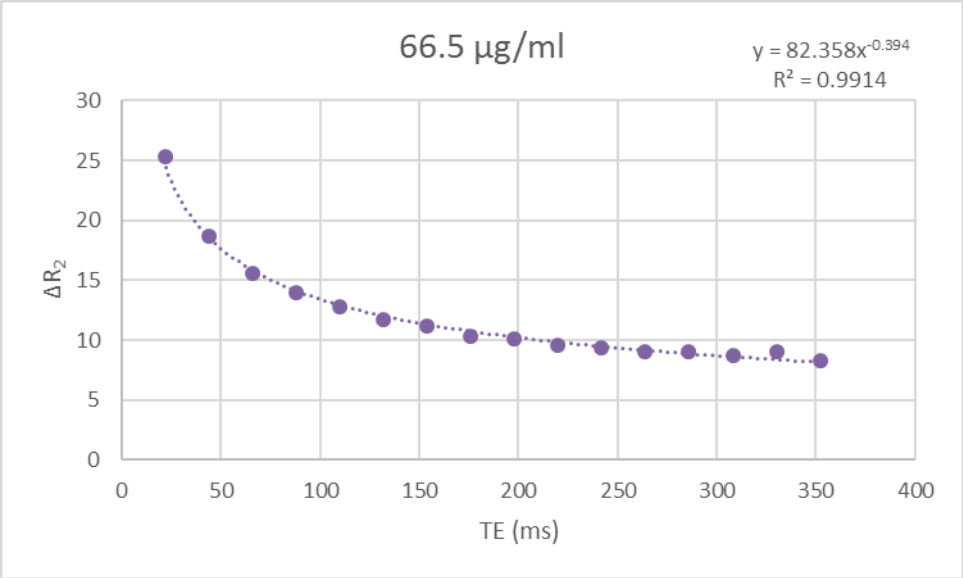

Figure 3.16: The change in R_2 relaxivity, intensity-decay profile of 66.5 µg/ml sample as determined at 1.5 T, of the dextran coated iron oxide nanoparticles has been graphed according to equation 2. A power trend line was fitted to the 16 echo data points as they were known to be exactly 22 ms apart from one another. The R^2 value from the graph equation demonstrates that the curve fit is excellent. This curve was created by plotting the T_2 response of iron oxide nanoparticles at a concentration of 66.5 µg/ml to the pulse sequence t2_se_COR_16-echoes at 1.5 T.

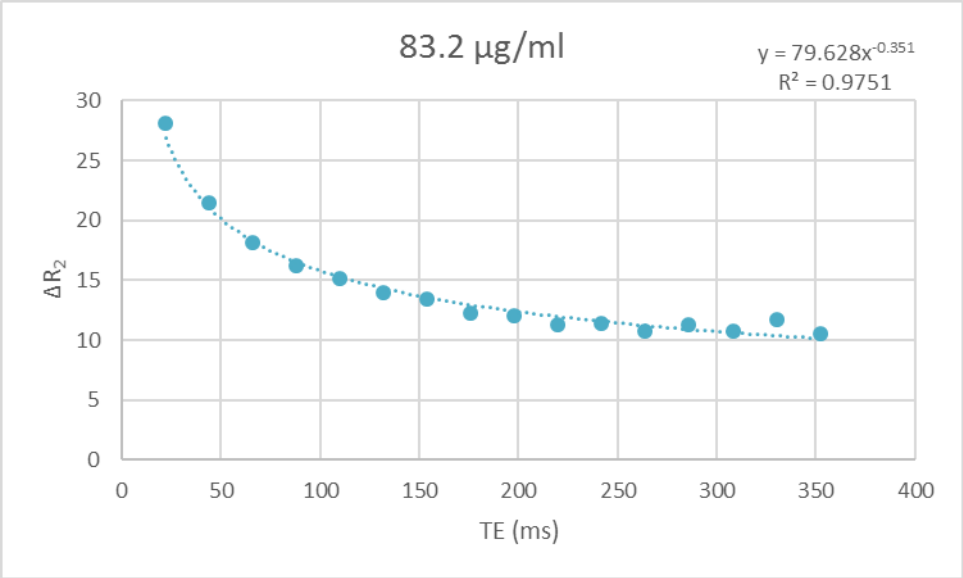

Figure 3.17: The change in R_2 relaxivity, intensity-decay profile of 83.2 µg/ml sample as determined at 1.5 T, of the dextran coated iron oxide nanoparticles has been graphed according to equation 2. A power trend line was fitted to the 16 echo data points as they were known to be exactly 22 ms apart from one another. The R^2 value from the graph equation demonstrates that the curve fit is excellent. This curve was created by plotting the T_2 response of iron oxide nanoparticles at a concentration of 83.2 µg/ml to the pulse sequence t2_se_COR_16-echoes at 1.5 T.

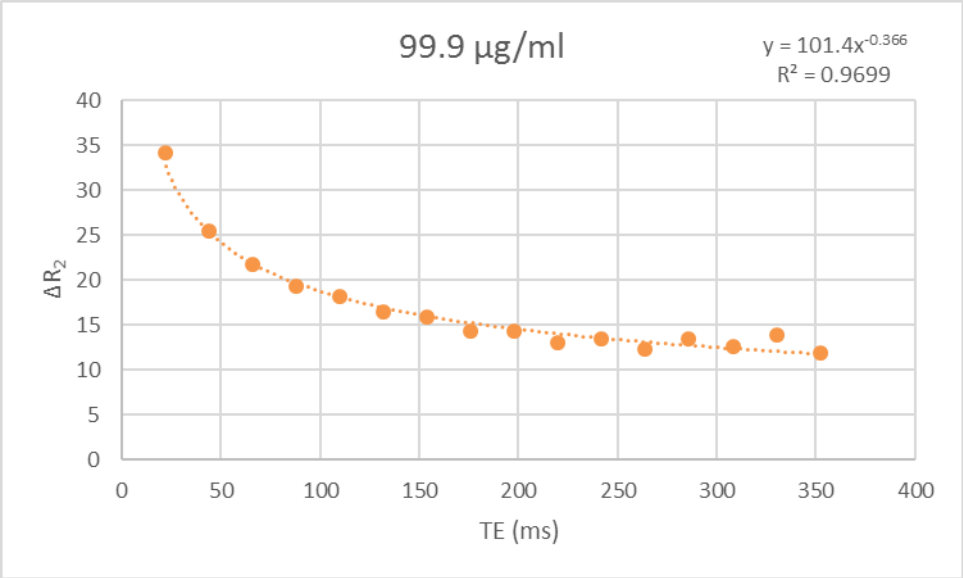

Figure 3.18: The change in R_2 relaxivity, intensity-decay profile of 99.9 µg/ml sample as determined at 1.5 T, of the dextran coated iron oxide nanoparticles has been graphed according to equation 2. A power trend line was fitted to the 16 echo data points as they were known to be exactly 22 ms apart from one another. The R^2 value from the graph equation demonstrates that the curve fit is excellent. This curve was created by plotting the T_2 response of iron oxide nanoparticles at a concentration of 99.9 µg/ml to the pulse sequence t2_se_COR_16-echoes at 1.5 T.

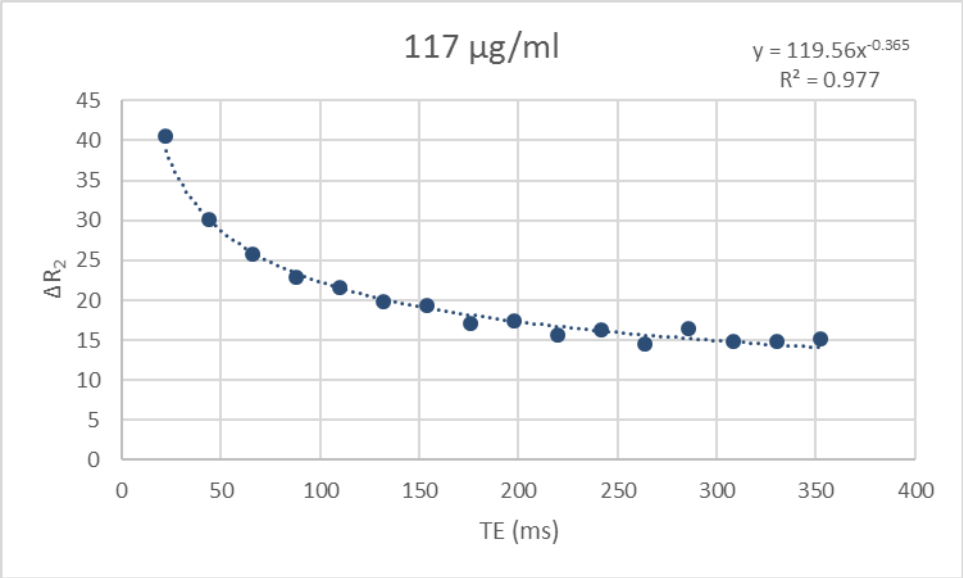

Figure 3.19: The change in R2 relaxivity, intensity-decay profile of 117.0 µg/ml sample as determined at 1.5 T, of the dextran coated iron oxide nanoparticles has been graphed according to equation 2. A power trend line was fitted to the 16 echo data points as they were known to be exactly 22 ms apart from one another. The R^2 value from the graph equation demonstrates that the curve fit is excellent. This curve was created by plotting the T_2 response of iron oxide nanoparticles at a concentration of 117.0 µg/ml to the pulse sequence t2_se_COR_16-echoes at 1.5 T.

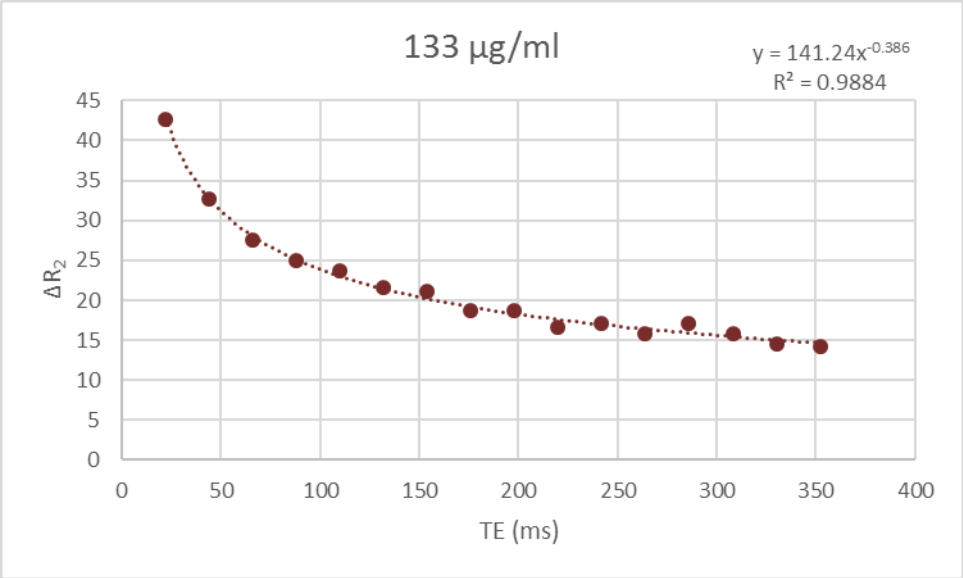

Figure 3.20: The change in R_2 relaxivity, intensity-decay profile of 133.0 µg/ml sample as determined at 1.5 T, of the dextran coated iron oxide nanoparticles has been graphed according to equation 2. A power trend line was fitted to the 16 echo data points as they were known to be exactly 22 ms apart from one another. The R^2 value from the graph equation demonstrates that the curve fit is excellent. This curve was created by plotting the T_2 response of iron oxide nanoparticles at a concentration of 133.0 µg/ml to the pulse sequence t2_se_COR_16-echoes at 1.5 T.

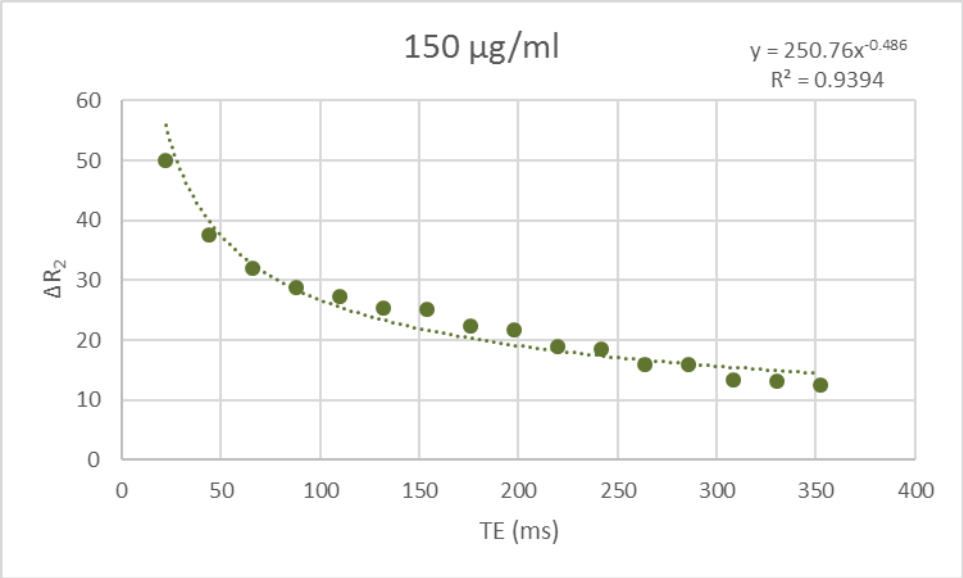

Figure 3.21: The change in R_2 relaxivity, intensity-decay profile of 150.0 µg/ml sample as determined at 1.5 T, of the dextran coated iron oxide nanoparticles has been graphed according to equation 2. A power trend line was fitted to the 16 echo data points as they were known to be exactly 22 ms apart from one another. The R^2 value from the graph equation demonstrates that the curve fit is excellent. This curve was created by plotting the T_2 response of iron oxide nanoparticles at a concentration of 150.0 µg/ml to the pulse sequence t2_se_COR_16-echoes at 1.5 T.

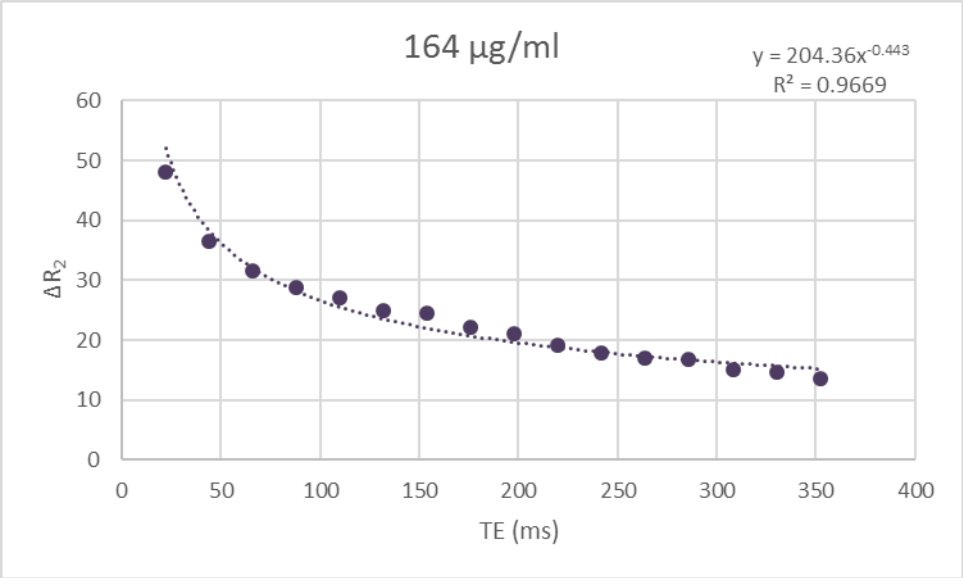

Figure 3.22: The change in R_2 relaxivity, intensity-decay profile of 164.0 µg/ml sample as determined at 1.5 T, of the dextran coated iron oxide nanoparticles has been graphed according to equation 2. A power trend line was fitted to the 16 echo data points as they were known to be exactly 22 ms apart from one another. The R^2 value from the graph equation demonstrates that the curve fit is excellent. This curve was created by plotting the T_2 response of iron oxide nanoparticles at a concentration of 164.0 µg/ml to the pulse sequence t2_se_COR_16-echoes at 1.5 T.

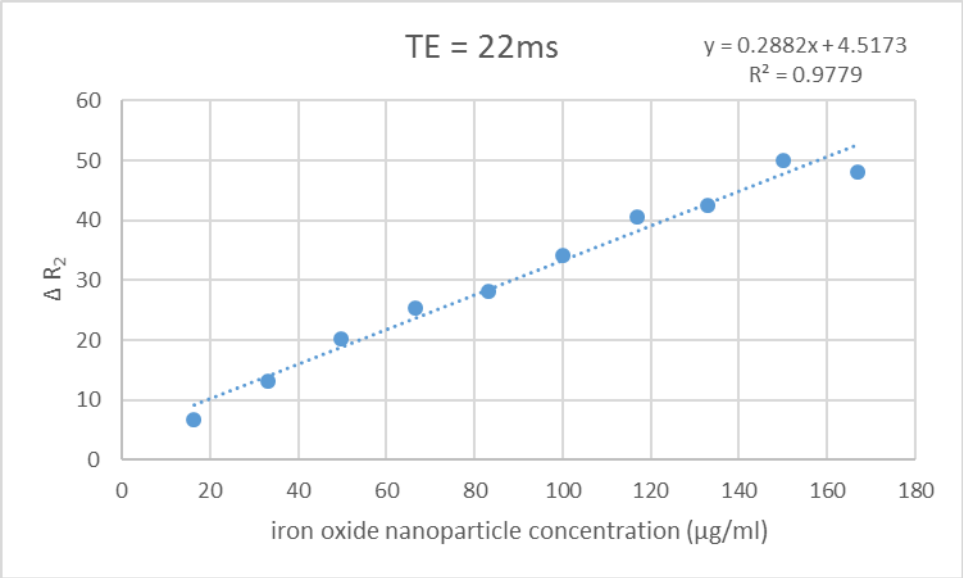

Figure 3.23: The linear fit to the T_2 relaxivity rate as a function of iron oxide nanoparticle concentration, at a TE of 22 ms at 1.5 T. A linear trend line was fitted to the plotted values of the increasing 10 concentration samples, as there is a linear dependence of the relaxation rate on concentration.

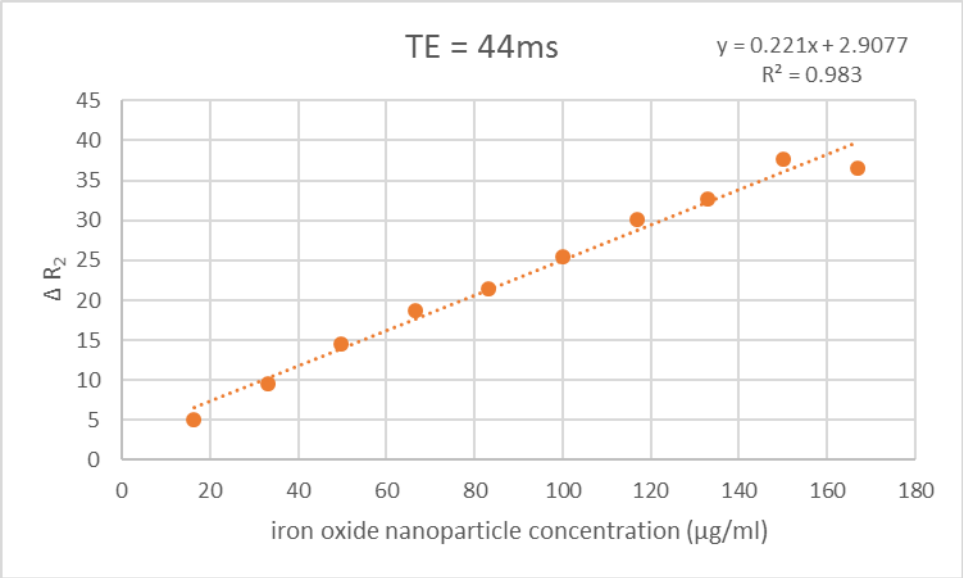

Figure 3.24: The linear fit to the T_2 relaxivity rate as a function of iron oxide nanoparticle concentration, at a TE of 44 ms at 1.5 T. A linear trend line was fitted to the plotted values of the increasing 10 concentration samples, as there is a linear dependence of the relaxation rate on concentration.

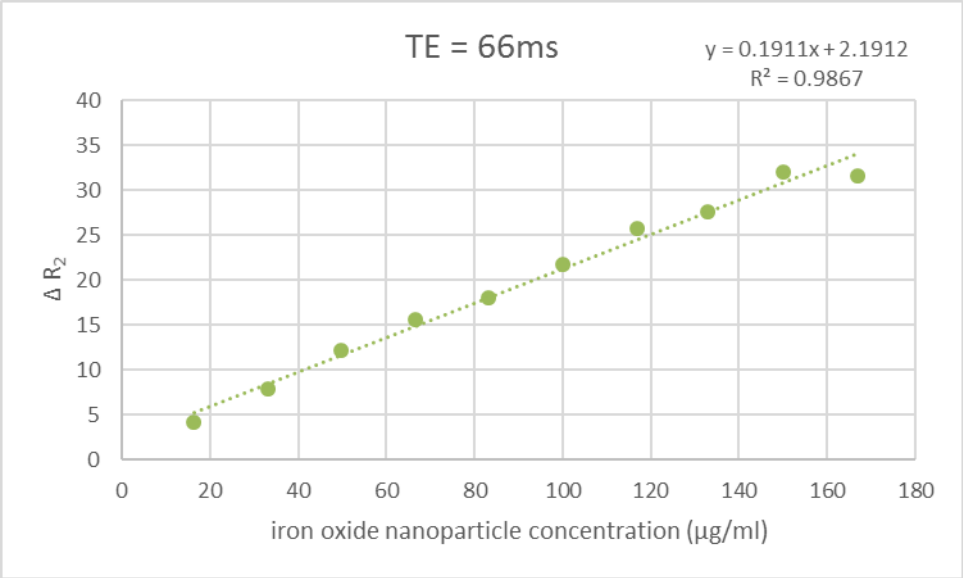

Figure 3.25: The linear fit to the T_2 relaxivity rate as a function of iron oxide nanoparticle concentration, at a TE of 66 ms at 1.5 T. A linear trend line was fitted to the plotted values of the increasing 10 concentration samples, as there is a linear dependence of the relaxation rate on concentration.

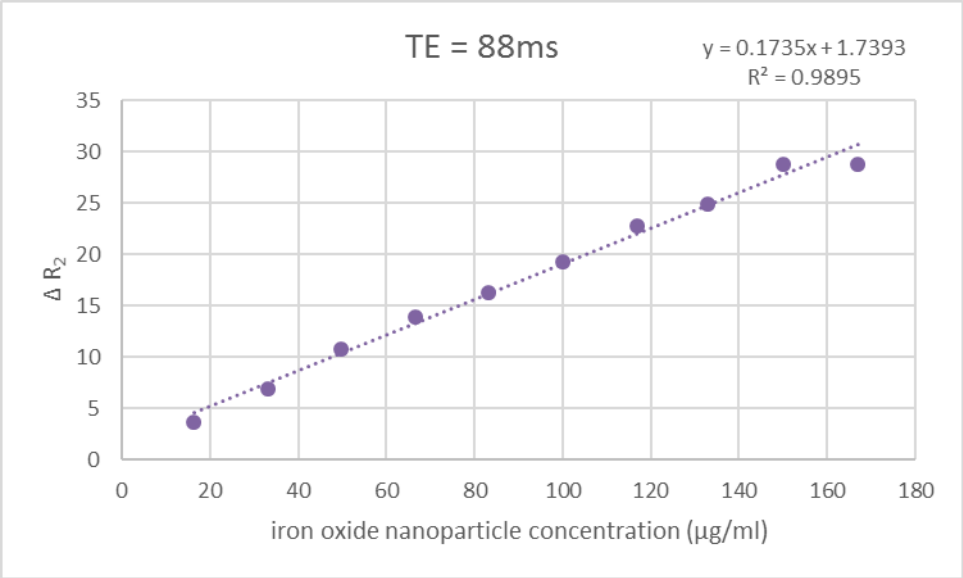

Figure 3.26: The linear fit to the T_2 relaxivity rate as a function of iron oxide nanoparticle concentration, at a TE of 88 ms at 1.5 T. A linear trend line was fitted to the plotted values of the increasing 10 concentration samples, as there is a linear dependence of the relaxation rate on concentration.

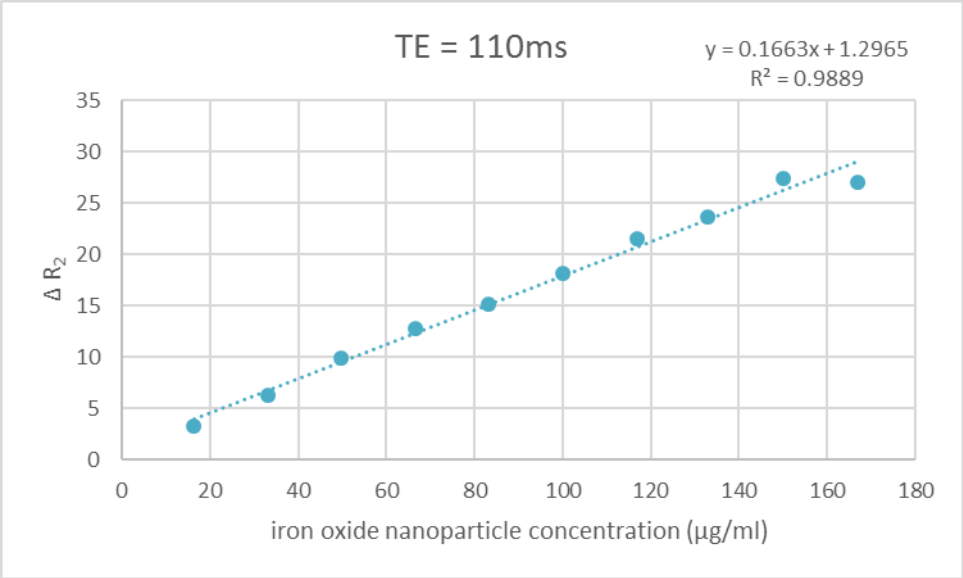

Figure 3.27: The linear fit to the T_2 relaxivity rate as a function of iron oxide nanoparticle concentration, at a TE of 110 ms at 1.5 T. A linear trend line was fitted to the plotted values of the increasing 10 concentration samples, as there is a linear dependence of the relaxation rate on concentration.

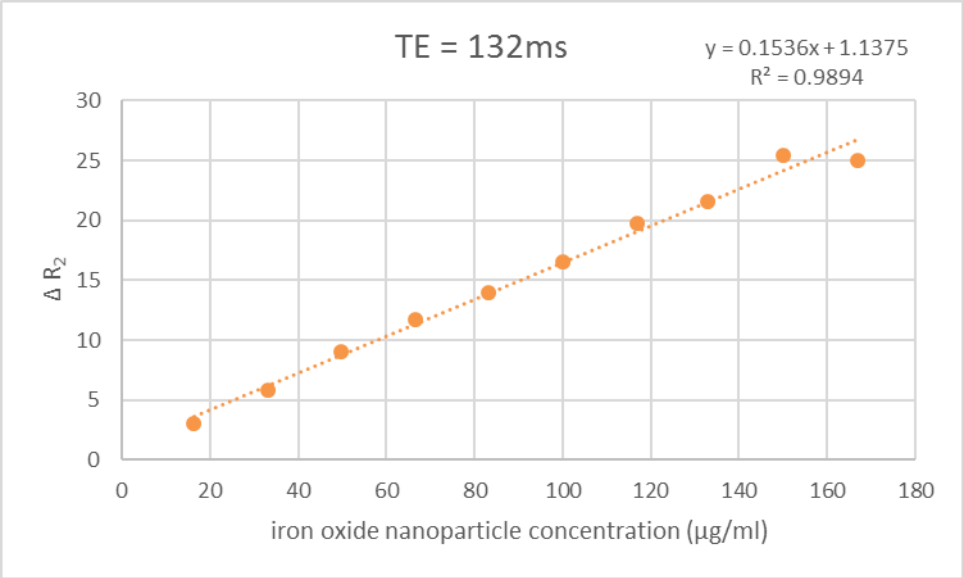

Figure 3.28: The linear fit to the T_2 relaxivity rate as a function of iron oxide nanoparticle concentration, at a TE of 132 ms at 1.5 T. A linear trend line was fitted to the plotted values of the increasing 10 concentration samples, as there is a linear dependence of the relaxation rate on concentration.

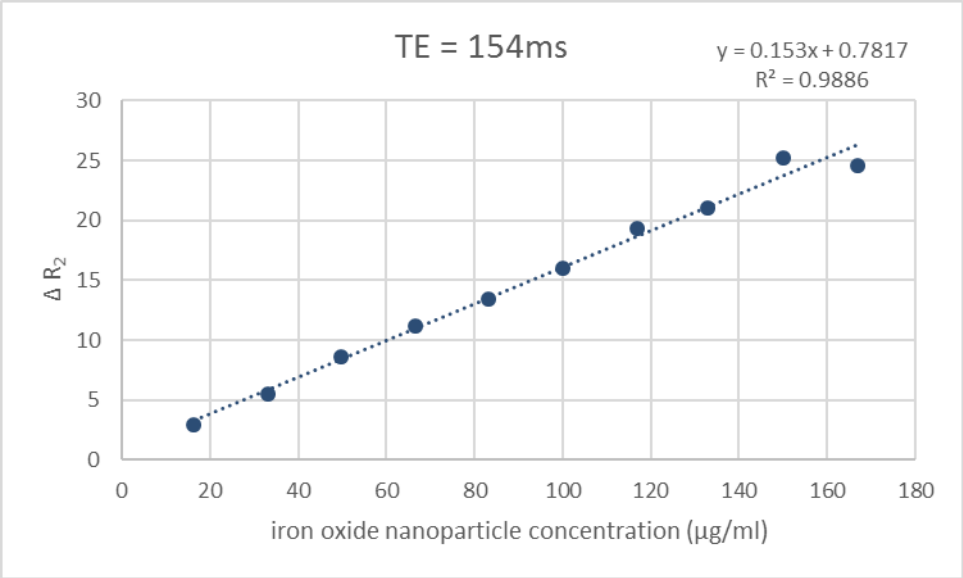

Figure 3.29: The linear fit to the T_2 relaxivity rate as a function of iron oxide nanoparticle concentration, at a TE of 154 ms at 1.5 T. A linear trend line was fitted to the plotted values of the increasing 10 concentration samples, as there is a linear dependence of the relaxation rate on concentration.

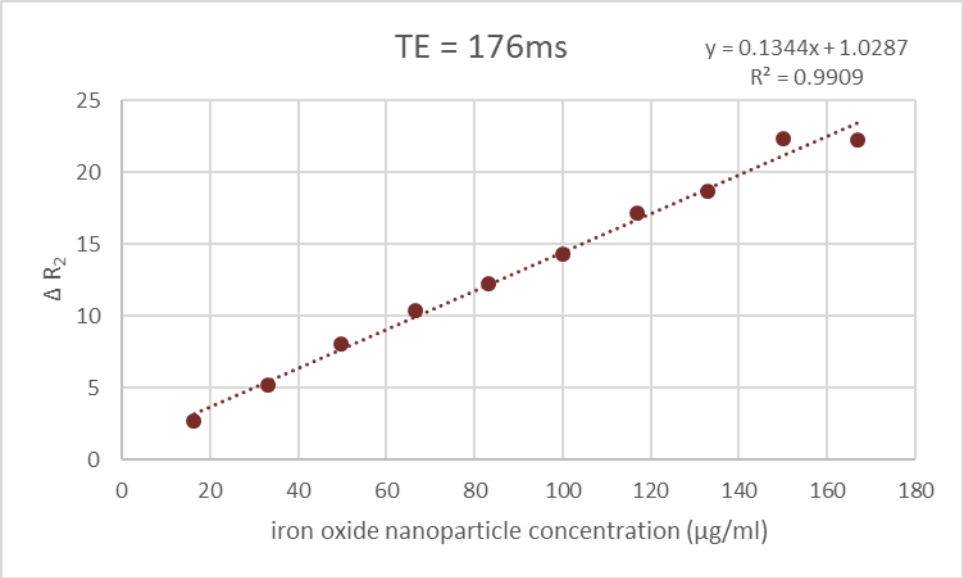

Figure 3.30: The linear fit to the T_2 relaxivity rate as a function of iron oxide nanoparticle concentration, at a TE of 176 ms at 1.5 T. A linear trend line was fitted to the plotted values of the increasing 10 concentration samples, as there is a linear dependence of the relaxation rate on concentration.

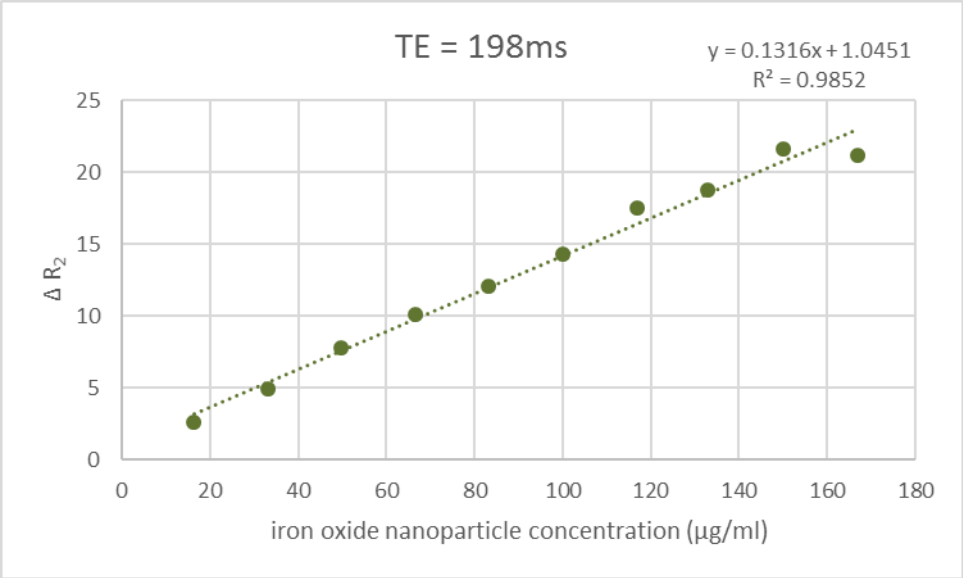

Figure 3.31: The linear fit to the T_2 relaxivity rate as a function of iron oxide nanoparticle concentration, at a TE of 198 ms at 1.5 T. A linear trend line was fitted to the plotted values of the increasing 10 concentration samples, as there is a linear dependence of the relaxation rate on concentration.

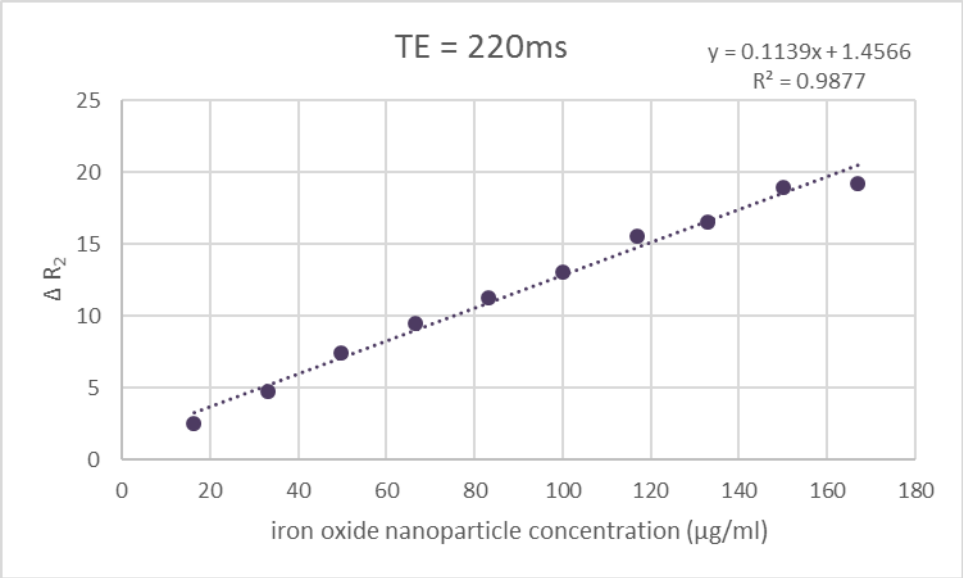

Figure 3.32: The linear fit to the T_2 relaxivity rate as a function of iron oxide nanoparticle concentration, at a TE of 220 ms at 1.5 T. A linear trend line was fitted to the plotted values of the increasing 10 concentration samples, as there is a linear dependence of the relaxation rate on concentration.

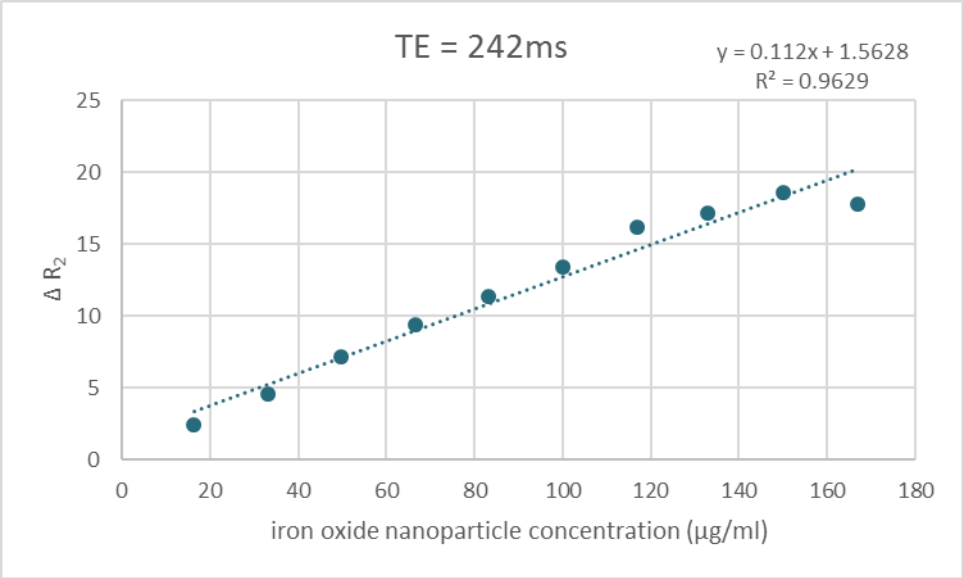

Figure 3.33: The linear fit to the T_2 relaxivity rate as a function of iron oxide nanoparticle concentration, at a TE of 242 ms at 1.5 T. A linear trend line was fitted to the plotted values of the increasing 10 concentration samples, as there is a linear dependence of the relaxation rate on concentration.

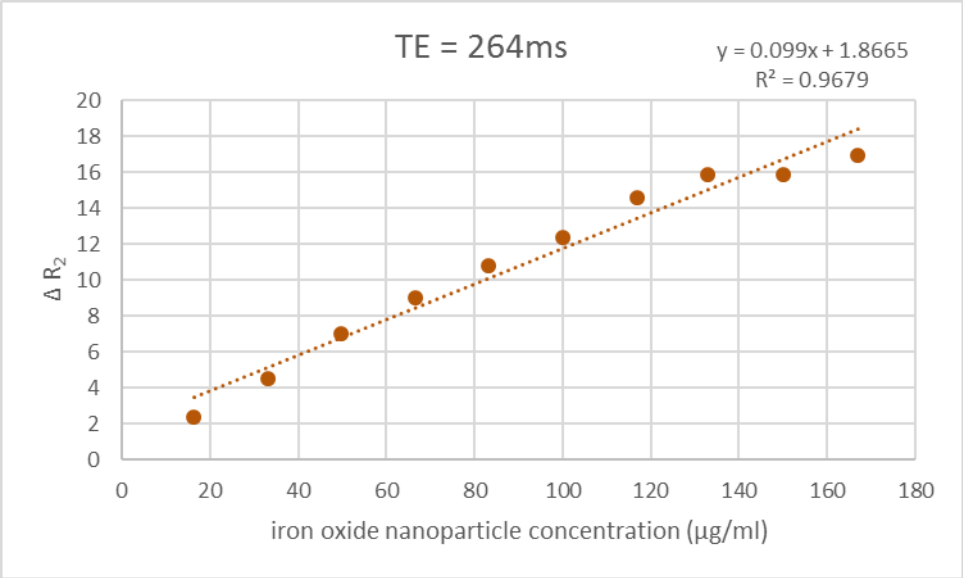

Figure 3.34: The linear fit to the T_2 relaxivity rate as a function of iron oxide nanoparticle concentration, at a TE of 264 ms at 1.5 T. A linear trend line was fitted to the plotted values of the increasing 10 concentration samples, as there is a linear dependence of the relaxation rate on concentration.

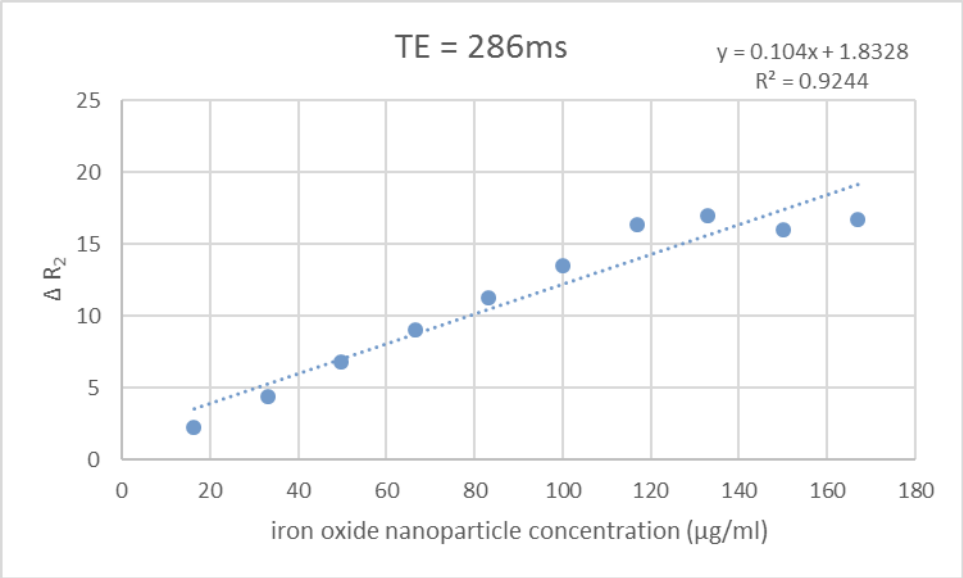

Figure 3.35: The linear fit to the T_2 relaxivity rate as a function of iron oxide nanoparticle concentration, at a TE of 286 ms at 1.5 T. A linear trend line was fitted to the plotted values of the increasing 10 concentration samples, as there is a linear dependence of the relaxation rate on concentration.

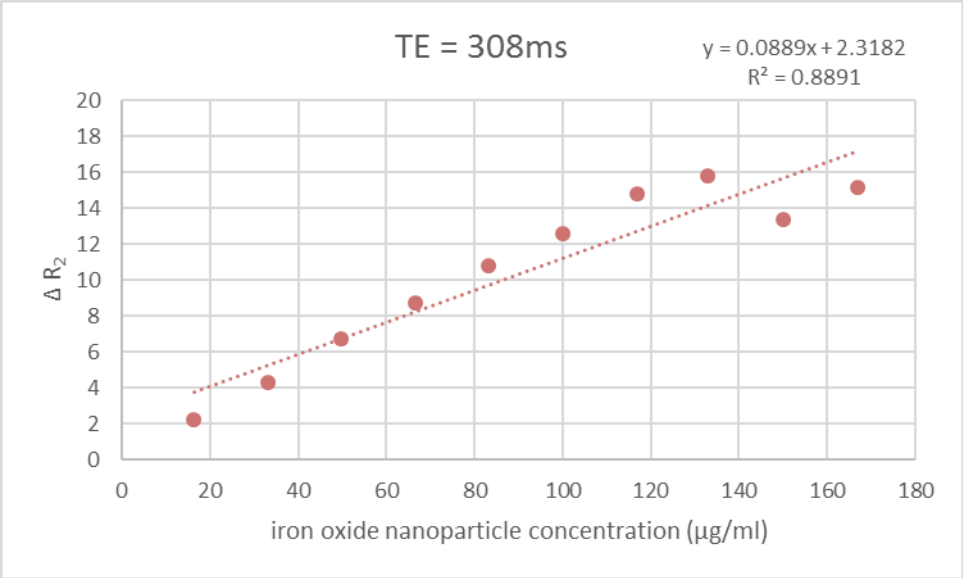

Figure 3.36: The linear fit to the T_2 relaxivity rate as a function of iron oxide nanoparticle concentration, at a TE of 308 ms at 1.5 T. A linear trend line was fitted to the plotted values of the increasing 10 concentration samples, as there is a linear dependence of the relaxation rate on concentration.

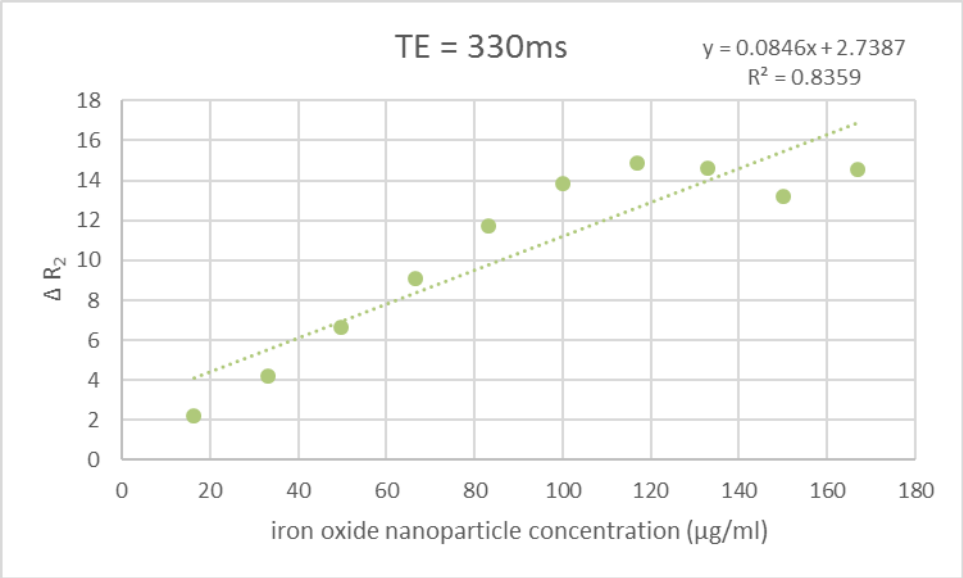

Figure 3.37: The linear fit to the T_2 relaxivity rate as a function of iron oxide nanoparticle concentration, at a TE of 330 ms at 1.5 T. A linear trend line was fitted to the plotted values of the increasing 10 concentration samples, as there is a linear dependence of the relaxation rate on concentration.

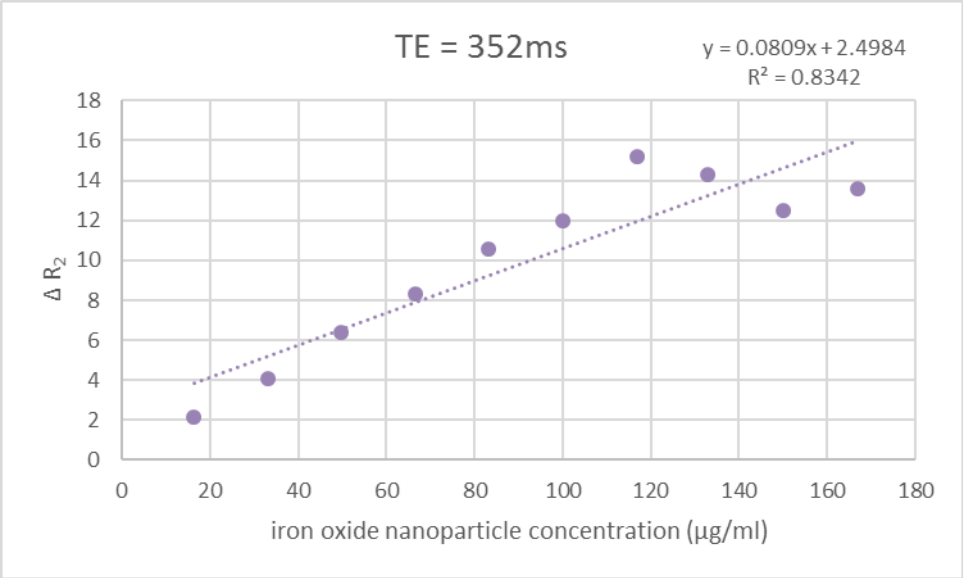

Figure 3.38: The linear fit to the T_2 relaxivity rate as a function of iron oxide nanoparticle concentration, at a TE of 352 ms at 1.5 T. A linear trend line was fitted to the plotted values of the increasing 10 concentration samples, as there is a linear dependence of the relaxation rate on concentration.

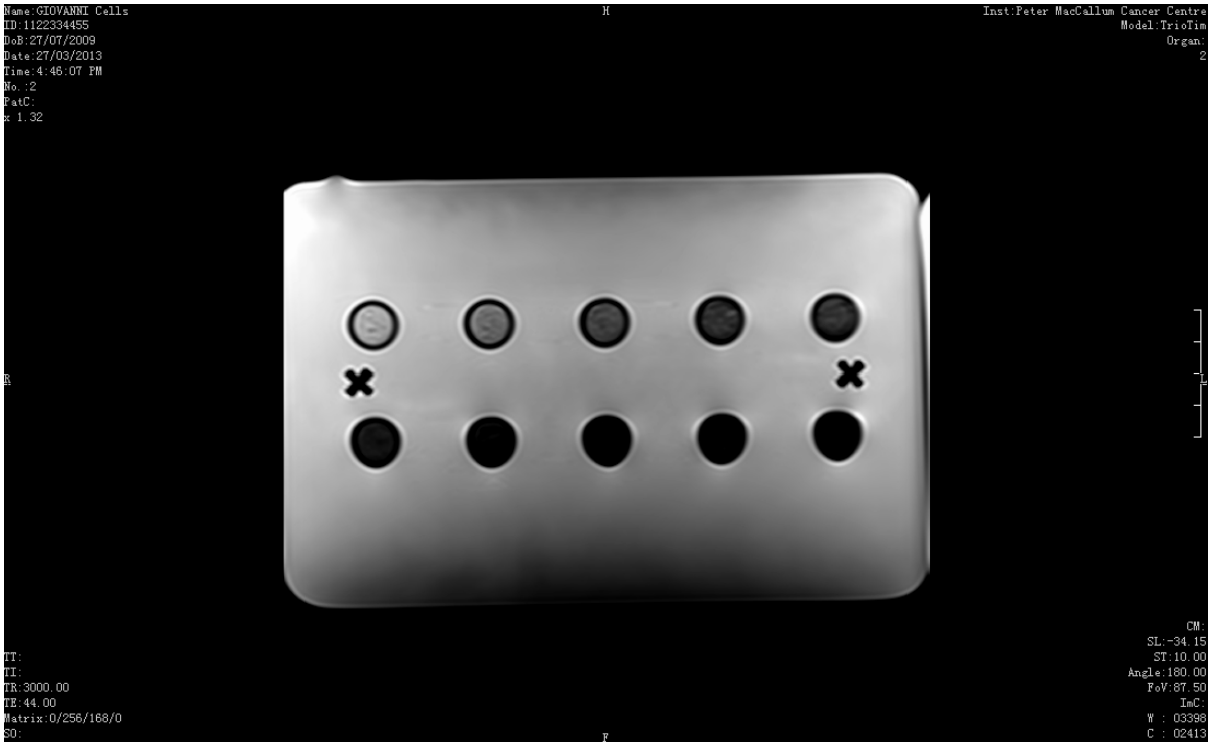

Figure 3.39: Top view of plastic container filled with water and containing plastic tubes filled with gel of increasing concentration of iron oxide nanoparticles; scanned at 3.0 T.
A T_2 weighted image generated from a 16 echo spin echo pulse sequence scanned at 3.0 T. This image was acquired with a TE value of 44 ms and a TR value of 3,000 ms and a 12-channel head coil was used.

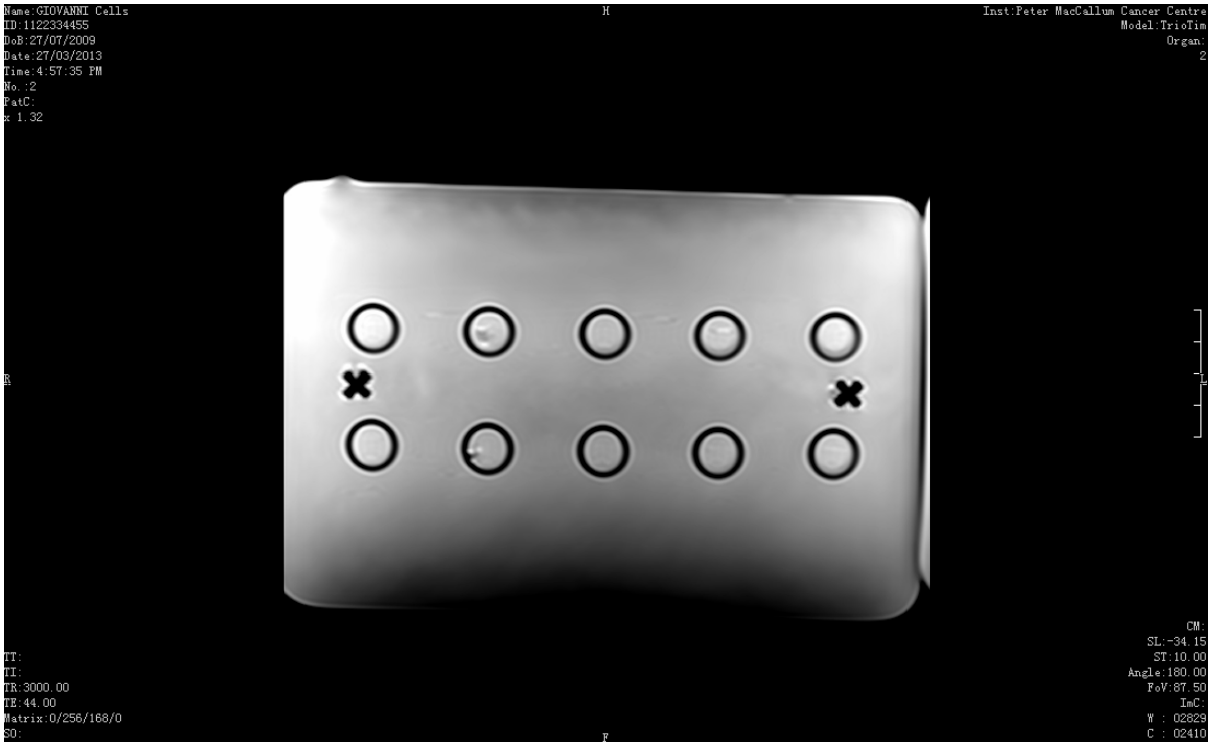

Figure 3.40: Top view of plastic container filled with water and the control tubes – plastic tubes filled with gel only (no iron oxide nanoparticles); scanned at 3.0 T

A T_2 weighted image generated from a 16 echo spin echo pulse sequence at 3.0 T. This image was acquired with a TE value of 44 ms and a TR value of 3,000 ms and a 12-channel head coil was used.

The series of graphs from Figure 3.39 to Figure 3.48 exhibit the change in T_2 relaxivity, ΔR_2 response (or intensity decay profile), for each concentration sample across the 16 echoes in the pulse sequence, at 3.0 T. The next series of graphs (Figure 3.41 to Figure 3.65) documents the linear fit to the T_2 relaxivity as a function of nanoparticle concentration and each of the known 16 TE echoes in the pulse sequence used, at 3.0 T.

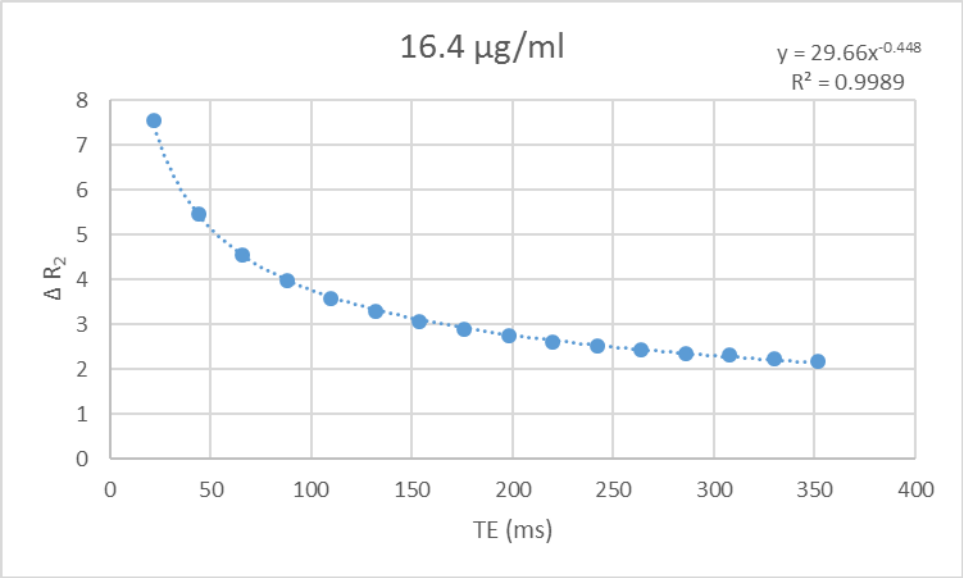

Figure 3.41: The change in R_2 relaxivity, intensity-decay profile of 16.4 µg/ml sample as determined at 3.0 T, of the dextran coated iron oxide nanoparticles has been graphed according to equation 2. A power trend line was fitted to the 16 echo data points as they were known to be exactly 22 ms apart from one another. This curve was created by plotting the T_2 response of iron oxide nanoparticles at a concentration of 16.4 µg/ml to the pulse sequence t2_se_COR_16-echoes at 3.0 T.

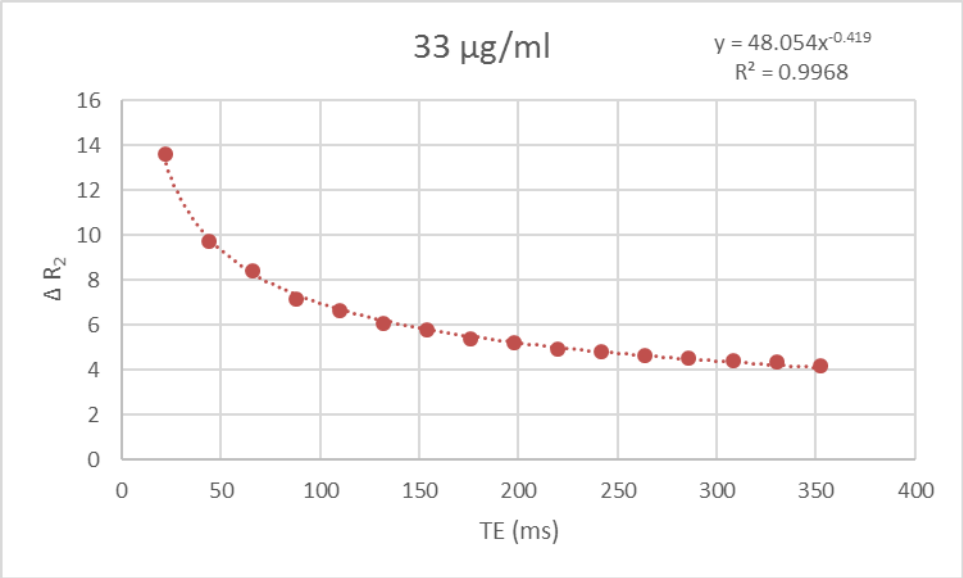

Figure 3.42: The change in R_2 relaxivity, intensity-decay profile of 33.0 µg/ml sample as determined at 3.0 T, of the dextran coated iron oxide nanoparticles has been graphed according to equation 2. A power trend line was fitted to the 16 echo data points as they were known to be exactly 22 ms apart from one another. This curve was created by plotting the T_2 response of iron oxide nanoparticles at a concentration of 33.0 µg/ml to the pulse sequence t2_se_COR_16-echoes at 3.0 T.

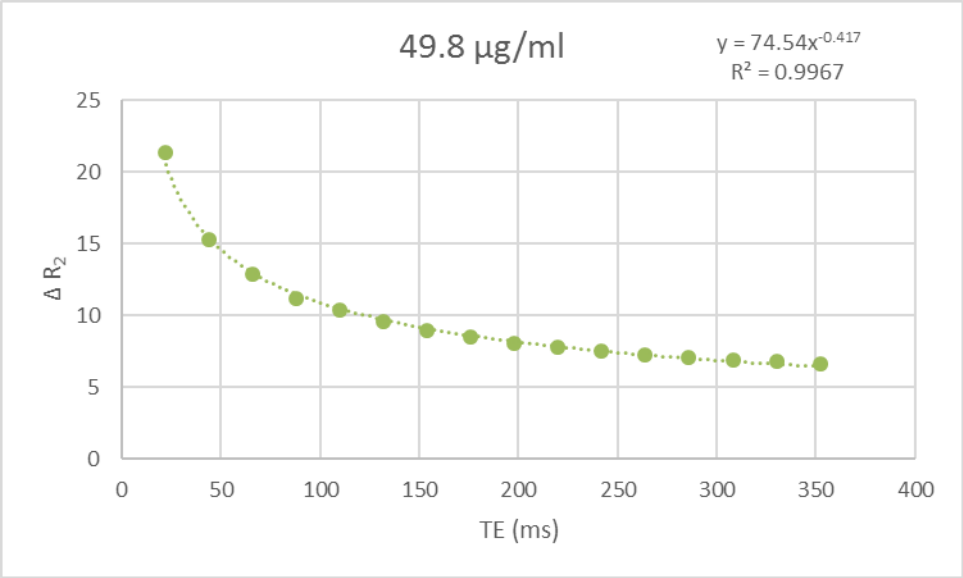

Figure 3.43: The change in R_2 relaxivity, intensity-decay profile of 49.8 µg/ml sample as determined at 3.0 T, of the dextran coated iron oxide nanoparticles has been graphed according to equation 2. A power trend line was fitted to the 16 echo data points as they were known to be exactly 22 ms apart from one another. This curve was created by plotting the T_2 response of iron oxide nanoparticles at a concentration of 49.8 µg/ml to the pulse sequence t2_se_COR_16-echoes at 3.0 T.

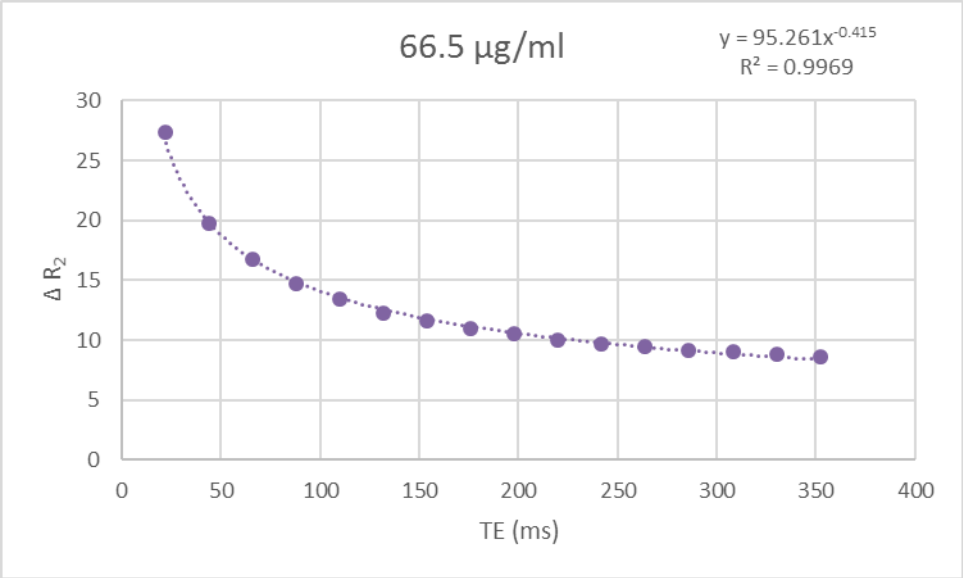

Figure 3.44: The change in R_2 relaxivity, intensity-decay profile of 66.5 µg/ml sample as determined at 3.0 T, of the dextran coated iron oxide nanoparticles has been graphed according to equation 2. A power trend line was fitted to the 16 echo data points as they were known to be exactly 22 ms apart from one another. This curve was created by plotting the T_2 response of iron oxide nanoparticles at a concentration of 66.5 µg/ml to the pulse sequence t2_se_COR_16-echoes at 3.0 T.

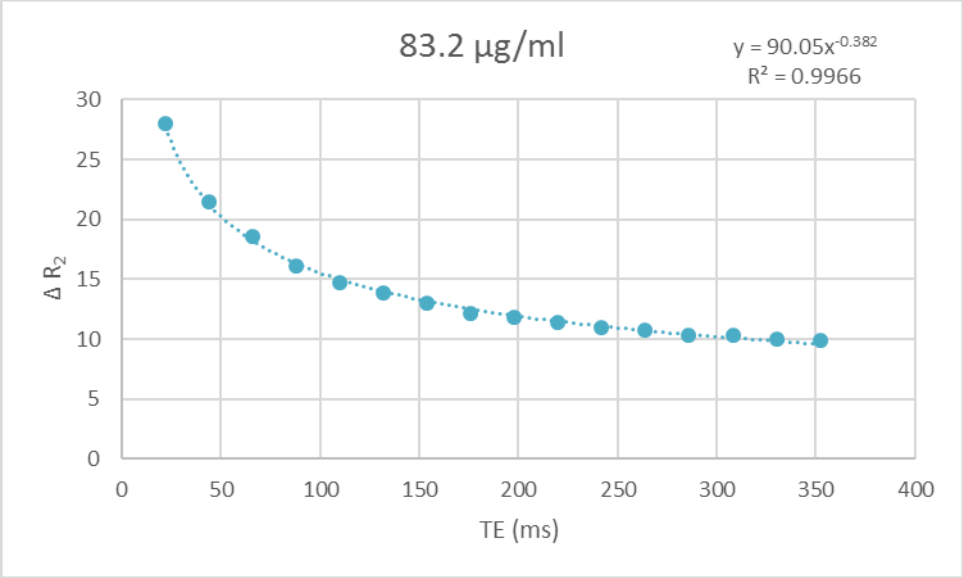

Figure 3.45: The change in R_2 relaxivity, intensity-decay profile of 83.2 µg/ml sample as determined at 3.0 T, of the dextran coated iron oxide nanoparticles has been graphed according to equation 2. A power trend line was fitted to the 16 echo data points as they were known to be exactly 22 ms apart from one another. This curve was created by plotting the T_2 response of iron oxide nanoparticles at a concentration of 83.2 µg/ml to the pulse sequence t2_se_COR_16-echoes at 3.0 T.

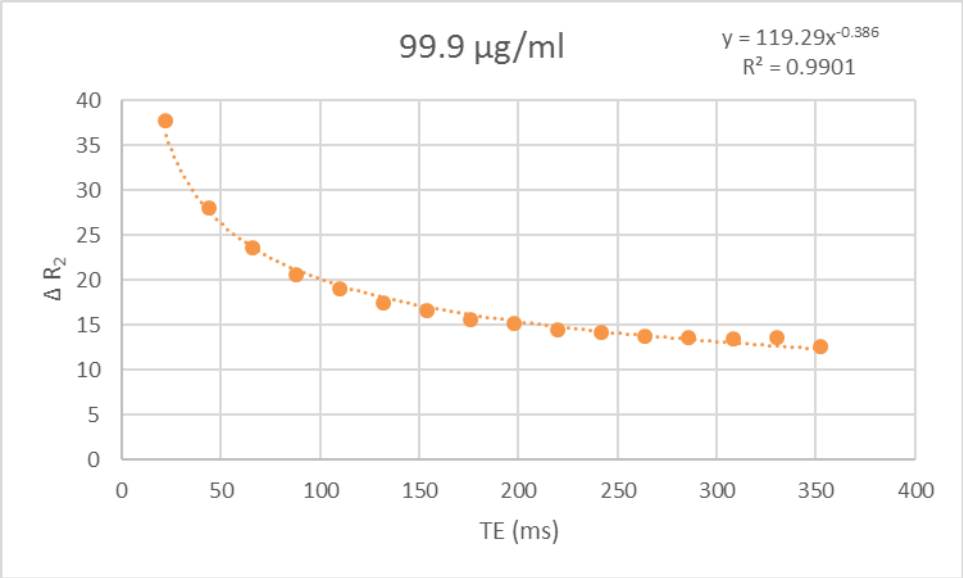

Figure 3.46: The change in R_2 relaxivity, intensity-decay profile of 99.9 µg/ml sample as determined at 3.0 T, of the dextran coated iron oxide nanoparticles has been graphed according to equation 2. A power trend line was fitted to the 16 echo data points as they were known to be exactly 22 ms apart from one another. This curve was created by plotting the T_2 response of iron oxide nanoparticles at a concentration of 99.9 µg/ml to the pulse sequence t2_se_COR_16-echoes at 3.0 T.

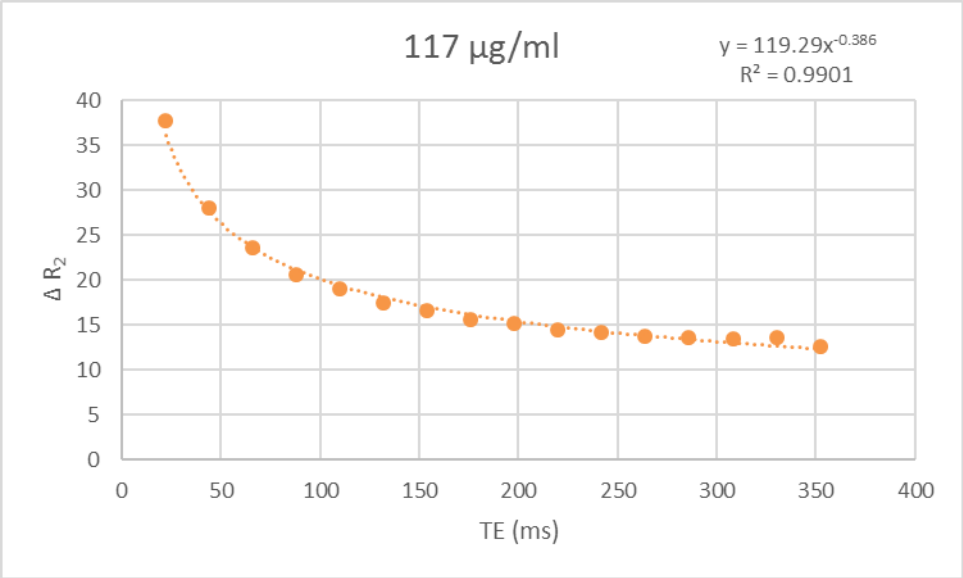

Figure 3.47: The change in R_2 relaxivity, intensity-decay profile of 117.0 µg/ml sample as determined at 3.0 T, of the dextran coated iron oxide nanoparticles has been graphed according to equation 2. A power trend line was fitted to the 16 echo data points as they were known to be exactly 22 ms apart from one another. This curve was created by plotting the T_2 response of iron oxide nanoparticles at a concentration of 117.0 µg/ml to the pulse sequence t2_se_COR_16-echoes at 3.0 T.

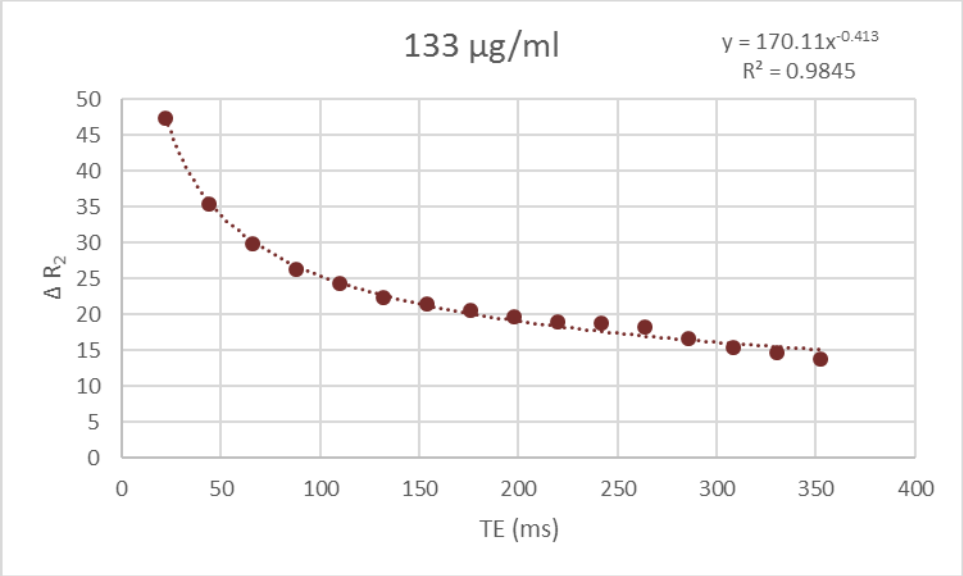

Figure 3.48: The change in R_2 relaxivity, intensity-decay profile of 133.0 µg/ml sample as determined at 3.0 T, of the dextran coated iron oxide nanoparticles has been graphed according to equation 2. A power trend line was fitted to the 16 echo data points as they were known to be exactly 22 ms apart from one another. This curve was created by plotting the T_2 response of iron oxide nanoparticles at a concentration of 113.0 µg/ml to the pulse sequence t2_se_COR_16-echoes at 3.0 T.

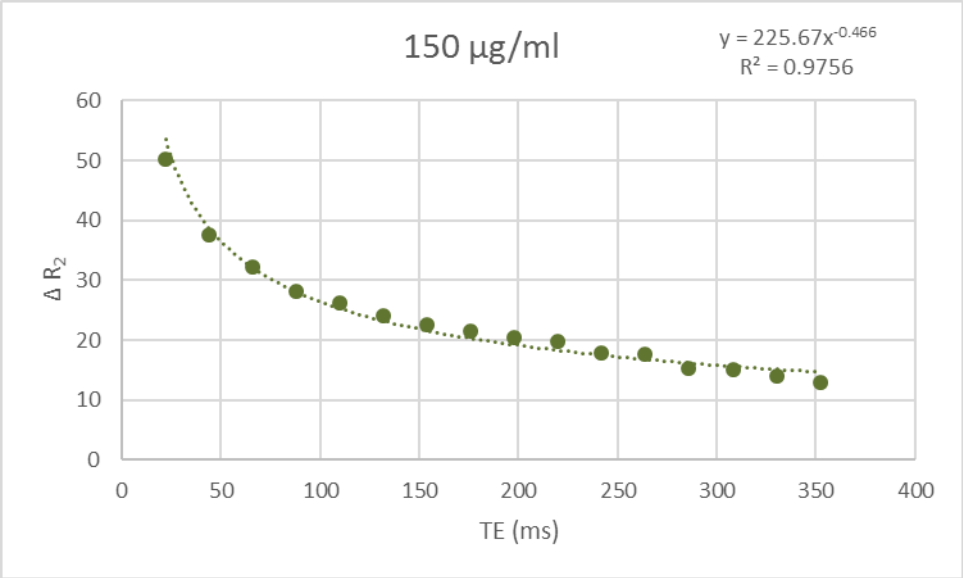

Figure 3.49: The change in R_2 relaxivity, intensity-decay profile of 150.0 µg/ml sample as determined at 3.0 T, of the dextran coated iron oxide nanoparticles has been graphed according to equation 2. A power trend line was fitted to the 16 echo data points as they were known to be exactly 22 ms apart from one another. This curve was created by plotting the T_2 response of iron oxide nanoparticles at a concentration of 150.0 µg/ml to the pulse sequence t2_se_COR_16-echoes at 3.0 T.

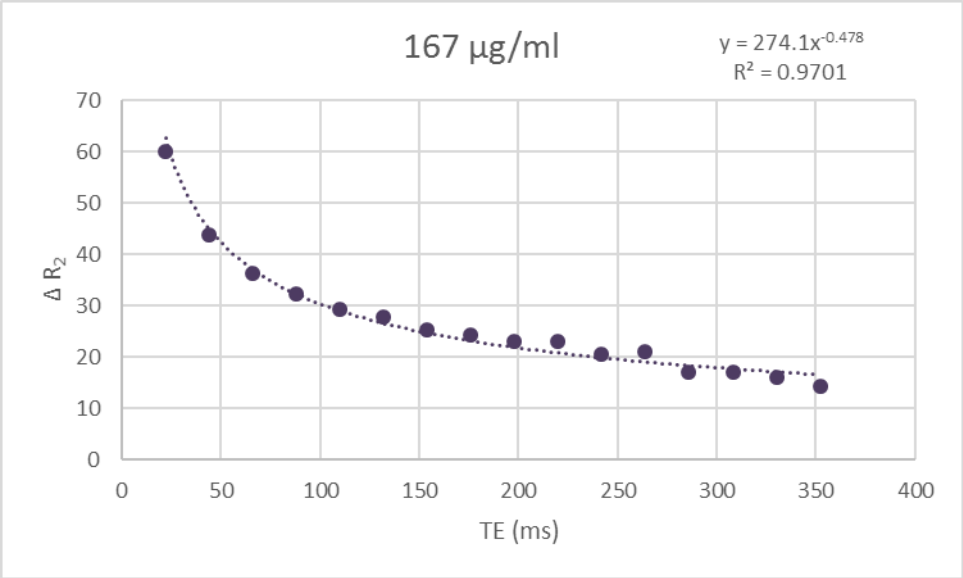

Figure 3.50: The change in R_2 relaxivity, intensity-decay profile of 167.0 µg/ml sample as determined at 3.0 T, of the dextran coated iron oxide nanoparticles has been graphed according to equation 2. A power trend line was fitted to the 16 echo data points as they were known to be exactly 22 ms apart from one another. This curve was created by plotting the T_2 response of iron oxide nanoparticles at a concentration of 167.0 µg/ml to the pulse sequence t2_se_COR_16-echoes at 3.0 T.

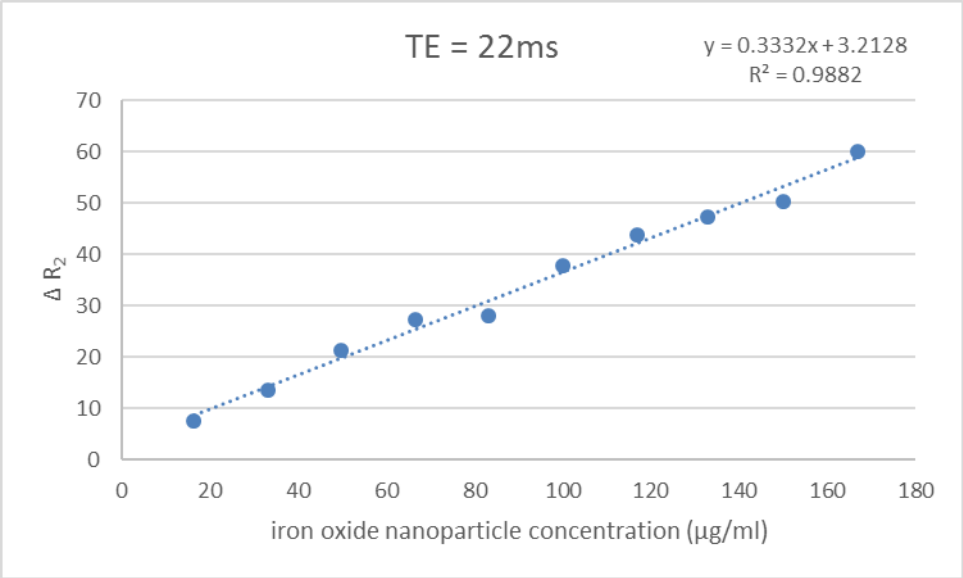

Figure 3.51: The linear fit to the T_2 relaxivity rate as a function of iron oxide nanoparticle concentration, at a TE of 22 ms at 3.0 T. A linear trend line was fitted to the plotted values of the increasing 10 concentration samples, as there is a linear dependence of the relaxation rate on concentration.

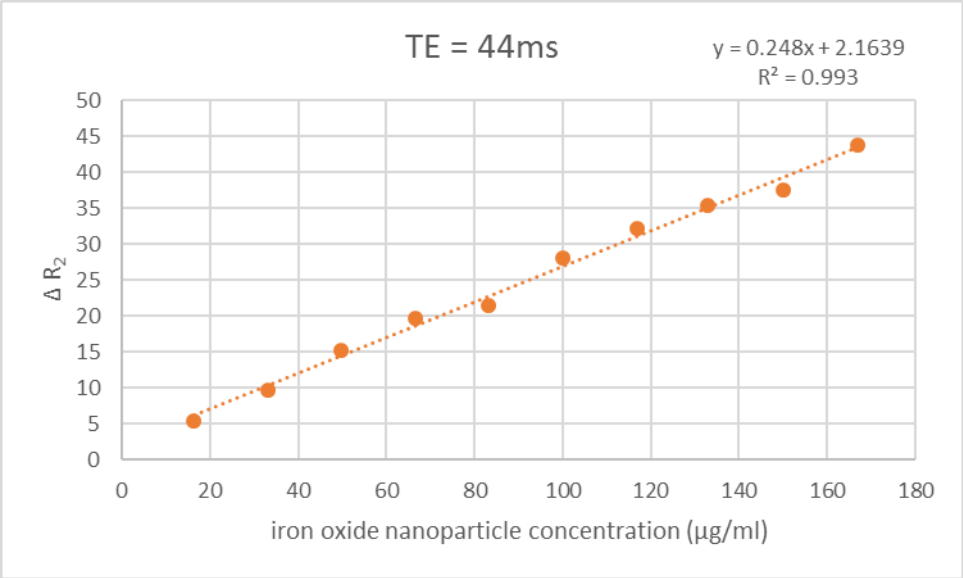

Figure 3.52: The linear fit to the T_2 relaxivity rate as a function of iron oxide nanoparticle concentration, at a TE of 44 ms at 3.0 T. A linear trend line was fitted to the plotted values of the increasing 10 concentration samples, as there is a linear dependence of the relaxation rate on concentration.

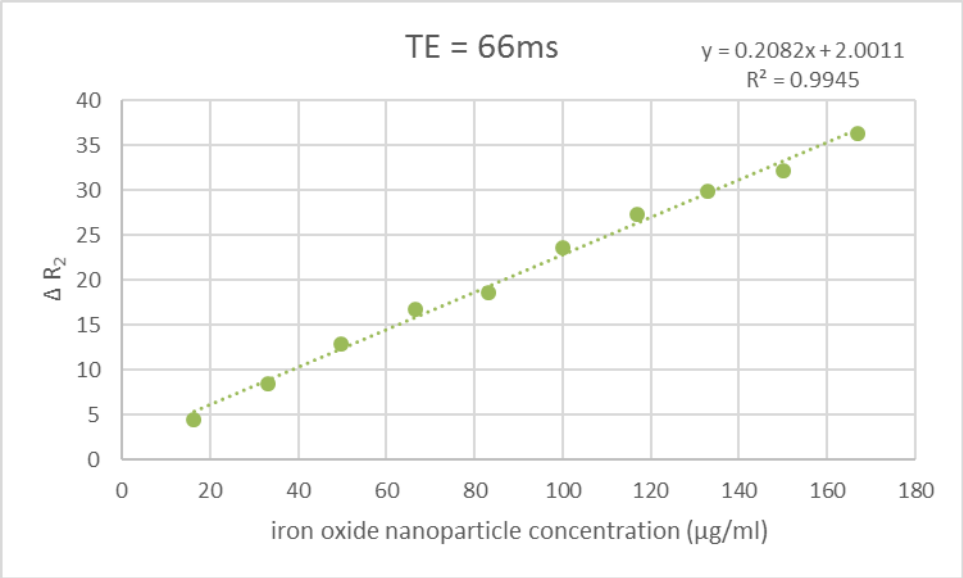

Figure 3.53: The linear fit to the T_2 relaxivity rate as a function of iron oxide nanoparticle concentration, at a TE of 66 ms at 3.0 T. A linear trend line was fitted to the plotted values of the increasing 10 concentration samples, as there is a linear dependence of the relaxation rate on concentration.

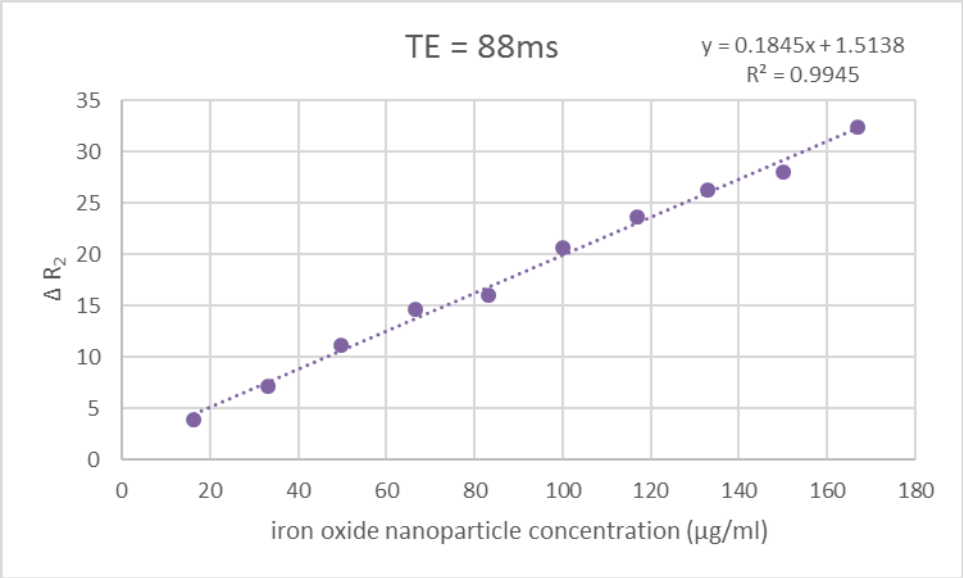

Figure 3.54: The linear fit to the T_2 relaxivity rate as a function of iron oxide nanoparticle concentration, at a TE of 88 ms at 3.0 T. A linear trend line was fitted to the plotted values of the increasing 10 concentration samples, as there is a linear dependence of the relaxation rate on concentration.

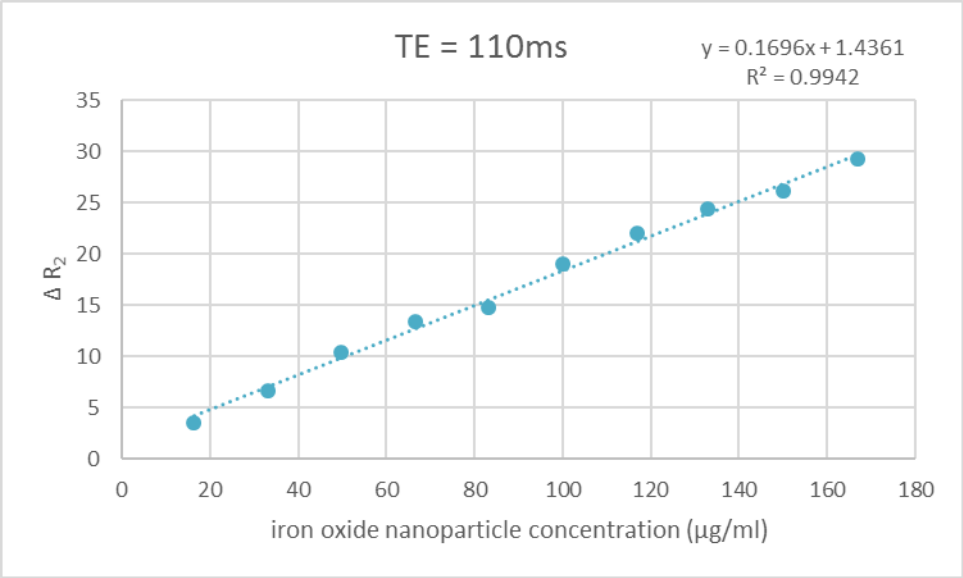

Figure 3.55: The linear fit to the T_2 relaxivity rate as a function of iron oxide nanoparticle concentration, at a TE of 110 ms at 3.0 T. A linear trend line was fitted to the plotted values of the increasing 10 concentration samples, as there is a linear dependence of the relaxation rate on concentration.

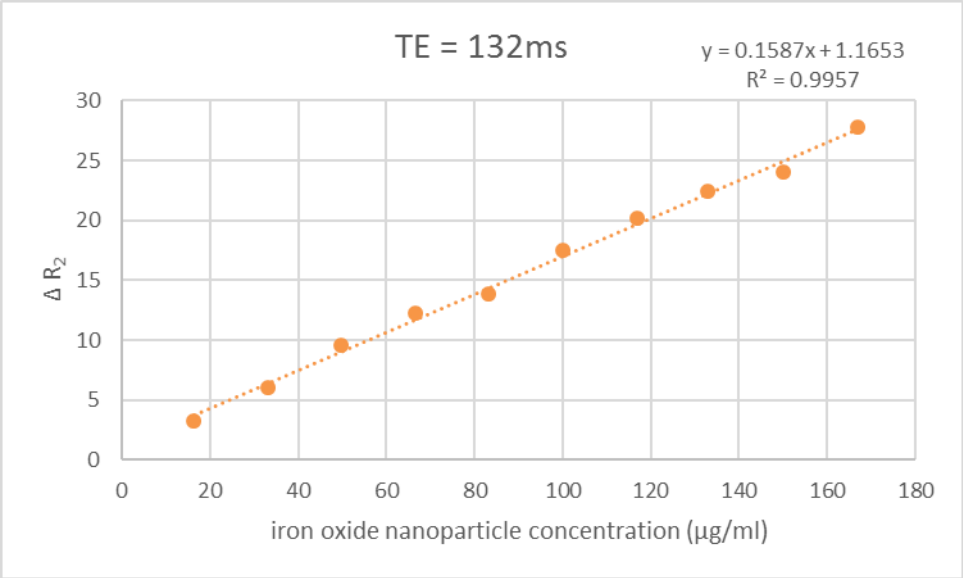

Figure 3.56: The linear fit to the T_2 relaxivity rate as a function of iron oxide nanoparticle concentration, at a TE of 132 ms at 3.0 T. A linear trend line was fitted to the plotted values of the increasing 10 concentration samples, as there is a linear dependence of the relaxation rate on concentration.

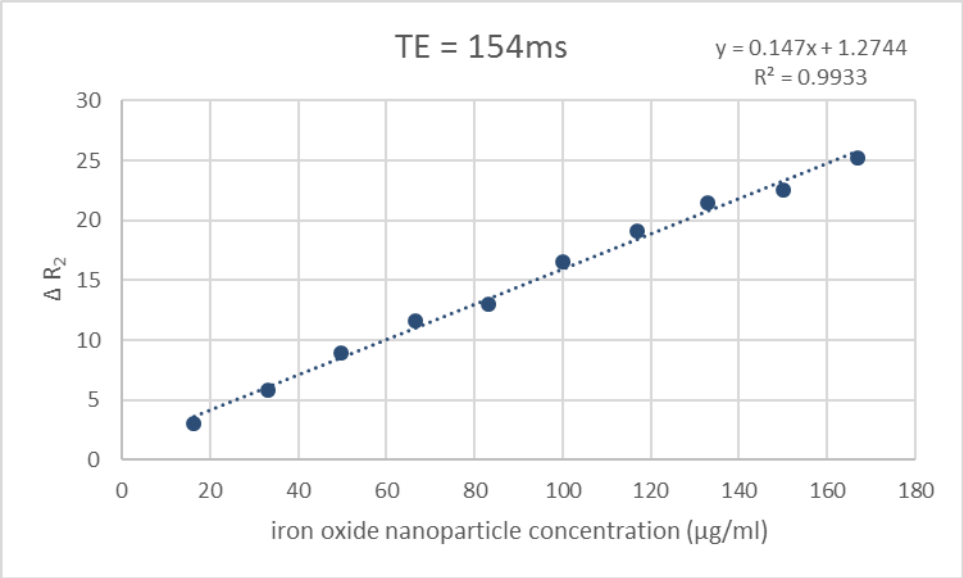

Figure 3.57: The linear fit to the T_2 relaxivity rate as a function of iron oxide nanoparticle concentration, at a TE of 154 ms at 3.0 T. A linear trend line was fitted to the plotted values of the increasing 10 concentration samples, as there is a linear dependence of the relaxation rate on concentration.

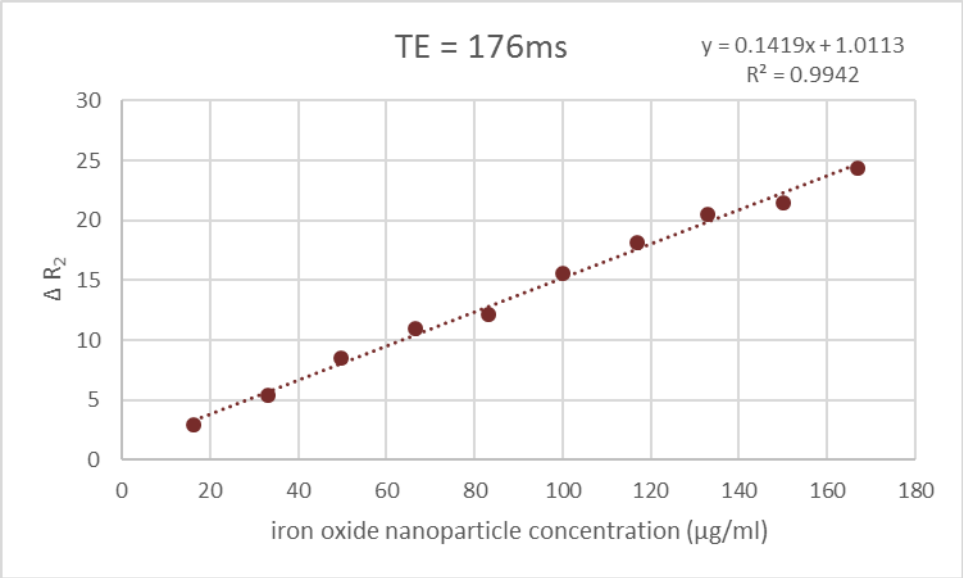

Figure 3.58: The linear fit to the T_2 relaxivity rate as a function of iron oxide nanoparticle concentration, at a TE of 176 ms at 3.0 T. A linear trend line was fitted to the plotted values of the increasing 10 concentration samples, as there is a linear dependence of the relaxation rate on concentration.

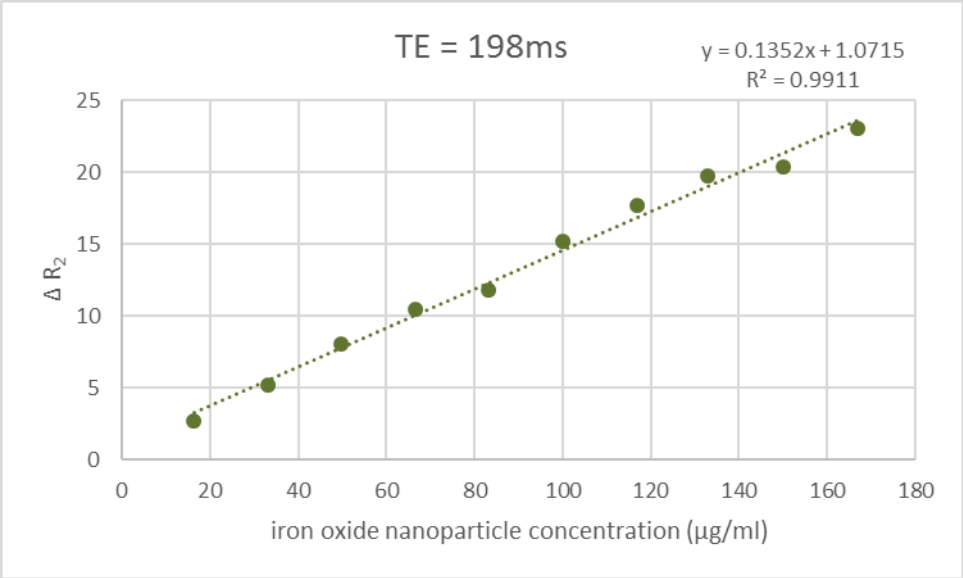

Figure 3.59: The linear fit to the T_2 relaxivity rate as a function of iron oxide nanoparticle concentration, at a TE of 198 ms at 3.0 T. A linear trend line was fitted to the plotted values of the increasing 10 concentration samples, as there is a linear dependence of the relaxation rate on concentration.

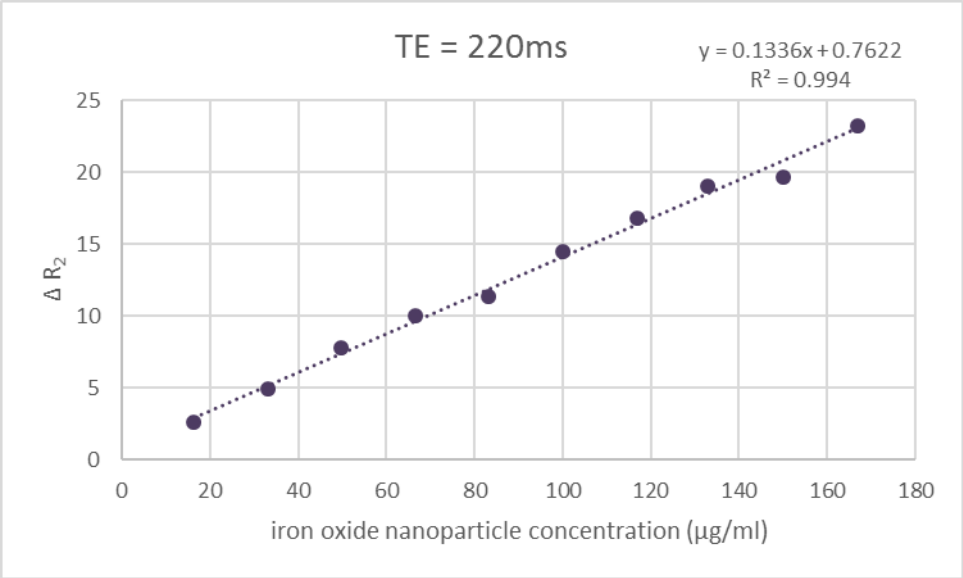

Figure 3.60: The linear fit to the T_2 relaxivity rate as a function of iron oxide nanoparticle concentration, at a TE of 220 ms at 3.0 T. A linear trend line was fitted to the plotted values of the increasing 10 concentration samples, as there is a linear dependence of the relaxation rate on concentration.

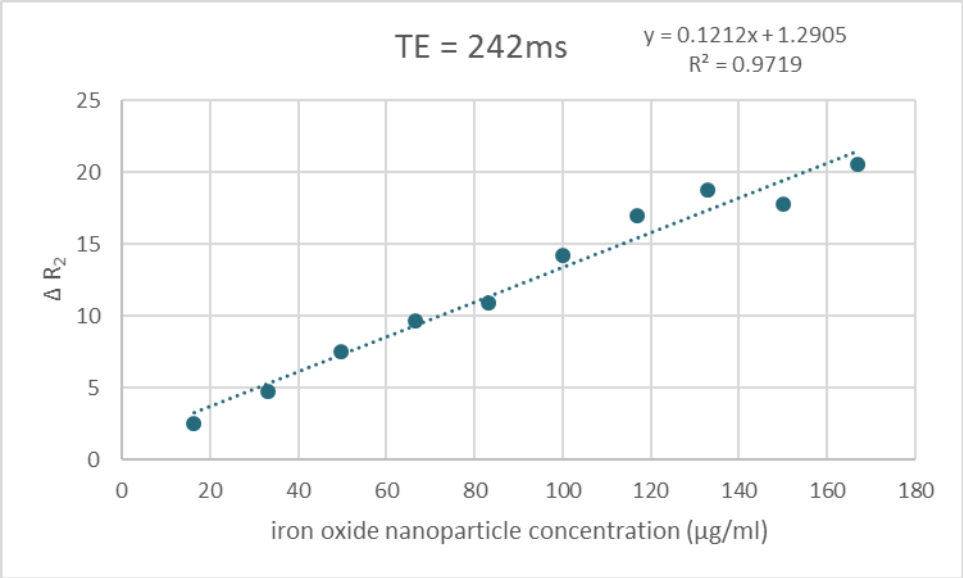

Figure 3.61: The linear fit to the T_2 relaxivity rate as a function of iron oxide nanoparticle concentration, at a TE of 242 ms at 3.0 T. A linear trend line was fitted to the plotted values of the increasing 10 concentration samples, as there is a linear dependence of the relaxation rate on concentration.

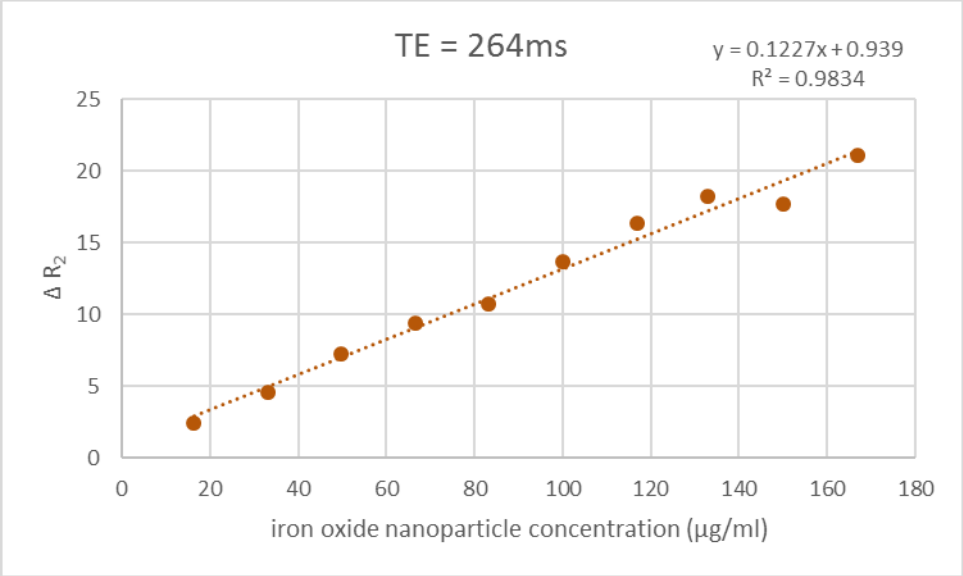

Figure 3.62: The linear fit to the T_2 relaxivity rate as a function of iron oxide nanoparticle concentration, at a TE of 264 ms at 3.0 T. A linear trend line was fitted to the plotted values of the increasing 10 concentration samples, as there is a linear dependence of the relaxation rate on concentration.

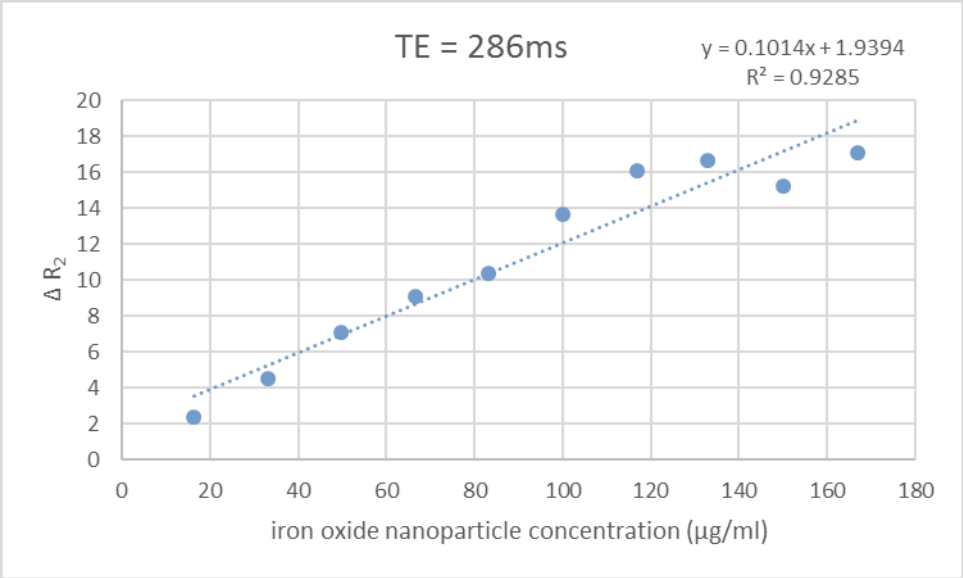

Figure 3.63: The linear fit to the T_2 relaxivity rate as a function of iron oxide nanoparticle concentration, at a TE of 286 ms at 3.0 T. A linear trend line was fitted to the plotted values of the increasing 10 concentration samples, as there is a linear dependence of the relaxation rate on concentration.

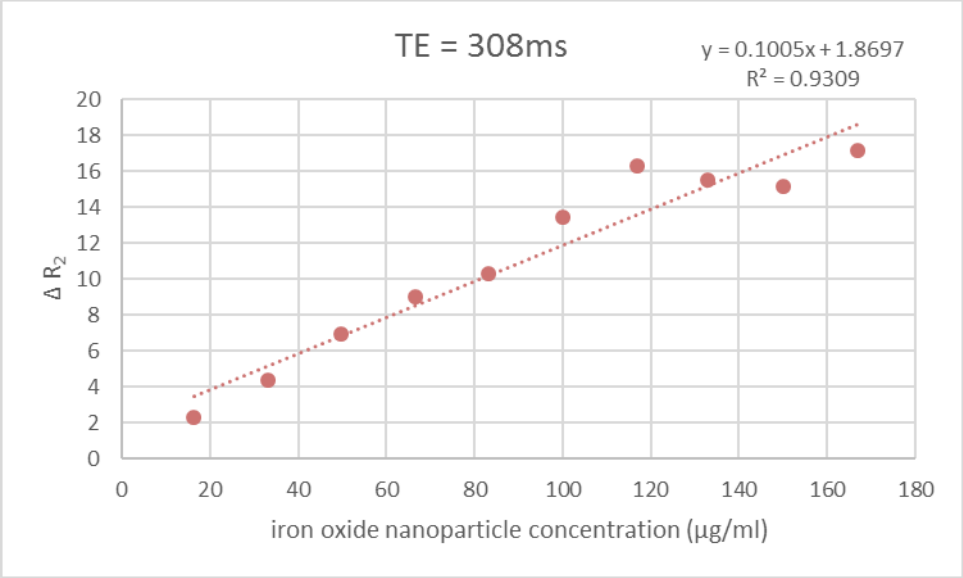

Figure 3.64: The linear fit to the T_2 relaxivity rate as a function of iron oxide nanoparticle concentration, at a TE of 308 ms at 3.0 T. A linear trend line was fitted to the plotted values of the increasing 10 concentration samples, as there is a linear dependence of the relaxation rate on concentration.

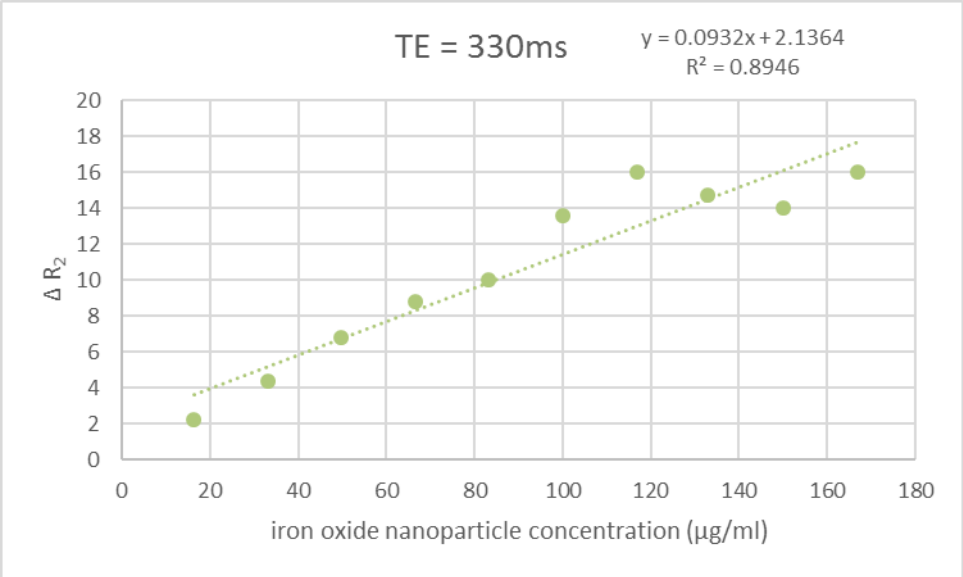

Figure 3.65: The linear fit to the T_2 relaxivity rate as a function of iron oxide nanoparticle concentration, at a TE of 330 ms at 3.0 T. A linear trend line was fitted to the plotted values of the increasing 10 concentration samples, as there is a linear dependence of the relaxation rate on concentration.

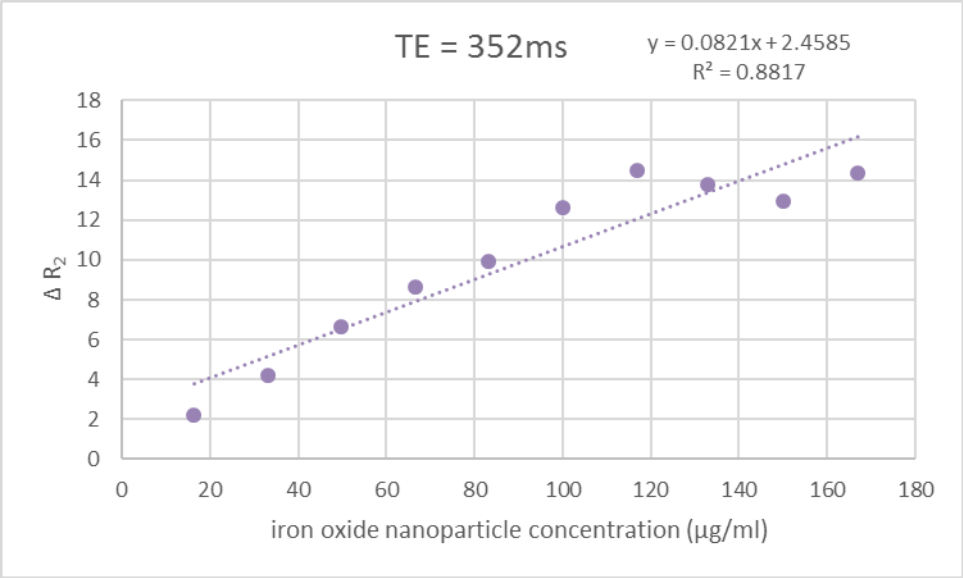

Figure 3.66: The linear fit to the T_2 relaxivity rate as a function of iron oxide nanoparticle concentration, at a TE of 352 ms at 3.0 T. A linear trend line was fitted to the plotted values of the increasing 10 concentration samples, as there is a linear dependence of the relaxation rate on concentration.

8.2 Appendix 2 – Publications and Presentations

8.2.1 Peer Reviewed Publications

Mandarano G, Lodhia J, Ferris N, Eu P, Davidson R, Cowell C, Development and use of iron oxide nanoparticles: Part 2 - The application of iron oxide contrast agents in Magnetic Resonance Imaging (MRI), Biomedical Imaging and Intervention Journal. 2010; 6(2):e13.

Lodhia J, Mandarano G, Ferris N, Eu P, Cowell C. Development and use of iron oxide nanoparticles: Part 1 - The Synthesis of Iron Oxide Nanoparticles for Magnetic Resonance Imaging, Biomedical Imaging and Intervention Journal. 2010; 6(2):e12.

8.2.2 Oral Presentations

Mallia A, Mandarano G, Pouniotis D, Cullinane C, Hicks R, Eu P; A Fluorescent PET/CT Lymphoscintigraphic Agent for Sentinel Lymph Node Imaging and Detection; Annual Congress of the European Association of Nuclear Medicine, 18-22 September, 2014, Gothenburg, Sweden

Mandarano G; Lodhia J; Pouniotis D, Eu P; Ferris N; Davidson R; Cowell S; The continued development of iron oxide based nanoparticles for clinical MRI scanning; International Society of Radiographers and Radiologic Technologists, 9th to 12th September, 2010, Gold Coast Convention and Exhibition Centre

Conference, CSM 2009 (October), Combined Scientific Meeting of four professional bodies (Royal Australian and New Zealand College of Radiologists, Australian Institute of Radiography, Faculty of Radiation Oncology, Australasian College of Physical Scientists and Engineers in Medicine). Two oral presentations, with their abstracts published. Details below:

Mandarano G, Lodhia J, Eu P, Ferris N, Cowell S, Davidson R; The possibility of a general purpose contrast agent for MRI based on iron oxide nanoparticles; Journal of Medical Imaging and Radiation Oncology; Volume 53; Supplement 1; October 2009; p. A36; Wiley-Blackwell; ISSN 1754-9477

Lodhia J, Mandarano G, Campbell J, Eu P, Ferris N, Cowell S; The synthesis, evaluation and future role of iron oxide nanoparticles in MRI; Journal of Medical Imaging and Radiation Oncology; Volume 53; Supplement 1; October 2009; p. A116; Wiley-Blackwell; ISSN 1754-9477

9.0 References

1. McRobbie D, Moore E, Graves M, Prince M. MRI – From Picture to Proton. 2nd Edition ed. Cambridge: Cambridge University Press; 2011.
2. Westbrook C, Kaut Roth C, Talbot J. MRI in practice. 4th edition ed. Oxford: Blackwell Publishing; 2011.
3. Bushong S. Magnetic Resonance Imaging – Physical and Biological Principles. 3rd ed. St. Louis: Mosby; 2003.
4. Brown MA, Semelka RC. MRI: Basic Principles and Applications. 2010.
5. Curry TS, Dowdey JE, Murry RC. Christensen's Physics of Diagnostic Radiology. 4th Edition ed1990.
6. Hashemi RH, Bradley WG, Lisanti CJ. MRI: The Basics. 3rd Edition ed2010.
7. Keogh MJ, Morris CM, Chinnery PF. Chapter Five - Neuroferritinopathy. In: Kailash PB, Susanne AS, editors. International Review of Neurobiology. Volume 110: Academic Press; 2013. p. 91-123.
8. Ohta E, Takiyama Y. MRI findings in neuroferritinopathy. Neurology research international. 2012;2012:197438.
9. Lehn A, Boyle R, Brown H, Airey C, Mellick G. Neuroferritinopathy. Parkinsonism & Related Disorders. 2012;18(8):909-15.
10. Castiella A, Alústiza JM, Zapata E, Emparanza JI. Is MRI becoming the new gold standard for diagnosing iron overload in hemochromatosis and other liver iron disorders? Imaging in Medicine. 2013;5(6):515-24.
11. Forschner A, Schmidt D, Garbe C. Hepatic hemangioma and hemochromatosis misdiagnosed by MRI as metastatic melanoma. JDDG: Journal der Deutschen Dermatologischen Gesellschaft. 2011;9(10):842-3.
12. Baur LHB. Patient screening for cardiac hemochromatosis, echocardiography or MRI? The International Journal of Cardiovascular Imaging. 2009;25(3):249-50.
13. Karçaaltıncaba M, İdilman İ, Çelik A. Focal sparing of iron and fat in liver tissue in patients with hemosiderosis: diagnosis with combination of R2* relaxometry and proton density fat fraction calculation by MRI 2011;17:323-7.
14. Rostoker G, Griuncelli M, Loridon C, Couprie R, Benmaadi A, Bounhiol C, et al. Hemodialysis-associated Hemosiderosis in the Era of Erythropoiesis-stimulating Agents: A MRI Study. The American Journal of Medicine. 2012;125(10).
15. Au WY, Lam WWM, Chu WWC, Tam S, Wong WK, Chan H, et al. A pilot MRI study of organ specific hemosiderosis and functional correlation in Chinese patients with myelodysplasia and aplastic anemia with raised ferritin levels. Hematological Oncology. 2008;26(4):225-8.
16. Hayflick SJ, Hartman M, Coryell J, Gitschier J, Rowley H. Brain MRI in Neurodegeneration with Brain Iron Accumulation with and without PANK2 Mutations. American Journal of Neuroradiology. 2006;27(6):1230-3.
17. Levi S, Finazzi D. Neurodegeneration with brain iron accumulation: update on pathogenic mechanisms. Frontiers in Pharmacology. 2014;5.
18. Corot C, Robert P, Idée J-M, Port M. Recent advances in iron oxide nanocrystal technology for medical imaging. Advanced Drug Delivery Reviews. 2006;58(14):1471-504.
19. Srinivas M, Boehm-Sturm P, Figdor CG, de Vries IJ, Hoehn M. Labeling cells for in vivo tracking using 19F MRI. Biomaterials. 2012;33(34):8830-40.

20. Dekaban GA, Hamilton AM, Fink CA, Au B, de Chickera SN, Ribot EJ, et al. Tracking and evaluation of dendritic cell migration by cellular magnetic resonance imaging. Wiley Interdisciplinary Reviews: Nanomedicine and Nanobiotechnology. 2013;5(5):469-83.
21. Harisinghani MG, Saksena MA, Hahn PF, King B, Kim J, Torabi MT, et al. Ferumoxtran-10-Enhanced MR Lymphangiography: Does Contrast-Enhanced Imaging Alone Suffice for Accurate Lymph Node Characterization? American Journal of Roentgenology. 2006;186(1):144-8.
22. Bushong S. Magnetic Resonance Imaging – Physical and Biological Principles. 2nd Edition ed. St. Louis: Mosby; 1996.
23. Berlex L. About Magnevist 2006 [cited 2008 20th March 2008]. Available from: http://www.pharma.bayer.com/scripts/pages/en/news_room/news_room/archive/newsroom_archive55.php
24. Sahani D. MRI Contrast Agents: A Dynamic Field in Flux. Imaging Technology. 2004(July).
25. Shellock F, Kanal E. Magnetic resonance – Bioeffects, Safety and patient Management. 2nd ed. Philadelphia: Lippincott Williams & Wilkins; 1996.
26. Radiologists RAaNZCo, Group MR, Committee SoPaA. RANZCR guidelines on the use of gadolinium-containing MRI contrast agents: Royal Australian New Zealand College Radiologists; 2008 [cited 2008 20th March 2008]. Available from: http://www.ranzcr.edu.au/documents/download.cfm/NSFguidelines2008.pdf?txtLibraryID=ranzcr&txtFileName=NSFguidelines2008%2Epdf
27. Bulte J, Modo M. Nanoparticles in Biomedical imaging – Emerging Technologies and applications. New York: Springer; 2007.
28. Mirkin C, Niemeyer C. Nanobiotechnology II – More Concepts and Applications. Wienheim: John Wiley & Sons; 2007.
29. High WA, Ayers RA, Chandler J, Zito G, Cowper SE. Gadolinium is detectable within the tissue of patients with nephrogenic systemic fibrosis. Journal of the American Academy of Dermatology. 2007;56(1):21-6.
30. Cowper SE, Robin HS, Steinberg SM, Su LD, Gupta S, LeBoit PE. Scleromyxoedema-like cutaneous diseases in renal-dialysis patients. The Lancet. 2000;356(9234):1000-1.
31. Broome DR. Nephrogenic systemic fibrosis associated with gadolinium based contrast agents: A summary of the medical literature reporting. European Journal of Radiology. 2008;66(2):230-4.
32. Cowper SE. Nephrogenic Systemic Fibrosis: The Nosological and Conceptual Evolution of Nephrogenic Fibrosing Dermopathy. American Journal of Kidney Diseases. 2005;46(4):763-5.
33. Pryor JG, Poggioli G, Galaria N, Gust A, Robison J, Samie F, et al. Nephrogenic systemic fibrosis: A clinicopathologic study of six cases. Journal of the American Academy of Dermatology. 2007;57(1):105-11.
34. Cowper SE, Rabach M, Girardi M. Clinical and histological findings in nephrogenic systemic fibrosis. European Journal of Radiology. 2008;66(2):191-9.
35. Danielle M. DeHoratius SEC. Nephrogenic Systemic Fibrosis: An Emerging Threat Among Renal Patients. Seminars in Dialysis. 2006;19(3):191-4.
36. Thomsen HS, Morcos SK, Dawson P. Is there a causal relation between the administration of gadolinium based contrast media and the development of nephrogenic systemic fibrosis (NSF)? Clinical Radiology. 2006;61(11):905-6.
37. Grobner T. Gadolinium - a specific trigger for the development of nephrogenic fibrosing dermopathy and nephrogenic systemic fibrosis? Nephrol Dial Transplant. 2006;21(4):1104-8.

38. Joffe P, Thomsen HS, Meusel M. Pharmacokinetics of gadodiamide injection in patients with severe renal insufficiency and patients undergoing hemodialysis or continuous ambulatory peritoneal dialysis. Academic Radiology. 1998;5(7):491-502.
39. Thomsen HS, Marckmann P. Extracellular Gd-CA: Differences in prevalence of NSF. European Journal of Radiology. 2008;66(2):180-3.
40. Morcos SK. Extracellular gadolinium contrast agents: Differences in stability. European Journal of Radiology. 2008;66(2):175-9.
41. Desreux J, Gilsoul D. Chemical synthesis of paramagnetic complexes. In: HS T, RN M, RF M, editors. Trends in contrast imaging. Berlin, Germany: Springer-Verlag; 1999. p. 161-9.
42. Dawson P. Gadolinium chelates: chemistry. In: Dawson P, Cosgrove D, Grainger R, editors. Textbook of contrast media. Oxford: Isis Medical Media; 1999. p. 291–6.
43. Cowper S. NSF and macrocyclics. In: Mandarano G, editor. email communication ed. Melbourne2009.
44. Comblin V, Gilsoul D, Hermann M, Humblet V, Jacques V, Mesbahi M, et al. Designing new MRI contrast agents: a coordination chemistry challenge. Coordination Chemistry Reviews. 1999;185-186:451-70.
45. Idée J-M, Port M, Medina C, Lancelot E, Fayoux E, Ballet S, et al. Possible involvement of gadolinium chelates in the pathophysiology of nephrogenic systemic fibrosis: A critical review. Toxicology. 2008;248(2-3):77-88.
46. Golding L, Provenzale J. Nephrogenic systemic fibrosis: Possible association with a predisposing infection. American journal of roentgenology 2008;190(4):1069 -75
47. Khurana A, Greene Jr JF, High WA. Quantification of gadolinium in nephrogenic systemic fibrosis: Re-examination of a reported cohort with analysis of clinical factors. Journal of the American Academy of Dermatology. 2008;59(2):218-24.
48. Marckmann P, Skov L, Rossen K, Dupont A, Damholt MB, Heaf JG, et al. Nephrogenic Systemic Fibrosis: Suspected Causative Role of Gadodiamide Used for Contrast-Enhanced Magnetic Resonance Imaging. J Am Soc Nephrol. 2006;17(9):2359-62.
49. Grobner T, Prischl FC. Gadolinium and nephrogenic systemic fibrosis. Kidney Int. 2007;72(3):260-4.
50. Agarwal R, Brunelli SM, Williams K, Mitchell MD, Feldman HI, Umscheid CA. Gadolinium-based contrast agents and nephrogenic systemic fibrosis: a systematic review and meta-analysis. Nephrol Dial Transplant. 2009;24(3):856-63.
51. Kuo PH. Gadolinium-Containing MRI Contrast Agents: Important Variations on a Theme for NSF. Journal of the American College of Radiology. 2008;5(1):29-35.
52. Swaminathan S, Shah SV. New Insights into Nephrogenic Systemic Fibrosis. J Am Soc Nephrol. 2007;18(10):2636-43.
53. Shellock FG, Spinazzi A. MRI Safety Update 2008: Part 1, MRI Contrast Agents and Nephrogenic Systemic Fibrosis. Am J Roentgenol. 2008;191(4):1129-39.
54. Rogers JL, Tarrant T, Kim JS. Nanoparticle-based Diagnostic Imaging of Inflammation in Rheumatic Disease. Current rheumatology reviews. 2014.
55. Christian P, Von der Kammer F, Baalousha M, Hofmann T. Nanoparticles: structure, properties, preparation and behaviour in environmental media. Ecotoxicology. 2008;17(5):326-43.
56. Neuberger T, Schöpf B, Hofmann H, Hofmann M, von Rechenberg B. Superparamagnetic nanoparticles for biomedical applications: Possibilities and limitations of a new drug delivery system. Journal of Magnetism and Magnetic Materials. 2005;293(1):483-96.
57. Kim EH, Ahn Y, Lee HS. Biomedical applications of superparamagnetic iron oxide nanoparticles encapsulated within chitosan. Journal of Alloys and Compounds. 2007;434-435:633-6.

58. Heidt T, Nahrendorf M. Multimodal iron oxide nanoparticles for hybrid biomedical imaging. NMR in Biomedicine. 2013;26(7):756-65.
59. Cormode DP, Naha PC, Fayad ZA. Nanoparticle contrast agents for computed tomography: a focus on micelles. Contrast Media & Molecular Imaging. 2014;9(1):37-52.
60. Rudin M, Weissleder R. Molecular imaging in drug discovery and development. Nat Rev Drug Discov. 2003;2(2):123-31.
61. ASHBURN WL, BRAUNWALD E, SIMON AL, PETERSON KL, GAULT JH. Myocardial Perfusion Imaging with Radioactive-Labeled Particles Injected Directly into the Coronary Circulation of Patients with Coronary Artery Disease. Circulation. 1971;44(5):851-65.
62. Fee HJ, Robinson DS, Sample WF, Graham LS, Holmes EC, Morton DL. The determination of lymph shed by colloidal gold scanning in patients with malignant melanoma: a preliminary study. Surgery. 1978;84(5):626-32.
63. Dias MHM, Lauterbur PC. Ferromagnetic particles as contrast agents for magnetic resonance imaging of liver and spleen. Magnetic Resonance in Medicine. 1986;3(2):328-30.
64. Renshaw PF, Owen CS, McLaughlin AC, Frey TG, Leigh JS. Ferromagnetic contrast agents: A new approach. Magnetic Resonance in Medicine. 1986;3(2):217-25.
65. Ohgushi M, Nagayama K, Wada A. Dextran-magnetite: A new relaxation reagent and its application to T2 measurements in gel systems. Journal of Magnetic Resonance (1969). 1978;29(3):599-601.
66. Jun Y-w, Lee J-H, Cheon J. Nanoparticle Contrast Agents for Molecular Magnetic Resonance Imaging. In: Mirkin PDCA, Niemeyer PDCM, editors. Nanobiotechnology 11: Wiley-VCH Verlag GmbH & Co. KGaA; 2007. p. 321-46.
67. De La Vega JC, Häfeli UO. Utilization of nanoparticles as X-ray contrast agents for diagnostic imaging applications. Contrast Media & Molecular Imaging. 2014:n/a-n/a.
68. Hainfeld JF, Slatkin DN, Focella TM, Smilowitz HM. Gold nanoparticles: a new X-ray contrast agent. The British Journal of Radiology. 2006;79(939):248-53.
69. Chien C-C, Chen H-H, Lai S-F, Wu K-C, Cai X, Hwu Y, et al. Gold nanoparticles as high-resolution X-ray imaging contrast agents for the analysis of tumor-related micro-vasculature. J Nanobiotechnol. 2012;10:10-1.
70. Kobayashi Y, Nagasu R, Shibuya K, Nakagawa T, Kubota Y, Gonda K, et al. Synthesis of a colloid solution of silica-coated gold nanoparticles for X-ray imaging applications. J Nanopart Res. 2014;16(8):1-13.
71. Cormode DP, Roessl E, Thran A, Skajaa T, Gordon RE, Schlomka J-P, et al. Atherosclerotic Plaque Composition: Analysis with Multicolor CT and Targeted Gold Nanoparticles. Radiology. 2010;256(3):774-82.
72. Li X, Zhou H, Yang L, Du G, Pai-Panandiker AS, Huang X, et al. Enhancement of cell recognition< i> in vitro</i> by dual-ligand cancer targeting gold nanoparticles. Biomaterials. 2011;32(10):2540-5.
73. Ninomiya K, Fukuda A, Ogino C, Shimizu N. Targeted sonocatalytic cancer cell injury using avidin-conjugated titanium dioxide nanoparticles. Ultrasonics Sonochemistry. 2014;21(5):1624-8.
74. Bonnemain B. Superparamagnetic agents in magnetic resonance imaging: physicochemical characteristics and clinical applications. A review. J Drug Target. 1998;6(3):167-74.
75. Teja AS, Koh P-Y. Synthesis, properties, and applications of magnetic iron oxide nanoparticles. Progress in Crystal Growth and Characterization of Materials.55(1-2):22-45.
76. Bulte JW, Kraitchman DL. Iron oxide MR contrast agents for molecular and cellular imaging. NMR Biomed. 2004;17(7):484-99.
77. Gupta AK, Gupta M. Synthesis and surface engineering of iron oxide nanoparticles for biomedical applications. Biomaterials. 2005;26(18):3995-4021.

78. Bulte JW, Arbab AS, Douglas T, Frank JA. Preparation of magnetically labeled cells for cell tracking by magnetic resonance imaging. Methods Enzymol. 2004;386:275-99.
79. Fleige G, Seeberger F, Laux D, Kresse M, Taupitz M, Pilgrimm H, et al. In vitro characterization of two different ultrasmall iron oxide particles for magnetic resonance cell tracking. Invest Radiol. 2002;37(9):482-8.
80. Mornet S, Vasseur S, Grasset F, Veverka P, Goglio G, Demourgues A, et al. Magnetic nanoparticle design for medical applications. Progress in Solid State Chemistry. 2006;34(2-4):237-47.
81. Cheng FY, Su CH, Yang YS, Yeh CS, Tsai CY, Wu CL, et al. Characterization of aqueous dispersions of Fe(3)O(4) nanoparticles and their biomedical applications. Biomaterials. 2005;26(7):729-38.
82. Morales MP, Bomati-Miguel O, Pérez de Alejo R, Ruiz-Cabello J, Veintemillas-Verdaguer S, O'Grady K. Contrast agents for MRI based on iron oxide nanoparticles prepared by laser pyrolysis. Journal of Magnetism and Magnetic Materials. 2003;266(1-2):102-9.
83. Wagner S, Schnorr J, Pilgrimm H, Hamm B, Taupitz M. Monomer-coated very small superparamagnetic iron oxide particles as contrast medium for magnetic resonance imaging: preclinical in vivo characterization. Invest Radiol. 2002;37(4):167-77.
84. LaConte L, Nitin N, Bao G. Magnetic nanoparticle probes. Materials Today. 2005;8(5, Supplement 1):32-8.
85. Weibo C, Xiaoyuan C. Nanoplatforms for Targeted Molecular Imaging in Living Subjects. Small. 2007;3(11):1840-54.
86. Thomas RM, Matthew DR, Cheryl AL. Pelvic lymph node visualization with MR imaging using local administration of ultra-small superparamagnetic iron oxide contrast. Journal of Magnetic Resonance Imaging. 2002;15(4):492-7.
87. Mark GT, Richard N, Rudy D, Jerome ML, James AT. Interstitial MR lymphangiography for the detection of sentinel lymph nodes. Journal of Surgical Oncology. 2001;78(3):151-6.
88. Zinderman CE, Landow L, Wise RP. Anaphylactoid reactions to Dextran 40 and 70: Reports to the United States Food and Drug Administration, 1969 to 2004. Journal of Vascular Surgery. 2006;43(5):1004-9.
89. Rosenthal MD, Glew RH. Medical Biochemistry - Human Metabolism in Health and Disease. New Jersey, USA: Wiley; 2009.
90. Thorek DL, Chen AK, Czupryna J, Tsourkas A. Superparamagnetic iron oxide nanoparticle probes for molecular imaging. Ann Biomed Eng. 2006;34(1):23-38.
91. Jeong U, Teng X, Wang Y, Yang H, Xia Y. Superparamagnetic colloids: Controlled synthesis and niche applications. Advanced Materials. 2006;19(1).
92. Roch A, Muller RN, Gillis P. Theory of proton relaxation induced by superparamagnetic particles. The Journal of Chemical Physics. 1999;110(11):5403-11.
93. Aime S, Caravan P. Biodistribution of gadolinium-based contrast agents, including gadolinium deposition. Journal of Magnetic Resonance Imaging. 2009;30(6):1259-67.
94. Ergün I, Keven K, Uruç I, Ekmekçi Y, Canbakan B, Erden I, et al. The safety of gadolinium in patients with stage 3 and 4 renal failure. Nephrology Dialysis Transplantation. 2006;21(3):697-700.
95. Erley CM, Bader BD, Berger ED, Tuncel N, Winkler S, Tepe G, et al. Gadolinium-based contrast media compared with iodinated media for digital subtraction angiography in azotaemic patients. Nephrology Dialysis Transplantation. 2004;19(10):2526-31.
96. Perazella M, Pope J, Cowper S. Nephrogenic Systemic Fibrosis and Other Scleroderma Mimickers. In: Stone J, editor. A Clinician's Pearls and Myths in Rheumatology: Springer London; 2010. p. 97-106.
97. Sam Ii AD, Morasch MD, Collins J, Song G, Chen R, Pereles FS. Safety of gadolinium contrast angiography in patients with chronic renal insufficiency. Journal of Vascular Surgery. 2003;38(2):313-8.

98. Lodhia J, Mandarano G, Ferris NJ, Eu P, Cowell SF. Development and use of iron oxide nanoparticles (Part 1): Synthesis of iron oxide nanoparticles for MRI. Biomedical Imaging and Intervention Journal. 2010;6(2).
99. Tamura I, Mizushima T. Explanation for magnetic properties of interacting iron oxide nanocrystals. Journal of Magnetism and Magnetic Materials. 2002;250:241-8.
100. Thorek DL, Tsourkas A. Size, charge and concentration dependent uptake of iron oxide particles by non-phagocytic cells. Biomaterials. 2008;29(26):3583-90.
101. Jacques V, Desreaux JF. New Classes of MRI Contrast Agents. In: Krause PDW, editor. Topics in Current Chemistry. 221/2002. Berlin, Heidelberg: Springer-Verlag; 2002. p. 123-64.
102. Hudgins PA, Anzai Y, Morris MR, Lucas MA. Ferumoxtran-10, a superparamagnetic iron oxide as a magnetic resonance enhancement agent for imaging lymph nodes: a phase 2 dose study. AJNR Am J Neuroradiol. 2002;23(4):649-56.
103. Artemov D, Mori N, Okollie B, Bhujwalla ZM. MR molecular imaging of the Her-2/neu receptor in breast cancer cells using targeted iron oxide nanoparticles. Magn Reson Med. 2003;49(3):403-8.
104. Reimer P, Weissleder R, Lee AS, Wittenberg J, Brady TJ. Receptor imaging: application to MR imaging of liver cancer. Radiology. 1990;177(3):729-34.
105. SchÃœTt W, GrÃœTtner C, HÃ„Feli U, Zborowski M, Teller J, Putzar H, et al. Applications of Magnetic Targeting in Diagnosis and Therapyâ€"Possibilities and Limitations: A Mini-Review. Hybridoma. 1997;16(1):109-17.
106. Thorek DLJ, Tsourkas A. Size, charge and concentration dependent uptake of iron oxide particles by non-phagocytic cells. Biomaterials. 2008;29(26):3583-90.
107. Portet D, Denizot B, Rump E, Lejeune JJ, Jallet P. Nonpolymeric Coatings of Iron Oxide Colloids for Biological Use as Magnetic Resonance Imaging Contrast Agents. J Colloid Interface Sci. 2001;238(1):37-42.
108. Rogers WJ, Meyer CH, Kramer CM. Technology Insight: in vivo cell tracking by use of MRI. Nat Clin Pract Cardiovasc Med. 2006;3(10):554-62.
109. Sun C, Lee JSH, Zhang M. Magnetic nanoparticles in MR imaging and drug delivery. Advanced Drug Delivery Reviews. 2008;60(11):1252-65.
110. Mulder WJ, Strijkers GJ, van Tilborg GA, Griffioen AW, Nicolay K. Lipid-based nanoparticles for contrast-enhanced MRI and molecular imaging. NMR Biomed. 2006;19(1):142-64.
111. Barrett T, Kobayashi H, Brechbiel M, Choyke PL. Macromolecular MRI contrast agents for imaging tumor angiogenesis. European Journal of Radiology. 2006;60(3):353-66.
112. Zhao M, Beauregard DA, Loizou L, Davletov B, Brindle KM. Non-invasive detection of apoptosis using magnetic resonance imaging and a targeted contrast agent. Nat Med. 2001;7(11):1241-4.
113. Hild WA, Breunig M, Goepferich A. Quantum dots - Nano-sized probes for the exploration of cellular and intracellular targeting. European Journal of Pharmaceutics and Biopharmaceutics. 2008;68(2):153-68.
114. Jeong U, Teng X, Wang Y, Yang H, Xia Y. Superparamagnetic Colloids: Controlled Synthesis and Niche Applications. Advanced Materials. 2007;19(1):33-60.
115. Waters EA. MRI molecular targeted imaging and therapy of angiogenesis in aortic valve disease using fluorinated nanoparticles [Ph.D.]. United States -- Missouri: Washington University in St. Louis; 2008.
116. Häfeli UO. Magnetically modulated therapeutic systems. International Journal of Pharmaceutics. 2004;277(1-2):19-24.
117. Wilhelm C, Gazeau F. Universal cell labelling with anionic magnetic nanoparticles. Biomaterials. 2008;29(22):3161-74.
118. Rabinow B, Chaubal MV. Injectable nanoparticles for efficient drug delivery. Drugs Pharmaceut Sci. 2006;159:199-229.

119. Lübbe AS, Alexiou C, Bergemann C. Clinical Applications of Magnetic Drug Targeting. Journal of Surgical Research. 2001;95(2):200-6.
120. Nagesha D, Devalapally H, Sridhar S, Amiji MM. Multifunctional Magnetic Nanosystems for Tumor Imaging, Targeted Delivery, and Thermal Medicine. Multifunctional Pharmaceutical Nanocarriers2008. p. 381-408.
121. Fortin J-P, Gazeau F, Wilhelm C. Intracellular heating of living cells through Néel relaxation of magnetic nanoparticles. European Biophysics Journal. 2008;37(2):223-8.
122. Jordan A, Scholz R, Wust P, Schirra H, Thomas S, Schmidt H, et al. Endocytosis of dextran and silan-coated magnetite nanoparticles and the effect of intracellular hyperthermia on human mammary carcinoma cells in vitro. Journal of Magnetism and Magnetic Materials. 1999;194(1-3):185-96.
123. Salado J, Insausti M, Lezama L, Rojo T, Echevarria JJ, Garcia-Alonso I, et al. FE3O4 Nanoparticles for MRI Contrast Enhancement. Trends in NanoTechnology; 03-07 September, 2007; San Sebastian, Spain2007.
124. Xu YH, Bai J, Wang J-P. High-magnetic-moment multifunctional nanoparticles for nanomedicine applications. Journal of Magnetism and Magnetic Materials. 2007;311(1):131-4.
125. Plotkin M, Gneveckow U, Meier-Hauff K, Amthauer H, FeuÃŸner A, Denecke T, et al. ¹⁸F-FET PET for planning of thermotherapy using magnetic nanoparticles in recurrent glioblastoma -- Hot Topic. International Journal of Hyperthermia. 2006;22(4):319 - 25.
126. Sun C, Fang C, Stephen Z, Veiseh O, Hansen S, Lee D, et al. Tumor-targeted drug delivery and MRI contrast enhancement by chlorotoxin-conjugated iron oxide nanoparticles. Nanomed. 2008;3(4):495-505.
127. Lee JH, Huh YM, Jun YW, Seo JW, Jang JT, Song HT, et al. Artificially engineered magnetic nanoparticles for ultra-sensitive molecular imaging. Nat Med. 2007;13(1):95-9.
128. Huh YM, Jun YW, Song HT, Kim S, Choi JS, Lee JH, et al. In vivo magnetic resonance detection of cancer by using multifunctional magnetic nanocrystals. J Am Chem Soc. 2005;127(35):12387-91.
129. Oghabian MA, Guiti M, Haddad P, Gharehaghaji N, Saber R, Alam NR, et al. Detection sensitivity of MRI using ultra-small super paramagnetic iron oxide nano-particles (USPIO) in biological tissues. Conf Proc IEEE Eng Med Biol Soc. 2006;1:5625-6.
130. Wang A, Z. , Bagalkot V, Vasilliou C, C. , Gu F, Alexis F, Zhang L, et al. Superparamagnetic Iron Oxide Nanoparticle-Aptamer Bioconjugates for Combined Prostate Cancer Imaging and Therapy. ChemMedChem. 2008;3(9):1311-5.
131. Enochs WS, Harsh G, Hochberg F, Weissleder R. Improved delineation of human brain tumors on MR images using a long-circulating, superparamagnetic iron oxide agent. J Magn Reson Imaging. 1999;9(2):228-32.
132. Neuwelt EA, Varallyay P, Bago AG, Muldoon LL, Nesbit G, Nixon R. Imaging of iron oxide nanoparticles by MR and light microscopy in patients with malignant brain tumours. Neuropathol Appl Neurobiol. 2004;30(5):456-71.
133. Varallyay P, Nesbit G, Muldoon LL, Nixon RR, Delashaw J, Cohen JI, et al. Comparison of two superparamagnetic viral-sized iron oxide particles ferumoxides and ferumoxtran-10 with a gadolinium chelate in imaging intracranial tumors. AJNR Am J Neuroradiol. 2002;23(4):510-9.
134. Kraitchman DL, Heldman AW, Atalar E, Amado LC, Martin BJ, Pittenger MF, et al. In Vivo Magnetic Resonance Imaging of Mesenchymal Stem Cells in Myocardial Infarction. Circulation. 2003;107(18):2290-3.
135. Heymer A, Haddad D, Weber M, Gbureck U, Jakob PM, Eulert J, et al. Iron oxide labelling of human mesenchymal stem cells in collagen hydrogels for articular cartilage repair. Biomaterials. 2008;29(10):1473-83.

136. Guzman R, Bliss T, De Los Angeles A, Moseley M, Palmer T, Steinberg G. Neural progenitor cells transplanted into the uninjured brain undergo targeted migration after stroke onset. J Neurosci Res. 2008;86(4):873-82.
137. Zhang Z, Mascheri N, Dharmakumar R, Li D. Cellular magnetic resonance imaging: potential for use in assessing aspects of cardiovascular disease. Cytotherapy. 2008:1-12.
138. Sosnovik DE, Nahrendorf M, Weissleder R. Molecular Magnetic Resonance Imaging in Cardiovascular Medicine. Circulation. 2007;115(15):2076-86.
139. Himes N, Min JY, Lee R, Brown C, Shea J, Huang X, et al. In vivo MRI of embryonic stem cells in a mouse model of myocardial infarction. Magn Reson Med. 2004;52(5):1214-9.
140. Sosnovik DE. Molecular imaging in cardiovascular magnetic resonance imaging: current perspective and future potential. Top Magn Reson Imaging. 2008;19(1):59-68.
141. Mulder WJM. Lipid-based nanoparticles for magnetic resonance molecular imaging: Design, characterization, and application [Ph.D.]. Netherlands: Technische Universiteit Eindhoven (The Netherlands); 2006.
142. Ruehm SG, Corot C, Vogt P, Kolb S, Debatin JF. Magnetic Resonance Imaging of Atherosclerotic Plaque With Ultrasmall Superparamagnetic Particles of Iron Oxide in Hyperlipidemic Rabbits. Circulation. 2001;103(3):415-22.
143. Waters E, Wickline S. Contrast agents for MRI. Basic Research in Cardiology. 2008;103(2):114-21.
144. Winter P, M. , Cai K, Chen J, Adair C, R. , Kiefer G, E. , Athey P, S. , et al. Targeted PARACEST nanoparticle contrast agent for the detection of fibrin. Magnetic Resonance in Medicine. 2006;56(6):1384-8.
145. Allkemper T, Bremer C, Matuszewski L, Ebert W, Reimer P. Contrast-enhanced Blood-Pool MR Angiography with Optimized Iron Oxides: Effect of Size and Dose on Vascular Contrast Enhancement in Rabbits1. Radiology. 2002;223(2):432-8.
146. Krombach GA, Wendland MF, Higgins CB, Saeed M. MR Imaging of Spatial Extent of Microvascular Injury in Reperfused Ischemically Injured Rat Myocardium: Value of Blood Pool Ultrasmall Superparamagnetic Particles of Iron Oxide1. Radiology. 2002;225(2):479-86.
147. Tombach B, Reimer P, Bremer C, Allkemper T, Engelhardt M, Mahler M, et al. First-pass and equilibrium-MRA of the aortoiliac region with a superparamagnetic iron oxide blood pool MR contrast agent (SH U 555 C): results of a human pilot study. NMR Biomed. 2004;17(7):500-6.
148. Li W, Tutton S, Vu AT, Pierchala L, Li BS, Lewis JM, et al. First-pass contrast-enhanced magnetic resonance angiography in humans using ferumoxytol, a novel ultrasmall superparamagnetic iron oxide (USPIO)-based blood pool agent. J Magn Reson Imaging. 2005;21(1):46-52.
149. Schellenberger E, Rudloff F, Warmuth C, Taupitz M, Hamm B, Schnorr Jr. Protease-Specific Nanosensors for Magnetic Resonance Imaging. Bioconjugate Chemistry. 2008;19(12):2440-5.
150. Colombo M, Ronchi S, Monti D, Corsi F, Trabucchi E, Prosperi D. Femtomolar detection of autoantibodies by magnetic relaxation nanosensors. Analytical Biochemistry. 2009;392(1):96-102.
151. Kaittanis C, Santra S, Perez JM. Role of Nanoparticle Valency in the Nondestructive Magnetic-Relaxation-Mediated Detection and Magnetic Isolation of Cells in Complex Media. Journal of the American Chemical Society. 2009;131(35):12780-91.
152. Jang J-t, Nah H, Lee J-H, Moon Seung H, Kim Min G, Cheon J. Critical Enhancements of MRI Contrast and Hyperthermic Effects by Dopant-Controlled Magnetic Nanoparticles13. Angewandte Chemie International Edition. 2009;48(7):1234-8.
153. Groman EV, Bouchard JC, Reinhardt CP, Vaccaro DE. Ultrasmall Mixed Ferrite Colloids as Multidimensional Magnetic Resonance Imaging, Cell Labeling, and Cell Sorting Agents. Bioconjugate Chemistry. 2007;18(6):1763-71.

154. Lu J, Ma S, Sun J, Xia C, Liu C, Wang Z, et al. Manganese ferrite nanoparticle micellar nanocomposites as MRI contrast agent for liver imaging. Biomaterials. 2009;30(15):2919-28.
155. Jendelova P, Herynek V, Urdzikova L, Glogarova K, Kroupova J, Andersson B, et al. Magnetic resonance tracking of transplanted bone marrow and embryonic stem cells labeled by iron oxide nanoparticles in rat brain and spinal cord. J Neurosci Res. 2004;76(2):232-43.
156. McFadden C, Mallett CL, Foster PJ. Labeling of multiple cell lines using a new iron oxide agent for cell tracking by MRI. Contrast Media & Molecular Imaging. 2011;6(6):514-22.
157. Wong RM, Gilbert DA, Liu K, Louie AY. Rapid Size-Controlled Synthesis of Dextran-Coated, 64Cu-Doped Iron Oxide Nanoparticles. ACS Nano. 2012;6(4):3461-7.
158. Pombo-Garcia K, Zarschler K, Barreto JA, Hesse J, Spiccia L, Graham B, et al. Design, synthesis, characterisation and in vitro studies of hydrophilic, colloidally stable, 64Cu(ii)-labelled, ultra-small iron oxide nanoparticles in a range of human cell lines. RSC Advances. 2013;3(44):22443-54.
159. Madru R, Kjellman P, Olsson F, Wingårdh K, Ingvar C, Ståhlberg F, et al. 99mTc-Labeled Superparamagnetic Iron Oxide Nanoparticles for Multimodality SPECT/MRI of Sentinel Lymph Nodes. Journal of Nuclear Medicine. 2012;53(3):459-63.
160. Zhang F, Niu G, Lu G, Chen X. Preclinical lymphatic imaging. Mol Imaging Biol. 2011;13(4):599-612.
161. Lucarelli RT, Ogawa M, Kosaka N, Turkbey B, Kobayashi H, Choyke PL. New Approaches to Lymphatic Imaging. Lymphatic Research and Biology. 2009;7(4):205-14.
162. Barrett T, Choyke PL, Kobayashi H. Imaging of the lymphatic system: new horizons. Contrast Media Mol Imaging. 2006;1:230.
163. Kwee T, Basu S, Torigian D, Saboury B, Alavi A. Defining the role of modern imaging techniques in assessing lymph nodes for metastasis in cancer: evolving contribution of PET in this setting. European Journal of Nuclear Medicine and Molecular Imaging. 2011;38(7):1353-66.
164. Jain R, Dandekar P, Patravale V. Diagnostic nanocarriers for sentinel lymph node imaging. Journal of Controlled Release. 2009;138(2):90-102.
165. Harisinghani MG, Barentsz J, Hahn PF, Deserno WM, Tabatabaei S, van de Kaa CH, et al. Noninvasive detection of clinically occult lymph-node metastases in prostate cancer. N Engl J Med. 2003;348(25):2491-9.
166. Nune SK, Gunda P, Majeti BK, Thallapally PK, Forrest ML. Advances in lymphatic imaging and drug delivery. Advanced Drug Delivery Reviews. 2011;63(10-11):876-85.
167. Solari N, Gipponi M, Stella M, Queirolo P, di Somma C, Villa G, et al. Predictive role of preoperative lymphoscintigraphy on the status of the sentinel lymph node in clinically node-negative patients with cutaneous melanoma. Melanoma research 2009;19(4).
168. Stacker SA, Achen MG, Turkbey B, Ravizzini G, Choyke PL, Kobayashi H. Lymphangiogenesis and Imaging of the Lymphatics in Cancer

Lymphangiogenesis in Cancer Metastasis. Cancer Metastasis - Biology and Treatment. 13: Springer Netherlands; 2009. p. 159-84.
169. Mai S, Welzel G, Hermann B, Wenz F, Haberkorn U, Dinter D. Can the Radiation Dose to CT-Enlarged but FDG-PET-Negative Inguinal Lymph Nodes in Anal Cancer Be Reduced? Strahlentherapie und Onkologie. 2009;185(4):254-9.
170. O'Malley M, Chung P, Haider M, Jang H-J, Jhaveri K, Khalili K, et al. Comparison of low dose with standard dose abdominal/pelvic multidetector CT in patients with stage 1 testicular cancer under surveillance. European Radiology. 2010;20(7):1624-30.
171. Hungerhuber E, Schlenker B, Frimberger D, Linke R, Karl A, Stief C, et al. Lymphoscintigraphy in penile cancer: limited value of sentinel node biopsy in patients with clinically suspicious lymph nodes. World Journal of Urology. 2006;24(3):319-24.

172. Guimaraes AR, Tabatabei S, Dahl D, McDougal WS, Weissleder R, Harisinghani MG. Pilot Study Evaluating Use of Lymphotrophic Nanoparticle-Enhanced Magnetic Resonance Imaging for Assessing Lymph Nodes in Renal Cell Cancer. Urology. 2008;71(4):708-12.
173. Koh D-M, George C, Temple L, Collins DJ, Toomey P, Raja A, et al. Diagnostic Accuracy of Nodal Enhancement Pattern of Rectal Cancer at MRI Enhanced With Ultrasmall Superparamagnetic Iron Oxide: Findings in Pathologically Matched Mesorectal Lymph Nodes. American Journal of Roentgenology. 2010;194(6):W505-W13.
174. Ross RW, Zietman AL, Xie W, Coen JJ, Dahl DM, Shipley WU, et al. Lymphotropic nanoparticle-enhanced magnetic resonance imaging (LNMRI) identifies occult lymph node metastases in prostate cancer patients prior to salvage radiation therapy. Clinical Imaging.33(4):301-5.
175. Heesakkers RAM, Hövels AM, Jager GJ, van den Bosch HCM, Witjes JA, Raat HPJ, et al. MRI with a lymph-node-specific contrast agent as an alternative to CT scan and lymph-node dissection in patients with prostate cancer: a prospective multicohort study. The Lancet Oncology. 2008;9(9):850-6.
176. Hsueh EC, Turner RR, Giuliano AE. Lymphoscintigraphy and Lymphatic Mapping for Identification of Sentinel Lymph Nodes. World Journal of Surgery. 2001;25(6):794-7.
177. Harvey NL, Srinivasan RS, Dillard ME, Johnson NC, Witte MH, Boyd K, et al. Lymphatic vascular defects promoted by Prox1 haploinsufficiency cause adult-onset obesity. Nat Genet. 2005;37(10):1072-81.
178. Cheng G, Kurita S, Torigian D, Alavi A. Current status of sentinel lymph-node biopsy in patients with breast cancer. European Journal of Nuclear Medicine and Molecular Imaging. 2011;38(3):562-75.
179. Scarsbrook AF, Ganeshan A, Bradley KM. Pearls and pitfalls of radionuclide imaging of the lymphatic system. Part 1: sentinel node lymphoscintigraphy in malignant melanoma. Br J Radiol. 2007;80(950):132-9.
180. Read E. Radio-active dose used per single injection for lymphoscintihraphy. personal communication. 2011.
181. Hoshida T, Isaka N, Hagendoorn J, di Tomaso E, Chen Y-L, Pytowski B, et al. Imaging Steps of Lymphatic Metastasis Reveals That Vascular Endothelial Growth Factor-C Increases Metastasis by Increasing Delivery of Cancer Cells to Lymph Nodes: Therapeutic Implications. Cancer Research. 2006;66(16):8065-75.
182. Cao HST, McElroy M, Kaushal S, Hoffman RM, Bouvet M. Imaging of the interaction of cancer cells and the lymphatic system. Advanced Drug Delivery Reviews. 2011;63(10-11):886-9.
183. Webb WR, Brant WE, Major N. Fundamentals of Body CT. 3rd ed: Saunders 2006.
184. Harisinghani MG, Dixon WT, Saksena MA, Brachtel E, Blezek DJ, Dhawale PJ, et al. MR Lymphangiography: Imaging Strategies to Optimize the Imaging of Lymph Nodes with Ferumoxtran-101. Radiographics. 2004;24(3):867-78.
185. Westbrook C, Kaut Roth C, Talbot J. MRI in practice. 3rd ed. Oxford: Blackwell Publishing; 2005.
186. McRobbie D, Moore E, Graves M, Prince M. MRI – From Picture to Proton. Cambridge: Cambridge University Press; 2003.
187. Korteweg M, Zwanenburg J, van Diest P, van den Bosch M, Luijten P, van Hillegersberg R, et al. Characterization of ex vivo healthy human axillary lymph nodes with high resolution 7 Tesla MRI. European radiology. 2011;21(2):310-7.
188. Korteweg MA, Zwanenburg JJM, Hoogduin JM, van den Bosch MAAJ, van Diest PJ, van Hillegersberg R, et al. Dissected Sentinel Lymph Nodes of Breast Cancer Patients: Characterization with High-Spatial-Resolution 7-T MR Imaging. Radiology. 2011;261(1):127-35.

189. Klerkx WM, Bax L, Veldhuis WB, Heintz APM, Mali WP, Peeters PHM, et al. Detection of Lymph Node Metastases by Gadolinium-Enhanced Magnetic Resonance Imaging: Systematic Review and Meta-analysis. Journal of the National Cancer Institute. 2010;102(4):244-53.
190. Mandarano G, Lodhia J, Eu P, Ferris N, Davidson R, Cowell S. Development and use of iron oxide nanoparticles (Part 2): The application of iron oxide contrast agents in MRI. Biomed Imaging Interv J. 2010;6((2)).
191. Kimura K, Tanigawa N, Matsuki M, Nohara T, Iwamoto M, Sumiyoshi K, et al. High-resolution MR lymphography using ultrasmall superparamagnetic iron oxide (USPIO) in the evaluation of axillary lymph nodes in patients with early stage breast cancer: preliminary results. Breast Cancer. 2010;17(4):241-6.
192. Will O, Purkayastha S, Chan C, Athanasiou T, Darzi AW, Gedroyc W, et al. Diagnostic precision of nanoparticle-enhanced MRI for lymph-node metastases: a meta-analysis. Lancet Oncol. 2006;7(1):52-60.
193. Saksena MA, Saokar A, Harisinghani MG. Lymphotropic nanoparticle enhanced MR imaging (LNMRI) technique for lymph node imaging. European Journal of Radiology. 2006;58(3):367-74.
194. McCauley TR, Rifkin MD, Ledet CA. Pelvic lymph node visualization with MR imaging using local administration of ultra-small superparamagnetic iron oxide contrast. Journal of Magnetic Resonance Imaging. 2002;15(4):492-7.
195. McCauley TR, Rifkin MD, Ledet CA. Pelvic lymph node visualization with MR imaging using local administration of ultra-small superparamagnetic iron oxide contrast. J Magn Reson Imaging. 2002;15(4):492-7.
196. Ferguson PM, Slocombe A, Tilley RD, Hermans IF. Using Magnetic Resonance Imaging to Evaluate Dendritic Cell-Based Vaccination. PLoS ONE. 2013;8(5).
197. Steinman RM, Cohn ZA. Identification of a novel cell type in peripheral lymphoid organs of mice I. Morphology, quantitation, tissue distribution. The Journal of experimental medicine. 1973;137(5):1142-62.
198. MacDonald KP, Munster DJ, Clark GJ, Dzionek A, Schmitz J, Hart DN. Characterization of human blood dendritic cell subsets. Blood. 2002;100(13):4512-20.
199. Pulendran B, Banchereau J, Burkeholder S, Kraus E, Guinet E, Chalouni C, et al. Flt3-ligand and granulocyte colony-stimulating factor mobilize distinct human dendritic cell subsets in vivo. The Journal of Immunology. 2000;165(1):566-72.
200. Martín-Fontecha A, Lanzavecchia A, Sallusto F. Dendritic cell migration to peripheral lymph nodes. Dendritic Cells: Springer; 2009. p. 31-49.
201. Randolph GJ, editor Dendritic cell migration to lymph nodes: cytokines, chemokines, and lipid mediators. Seminars in immunology; 2001: Elsevier.
202. Segura E, Valladeau-Guilemond J, Donnadieu M-H, Sastre-Garau X, Soumelis V, Amigorena S. Characterization of resident and migratory dendritic cells in human lymph nodes. The Journal of experimental medicine. 2012;209(4):653-60.
203. Bioscience B. Dendritic Cells - Tools for Mouse and Human Dendritic Cell Research. In: Bioscience B, editor.: BD Bioscience; 2005.
204. Wan H, Dupasquier M. Dendritic cells in vivo and in vitro. Cellular & molecular immunology. 2005.
205. Kobukai S, Baheza R, Cobb JG, Virostko J, Xie J, Gillman A, et al. Magnetic nanoparticles for imaging dendritic cells. Magnetic Resonance in Medicine. 2010;63(5):1383-90.
206. Pham W, Kobukai S, Hotta C, Gore JC. Dendritic cells: therapy and imaging. 2009.
207. Mou Y, Hou Y, Chen B, Hua Z, Zhang Y, Xie H, et al. In vivo migration of dendritic cells labeled with synthetic superparamagnetic iron oxide. International journal of nanomedicine. 2011;6:2633.

208. Magnitsky S, Watson DJ, Walton RM, Pickup S, Bulte JWM, Wolfe JH, et al. In vivo and ex vivo MRI detection of localized and disseminated neural stem cell grafts in the mouse brain. NeuroImage. 2005;26(3):744-54.
209. Farrell E, Wielopolski P, Pavljasevic P, van Tiel S, Jahr H, Verhaar J, et al. Effects of iron oxide incorporation for long term cell tracking on MSC differentiation in vitro and in vivo. Biochemical and Biophysical Research Communications. 2008;369(4):1076-81.
210. Andreas K, Georgieva R, Ladwig M, Mueller S, Notter M, Sittinger M, et al. Highly efficient magnetic stem cell labeling with citrate-coated superparamagnetic iron oxide nanoparticles for MRI tracking. Biomaterials. 2012;33(18):4515-25.
211. Jain TK, Richey J, Strand M, Leslie-Pelecky DL, Flask CA, Labhasetwar V. Magnetic nanoparticles with dual functional properties: Drug delivery and magnetic resonance imaging. Biomaterials. 2008;29(29):4012-21.
212. Chertok B, Moffat BA, David AE, Yu F, Bergemann C, Ross BD, et al. Iron oxide nanoparticles as a drug delivery vehicle for MRI monitored magnetic targeting of brain tumors. Biomaterials. 2008;29(4):487-96.
213. Maier-Hauff K, Rothe R, Scholz R, Gneveckow U, Wust P, Thiesen B, et al. Intracranial thermotherapy using magnetic nanoparticles combined with external beam radiotherapy: results of a feasibility study on patients with glioblastoma multiforme. J Neurooncol. 2007;81(1):53-60.
214. Lee J-H, Kim J-w, Cheon J. Magnetic nanoparticles for multi-imaging and drug delivery. Mol Cells. 2013;35(4):274-84.
215. Bouziotis P, Psimadas D, Tsotakos T, Stamopoulos D, Tsoukalas C. Radiolabeled Iron Oxide Nanoparticles As Dual-Modality SPECT/MRI and PET/MRI Agents. Current Topics in Medicinal Chemistry. 2012;12(23):2694-702.
216. Kim S-m, Chae MK, Yim MS, Jeong IH, Cho J, Lee C, et al. Hybrid PET/MR imaging of tumors using an oleanolic acid-conjugated nanoparticle. Biomaterials. 2013;34(33):8114-21.
217. Gupta AK, Naregalkar RR, Vaidya VD, Gupta M. Recent advances on surface engineering of magnetic iron oxide nanoparticles and their biomedical applications. Nanomed. 2007;2(1):23-39.
218. Zanoni G, Puccetti A, Dolcino M, Simone R, Peretti A, Ferro A, et al. Dextran-specific IgG response in hypersensitivity reactions to measles-mumps-rubella vaccine. Journal of Allergy and Clinical Immunology. 2008;122(6):1233-5.
219. Nahrendorf M, Zhang H, Hembrador S, Panizzi P, Sosnovik DE, Aikawa E, et al. Nanoparticle PET-CT imaging of macrophages in inflammatory atherosclerosis. Circulation. 2008;117(3):379-87.
220. Longmire M, Choyke PL, Kobayashi H. Clearance properties of nano-sized particles and molecules as imaging agents: considerations and caveats. 2008.
221. Thomas R, Park I-K, Jeong YY. Magnetic iron oxide nanoparticles for multimodal imaging and therapy of cancer. International journal of molecular sciences. 2013;14(8):15910-30.
222. Promega. CellTiter96 AQueous One Solution Cell Proliferation Assay - Technical Bulletin. Manufacturer's Instructions for Use of Products: Promega; 2012.
223. de Labriolle Vaylet C, Colas-Linhart N, Petiet A, Bok B. White Blood Cell Labeling with 99mTc-HMPAO. Journal of Nuclear Medicine. 2003;44(4):657-8.
224. Ak İ, Vardereli E, Durak B, Gülbaş Z, Basaran N, Stokkel MP, et al. Labeling of mixed leukocytes with 99mTc-HMPAO causes severe chromosomal aberrations in lymphocytes. Journal of Nuclear Medicine. 2002;43(2):203-6.
225. Tsopelas C. Particle size analysis of 99mTc-labeled and unlabeled antimony trisulfide and rhenium sulfide colloids intended for lymphoscintigraphic application. Journal of Nuclear Medicine. 2001;42(3):460-6.

226. Committee MIDA. FDA Advisory Committee Briefing Document. In: Administration FaD, editor. USA2013. p. 95.
227. Budjan J, Schoenberg SO, Morelli JN, Haneder S. MR Contrast Agent Safety in the Age of Nephrogenic Systemic Fibrosis: Update 2014. Curr Radiol Rep. 2014;2(9):1-6.
228. Ota T, Kimura J, Ishiguchi T. Safety and clinical usefulness of gadoteric acid including post-marketing surveillance. Imaging in Medicine. 2012;4(4):397-409.
229. Reimer P, Balzer T. Ferucarbotran (Resovist): a new clinically approved RES-specific contrast agent for contrast-enhanced MRI of the liver: properties, clinical development, and applications. European radiology. 2003;13(6):1266-76.
230. Villanueva A, Canete M, Roca AG, Calero M, Veintemillas-Verdaguer S, Serna CJ, et al. The influence of surface functionalization on the enhanced internalization of magnetic nanoparticles in cancer cells. Nanotechnology. 2009;20(11):115103.
231. Zhang Y, Yang M, Portney NG, Cui D, Budak G, Ozbay E, et al. Zeta potential: a surface electrical characteristic to probe the interaction of nanoparticles with normal and cancer human breast epithelial cells. Biomedical microdevices. 2008;10(2):321-8.
232. Koudelka KJ, Destito G, Plummer EM, Trauger SA, Siuzdak G, Manchester M. Endothelial targeting of cowpea mosaic virus (CPMV) via surface vimentin. PLoS pathogens. 2009;5(5):e1000417.
233. Lorenz MR, Holzapfel V, Musyanovych A, Nothelfer K, Walther P, Frank H, et al. Uptake of functionalized, fluorescent-labeled polymeric particles in different cell lines and stem cells. Biomaterials. 2006;27(14):2820-8.
234. Thiele L, Rothen-Rutishauser B, Jilek S, Wunderli-Allenspach H, Merkle HP, Walter E. Evaluation of particle uptake in human blood monocyte-derived cells in vitro. Does phagocytosis activity of dendritic cells measure up with macrophages? Journal of Controlled Release. 2001;76(1):59-71.
235. Foged C, Brodin B, Frokjaer S, Sundblad A. Particle size and surface charge affect particle uptake by human dendritic cells in an in vitro model. International journal of pharmaceutics. 2005;298(2):315-22.
236. Jarrett BR, Gustafsson Br, Kukis DL, Louie AY. Synthesis of 64Cu-labeled magnetic nanoparticles for multimodal imaging. Bioconjugate chemistry. 2008;19(7):1496-504.
237. Kang KW. Preliminary pre-clinical results and overview on PET/MRI/fluorescent molecular imaging. The Open Nuclear Medicine J. 2010;2:153-6.
238. Aryal S, Key J, Stigliano C, Landis MD, Lee DY, Decuzzi P. Positron Emitting Magnetic Nanoconstructs for PET/MR Imaging. Small. 2014.
239. Mérian J, Gravier J, Navarro F, Texier I. Fluorescent nanoprobes dedicated to in vivo imaging: from preclinical validations to clinical translation. Molecules. 2012;17(5):5564-91.
240. Gilliet M, Boonstra A, Paturel C, Antonenko S, Xu XL, Trinchieri G, et al. The development of murine plasmacytoid dendritic cell precursors is differentially regulated by FLT3-ligand and granulocyte/macrophage colony-stimulating factor. J Exp Med. 2002;195(7):953-8.
241. Li J, Mo HY, Xiong G, Zhang L, He J, Huang ZF, et al. Tumor microenvironment macrophage inhibitory factor directs the accumulation of interleukin-17-producing tumor-infiltrating lymphocytes and predicts favorable survival in nasopharyngeal carcinoma patients. The Journal of biological chemistry. 2012;287(42):35484-95.
242. Bellone G, Smirne C, Mauri FA, Tonel E, Carbone A, Buffolino A, et al. Cytokine expression profile in human pancreatic carcinoma cells and in surgical specimens: implications for survival. Cancer immunology, immunotherapy : CII. 2006;55(6):684-98.
243. Barton BE. Interleukin-6 and new strategies for the treatment of cancer, hyperproliferative diseases and paraneoplastic syndromes. Expert opinion on therapeutic targets. 2005;9(4):737-52.
244. Smolen JS, Maini RN. Interleukin-6: a new therapeutic target. Arthritis research & therapy. 2006;8 Suppl 2:S5.

245. van der Poll T, Keogh CV, Guirao X, Buurman WA, Kopf M, Lowry SF. Interleukin-6 gene-deficient mice show impaired defense against pneumococcal pneumonia. The Journal of infectious diseases. 1997;176(2):439-44.
246. Conti L, Gessani S. GM-CSF in the generation of dendritic cells from human blood monocyte precursors: Recent advances. Immunobiology. 2008;213(9–10):859-70.
247. Rovati B, Mariucci S, Manzoni M, Bencardino K, Danova M. Flow cytometric detection of circulating dendritic cells in healthy subjects. European Journal of Histochemistry. 2009;52(1):45-52.
248. Kassianos AJ, Jongbloed SL, Hart DN, Radford KJ. Isolation of human blood DC subtypes. Dendritic Cell Protocols: Springer; 2010. p. 45-54.
249. Erdmann M, Schuler-Thurner B. Towards a standardized protocol for the generation of monocyte-derived dendritic cell vaccines. Dendritic Cell Protocols: Springer; 2010. p. 149-63.
250. Liu Y-J. IPC: professional type 1 interferon-producing cells and plasmacytoid dendritic cell precursors. Annu Rev Immunol. 2005;23:275-306.
251. Shi J, Ikeda K, Maeda Y, Shinagawa K, Ohtsuka A, Yamamura H, et al. Identification of CD123+ myeloid dendritic cells as an early-stage immature subset with strong tumoristatic potential. Cancer Letters. 2008;270(1):19-29.
252. Pham W, Xie J, Gore JC. Tracking the migration of dendritic cells by in vivo optical imaging. Neoplasia. 2007;9(12):1130-7.
253. Kohrgruber N, Halanek N, Gröger M, Winter D, Rappersberger K, Schmitt-Egenolf M, et al. Survival, maturation, and function of CD11c− and CD11c+ peripheral blood dendritic cells are differentially regulated by cytokines. The Journal of Immunology. 1999;163(6):3250-9.
254. Frankenberger B, Schendel DJ. Third generation dendritic cell vaccines for tumor immunotherapy. European Journal of Cell Biology. 2012;91(1):53-8.
255. Sabado RL, Bhardwaj N. Directing dendritic cell immunotherapy towards successful cancer treatment. Immunotherapy. 2010;2(1):37-56.
256. Grolleau A, Sloan A, Mule J. Dendritic cell-based vaccines for cancer therapy. Tumor immunology and cancer vaccines: Springer; 2005. p. 181-205.
257. Auffray C, Sieweke MH, Geissmann F. Blood Monocytes: Development, Heterogeneity, and Relationship with Dendritic Cells. Annual Review of Immunology. 2009;27(1):669-92.
258. Jagannathan-Bogdan M, Zon LI. Hematopoiesis. Development (Cambridge, England). 2013;140(12):2463-7.
259. Biolegend. Hematopoiesis from pluripotent stem cell 2015 [cited 2015 05-04-2015]. Available from: http://www.biolegend.com/pop_pathway.php?id=6.
260. Willmann K, Olweus J. Peripheral Blood Dendritic Cells revealed by Flow Cytometry

Identification of CD123+ (anti-interleukin 3 receptor α chain) and CD11c+ dendritic cell subsets. In: Bioscience B, editor. Immunochemistry Systems. San Jose, CA, USA: Becton, Dickinson and Comapany; 2000.
261. Jiao Q, Li L, Mu Q, Zhang Q. Immunomodulation of Nanoparticles in Nanomedicine Applications. BioMed Research International. 2014.
262. Zitvogel L, Kepp O, Kroemer G. Decoding cell death signals in inflammation and immunity. Cell. 2010;140(6):798-804.
263. Ning Y, Manegold PC, Hong YK, Zhang W, Pohl A, Lurje G, et al. Interleukin-8 is associated with proliferation, migration, angiogenesis and chemosensitivity in vitro and in vivo in colon cancer cell line models. International Journal of Cancer. 2011;128(9):2038-49.
264. Stehlik C. Macrophages, the Inflammasome and Interleukin-1β in Cancer. " Do not go where the path may lead, go instead where there is no path and leave a trail. 2011:44.

265. Rodemann HP, Blaese MA. Responses of Normal Cells to Ionizing Radiation. Seminars in Radiation Oncology. 2007;17(2):81-8.
266. Wehling N, Palmer GD, Pilapil C, Liu F, Wells JW, Müller PE, et al. Interleukin-1β and tumor necrosis factor α inhibit chondrogenesis by human mesenchymal stem cells through NF-κB–dependent pathways. Arthritis & Rheumatism. 2009;60(3):801-12.
267. Information NCfB. IL1B interleukin 1, beta [Homo sapiens (human)]: National Institute of Health; 2015 [updated 5-Apr-2015; cited 2015 08/04/2015]. Available from: http://www.ncbi.nlm.nih.gov/gene/3553.
268. Ahrens ET, Bulte JW. Tracking immune cells in vivo using magnetic resonance imaging. Nature Reviews Immunology. 2013;13(10):755-63.
269. Girard J-P, Moussion C, Forster R. HEVs, lymphatics and homeostatic immune cell trafficking in lymph nodes. Nat Rev Immunol. 2012;12(11):762-73.
270. Akins EJ, Dubey P. Noninvasive Imaging of Cell-Mediated Therapy for Treatment of Cancer. The Journal of Nuclear Medicine. 2008;49:180S.
271. Shenoi MM, Shah NB, Griffin RJ, Vercellotti GM, Bischof JC. Nanoparticle preconditioning for enhanced thermal therapies in cancer. Nanomedicine. 2011;6(3):545-63.
272. Bhirde A, Xie J, Swierczewska M, Chen X. Nanoparticles for cell labeling. Nanoscale. 2011;3(1):142-53.
273. Naik SH. Generation of large numbers of pro-DCs and pre-DCs in vitro. Dendritic Cell Protocols: Springer; 2010. p. 177-86.
274. Agrawal A, Gupta S. Impact of aging on dendritic cell functions in humans. Ageing research reviews. 2011;10(3):336-45.
275. Conniot J, Silva JM, Fernandes JG, Silva LC, Gaspar R, Brocchini S, et al. Cancer immunotherapy: nanodelivery approaches for immune cell targeting and tracking. Frontiers in chemistry. 2014;2.
276. de Vries IJM, Lesterhuis WJ, Barentsz JO, Verdijk P, van Krieken JH, Boerman OC, et al. Magnetic resonance tracking of dendritic cells in melanoma patients for monitoring of cellular therapy. Nature biotechnology. 2005;23(11):1407-13.
277. Ziegler-Heitbrock L, Ancuta P, Crowe S, Dalod M, Grau V, Hart DN, et al. Nomenclature of monocytes and dendritic cells in blood2010 2010-10-21 00:00:00. e74-e80 p.
278. Ju X, Clark G, Hart DN. Review of human DC subtypes. Dendritic Cell Protocols: Springer; 2010. p. 3-20.
279. Thorek DL, Ulmert D, Diop N-FM, Lupu ME, Doran MG, Huang R, et al. Non-invasive mapping of deep-tissue lymph nodes in live animals using a multimodal PET/MRI nanoparticle. Nature communications. 2014;5.
280. Larson SM, Nelp WB. Radiopharmacology of a simplified technetium-99m-colloid preparation for photoscanning. Journal of Nuclear Medicine. 1966;7(11):817-26.
281. Schöder H, Glass EC, Pecking AP, Harness JK, Wallace AM, Hirnle P, et al. Molecular targeting of the lymphovascular system for imaging and therapy. Cancer and Metastasis Reviews. 2006;25(2):185-201.
282. Choi SH, Moon WK. Contrast-enhanced MR imaging of lymph nodes in cancer patients. Korean Journal of Radiology. 2010;11(4):383-94.
283. Moses WW. Fundamental limits of spatial resolution in PET. Nuclear Instruments and Methods in Physics Research Section A: Accelerators, Spectrometers, Detectors and Associated Equipment. 2011;648:S236-S40.
284. Andersen FL, Klausen TL, Loft A, Beyer T, Holm S. Clinical evaluation of PET image reconstruction using a spatial resolution model. European Journal of Radiology. 2013;82(5):862-9.
285. Banerjee SR, Pomper MG. Clinical applications of Gallium-68. Applied Radiation and Isotopes. 2013;76(0):2-13.

286. Nanni C, Errani C, Boriani L, Fantini L, Ambrosini V, Boschi S, et al. 68Ga-citrate PET/CT for evaluating patients with infections of the bone: preliminary results. Journal of Nuclear Medicine. 2010;51(12):1932-6.
287. Ravizzini G, Turkbey B, Barrett T, Kobayashi H, Choyke PL. Nanoparticles in sentinel lymph node mapping. Wiley Interdisciplinary Reviews: Nanomedicine and Nanobiotechnology. 2009;1(6):610-23.
288. Moore A, Marecos E, Bogdanov A, Jr., Weissleder R. Tumoral distribution of long-circulating dextran-coated iron oxide nanoparticles in a rodent model. Radiology. 2000;214(2):568-74.
289. Bumb A, Regino CA, Egen JG, Bernardo M, Dobson PJ, Germain RN, et al. Trafficking of a dual-modality magnetic resonance and fluorescence imaging superparamagnetic iron oxide-based nanoprobe to lymph nodes. Mol Imaging Biol. 2011;13(6):1163-72.
290. Zubris KAV, Khullar OV, Griset AP, Gibbs-Strauss S, Frangioni JV, Colson YL, et al. Ease of Synthesis, Controllable Sizes, and In Vivo Large-Animal-Lymph Migration of Polymeric Nanoparticles. ChemMedChem. 2010;5(9):1435-8.
291. Zhou Z, Chen H, Lipowska M, Wang L, Yu Q, Yang X, et al. A dual-modal magnetic nanoparticle probe for preoperative and intraoperative mapping of sentinel lymph nodes by magnetic resonance and near infrared fluorescence imaging. Journal of biomaterials applications. 2013;28(1):100-11.
292. Tseng Y-C, Xu Z, Guley K, Yuan H, Huang L. Lipid–calcium phosphate nanoparticles for delivery to the lymphatic system and SPECT/CT imaging of lymph node metastases. Biomaterials. 2014;35(16):4688-98.
293. Mazzaccara C, Labruna G, Cito G, Scarfò M, De Felice M, Pastore L, et al. Age-related reference intervals of the main biochemical and hematological parameters in C57BL/6J, 129SV/EV and C3H/HeJ mouse strains. PloS one. 2008;3(11):e3772.
294. Schnell MA, Hardy C, Hawley M, Propert KJ, Wilson JM. Effect of blood collection technique in mice on clinical pathology parameters. Human gene therapy. 2002;13(1):155-61.
295. Stevens A, Lowe JS, Young B. Basic Histopathology Wheater's: A Colour Atlas and Text: Churchil Livingstone; 2002.
296. Anzai Y, Piccoli CW, Outwater EK, Stanford W, Bluemke DA, Nurenberg P, et al. Evaluation of Neck and Body Metastases to Nodes with Ferumoxtran 10–enhanced MR Imaging: Phase III Safety and Efficacy Study 1. Radiology. 2003;228(3):777-88.
297. Winter A, Woenkhaus J, Wawroschek F. A Novel Method for Intraoperative Sentinel Lymph Node Detection in Prostate Cancer Patients Using Superparamagnetic Iron Oxide Nanoparticles and a Handheld Magnetometer: The Initial Clinical Experience. Annals of surgical oncology. 2014;21(13):4390-6.
298. Heesakkers RA, Hövels AM, Jager GJ, van den Bosch H, Witjes JA, Raat HP, et al. MRI with a lymph-node-specific contrast agent as an alternative to CT scan and lymph-node dissection in patients with prostate cancer: a prospective multicohort study. The lancet oncology. 2008;9(9):850-6.
299. Afshar-Oromieh A, Haberkorn U, Hadaschik B, Habl G, Eder M, Eisenhut M, et al. PET/MRI with a 68Ga-PSMA ligand for the detection of prostate cancer. Eur J Nucl Med Mol Imaging. 2013;40(10):1629-30.
300. Stevens Alan, Lowe James S., Young B. Wheater's Basic Histopathology - a colour atlas and text. Edinburgh: Churchill Livingstone Elsevier; 2002.
301. Srichairatanakool S, Pangjit K, Phisalaphong C, Fucharoen S. Evaluation of a novel oral iron chelator 1-(N-acetyl-6-aminohexyl)-3-hydroxypyridin-4-one (CM1) for treatment of iron overload in mice. 2013.
302. Nicolas G, Bennoun M, Porteu A, Mativet S, Beaumont C, Grandchamp B, et al. Severe iron deficiency anemia in transgenic mice expressing liver hepcidin. Proceedings of the National Academy of Sciences. 2002;99(7):4596-601.

303. Foretz M, Hébrard S, Guihard S, Leclerc J, Do Cruzeiro M, Hamard G, et al. The AMPKγ1 subunit plays an essential role in erythrocyte membrane elasticity, and its genetic inactivation induces splenomegaly and anemia. The FASEB Journal. 2011;25(1):337-47.
304. Kohgo Y, Ikuta K, Ohtake T, Torimoto Y, Kato J. Body iron metabolism and pathophysiology of iron overload. International journal of hematology. 2008;88(1):7-15.
305. Knovich MA, Storey JA, Coffman LG, Torti SV, Torti FM. Ferritin for the clinician. Blood reviews. 2009;23(3):95-104.
306. Arosio P, Ingrassia R, Cavadini P. Ferritins: a family of molecules for iron storage, antioxidation and more. Biochimica et Biophysica Acta (BBA)-General Subjects. 2009;1790(7):589-99.
307. Recalcati S, Invernizzi P, Arosio P, Cairo G. New functions for an iron storage protein: the role of ferritin in immunity and autoimmunity. Journal of autoimmunity. 2008;30(1):84-9.
308. Matsuno T, Mori M, Awai M. Distribution of ferritin and hemosiderin in the liver, spleen and bone marrow of normal, phlebotomized and iron overloaded rats. Acta Med Okayama. 1985;39(5):347-60.
309. Orchard G, Nation B. Histopathology. Orchard G, Nation B, editors. Oxford, England: Oxford University Press; 2012.
310. Mori Y, Umeda M, Fukunaga M, Ogasawara K, Yoshioka Y. MR contrast in mouse lymph nodes with subcutaneous administration of iron oxide particles: size dependency. Magnetic Resonance in Medical Sciences. 2011;10(4):219-27.
311. Pimlott SL, Sutherland A. Molecular tracers for the PET and SPECT imaging of disease. Chemical Society Reviews. 2011;40(1):149-62.
312. Bal H, Guerin L, Casey M, Conti M, Eriksson L, Michel C, et al. Improving PET spatial resolution and detectability for prostate cancer imaging. Physics in medicine and biology. 2014;59(15):4411.
313. Farsad M, Schiavina R, Franceschelli A, Sanguedolce F, Castellucci P, Bertaccini A, et al. Positron-emission tomography in imaging and staging prostate cancer. Cancer Biomarkers. 2008;4(4):277-84.
314. Apolo AB, Pandit-Taskar N, Morris MJ. Novel tracers and their development for the imaging of metastatic prostate cancer. Journal of Nuclear Medicine. 2008;49(12):2031-41.
315. Jadvar H. Molecular imaging of prostate cancer: PET radiotracers. AJR American journal of roentgenology. 2012;199(2):278.
316. Lütje S, Boerman OC, van Rij CM, Sedelaar M, Helfrich W, Oyen WJ, et al. Prospects in radionuclide imaging of prostate cancer. The Prostate. 2012;72(11):1262-72.
317. Harisinghani MG, Barentsz J, Hahn PF, Deserno WM, Tabatabaei S, van de Kaa CH, et al. Noninvasive detection of clinically occult lymph-node metastases in prostate cancer. New England Journal of Medicine. 2003;348(25):2491-9.
318. Vermeeren L, Olmos RAV, Meinhardt W, Bex A, van der Poel HG, Vogel WV, et al. Value of SPECT/CT for detection and anatomic localization of sentinel lymph nodes before laparoscopic sentinel node lymphadenectomy in prostate carcinoma. Journal of Nuclear Medicine. 2009;50(6):865-70.
319. Mao Y, Hedgire S, Prapruttam D, Harisinghani M. Imaging of Pelvic Lymph Nodes. Curr Radiol Rep. 2014;2(11):1-13.
320. Weckermann D, Dorn R, Trefz M, Wagner T, Wawroschek F, Harzmann R. Sentinel lymph node dissection for prostate cancer: experience with more than 1,000 patients. The Journal of urology. 2007;177(3):916-20.
321. Mattei A, Fuechsel FG, Bhatta Dhar N, Warncke SH, Thalmann GN, Krause T, et al. The template of the primary lymphatic landing sites of the prostate should be revisited: results of a multimodality mapping study. European urology. 2008;53(1):118-25.

322. Ganswindt U, Schilling D, Müller A-C, Bares R, Bartenstein P, Belka C. Distribution of Prostate Sentinel Nodes: A SPECT-Derived Anatomic Atlas. International Journal of Radiation Oncology • Biology • Physics. 2010;79(5):1364-72.
323. Afshar-Oromieh A, Haberkorn U, Eder M, Eisenhut M, Zechmann CM. [68Ga]Gallium-labelled PSMA ligand as superior PET tracer for the diagnosis of prostate cancer: comparison with 18F-FECH. European Journal of Nuclear Medicine and Molecular Imaging. 2012;39(6):1085-6.